Green Chemistry and Sustainable Technology

Juan Carlos Colmenares
Yi-Jun Xu *Editors*

Heterogeneous Photocatalysis

From Fundamentals to Green Applications

Springer

Green Chemistry and Sustainable Technology

Aims and Scope

The series *Green Chemistry and Sustainable Technology* aims to present cutting-edge research and important advances in green chemistry, green chemical engineering and sustainable industrial technology. The scope of coverage includes (but is not limited to):

- Environmentally benign chemical synthesis and processes (green catalysis, green solvents and reagents, atom-economy synthetic methods etc.)
- Green chemicals and energy produced from renewable resources (biomass, carbon dioxide etc.)
- Novel materials and technologies for energy production and storage (biofuels and bioenergies, hydrogen, fuel cells, solar cells, lithium-ion batteries etc.)
- Green chemical engineering processes (process integration, materials diversity, energy saving, waste minimization, efficient separation processes etc.)
- Green technologies for environmental sustainability (carbon dioxide capture, waste and harmful chemicals treatment, pollution prevention, environmental redemption etc.)

The series *Green Chemistry and Sustainable Technology* is intended to provide an accessible reference resource for postgraduate students, academic researchers and industrial professionals who are interested in green chemistry and technologies for sustainable development.

More information about this series at http://www.springer.com/series/11661

Juan Carlos Colmenares • Yi-Jun Xu
Editors

Heterogeneous Photocatalysis

From Fundamentals to Green Applications

Springer

Editors
Juan Carlos Colmenares
Institute of Physical Chemistry
Polish Academy of Sciences
Warsaw, Poland

Yi-Jun Xu
State Key Laboratory of Photocatalysis
on Energy and Environment
Fuzhou University
Fuzhou, China

ISSN 2196-6982 ISSN 2196-6990 (electronic)
Green Chemistry and Sustainable Technology
ISBN 978-3-662-48717-4 ISBN 978-3-662-48719-8 (eBook)
DOI 10.1007/978-3-662-48719-8

Library of Congress Control Number: 2015959972

Springer Heidelberg New York Dordrecht London

Printed on acid-free paper

Springer-Verlag GmbH Berlin Heidelberg is part of Springer Science+Business Media (www.springer.com)

Preface

Heterogeneous photocatalysis has become a comprehensively studied area during the past several decades because of its great potential for solving the problems of environmental pollution and the world energy crisis. As a green technology featured with the unique advantages of operation at room temperature and utilization of clean, renewable solar light as the driving force, heterogeneous photocatalysis continues to be an important component of modern chemistry in the twenty-first century.

The available existing literature in heterogeneous photocatalysis mainly focused on the advances of semiconductor TiO_2 for degradation of pollutants in water and air. However, recent researches have proven that heterogeneous photocatalysis is effective and promising for many other reactions, such as carbon dioxide reduction, photocatalytic water splitting and organic transformations. In addition, the research reports have also shown that a lot of alternative semiconductors and photoactive organic species can apply to these photocatalytic reactions. Therefore, in this book, we highlight and summarize recent progress in green-chemistry-oriented application fields (e.g. carbon dioxide reduction, selective organic transformations, water splitting) over TiO_2-based and other new photocatalysts alternative to TiO_2. The synthetic consideration of the proper design of photocatalytic reactors and modelling of light has also been discussed, which are often neglected in literature but rather important for improving efficacy and scale-up applications of photocatalytic systems.

The book *Heterogeneous photocatalysis: from fundamentals to green applications* is aimed at providing researchers with the up-to-date advances related to the field of photocatalysis in the shape of a collective work of reviews illustrative of recent advances in exploitation and green application of heterogeneous photocatalysis towards solar energy conversion and utilization. The book consists of 11 chapters including the principles and fundamentals of heterogeneous photocatalysis (Chap. 10), the mechanisms and dynamics of surface photocatalysis (Chap. 11), the researches on the TiO_2-based composites with unique nanostructures (Chap. 5), the latest developments and new advances of exploiting new photocatalyst materials alternative to TiO_2 (Chap. 4) and photocatalytic materials for new applications different from the traditional degradation of pollutants: carbon dioxide reduction (Chap. 1), water oxidation (Chap. 2), a complete spectrum on selective organic transformations (Chaps. 8 and 9) and water splitting by photocatalytic reduction (Chap. 6). In addition, heterogeneized polyoxometalate materials for photocatalytic purposes (Chap. 3) and the proper design of photocatalytic reactors and modelling of light (Chap. 7) have also been discussed. These progresses in heterogeneous photocatalysis provide new directions and tremendous opportunities for developing new generations of effective and selective photocatalysts towards target practical applications.

In this book the high quality and geographic distribution of the contributions are taken into consideration when inviting worldwide respected and well-known leaders in the relative field including Prof. Pierre Pichat, Prof. Leonardo Palmisano, Prof. Flemming Besenbacher, Prof. Graham J. Hutchings, Prof. Hermenegildo Garcia and Prof. Xueming Yang, as well as excellent emerging young scientists, among them Prof. Bin Liu, Prof. Nurxat Nuraje, Prof. Adriana Zaleska-Medynska, Prof. Elisa Garcia Lopez, Dr. Ren Su and Prof. Hiroshi Kominami.

The book is able to serve as a self-contained major reference for heterogeneous photocatalysis towards solar energy conversion and utilization. This book appeals to a wide readership of the academic and industrial researchers and can also be used in the classroom for undergraduate and graduate students who focus on heterogeneous photocatalysis, sustainable chemistry, energy conversion and storage, nanotechnology, chemical engineering, environmental protection, optoelectronics, sensors and surfaces and interfaces sciences.

We would like to express our sincere thanks to all authors for their excellent contributions to this impressive book. We are also thankful to the whole Springer team, especially to Heather Feng and June Tang for their priceless support in publishing this book.

Warsaw, Poland J.C. Colmenares
Fuzhou, China Y.-J. Xu

Contents

Chapter 1
Photocatalytic CO_2 Reduction

Josep Albero and Hermenegildo García

Abstract In the context of finding sustainable and environmentally neutral alternatives to fossil fuels, there is much current interest in the production of chemicals that can be used as fuels using solar light (*solar fuels*). In the present chapter, we describe the fundamentals and the current state of the art for the photocatalytic reduction of CO_2, making emphasis on the importance of the co-substrate (either water, hydrogen, or other electron donors), the differences of the process with respect to the photocatalytic hydrogen generation from water, and the importance to control the selectivity towards a single product of the many possible ones. After this part describing some basic issues of the photocatalytic CO_2 reduction, some of the currently more efficient photocatalysts are described, delineating similarities and differences among those materials. The final section summarizes the main points of the chapter and presents our view on future developments in the field.

Keywords Solar fuels • CO_2 reduction • Photocatalysts • Semiconductor photocatalysts • Graphene-based photocatalysts

1.1 Solar Fuels: Concept and Importance

Modern societies consume an enormous amount of energy to perform their activities including transportation, industrial processes, and heating, among other main uses. The current scenario is based on the massive consumption of fossil fuels, including oil and natural gas, not only for transportation but also for the production of electricity and heating. Considering the limited resources on fossil fuels, it is clear that at the high current consumption rate these resources will become depleted, making the present energy source scheme unsustainable.

Besides sustainability, a second driving force to develop alternative energy sources is climate change and, specifically, atmospheric pollution by greenhouse effect gases. The limited resources of fossil fuels together with global warming

---

J. Albero • H. García (✉)
Departamento de Química, Instituto Universitario de Tecnología Química CSIC-UPV,
Universidad Politécnica de Valencia, Avda. de los Naranjos s/n, 46022 Valencia, Spain
e-mail: hgarcia@qim.upv.es

J.C. Colmenares, Y.-J. Xu (eds.), *Heterogeneous Photocatalysis*, Green Chemistry
and Sustainable Technology, DOI 10.1007/978-3-662-48719-8_1

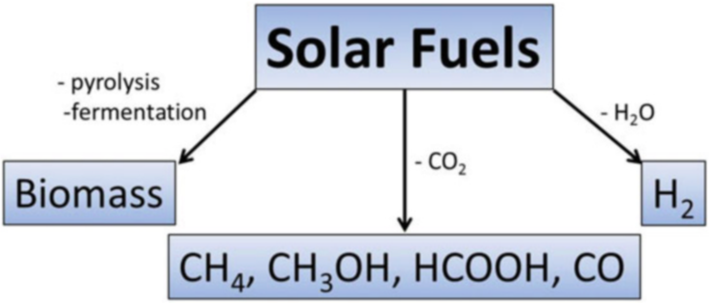

Scheme 1.1 Most common chemicals considered as solar fuels

concerns as well as geostrategic considerations derived from the uneven geographical distribution of oil and natural gas reserves have motivated a strong interest in developing alternative energy resources that should be characterized by sustainability and lack polluting emissions.

In this regard, one almost inexhaustible natural energy resource is sunlight reaching the Earth's crust [1]. While there is a series of competing alternative technologies to convert solar light into other types of energy, particularly electricity, including thermal conversion and photovoltaic devices, the use of sunlight directly in transportation and many other applications is problematic due to the low energy density of sunlight, circadian cycles between day and night, and dependence on weather and seasonal conditions [2].

In this context, one possibility would be to accumulate the energy of the sunlight into chemical compounds that could later be used in transportation or when required on demand [3–7]. The use of chemicals obtained from solar light as fuels in transportation has led to the concept of solar fuels (Scheme 1.1). These solar fuel chemicals have in common to correspond to a reduced compound that when reacted with atmospheric oxygen should undergo combustion or oxidation, releasing the accumulated energy. Among the possible solar fuels, hydrogen has been identified by the US Department of Energy as an ideal energy vector since when oxidized at moderate temperatures it will form water as the only product [8]. However, the use of hydrogen as fuel cannot be readily implemented due to the lack of technology concerning its production, storage, and use. Due to the extremely low boiling point (−253 °C), hydrogen has to be handled as compressed gas, and this creates problems concerning filling fuel tanks and storage of enough energy to achieve autonomy in transportation.

Besides hydrogen one alternative that is increasingly being considered is the use of C1 chemicals obtained by CO_2 reduction, including methane, methanol, formic acid, and others. Although the use of solar fuels derived from CO_2 has a major drawback in that CO_2 having a greenhouse effect is formed in their combustion, the overall CO_2 footprint should be neutral when these solar fuels are prepared from CO_2 as feedstock [9, 10].

Scheme 1.2 Elementary steps taking place in a photocatalytic cycle: light absorption (i), electron excitation (ii), electron and hole migration (iii), oxidation and reduction reactions (iv), or geminate electron recombination (v)

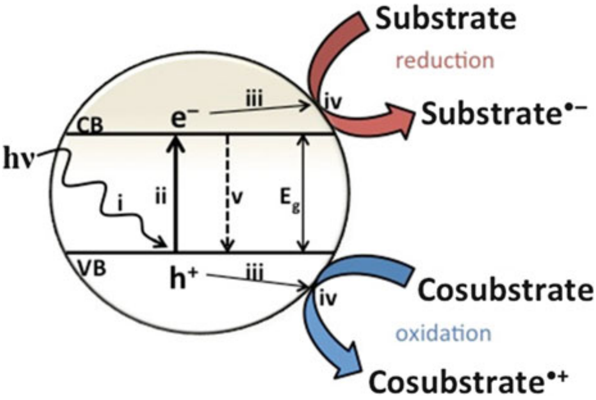

Besides hydrogen and CO_2-derived chemicals, fuels from biomass are also considered in the broad sense as solar fuels since biomass is based on natural photosynthesis by green algae and plants [11].

Solar fuels can be obtained in an indirect way by first converting solar energy into electricity and subsequently carrying out the electrochemical reduction of water or CO_2 [12]. This possibility has some advantages as a way to store the excess of electricity from renewables. However, also appealing is to devise systems for the direct conversion of sunlight into solar fuels, since this approach could require much less capital investment and is flexible enough to be implemented for small-scale production. This strategy is based on the use of materials that are capable to absorb sunlight generating a charge separation state, generally electrons and positive holes. These materials are generally termed as photocatalysts since they should perform many turnovers absorbing photons and generating a product [13, 14]. The most typical photocatalyst are solid semiconductors, such as some metal oxides, chalcogenides, and carbonaceous materials.

In photocatalysis photons, having energy higher than the bandgap of the semiconductor promotes excitation of electrons from the occupied state of highest energy to unoccupied states of lowest energy. This electronic excitation is generally described as charge separation since, very often in a semiconductor, electrons and/or holes are mobile and electronic excitation results in uncoupled electrons and holes (Scheme 1.2).

The state of charge separation can decay through different pathways, the most important ones being charge recombination of geminate electrons and holes generated in the same event of photon absorption or charge recombination after random migration of electrons or holes through the material [15]. The difference between geminate and random recombination is the time scale in which they take place, sub-microsecond for geminate recombination and microsecond time scale after random migration of the charges. During the lifetime of charge separation, the semiconducting particle behaves simultaneously as an oxidizing reagent (by capturing electrons from a substrate and placing them at the positive holes) or reductant (by transferring electrons to substrates). Scheme 1.3 illustrates the dual nature of charge-separated states as reducing and oxidizing agents. As briefly

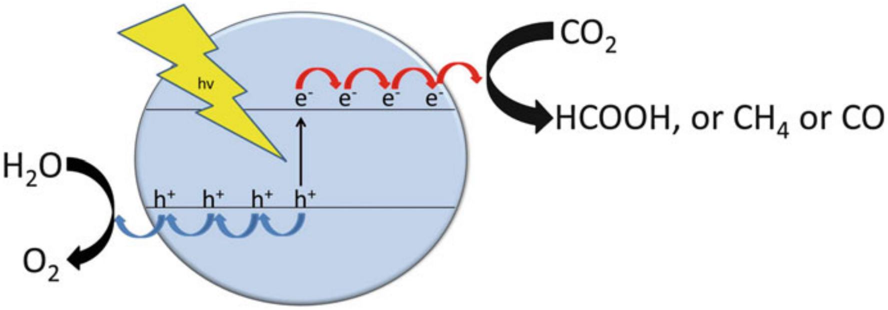

Scheme 1.3 Schematic representation of an ideal photocatalyst performing CO_2 reduction by water

indicated above, for the sake of solar fuel production, the most wanted process is reduction of a substrate (H_2O or CO_2) by photogenerated electrons at the semiconductor to form the solar fuel. However, for the sake of fulfilling the electroneutrality principle, reduction in the photocatalytic process has to occur at the same reaction rate as the oxidation reaction by holes. This requirement of simultaneous oxidation and reduction of different chemicals in the same particle makes necessary that in the photocatalytic process, besides the targeted solar fuels, some oxidized compound has to be simultaneously formed.

In order to decouple oxidation and reduction at the semiconductor, achieving the maximum possible efficiency in the reduction semireaction leading to solar fuels, it is very common that model studies use a sacrificial agent whose role is to quench efficiently at a high rate photogenerated holes, allowing the study of the reduction process as the rate-limiting step. Preferred hole quenchers in this type of photocatalytic studies are tertiary amines, particularly triethanolamine and triethylamine, and alcohols, especially methanol and ethanol, and also inorganic ions such as sulfide, sulfite, and nitrate. To differentiate those photocatalytic experiments in the absence of a sacrificial electron donor with those having present these reagents, it is common to indicate the term “overall” to denote that photocatalytic oxidation and reduction of the same substrate are simultaneously carried out without any sacrificial electron donor (Scheme 1.4). Photocatalytic generation of solar fuels has the advantage with respect to indirect strategies based on electrolysis in that they require much less infrastructure and lower capital investment in equipment, and therefore, it could be more amenable for on-site implementation in small- or medium-sized plants, rather than application in large facilities.

1.2 Advantages of Solar Fuels Derived from CO_2

As commented earlier, the current energy production is largely based on fossil fuel combustion in which vast amounts of CO_2 is formed. These power plants are an interesting source of CO_2 that at the moment has to be captured and stored. It would

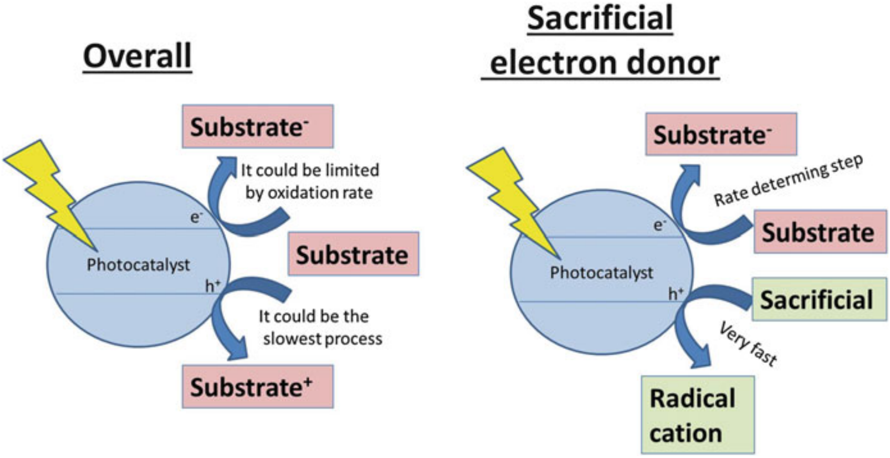

Scheme 1.4 Photocatalytic oxidation and reduction of a substrate with and without a sacrificial electron donor

be interesting to use this CO_2 as feedstock of chemical processes and, particularly, as source of solar fuels. International treaties currently enforced require a gradual reduction of CO_2 emissions to the atmosphere, and one of the most appealing ways to reduce CO_2 emissions is their use as feedstock. It should be taken into account that solar fuels based on CO_2 will be neutral from the point of view of greenhouse emission gases. Another advantage of CO_2-derived solar fuels with respect to hydrogen is that some of the possible products such as formic acid or methanol are liquids under ambient conditions and this physical state will simplify enormously their storage and all the technology involved in their manipulation. Even in the case of methane as CO_2 reduction product, there are nowadays a large number of implemented energy systems using natural gas that would be straightforwardly adapted to methane as solar fuel. Thus, solar fuels derived from CO_2 would overcome the major problems encountered in hydrogen technology related to storage and manipulation [16, 17].

However, compared to hydrogen generation from water, the use of CO_2 as feedstock for the preparation of solar fuel is extremely challenging from the photocatalytic point of view. One of the major problems related to the use of CO_2 as feedstock for the generation of solar fuels is that the “overall” CO_2 splitting has never been reported. Thus, in contrast to H_2O which photocatalytically can be reduced to hydrogen and oxidized to oxygen, in the case of CO_2, it is necessary to add another substrate that should undergo oxidation concurrently to CO_2 reduction. The most advantageous reductant promoting CO_2 reduction would be water. Equation 1.1 illustrates one of the possible stoichiometries for this reaction:

$$CO_2 + 2H_2O \rightarrow CH_3OH + 3/2O_2 \quad \Delta G^0 = 702.27\ \mathrm{kJ/mol} \tag{1.1}$$

In this case water would be oxidized to oxygen while CO_2 will be reduced to methanol. This process of CO_2 reduction by water is the one that is taken place in

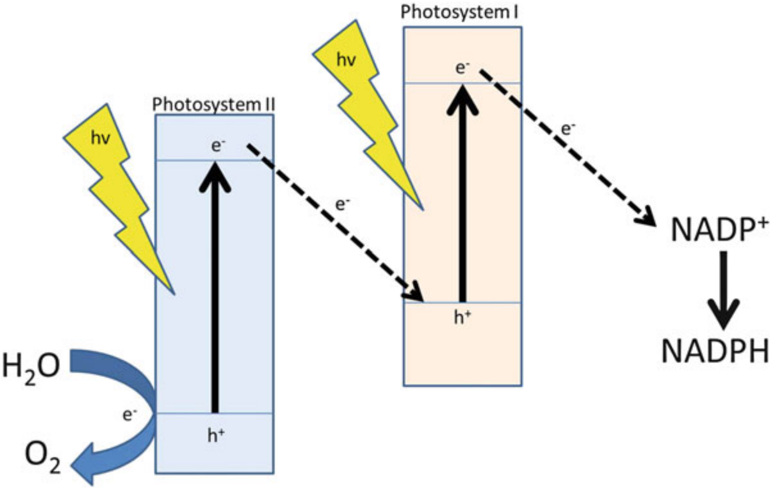

Scheme 1.5 Pictorial illustration of some of the processes taking place in natural photosynthesis

natural photosynthesis carried out by algae and green plants. Unfortunately, the current state in photocatalysis is very far from mimicking natural photosynthetic centers, and the present efficiency using semiconductors for CO_2 reduction from water is very low. Below in this chapter, we will describe some of the most efficient artificial photocatalyst for this process.

The reasons why CO_2 reduction by water is so inefficient are both thermodynamic and kinetic. From the thermodynamic point of view, CO_2 reduction is highly endothermic and consequently requires more than one photon to occur. It should be noted that in natural photosynthesis the transfer of one electron requires the absorption of two photons, one in each of the two photosynthetic centers (Scheme 1.5) [18]. Also from the kinetic point of view, the process of CO_2 reduction is very complex since, depending on the products formed, several steps of reduction and protonation have to take place. For instance, conversion of CO_2 into methane is a process that requires eight electrons and eight protons, and most probably this transformation has to occur stepwise, each step consisting in the transfer of one electron followed more or less synchronously by protonation. For the reaction of Eq. 1.1, formation of methanol requires the reduction of six electrons and six protons.

Besides water other reducing agents can also be considered for photocatalytic CO_2 reduction. Particularly interesting is the use of hydrogen as reducing agent. In contrast to CO_2 reduction by water, the reaction of CO_2 with hydrogen is exothermic, thus making the reaction favorable from the thermodynamic point of view (Eq. 1.2):

$$CO_2 + 4H_2 \rightarrow CH_4 + 2H_2O \quad \Delta G^0 = -165\ \text{kJ/mol} \tag{1.2}$$

In fact, CO_2 reduction by hydrogen, the so-called Sabatier reaction, can be carried out thermally in the absence of light at high temperature [19]. However, the use of sunlight to assist the reaction is interesting from the point of view of saving energy in the process. The main problem of the Sabatier reaction is the source of hydrogen that has to be supplied to the system. Hydrogen can be obtained by steam reforming of methane and fossil fuels [20], a process based on nonrenewable chemicals that cannot be considered for CO_2 reduction since it would not make sense to use methane to generate hydrogen to react with CO_2 to form methane again. However, hydrogen can be also obtained in thermal water splitting, electrolytically from alternative renewable electricity or even photocatalytically. In this scenario, the advantage of the Sabatier reaction would be to provide methane as substitute of natural gas from renewable resources and avoiding the direct use of hydrogen as fuel. In other words, since natural gas is widely used as fuel and its technology is fully developed, the shift will be in the origin of this fuel moving from nonrenewable resources to a renewable process based on CO_2 and hydrogen coming from a sustainable primary energy.

From the point of view of a desirable C1 fuel, methanol is probably the best choice since it is liquid under ambient conditions and has high volumetric energy content [21]. In addition, burners and combustion engines for gasoline can be easily adapted to use methanol as fuel. In addition, methanol can also be the fuel for proton-exchange membrane fuel cells (PEM-FC) instead of hydrogen [22]. In this regard, the use of methanol as fuel and PEM-FC as an electricity provider device could represent a temporary transition towards the complete implementation of hydrogen technology that still needs scientific knowledge and technical developments to be close to application. However, as it will be commented below, it is very unlikely that methanol could be obtained photocatalytically from CO_2 by reduction since due to its high chemical reactivity, the same photocatalytic process would decompose methanol if this molecule is present in high concentrations in contact with the photocatalyst. Thus, under batch conditions, the stationary concentration of methanol in a photocatalytic experiment has to be very low.

1.3 Differences Between Photocatalytic Hydrogen Generation from Water and CO_2 Reduction

Photocatalysis is aimed at converting light into chemical energy. However, the nature of the substrates that are going to be converted photocatalytically and the nature of the products formed are extremely important for the success of the reaction and for efficiency of the photocatalytic process. In this regard there are remarkable differences between water reduction to generate hydrogen and photocatalytic CO_2 reduction that are worth to be commented in order to understand the reasons why the level of development in photocatalytic CO_2 reduction is always lower than photocatalytic hydrogen evolution from water.

One of the first differences from the fundamental point of view is the higher reduction potential to inject a single electron to CO_2 compared to water.

Equations 1.3 and 1.4 indicate the redox potential for the simplest elementary step of one electron reduction to water or CO_2:

$$H^+ + e^- \rightarrow ½\,H_2 \quad E^0_{redox} = -0.41\ V\ vs.\ NHE \tag{1.3}$$

$$CO_2 + e^- \rightarrow CO_2{}^{-} \quad E^0_{redox} = -1.90\ V\ vs.\ NHE \tag{1.4}$$

These represents the thermodynamic requirements of the photocatalytic process, meaning that, in order to start the photocatalytic reduction, electrons in the conduction band of the semiconductor have to have enough reduction potential to initiate the process. As it is indicated in Eqs. 1.3 and 1.4, the reduction potential required for CO_2 is considerably higher than in the case of H_2O. It should be noted that if instead of Eq. 1.4 an alternative Eq. 1.5 is considered in which electron reduction is accompanied simultaneously by protonation of the reduced species, then a significant decrease in the energy of the process from the thermodynamic point of view occurs. It has to be, however, noted that mechanistically to transfer an electron and a proton simultaneously can be rather difficult since as it is indicated in Eqs. 1.3 and 1.4 they are incompatible in the sense that protons and electrons react to give hydrogen at much lower potential without requiring CO_2.

Naturally, in certain enzymes, proton-assisted electron transfer is promoted by having one redox center near a proton donor center in a relatively rigid environment that keeps the two sites separated. The problem is that artificial photocatalysis is based on considerably simpler and not ordered systems than those occurring in natural photosynthetic systems or enzymes and artificial photosynthesis is still far behind the complexity characteristic of natural systems. Moreover, if instead of Eqs. 1.3 or 1.5 referring to single electron reduction of CO_2, assisted or not by proton transfer, other possible equations in which two electrons and two protons (Eq. 1.6) leading to formic acid or six electrons and six protons leading to methanol (Eq. 1.7) or eight electrons and eight protons leading to methane (Eq. 1.8) are considered, then the thermodynamic potential decreases gradually for each reaction. This relaxation of the thermodynamic reduction potential is, as just commented, a reflection of the assistance of protons to the electron transfer. However, from the mechanistic point of view, none of the Eqs. 1.7 and 1.8 have any sense as occurring in a single step and have to be considered only as the thermodynamic potential between reactants and products rather than having any mechanistic implication:

$$CO_2 + H^+ + e^- \rightarrow HCO_2{}^{-} \quad E^0_{redox} = -0.53 Vvs.NHE \tag{1.5}$$

$$CO_2 + 2H^+ + 2e^- \rightarrow HCOOH + H_2O \quad E^0_{redox} = -0.61\ V\ vs.\ NHE \tag{1.6}$$

$$CO_2 + 6H^+ + 6e^- \rightarrow CH_3OH + H_2O \quad E^0_{redox} = -0.38\ V\ vs.\ NHE \tag{1.7}$$

$$CO_2 + 8H^+ + 8e^- \rightarrow CH_4 + H_2O \quad E^0_{redox} = -0.24\ V\ vs.\ NHE \tag{1.8}$$

The previous comment on the higher reduction potential to convert CO_2 in respect to H_2O reduction raises the issue of whether or not all the photocatalysts reported for hydrogen generation from water are applicablet for photocatalytic CO_2 reduction. Experimentally, virtually all the photocatalysts reported for hydrogen evolution from water have been in a second study tested as photocatalysts for CO_2 reduction, observing that efficiency for CO_2 reduction is always considerably lower than for hydrogen evolution. As a rule of thumb, photocatalytic CO_2 reduction is three orders of magnitude less efficient than water reduction under the same conditions, this poor efficiency being a reflection of the stringent thermodynamic and kinetic requirements for CO_2 reduction compared to water reduction.

Besides thermodynamic considerations, an additional problem in photocatalytic CO_2 reduction with respect to water is that, while overall water splitting into hydrogen and oxygen is a possible process, the overall CO_2 process has never been reported. In other words, H_2O can be simultaneously oxidized by positive holes on the semiconductor into molecular oxygen and reduced to hydrogen by conduction band electrons (Scheme 1.4). Accordingly water is acting as an electron donor in the reduction to form hydrogen. In contrast CO_2 has never been reported as an electron donor and photocatalytic CO_2 reduction requires always the presence of a sacrificial electron donor.

Based on natural photosynthesis in where H_2O is the electron donor molecule for CO_2 reduction to sugars performed by all the complex machinery present in photosynthetic systems I and II and enzymatic reduction, the ideal photocatalytic process will be the reduction of CO_2 by H_2O. In this case there are several possibilities depending on the final product, either formic acid, methanol, or methane (Eqs. 1.6, 1.7, and 1.8).

Each of these equations is thermodynamically unfavorable, the endoergonicity of the process decreasing along the reduction degree of CO_2. In any case, consideration of the high positive value of the ΔG^0 for these processes using H_2O as the electron donor clearly shows that they are difficult from the thermodynamic point of view.

Also from the kinetic point of view, the processes indicated in Eqs. 1.6, 1.7, and 1.8 are not straightforward, particularly considering that reduction of water can occur at lower potentials and faster reaction rates than CO_2 reduction. In other words, water is required as a sacrificial electron donor, but, when present in the system, water can compete favorably with CO_2 for reduction. For this reason, it is also generally observed that hydrogen evolution accompanies or is even the more favorable process with respect to CO_2 reduction. The solution to this dilemma (i.e., water is needed for reduction but then competes for electrons with CO_2) is the presence of centers active as co-catalyst that should exhibit preference for CO_2 reduction vs. H_2O reduction. While H_2O is an amphoteric molecule, CO_2 is relatively acidic and adsorbs on the surface of basic sites. It is possible to take advantage of the adsorption of CO_2 on basic sites to drive the photocatalytic process towards CO_2 reduction, preferentially to H_2O reduction.

Another important difference of CO_2 reduction vs. H_2O reduction is that the former has to be carried out in the gas phase or dissolved in a certain medium. If the reaction is performed in the gas phase, then the hydrogen donor reducing agent has also to be present at the interface of the solid photocatalyst to promote the

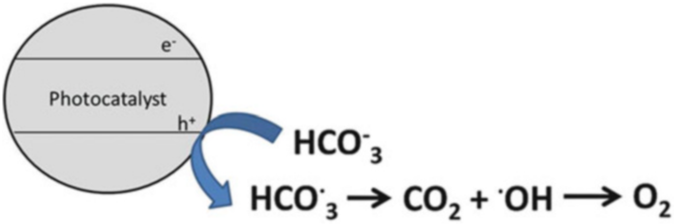

Scheme 1.6 Bicarbonate and carbonate can act as electron donors quenching positive h^+ and resulting in the formation of CO_2 and O_2. This process is opposed to CO_2 reduction

photocatalytic reduction. However, in many examples in the literature, CO_2 has been photocatalytically reduced in liquid water or in other media. In the case of water, due to the submillimolar solubility of CO_2 at acid or neutral pH, basic solutions are generally employed. However, under these conditions, CO_2 is dissolved to form $HCO_3{}^-$ or $CO_3{}^{-2}$ depending on the pH value (see Eqs. 1.9, 1.10, 1.11, and 1.12). It happens that reduction of carbonate and bicarbonate has a potential even higher than that of CO_2. In addition, these negative anions can act as sacrificial electron donors quenching the photogenerated electrons (Scheme 1.6). In those cases in which carbonate and bicarbonate quench holes, the whole process is again the overall water splitting into hydrogen and oxygen rather than photocatalytic CO_2 reduction. In addition, it has to be considered that using water makes favorable the overall water splitting over photocatalytic CO_2 reduction due to its large concentration. For this reason, it could be preferable to use gas phase reactions:

$$CO_2 + H_2O \rightarrow H_2CO_3 \quad K_{eq} = 2.58 \cdot 10^{-3} \tag{1.9}$$

$$H_2CO_3 \rightarrow H^+ + HCO_{3^-} \quad K_1 = 4.3 \cdot 10^{-7} \tag{1.10}$$

$$HCO_{3^-} \rightarrow H^+ + CO_{3^{-2}} \quad K_2 = 5.6 \cdot 10^{-11} \tag{1.11}$$

$$HCO_{3^-} + 3H^+ + 2e^- \rightarrow CO + 2H_2O \quad E^0_{redox} = -0.66\ V\ vs.\ NHE \tag{1.12}$$

$$CO_{3^{-2}} + 4H^+ + 2e^- \rightarrow CO + 2H_2O \quad E^0_{redox} = -0.87\ V\ vs.\ NHE \tag{1.13}$$

A final difference between photocatalytic CO_2 reduction and hydrogen evolution from water is the large number of possible reaction products that can be formed in the process. The products that have been detected in photocatalytic CO_2 conversion include oxalic acid or oxalate, formate, methanol, methane, ethane, CO, and even elemental C. The problem arises from the fact that some of the possible products are gaseous, while others are liquids or even solids. If solids are deposited on the photocatalyst surface performing the reaction in the gas phase at low temperatures, deactivation of the catalyst should occur by blocking of the surface by carbon and liquid products that poison the photocatalyst. The large diversity of products that can be formed in CO_2 reduction and their difference in physical states at ambient temperature determine the need to apply adequate analytic procedures to detect and quantify all the possible products in gas, liquid, and solid phases. A good practice in this photocatalytic CO_2 conversion is to include always a mass balance in which the number of moles of CO_2 reacted is compared with the moles of products that had been detected and quantified. Also, this diversity in the nature of the products that can be formed determines that a combination of various analytical techniques have to be applied to ensure the detection and quantification of all products. The possible formation of elemental carbon on the photocatalyst or strongly bound formate or oxalate requires analysis of the carbon content present on the photocatalyst after the reaction. Also, the possible formation of hydrogen from water together with CO_2 reduction products makes necessary the use of gas chromatography combining different types of columns and detectors. For instance, methanol is typically characterized in cross-linked phenyl methyl silicone columns with flame ionization detectors, while analysis of hydrogen requires the use of argon as carrier gas, packed columns of molecular sieves, and a thermoconductivity detector. Also CO and the remaining CO_2 have to be detected and quantified together with hydrogen.

The above issue of possible formation of various products on photocatalytic CO_2 reduction raises the important point of how to control the product distribution and the selectivity of the photocatalytic reaction. This goal requires further understanding on the reaction mechanisms and the rate-determining steps leading to the formation of each product. This understanding should be gained by a combination of theoretical calculations and in situ characterization techniques allowing detection reaction intermediates. This basic knowledge should lead to modification of the photocatalyst surface creating selective sites, frequently termed as *co-catalysts*, for the formation of some products, disfavoring the appearance of unwanted compounds.

1.4 Current State of the Art in Photocatalytic CO_2 Reduction

In the previous section, we have tried to convey the idea that due to the combination of various reasons, photocatalytic CO_2 reduction is a considerably more difficult and complex process than hydrogen generation from water. A simple way to illustrate and summarize these differences is that while for hydrogen generation rates well above 1000 $\mu mol \cdot g^{-1} \cdot h^{-1}$ are not uncommon, for many of the most efficient photocatalytic reduction process, the production reaction rates are measured in hundreds of $nmol \cdot g^{-1}h^{-1}$. Of course these values represent an oversimplification, since photocatalytic data from different laboratories are almost impossible to be compared, due to the strong influence of many experimental parameters playing a role in the production rate. Among them, the two most important are probably the lamp employed in the photocatalytic experiment and the geometry of photochemical reactor. But there are many other parameters, such as the amount of photocatalyst employed, the way in which the photocatalyst is exposed to the light, the gas or liquid phase condition, the reaction temperature, the stirring procedure and speed, and many other parameters that certainly alter the production rate. One important consideration is that to have some interest from the point of view of energy storage, photocatalytic experiments should be carried out with sunlight or at least with simulated solar light. However, since the percentage of UV light present in the solar emission spectrum is very low (about 4 %) and considering that common photocatalyst are wide bandgap semiconductors absorbing in the UV but not in the visible region, much higher production rates are obtained when using artificial lamps that have an intense emission in the UV. Also another factor to be considered is the distribution of energy emitted by the lamp as a function of the wavelength, since different types of lamps have different emission spectra that surely influence the efficiency of the photocatalytic process.

Besides the lamp the design of the photochemical reactor is extremely important to achieve high production rates. Ideally, the photoreactor should ensure that the maximum number of photons from the light source enter into the reactor and at the same time disperse the photocatalyst allowing the maximum amount of particles to be illuminated. In photocatalysis, it is very convenient to make a preliminary study in which the efficiency of the photocatalytic process is studied as a function of the amount of photocatalyst present in the medium. Frequently, a volcano shape is found indicating that there is an optimum amount of photocatalyst to achieve the highest production rate of the process. Higher amounts than the optimal lead to a decrease in the efficiency of the process as result of the higher light scattering that makes difficult the penetration of the light beam in the reactor body. In many cases the production rate can be simply increased by designing an appropriate way to illuminate the maximum number of photocatalyst particles. For gas phase irradiation, one simplest way is to prepare a thin layer of the photocatalyst of a few micrometers depth coating an inert substrate such as glass. Experimental measurements have shown that for many opaque materials, light can penetrate a maximum depth of a few micrometers on the photocatalyst film and, therefore, there should not be increase in photocatalytic efficiency by increasing the photocatalyst amount to prepare thicker coatings.

Reactor design and the way in which heat from the lamp or Sun is dissipated can also be important, influencing photocatalytic efficiency. Solar simulators can reach temperatures above 60 °C on surfaces that are 10 cm away from the light output. In other cases in which the lamp is immersed into the photoreactor, the maximum temperature can be even higher, and it is necessary to cool the lamp by a circulating water flow. As in any catalytic process, the temperature is an important parameter influencing the reaction rate. Although many photocatalytic process can occur even at low temperatures, well below ambient temperature, this is not always the case, and some elementary steps in the mechanism can be activated thermally, including adsorption and desorption of substrate and products on the solid surface. The main conclusion of the above comments is that there is no point in comparing photocatalytic activity data obtained in different laboratories under different conditions unless quatum efficiencies are given. Furthermore, most of the reported photocatalytic activity data can be surely increased by optimization of reactor design and operation conditions. However, even considering the above limitations, the difference in photocatalytic activity for hydrogen generation and photocatalytic CO_2 reduction by water is so high for many orders of magnitude that it is reasonable to conclude that they reflect the intrinsic different reactivity of the two processes.

1.5 Photocatalytic CO_2 Reduction by Water

As commented above photocatalytic CO_2 reduction always requires a hydrogen source, even if CO is the main C-containing product formed. We have already indicated that natural photosynthesis transforms CO_2 into glucose and sugars by using the energy of the Sun and water as reducing agent. However, the current artificial photocatalytic systems for the CO_2 reduction by water are considerably inefficient and maximum quantum yields for this process are currently being estimated much below 0.1 %, thus being considerable room for improvement [23, 24].

At present the most efficient solid photocatalyst for CO_2 reduction by H_2 is based on TiO_2, a semiconductor that is suitably modified to increase the efficiency under solar light irradiation and contain co-catalysts to increase production rate and selectivity of the process. One of the most efficient photocatalysts has been reported by Grimes and coworkers who have used anodized titania nanotubes in the anatase phase doped with nitrogen and platinum and copper nanoparticles as photocatalyst for the gas phase; CO_2 reduction by H_2O production rates to methane as high as 75 $\mathrm{ppm \cdot cm^{-1} \cdot h^{-1}}$ have been achieved for this type of titania photocatalyst under solar light illumination [23, 25].

This example illustrates several of the strategies that can be employed to increase the efficiency of TiO_2 for the photocatalytic CO_2 reduction. In this way, spatial structuring of the anatase TiO_2 photocatalyst as nanotubes of a few micrometers long and hundreds of nanometers wide has been proposed to increase charge separation and the intrinsic efficiency of TiO_2 as photocatalyst. Evidence by transient absorption spectroscopy suggests that depending on the shape of TiO_2 as rods or tubes, charge migration takes place preferentially along the main direction of the tube or rod. The diffusion length of the charge carriers along the direction of the tubes is much longer than for spherical nanoparticles, this meaning that electrons and holes can travel longer distances in these structured materials than in conventional TiO_2 nanoparticles.

By doping with nitrogen atoms, a certain reduction of TiO_2 bandgap can be obtained. Doping with no metallic elements introduces energy levels, mainly lone sp^2 electrons on the nitrogen atom in the inter-bandgap space of conventional TiO_2. This bandgap reduction is reflected in the yellow color characteristic of N-doped TiO_2 that allows a certain absorption of visible light by TiO_2. In the

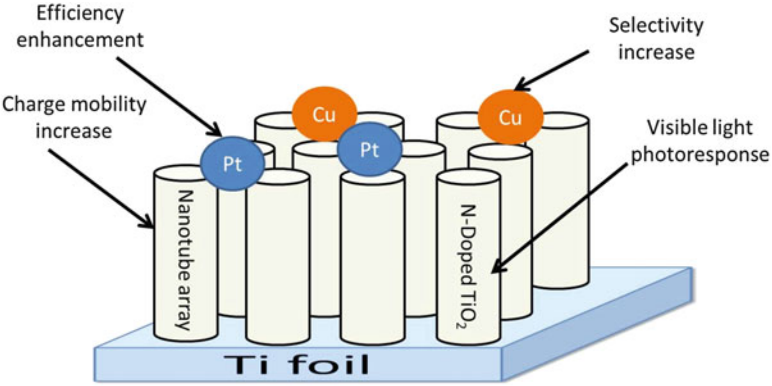

Scheme 1.7 Pictorial illustration of N–TiO_2 anodized photocatalyst containing Pt and Cu nanoparticles and the role of each component

present case, N-doping can be obtained when performing the formation of titania nanotubes electrochemically by contacting the titanium metal electrode precursor with atmospheric nitrogen gas. However, ammonia and ammonium are among the two most convenient doping agents for TiO_2, since these chemicals are considerably more reactive than molecular N_2. Besides structuring to prolong charge separation lifetime and N-doping to increase TiO_2 photoresponse into the visible region, the system contains platinum and copper nanoparticles to facilitate CO_2 adsorption, electron reduction, and gas evolution. Scheme 1.7 illustrates the components of the anodized n-TiO_2 photocatalyst and the main purpose of each of the components.

In another relevant example of an efficient titania-based photocatalyst for CO_2 reduction, we reported that over 2000 μmoles · $g^{-1}h^{-1}$ of methane can be achieved by using a commercial titanium dioxide photocatalyst (Evonik P25) that has been conveniently modified by Au–Cu nanoalloys [26]. The photocatalyst is presented in a gas phase photoreactor as a thin film of a few micrometers deep, exposing in this way the maximum amount of particles to the light, thus ensuring the maximum photoactivity per mass of photocatalyst in the reactor. Besides the use of a thin film, the key point of this photocatalytic system is to use a highly active commercial anatase (80 %)–rutile (20 %) titania that is conveniently modified by nanoparticles of Au–Cu in about 2 % weight. While Au introduces visible light photocatalytic activity, the presence of copper drives the selectivity of the system towards CO_2 reduction and methane formation, preferentially to H_2O reduction. Comparison of the performance of Au–Cu/P25 with that of Au/P25 shows that the latter has high photocatalytic efficiency for hydrogen generation from water, even in the presence of CO_2. But addition of Cu in the nanoalloy changes the preference of the photocatalytic activity towards CO_2 reduction.

FTIR spectroscopy has shown that adsorption of CO_2 forms spontaneously, even in the dark, a small population of CO_2^{-} by single electron reduction of CO_2 by Ti^{3+} sites present in the material. Upon illumination appearance of a band attributable to

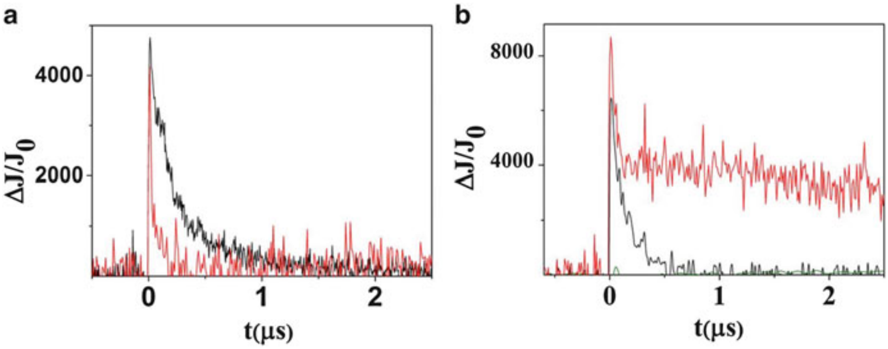

Fig. 1.1 Temporal profiles of transient signals monitored at 720 nm recorded for Cu/P25 (**a**) and Au/P25 (**b**) samples upon 532 nm laser excitation under CO_2 (*red*) or Ar (*black*) atmosphere

CO absorbed on Cu nanoparticles is detected, and based on this observation, it is proposed that the photocatalytic CO_2 reduction takes place on copper atoms of the nanoalloy. Furthermore, transient absorption spectroscopy has provided an useful spectroscopic evidence showing that CO_2 only quenches the charge separation state of the photocatalyst when Cu is present on titania [27]. Figure 1.1 presents selected temporal profiles of the transient signal monitored at long wavelengths in the absence and in the presence of CO_2 for a sample of Cu/P25 and Au/P25.

These spectroscopic studies still need to be complemented by theoretical calculations and modeling to understand in deeper detail why the presence of copper is able to control the outcome of the photocatalytic process and, more specifically, the product distribution. It is very likely that reactive CO_2 adsorbs preferentially near copper atoms, probably forming some type of carbonate-like species, and that this adsorption is the key feature controlling the photocatalytic process. It is worth to comment that noble metals and particularly Pt and Au do not interact with CO_2. The presence of copper should introduce some affinity for CO_2 adsorption on the metal co-catalyst, this being the origin of the change in selectivity.

1.6 Photocatalytic CO_2 Reduction in the Presence of Sacrificial Electron Donors

Although the case that has been previously commented consisting in the photocatalytic reduction of CO_2 by water is the one that could have potential application for the generation of solar fuels, the high endoergonicity of the process and the complex reaction mechanism determine that the efficiency of the process is currently very far from any possible commercial application. As commented earlier, most of the reports on the photocatalytic reduction of CO_2 by water describe the formation of a few $\mu mol \cdot g^{-1} \cdot h^{-1}$ production rate under solar light irradiation, and several orders of magnitude of enhancement are at least needed to consider the viability of the process.

In this context, for fundamental studies, it is of interest to increase the efficiency of the photocatalytic reduction process by performing it in the presence of some compounds that can act as sacrificial electron donors more efficiently than water. Since in the photocatalytic process the same amount of electrons in the conduction band and holes in the valence band, leading to reduction and oxidation respectively, are formed, for the purpose of understanding CO_2 reduction, it is convenient to carry out the reaction under conditions in which the evolution of holes do not limit the efficiency and rate of the process. This can be achieved by performing the reaction in the presence of sufficient amounts of tertiary amines that are well-known excellent electron donors, quenching immediately holes in the valence band, increasing charge separation efficiency by reducing e^{-}/h^{+} recombination, and leading to electrons in the conduction band. The use of a tertiary amine is more convenient due to the lower chemical reactivity of these amines compared to primary and secondary ones, while still being good electron donors. The presence of amines also enhances solubility of CO_2 in aqueous media by increasing the pH of the solution and also by forming carbamates by formation of adducts with CO_2 (Eq. 1.14).

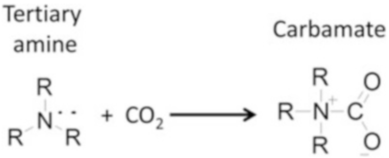

(1.14)

This approach of CO_2 reduction in the presence of tertiary amines has been frequently used in photocatalytic systems based on metallic complexes and particularly with Ru(II) polypyridyl complexes [28]. In these cases excitation with visible light of the Ru(II) polypyridyl complexes results in the generation of a triplet excited state with intramolecular metal-to-ligand charge transfer character that will transfer an electron to CO_2 forming Ru(III) and $CO_2^{\cdot-}$. Subsequent Ru(III) will undergo reduction to Ru(II) in the presence of amine that will be the reducing species in the system (Scheme 1.8).

While initial systems were reported in solution, these molecular-based photocatalysts can subsequently be adsorbed or attached to solids, and then, the homogeneous photocatalytic system is converted to a heterogeneous one. One example of this strategy is the development of metal organic frameworks comprising Ru(II) polypyridyl complexes in their structure [29]. MOFs are crystalline porous materials in which the structure is formed by nodes of metal or metal clusters held in place by rigid bi- or multipodal organic linkers. In the present case, Ru(II) complex replaces a percentage of biphenyl-4,4′-dicarboxylate linkers of the structure (Scheme 1.9).

Overall, the use of amines as sacrificial donors in CO_2 reduction can serve to prove that the reduction potential of electrons in the photocatalytic system is high

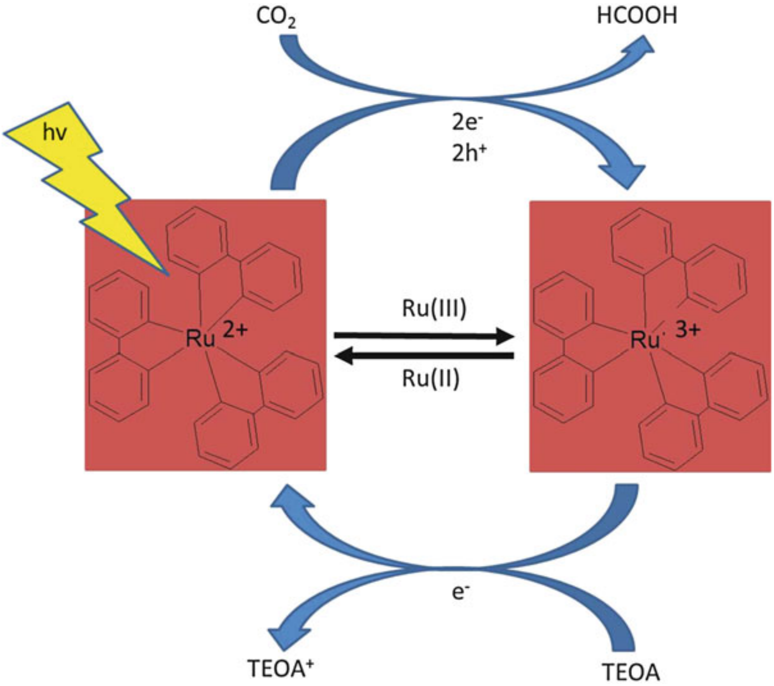

Scheme 1.8 Mechanism of photocatalytic CO_2 reduction by visible light excitation of Ru (II) polypyridyl complex and the subsequent reduction of Ru(III) by triethanolamine (TEOA) as sacrificial electron donor

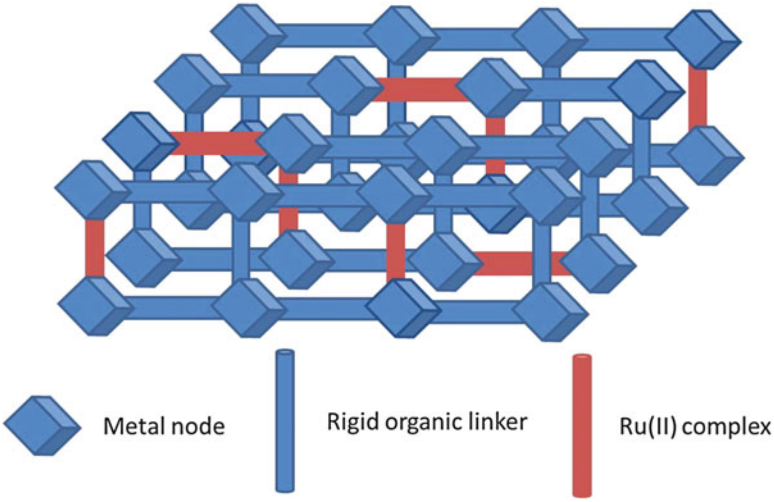

Scheme 1.9 Simplified illustration of the general structure of a MOF where a percentage of Ru (II) complex is replacing the typical organic linker

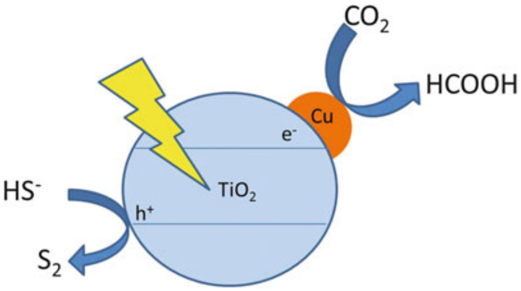

Scheme 1.10 Photocatalytic CO_2 reduction by Cu-doped TiO_2 using hydrogen sulfide (HS^-) as sacrificial electron donor and subsequent sulfur formation

enough to promote CO_2 reduction and also to determine the products formed in the process. For instance, in the above commented case of a MOF comprising a Ru (II) complex, formate is the only product observed upon photocatalyst reduction of CO_2 in aqueous solution.

Continuing with the use of sacrificial electron donors, it has been found that Cu-doped TiO_2 can also form formate by CO_2 reduction in aqueous phase using sulfide as a sacrificial electron donor. The process is accompanied by the generation of a large amount of hydrogen in the gas phase. The use of sulfide as electron donor may have an additional interest besides photocatalytic CO_2 reduction, since as consequence of CO_2 reduction and hydrogen generation, elemental sulfur is formed during the photocatalytic reaction. In this way, the whole process can have interest for purification of wastewaters containing unwanted sulfides (Scheme 1.10).

1.7 Photoassisted CO_2 Reduction by Hydrogen

The reaction of CO_2 with hydrogen to form methane (*the Sabatier reaction*) is an exothermic process (Eq. 1.15) that can be performed in the dark at moderate temperatures using adequate nickel catalyst, but also there are several reports describing the process photocatalytically [30, 31]:

$$CO_2 + 4H_2 \rightarrow CH_4 + 2H_2O \quad \Delta H = -165 kJ/mol \tag{1.15}$$

In the photocatalytic process, the reaction is initiated at room or near room temperature, although as the reaction progresses, a sudden increase of the reaction temperature is observed and combination of catalytic and photocatalytic process could take place in various proportions depending on the temperature. If the reaction temperature reaches a sufficient high value to start the catalytic pathway, then the use of light may be no longer needed. For this reason, this process is probably better described as *photoassisted* rather than being a true photocatalytic process.

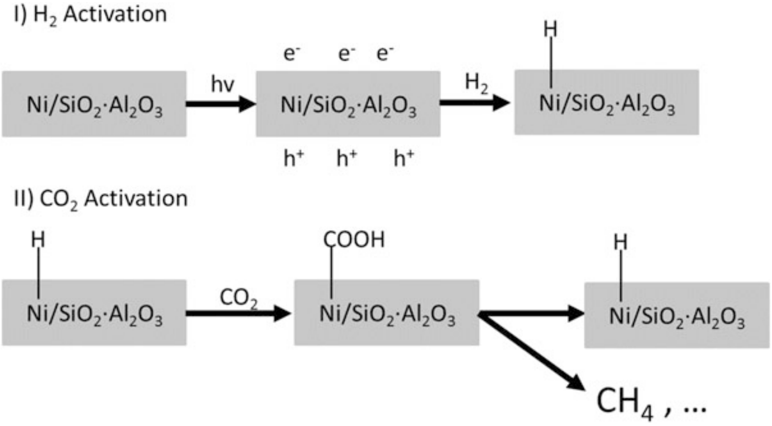

Scheme 1.11 Mechanistic proposal of photocatalytic CO_2 reduction by supported NiO as catalyst

The *photoassisted* CO_2 reduction by hydrogen using NiO nanoparticles supported on SiO_2–Al_2O_3 has the advantage of taking place with complete CO_2 conversion using quasi-stoichiometric amounts of hydrogen into CH_4 with minor a percentage of CO or elemental carbon. Similarly, other solid photocatalysts based on $In_2O_{3-x}(OH)_y$ also achieve complete conversion [31]. In the case of NiO, it is proposed that light irradiation with the generation of electrons and holes will form some Ni–H species by reduction of H_2 by electrons and that Ni–H will reduce CO_2 (Scheme 1.11).

The Sabatier reaction requires H_2 as feedstock and it may seem that it will never be suitable for developing large-scale industrial processes. However, in the context of an integrated view of renewable energy, it has been claimed that the Sabatier process can be suitable for achieving two goals in the same process [32]. On one hand, large-scale implementation of the Sabatier reaction will serve to control atmospheric CO_2 emissions, particularly during the transitory period in which fossil fuels will still contribute in a significant percentage to the total energy consumed. On the other hand, the Sabatier reaction can serve as a way to convert hydrogen, a chemical difficult to store in large quantities, into a useful fuel for transportation or for its use in power plants. In this integrated scheme of electricity management, the point to solve is the mismatch between the production of energy from renewable resources and electricity consumption. In this way windmills can generate a significant amount of electricity in periods and times in which this energy production cannot be coupled with consumer's electricity demand. In the situation in which a surplus of electricity is produced, one way to store this electricity production excess could be the electrolytic hydrogen generation from water in large amounts. This hydrogen would be the one reacted with CO_2 to form methane that would be the fuel finally burned either in power plants to generate electricity on demand or for transportation. Scheme 1.12 shows the way in which the Sabatier reaction can act as a buffer making possible the chemical storage of electricity [32].

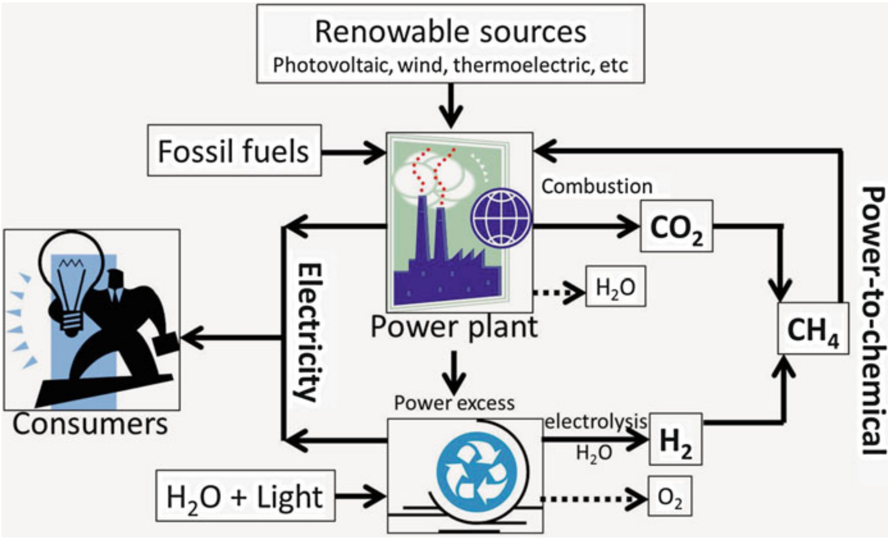

Scheme 1.12 Description of the possible role of the Sabatier reaction of CO_2 and H_2 for the coupling of electricity and production of chemicals, allowing the matching of production and consumption

1.8 Photocatalyst Types for CO_2 Reduction

1.8.1 Semiconductor-Based Photocatalyst

Since the seminal report by Fujishima and Honda [33] describing the photoelectrochemical CO_2 reduction by TiO_2, this metal oxide semiconductor has became by far the most important photocatalyst. TiO_2 has several crystal phases in addition to an amorphous phase. However, for photocatalysis, it has been found that anatase is the most active form of TiO_2. The presence of defects in the crystal structure is detrimental for the photocatalytic activity, and for this reason, amorphous titania is always considerably much less active. When prepared by sol–gel at moderate temperatures, amorphous titania is the first material obtained, but thermal annealing at temperatures below 350 °C increases significantly the crystallinity of the solid towards the thermodynamically more stable anatase phase. This phase transition results in a considerable increase in photocatalytic activity. Annealing at higher temperatures converts anatase into rutile. Although rutile is also a semiconductor and has somewhat smaller bandgap with an absorption tail into the visible region, the photocatalytic activity of this titania crystal phase is generally lower than that of anatase, and therefore, attention has to be paid to thermal treatment to avoid conversion of TiO_2 in rutile. Much higher temperatures result in the formation of brookite that is totally inactive from the photocatalytically point of view. Crystal phases of TiO_2 can be conveniently distinguished by XRD or Raman spectroscopy. The last technique is also valid to characterize amorphous titania. Due to the wide use of TiO_2 as photocatalyst, there are many commercial samples currently available. However, it is important to note that the photocatalytic activity of different commercial TiO_2 can vary by several orders of magnitude. One of the photocatalytically most active commercial samples is Evonik P25 that consists in a pyrolytic TiO_2 sample obtained by hydrolysis of $TiCl_4$ at high temperatures (Eq. 1.15):

$$TiCl_4 + O_2 + 2\,H_2 \rightarrow TiO_2 + 4\,HCl \quad (\text{Temperature} = 400 - 600^{o}C) \tag{1.16}$$

P25 is constituted by approximately 80/20 % of anatase and rutile phases, and it has been proposed that the combination of these two phases in the correct proportion is the factor responsible for its high photocatalytic activity. When two semiconductors of adequate bandgap and energy levels are in intimate contact, a heterojunction can be developed, and upon excitation of one of the semiconductors and generation of the corresponding charge-separated state, either electrons or holes can move through the interface to the second semiconductor with adequate energy potentials. This interfacial electron migration creates a Schottky barrier between the two semiconductors that increases considerably the lifetime of the charge separation state, and this can be reflected in a more efficient photocatalytic process. It is proposed that in P25, the combination of anatase and rutile is acting as a heterojunction, and for this reason, the photocatalytic efficiency of this particular commercial sample is much better than other TiO_2 materials even if they are exclusively constituted by anatase or even if the sample exhibits higher crystallinity (Scheme 1.13).

The photocatalytic efficiency of semiconductors, including TiO_2, can be low and notably enhanced by deposition of other components that are generally described as co-catalysts. These particles on the surface of the semiconductor can influence the outcome of the photocatalytic process in several ways, resulting in the observation of a higher efficiency of the wanted product. One of these roles is the management of electrons or holes reaching these co-catalysts. The rates of reduction by conduction band electrons and oxidation by valence band holes had to be, under steady-state conditions, the same, and one of the two processes is typically the rate-limiting one. For instance, in the overall water splitting, reduction of water by conduction band electrons can be the rate-determining process, and in this case, the rate can be increased by the presence of a co-catalyst. Typical co-catalysts for conduction band

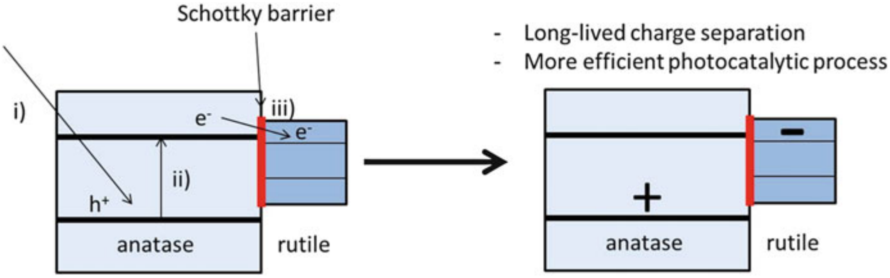

Scheme 1.13 Pictorial illustration of the formation of long-lived charges after light absorption (i), electron excitation (ii), and electron migration through the Schottky barrier in a heterojunction anatase–rutile of P25 titania

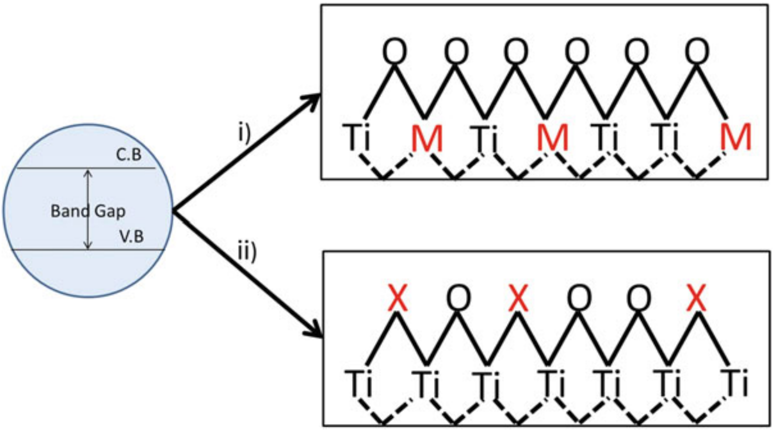

Scheme 1.14 Pictorial illustration of the possible strategies to reduce the bandgap energy of a TiO_2 through doping with (i) metallic or (ii) nonmetallic elements

electron management are noble metals, particularly Pt and Au [34]. On the other hand, the oxidation semireaction by holes are frequently catalyzed by metal oxide co-catalysts such as RuO_2, IrO_2, and Co_2O_3 present as small nanoparticles on the semiconductor surface [35]. In this regard in a seminal work, Fujishima and Honda reported that upon UV irradiation Pt containing TiO_2 submitted to an overpotential is able to act as photoanode for CO_2 reduction in water [33]. After this report, several studies have shown the ability of various forms of TiO_2 modified with co-catalysts to promote CO_2 reduction by UV.

In general the photocatalytic activity upon UV irradiation of TiO_2 conveniently modified by co-catalysts is excellent and among the highest for all photocatalysts. However, as commented earlier, solar light contains only about 4 % of the energy in the UV region and consequently the photocatalytic activity of TiO_2 under these conditions is far from optimum. Several strategies have been reported to increase the photocatalytic response of TiO_2 to the visible region. Visible light is about 46 % of the solar light energy reaching the Earth's surface and there is about 50 % of infrared radiation. Infrared photons have generally not enough energy to promote electronic transitions between orbitals, and for this reason, they cannot directly be useful to excite a photocatalyst.

In order to introduce a visible light response in TiO_2, it is necessary to reduce the bandgap energy below 3.2 eV that is the value corresponding to TiO_2 anatase. One possibility to reduce the bandgap is metal doping in which a few percentage of Ti^{4+} ions are replaced by other transition metal ion. In this case the metal ion dopant introduces empty orbitals below the conduction band of anatase. Typical metal dopants are Pt, Pd, Cu, and Fe [36–38]. In a complementary alternative, the bandgap energy can be decreased by replacing some oxygen atoms by nonmetallic elements like N, S, or C among others [39]. In this case, orbitals of nonmetallic elements having electron pairs are located above in energy with respect to valence band electrons. Scheme 1.14 illustrates the two alternative strategies to diminish the bandgap energy by doping with metallic or nonmetallic elements.

As commented earlier, one of the most efficient photocatalysts for CO_2 reduction by water to form methane consists of N-doped TiO_2 anatase nanotubes modified by Pt and Cu as co-catalysts (Scheme 1.7). In this case, N atoms, introduced during the anodization process of TiO_2 nanotubes, come from the NH_4^+ electrolyte or even atmospheric N_2, and its presence increases the photocatalytic activity by allowing visible light absorption by the photocatalyst.

A third alternative to introduce visible light photoresponse that was commented above is deposition of metal nanoparticles exhibiting surface plasmon band [40]. Due to the chemical stability and inertness against oxidation, Au nanoparticles are the most adequate metal for the purpose of introducing visible light photoresponse. We have already commented the case of Au–Cu/P25 as a photocatalyst for CO_2 reduction reaching high CO_2 conversion rates.

Besides $TiO_{2,}$ ZnO is probably the second most used metal oxide semiconductor. ZnO is also a wide bandgap material with similar bandgap energy as TiO_2 anatase (3.2 eV), and, therefore, ZnO has only photocatalytic activity upon UV irradiation. In one report comparing the photocatalytic activity of ZnO and TiO_2, it was concluded that the former can be even more efficient than the later. In general, the photocatalytic activity of TiO_2 and ZnO are expected to be similar and dependent on the crystal phase, particle size, surface area, and experimental setup (lamps and photoreactor). It can be anticipated that the concepts of doping and deposition of plasmonic nanoparticles as co-catalysts can be also applicable equally well for ZnO and for TiO_2. The main problem that limits the use of ZnO as photocatalyst is its instability at acid pH values.

Besides metal oxides, photocatalytic systems based on metal chalcogenides and particularly metal sulfides have also been reported to promote the photocatalytic CO_2 reduction. In particular, CdS and Bi_2S_3 quantum dots having visible light absorption have been reported also to act as visible light photocatalysts for CO_2 reduction by H_2O [41].

1.8.2 Layered Double Hydroxide (LDH)-Based Photocatalysts

Other types of materials that are attracting increasing interest as photocatalysts are LDH. LDHs contain two different metals, one divalent and other trivalent, the latter being present in lower proportion, generally below 33 % respect to the divalent cation. LDHs are isostructural with brucite ($Mg(OH)_2$), whose structure is constituted by MgO_6 octahedra sharing the edges forming sheets. In the case LDHs, these octahedra contain the di- or trivalent cation. As consequence of the presence of a certain percentage of trivalent cations, LDH layers have an excess of positive charge that has to be compensated by the presence of charge-balancing anions located at the intergallery space. Scheme 1.15 illustrates the structure of LDHs.

Due to the intrinsic basicity of hydroxides, carbonate is one of the most common ions forming part of LDHs. This affinity of LDHs for carbonate can be advantageously used to perform the photocatalytic CO_2 reduction. In a certain way, it can be considered that LDHs are similar to metal oxides (such as ZnO) with a variable

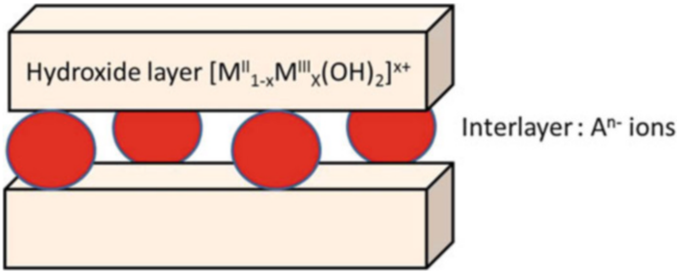

Scheme 1.15 Pictorial illustration of the LDH structure

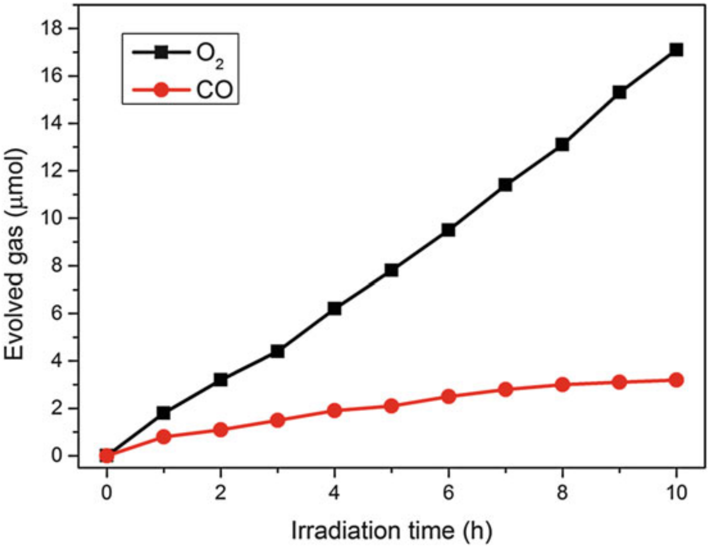

Fig. 1.2 CO and O_2 evolution in the photocatalytic reduction of CO_2 in water at pH 10 using Mg–In LDH as photocatalyst

amount of metal doping (as trivalent cation) that can be large. LDHs behave as semiconductors and their photocatalytic activity for hydrogen evolution from water/methanol mixtures as well as oxygen evolution from water has been reported [12]. In this regard, Zn–Cr LDH exhibits photocatalytic activity for the conversion of CO_2 into CO upon UV light irradiation, and the photocatalytic efficiency in CO evolution increases upon deposition of metal nanoparticles such as Pt, Pd, or Au [42].

Ni–Al LDH also exhibits high photocatalytic activity for this CO_2 into CO conversion that depends on the Ni/Al ratio, reaching an optimal photocatalytic activity for Ni/Al ratio of 4 with 36.6 and 12.2 μmol of CO and H_2, respectively, at 10 h UV light irradiation [43]. The photocatalytic CO_2 reduction for Ni–Al LDH is about three times higher than the value observed for $Ni(OH)_2$. Mg–In LDH ($Mg^{2+}/In^{3+} = 3$) is also able to split CO_2 into CO in water upon UV irradiation [44]. In this case the simultaneous evolution of oxygen was observed as depicted in Fig. 1.2.

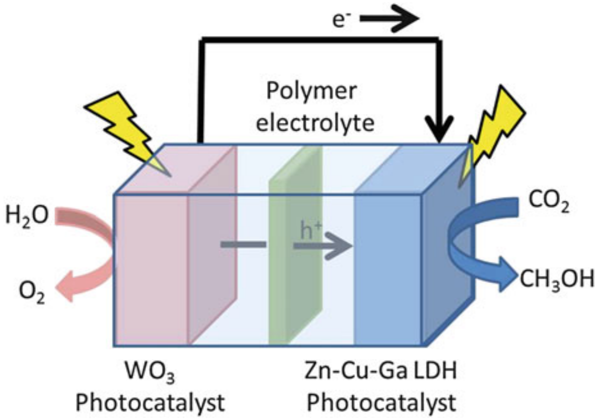

Scheme 1.16 Illustration of the photocatalytic CO_2 reduction in a reverse photofuel cell including WO_3 and Zn–Cu–Ga LDH

Photocatalytic CO_2 reduction by a ternary Zn–Cu–Ga LDH has been combined with WO_3 photocatalytic oxygen generation [45]. The two processes have been coupled electrically, allowing the transfer of electrons from water oxidation to Zn–Cu–Ga LDH photocatalytic CO_2 reduction, while protons diffuse through a polymer electrolyte (Scheme 1.16). The overall process taking place separately in two compartments forms methanol and water from CO_2 and O_2.

The process is in fact just the reverse of a fuel cell for methanol oxidation, and the two photocatalytic processes (water oxidation by WO_3 and CO_2 reduction Zn–Cu–Ga LDH) require light irradiation and should occur at the same rate transferring electrons (through the metallic conductor) and protons (through the membrane).

1.8.3 *Graphene-Based Photocatalyst*

Graphene is a one-atom-thick sheet of sp^2 carbons in hexagonal geometry. The 2D morphology of graphene represents the limit of miniaturization of a material approaching a surface and is analogous to an ideal surface with extended π orbitals. Graphene is a conductive material that has no photocatalytic properties. However, graphene as additive in a small weight percentage has been found to increase the photocatalytic activity of TiO_2 for CO_2 reduction. In this system graphene increases the intrinsic efficiency of TiO_2 by accepting electrons from the TiO_2 conduction band in an analogous way as commented earlier for metal co-catalyst (Scheme 1.17). The presence of graphene can lead to more than one order of magnitude enhancement of TiO_2 photocatalytic activity for CO_2 reduction due to the more efficient charge separation. Similarly to the case of graphene/TiO_2 composites, graphene has also been reported to increase the photocatalytic activity for CO_2 reduction of other semiconductors including ZnO, WO_3, and CdS [46].

Besides the use of graphene as additive, graphene-derived materials can be themselves semiconductors and they can act as active photocatalysts, particularly

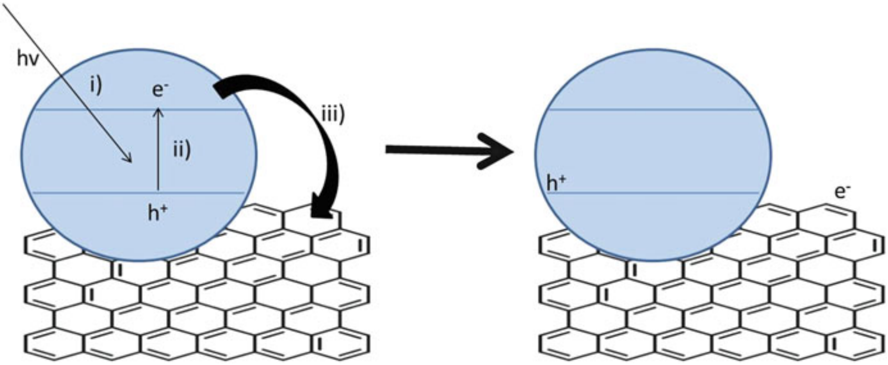

Scheme 1.17 Mechanism through which graphene increases the photocatalytic activity of TiO_2 in intimate contact with it. (i) Light absorption, (ii) electron promotion from the valence to the conduction band, and (iii) electron transfer from TiO_2 conduction band to graphene

graphene oxide [47]. While graphene is a conducting material, graphene oxide prepared by deep chemical oxidation of graphite and subsequent exfoliation of graphite oxide is a semiconductor that exhibits photocatalytic activity in the UV region for hydrogen generation or, in combination with dyes as light harvesters, can be activated with visible light [48].

Graphene oxide has been found to be a promising material for the photocatalytic reduction of CO_2 to methanol. Methanol is considered as the most valuable photoproduct by CO_2 reduction from the point of view of solar fuels since this chemical is liquid under ambient conditions and has high volumetric energy content. However, due to its high reactivity, particularly in the presence of holes and their tendency to decompose catalytically into CO_2, it is very unlikely that high yields to methanol can be achieved photocatalytically. In the case of graphene oxide, it was found that a sample of this material with high oxygen content was about six times more efficient than commercial P25 for the generation of methanol by photocatalytic CO_2 reduction by water upon simulated solar light irradiation [47].

One point of large importance when considering the photocatalytic activity of graphene oxide is its stability under reaction conditions for long operation times. Graphene oxide has a tendency to become reduced to a type of reconstituted graphene by expelling CO_2 and CO. This chemical reduction of graphene oxide can be done under hydrothermal conditions at moderate temperatures below 200 °C, but also it has been found that upon light exposure evolution of CO_2 and CO from graphene oxide can occur. In the context of the variation of the semiconducting properties going from graphene to graphene oxide, it has been observed that the degree of oxidation plays a strong influence on its photocatalytic activity, probably because the redox potential of the valence and conduction bands depends on the degree of oxidation of graphene oxide and it can be modulated in a certain range by the percentage of oxygenated functional groups introduced on the graphene sheet.

A more elaborated alternative for CO_2 reduction using graphene consists in coupling the photocatalytic activity of these materials having covalently attached light-harvesting organic units with an enzymatic system able to produce formic acid by CO_2 conversion [49]. Formate dehydrogenase consumes NADH as cofactor transferring protons and electrons to CO_2 in the prosthetic center of the enzyme. Upon CO_2 reduction to formate, NADH becomes oxidized to NAD^+, and this enzymatic system can continuously operate if additional amounts of NADH are provided (Scheme 1.18).

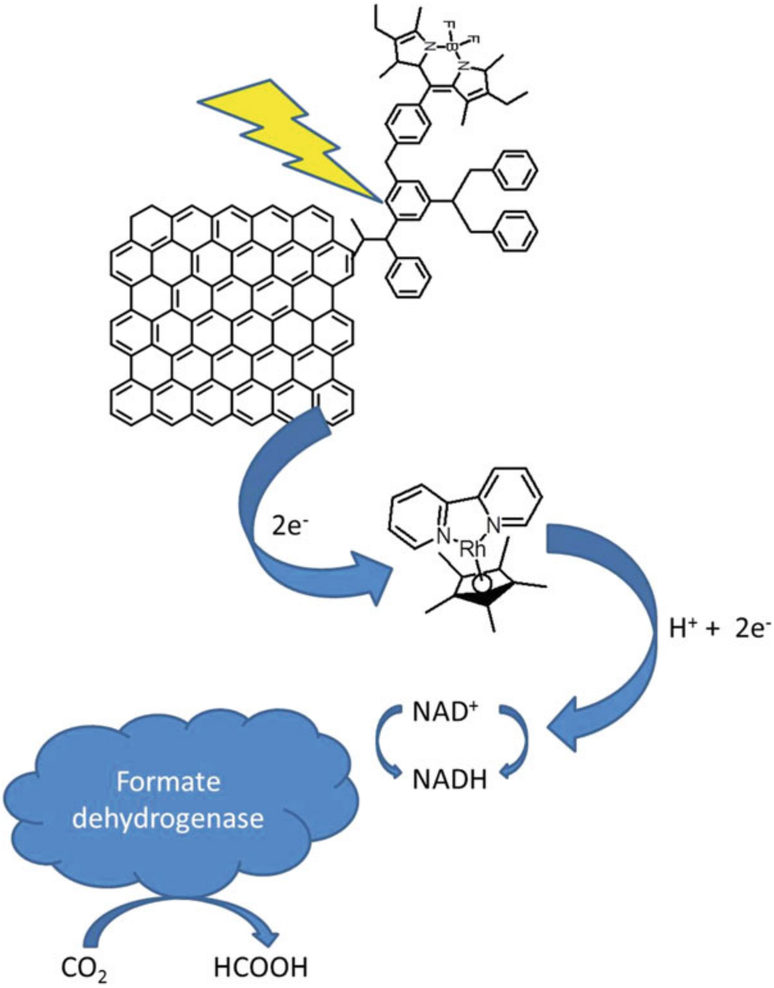

Scheme 1.18 Illustration of the enzymatic system operating by NADH regeneration using a graphene–BODIPY photocatalyst and a Rh complex as mediator. The photobiocatalytic system can promote the photocatalytic CO_2 reduction to formic acid

One way to continuously provide NADH is to regenerate this species photocatalytically by reduction of NAD^+. In this regard it has been reported that graphenes having covalently attached a multi-anthraquinone substituted porphyrin or moieties having BODIPY chromophores can effect NAD^+ reduction to NADH with visible light if a Rh–bipyridyl complex is present as mediator [49]. Considering the large variety of enzymatic reductions based on NADH, it is worth exploring further the advantages of combining substituted graphenes with dehydrogenases to obtain solar fuels and particularly other reduction products from CO_2.

1.9 Concluding Remarks and Future Perspectives

Current energy demand is largely satisfied by fossil fuels and it can be anticipated that the percentage of contribution to the total energy consumption of fossil fuels will continue to be high in the near future, although with a gradual tendency to decline. During this transitory period, it is expected that energy from fossil fuels will coexist with an increasing percentage of energy from renewable sources, particularly aerogenerators and photovoltaics. The nominal power of renewable power resources will steadily increase until it becomes a substantial percentage of the total energy supply. However, one of the major drawbacks of renewable energies is their dependence on weather conditions and that their production does not match in time with the energy demand. In contrast conventional power plants based on fossil fuels are flexible enough to adjust their production to the consumption. One possible solution to this mismatch of energy from renewable resources and consumption would be to utilize CO_2 from conventional power plants as feedstock that with the energy of renewable sources is converted into fuels. The overall cycle would be neutral from the CO_2 footprint. Also, direct conversion of CO_2 into solar fuels either electrocatalytically or photocatalytically could serve later as a way to supply energy on demand, since the products of CO_2 reduction will store the energy until needed. In this scheme, the development of efficient photocatalytic methods for CO_2 reduction will become increasingly used.

In the previous sections, we have presented several possibilities to effect the photocatalytic reduction. By far the most efficient and promising one is the reaction of CO_2 with hydrogen that can lead to the complete conversion of both feedstocks, but this efficient process depends on the availability of hydrogen supply obtained from renewables. Other processes and particularly CO_2 reduction by water are very appealing, but their efficiency is still many orders of magnitude lower than required for commercial applications. Any improvement in this field has to derive from the development of an efficient photocatalytic system. We have shown that much research effort has been focused on modification of $TiO_{2,}$, and today this material conveniently modified is the one exhibiting the highest photocatalytic activity.

In this area, techniques to gain information on the reaction mechanism by detecting intermediates have to be developed to gain insights into the bottleneck that limits the efficiency of the process and to provide hints of how to control the product distribution. Theoretical calculations are needed also to assist the design of novel photocatalyst and to provide a conceptual framework to rationalize the experimental results.

Therefore, the progress in the development of efficient photocatalyts for CO_2 reduction has to come from multidisciplinary skills with expertise in material science synthesis, surface characterization with detection of adsorbed species, and experts in computational chemistry. Besides TiO_2, materials providing flexibility in the composition and properties are promising and will be increasingly studied. They include not only inorganic solids like LDHs but particularly carbon nanoforms such as graphenes, layered carbon nitrides, and silicon carbides among others. Considering the large economic and societal impact that the process may have, the long-term goal in this area is to reach commercial application, although initially the process of photocatalytic CO_2 reduction could be applied solely in certain circumstances and under favorable conditions and environment. This initial proof of concept of a commercial application will surely accelerate research and subsequent implementation of other photocatalytic CO_2 reduction processes.

Acknowledgments Financial support by the Spanish Ministry of Economy and Competitiveness (Severo Ochoa and CTQ2012-32315) and Generalitat Valenciana (Prometeo 2013/2014) is gratefully acknowledged. J.A. thanks the Spanish Ministry of Economy and Competitiveness for the Severo Ochoa research associate contract.

References

1. Gust D, Moore TA, Moore AL (2001) Mimicking photosynthetic solar energy transduction. Acc Chem Res 34:40–48
2. Heller A (1981) Conversion of sunlight into electrical power and photoassisted electrolysis of water in photoelectrochemical cells. Acc Chem Res 14:154–162
3. Corma A, Iborra S, Velty A (2007) Chemical routes for the transformation of biomass into chemicals. Chem Rev 107:2411–2502
4. Lewis NS, Nocera DG (2006) Powering the planet: chemical challenges in solar energy utilization. Proc Natl Acad Sci 103:15729–15735
5. Alstrum-Acevedo JH, Brennaman MK, Meyer TJ (2005) Chemical approaches to artificial photosynthesis. 2. Inorg Chem 44:6802–6827
6. Blankenship RE, Tiede DM, Barber J, Brudvig GW, Fleming G, Ghirardi M, Gunner MR, Junge W, Kramer DM, Melis A, Moore TA, Moser CC, Nocera DG, Nozik AJ, Ort DR, Parson WW, Prince RC, Sayre RT (2011) Comparing photosynthetic and photovoltaic efficiencies and recognizing the potential for improvement. Science 332:805–809
7. Corma A, dela Torre O, Renz M, Villandier N, Renz M, Villandier N (2011) Production of high-quality diesel from biomass waste products. Angew Chem Int Ed 50:2375–2378
8. U S D o Energy (2013) Energy efficiency & renewable energy, hydrogen delivery. Available online: http://www1.eere.energy.gov/hydrogenandfuelcells/delivey/. Accessed 30 Nov 2013
9. Balzani V, Credi A, Venturi M (2008) Photochemical conversion of solar energy. Chem Sus Chem 1:26–58
10. Gust D, Moore TA, Moore AL (2009) Solar fuels via artificial photosynthesis. Acc Chem Res 42:1890–1898

11. Hannon M, Gimpel J, Tran M, Rasala B, Mayfield S (2010) Biofuels from algae: challenges and potential. Biofuels 1:763–784
12. Corma A, Garcia H (2013) Photocatalytic reduction of CO2 for fuel production: possibilities and challenges. J Catal 308:168–175
13. de_Richter RK, Ming T, Caillol S (2013) Fighting global warming by photocatalytic reduction of CO2 using giant photocatalytic reactors. Renew Sust Energ Rev 19:82–106
14. Morris AJ, Meyer GJ, Fujita E (2009) Molecular approaches to the photocatalytic reduction of carbon dioxide for solar fuels. Acc Chem Res 42:1983–1994
15. Habisreutinger SN, Schmidt-Mende L, Stolarczyk JK (2013) Photocatalytic reduction of CO2 on TiO2 and other semiconductors. Angew Chem Int Ed 52:7372–7408
16. Huber GW, Corma A (2007) Synergies between bio- and oil refineries for the production of fuels from biomass. Angew Chem Int Ed 46:7184–7201
17. Huber GW, Iborra S, Corma A (2006) Synthesis of transportation fuels from biomass: chemistry, catalysts, and engineering. Chem Rev 106:4044–4098
18. Barber J (2009) Photosynthetic energy conversion: natural and artificial. Chem Soc Rev 38:185–196
19. Lunde PJ (1974) Modeling, simulation, and operation of a Sabatier reactor. Ind Eng Chem Process Des Dev 13:226–233
20. Agrell J, Birgersson H, Boutonnet M (2002) Steam reforming of methanol over a Cu/ZnO/Al2O3 catalyst: a kinetic analysis and strategies for suppression of CO formation. J Power Sources 106:249–257
21. Trimm DL, Önsan ZI (2001) Onboard fuel conversion for hydrogen-fuel-cell-driven vehicles. Catal Rev 43:31–84
22. Zhang H, Shen PK (2012) Recent development of polymer electrolyte membranes for fuel cells. Chem Rev 112:2780–2832
23. Roy SC, Varghese OK, Paulose M, Grimes CA (2010) Toward solar fuels: photocatalytic conversion of carbon dioxide to hydrocarbons. ACS Nano 4:1259–1278
24. Indrakanti VP, Kubicki JD, Schobert HH (2009) Photoinduced activation of CO2 on Ti-based heterogeneous catalysts: current state, chemical physics-based insights and outlook. Energy Environ Sci 2:745–758
25. Varghese OK, Paulose M, LaTempa TJ, Grimes CA (2009) High-rate solar photocatalytic conversion of CO2 and water vapor to hydrocarbon fuels. Nano Lett 9:731–737
26. Neaţu Ş, Maciá-Agulló JA, Concepción P, Garcia H (2014) Gold–copper nanoalloys supported on TiO2 as photocatalysts for CO2 reduction by water. J Am Chem Soc 136:15969–15976
27. Baldoví HG, Neaţu Ş, Khan A, Asiri AM, Kosa SA, Garcia H (2015) Understanding the origin of the photocatalytic CO2 reduction by Au- and Cu-loaded TiO2: a microsecond transient absorption spectroscopy study. J Phy Chem C 119:6819–6827
28. Chen Z, Chen C, Weinberg DR, Kang P, Concepcion JJ, Harrison DP, Brookhart MS, Meyer TJ (2011) Electrocatalytic reduction of CO2 to CO by polypyridyl ruthenium complexes. Chem Commun 47:12607–12609
29. Wang C, Xie Z, deKrafft KE, Lin W (2011) Doping metal–organic frameworks for water oxidation, carbon dioxide reduction, and organic photocatalysis. J Am Chem Soc 133:13445–13454
30. Sastre F, Puga AV, Liu L, Corma A, García H (2014) Complete photocatalytic reduction of CO2 to methane by H2 under solar light irradiation. J Am Chem Soc 136:6798–6801
31. Ozin GA (2015) Throwing new light on the reduction of CO2. Adv Mater 27:1957–1963
32. Schlögl R (2015) The revolution continues: energiewende 2.0. Angew Chem Int Ed 54:4436–4439
33. Fujishima A, Honda K (1972) Electrochemical photolysis of water at a semiconductor electrode. Nature 238:37–38
34. Abad A, Concepción P, Corma A, García H (2005) A collaborative effect between gold and a support induces the selective oxidation of alcohols. Angew Chem Int Ed 44:4066–4069

35. Yan S, Wan L, Li Z, Zou Z (2011) Facile temperature-controlled synthesis of hexagonal Zn2GeO4 nanorods with different aspect ratios toward improved photocatalytic activity for overall water splitting and photoreduction of CO2. Chem Commun 47:5632–5634
36. Slamet HWN, Purnama E, Kosela S, Gunlazuardi J (2005) Photocatalytic reduction of CO2 on copper-doped Titania catalysts prepared by improved-impregnation method. Catal Commun 6:313–319
37. Ishitani O (1993) Photocatalytic reduction of carbon dioxide to methane and acetic acid by an aqueous suspension of metal-deposited TiO2. J Photochem Photobiol A: Chem 72:269–271
38. Pan J, Wu X, Wang L, Liu G, Lu GQ, Cheng H-M (2011) Synthesis of anatase TiO2 rods with dominant reactive {010} facets for the photoreduction of CO2 to CH4 and use in dye-sensitized solar cells. Chem Commun 47:8361–8363
39. Tsai C-W, Chen HM, Liu R-S, Asakura K, Chan T-S (2011) Ni@NiO core–shell structure-modified nitrogen-doped InTaO4 for solar-driven highly efficient CO2 reduction to methanol. J Phys Chem C 115:10180–10186
40. Daniel M-C, Astruc D (2004) Gold nanoparticles: assembly, supramolecular chemistry, quantum-size-related properties, and applications toward biology, catalysis, and nanotechnology. Chem Rev 104:293–346
41. Navalón S, Dhakshinamoorthy A, Álvaro M, Garcia H (2013) Photocatalytic CO2 reduction using non-titanium metal oxides and sulfides. ChemSusChem 6:562–577
42. Katsumata K-i, Sakai K, Ikeda K, Carja G, Matsushita N, Okada K (2013) Preparation and photocatalytic reduction of CO2 on noble metal (Pt, Pd, Au) loaded Zn–Cr layered double hydroxides. Mater Lett 107:138–140
43. Iguchi S, Teramura K, Hosokawa S, Tanaka T (2015) Photocatalytic conversion of CO2 in an aqueous solution using various kinds of layered double hydroxides. Catal Today 251:140–144
44. Teramura K, Iguchi S, Mizuno Y, Shishido T, Tanaka T (2012) Photocatalytic conversion of CO2 in water over layered double hydroxides. Angew Chem Int Ed 51:8008–8011
45. Morikawa M, Ogura Y, Ahmed N, Kawamura S, Mikami G, Okamoto S, Izumi Y (2014) Photocatalytic conversion of carbon dioxide into methanol in reverse fuel cells with tungsten oxide and layered double hydroxide photocatalysts for solar fuel generation. Catal Sci Technol 4:1644–1651
46. Tu W, Zhou Y, Zou Z (2013) Versatile graphene-promoting photocatalytic performance of semiconductors: basic principles, synthesis, solar energy conversion, and environmental applications. Adv Funct Mater 23:4996–5008
47. Liang YT, Vijayan BK, Gray KA, Hersam MC (2011) Minimizing graphene defects enhances titania nanocomposite-based photocatalytic reduction of CO2 for improved solar fuel production. Nano Lett 11:2865–2870
48. Latorre-Sánchez M, Lavorato C, Puche M, Fornés V, Molinari R, Garcia H (2012) Visible-light photocatalytic hydrogen generation by using dye-sensitized graphene oxide as a photocatalyst. Chem Eur J 18:16774–16783
49. Yadav RK, Baeg J-O, Oh GH, Park N-J, Kong K-j, Kim J, Hwang DW, Biswas SK (2012) A photocatalyst–enzyme coupled artificial photosynthesis system for solar energy in production of formic acid from CO2. J Am Chem Soc 134:11455–11461

Chapter 2
Photocatalytic Water Oxidation

Tanvi Gadgil, Niyaz Ibrayev, and Nurxat Nuraje

Abstract Depletion in the resources of fossil fuels and its hazardous effects on environment are the biggest concerns of this century. Researchers have suggested solar energy as a sustainable and viable solution to overcome this problem. But due to the sporadic nature of solar energy, it is essential to store it. The hydrogen fuel is one of the chemical energy forms for storing solar energy. However, the production of hydrogen is the most demanding step in the overall energy-harnessing process. The water-splitting process is one of the most innovative ways to produce hydrogen. The sustainable evolution of hydrogen gas depends on well-designed water oxidation step in the overall water-splitting process. Water oxidation is a challenging half reaction because of the four electron process. The oxidation reaction taking place at the photoanode can be significantly improved with better design of the photocatalytic system. An enhanced water oxidation reaction proves to improve the efficiency of hydrogen production and thus more storage of solar energy as well.

Keywords Solar energy • Water splitting • Hydrogen production • Water oxidation • Heterogeneous photocatalyst • Photoelectrochemical cell

2.1 Introduction

The fossil fuel is an important source of energy. Sustainable supply of fossil fuel energy as per increasing needs of a mankind has always been a matter of concern for present era. This century has witnessed depletion in the resources of fossil fuel. Furthermore, exploitation of fossil fuel energy has caused major environmental hazards in the past decade including global warming. Therefore, increasing demand for the energy and further requirement for protecting the environments have generated a need for alternative and equally effective resource of energy. The

---

T. Gadgil • N. Nuraje (✉)
Department of Chemical Engineering, Texas Tech University, Lubbock, TX 79409, USA
e-mail: Nurxat.nuraje@ttu.edu

N. Ibrayev
Institute of Molecular Nanophotonics, E.A. Buketov Karaganda State University, Karaganda 100028, Kazakhstan

J.C. Colmenares, Y.-J. Xu (eds.), *Heterogeneous Photocatalysis*, Green Chemistry and Sustainable Technology, DOI 10.1007/978-3-662-48719-8_2

renewable energy is the best possible alternative to replace fossil fuels. Sun is an inexhaustible source of renewable energy. The solar energy obtained from Sun is not only ample in amount to serve rising energy demand but environmentally friendly also. Estimated magnitude of solar energy is 3×10^{24} J year^{-1} (i.e., 10^5 terawatts) [1]. The general energy consumption of the world is around 4.0×10^{20} J year^{-1} (i.e., 12 terawatts) [1].

Although Sun is a viable alternative for fossil fuel energy in coming years, it has to be noted that density of solar energy changes as per the locations and seasonal changes on the earth. In other words, considerable contrast can be observed in availability of solar energy in Sahara desert and North Pole. Therefore, in order to maintain constant supply of solar energy throughout the year, it is important to harness it in a proper way. Photosynthesis is one of the good examples for the natural way of storage and harnessing of solar energy. The idea from nature inspired researchers to design an artificial photosynthesis system for storage of solar energy.

Thus, the photocatalytic water splitting is a man made and green solution for storage of solar energy. The splitting of water molecule into hydrogen and oxygen by photocatalyst particles in a photoelectrochemical cell is an attractive feature of water-splitting process. As a result solar energy is stored in the form of hydrogen gas. Currently, hydrogen-based technologies are of great interest because of their use and environmentally clean nature [2].

2.2 Thermodynamics of Water-Splitting Process

In this chapter, the water oxidation reaction in water-splitting process is taken under consideration. It is important to understand overall water-splitting process before focusing on the water oxidation reaction alone. Therefore, in the next two sections, thermodynamics and mechanism of overall water-splitting process is described in detail.

2.2.1 General

In this century, hydrogen-based energy is one of the highly used forms of renewable energy. The available data on efficiency of hydrogen fuel has estimated that 2.2 pounds of hydrogen gas is as good as 1 gal of gasoline [2]. In the era of stringent environmental demands, this “zero emission fuel” serves as an appropriate choice to replace conventional fossil fuel energy. Therefore, hydrogen is the beneficial choice to store inexhaustible solar energy in the absence of sunlight.

Production of hydrogen is the most crucial step in the harnessing of solar energy.

Traditionally, hydrogen is produced from fossil fuels as shown in the reaction (2.1) and (2.2). Production of *syngas*[1] from reaction between water molecule and methane gas is a highly practiced technique in petroleum industry [2].

$$CH_4 + H_2O \rightarrow 3H_2 + CO \tag{2.1}$$

$$CO + H_2O \rightarrow H_2 + CO_2 \tag{2.2}$$

The syngas at the product side is a primary combination of hydrogen gas and carbon monoxide and often carbon dioxide [2]. The carbon dioxide is a major contributor to a greenhouse effect. Therefore, although efficient, this process is not the best way to obtain hydrogen gas and, hence, has been called into a question recently by researchers.

Scientists are researching a better and greener solution for hydrogen production. *Artificial photosynthesis*[2] is an equally efficient and environmentally friendly approach suggested for production of hydrogen gas. Water splitting is one of the techniques that applies principles of natural photosynthesis. Decomposition of water molecule into hydrogen and oxygen using heterogeneous photocatalyst is the fundamental to the overall water-splitting process as shown in the reaction (2.3) [1]:

$$H_2O \xrightarrow[\text{catalyst}]{h\vartheta} H_2 + 1/2\ O_2 \tag{2.3}$$

In this chapter we will focus on understanding intricacies related to the reaction of water splitting.

2.2.2 *Thermodynamics of Overall Water-Splitting Process*

As discussed earlier, overall water-splitting process is a combination of two reactions: oxidation and reduction. These two half reactions can also be termed – the two-electron stepwise process. The evolution of oxygen at the photoanode and that of hydrogen at cathode in a photoelectrochemical cell is observed as shown in reactions (2.4) and (2.5) [3, 9].

At anode (oxidation) [3],

$$H_2O \rightarrow 1/2O_2 + 2H^+ + 2e^- \tag{2.4}$$

At cathode (reduction) [3],

---

[1] *Syngas* is an abbreviation for synthesis gas. Syngas is a mixture of carbon dioxide, carbon monoxide, and hydrogen gas. General producers of syngas are chemical processes in oil and gas industries such as gasification of coal.

[2] *Artificial photosynthesis* is mimicking of natural process of photosynthesis but with the use of photocatalysts.

$$2H^+ + 2e^- \rightarrow H_2 \tag{2.5}$$

Overall reaction [1],

$$H_2O \rightarrow H_2 + 1/2\ O_2 \tag{2.6}$$

However, positive Gibbs free energy change ($\Delta G = +237.2$ kJ mol^{-1} and 2.46 eV per molecule) [1] is observed in the overall water-splitting reaction. Positive Gibbs free energy indicates that the process is endothermic. Therefore, energy is required to overcome positive Gibbs free energy.

Photon energy emitted by the Sun is used for breaking the barrier formed by positive Gibbs free energy. Hence, the material capable of absorbing photon energy has to be included for complete separation of water molecule. Semiconductors efficiently absorb photon and initiate electron and hole pair required for oxidation and reduction reaction. Due to this property of semiconductors, they are widely used as photocatalyst in decomposition of water.

2.3 Mechanism of Overall Water-Splitting Process

2.3.1 Principle

Fujishima and Honda have carried out significant research in the field of water splitting. Most of their work is conducted using a photoelectrochemical cell consisting of titania as the photoanode and platinum as the cathode under UV radiation. In other words, generation of solar hydrogen is carried out in the photoelectrochemical cell (PEC) which consists of a photoanode made up of semiconductor material and a cathode of metal immersed in an electrolyte [3].

In general, the process takes place in a sequential manner. The photocatalysts absorb the light radiation (either UV/visible). The absorbance of light causes excitation of electron in a conduction band of a photocatalyst. These excited electrons initiate the reduction reaction of water molecules into hydrogen gas on active sites of the photocatalysts. Simultaneously, a positive hole is created in the valence band. The positive hole assists in oxidation of water molecule into oxygen gas.

It has to be noted that semiconductors when used as photocatalysts absorb the energy of incident light which is greater than their band gap. Also, the smaller the size of photocatalyst particles, the more sites there are for water decomposition. Furthermore, on the surface active sites, cocatalyst is usually applied to reduce the overpotential at the interface between liquid and semiconductor and conduct the water redox reaction. The cocatalyst plays important role during the water-splitting process. High crystallinity and small dimension of the photocatalyst can reduce the

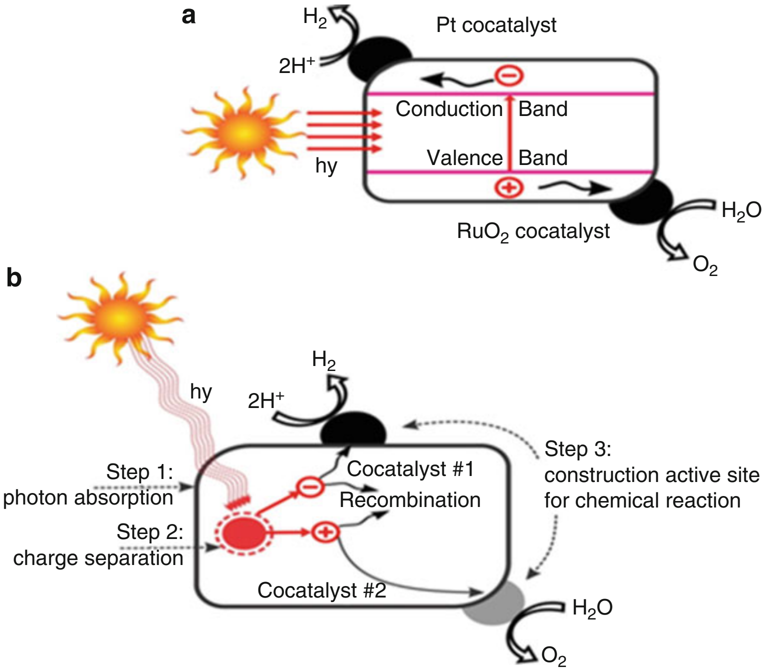

Fig. 2.1 (**a**) Overall water-splitting reaction on a solid photocatalyst and (**b**) Process of electron transport in overall water-splitting reaction

recombination of photogenerated electron–hole pairs. As shown in Fig. 2.1, the cocatalysts (e.g., Pt and RuO_2) are attached to the surface of the photocatalyst [1].

Recently, metal oxides are widely being explored as photocatalysts. They have particular advantages including a naturally abundant availability, a negative band gap, and chemical stability. Moreover, the 2p orbital in the oxygen of the metal oxide is mainly contributed to the formation of the valence band of the metal oxide semiconductors which are able to oxidize water molecules [1].

2.3.2 Cocatalyst and Sacrificial Agent

The efficiency of the redox reaction can be enhanced by the addition of an agent that serves as cocatalyst. The cocatalyst plays an important role in the generation of hydrogen and oxygen by reducing overpotential, improving electron–hole pair transport, and providing active sites for the reaction to occur [1, 4].

The metal oxide, paired with the cocatalyst, absorbs UV/Vis irradiation. The excited electrons in the conduction band initiate hydrogen formation at the interface of the water layer and cocatalyst [1, 4]. In the next step these sacrificial agents such as methanol, diethanol amine, triethanol amine, and ethanol are able to donate or accept electrons, so are also known as electron donor/acceptor elements. These electrons are provided to the positive holes in the valence band of the metal oxide. This is why, electron donor elements are used for reduction reactions. Certain dyes are also sometimes included in this process to absorb visible light. Most of metal oxide particles are more sensitive to the UV irradiation than visible light because of their band gaps. The sacrificial agent improves the efficiency of the process by involving catalytic reactions. The entire process continues until the exhaustion of sacrificial agent [1, 4]. The electron acceptor sacrificial agents such as silver nitrate are used for oxidation reaction. The agents speed up oxidation process under the solar light irradiations [4].

2.3.3 Different Designs in Overall Water-Splitting Process

The process of water splitting under solar energy can be usually designed in following two configurations:

1. Z-scheme reaction (a.k.a. dual-bed configuration)
2. Dye-sensitized photoelectrochemical cell

The first configuration does not involve an external wire for the decomposition of water molecule, whereas in the second configuration, an external circuit is required for smooth transfer of electron between two electrodes [1, 5].

The Z-scheme approach involves two semiconductor photocatalysts with different band gap. One of the photocatalysts is assigned for oxidation and the other photocatalyst for reduction reaction of water. An excited electron initiates the reduction reaction on the surface of photocatalyst (Fig. 2.2 (right)) with the help of

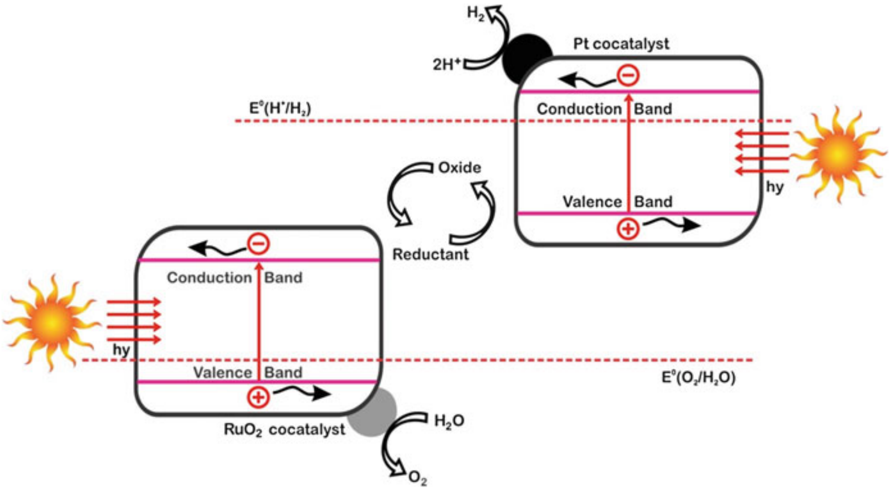

Fig. 2.2 Z-scheme reaction (Dual-bed configuration) on two different solid catalysts (*left* n-type photocatalyst, *right* p-type photocatalyst)

an electron donor of a redox shuttle. This electron donor species of the redox shuttle is further converted into its electron acceptor form by its oxidation through holes. During oxidation process, the electron acceptor is converted back to its initial electron donor stage through accepting electron from the conduction band of the n-type photocatalyst (Fig. 2.2 (left)) as oxidization of water at positive holes takes place.

In the dye-sensitized photoelectrochemical cell [7], the dye molecule in the photoelectrode absorbs visible light radiations. Absorption of the visible light photon causes an excitation of electrons which are carried toward the counter electrode for the reduction reaction. This transfer of electrons takes place via conduction wires. The oxidation reaction takes place at the photoanode. The dye can be regenerated after receiving electrons from water molecule or water oxidation process.

2.4 Standard of Measurements

Analysis of effective standards of measurement of the photocatalyst and photoelectrode is of utmost importance in order to determine efficiency of solar-to-fuel energy process. The common standard of measurements is discussed below.

2.4.1 Solar-to-Hydrogen Efficiency (STH)

The product of the rate of hydrogen production ($\mathrm{r}_{\mathrm{H}_2}$) and gain in Gibbs energy (ΔG) of 237 mol gives output energy as H_2. P_{sun} is defined as the energy flux of the sunlight. The ratio of output energy as H_2 to energy of incident solar light P_{sun} gives solar-to-hydrogen efficiency (STH) [8, 9]:

$$\mathrm{STH} = \frac{\text{Output energy as H}_2}{\text{Energy of incident solar light}} = \frac{\mathrm{r}_{\mathrm{H}_2} \times \Delta\mathrm{G}}{\mathrm{P}_{\mathrm{sun}}} \tag{2.7}$$

Solar irradiation has an energy flux of 1.0×10^3 Wm^{-2} and well-defined spectrum, according to the ASTM-G173 AM1.5 global tilt [1]. Under an external voltage applied to photoelectrochemical cell, the electrical energy has to be subtracted from the energy gain.

Applied bias photon-to-current efficiency (ABPE) is used for two-electrode measurements [8, 9]:

$$\mathrm{ABPE} = \frac{|j| \times (V_{\mathrm{th}} - V_{\mathrm{bias}})}{P_{\mathrm{sun}}} \tag{2.8}$$

where j represents photocurrent density, V_{th} the theoretical water electrolysis voltage (1.23 V), andV_{bias} the applied voltage

2.4.2 Faradaic Efficiency

The ratio of the current contributing to water splitting into hydrogen and oxygen to the observed current is called the faradaic efficiency, η_F, of water splitting [9]:

1. Faradaic efficiency $(\eta_F) = 1$: the photocurrent is contributed to water splitting completely.
2. Faradaic efficiency $(\eta_F) < 1$: part of the current should be attributed to other redox processes rather than water splitting.

2.4.3 Applied-Bias-Compensated Solar-to-Hydrogen (AB-STH) Efficiency

Applied-bias-compensated solar-to-hydrogen (AB-STH) efficiency is given by [8, 9]

$$\mathrm{ABSTH} = \frac{|j| \times \eta_F (V_{\mathrm{th}} - V_{\mathrm{bias}})}{P_{\mathrm{sun}}} \tag{2.9}$$

AB-STH is also known as energy conversion efficiency or quantum efficiency for a general expression of solar to hydrogen via photoelectrochemical water splitting under sunlight. Quantification of the evolved amounts of H_2 and O_2 based on known η_F to avoid side reactions involving hydrogen and oxygen with PEC cells purged with an inert gas is required. Accurate estimation of AB-STH efficiency can be obtained by employing a two electrode system.

2.4.4 Hypothetical Half-Cell Solar-to-Hydrogen (HCSTH) Efficiency

Hypothetical half-cell solar-to-hydrogen (HCSTH) efficiency is used in the three-electrode configuration. It is the product of the potential gain and the photocurrent.

The difference of the potential of a photoanode (photocathode) from the oxygen (hydrogen) equilibrium potential can be calculated by gain in potential by PEC water splitting [8, 9].

At photoanode,

$$\mathrm{HCSTH} = \frac{|j| \times \left(E_{\mathrm{O_2/H_2O}} - E_{\mathrm{RHE}}\right)}{P_{\mathrm{sun}}} \tag{2.10}$$

At photocathode,

$$\text{HCSTH} = \frac{|j| \times \left(E_{\text{RHE}} - E_{\text{H}^+/\text{H}_2}\right)}{P_{\text{sun}}} \tag{2.11}$$

where E_{O_2/H_2O} is equilibrium potentials of oxygen evolution (+1.23 V vs. RHE) and E_{H^+/H_2} is hydrogen evolution (0 V vs. RHE) [5, 6].

There are two ways to identify photocatalytic activity of the water-splitting system:

1. Direct measurement of the amounts of hydrogen
2. Indirect method where the electron is transported from the semiconductor to the water within a certain time period under light irradiation

The units used for measuring the rate of O_2 and H_2 gas evolution are μmol h^{-1} and μmol h^{-1} g^{-1} catalyst.

2.4.5 *Quantum Yield*

The quantum yield is always used to make a direct comparison. Results from different research groups and the photocatalytic hydrogen generation systems for the same catalyst vary as per the different experimental setups. Rate of O_2 and H_2 gas evolution is applied for the comparison purpose [9].

The *real quantum yield* is given by the following equation [9]:

$$\text{Overall quantum yield}(\%) = \frac{\text{Number of reacted electrons}}{\text{Number of absorbed photons}} \times 100\% \tag{2.12}$$

Because of the smaller number of absorbed photons than that of the incident light, real quantum yield is larger than the apparent quantum yield [9]:

$$\text{Apparent quantum yield }(\%) = \frac{\text{Number of reacted electrons}}{\text{Number of incident photons}} \times 100\% \tag{2.13}$$

The number of reacted electrons is calculated from the amount of produced hydrogen gas [9].

It is important to achieve efficient solar energy conversion efficiency at reasonable quantum efficiency. Active participation of photocatalysts and photoelectrodes in water splitting under irradiation of 600 nm is suggested to achieve efficient solar energy conversion efficiency [8]:

$$\text{Solar energy conversion } (\%) = \frac{\text{Output energy as } H_2}{\text{Energy of incident solar light}} \times 100\% \tag{2.14}$$

2.5 Role of Photocatalyst

The focus of this chapter is on water oxidation reaction in water-splitting process. Water oxidation catalyst ensures efficient and sustainable conversion of solar-to-fuel energy cycle. The water oxidation reaction includes four-electron transfer process. Before studying various water oxidation catalysts, it is important to understand the role of photocatalyst in overall water-splitting process and reactions associated with it.

2.5.1 Principle

As we have discussed earlier, semiconductors and metal oxides are highly used as photocatalysts in the water-splitting process. The principle of electrolysis is exploited in the process of decomposition of water molecule into hydrogen and oxygen gas. In addition to this principle, it is necessary to understand the thermodynamics between semiconductor and electrolyte solution.

Earlier in this chapter we have been introduced to the concept of using semiconductor as the photocatalyst. Additionally, the particulate photocatalyst in an electrolyte solution is also discussed. The methods given in this section will familiarize the reader with mechanism of these reactions.

2.5.2 Semiconductor-Liquid Interface

Electronic properties of the semiconductor such as band gap have to be understood in order to design an accurate photocatalyst for water-splitting process. The energy level occupied at a given temperature can be predicted by the Fermi–Dirac statistics. Fermi energy level is related to the collection of electron energy levels at absolute zero temperature. This is the lowest available energy state achieved by electrons basically due to low temperature [9].

The Fermi level of the intrinsic semiconductor is halfway between the conduction band and valence band. However, this level fluctuates on addition of impurities into the pure semiconductor. There are two types of doped semiconductors: n-type semiconductor and p-type semiconductor.

N-type semiconductor consists of electron donor elements and, hence, the Fermi level is higher. N-type photoanode, therefore, has higher Fermi level than that of the solution. The n-type photoanode when brought in contact with the solution, the electrons in the conduction band are accepted by the acceptor. This process continues until Fermi level of n-type photoanode and the solution become equal. Depletion of electrons at the interface of photoanode and solution is observed. Positive particles accumulate in the depletion region and upward bending electric potential gradient is developed. This avoids further electron transfer [9, 10].

On the other hand, Fermi level in the p-type semiconductor is lower than that of the solution. Positive hole concentration in p-type semiconductors is higher relatively. Therefore, the electrons are transferred from solution to the p-type photocathode [10]. The electrons are then accumulated at the interface of the photocathode and solution. The process continues until Fermi level of both p-type photocathode and solution becomes equal. The downward bending electric potential gradient is developed in this system [10].

2.5.3 Z-Scheme Reaction: Innovative Approach

Traditionally, the process of water splitting is carried out in a single metal oxide photocatalyst. This approach encourages oxidation and reduction reaction to occur in conduction and valence band of a single photocatalytic particle. Back reaction of water formation and limited range of absorption of light irradiations as per the band gap of the selected photocatalyst are major drawbacks observed in this system.

In order to overcome these limitations, an innovative approach called as Z-scheme is suggested. In the Z-scheme reaction, two separate photocatalysts are involved according to their suitability for reduction or oxidation reaction of water molecule [9, 10]. Redox couple plays a vital role in this reaction for transfer of electrons. The generated electron during the oxidation reaction on one photocatalyst is passed on to the redox couple. The redox couple forwards this electron to the hydrogen photocatalyst for reduction reaction.

Choice of an appropriate photocatalyst for respective redox reactions is a crucial decision in the Z-scheme reaction. $BaTaO_2N$ (660 nm) can be applied to the hydrogen evolution electrode, while WO_3 or $BiVO_4$ can be used for the oxygen evolution [9]. Ru-load $SrTiO_3$ doped with Rh as a H_2-photocatalyst and $BiVO_4$ as a O_2-photocatalyst with a redox couple is used for a Z-scheme system, which gives a highest average quantum yield of 2.1 % at 420 nm [9]. The pH of the system was observed throughout the photocatalytic reaction. The shift in pH can cause imbalance in the system and lead to undesirable reactions. For example, more acidic pH on decreasing value of pH leads to negative potential in redox couple. As a result, more evolution of the hydrogen is obtained. On the other hand, energy difference between redox couple and oxygen photocatalyst shrinks. The less energy available for oxidation will affect the oxygen evolution. Therefore, it is ideal to maintain neutral pH in Z-scheme reaction.

2.6 Water Oxidation

2.6.1 General

As we have already discussed, water oxidation is the half reaction of the overall water-splitting process. Oxygen is the main by-product of the natural photosynthesis. Oxidation reaction is the crucial step in the water-splitting process as it involves four proton and four electron transfer as well as formation of oxygen–oxygen bonding [11, 13,14]. Moreover, the oxidation reaction in the water-splitting process using photoelectrochemical cell takes place at the photoanode. The reaction at photoanode experiences substantial energy loss due to high potential at oxygen evolving anode. These observations may prove to be barriers in the final product formation. Hence, effective techniques have to be analyzed for sustainable production of oxygen at photoanode.

In this chapter, we will focus on various techniques used for production of "visible light-absorbing photocatalysts" used in water oxidation reaction.

2.6.2 Innovative Techniques: Photocatalysts in Water Oxidation

Artificial photosynthesis is one of the promising techniques used in water-splitting process. However, the photocatalyst in the process plays a key role in the success of artificial photosynthesis [11]. Therefore, in order to increase the efficiency and range of artificial photosynthesis, it is important to develop visible light-absorbing photocatalysts since the visible light spectrum possesses approximately 43 % of solar spectrum [12]. Some of the UV/visible light irradiation-absorbing photocatalysts are discussed in this section.

2.6.2.1 Water Oxidation on TiO_2 Surface

Fujishima and Honda have done substantial work on the photoelectrolysis of water. Most of their work focused on the use of semiconductor metal oxides as a photocatalyst. Amongst all other metal oxides available on earth, TiO_2 has been a special area of interest for both researchers. The chemical and biological inert nature, stability, and cheap cost are attractive features of TiO_2 semiconductor catalyst [15–17]. Furthermore, light absorption range of rutile TiO_2 can be extended from ultraviolet to visible light spectra after chemical doping.

The band gap of rutile TiO_2 is larger as compared to that of WO_3 and Fe_2O_3. The wide band gap of TiO_2 proves to be an obstacle in absorption of visible light and also decreases photoenergy conversion factor to less than 1 % since the UV spectrum is only around 4 % of the whole solar spectrum [18, 20].

The enhancement in the light absorption range improves photoactivity of the catalyst. But, our aim is to improve efficiency of photocatalyst for water oxidation. Therefore, in order to enhance overall photoactivity, it is important to understand the oxidation of water on oxide surfaces.

The reactions taking place at the anode with respect to the surface termination of the TiO_2 face are observed. The types of surface termination under consideration are as follows [19]:

1. Surface with all bridge sites occupied by oxygen ($TiO_2 + 2O_b$)
2. Totally O* covered surface with unsaturated sites also covered by O* ($TiO_2 + 2O_b + 2O^*$)

where * is the reaction site and O_b is the bridging oxygen atom.

Mechanism for water oxidation reaction takes place in four steps with release of one electron per step [19]:

$$H_2O + * \rightarrow HO^* + H^+ + e^- \tag{2.15}$$

$$HO^* \rightarrow O^* + H^+ + e^- \tag{2.16}$$

$$H_2O + O^* \rightarrow HOO^* + H^+ + e^- \tag{2.17}$$

$$HOO^* \rightarrow O_2 + * + H^+ + e^- \tag{2.18}$$

Reactions (2.15, 2.16, 2.17 and 2.18) occur on the surface of rutile TiO_2. In the surface with all bridge sites occupied by oxygen, the electron release sequence starts with reaction between water molecule and free reaction site, resulting into OH* at reaction site. In addition, on the surface of totally O*-covered surface with unsaturated sites also covered by O*, reaction begins with reaction between O* and water molecule, resulting into OOH*. At both reactions, oxygen is evolved along with $4H^+$ and $4e^-$ [19].

It is observed that relative stability of the surfaces is a function of applied bias and pH of the electrolyte. The pH determines thermodynamic stability of the different surface terminations. Also, illumination provides overpotential required for water oxidation. The estimated intrinsic overpotential is between 0.9 and 1.1 eV [19]. It can be concluded that, only anodic bias is required to reduce from H^+ ions to H_2. The overall photo oxidation of water on the ideal rutile TiO_2 surface leads to a conclusion that, moderate overpotential in the range of 0.78 V with zero pH is efficient for water oxidation on rutile TiO_2 surface [19].

2.6.2.2 Cu_2O: A Visible Light Irradiation Photocatalyst

Cuprous oxide (Cu_2O) is a p-type metal oxide semiconductor with the band gap between 2.0 and 2.2 eV [20]. The small band gap energy is beneficial for reduction and oxidation of water under visible light irradiation. Also, its lattice structure is mainly made up of the chains of linear bonds (–O–Cu^I–O–). Therefore, the material

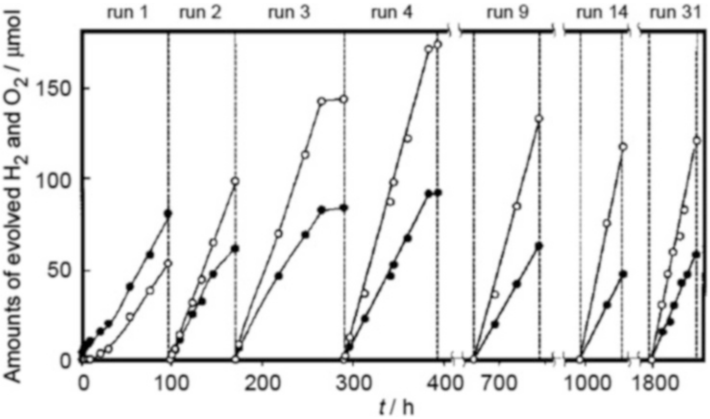

Fig. 2.3 Time courses of H_2 (*open circles*) and O_2 (*filled circles*) evolution in Cu_2O under visible light ($\lambda > 460$ nm) irradiation (Reproduced from Ref. [20] with permission from The Royal Society of Chemistry. ©Royal Society of Chemistry 1998)

containing Cu^I is able to decompose water under visible light irradiation. Hara et al. [20] have conducted a series of experiments on the Cu_2O powder under visible light irradiation.

The Cu_2O powder is the product of the hydrolysis of CuCl in the presence of 1 M Na_3PO_4 (40 cm^3) to a 5 M aqueous NaCl solution containing 0.04 mol of CuCl (400 cm^3). The mixture is vigorously stirred under an Ar flow condition. The resulting yellow precipitate is further heated at 673 K for 24 h in vacuum and boiled in water under Ar atmosphere. The impurity-free Cu_2O powder is thus obtained. The water-splitting experiments are carried out on the mixture of cuprous oxide powder (0.5 g) with 200 cm^3 of distilled water in Pyrex cell [20]. Under visible light irradiation more than 460 nm (300 W Xe lamp with a cutoff filter), a gas chromatograph is applied to measure the amount of evolved gas. The results obtained from this system are presented in Fig. 2.3.

The data analyzes a total of 31 runs of the experiments to understand behavior pattern of hydrogen and oxygen evolution with respect to the time courses. The open circles in Fig. 2.3 stand for evolution of H_2 and filled circles are of evolution of O_2. In the first run of the reaction system, O_2 evolved for 10 h on beginning of the reaction, followed by the H_2 evolution as the reaction proceeded. The evolution of H_2/O_2 ratio increased from 0.8 in first run to 1.8 in 4th run. The final composition of H_2 after 31st run was of 3.8 mmol and that of O_2 was of 1.9 mmol. Also, the pH of the reaction system remained relatively unaffected from before the start of reaction (pH 7.3) to the pH after 31st run (pH 7.1) [20]. The pH reading and the H_2/O_2 evolution ratio are compatible with the initial concentration of the reaction system (0.5 g, 3.5 mmol) [20].

Figure 2.3 also reflects the excess O_2 evolution in the starting runs of the reaction system. As shown in the figure, the observed O_2 evolution is more in run 1 and run

2. This can be attributed to the characteristic of Cu_2O to absorb more oxygen in the bulk and also in the form of O^- and O_2^- on the surface [20]. This results in the p-type semiconducting nature of Cu_2O and confirms its strong oxidation catalyst characteristics. Furthermore, the run 3 and run 4 describe the dependence of O_2 evolution on the reaction system pressure. It is observed that, the H_2 and O_2 evolution slows down in run 3 and 4 when oxygen evolution exceeds 80 μmol which corresponds to the reaction system pressure of 500 Pa. The evolution of O_2 at more than 500 Pa leads to the inhibition in overall water-splitting process [20]. This can be attributed to the photoadsorption of oxygen on the surface of p-type semiconductors on exceeding a certain pressure.

The obtained results from the experiments carried out on the Cu_2O powder reveal the importance of Cu_2O as a visible light irradiation photocatalyst in the overall water-splitting process.

2.6.2.3 $BiVO_4$

Earlier we have discussed TiO_2 as a stable semiconductor photocatalyst. However, large band gaps in TiO_2 formed by O 2p orbital are the problem areas in its direct application as a photocatalyst. Therefore, researchers have directed their attention to a catalyst that avoids O 2p orbital. It is estimated that instead of O 2p orbital, in the $BiVO_4$, 6 s orbital of Bi^{3+} may form its valence band [21]. Its conduction bands are still formed from V 3d orbital. $BiVO_4$ is able to produce O_2 under visible light irradiation, and its photocatalytic activity strongly depends on the crystal form. The band gaps for the three main crystal forms which are monoclinic system with scheelite structure $BiVO_4$ (m-s), tetragonal system with zircon structure $BiVO_4$ (t-z), and scheelite structure $BiVO_4$ (t-s) are reported to be 2.40, 2.34, and 2.90 eV, respectively [21, 22].

$BiVO_4$ in aqueous $AgNO_3$ solution is used as a potential photocatalyst assembly for evolution of oxygen gas. $BiVO_4$ can be formed by calcinating Bi_2O_3 and NH_4VO_3 at 970 K or 1170 K. This material is kept in air for 5 h using alumina crucible [21]. The powdered mixture is then dispersed in the aqueous $AgNO_3$ solution. The photocatalytic activity of this mixture is studied with reference to highly used visible light photocatalyst WO_3.

The reaction cell for this process is made up of Pyrex glass. The light source used in the experiment is an ozone-free 300 W Xe illuminator. Diffuse reflection spectrum of $BiVO_4$ was measured and the onset started at 540 nm. The band gap of this $BiVO_4$ is 2.3 eV [21]. The experiments carried out by Kudo et al. identified that for a cutoff filter of wavelength greater than 560 nm, the oxygen evolution is very less. But for a cutoff filter of wavelength greater than 520 nm, more oxygen evolution is observed. This wavelength range (greater than 520 nm) matches with the wavelength of diffuse diffraction spectrum of $BiVO_4$, that is, 540 nm [21]. This indicates that the $BiVO_4$ photocatalyst can also be treated as an oxygen evolution photocatalyst used in Z-scheme reactions.

In order to confirm the workability of $BiVO_4$ as a photocatalytic oxidation catalyst functioning under the visible light, Kudo [21] compared it with WO_3. The evolution of oxygen on WO_3 and $BiVO_4$ from aqueous $AgNO_3$ solution was tested under the visible light of wavelength greater than 420 nm. The XRD pattern of $BiVO_4$ observed in the reaction was constant even after 50 h [21]. This result confirms chemical stability of $BiVO_4$. Also it was observed that, wavelength range absorbed by $BiVO_4$ is wider than that by WO_3. The setup of gas chromatography was used to determine amount of evolved oxygen [21].

$BiVO_4$ in aqueous $AgNO_3$ solution involves less chemical and structural alterations as compared to that of rutile TiO_2. The mixing of Bi^{3+} with oxides proves to be a step forward in development of visible light-absorbing photo oxidation catalysts [21, 26, 27].

2.6.2.4 Biologically Templated Nanostructures

Extensive research has been carried out on metal oxide colloids as current and potential photocatalysts for water oxidation. The photocatalysts that we have discussed earlier fall under the category of metal oxides. However, the systems involving metal oxides as a photocatalysts highly depend upon certain components such as photosensitizer, electron acceptors, and catalyst. The photosensitizer absorbs visible light radiations and initiates the photocatalytic action [29, 34, 35]. The electron–hole pair transport is thus established, and the repeated action results into an accumulation of four holes in the catalysts which leads to sustainable evolution of oxygen gas. However, the spacing between photosensitizer, electron acceptor, and catalyst is very crucial and has to be maintained at certain ordered structure for efficient energy transfer and electron or hole transport in the water-splitting system. However, it is difficult to create controlled structural system at molecular level.

Nam et al. have suggested a solution to design an artificial water-splitting system. According to these researchers, multiple functional materials can be spatially organized with the help of biological scaffolds for photochemical water splitting. The system suggested in this research consists of a photosensitizer and metal oxide catalyst co-assembled in proximity of M13 virus scaffolds. This structure forms a hierarchically ordered photocatalytic nanostructure. Zn (II) deuteroporphyrin IX 2,4 bis-ethylene glycol (ZnDPEG) is used as a photosensitizer [29]. Iridium oxide, a catalyst with stability under oxidizing conditions, is placed as an oxygen evolution center, and genetically engineered M13 virus serves as scaffolds for growth of IrO_2 through biomineralization approach. IrO_2 nanocatalysts are formed on the surface of M13 virus via aqueous sodium hexachloroiridate as precursor. ZnDPEGs were assembled along with linkage to M13 virus [29, 30].

According to the experimental observations, IrO_2–ZnDPEG nanowires precipitated after evolution of oxygen. Aggregation of photochemical colloidal catalyst is an undesirable outcome [28, 29, 30]. Therefore, porous microgels were introduced as matrix for immobilization of IrO_2–ZnDPEG nanostructures. M13 viruses encapsulated microgels produced by microfluidic device serve as a template for IrO_2 hydrosol clusters and photosensitizer. The photosensitizer was covalently introduced into M13 virus encapsulated by the microgel.

IrO_2–ZnDPEG microgels with radius of 35 and 109 microns were studied in this experiment. It was observed that the lower the ratio of IrO_2–ZnDPEG, the more the evolution of oxygen from microgels [29, 30]. Reuse of the microgel matrix is also studied in order to develop data for efficiency of the prepared oxidation photocatalyst. The regenerated microgels showed approximately 94 % oxygen evolution as that of the fresh microgel used in first cycle. The efficiency of the microgel started to decrease from the fourth cycle as per the experiments [30, 32].

Turnover number (TON) is used as a standard of measurement for oxygen evolution. Turnover number indicates number of water molecules that can be split by the catalyst. It is estimated that IrO_2 hydrosol cluster dispersed with pH11 and dispersed in unconjugated ZnDPEG has TON approx. equal to 180. This number is four times the evolution of oxygen by sole iridium atom. TON approx. equal to 76 is observed in IrO_2 nanowires with unconjugated ZnDPEG. The exposure of the catalyst to water molecule plays key role in this process. This could be due to reduced surface area from hydrosol to nanowires. Significant increase in the turnover number was observed on the introduction of M13 virus into the IrO_2–ZnDPEG matrix on nanowires and hydrosol cluster [29, 31, 33]. However, this type of nanowires containing M13 virus with IrO_2–ZnDPEG showed TON ~ 790, whereas IrO_2–ZnDPEG hydrosol cluster with M13 virus showed TON ~ 310 [29, 30]. Combination of excitonic migration between photosensitizers and close arrangement of photosensitizer with IrO_2 supports the higher turnover number of nanowires containing M13 virus with IrO_2–ZnDPEG [29]. However, these results prove that introduction of M13 virus has resulted into significant improvement in the oxygen evolution [30, 32]. The turnover number has also been calculated to verify ideal amount of photosensitizer [30, 31].

In sum, quantum yield and TON are helpful in determining appropriate assembly of catalyst with photosensitizer. Accurate estimations of these physical quantities can improve water oxidation reaction.

2.7 Photoelectrochemical Cell

Photoelectrochemical cell is one of the basic devices used for the decomposition of water molecule into hydrogen and oxygen [36, 37]. The working and construction of the photoelectrochemical cell is inspired by the normal electrochemical cell. However, it is modified by introduction of photocatalysts and particular electrodes that show ability to absorb visible/UV light.

2.7.1 Principle

The process of water electrolysis is driven by water-splitting photoelectrode devices. An external bias is required for continuous working of water electrolysis. Two-electrode configurations of electrochemical cell are used for these measurements [39, 40].

In case of a back-to-back photoelectrode with no external wiring, the efficiency is calculated by physically collecting the hydrogen and oxygen. The free energy contained in the chemical products is related to the energy of the incoming light. The solar-to-hydrogen production efficiency with inputs of only sunlight and water is calculated by measuring the photocurrent (J) at $V_{\mathrm{app}} = 0$, where V_{app} is the applied voltage measured between the oxygen-evolving photoanode and the hydrogen-evolving photocathode in J-V data.

The efficiencies of a photoanode or photocathode can be calculated separately from the other half of the water-splitting reaction. This way optimization of materials can be done independently. An individual photoelectrode produces the power equal to only a portion of the Gibbs free energy needed to split water.

The efficiency of the photoelectrode can be calculated by using the equation given below [39]:

$$\eta = \frac{J_{\mathrm{mp}} V_{\mathrm{mp}}}{P_{\mathrm{in}}} \tag{2.19}$$

Maximum power point (P_{PA}) and fill factor can be calculated by using equations given below [1, 32]:

$$P_{\mathrm{PA}} = J_{\mathrm{mp}} V_{\mathrm{mp}} \tag{2.20}$$

$$\mathrm{ff} = \frac{J_{\mathrm{mp}} V_{\mathrm{mp}}}{J_{\mathrm{SC}} V_{\mathrm{OC}}} \tag{2.21}$$

where:

η: Efficiency of photoelectrode based on its current–voltage data
V_{mp}: Voltage at the maximum power point
P_{in}: Power of the incoming illumination (in W cm^{-2})
J_{mp}: Current density at the maximum power point
V_{oc}: Open-circuit voltage
J_{sc}: Short-circuit current density
ff: Fill factor

The above formulae support that a semiconductor of band gap between 1.6 and 1.7 eV [39, 44] is required to generate V_{oc} for water-splitting process, whereas in case of voltage-loss mechanism it is around 2 eV.

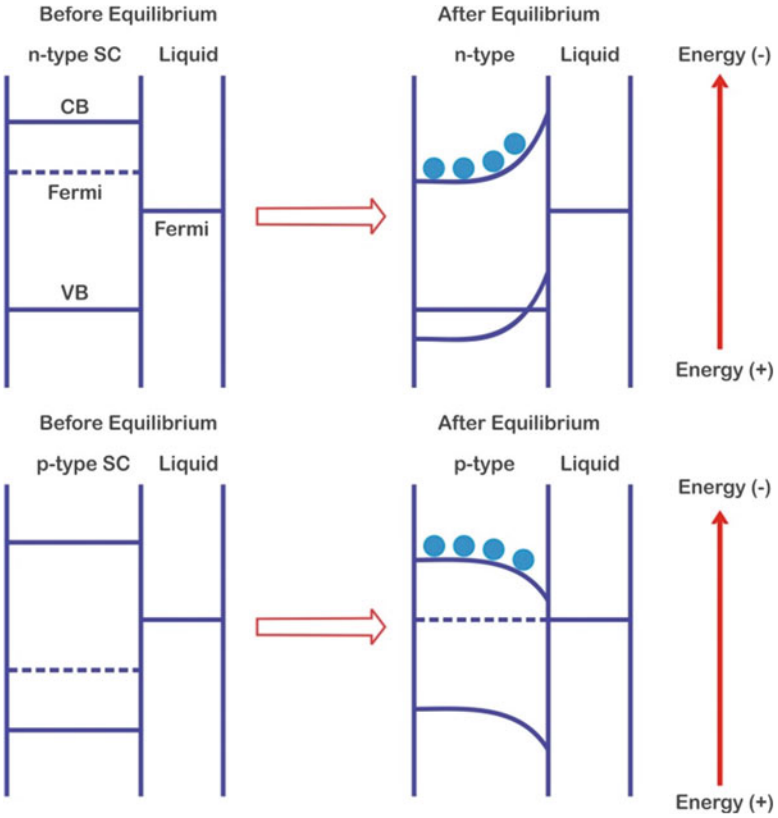

Fig. 2.4 N-type semiconductor before and after illumination (*top*); p-type semiconductor before and after illumination (*bottom*) [1]

2.7.2 Working of Semiconductor Photoelectrochemical Cell

When a semiconductor electrode is immersed in an electrolyte, the semiconductor-liquid junction is thus established. As a result, electrons flow from semiconductor to the electrolyte until the equilibrium is achieved (Fig. 2.4). The electrolyte solution contains redox couple. The charge transfer develops an interfacial electric field and thus electrostatic potential builds up. The electrostatic potential balances the electrochemical potential between electrolyte solution and semiconductor. The electrochemical potential is observed throughout the system after equilibrium stage is achieved. It is also referred as Fermi level [38, 39, 42].

The ideal device for water-splitting process consists of an n-type semiconductor as photoanode and p-type semiconductor as photocathode (Fig. 2.5). The n-type photoanode consists of excess positive charge due to doping. As a result, the electrolyte solution will have excess negative charge after equilibrium with redox couple (O_2/H_2O) [42, 43].

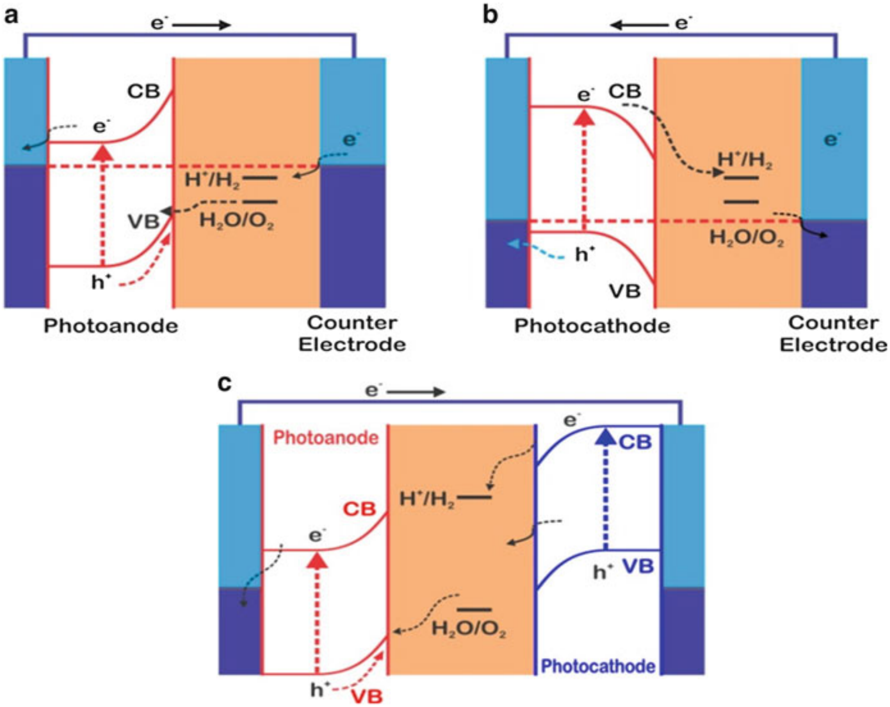

Fig. 2.5 Water splitting in photoelectrochemical cell using (**a**) photoanode (**b**) photocathode and (**c**) photoanode, and photocathode in tandem configuration (Reproduced from Ref. [8] with permission from The Royal Society of Chemistry. ©Royal Society of Chemistry 2014)

This causes formation of depletion region in semiconductor, leading to carrier of positive charge. In the case of photo-illumination, holes move into the electrolyte solution; thus, the band bending is observed. On the other hand, in the case of p-type semiconductor electrodes, solution is positively charged (Fig. 2.4). The difference between initial energy level of Fermi level and electrochemical potential gives electric field strength and potential energy barrier in the semiconductor.

Photogenerated charge carriers are the area of interest for photochemical water-splitting process (Fig. 2.5). These photogenerated electron–hole pairs can be separated effectively. The charge carriers generated have very large mobility (10–-1000 $cm^2\ V^{-1}\ s^{-1}$) in crystalline inorganic semiconductors. The free energy generated by semiconductors can be calculated [42]. But for that, the concept of quasi-Fermi level has to be understood. It is defined as the electrochemical potential of either electrons or holes under nonequilibrium conditions. Illuminated conditions represent nonequilibrium. Population of electrons and holes can be calculated using Fermi–Dirac statistics.

The photoelectrochemical reactions are driven by photo excited electron–hole pair. The potential of Fermi level of the photoelectrode under photo excitation is similar to the potential of electron on counter electrode.

2.7.3 Fabrication of Semiconductor Photoelectrode

The fabrication of semiconductor photoelectrode is one of the key features in photoelectrochemical cell device. It ensures reduction in the series resistance. The high resistance between particles and substrates causes poor photoelectrochemical performance. High resistance also affects the mechanical strength which can be improved by drop casting and electrophoretic deposition by building the layer of powdered semiconductor materials on conductive substrates. Charge transfer between semiconducting particles and a conductive substrate can be improved by necking treatment [1, 39, 42]. In the case of necking treatment, the photoelectrode is treated with the solution of metal salt precursor that is annealed [1, 39]. The metal salt precursor decomposes into the metal oxide, during the heating period [1]. The decomposition into metal oxide helps to bridge the semiconducting particles.

The following approaches are being exploited recently to fabricate photoelectrodes:

1. A particle transfer method
2. A mask anodization method

In the case of the particle transfer method (Fig. 2.6), a glass substrate is covered with a semiconducting powder. This substrate is then sputtered with metals as a contact layer of approximately 100–300 nm. Many such micrometer thick films are deposited continuously by sputtering method. Resin is used to transfer such metal film of proper conductivity and mechanical strength. Loosely bound powder is removed by ultrasonication in water and the primary substrate is peeled off. Thus, after ultrasonication, a monolayer of particle forms metal contactor film. Good electrical contact between the semiconducting particles and the metal layer is established [1, 42].

In the second method (Fig. 2.6), nanorods are grown vertically on conductive substrates. For example, in nitridation of Ta_2O_5 nanorod arrays, a through-mask anodization method is used to grown them. A porous anodic alumina (PAA) mask is created on the top of a Ta substrate. This can be done by anodizing an evaporated Al layer. An aqueous solution of boric acid (0.5 M) is used so that Ta substrate is anodized (Fig. 2.7).

An aqueous solution of boric acid (0.5 M) is used so that Ta substrates are anodized through the PAA mask. Ta^{5+} has the low solubility in the boric acid solution. Also, with volume expansion by anodization of Ta into Ta_2O_5, Ta_2O_5 is packed into the nanochannels of the PAA. This is then masked under a high electrical field. Phosphoric acid (5 %) is applied to PAA mask. Nitrided nanorods

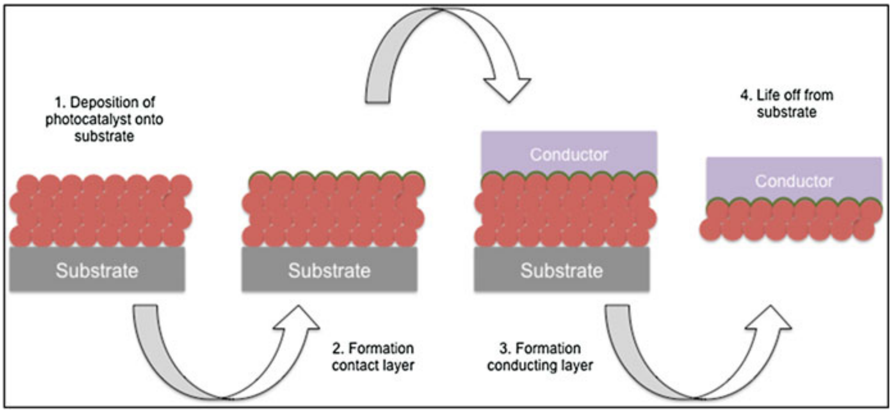

Fig. 2.6 Particle transfer method (Reproduced from Ref. [53] with permission from The Royal Society of Chemistry. ©Royal Society of Chemistry 2012)

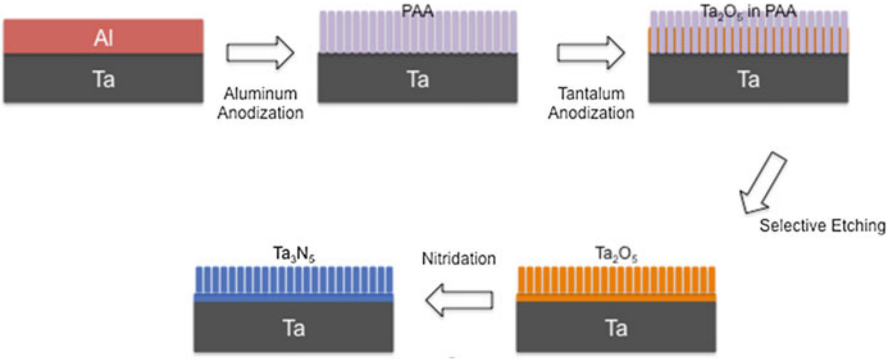

Fig. 2.7 Nanorod photoelectrode fabrication process (Reproduced from Ref. [54] with permission from John Wiley & Sons Ltd)

of Ta_2O_5 arrays are converted into Ta_3N_5 nanorod arrays under a heated NH_3 flow [42, 44].

2.7.4 *Metal Oxide-Based Photoelectrochemical Cell*

Minegishi et al. [44] studied current-potential curves of $LaTiO_2N$ photoanode in an aqueous Na_2SO_4 solution (1 M) at pH = 13.5. In this research, the photoelectrode was prepared using Ta and Ti layers as the contact layer and conductor layer, respectively. The particle transfer method was thus applied. Oxygen evolution catalyst IrO_2 was applied for modifying surface of the photoanode [42]. It was observed that, $LaTiO_2N$ has conduction band which is more negative than the equilibrium potential of hydrogen evolution. The results were confirmed due to anodic photocurrent below 0 V vs. RHE [42].

Most of the oxides, nitrides, and sulfides have anion defects and hence are n-type semiconductors. Molecular beam epitaxy (MBE) is used to prepare $CuGaSe_2$ photoelectrodes on a Mo-coated glass substrate which was suggested by Moriya et al. Hydrogen evolution reaction was initiated by modifying surface with Pt. Because of hydrogen evolution, cathodic photocurrent observed was below ca. 0.7 V vs. RHE [42, 44]. CdS forms a good p-n heterojunction with $CuGaSe_2$; hence, the photocurrent was noticeably improved. This indicates that band formation between CdS and $CuGaSe_2$ is important to raise photocurrent.

Another example is of n-type TaON photoelectrode coated with p-type semiconductor $CaFe_2O_4$. This newly formed p-n heterojunction photoelectrochemical cell enhances photocurrent during the oxygen evolution.

In general, splitting of water by only light energy is possible by combining p-type photoelectrodes in with n-type photoelectrodes. Such system can split water without electrical power given that the photocurrents of the photoanode and photocathode are balanced at a certain potential.

2.7.5 Dye-Sensitized Photoelectrochemical Cell

Dye-sensitized photoelectrochemical cell is used to split water under visible light. For example, an O_2 evolution catalyst is formed by hydrated iridium oxide ($IrO_2 \cdot nH_2O$) nanoparticles attached to Ru-complex sensitizer molecules. An excited electron from LUMO is injected into the conduction band of TiO_2. The outer circuit transfers this electron to a counter electrode (Pt). The water is then reduced to form hydrogen gas [41]. After water oxidation to O_2, the dye returns to the ground state on accepting an electron from the $IrO_2 \cdot nH_2O$ nanoparticle.

An example of water-splitting dye-sensitized photoelectrochemical cell will help us to understand working of dye-sensitized photoelectrochemical cell. A recent development in the photocatalytic system is semiconductor particles of oxynitride. As we have already mentioned in this chapter, hydrated iridium oxide can be used as an effective water oxidation catalyst. The Ru(III)tris(bipyridine) is generated photochemically and helps to carry out oxidation reaction. Recently, it has been discovered that the size and polydispersity of colloidal $IrO_2 \cdot nH_2O$ particles (10–30 nm) can be decreased to 1–5 nm by using bidentate carboxylic acid stabilizers [42]. Effective stabilizers such as ruthenium polypyridyl dyes modified with bidentate carboxylates are used for the size and polydispersity modifications. It is reported that it causes significant increase in the rate of electron transfer for chemisorbed dyes on $IrO_2 \cdot nH_2O$ (in the range of $10^3\ s^{-1}$) than that for unbound dyes in the presence of $IrO_2 \cdot nH_2O$ colloids [42].

It is important to create a connection between $IrO_2 \cdot nH_2O$ particles and a metal oxide semiconductor. Therefore, a dye that serves as both sensitizer component and a molecular bridge such as dye 1 was created. In dye 1 phosphonates are chemically

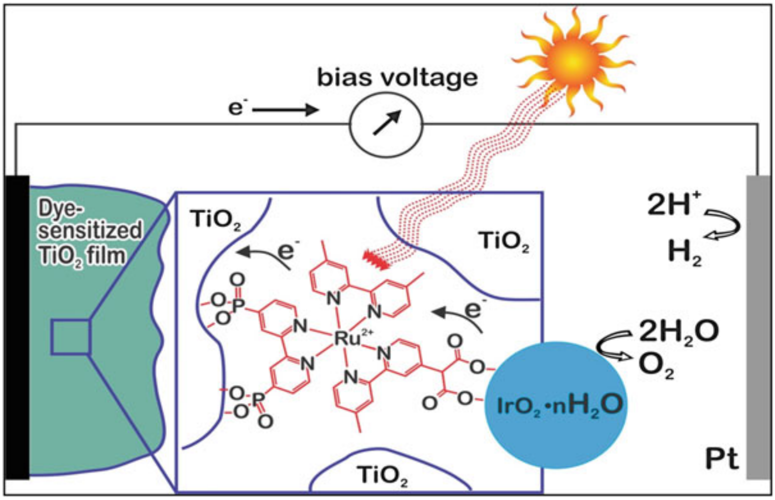

Fig. 2.8 Assembly of water splitting in dye-sensitized solar cell (Reproduced from Ref. [42] with permission from American Chemical Society. Copyright © 2009 American Chemical Society)

selective for TiO_2 and malonate group is selective for $IrO_2 \cdot nH_2O$ particles. A well-dispersed particle of $IrO_2 \cdot nH_2O$ approximately 2 nm in diameter has been successfully produced by using dye 1 [41, 42]. Therefore, the combination of dye–-$IrO_2 \cdot nH_2O$ colloid complex when absorbed onto anatase TiO_2 results in rapid injection of electrons. This provides us with general factors involved in dye production [42].

It is a known fact that the reaction of water splitting can be exploited most when absorption of visible light radiation is augmented.

This idea of water splitting with sensitized oxide semiconductor induced by visible light absorption can be implemented practically in a photoelectrochemical cell. The main advantage of mimicking electrochemical cell is that, in the assembly of electrochemical cell, the evolution of H_2–O_2 can be separated in physically different compartments.

Figure 2.8 shows assembly of a water-splitting dye-sensitized solar cell. The dye-sensitized photochemical cell consists of two electrodes as in electrochemical cell. The difference in the two cells is that, in dye-sensitized photochemical cell, the dye sensitizer is an add-on feature. The photoanode is made up of mesoporous TiO_2 electrode. The dye used in this experimental setup is a monolayer of $IrO_2 \cdot nH_2O$ particles. The $[Ru(bpy)_3]^{2+}$ sensitizer is used. The $IrO_2 \cdot nH_2O$ particle dye is sensitizer capped. The $[Ru(bpy)_3]^{2+}$ is modified with phosphonate and malonate ligands [42, 44]. This modification in the 4th position of 2,2′-bipyridyl ligands helps to absorb TiO_2 and in $IrO_2 \cdot nH_2O$, respectively. The cathode is of platinum wire electrode. Also, the bias voltage of $\geq$300 mV has to be applied for efficient water splitting in the water-splitting dye-sensitized solar cell (DSSC) [42, 46].

The electron donor is Ir(IV). Therefore, the oxidized sensitizer reduces at a slower time scale. However, the rate of electron transfer (2 ms) of this process fails to compete with fast charge recombination reaction of photo-injected electron (0.37 ms) and Ru

(III). Each of the $IrO_2 \cdot nH_2O$ particle in this reaction is sensitizer capped. There are around 10–20 molecules of sensitizer that are capped onto single $IrO_2 \cdot nH_2O$ particle [42]. Only a few of these complexes can bind to the TiO_2 surface. The remaining are subjected to excited state quenching by electron transfer to Ir(IV). As a result of this, steady-state quantum efficiency of this cell is about 1 % [42, 47].

There are few rectifications suggested in this system by researchers for obtaining better efficiency. It is suggested that, in order to increase the quantum yield of this process, the catalyst particle should be connected to only one sensitizer molecule [45, 48]. This way, each sensitizer can bind efficiently with TiO_2 and $IrO_2 \cdot nH_2O$ particle. Another drawback of this system is current decay due to pH drop in the TiO_2 film. This current decay due to pH drop is observed due to the protons created by oxidation reaction. The more effective buffer can avoid current decay by penetrating into the porous film.

In spite of few limitations, the water-splitting dye-sensitized solar cell convinces the use of sensitizer-based photosystem in water-splitting reaction. The overall water-splitting dye-sensitized solar cell system can be improved by increasing its quantum yield to unity [41, 49, 50, 51, 52].

2.7.6 *$CuWO_4$–WO_3 Composite Electrode in the Presence of $[Fe(CN)_6]^{3-}$*

The WO_3 is a traditionally used photoanode material for solar-driven water oxidation reactions. WO_3 metal oxide semiconductor consists of the sufficiently positive valence band edge for production of oxygen. However, the large band gap and instability under neutral and basic conditions limit the use of WO_3 as an oxidation photocatalyst. These limitations can be overcome by forming a first row transition-metal tungstate compounds. $CuWO_4$ is one of the best suggested and well-researched alternatives for WO_3. The band gap of $CuWO_4$ (2.25 eV) is smaller than that of WO_3 (2.7 eV). As a result, $CuWO_4$ shows shift to longer wavelengths as compared to WO_3 in absorption spectrum. Therefore, the yellow electrodes of $CuWO_4$ absorb more visible light irradiations in contrast to the white color electrodes of WO_3 which absorb more light in the UV region [55]. Another advantage of using $CuWO_4$ electrodes is their stability at the neutral pH (approximately 8). The stability at neutral pH is important for use of the $CuWO_4$ electrodes as photocatalysts at industrial level.

The efficiency of the solar energy conversion can be improved by using the photoelectrochemical cell. The redox mediator $[Fe(CN)_6]^{3-}$ is used to transfer electrons between $CuWO_4$–WO_3 photoanode and Pt photocathode as shown in the Fig. 2.9. The reactions (2.22), (2.23), and (2.24) are observed in the Fig. 2.9 [55]:

$$2H_2O \rightarrow O_2 + 4H^+ + 4e^- \quad E^\circ = 0.82\ \text{V} \tag{2.22}$$

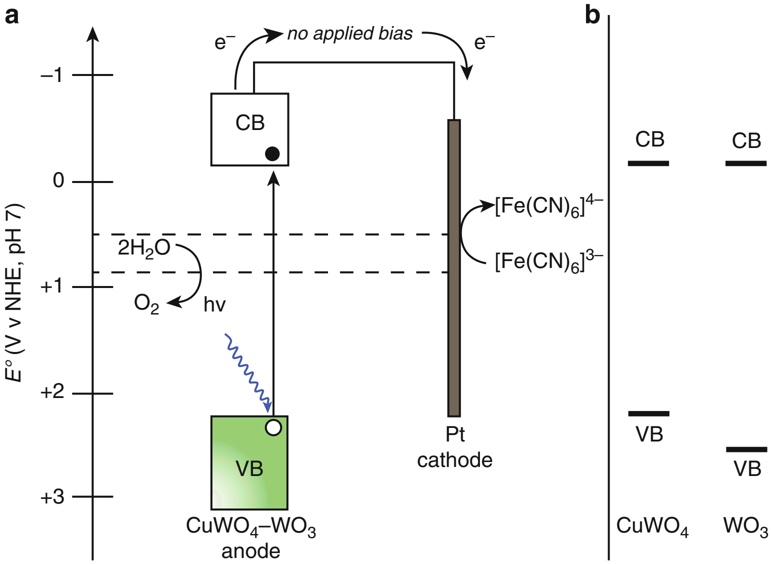

Fig. 2.9 (**a**) Band structure of $CuWO_4$–WO_3 composite electrodes superimposed with the chemical potentials for water oxidation and ferricyanide reduction at pH 7; (**b**) Measured band edges of 1.2:1 W:Cu and for pure WO_3 for comparison purposes (Reproduced from Ref. [55] with permission from American Chemical Society. Copyright © 2012 American Chemical Society)

$$4\left[\mathrm{Fe(CN)_6}\right]^{3-} + 4\mathrm{e}^- \rightarrow 4\left[\mathrm{Fe(CN)_6}\right]^{4-} \quad \mathrm{E}^\circ = 0.44\ \mathrm{V} \tag{2.23}$$

$$2\mathrm{H_2O} + 4\left[\mathrm{Fe(CN)_6}\right]^{3-} \rightarrow \mathrm{O_2} + 4\mathrm{H}^+ + \left[\mathrm{Fe(CN)_6}\right]^{4-} \quad \mathrm{E}^\circ = -0.38\ \mathrm{V} \tag{2.24}$$

As indicated by overall reaction (2.24), the use of $[Fe(CN)_6]^{3-}$ decreases the overall E° to −0.38 V for overall water-splitting process at pH 7. The overall reaction can be illustrated briefly with the help of Fig. 2.9. The water is oxidized at $CuWO_4$–WO_3 photoanode [55]. The reaction of oxidation is followed by the reduction of redox mediator $[Fe(CN)_6]^{3-}$. The reduction potential of $[Fe(CN)_6]^{3-}$ is more positive than that of the conduction band edge of the $CuWO_4$–WO_3 composite photoelectrode. Finally, the redox mediator $[Fe(CN)_6]^{3-}$ is able to receive electron from photoanode through external wire [55]. This half reaction is a substitute for water reduction or H_2 production. The entire reaction scheme indicates that $CuWO_4$–WO_3 composite electrodes in the presence of $[Fe(CN)_6]^{3-}$ are capable of water splitting with no applied bias [55].

2.8 Summary

The water oxidation reaction is the main part of the overall water-splitting process. The choice of oxidation catalyst without degradation during continuous exchange of four electron–hole pair is the most important step in the water oxidation process.

An efficient water oxidation catalyst is the one that can easily form O–O bond and simultaneously allow release of dioxygen from active sites. This chapter presents the mechanism and working of overall water-splitting process. Then the chapter mainly concentrates on the water oxidation reaction. As we have already discussed in this chapter, the photocatalyst is a key element in oxidation; so we summarized various available water oxidation catalysts in the research field. Inorganic and organic photocatalysts are described for understanding of their role in photocatalytic water oxidation process. In addition to this, effective standard of measurements is discussed. Harnessing of solar energy in the form of hydrogen is undoubtedly one of the most profitable and promising techniques. Intense research in the field of solar energy shows potential to solve energy crisis faced worldwide.

References

1. Nuraje N, Asmatulu R, Kudaibergenov S (2012) Metal oxide-based functional materials for solar energy conversion: a review. Curr Inorg Chem 2(2):1–23
2. Rostrup-Nielsen J, Christianse L (2011) Concepts in syngas manufacture, Catalytic science series (10). London: Imperial College Press.
3. Fujishima A, Honda K (1972) Electrochemical photolysis of water at a semiconductor electrode. Nature 238(5358):37–38
4. Duan L (2011) Artificial water splitting: ruthenium complexes for water oxidation. KTH Chemical Science and Engineering, Royal Institute of Technology, Stockholm
5. Koroidov S (2014) Water splitting in natural and artificial photosynthetic systems. Umeå University, Umeå, p 96
6. Ollis DF, Pelizzetti E, Serpone N (1991) Photocatalyzed destruction of water contaminants. Environ Sci Technol 25(9):1522–1529
7. Kudo A, Miseki Y (2009) Heterogeneous photocatalyst materials for water splitting. Chem Soc Rev 38(1):253–278
8. Hisatomi T, Kubota J, Domen K (2014) Recent advances in semiconductors for photocatalytic and photoelectrochemical water splitting. Chem Soc Rev 43(22):7520–7535
9. Lei Y, Asmatulu R, Nuraje N (2015) Photo-active metal oxide nanomaterials for water splitting. ScienceJet 4:169
10. Chen X, Shen S, Guo L, Mao S (2010) Semiconductor-based photocatalytic hydrogen generation. Chem Rev 110(11):6503–6570
11. Joya KS, Joya YF, Ocakoglu K, van de Krol R (2013) Water-splitting catalysis and solar fuel devices: artificial leaves on the move. Angew Chem Int Ed Engl 52(40):10426–10437
12. Mills A, Hunte S (1997) An overview of semiconductor photocatalysis. J Photochem Photobiol A Chem 108:1–35
13. Kanan M, Nocera D (2008) In situ formation of an oxygen-evolving catalyst in neutral water containing phosphate and Co^{2+}. Science 321(5892):1072–1075
14. Tagore R, Crabtree R, Brudvig G (2008) Oxygen evolution catalysis by a dimanganese complex and its relation to photosynthetic water oxidation. Inorg Chem 47:1815–1823
15. Shibata M, Kudo A, Tanaka A, Domen K, Maruya K, Onishi T (1987) Photocatalytic activities of layered titanium compounds and their derivatives for H_2 evolution from aqueous methanol solution. Chem Lett 16:1017–1018
16. Park JH, Kim S, Bard AJ (2005) Novel carbon-doped TiO_2 nanotube arrays with high aspect ratios for efficient solar water splitting. Nano Lett 6(1):24–28

17. Bonetta S (2013) Photocatalytic bacterial inactivation by TiO_2-coated surfaces. AMB Express 3(1):1–8
18. Khan S, Al-Shahry M, Ingler W (2002) Efficient photochemical water splitting by a chemically modified n-TiO_2. Science 297(5590):2243–2245
19. Valde's Z, Kroes GJ, Rossmeisl J, Nørskov JK (2008) Oxidation and photo-oxidation of water on TiO_2 surface. J Phys Chem C 112:9872–9879
20. Hara M, Kondo T, Komoda M, Ikeda S, Shinohara K, Tanaka A, Kondo J, Domen K (1998) Cu_2O as a photocatalyst for overall water splitting under visible light irradiation. Chem Commun 3:357–358
21. Kudo A, Ueda K, Kato H, Mikami I (1998) Photocatalytic O_2 evolution under visible light irradiation on $BiVO_4$ in aqueous $AgNO_3$ solution. Catal Lett 53:229–230
22. Seabold JA (2014) Efficient solar photoelectrolysis by nanoporous Mo:$BiVO_4$ through controlled electron transport. Phys Chem Chem Phys 16(3):1121–1131
23. Aroutiounian VM, Arakelyan VM, Shahnazarya GE, Stepanyan GM, Turner JA, Khaselev O (2002) Investigation of ceramic Fe_2O_3<Ta> photoelectrodes for solar energy photoelectrochemical converters. Int J Hydrog Energy 27:33–38
24. Konduri R, Ye H, MacDonnell FM, Serroni S, Campagna S, Rajeshwar K (2002) Ruthenium photocatalysts capable of reversibly storing up to four electrons in a single acceptor ligand: a step closer to artificial photosynthesis. Angew Chem Int Ed 41:3185–3187
25. Reber JF, Rusek M (1986) Photochemical hydrogen production with platinized suspensions of cadmium sulfide and cadmium zinc sulfide modified by silver sulfide. J Phys Chem 90 (5):824–834
26. Zhong DK (2009) Solar water oxidation by composite catalyst/α-Fe_2O_3 photoanodes. J Am Chem Soc 131(17):6086–6087
27. Kudo A, Kato H (1997) Photocatalytic activities of $Na_2W_4O_{13}$ with layered structure. Chem Lett 26(5):421–422
28. Domen K, Kudo A, Shinozaki A, Tanaka A, Maruya K-I, Onishi T (1986) Photodecomposition of water and hydrogen evolution from aqueous methanol solution over novel niobate photocatalysts. J Chem Soc Chem Commun 4:356–357
29. Nam YS (2010) Biologically templated photocatalytic nanostructures for sustained light-driven water oxidation. Nat Nanotechnol 5(5):340–344
30. Nam YS (2010) Virus-templated assembly of porphyrins into light-harvesting nanoantennae. J Am Chem Soc 132:1462–1463
31. Yanagida T, Sakata Y, Imamura H (2004) Photocatalytic decomposition of H_2O into H_2 and O_2 over Ga_2O_3 loaded with NiO. Chem Lett 33(6):726–727
32. Jun K (2011) Iron-oxide catalyzed silicon photoanode for water splitting. Thesis (PhD) Massachusetts Institute of Technology, Department of Mechanical Engineering, pp 130–139
33. McDaniel ND, Coughlin FJ, Tinker LL, Bernhard S (2008) Cyclometalated iridium(III) aquo complexes: efficient and tunable catalysts for the homogeneous oxidation of water. J Am Chem Soc 130:210–217
34. Hinnemann B, Moses PG, Bonde J, Jørgensen KP, Nielsen JH, Horch S, Chorkendorff I, Nørskov JK (2005) Biomimetic hydrogen evolution: MoS_2 nanoparticles as catalyst for hydrogen evolution. J Am Chem Soc 127(15):5308–5309
35. Brimblecombe R, Swiegers GF, Dismukes GC, Spiccia L (2008) Sustained water oxidation photocatalysis by a bioinspired manganese cluster. Angew Chem Int Ed 47:7335–7338
36. Benniston AC, Mackie PR, Harriman A (1998) Artificial photosynthesis: mimicking redox asymmetry. Angew Chem Int Ed 37:354–356
37. Tachibana Y (2012) Artificial photosynthesis for solar water-splitting. Nat Photon 6 (8):511–518
38. Eisenberg R, Gray HB (2008) Preface on making oxygen. Inorg Chem 47:1697–1699
39. Fahrenbruch AL, Bube RH (1983) Fundamentals of solar cells. Academic Press, New York
40. Walter MG, McKone JR, Boettcher SW, Mi Q, Santori EA, Lewis NS (2010) Solar water splitting cells. J Am Chem Soc 110:6446–6473

41. Shimidzu T, Iyoda T, Koide Y (1985) An advanced visible-light-induced water reduction with dye-sensitized semiconductor powder catalyst. J Am Chem Soc 107(1):35–41
42. Youngblood WJ, Lee SHA, Maeda K, Mallouk TE (2009) Visible light water splitting using dye-sensitized oxide semiconductors. Acc Chem Res 42:1966–1973
43. Bard AJ, Fox MA (1995) Artificial photosynthesis: solar splitting of water to hydrogen and oxygen. Acc Chem Res 28(3):141–145
44. Moriya M, Minegishi T, Kumagai H, Katayama M, Kubota J, Domen K (2013) Stable hydrogen evolution from CdS-modified $CuGaSe_2$ photoelectrode under visible-light irradiation. J Am Chem Soc 135(10):3733–3735
45. Gratzel M (2001) Photoelectrochemical cells. Nature 414(6861):338–344
46. Brixner T (2005) Two-dimensional spectroscopy of electronic couplings in photosynthesis. Nature 434:625–628
47. Izawa S (1969) The role of chloride ion in photosynthesis III. The effect of artificial electron donors upon electron transport. Biochim Biophys Acta, Bioenerg 180(2):388–398
48. Hoshikawa T, Yamada M, Kikuchi R, Eguchi K (2005) Impedance analysis of internal resistance affecting the photoelectrochemical performance of dye-sensitized solar cells. J Electrochem Soc 152(2):E68–E73
49. Dloczik L, Ileperuma O, Lauermann I, Peter E, Ponomarev A, Redmond G, Shaw NJ, Uhlendorf I (1997) Dynamic response of dye-sensitized nanocrystalline solar cells: characterization by intensity-modulated photocurrent spectroscopy. J Phys Chem B 101 (49):10281–10289
50. Furube A, Shiozawa T, Ishikawa A, Wada A (2002) Transient absorption spectroscopy on photocatalysts: $K_4Nb_6O_{17}$ and $Ru(bpy)^{32+}$-intercalated $K_4Nb_6O_{17}$ thin films. J Phys Chem B 106(12):3065–3072
51. Umena Y, Kawakami K, Shen JR, Kamiya N (2011) Crystal structure of oxygen-evolving photosystem II at a resolution of 1.9 angstrom. Nature 473:55–60
52. Osterloh FE, Parkinson BA (2011) Recent developments in solar water-splitting photocatalysis. MRS Bull 36(01):17–22
53. Minegishi T, Nishimura N, Kubota J, Domen K (2013) Photoelectrochemical properties of $LaTiO_2N$ electrodes prepared by particle transfer for sunlight-driven water splitting. Chem Sci 4:1120–1124
54. Li Y, Takata T, Cha D, Takanabe K (2013) Vertically aligned Ta_3N_5 nanorod arrays for solar-driven photoelectrochemical water splitting. Adv Mater 25:125–131
55. Yourey J, Kurtz J, Bartlett B (2012) Water oxidation on a $CuWO_4$-WO_3 composite electrode in the presence of $[Fe(CN)_6]^{3-}$: towards solar Z-scheme water splitting at zero bias. J Phys Chem C 116:3200–3205

Chapter 3
Heteropolyacid-Based Heterogeneous Photocatalysts for Environmental Application

Elisa I. García-López, Giuseppe Marcì, and Leonardo Palmisano

Abstract Polyoxometalates (POMs) are a wide class of discrete nanosized transition metal–oxygen clusters. The synthesis of POMs has received great interest not only because they present intriguing architectures but also because they have potential applications in catalysis, medicine, electrochemistry, materials design or models for self-assembling nanoscale systems. Recently, POMs have also been studied as green and cheap photocatalysts. The potentialities of POMs are attributed to their unique structural features; indeed, POMs are photostable and non-toxic, have oxygen-rich surfaces and excellent redox properties and possess photochemical characteristics similar to those of the semiconductor photocatalysts. Heteropolyacids (HPAs), including their anions, are a POM subclass. In this chapter their photocatalytic properties when they are immobilized on various supports are described citing a part of the existing literature.

Keywords Photocatalysis • Heteropolyacids • Polyoxometalates • Inorganic clusters • Semiconductors

3.1 Introduction

Since Fujishima and Honda achieved UV light-induced water cleavage using a TiO_2 photoanode [1], photocatalysis has attracted significant attention because of its promising applications, mainly focused on the degradation of organic and inorganic pollutants both in vapour and liquid phase under mild experimental conditions [2–4]. The recent scientific efforts in this field have been addressed to increase the selectivity of the photocatalytic process for partial oxidation [5] or synthetic purposes [6]. The semiconductor metal oxides that are traditionally used as photocatalysts, as, for instance, TiO_2, have evidenced several drawbacks. Among

---

E.I. García-López (✉) • G. Marcì • L. Palmisano
"Schiavello-Grillone" Photocatalysis Group. Dipartimento di Energia, Ingegneria dell'informazione e modelli Matematici (DEIM), Università di Palermo, Viale delle Scienze, 90128 Palermo, Italy
e-mail: elisaisabel.garcialopez@unipa.it

J.C. Colmenares, Y.-J. Xu (eds.), *Heterogeneous Photocatalysis*, Green Chemistry and Sustainable Technology, DOI 10.1007/978-3-662-48719-8_3

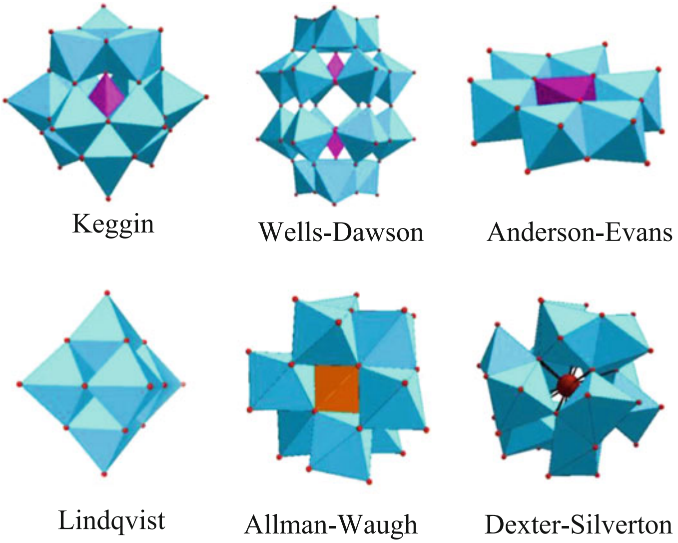

Fig. 3.1 Polyhedral representation of some classical POM structures

them we can cite the small amount of photons absorbed in the visible region, the high recombination rate for the photoproduced electron–hole pairs, the difficulty to enhance the activity by loading or doping and the deactivation in the absence of water vapour, particularly in the gas–solid regime for the degradation of aromatics. All these drawbacks account for the difficulties to improve the photocatalytic system [7]. Consequently, strong efforts have been devoted to develop alternative materials [8]. In this context relatively very low attention has been focused on the use of polyoxometalates or polyoxometalate-based materials as heterogeneous photocatalysts. These clusters exhibit interesting physico-chemical properties that allow their wide use in catalysis, materials science, analytical chemistry, surface and interface science, medicine and life science and electro-, photo- and magnetic chemistry [9]. The large number of structural types of POMs can be divided in three classes: heteropolyanions (HPAs), isopolyanions (IPAs) and Mo-blue- and Mo-brown-reduced POM centres [10]. Several types of HPAs are known, including acids and their salts; however, according to Pope and Muller [11], it is convenient to classify them starting from the symmetrical 'parent' polyanion, i.e. Keggin, Wells–Dawson, Anderson–Evans or Dexter–Silverton and other structures as reported in Fig. 3.1. In general, we can define POMs as a class of discrete anionic metal oxides of groups 5 and 6 constructed via the condensation of metal oxide polyhedra (MO_x, where M can be W(VI), Mo(VI), V(V), Nb(V), Ta(V), etc.) [11, 12]. The metal atoms are referred to as addenda atoms. The addenda atoms include those that can change their coordination with oxygen from four to six because the MO_x polyhedra condense in solution upon acidification. Although oxygen is the main ligand that coordinates with the addenda atoms, other atoms/groups such as sulphur, bromine, nitrosyl and alkoxy are also reported in POM clusters [13]. When the POM frameworks exclusively contain the addenda metals (from groups 5 and/or 6) and oxygen, the clusters are called isopolymetalates or isopolyanions (IPAs), such as the Lindqvist-type anion $[M_6O_{19}]^{2-}$. When the POMs include additional elements along with the addenda metals and oxygen, they are known as heteropoly complexes or heteropolyanions (HPAs) which can be formed via condensation of MO_x polyhedra around the central heteroatom. Many different elements can act as heteroatoms in heteropoly complexes with various coordination numbers: 4-coordinate (tetrahedral) in Keggin and Wells–Dawson structures (e.g. PO_4^{3-}, SiO_4^{4-} and AsO_4^{3-}), 6-coordinate (octahedral) in Anderson–Evans structures (e.g. $Al(OH)_6^{3-}$ and TeO_6^{6-}) and 12-coordinate (Silverton) in $[(UO_{12})Mo_{12}O_{30}]^{8-}$.

In this chapter we will only treat the Keggin structure, the first to be characterized and the most used in heterogeneous photocatalysis. Keggin $\{XM_{12}O_{40}\}^{-y}$ anions include a heteroatom, X in the $XO_4{}^{-}$, that could be PO_4^{3-} or SiO_4^{3-} and the addenda atom, commonly W or Mo. The HPA tungstophosphates are the largest POM subclass. The Keggin structure, for instance, in the polyanion $[PW_{12}O_{40}]^{3-}$, can be described as an assembly of a central tetrahedron of oxygen with phosphorus in the centre and 4 peripheral $[W_3O_{13}]$ blocks that complete 12 octahedra in total, whose centres are occupied by tungsten. In each $[W_3O_{13}]$ block, three octahedra are connected by an edge of oxygens, and each block shares with an oxygen each of the other blocks as well as the central tetrahedron. This cluster has a diameter of ca. 1.2 nm [14–16]. The current research is often focused on the HPA functionalization in order to covalently attach these clusters to organic or inorganic species. To this aim the first step is the removal of one or several metal 'octahedra' from the original HPA in order to generate the so-called lacunary species. In a non-lacunary cluster, i.e. the plenary structure, the negative charge is delocalized over the entire structure, whereas in the lacunary HPAs the oxygen atoms are more nucleophilic and hence more reactive towards electrophilic organic and inorganic groups to form covalent bonds. The lacunary HPAs can also assemble to form new species. In general HPAs are prepared in aqueous medium by acidification of a solution containing the parent species, but the preparation conditions can give rise to a large family of compounds. The variables are (i) concentration/type of metal oxide anions, (ii) pH and type of acid, (iii) type and concentration of electrolyte, (iv) heteroatom concentration, (v) possibility to introduce additional ligands, (vi) reducing agent and (vii) temperature and solvent [10]. As an example, the Keggin cluster can be obtained by a simple polycondensation reaction in an acidic medium between the phosphate (or silicate) and tungstate ions:

$$PO_4^{3-} + 12WO_4^{2-} + 24H^+ \rightarrow PW_{12}O_{40}^{3-} + 12H_2O \qquad (3.1)$$

The heteropolyanion itself forms the so-called primary structure (Fig. 3.2a corresponding also to the Keggin cluster in Fig. 3.1), whereas in the solid material it is present the anionic cluster, the countercation and also some polar molecules, such as water or alcohols. The secondary structure is formed by the union of several primary units and the assembly neutralized by countercations (H^+ or monovalent cations such as Na^+, NH_4^+, Cs^+). Primary structures form secondary rather mobile

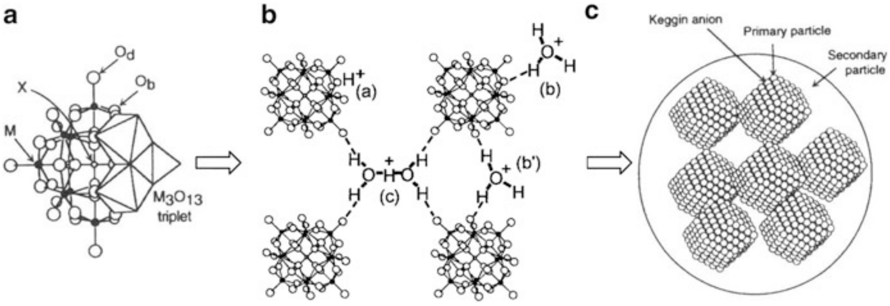

Fig. 3.2 Structural hierarchy of heteropoly compounds: (**a**) Keggin cluster (primary particle), (**b**) secondary structure and (**c**) tertiary structure (texture: particle size, porosity, surface area, etc.) (Adapted with permission from Ref. [16]. Copyright 2001, Royal Society of Chemistry)

structures by interacting with polar molecules as water which are present into the bulk of crystallites giving rise to the protonated clusters (see Fig. 3.2b). The primary structure of $H_3PW_{12}O_{40}$ presents a molecular dimensions of ca. 11.7 × 11.7 Å [17]. The secondary structures condense in small particles of different sizes that can exceed several tens of nanometres. The countercation H^+ appears as a protonated dimer of water in the form of dioxonium $H_5O_2{}^+$. Each $H_5O_2^+$ links four $[PW_{12}O_{40}]^{3-}$ anions, forming with them hydrogen bonds involving terminal O atoms [18], as reported in Fig. 3.2b.

The presence of water in the secondary structure is paramountly important; for instance, considering the use of HPAs as catalysts, water influences the acidity and the adsorption properties of HPAs and consequently their catalytic activity [14–16]. HPAs contain up to 30 H_2O molecules of crystallization per anion, which desorb progressively by increasing the temperature. The solid becomes completely dehydrated at ca. 350–500 °C and dioxonium is removed at ca. 150–200 °C [18]. HPAs are thermally unstable and in particular the thermal stability of the Keggin structure decreases in the following order: $H_3[PW_{12}O_{40}] > H_3[SiW_{12}O_{40}] > H_3[PMo_{12}O_{40}] > H_3[SiMo_{12}O_{40}]$. Anyway, the thermal stability can be enhanced by the formation of appropriate salts [19]. HPAs possess strong acidity both in solid state and in solution that can be attributed to the large dimension of the polyanion which favours the delocalization of protons in the structure. HPAs, such as $H_3PW_{12}O_{40}$, $H_4SiW_{12}O_{40}$, $H_3PMo_{12}O_{40}$, $H_4SiMo_{12}O_{40}$, $H_6P_2W_{18}O_{62}$, have stronger Brønsted acidity than conventional inorganic acids, and consequently, the corresponding anions have weak Brønsted basicity, softer than that of nitrate and sulphate anions [20], which makes these molecules easy to handle without hazardous corrosive problems unlike mineral acids [21]. The order of acidity for the Keggin structures is the following: $H_3[PW_{12}O_{40}] > H_3[SiW_{12}O_{40}] \geq H_3[PMo_{12}O_{40}] > H_3[SiMo_{12}O_{40}]$ [22, 23], and the acidity strength in the available surface of the solid HPAs depends on the nature of the countercation. When it is small (as Na^+), the behaviour of the HPA is very similar to that of the acidic form, and the species is highly soluble in water and polar solvents; conversely, when it is voluminous (K^+, Cs^+, NH_4^+), HPAs are insoluble in water. The usable acidity for a (photo)catalytic reaction depends on the size of particles (tertiary structure, Fig. 3.2c). In most cases the reagent molecules cannot penetrate in the tertiary structure and only a small fraction of the total acidity is accessible. However, due to the ability of HPAs to solve polar molecules, the latter can react more easily (reaction in 'pseudo-liquid phase') [14]. Another important feature of many HPAs and particularly of the Keggin is that they are reduced easily. The addenda metal atoms are mostly in their highest oxidation states (d^0), and thus these clusters exhibit fast reversible redox transformations under mild conditions. This property is very useful in the application of POMs as photocatalysts in pollutant photodegradation. When they accept one or more electrons, mixed-valence species are formed, the so-called heteropoly blues, that retain the structure of the parent oxidized anions [19]. Moreover, most POMs are highly soluble in a variety of polar and polar-organic solvents. This is due to the ability of POMs to interact with most solutions via electrostatic forces, hydrogen bonding and covalent and non-covalent interactions.

Further details on the chemistry of POMs have been summarized in various books, reviews and thematic issues [11, 24–29]. As mentioned above, POMs have been used in the design of various multifunctional materials with different techniques, and they are the base of multifunctional materials used to solve different emerging issues. Omwoma et al. [30] have recently revised the abilities of POM-based molecular compounds and functionalized POM-containing composites in providing effective solutions to various environmental problems, including the sequestration of CO_2, CH_4, N_2O and SO_2 and the adsorption/mineralization of cations, contaminants, dyes and pesticides from wastewater. Their contributions handling environmental problems such as toxic gas sequestration, wastewater decontamination, fine chemical production, corrosion and radioactive waste processing are particularly important.

By keeping in mind that photocatalysis is a branch of catalysis, it is worth highlighting the important role of HPA-based materials in catalysis both in solution and in solid state. The long list of review articles and special issues devoted to this field published in the last decades [11, 14, 19, 22–35], along with several patents and the commercialization of several catalytic processes involving HPAs, is a clear indication of their practical significance. Looking for strong acid catalysts, heteropolyacids such as $H_3PW_{12}O_{40}$ are able to catalyze a wide range of homogeneous catalytic processes at low temperatures [14]. They exhibit very strong Brønsted type acidity, making them suitable for various acidic reactions, such as esterification, transesterification, hydrolysis, Friedel–Crafts alkylation and acylation and Beckmann rearrangement [36, 37]. Interestingly, some special POMs also possess basic properties and can be used in base-catalytic reactions [38]. Above all, the chemical properties of HPAs, as their acid–base strength, redox potential and solubility in aqueous and/or organic media, can be tailored varying their composition and structure. Consequently, owing to the mentioned above unique properties, HPAs have been used extensively as efficient homogeneous catalysts in numerous catalytic reactions.

From the practical point of view, heterogeneous catalysis is usually preferred because of the advantages of the facile catalyst separation from the reaction products. The POM solubility in water and polar solvents cause difficulties in the recovery, separation and recycling of the catalysts, which affect their use in systems that require environmentally friendly efficient transformations. Therefore, an imperative is to develop easily recoverable and recyclable HPA-based catalysts for practical industrial applications. The heterogeneization of HPA clusters have been also an important issue because of the low specific surface area of unsupported HPAs ($1 \div 10\ \mathrm{m}^2\ \mathrm{g}^{-1}$). HPA dispersion on supports with high surface area increases the accessibility to their acidic sites and consequently increases their catalytic activity. The classical strategy to heterogeneize HPA clusters consists of supporting them on an oxide. Alternatively, the caesium or potassium salts ($Cs_{2.5}H_{0.5}PW$ or $K_{2.5}H_{0.5}PW$) are insoluble solids with micro- and mesoporosity [39]; however, the sizes of their particles are very small and problems can arise during the separation procedure. Recently, heterogeneized HPAs have been prepared associated with inorganic, organic or organometallic moieties. The supported HPAs evidenced important changes in structure, acid strength and redox properties with respect to the unsupported material. It is important to remind that in general for heterogeneous catalysis and in particular for a photocatalytic process, the reaction occurs on the solid surface, and the substrates need to diffuse into the active sites to be chemically adsorbed, while the products need to be desorbed from the solid through a reverse process. Therefore, the pore structures as well as the hydrophilic–hydrophobic properties significantly affect both activity and selectivity. Consequently, a porous material support is generally preferred in order to uniformly distribute the active sites and to decrease the mass transfer resistance. Several oxides have been used as HPA supports for (photo)catalytic purposes, for instance, SiO_2 [40–44], Al_2O_3 [45, 46], ZrO_2 [47, 48], Ta_2O_5 [49] or carbon [40, 50]. Silica has been widely favoured as supporting material because it interacts weakly with the Keggin anions preserving their structure. Conversely, interaction with basic solids, as MgO, ZnO or Al_2O_3, induces their decomposition, resulting in a decline of acidity [51]. The detrimental effect of such interactions on the catalytic activity has been well documented [44–46, 52]. Metal–organic frameworks (MOFs), mesoporous polymers, magnetic nanoparticles, porous carbons and zeolites, have been also used.

Parallel studies have been extensively devoted to the use of HPAs as photocatalysts in homogeneous systems [53]. In fact, absorption of light by the ground electronic state of the solubilized HPA produces an excited state HPA^*. The light absorption gives rise to a $O \rightarrow M$ ligand-to-metal charge transfer (LMCT) in the HPA cluster, for instance, in the $PW_{12}O_{40}^{3-}$ Keggin structure, from an O^{2-} to a W^{6+} at the W–O–W bonds. An electron is promoted from a spin-paired, doubly occupied bonding orbital (HOMO) to an empty, antibonding orbital (LUMO), resulting in the generation of a species with a hole centre (O^-) and a trapped electron centre (W^{5+}). This charge transfer observed at 260 nm, corresponding to

4.8 eV, for the plenary Keggin $H_3[PW_{12}O_{40}]$ is qualitatively analogous to the band gap of a solid semiconductor metal oxide that also generates an electron–hole pair under irradiation [54]. The proposed mechanism of the HPA-based photocatalysis involves several steps [53]. The first step is the preassociation between the HPA and the substrate (S), followed by absorption of light by the formed complex forming the excited state species (HPA^*) with a high reduction potential. The latter, in the presence of an electron donor (substrate S), gives rise to the heteropoly blue-reduced form (HPA^-) that absorbs at 650 nm (reactions 3.2, 3.3 and 3.4). The further step is the reoxidation of HPA^- upon exposure to an oxidant, for instance, O_2 (reaction 3.5):

$$\mathrm{HPA} + \mathrm{S} \rightarrow (\mathrm{HPA} - \mathrm{S}) \tag{3.2}$$

$$(\mathrm{HPA} - \mathrm{S})(\lambda < 260\,\mathrm{nm}) \rightarrow \left(\mathrm{HPA}^* - \mathrm{S}\right) \tag{3.3}$$

$$\left(\mathrm{HPA}^* - \mathrm{S}\right) \rightarrow \mathrm{HPA}^- + \mathrm{S}^+ \tag{3.4}$$

$$\mathrm{HPA}^- + \mathrm{O}_2 \rightarrow \mathrm{HPA} + \mathrm{O}_2^- \tag{3.5}$$

The formation of highly reactive $^{\bullet}OH$ radicals, according to reactions 3.6, 3.7 and 3.8, has been proposed to enhance the photo-oxidation performance:

$$\mathrm{O}_2^- + \mathrm{H}_2\mathrm{O} \rightarrow \mathrm{HO}_2 + \mathrm{OH}^- \tag{3.6}$$

$$2\mathrm{HO}_2 \rightarrow \mathrm{O}_2 + \mathrm{H}_2\mathrm{O}_2 \tag{3.7}$$

$$\mathrm{O}_2^- + \mathrm{H}_2\mathrm{O}_2 \rightarrow {}^{\cdot}\mathrm{OH} + \mathrm{OH}^- + \mathrm{O}_2 \tag{3.8}$$

Hydroxyl radical species have been experimentally detected in the presence of HPAs by photolysis or EPR experiments. The reoxidation of the HPA catalyst to its original oxidation state (reaction 3.5) is reported to be the rate-determining step in the HPA photocatalytic cycle [55], and it is performed by an electron acceptor, such as O_2 dissolved in the suspension or, in the absence of O_2, by other electrophilic species [56].

We have mentioned above the importance of using an immobilized HPA for (photo)catalysis, because of facile catalyst/product separation. Nevertheless, heterogeneous POM-based catalysts can entail some disadvantages, such as leaching of the active sites. Moreover, heterogeneous POM-based catalysts usually exhibit inferior catalytic performance than their homogeneous counterparts, mainly due to the mass transfer resistance and the diffusion limitation on the active sites. In order to overcome the above limitations, many approaches have been proposed to improve the stability and catalytic performance. Wang's workgroup reviewed the strategies to obtain POM-based heterogeneous catalysts and concluded that mainly two pathways can be undertaken: 'immobilization' or 'solidification' [23]. Figure 3.3 introduces the different pathways that can be used to 'heterogeneize' the POM active species. Based on the different host–guest interactions, POM-based active sites can be immobilized through adsorption, ion exchange, covalent linkage, encapsulation, substitution, etc. The porous supports will not only provide a larger surface to highly distribute the active sites but will also greatly influence the activity

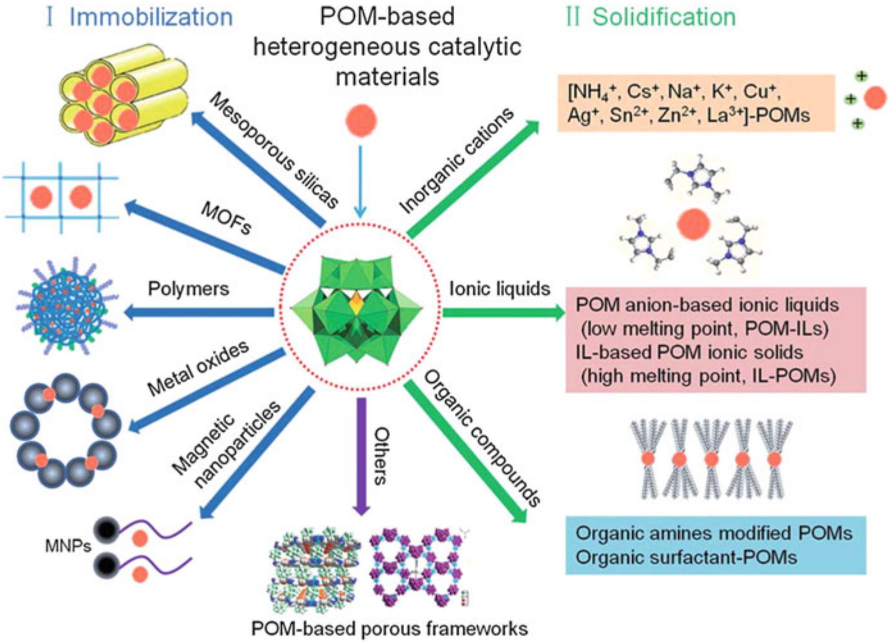

Fig. 3.3 Strategies for preparing heterogeneous POM-based materials for catalytic/photocatalytic purposes (Reprinted with permission from Ref. [23]. Copyright 2014, Royal Society of Chemistry)

and selectivity because the host–guest interaction can affect the physico-chemical features of the HPA-active centre. In order to design an efficient supported heterogeneous POM-based material, it is necessary to choose an appropriate heterogeneization methodology.

In the present chapter, we classify the methodologies devoted to heterogeneize HPAs in three main groups. In the first one the HPA is immobilized by a photocatalytically inactive support, in the second one HPA is immobilized onto a photocatalytically active material (generally a semiconductor oxide) and in the third one HPA is not supported but heterogeneized by immobilization in a host–guest insoluble composite.

3.2 HPA-Based Heterogeneous Photocatalysts: HPA Immobilized on Different Supports Which Are Not Activated Under Irradiation

When the HPA is supported onto a photocatalytically inactive material, the mechanism of the photocatalytic process corresponds to what explained before for the activation of the HPA in a homogeneous system. In these composite materials, the support can play the double role, i.e. modifying some of the physico-chemical features of the HPA and/or improving the adsorption ability of the substrates to react with the active species.

3.2.1 HPAs Immobilized on SiO_2-Based Materials

Guo et al. reported [57–60] the use of $H_3PW_{12}O_{40}/SiO_2$ and $H_4SiW_{12}O_{40}/SiO_2$ prepared by incorporating the HPAs into the silica matrix via a sol–gel technique. The photocatalytic activity of the composites was tested by degradation of malic acid, which was totally mineralized in ca. 2 h by UV irradiation. The intermediate products produced using supported HPAs or bare TiO_2 were the same, indicating that in both systems $^{\bullet}OH$ radical was the main oxidant species, as previously reported in reactions (3.2, 3.3, 3.4, 3.5, 3.6, 3.7 and 3.8). Alternatively, amine-functionalized silica can be used as support for transition-metal-substituted polyoxometalate (TMSP) [61]. The TMSPs are considered as inorganic porphyrins where the incorporation of the transition metal into the HPA cluster can facilitate the formation of elaborate structures, due to their variable coordination number and geometry. To obtain the TMSPs, the vacant sites of the lacunary cluster must accommodate the transition metal. The presence of a transition metal different from the addenda gives different physical properties to the TMSP compared to the original non-substituted HPA, due to the variable electronic and magnetic states of the incorporated transition metal. In these TMSPs the addenda transition metal is coordinated to five oxygen atoms, and according to Guo et al., it possesses the sixth coordination site occupied by a water molecule. The water molecule of most TMSPs can be displaced in aqueous media by ligands such as pyridines or ammonia. Guo et al. replaced a W(VI) addenda atom with a Ni(II). The TMSP, $[Ni(H_2O)SiW_{11}O_{39}]$, was covalently coordinated by the Ni centres to the amine surface groups of the silica. Rhodamine B dye was completely mineralized by using these heterogeneous photocatalysts and no heteropolyacid leaching occurred. By comparing the photocatalytic activity of the solubilized TMSP with that of the heterogeneized one, Guo et al. reported an improvement by using the supported material. However, although the photocatalytic activity of the plenary HPAs is higher than that of the lacunary one and of the TMSP, the use of the transition-metal-substituted cluster is preferable due to the strong chemical interaction with the matrix that prevents leaching. It is worth to mention that, according to Cronin et al., the lacunary clusters are known to reorganize in solution, which increases the complexity of the reaction mixture, and it is more difficult to postulate and to determine the likely mechanisms underlying the assembly processes [62].

Another possibility is to use silica as support. Shen et al. propose the use of $H_3PW_{12}O_{40}$/MCM-41 supported by impregnation of fluorinated Si–MCM-41 for the selective oxidation of alcohols to aldehydes in ionic liquid (IL) medium [63]. The photocatalytic activity of this material was higher than that of bare HPA. Authors observed an optimal loading amount of 30 wt% HPA. The use of

ILs instead of CH_3CN improved the reactivity. Imidacloprid pesticide was partially degraded (58.0 %) after 5 h of irradiation at 365 nm by using $H_3PW_{12}O_{40}$/MCM-41, prepared by impregnation with 50 wt% of HPA loading [64].

Tao et al. have recently supported $H_3PW_{12}O_{40}$ onto hierarchically porous silica. Neutral red, rhodamine B and fuchsin basic dyes were efficiently degraded under visible-light irradiation [65]. The HPA was successfully immobilized in the pores as the silica was previously treated with 3-aminopropyltriethoxysilane that provided amino groups to the silica to interact with the HPA through electrostatic interactions. Comparing with other porous catalyst supports (as MCM-41 or SBA-15), the hierarchically porous structure was considered to be an important factor to improve the molecular diffusion in the heterogeneous photocatalytic process. Notably, dyes are generally inappropriate as model compounds for the evaluation of photocatalytic activity of novel photocatalysts under visible light. The advantage of using these molecules as substrates to test a photocatalyst in the visible range of the spectrum is severely limited by the presence of a sensitization mechanism as highlighted by Choi [66] and then deeply explained by Paz et al. [67]. This important point should be considered for future advancements in the photocatalysis field as far as until now the great majority of the papers on heteropolyacid-based heterogeneous photocatalysts has been carried out by using dyes as model molecules.

The design and synthesis of HPA supported on magnetic materials attract substantial interest because the core–shell structured microspheres composed, for instance, by $Fe_3O_4@SiO_2$ exhibit paramagnetic features, and they can be efficiently recovered by magnetic separation. Following this idea, $H_3PW_{12}O_{40}$ can be anchored to an amino-functionalized Fe_3O_4/SiO_2/meso-SiO_2 microsphere by means of chemical bonds to the aminosilane groups. Zhao et al. prepared a composite where the resultant microspheres contained an HPA loading of ca. 17 % wt. and used them to degrade rhodamine B under UV irradiation more quickly than by using the solubilized HPA [68]. In this composite HPA interacts with the silica support through an acid–base reaction and hydrogen and covalent bonds, between -NH_2 and $H_3PW_{12}O_{40}$; however, authors admitted that slight leaching of HPA unit is inevitable. Also Li et al. have focused their work on core–shell structured magnetic photocatalysts, but they used $H_3PW_{12}O_{40}$ sensitized by thionine deposited by the so-called layer-by-layer (LbL) self-assembly method [69]. The thionine excited by visible light can inject electrons in the LUMO of the HPA improving the overall efficiency of the process. These microspheres exhibit better photocatalytic activity towards the degradation of methyl orange under visible-light irradiation than the same photocatalytic material deposited on quartz slides. The deposition procedure is reported in Fig. 3.4. The $Fe_3O_4@SiO_2$ magnetic microspheres were used as the supporting substrate, and they were impregnated and coated several times to obtain the final material.

The preparation of cellulose/silica hybrid materials functionalized with Keggin-type polyoxometalates employing sol–gel synthesis under mild conditions has been also developed. These bio-based materials were composed by a 37 % of propylamine-modified silica dispersed over cellulosic fibres (56 wt%) and a small

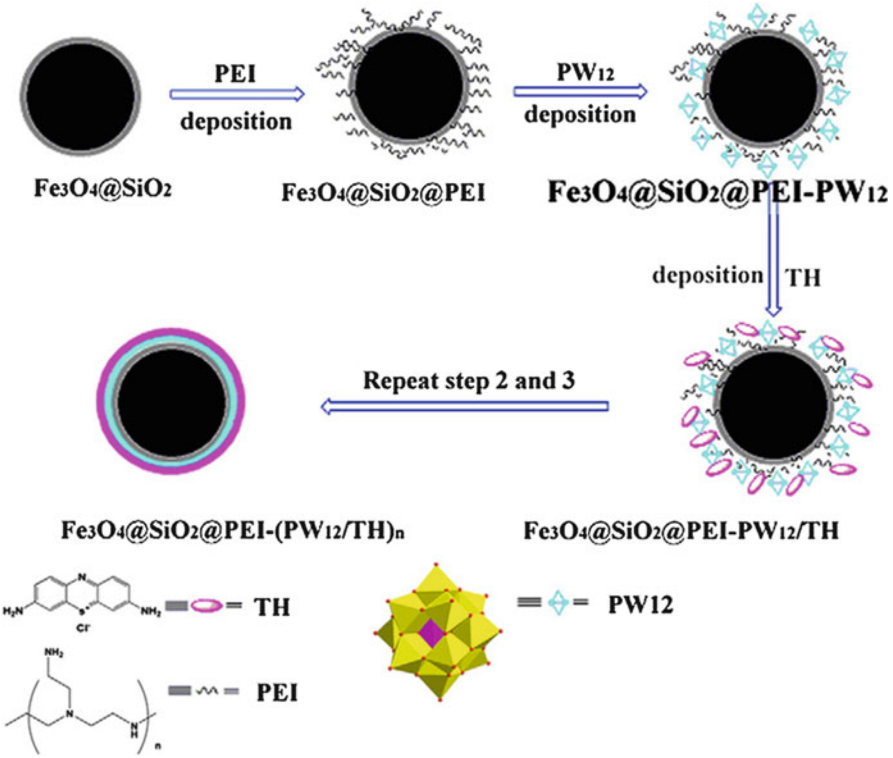

Fig. 3.4 Self-assembly procedure of PW_{12}-TH multilayer films on magnetic microspheres (Reprinted with permission from Ref. [69]. Copyright 2013, Elsevier)

amount (2 %) of Keggin-type polyoxoanions attached electrostatically to the protonated amino groups, as reported in Fig. 3.5. The HPA species consisted of $[PV_2Mo_{10}O_{40}]_{52}$, $[PVMo_{11}O_{40}]_{42}$, and $[PMo_{12}O_{40}]_{32}$ or $[PW_{12}O_{40}]_{32}$ groups. The silica was functionalized with the heteropolyacids via electrostatic interactions between HPA and protonated propylamino groups of modified silica. No covalent bond (C–O–Si) between cellulose and silica has been detected. Despite their high silica content, cellulose/silica hybrids retained basic cellulosic properties such as fibrous structure, crystallinity, high porosity and low density. The bio-based material, functionalized with 2 % of $[PVMo_{11}O_{40}]_{42}$, shows high activity towards the oxidation of volatile organic compounds [70]. The composite of poly(vinylidene-fluoride) (PVDF) and the Keggin HPA, formed via combining a doctor-blade method, immersion precipitation and colloid interface techniques, acts as a good photocatalyst for the methyl orange decolorization in the presence of H_2O_2, maintaining its efficiency even after eight cycles. The mechanism of the photocatalytic activation of all of these composites has been explained in the same way, i.e. excitation of HPA to form the heteropoly blue. This has a highly oxidizing power, strong enough to oxidize H_2O to generate hydroxyl radicals,

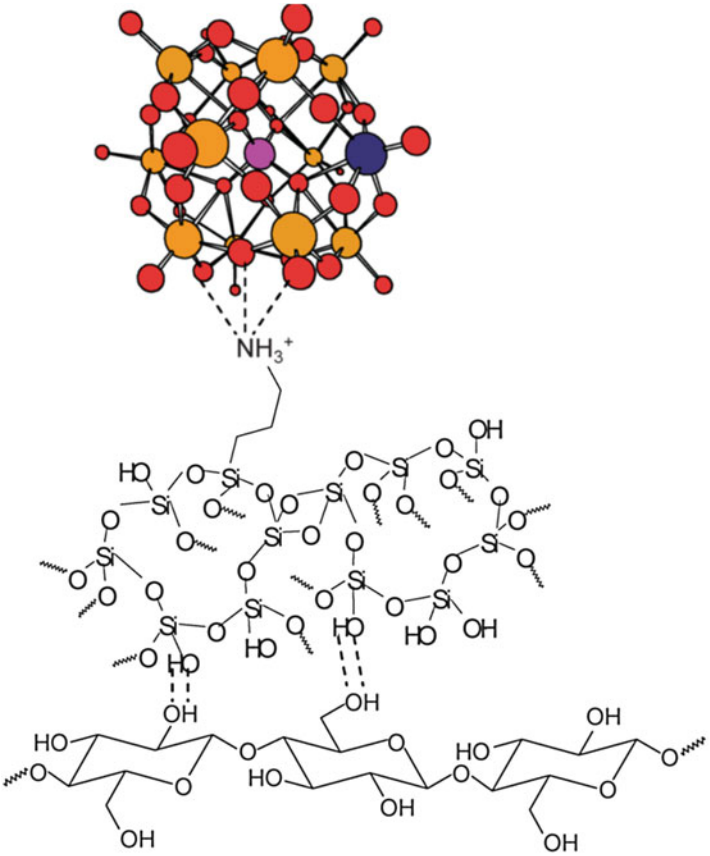

Fig. 3.5 Schematic representation of the chemical interactions in the cellulose/silica hybrids functionalized with HPA. In the ball and stick representation of the Keggin structure, the substituting heteroatom (vanadium) is shown in *blue* (Reprinted with permission from Ref. [70]. Copyright 2012, Royal Society of Chemistry)

which promotes the substrate photodegradation efficiency, as described before in reactions (3.2, 3.3, 3.4, 3.5, 3.6, 3.7 and 3.8).

3.2.2 HPAs on Zeolites

The use of a zeolite as an HPA support has been explored in a classical research work by Ozer and Ferry, who reported the use of a NaY zeolite with $H_2NaPW_{12}O_{40}$, $H_4SiW_{12}O_{40}$ or $H_3PMo_{12}O_{40}$ as photocatalysts for the degradation of 1,2-dichlorobenzene [71]. In this case HPA has not been previously heterogeneized but just added to the irradiated zeolite suspension. Authors attributed an important role to the zeolite surface in the enhancement of the photocatalytic degradation rate of the substrate; indeed, they claimed that the zeolite surface enhances the 'local concentration' of both substrate and excited HPA, which consequently can react more efficiently in the adsorbed phase. Moreover, according to Ozer and Ferry, the zeolite surface stabilizes charge-transfer states and transient species as $^{\bullet}OH$. The immobilization of $H_3PW_{12}O_{40}$ by wet impregnation on NH_4Y and NH_4ZSM5 zeolites with loading in the range 5 to 30 wt% has been done by Leal Marchena et al. [72]. The Keggin anion was partially transformed into $[P_2W_{21}O_{71}]^{6-}$ anion during the synthesis and the soft drying (vacuum at 80 °C). The acid properties of both series of composites are rather similar, despite the higher acid strength of NH_4ZSM5. These materials were active for the photocatalytic degradation of 4-chlorophenol in liquid–solid regime, and the OH radical production by the mechanism illustrated in reactions 3.2, 3.3, 3.4, 3.5, 3.6, 3.7 and 3.8 was claimed to be responsible for the substrate degradation.

3.2.3 HPAs Immobilized on Carbon Nanotubes

Also carbon nanotubes have been used as HPA support. Tri-component Au/HPA/carbon nanotubes (CNTs) with visible-light photocatalytic activity were obtained when Keggin structures were employed as both reducing and bridging molecules between Au metallic nanoparticles and CNTs [73]. A thin HPA layer (ca. 2 nm) around gold nanoparticles supports Au on the CNTs surface. The composite Au/HPA/CNTs was more active for the photocatalytic degradation of rhodamine B under visible light than the mono- or bicomponent photocatalyst. The enhanced photocatalytic activity was attributed to a synergistic effect between the three components. Indeed, the visible-light excitation of the surface plasmon resonance of the Au nanoparticles induces electron transfer from Au to HPA. In this way the electron-deficient Au nanoparticles can oxidize the organic compounds. On the other hand, the electron transfer from the reduced HPA to the CNTs can decrease the electron–hole recombination. Finally, the trapped electrons on CNTs can react with O_2 as reported in Fig. 3.6.

As far as the HPAs supported on photocatalytically active semiconductors are concerned, the activity of heterogeneized HPAs is further enhanced by the use of a support activated by irradiation. The synergistic effect between the HPA and the semiconductor, particularly when TiO_2 is used as support, has been extensively reported. In the photocatalytic reaction, the heterogeneized HPA enhances the activity by playing the double role of (i) acting as an electron scavenger delaying the recombination of h^+ and e^- pairs [54] and (ii) catalyzing the photodegradation of the substrate by means of HPA^- that can react with molecular oxygen or another electrophilic species [56, 74] (see Fig. 3.7).

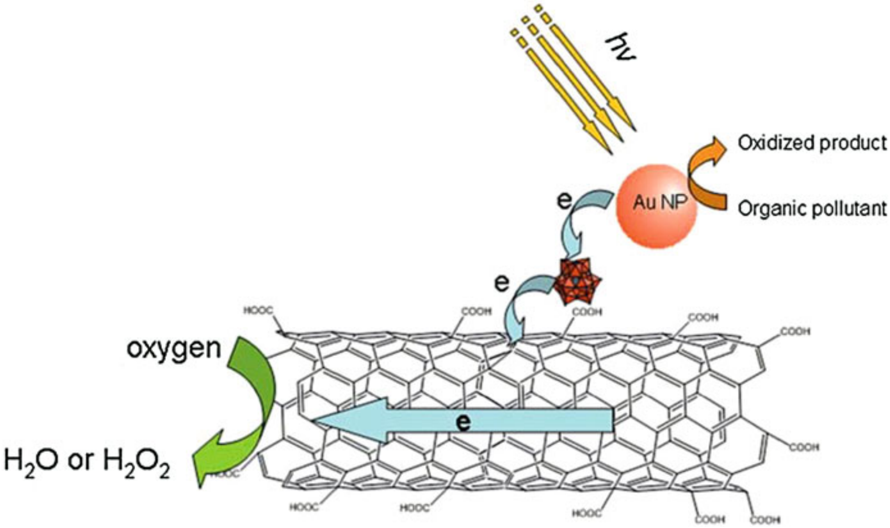

Fig. 3.6 Photocatalytic mechanism on Au nanoparticles/HPA/CNT tri-component nanohybrid (Reprinted with permission from Ref. [73]. Copyright 2011, Royal Society of Chemistry 3). HPA-based heterogeneous photocatalysts: HPA supported on semiconductor materials which are activated under irradiation

3.3 HPA Immobilized on TiO_2

The Keggin-type HPA supported on TiO_2 has been the most studied photocatalyst. A perusal of Fig. 3.7 shows how the semiconductor directly transfers the photogenerated electrons from the conduction band to the HPA^* formed by excitation of the HPA (see reaction 3.3). The Keggin anion $[PW_{12}O_{40}]^{3-}*$, from a thermodynamic point of view, is a better electron acceptor than O_2 (+0.22 V (pH independent) and −0.33 V (at pH = 0) vs. NHE, respectively) [76]. Notably, the reduction potential of $[PW_{12}O_{40}]^{3-}*$ is more positive than the flat band potential of the conduction band of TiO_2 particles (ca. −0.19 V vs. NHE (at pH = 0)) [77]. In this way the electron transfer from the conduction band of TiO_2 to $[PW_{12}O_{40}]^{3-}*$ is thermodynamically favourable to yield $[PW_{12}O_{40}]^{4-}$ species. The enhanced degradation of organic compounds by using HPAs on semiconductor oxides in the presence of UV light has been on this basis thoroughly explained in the literature. The first attempt to understand such a process has been done by Yoon et al. who prepared an HPA/TiO_2 reacting medium by incorporating $H_3PW_{12}O_{40}$ into a polyvinyl alcohol TiO_2 colloidal suspension and illuminated the system with UV light (300–375 nm) for the photodegradation of methyl orange [78]. HPA was simply added (not immobilized) to the TiO_2 suspension, and the extent of the photoinduced reaction depended not only on the HPA/TiO_2 ratios but also on the irradiation wavelength and intensity. The photoinduced charge-carrier generation at the heterojunction HPA–TiO_2 was very efficient, and it was synergistically

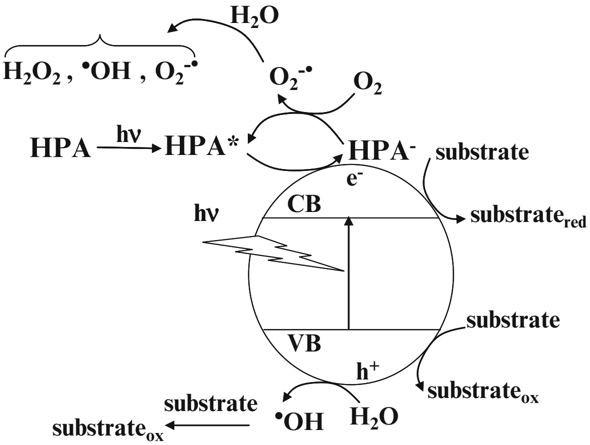

Fig. 3.7 Scheme of the mechanism acting in synergism between HPA and a photocatalytically active semiconductor under irradiation (Reprinted with permission from Ref. [75]. Copyright 2014, Wiley)

enhanced by illuminating both with visible and UV light. Interestingly, authors evidenced much stronger hydrogen bonds, between the oxygen atoms of Keggin anion and the hydroxyl groups of the titania, in the solution phase than in the dried state. An acid–base interaction between the HPA unit and the TiO_2 matrix exists. The ($TiOH^{2+}$) and $\left(H_2PW_{12}O_{40}^{-}\right)$ species are responsible for that interaction [19].

Further studies by Majima's group demonstrated that the initial reduction rate of HPA is greatly enhanced in the presence of TiO_2 upon UV irradiation [79]. Yoon et al. suggested that such reaction scheme with a double electron-transfer mechanism resembles the 'Z-scheme' mechanism invoked in the photosynthesis process, reported in Fig. 3.8. This mechanism implies that an interfacial photoinduced electron transfer takes place from conduction band of TiO_2 to HPA, resulting in a reduction of $PW_{12}O_{40}^{3-}$ to $PW_{12}O_{40}^{4-}$, the heteropoly blue species. The former can inject electron to the conduction band of TiO_2 in the presence of polyvinyl alcohol (PVA). It is interesting to note that the heteropoly blue can be also photoexcited with visible light to $PW_{12}O_{40}^{4-}$ which can be oxidized back to $PW_{12}O_{40}^{3-}$ through hydrogen atom abstraction reacting from polyvinyl alcohol (PVA) as supported by observation that the rate of reoxidation of $PW_{12}O_{40}^{4-}$ under irradiation is higher than that measured in the dark [78]. In Fig. 3.8, $PW_{12}O_{40}^{3-}$ is denoted as HPA and $PW_{12}O_{40}^{4-}$ as heteropoly blue (HPB), and it is produced by direct electron transfer from the TiO_2 conduction band to the ground-state HPA in addition to photoreduction through the excited state of HPA. It is also noteworthy that the ground-state HPB formed by illumination of near-UV light can be recovered photochemically as well as thermally.

Tachikawa et al. [79, 80] demonstrated the one-electron oxidation and reduction processes in the HPA-mediated TiO_2 photocatalytic reaction, by using the two-colour two-laser flash photolysis technique [80]. The efficiency of this electron transfer increased by using $PW_{12}O_{40}^{3-}$ instead of $SiW_{12}O_{40}^{4-}$. They attributed this

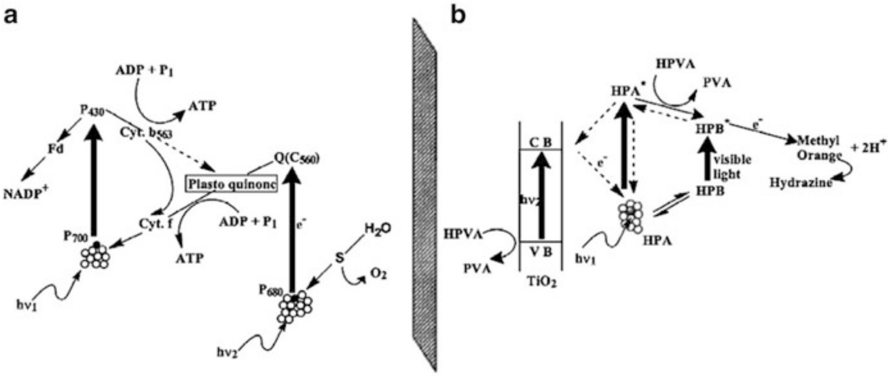

Fig. 3.8 Energy diagram: (**a**) photosynthesis in green plants; (**b**) photoinduced electron transfer at the heterojunction of HPA/TiO_2 colloids in the presence of 0.1 % PVA as an electron donor (Reprinted with permission from Ref. [78]. Copyright 2001, American Chemical Society)

behaviour to the reduction potentials of the two different HPAs [76]. The results clearly indicate that the electron injection from $PW_{12}O_{40}^{4-}$* to the conduction band of TiO_2 is the main reason for the significant enhancement in the one-electron oxidation of aromatic sulphides. It was also found that the efficiency of electron transfer increases in the order $H_2W_{12}O_{40}^{6-} < SiW_{12}O_{40}^{4-} < PW_{12}O_{40}^{3-}$, depending on the reduction potential of the HPA. In the presence of an electron acceptor such as methylviologen, an electron transfer from $PW_{12}O_{40}^{4-}$* to MV^{2+} occurs, and finally HPA accepts electron from $MV^{+\cdot}$ to form the HPA^{-} species because of the redox potential difference. The overall energy diagram for the TiO_2/HPA/MV^{2+} photocatalytic redox process is shown in Fig. 3.9. The ability of HPA as acceptor of the electrons generated in the conduction band of UV-irradiated TiO_2 suspensions was also demonstrated by Park and Choi, by using a photoelectrochemical method [54]. Time-resolved microwave conductivity (TRMC) technique also helps to demonstrate the electron transition from the semiconductor to the HPA. It gives information on the lifetimes of charge carriers created on the semiconductor and on recombination and/or trapping phenomena. We have experimentally observed that the Keggin HPA has a favourable effect on the charge-carrier separation in the photocatalytic process when it is supported on TiO_2 and on WO_3 [74].

The use of HPAs immobilized on polycrystalline TiO_2 has been extensively studied in liquid–solid regime for several photocatalytic model reactions. In general, authors reported that the primary Keggin structure remained unmodified after the immobilization on TiO_2 or inside the TiO_2 network. They explained the increasing activity of the composite material with respect to the homogeneous HPA or bare semiconductor according to the above exposed mechanism (see Figs. 3.7 and 3.8). In this mechanism an interfacial electron transfer from the conduction band of TiO_2 to the incorporated HPA occurs; hence, a reduction of the HPA after its activation by UV light takes place, and eventually the oxidation of

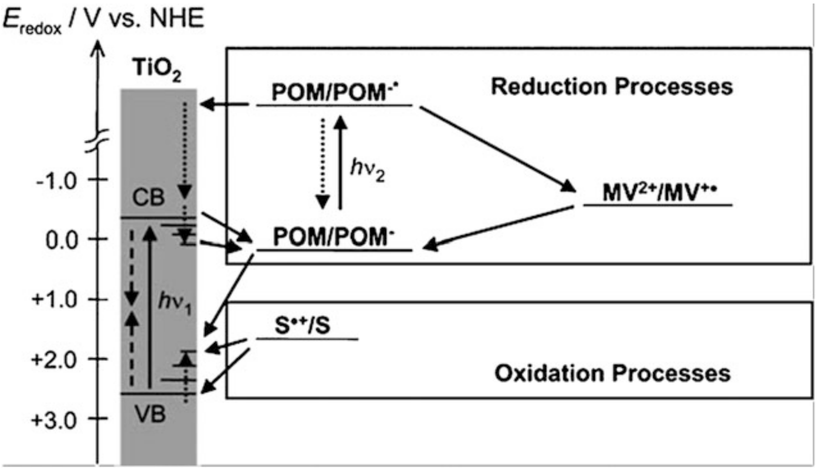

Fig. 3.9 Energy diagram for the TiO_2/POM/MV^{2+} photocatalytic redox processes, in which MV^{2+} is methylviologen ion (Reprinted with permission from Ref. [79]. Copyright 2007, American Chemical Society)

the reduced HPA species gave rise to $^{\bullet}OH$ radicals, the ultimate species responsible of the oxidation processes.

Analogously to Yoon et al., also Ozer and Ferry [81] added $PW_{12}O_{40}^{3-}$ and $SiW_{12}O_{40}^{4-}$ to a TiO_2 suspension. In the presence of O_2, the addition of HPA anions to TiO_2 suspensions resulted in a significant rate enhancement for 1,2-dichlorobenzene oxidation. The reduction potentials of the HPA used by these authors are +0.219 V vs. NHE for $H_2NaPW_{12}O_{40}$ [82] and +0.055 V vs. NHE for $H_4SiW_{12}O_{40}$ [83]. Mixtures of $H_3PW_{12}O_{40}$ with commercial TiO_2 Degussa P25 were used for 2,4-dichlorophenol photocatalytic degradation in aqueous media [84]. $H_3PW_{12}O_{40}$ species on the surface of TiO_2 accelerated the hydroxylation of the substrate but not its mineralization, which was somewhat suppressed in the presence of the HPA. An increase of the HPA loading increased the concentration of the toxic intermediates. This important result indicates that the enhancement of charge separation in TiO_2 photocatalysis does not always result in improvement of the efficiency of mineralization of the organic substrates.

Guo's group has intensively worked in this field [85–90]. A first composite was prepared as hydrogel by mixing titanium isopropoxide and a $H_3PW_{12}O_{40}$ solution. The material was successively autoclaved and calcined. The obtained $H_3PW_{12}O_{40}$/TiO_2 photocatalytically decolorizes ten organic dyes in aqueous systems under visible-light irradiation ($\lambda > 420$ nm) [85]. An electrostatic interaction between HPA and TiO_2 occurred during the hydrolysis of titanium tetraisopropoxide in the presence of the Keggin ion that remained entrapped by the protonated hydroxyl groups on the TiO_2 surface ($\equiv$Ti–OH), resulting in interactions between ($\equiv TiOH_2^+$) and ($H_2PW_{12}O_{40}^-$). Moreover, hydrogen bonds could be formed between the oxygen atoms of Keggin ion and the hydroxyl groups of the TiO_2

surface (WO· · ·HO–Ti). Authors attributed the photocatalytic activity not only to the synergistic effect of the HPA on the semiconductor oxide, expressed by the mechanism reported in Fig. 3.7, but also to the porous structure of the nanocomposite that enhanced mass transport and increased adsorption of the reactants. An important point was the use of visible irradiation to carry out these experiments. The mineralization was not systematically followed, but some intermediates were identified along with the presence of some final products as NH_4^+, SO_4^{2-}, NO_3^- and Cl^-. The same research group tested this catalyst in the visible-light photocatalytic degradation of parathion-methyl insecticide [86]. The activity was attributed not only to the synergistic effect between HPA and TiO_2 but also to the narrow band gap and porous structures; moreover, they loaded on TiO_2 a series of Keggin HPAs presenting different heteroatom, i.e. $[X^{n+}W_{12}O_{40}]^{(8-n)-}$, where $X^{n+} = P^{5+}$, Si^{4+}, Ge^{4+}. Interestingly, no thermal treatment was followed in this case [87]. These materials showed higher photocatalytic activity than both bare TiO_2 and HPAs (or a mechanical mixture of them) for the dye reactive brilliant red X-3B degradation under visible light. Two variables influenced the bleaching rate: HPA loading ($30 > 15 > 45$ wt%) and the presence of different heteroatoms in the HPA ($P > Si > Ge$). Authors reported that their HPAs are better dispersed in TiO_2 using the sol–gel method than using the incipient wetness impregnation, but they do not give any explanation for the observed behaviours. The same group also used $Cs_xH_{3-x}PW_{12}O_{40}/TiO_2$ ($x = 0.5$–3.0), prepared via the combination of the sol–gel and hydrothermal processes for the photocatalytic degradation of 4-nitrophenol, methyl orange and rhodamine B under UV irradiation by following both the total organic carbon and the substrate degradation [88]. The composites were more effective than the bare $Cs_xH_{3-x}PW_{12}O_{40}$ or TiO_2 Degussa P25, particularly the material with $x = 2.5$. The photoactivity was attributed to the higher surface acidity, the mesoporosity and the synergistic effect between HPA and TiO_2. $H_3PW_{12}O_{40}$ was also deposited on mesoporous TiO_2 (3.2–16.6 wt% loadings). The preparation method included both sol–gel (in the presence of a template, pluronic 123) and hydrothermal treatments, and it was used to obtain a well-distributed 3D interconnected mesopore structure partially covered by the HPA [89]. The solid acted as a photocatalyst for degradation/mineralization of dyes under UV, i.e. methyl orange, methylene blue, crystal violet and rhodamine B. The composite material $H_3PW_{12}O_{40}/TiO_2$ prepared by Guo et al. using their usual methodology was also successfully applied to the degradation/mineralization of aqueous phthalate esters: di-n-butyl phthalate (DBP), diethyl phthalate (DEP) and dimethyl phthalate (DMP) under simulated sunlight irradiation (Xe lamp) [90]. Degradation of DBP, DEP and DMP reached 98 %, 84 % and 80 %, respectively, after 90 min, and nearly total mineralization of DBP and DEP was achieved after 12 h of reaction. Authors attributed the photocatalytic performance to a synergistic effect between the Keggin unit and the TiO_2 network. The synergism can be explained not only by considering the presence of $^{\bullet}OH$, h^+ and $O_2^{\bullet-}$ formed under irradiation of HPA/TiO_2 samples (see Fig. 3.7) but also the porous morphology of the photocatalyst that favoured the adsorption of the substrate. The successful use of

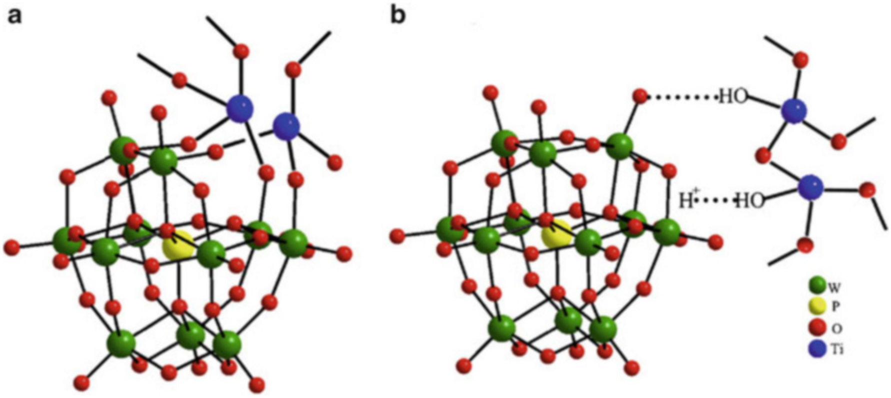

Fig. 3.10 The proposed structures of the composites formed between (**a**) 'lacunary' HPA and TiO_2 ($K_7PW_{11}O_{39}/TiO_2$) and (**b**) 'plenary' HPA and TiO_2 ($H_3PW_{12}O_{40}/TiO_2$) (Reprinted with permission from Ref. [91]. Copyright 2012, Elsevier)

simulated sunlight irradiation depended on the kind of composite HPA/TiO_2, but it was not satisfactorily clarified. In fact, as we have mentioned before, the absorption of light and the photoreactivity could be compromised by the type of molecule used. The formation of surface complexes activated by visible light when dyes are used, for instance, makes the latter species unsuitable for these studies [66, 67].

Saturated and monovacant Keggin unit functionalized TiO_2 materials, $H_3PW_{12}O_{40}/TiO_2$ and $K_7PW_{11}O_{39}/TiO_2$, have been also prepared by one-step sol–gel co-condensation followed by solvothermal treatment. Simulated sunlight photocatalytic activity for rhodamine B and diethyl phthalate were used as test reactions [91]. $H_3PW_{12}O_{40}/TiO_2$ and $K_7PW_{11}O_{39}/TiO_2$ showed better photocatalytic performance with respect to bare TiO_2. Moreover, the different photocatalytic activity between the saturated and monovacant Keggin unit functionalized TiO_2 was attributed to their different structures, which resulted in different electron-accepting ability. Figure 3.10 shows the bonds between the HPA and the TiO_2 support in the case of both the 'plenary' Keggin and the 'lacunary' derivative. Usually, the preparation of HPA supported on TiO_2 gives rise to a composite where an electrostatic acid–base interaction and/or hydrogen bonds between the HPA and the semiconductor occur(s). By using the lacunary HPA, the composite $K_7PW_{11}O_{39}/TiO_2$ shows a covalent bond between the terminal nucleophilic oxygen atoms of the $K_7PW_{11}O_{39}$ and the electrophilic titanium atoms in Ti–OH groups. This approach is particularly interesting because it opens the possibility to use functionalized HPAs that can be covalently linked to the support.

The attractiveness of the covalent approach has been stressed by Proust [92], who indicates as benefits (i) the enhanced stability despite external variation of pH (in the stability range of the HPA) or ionic strength, (ii) the enhanced control on the number and relative orientation of the components and (iii) the better dispersion in a polymer or on a surface.

It is worth mentioning that Lv et al. observed that the adsorption ability of the 'reactive orange 86' dye changed on the TiO_2 Degussa P25 surface along with its photocatalytic degradation rate when TiO_2 was covered by HPAs [93]. Due to the presence of HPA, the positive superficial charges of TiO_2 were greatly reduced giving rise to a significant decrease in the adsorption of the anionic dye. Moreover, the presence of HPA, replacing the surface hydroxyl groups ($Ti–OH_2^+$ sites), favours the production of surface-bound $^{\bullet}OH$ radicals that are less reactive than free $^{\bullet}OH$ radicals. That is why, according to Lv et al., the presence of the HPA can give rise to a detrimental effect on the photocatalytic activity of the loaded sample with respect to the bare TiO_2.

In another study visible-light-responsive spherical particles composed by TiO_2 and 20 or 30 wt% of $H_3PW_{12}O_{40}$ were prepared via the sol–gel process and by using urea as pore-forming agent. Malachite green oxalate dye bleaching reaction under UV and blue-light irradiation in aqueous phase was used as a model reaction [94, 95]. The prepared materials showed visible-light absorption due to the presence of WO_3 resulting from the partial degradation of the HPA during the preparation drying step, which gives rise also to lacunary $[PW_{11}O_{39}]^{7-}$ or dimeric species $[P_2W_{21}O_{71}]^{6-}$. Dye solutions were efficiently bleached after 60 min with the most active composite, containing 30 wt% HPA on TiO_2. By using blue-light irradiation, this powder also revealed the highest photocatalytic bleaching. In this case WO_3 could be responsible for the photocatalytic activity observed. The same group treated at high temperatures the same $H_3PW_{12}O_{40}$/mesoporous titania composites [96]. Keggin structure was partially transformed when the samples were thermally treated up to 600 °C. The HPA loading and the thermal treatment temperature influenced the activity of the photocatalyst.

Biboum et al. have synthesized the multi-cobalt- and multi-nickel-substituted HPAs shown in Fig. 3.11 [97] where (A) corresponds to $K_{10}Na_{12}[\{Co_3(B\text{-}\beta\text{-}SiW_9O_{33}(OH))(B\text{-}\beta\text{-}SiW_8O_{29}(OH)_2)\}_2]\cdot 49H_2O$, (B) to $K_{20}[\{(B\text{-}\beta\text{-}SiW_9O_{33}(OH))(B\text{-}\beta\text{-}SiW_8O_{29}(OH)_2)Co_3\text{-}(H_2O)\}_2Co(H_2O)_2]\cdot 47H_2O$ and (C) to $Na_{17}[Ni_6As_3W_{24}O_{94}$-

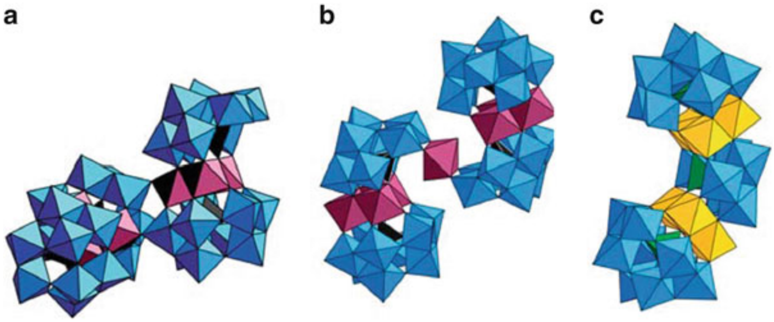

Fig. 3.11 Polyanions of the salts synthesized: (**a**), (**b**), (**c**). WO_6, CoO_6 and NiO_6 are represented as *blue*, *purple* or *yellow octahedral*, respectively. SiO_4, AsO_4 and PO_4 are represented as *black*, *green* and *orange tetrahedral*, respectively (Adapted from Ref. [97] with permission from The Royal Society of Chemistry)

$(H_2O)_2]\cdot 54H_2O$. These HPAs absorb visible light due to the presence of cobalt and nickel colour centres in contrast to other HPAs which are able to absorb only UV light. A and B formed two-electron and four-electron-reduced species, whereas C formed a six-electron-reduced species. Their photocatalytic activities were tested for the degradation of acid orange 7 dye in aqueous solution in the absence and in the presence of colloidal TiO_2 and in the presence of 2-propanol or polyvinyl alcohol, used as electron donors, to study the photosensitivity of these HPAs in homogeneous medium and in the presence of TiO_2.

The reduction of the HPA occurred along with the oxidation of 2-propanol in the homogeneous system, whereas 2-propanol oxidation decreased under visible light in the sequence $A > B >> H_3PW_{12}O_{40} > C$. The mechanism is reported below:

$$\mathrm{HPA} + h\nu \rightarrow \mathrm{HPA}^* \tag{3.9}$$

$$\mathrm{HPA}^* + 2\,\mathrm{CH_3 - CHOH - CH_3} \rightarrow \mathrm{HPA}^{2-} + 2\,\mathrm{CH_3 - CO - CH_3} + 2\,\mathrm{H}^+ \tag{3.10}$$

$$\mathrm{HPA}^{2-} + 2\,\mathrm{CH_3 - CHOH - CH_3} \rightarrow \mathrm{HPA}^{4-} + 2\,\mathrm{CH_3 - CO - CH_3} + 2\,\mathrm{H}^+ \tag{3.11}$$

The photoreduction kinetics when using $H_3PW_{12}O_{40}$ is negligible, despite the more positive formal potential, compared with that of A and B. The higher photoreduction yield of these HPAs compared to the Keggin anions was mainly attributed to their extended absorption in the visible region and the ability to undergo multielectron photoreduced species. As far as the dye degradation under visible irradiation (at $pH = 1$ in the presence of 2-propanol or PVA) is concerned, the photodegradation rate when using a suspension containing A and TiO_2 was three times higher than that observed using a homogeneous system containing A. The photodegradation efficiency in the presence of the colloidal TiO_2 follows the order: $A > B > C >> H_3PW_{12}O_{40}$. The TiO_2 role is associated by the authors to the kinetics of surface-adsorbed species. For comparison purposes, the dye bleaching was also carried out under UV irradiation ($\lambda > 320$ nm) in suspension containing both HPA and TiO_2 in the presence of PVA. The order in the photocatalytic efficiency was the same. Under UV irradiation the reaction was faster due to the synergistic mechanism explained in Fig. 3.7. In the presence of O_2 the activity was reduced due to a competition between dye and oxygen for the reoxidation of the reduced HPA.

Yoon and co-workers prepared composites containing $H_3PW_{12}O_{40}$ and nanochains Ag^+–N–TiO_2. These materials are highly visible-light-sensitive photocatalysts for efficient two-colour solar cells [98]. The visible-light absorption of Ag^+–N–TiO_2 became broader and stronger upon formation of composites with the HPA, due to the charge transfer between the HPA and TiO_2 nanochains. Shi et al. [99] prepared Ce-$H_3PMo_{12}O_{40}/TiO_2$ and La-$H_3PW_{12}O_{40}/TiO_2$ rare earth and HPA co-doped composite photocatalysts by the sol–gel method. These catalysts presented higher photocatalytic activity for the degradation of methylene blue dye as compared with bare TiO_2. Authors claimed the synergistic effect between the rare-earth ions and HPA that inhibited the recombination of photo-generated electron–hole pairs, but they did not clarify the roles of the so-called co-doping and the rare elements in the reaction mechanism. TiO_2/fly-ash cenosphere photocatalysts, modified with $H_3PW_{12}O_{40}$ or $H_3SiW_{12}O_{40}$, were prepared via the sol–gel method followed by a solvothermal method [100]. The composite materials shifted the absorption edge of the bare fly-ash TiO_2 to the visible-light region. The photocatalytic mineralization of ciprofloxacin under visible-light irradiation was enhanced by using the sample containing HPA, but no explanation was offered by authors about this result. Feng et al. prepared $H_3PW_{12}O_{40}/TiO_2$ catalysts with different HPA loading levels by an impregnation method [101]. The visible-light activity of the samples was affected by both the HPA loading and the amount of lanthanum used as doping element of TiO_2. The prepared composites were used as photocatalysts for the imidacloprid pesticide degradation, and the 20 wt% $H_3PW_{12}O_{40}$/0.3 % La–TiO_2 sample showed the best photocatalytic activity, achieving 98 % pesticide conversion after 60 min. The plenary Keggin cluster encapsulated into a titanium-exchanged HY (TiHY) zeolite was also used for the photocatalytic degradation of methyl orange [102]. Photoreaction rate increased 20 times as compared to the rate observed in the presence of HPA-encapsulated HY zeolite without Ti and nine times compared to the TiHY zeolite without HPA. The reaction rate increased four times by using HPA-encapsulated TiHY zeolite with respect to a home-prepared colloidal TiO_2. Authors explain this fact by considering that the zeolite matrix provides a good dispersion of active titanium sites and free access of the dye molecules to these isolated sites, which helps to enhance the photocatalytic activity. NaY zeolite incorporating TiO_2, $H_3PMo_{12}O_{40}$ and Co (II) [103], Ni(II) and Ru(III) [104] were prepared for methyl orange photocatalytic degradation. Authors reported that the photoreduction of the dye using the composite materials occurred via the reduced HPA species formed under solar irradiation, which transfer electrons to the transition metals with the assistance of the zeolite framework. The electron transfer is proposed to occur from the reduced HPA species to the Lewis acid sites of the zeolite and not directly to the transition metals, which then provide electrons to methyl orange that is photoreduced to hydrazine. Unfortunately, authors did not report the fate of the aromatic rings of the dye and provide the information about the substrate mineralization.

The pH value of the HPA solution plays an important role in the impregnation process of HPA onto TiO_2. Rengifo et al. impregnated $H_3PW_{12}O_{40}$ on TiO_2 nanoparticles at pH ranging from 1 to 10 [105]. Visible-light-absorbing TiO_2 materials were obtained only at pH 1 and 2, where the unchanged Keggin cluster was present on the TiO_2 surface. Authors suggest that visible-light absorption of the composite can be attributed to the formation of a complex between the Keggin anion and surface defects of TiO_2. In our view, a further effort is necessary to clarify the nature of this complex. The visible-light photocatalytic activity of these materials in the destruction of waterborne pollutants is explained by the fact that the surface HPA–TiO_2 complex might be excited by visible light, yielding an excited state of HPA–TiO_2 complex able to inject an electron to the TiO_2 conduction band. The resulting oxidized HPA^+–TiO_2 complex could accept an electron from the

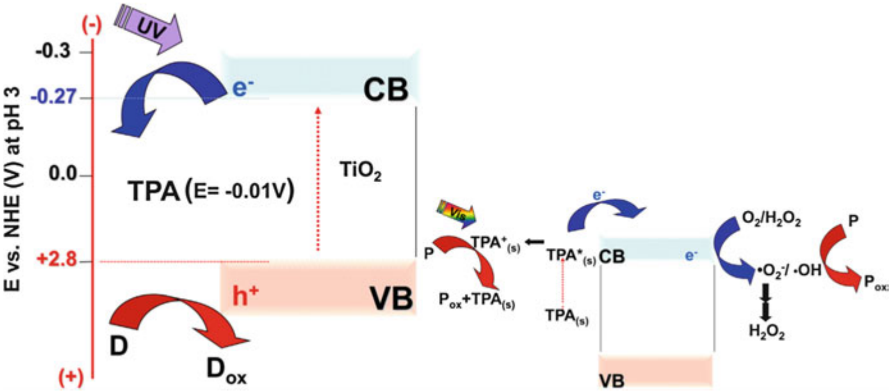

Fig. 3.12 Scheme suggested for the photocatalytic process occurring in HPA–TiO_2 systems under UV light (*left*) or visible-light irradiation (*right*). TPA corresponds to tungstophosphoric acid ($H_3PW_{12}O_{40}$) (Reprinted with permission from Ref. [105]. Copyright 2014, Elsevier)

organic pollutant. On the other hand, the electron injected into the TiO_2 conduction band could be trapped by molecular oxygen previously adsorbed on the metal oxide surface leading to the formation of H_2O_2 and consequently to OH radicals, as reported in Fig. 3.12.

Mesoporous TiO_2, prepared with urea as a low-cost pore-forming agent, was used also as support for $H_4SiW_{12}O_{40}$. This composite was a visible-light-absorbing material [106]. Interestingly, the presence of HPA shifted the anatase–rutile transition temperature towards temperatures higher than 600 °C. In the composites annealed up to 500 °C, the $[SiW_{12}O_{40}]^{4-}$ anion exhibited a strong interaction with TiO_2 surface probably due to the formation of surface complexes that should be responsible for its visible-light absorption. The photocatalytic activity of these materials has been tested using 4-chlorophenol as model pollutant revealing that the photocatalytic activity mainly depended on the HPA amount and on the annealing temperature. Also Feng et al. prepared a mesoporous TiO_2 to support $H_3PW_{12}O_{40}$ and $H_4SiW_{12}O_{40}$. The templating agent in this case was the nonionic surfactant P123 [107]. The photocatalysts were tested by using dinitrotoluene as the substrate to degrade (ca. 95 % disappeared after 4 h of irradiation in the presence of $H_3PW_{12}O_{40}/TiO_2$).

Composite catalysts $H_3PW_{12}O_{40}$/La-doped TiO_2 with different loading levels were synthesized using the impregnation method [108]. The visible-light activity of the composites in the degradation of the pesticide imidacloprid was higher with respect to that observed in the presence of bare TiO_2. The 20 % $H_3PW_{12}O_{40}$/0.3 % La–TiO_2 evidenced the best performance.

In the previous section, transition-metal-substituted polyoxometalates (TMSPs) supported on SiO_2 [61, 62] have been mentioned. TMSPs have been also tested when immobilized on TiO_2. For instance, the $H_5PW_{10}V_2O_{40}$ supported on TiO_2 was active in the photocatalytic decomposition of dimethyl sulphide (DMS) in gas–

solid regime [109]. DMS was irradiated with visible light from LED ($\lambda > 400$ nm), black light UV-A ($\lambda < 400$ nm) and visible fluorescent lamp 'daylight' (variable emission in the UV-A and visible range). DMS decomposition was almost 100 % for the system containing the composite material with exposure to visible daylight. This system maintained stable catalytic activity up to 500 min. Also, an amine-functionalized three-dimensionally ordered macroporous material has been used to deposit a transition-metal-monosubstituted polyoxometalate. The material was prepared by soaking polystyrene spheres in methanol to obtain a large size three-dimensionally ordered macroporous TiO_2, which was further functionalized using 3-aminopropyltriethoxysilane. The amine-functionalized TiO_2 was impregnated with $K_5[Co(H_2O)PW_{11}O_{39}]$ [110]. The primary Keggin structures remained intact and bonded by the coupling agent to the surface of the anatase crystalline structure. The three-dimensional structure retained in the final composite improved the accessibility of the diffusing species because of the permeability offered by the macroporous structure. This material exhibited very interesting photocatalytic activity for the degradation of rhodamine B, salicylic acid, Congo red and malachite green oxalate under microwave-assisted irradiation. No leakage of the HPA from the hybrid photocatalyst was observed, due to the strong coordination interactions between the Keggin units and the amine-functionalized TiO_2 surface.

3.4 HPA on ZnO, ZrO_2 and Ta_2O_5

ZnO (band gap = 3.2 eV) is a photocatalytically active oxide which has been proposed as an alternative to TiO_2. Unfortunately, its basic surface is not an ideal substrate for the anchorage of the strongly acidic HPAs; in fact an acid–base reaction occurs on the surface giving rise to the total or partial decomposition of the cluster [74]. ZrO_2 has been seldom used as photocatalyst due to its wide band gap (5.0 eV, ca. 250 nm) [111]. $H_3PW_{12}O_{40}/ZrO_2$ composites with loading levels 5–20 wt% have been prepared by a wet impregnation method in ethanolic medium. Authors reported that the interaction between ZrO_2 and HPA, analogous to what occurred between HPA and TiO_2, can occur both by electrostatic forces and by means of hydrogen bonds. These interactions should avoid the HPA leaching. The presence of HPA on the ZrO_2 surface gave rise to a red shift in the absorption spectrum of the material and hence to a narrowing of the band gap [112]. Furthermore, the mesoporosity and homogeneous dispersion of the HPA on the oxide surface played an important role to improve the photocatalytic degradation of 4-nitrophenol and methylene blue dye. The composites showed the best photocatalytic activity at HPA loadings not higher than 15 wt%, being more active than both bare HPA and ZrO_2. ZrO_2-supported Ti-substituted Keggin-type polyoxometalates, $Li_5PW_{11}TiO_{40}/ZrO_2$ and $K_7PW_{10}Ti_2O_{40}/ZrO_2$, were prepared by incorporating the Keggin-type cluster into ZrO_2 matrix by the sol–gel method giving rise to a cluster chemically attached to the support [113]. The photocatalytic activity of these heterogeneized HPAs was tested for the dye naphthol blue black degradation, which was bleached and mineralized under UV illumination. The composites were more active than the homogeneous HPAs. The activity of the composites was attributed to the surface area of the composite and to the electron transfer to the Keggin unit. ZrO_2 precipitated by the sol–gel method in a solution containing $H_3PW_{12}O_{40}$ was used for the partial oxidation of primary and secondary benzylic alcohols to the corresponding aldehydes or ketones [114]. Aliphatic alcohols were also oxidized in good yields but at longer reaction times in comparison with benzylic alcohols. The reaction mechanism proposed involves a direct H-atom abstraction from the benzylic active C–H bond of the alcohol by photoexcited HPA rather than an electron transfer:

$$R_1R_2CHOH + POM^* \rightarrow R_1R_2C - OH + POM^- + H^+ \tag{3.12}$$

$$R_1R_2C - OH + POM^* \rightarrow R_1R_2C = O + POM^- + H^+ \tag{3.13}$$

The composite HPA/ZrO_2 was more active than the bare HPA for the partial alcohol oxidation. The HPA/ZrO_2 was activated by light absorption, and it reacted with alcohol to give the corresponding carbonyl compound. Reoxidation of photoreduced HPA by the dissolved O_2 in suspension completed the photocatalytic cycle. No indications are given about the light source employed. The higher photocatalytic activity of the HPA/ZrO_2 was explained analogously to that of the HPA/TiO_2 materials (see Fig. 3.7). Authors suggested a synergistic effect between ZrO_2 and the photoactivated HPA. In another paper, $H_3PMo_{12}O_{40}/ZrO_2$ was prepared by incorporating the HPA into a ZrO_2 matrix via the sol–gel method. In this way $H_3PMo_{12}O_{40}$ was chemically attached to the ZrO_2 support and primary Keggin structure remained unchanged [115]. The photocatalytic activity was tested via degradation of methylene blue, rhodamine B, Congo red, bromothymol blue and alizarin dyes in aqueous solutions under UV light. Some characterization results reported in this paper are exactly the same as that reported in [114]; however, in this case authors used a high-pressure mercury lamp as the light source. The HPA/ZrO_2 nanocomposite showed higher photocatalytic activity than bare HPA and ZrO_2 samples.

Ta_2O_5 is not a very popular material in photocatalysis. It presents the band gap energy of 3.9 eV and showed photoactivity only under UV irradiation [116] or under visible light when doped with N [117]. Jiang et al. prepared HPA/Ta_2O_5 composites by a sol–gel/hydrothermal method in the presence of a pluronic surfactant giving rise to high surface area tridimensional interconnected framework. They deposited $H_3PW_{12}O_{40}$ on Ta_2O_5, with loading levels 5.6–15.3 wt%, and used these composites to decompose and mineralize salicylic acid and rhodamine B under visible-light excitation [118]. Analogously to what was reported for the HPA/TiO_2 composite [89], the similar electronegativity and ionic radius of Ta^{5+} and W^{6+} allows the existence of an electrostatic interaction. This exists between the terminal W=O groups of the Keggin cluster and the Ta–OH_2^+ groups (formed by an acid–base reaction between the surface of the oxide and the $H_3PW_{12}O_{40}$) on the surface of the oxide, i.e. the formation of the species $(TaOH_2)^+[H_2PW_{12}O_{40}]^-$ or

$(TaOH_2)^+[H_5P_2W_{18}O_{62}]^-$. The absorption threshold onset of these HPA/Ta_2O_5 composites was extended to the visible region (420 nm), which enhanced the photocatalytic activity of the composites compared with that of both bare HPA and Ta_2O_5. In order to explain the increase of photocatalytic activity, authors attributed a role to the physico-chemical features of the HPA/Ta_2O_5 composites (porous structure, small particle size, homogeneous dispersion) as reported for an HPA/TiO_2 system prepared by the same group in the same way [89]. In any case, authors claimed that the synergism between HPA and the Ta_2O_5 semiconductor oxide is the same as explained in Fig. 3.7 for the composites HPA/TiO_2.

3.5 HPA Supported on C_3N_4, CdS and $BiVO_4$

Very recently graphitic carbon nitride (g-C_3N_4) has been developed as an effective semiconductor photocatalyst [119]. It possesses great practical value because of its stable chemical structure, narrow band gap (2.7 eV) and low preparation cost. However, g-C_3N_4 presents some disadvantages when used as a metal-free photocatalyst, due to its bulk layered structure, a rapid recombination of the photo-generated electron–hole pairs (e^-/h^+) and a low visible-light utilization efficiency [120–122]. Li et al. prepared composites $H_3PW_{12}O_{40}/C_3N_4$ nanotubes by a one-step hydrothermal treatment, and the latter were used for methyl orange and diethyl phthalate degradation under visible-light ($\lambda > 420$ nm) irradiation [123]. The photocatalytic activity of $H_3PW_{12}O_{40}/C_3N_4$ was significantly enhanced compared with that of bare C_3N_4.

The tubular nanostructures are formed through a nanosheet roll-up mechanism illustrated in Fig. 3.13. The high catalytic stability of the composites is attributed to the strong chemical interaction between the Keggin unit and the C_3N_4. The mechanism explaining the photocatalytic activity of these composites, also illustrated in Fig. 3.13, is the same proposed before for the HPA supported on semiconductor materials.

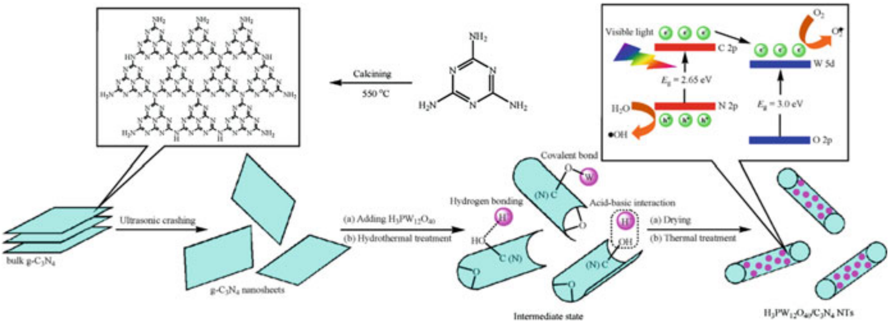

Fig. 3.13 The designed route for fabrication of $H_3PW_{12}O_{40}/C_3N_4$ NTs and the separation and transportation of photoinduced charge carriers under visible-light irradiation in this composite material (Reprinted with permission from Ref. [123]. Copyright 2014, Elsevier)

Cadmium sulphide (CdS) is a semiconductor that absorbs light at shorter wavelength than 520 nm; therefore, it could exhibit photocatalytic activity under visible-light irradiation. However, it shows low charge-carrier separation efficiency and poor photochemical stability. Zhao's group prepared the molecular self-assembled nanohybrids CdS quantum dots–$H_3PW_{12}O_{40}$–Au nanoparticles [124]. This nanohybrid tri-component material is analogous to that discussed in Fig. 3.5 and studied in [72] where CNTs are reported to be used instead of CdS quantum dots particles. Of course, in this case the role played by CdS was different from that played by CNTs. This composite showed photocatalytic activity in the photoproduction of H_2 and in the photodegradation of rhodamine B and methyl orange under visible irradiation. It was synthesized by the molecular self-assembly between the amine-modified CdS and the HPA-wrapped Au nanoparticles. In this way the Keggin cluster coupled with the CdS and Au nanoparticles. The photocatalytic activity of bare CdS, HPA and Au was negligible; on the contrary the three-component nanohybrid material showed some photocatalytic activity. Moreover, the activity increased by increasing the Au loading at least up to 6 % in weight of the metal with respect to the support, which was the maximum quantity used. Authors reported also that the bicomponent CdS–Au hybrid with the same Au loading showed lower activity because the composite contains HPA, indicating that HPA played a fundamental role because it promoted the separation of photoproduced electron–hole pairs on CdS quantum dots.

Figure 3.14 reports this hypothesized electron–hole pair separation mechanism in which the role of HPA in the electron transfer from the CB of CdS to Au NPs is illustrated. In the same figures also, SO_4^{2-}/SO_3^{2-} and S/S^{2-} redox couples appear

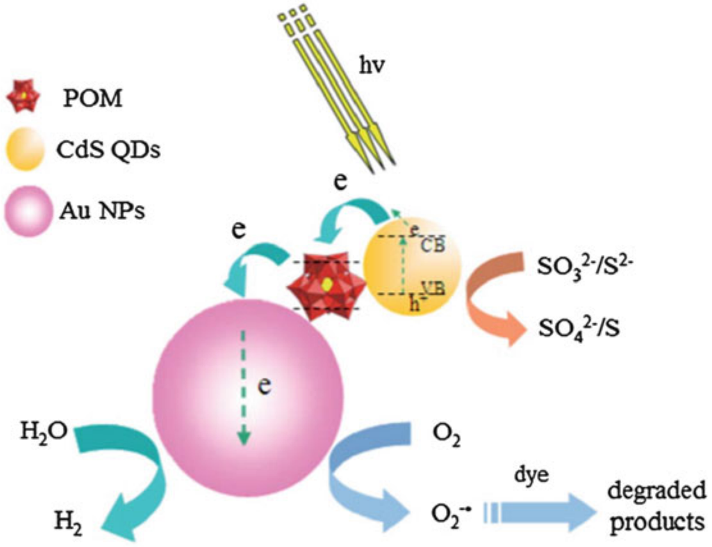

Fig. 3.14 The photocatalytic mechanism of the CdS QDs–Au NPs–HPA nanohybrid (Reprinted with permission from Ref. [124]. Copyright 2013, Royal Society of Chemistry)

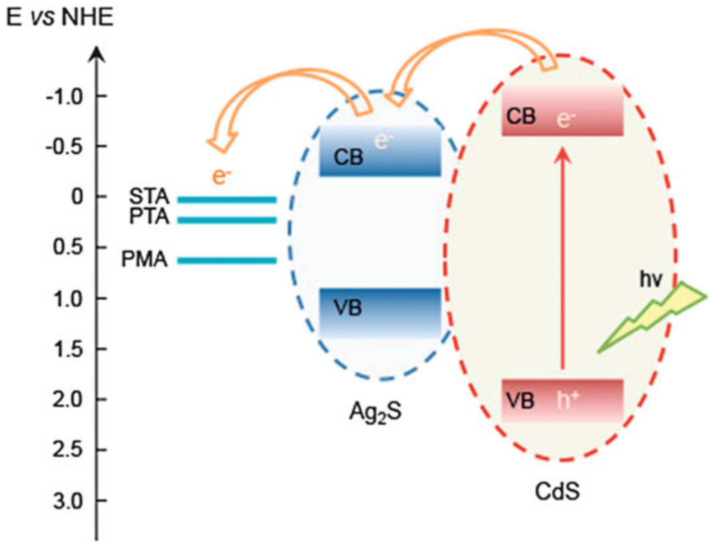

Fig. 3.15 Electron transfer in the band structure of the ternary material HPA–Ag_2S–CdS under visible-light irradiation ($\lambda > 420$ nm) (STA, $SiW_{12}O_{40}$; PTA, $PW_{12}O_{40}$; and PMA, $PMo_{12}O_{40}$) (Reprinted with permission from Ref. [125]. Copyright 2014, Royal Society of Chemistry)

because the photoproduction of H_2 was carried out in the presence of SO_3^{2-} or S^{2-} as sacrificial species.

Kornarakis et al. have prepared hybrid mesoporous materials consisting of a heteropolyacid along with Ag_2S and CdS nanocrystals [125]. They used HPAs as electron acceptors in the CdS-based heterojunction photocatalysts. Ag_2S is a semiconductor that possesses favourable band edge positions with respect to the reduction potential of CdS and HPA. In particular, the CB level of Ag_2S (−0.20 V vs. NHE) lies below that of CdS (−0.66 V vs. NHE) and above the reduction potential of the Keggin clusters. Therefore, the incorporation of the HPA and Ag_2S in the CdS matrix can induce delocalization of photoexcited electrons at CdS along the potential gradient of HPA–Ag_2S–CdS heterostructures. Figure 3.15 illustrates the electron transfer from the conduction band of CdS to that of the Ag_2S and hence to the empty lowest unoccupied molecular orbital (LUMO) of the HPA. The ternary structures HPA–Ag_2S–CdS can drive the photoexcited electrons from CdS to the HPAs, enhancing the charge separation efficiency and thereby the photocatalytic activity.

These ternary materials were active in the photocatalytic oxidation of various para-substituted benzyl alcohols to the corresponding carbonyl compounds. The thermodynamic band alignment of the components is the driving force for the increased photoactivity compared to the parent Ag_2S–CdS and CdS samples. The photocatalytic activity changes with the HPA employed, due to the different position of their LUMO energy level.

$BiVO_4$, with a band gap of 2.32 eV, has been also proposed as a promising photocatalyst. The photocatalytic activity of pure $BiVO_4$, however, is limited due to the fast recombination rates of photo-generated electron–hole pairs [126]. Zhang et al. proposed to load the $H_3PW_{12}O_{40}$ on the surface of $BiVO_4$ prepared using a hydrothermal and impregnation method. The band gap of the composite was narrower compared with that of bare $BiVO_4$, and the photocatalytic performance, investigated by the degradation of methylene blue dye (MB) under visible-light irradiation, was higher [127]. The highest photodegradation efficiency of MB was obtained at 10 wt% HPA content. The enhanced photocatalytic performance under visible-light irradiation was attributed to the efficient separation of photo-generated electron–hole pairs in the HPA- and $BiVO_4$-coupled system.

3.6 HPA-Based Materials with HPA Associated to Inorganic, Organic or Organometallic Moieties

HPA-based inorganic/organic hybrids have drawn much attention in various areas because these hybrids present properties both of inorganic materials and organic compounds.

The heterogeneization of the HPAs for photocatalytic purposes in environmental remediation can be successfully performed, but various strategies of catalysts preparation to avoid shortcomings, such as limited activity or stability during the reaction, are still explored by researchers.

Cao and co-workers coupled an organic cation, i.e. the macrocyclic cucurbituril, to form a water-insoluble composite with the Keggin-type $[SiW_{12}O_{40}]^{3-}$ anion [128]. Cucurbit[6]uril (CB[6]) is a hexameric macrocyclic compound comprising 6 glycoluril units and 12 methylene bridges. Due to its strong affinity towards organic dye molecules, CB[6] is considered suitable for treatment of effluents from dye industries just by sorption. Figure 3.16 shows the interaction between CB [6] and HPA (Fig. 3.16a) and the packing structure of the composite (Fig. 3.16b).

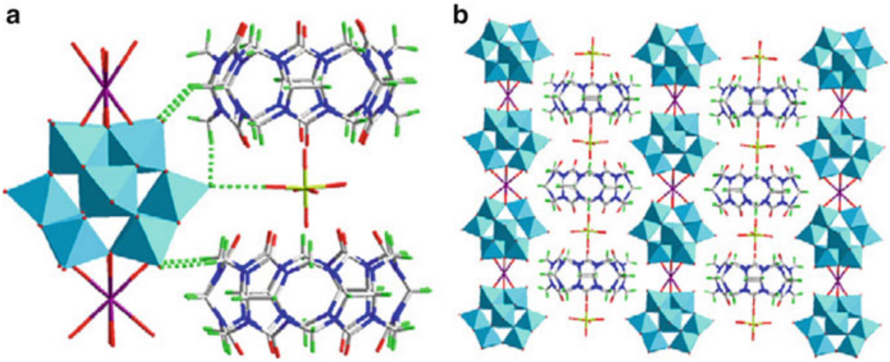

Fig. 3.16 (**a**) Hydrogen bond interaction between neighbouring Keggin HPA $[SiW_{12}O_{40}]^{4-}$ and CB[6] units to form the composite (**b**) (Adapted with permission from Ref. [128]. Copyright 2011, Elsevier)

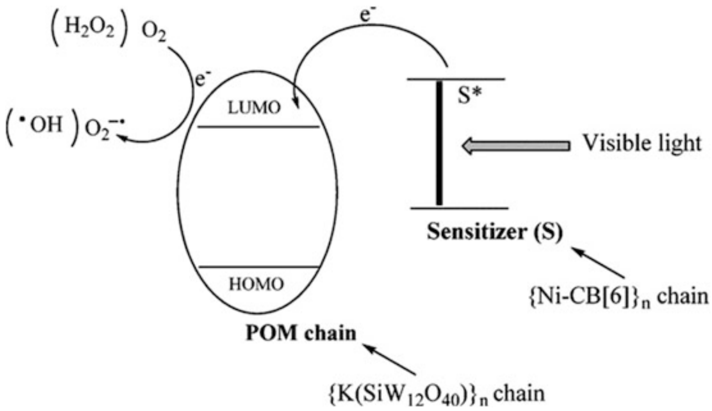

Fig. 3.17 Proposed photocatalytic degradation mechanism by using CB[6]–HPA composite as heterogeneous photocatalysts (Reprinted with permission from Ref. [128]. Copyright 2011, Elsevier)

The photocatalytic test reaction was the degradation of methyl orange under visible-light irradiation. As schematized in Fig. 3.17, the macrocyclic organic chain can act as a sensitizer under visible light, whereas the HPAs chain as an electron acceptor.

Another explored way in the water-insoluble composite HPA-based inorganic/organic hybrids preparation is to couple Keggin HPA and thionine (TH) with a simple precipitation method to obtain $(TH)_3PW_{12}O_{40}$ powders with specific surface area of ca. 20 $m^2\ g^{-1}$. Rhodamine B was bleached and mineralized under visible light ($\lambda > 420$ nm). TH acted as a sensitizer extending the spectrum of the $H_3PW_{12}O_{40}$ into the visible region [129]. Indeed, TH is excited by visible light and subsequently it could inject electrons in the HPA LUMO. In this way O_2 trapped an electron to generate oxidant radicals able to mineralize the rhodamine B molecules. The mechanism proposed for the sensitization is schematized in Fig. 3.18. In this paper authors did not explain the fate of the oxidized TH (TH^{*+}); consequently, from the reported mechanism, it seems that also TH can be degraded during the photocatalytic tests, and this should give rise to a deactivation of the catalyst that, anyway, was not observed, at least after five reaction cycles.

Another type of HPA-based composite material was prepared by Bonchio et al. that obtained an organic sensitized HPA heterogeneous photocatalyst by using a modified fullerene as sensitizer [130]. They followed two strategies: the covalent functionalization of lacunary decatungstosilicate with organosilylfulleropyrrolidines or the electrostatic interaction between cationic sensitizer and the HPA. The Keggin-based lacunary HPA ($[SiW_{10}O_{36}]^{8-}$) functionalized with tris (alkoxysilane)-C60-fulleropyrollidines (see Fig. 3.19) showed good photocatalytic activity for phenol photo-oxidation or L-methionine methylester photo-oxidation to the corresponding sulphoxide. The reactions were carried out in aqueous solution

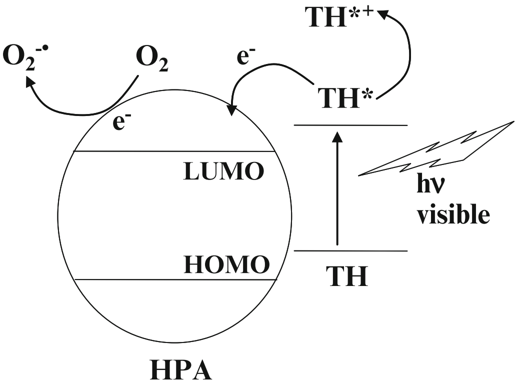

Fig. 3.18 Proposed mechanism for the HPA sensitization by thionine (Adapted with permission from Ref. [129]. Copyright 2012 Elsevier)

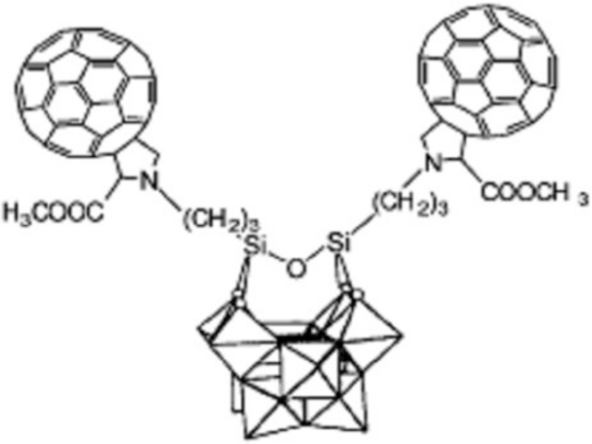

Fig. 3.19 Structure of the lacunary HPA functionalized with the fullerene derivative (Adapted with permission from Ref. [130]. Copyright 2004, Wiley)

under irradiation with $\lambda > 375$ nm. Phenol was partially oxidized to benzoquinone with ca. 90 % conversion. The solid photocatalyst was recycled three times without losing its activity. The presence of fullerene was essential for the photocatalytic activity; in fact photocatalysts functionalized with $Si(CH_2)_xR$ groups (R = Me, NH_2, Ph) were inactive. The type of bonding between fullerene and HPA has a huge effect on the system stability and can be used to modify the photocatalytic performance (see Fig. 3.19).

Zhou et al. prepared an HPA-based plasmonic visible-light $Ag/Ag_xH_{4-x}SiW_{12}O_{40}$ (Ag/AgHSiW) photocatalyst [131, 132]. The composite nanoparticles, possessing more OH surface groups than TiO_2 Degussa P25, showed a strong and broad absorption in the visible region and a weak plasmonic emission. The Ag/AgHSiW material showed higher photocatalytic activity for the decomposition of methylene blue dye under visible-light irradiation than bare Ag nanoparticles, $H_4SiW_{12}O_{40}$ and $Ag_4SiW_{12}O_{40}$ [132]. The composite activity was attributed to the

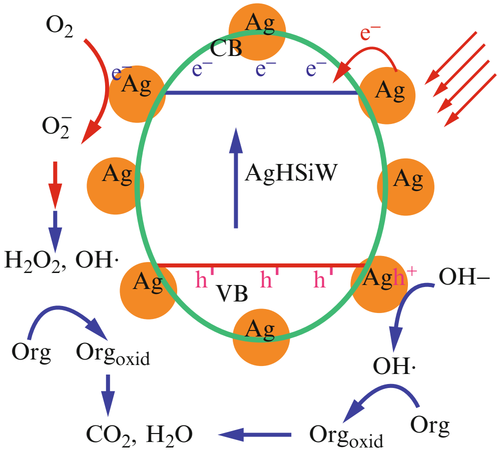

Fig. 3.20 Schematic diagram showing the energy band structure and electron–hole pair separation in Ag/AgHSiW NPs (Reprinted with permission from Ref. [132]. Copyright 2013, Elsevier)

synergistic effect of photoexcited HPA (AgHSiW) and plasmon-excited Ag nanoparticles (see Fig. 3.20). HPA showed redox ability and photocatalytic activity, whereas Ag could effectively accelerate the separation of electrons and holes.

Immobilization inside a suitable solid host matrix could be considered as a convenient approach to develop a (photo)catalyst. An optimum host should possess some features as (i) suitable cavities with adequate size and shape to encapsulate the HPA guest molecule allowing the homogeneous HPA dispersion inside the solid, (ii) appropriate openings for the diffusion of reactants and products, (iii) mild and simple preparation conditions of the composite and (iv) stability. Metal–organic frameworks (MOFs) are organic–inorganic hybrid solids, which have recently emerged as a particular class of functional solid-state materials, and they have been identified as adequate candidates for the scopes above claimed [133]. HPAs decorating the MOFs surface were reported as good heterogeneous catalysts because they exhibited a satisfactory immobilization along with an improvement of other catalytic properties [134]. Interestingly, the introduction of HPAs into the metal–organic frameworks (MOFs) to form PMOFs (where P stands for POM, polyoxometalate) was found as one of the most promising strategies to optimize the performance of the HPA clusters [135, 136].

Several networks can be obtained from polyoxometalates-based metal–organic frameworks (PMOFs), as a new class of materials. The archetypal and lacunary Keggin and Wells–Dawson anions have gone through extensive development to construct POMOFs with excellent catalytic efficiency in a heterogeneous manner [137, 138]. Zhu et al. have started the exploration of a new POM-based MOF in situ assembled and used as photocatalyst. This compound is a water-stable and insoluble photocatalyst that exhibits not only photocatalytic activity for the degradation of RhB under visible-light irradiation but also high stability, and it was easily separated from the reaction system for reuse [139]. It was hydrothermally synthesized by reaction of $FeCl_2$, Na_2MoO_4, H_3PO_4 and imidazole at 180 °C for 3 days.

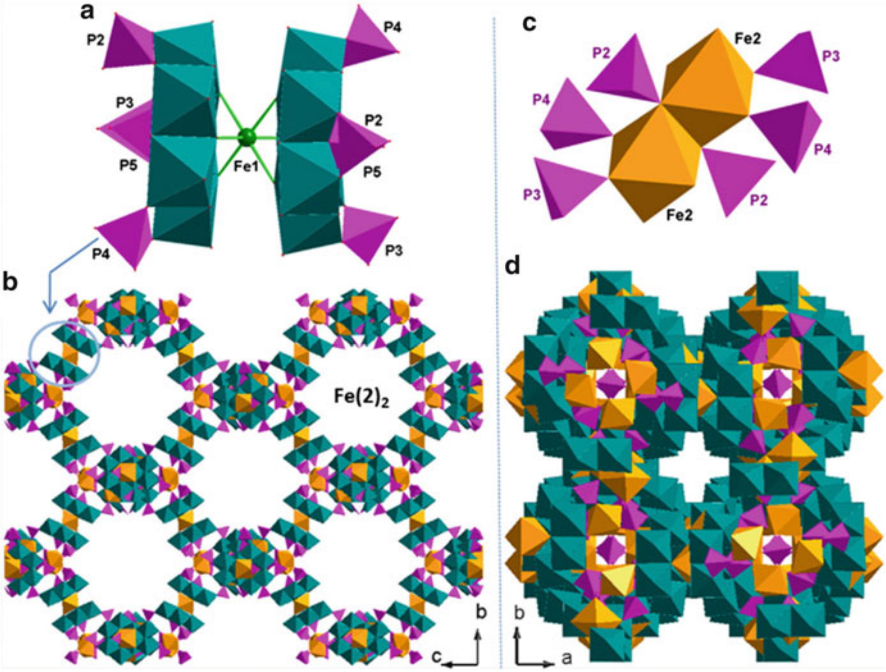

Fig. 3.21 (**a**) A sandwich-type $Fe^{II}[P_4Mo_6]_2$ cluster; (**b**) a 3D porous framework along [100] direction; (**c**) a Fe(II)$_2$ dimer; (**d**) the total 3D porous framework along [001] direction with cross-shaped channel. The free water molecules are omitted for clarity (Reprinted with permission from Ref. [139]. Copyright 2014, Elsevier)

A schematic representation of this novel molybdophosphate-based Fe(II) and (III)-metal–organic framework (FeMoP-MOF), with the formula $\{Na_6(H_2O)_{12}[Fe^{II}{}_2]_2[Fe^{III}{}_4(PO_4)][Fe^{II}(Mo_6O_{15})_2(PO_4)_8]_2\}(OH)_3{\cdot}33H_2O$, is reported in Fig. 3.21.

Guo et al. have also prepared a PMOF with the supramolecular compound with formula, $[(H_2toym)_2(SiW_{12}O_{40})]{\cdot}6H_2O$, where ‘toym’ is a multidentate O-donor ligand, i.e. (2,4,6-tris[1-(4-oxidroxypyridinium)-ylmethyl]-mesitylene) [140]. The solid network is templated by the HPA. The ‘host’ supramolecular network, with large pores, is composed by the partly protonated O-donor ligands, whereas the HPA ‘guest’ is located in the pores and dispersed between two organic layers in the complexes. The compound exhibited photocatalytic activity for methylene blue bleaching under UV light irradiation. The optical absorbance allowed to calculate the band gap of the solid which resulted 2.65 eV. No explanation is given by the authors about the mechanism of the photocatalytic reaction. Liu et al. prepared four PMOFs by using a bis(triazole) N-donor ligands. They used the HPA $[Mo_6O_{18}(O_3AsPh)_2]^{4-}$ and copper(I)-organic fragments containing the triazole ligands [141]. The structures possessed band gap between 2.7 and 1.9 eV, and they were used for the methylene blue bleaching by irradiating with a 500 W Xe

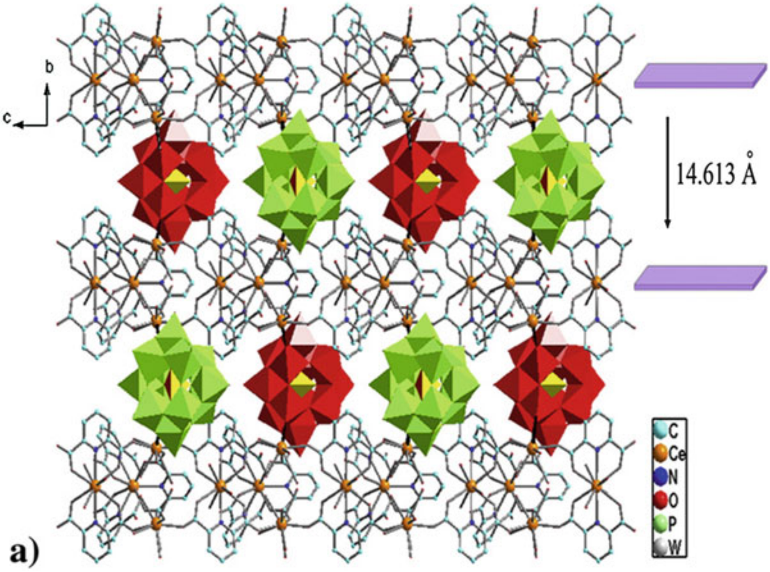

Fig. 3.22 Pillared layer architecture containing the Keggin HPA (Reprinted with permission from Ref. [142]. Copyright 2011, Elsevier)

lamp. Authors claimed that the presence of O_2 was essential for the photocatalytic process but no additional explanation about the mechanism was given.

The layered double hydroxides (LDHs) architecture was also used to design 3D frameworks with large channels hosting the plenary Keggin HPA [142]. The material exhibited a 3D Ce(III) hydrotalcite-like structure constructed from 2D cationic $[\{Ce(H_2O)_5\}_2\{Ce(pdc)_2(H_2O)_4\}\{Ce(pdc)_3\}]^{2+}$ layers, where pdc = pyridine-2,6-dicarboxylate, pillared by $[PW_{12}O_{40}]^{3-}$ anions (see Fig. 3.22).

This material was active for photocatalytic H_2 evolution in methanol aqueous solution under UV irradiation, but further efforts should be addressed to understand the mechanism of this reaction by using the HPA–LDHs material.

Biboum et al. synthesized polyionic liquids (PILs) with an HPA to form water-insoluble nanomaterials [143]. The macrocyclic HPA $[H_7P_8W_{48}O_{184}]^{33-}$ (see Fig. 3.23) synthetized by the authors resulted stable in aqueous media, underwent fast and chemically reversible 8-electron reduction processes and interacted with different imidazolium-based PILs to form a water-insoluble heterogeneous photocatalyst. This photocatalyst was able to bleach acid orange 7 dye also in the absence of O_2 and under visible-light irradiation ($\lambda > 400$ nm). On the contrary, the bare HPA or PIL showed a negligible activity indicating that a synergistic effect occurred when the two species were coupled. Moreover, authors claimed that the complete mineralization of acid orange 7 dye was also achieved with their photocatalyst, although they did not report any strong experimental evidence to prove this insight; indeed, they followed only the disappearance of the characteristic peaks in the AO7 UV-visible spectrum.

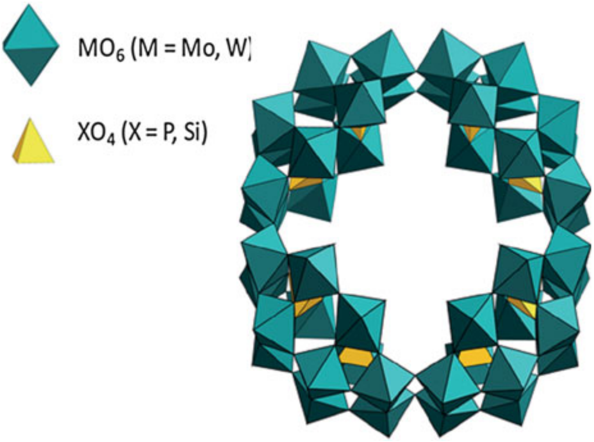

Fig. 3.23 Scheme of the heteropolyacid prepared by Biboum et al. and used as homogeneous photocatalyst in solution and as heterogeneous one when bonded to PILs (Adapted with permission from Ref. [143]. Copyright 2012, Royal Society of Chemistry)

Porous coordination polymers (PCPs) were also used as host to guest HPAs. Fu et al. report a kind of PCPs/HPA host–guest compound consisting of $[Cu(II)_2Cu(I)_3(OH)_4(H_2O)_2(TPT)_4][PW_{12}O_{40}]$, where TPT corresponds to tris(4-pyridyl) triazine. This supramolecular compound locates the Keggin anion at the centre of a large cationic ring containing TPT and Cu cations [144]. According to the authors, this metal–organic host framework strengthened the photocatalytic activity of the HPA, which was able to bleach methyl orange under UV irradiation. The bleaching rate was low by using only the supramolecular compound, but it dramatically increased when H_2O_2 was also present.

Among the classical conventional methods to heterogeneize HPA, we have reported the immobilization on a support and the precipitation with monovalent cations such as K^+, Cs^+ or NH_4^+ to form insoluble salts. Moreover, also rare-earth ions can be used to change the solubility of HPAs. Indeed, rare-earth ions have the ability to form complexes with various Lewis bases by the interaction of the functional groups with their f-orbitals. Li et al. have prepared an insoluble rare-earth-doped phosphotungstic acid by hydrothermal method. The photocatalytic activities of La^{3+}/Ce^{3+}-$H_3PW_{12}O_{40}$ were evaluated in the photobleaching of methyl orange and rhodamine B under UV and visible-light irradiation [145]. Authors observed that the behaviour of La(III)-loaded samples was better than that of Ce (III)-loaded HPA. The activity has been attributed to the synergistic effect existing between the rare-earth ions and the heteropolyacids, which can enlarge the light absorption and inhibit the recombination of photo-generated electron–hole pairs. Xue et al. report the hydrothermal synthesis and physico-chemical characterization of a complicated high-dimensional and high-connected HPA-based hybrid compound, namely, $[Ag_3(pytz)_2(H_2O)]_2 \cdot [HAgGe\text{-}Mo_{12}O_{40}] \cdot H_2O$, which has been synthesized by reactions of pyridyltetrazoles (pytz) and Keggin HPAs. The compound presents HPA chains pillaring transition-metal complexes, which represents the highest coordination number of a Keggin HPA [146]. This material was photocatalytically active in the decomposition of rhodamine B dye under UV irradiation.

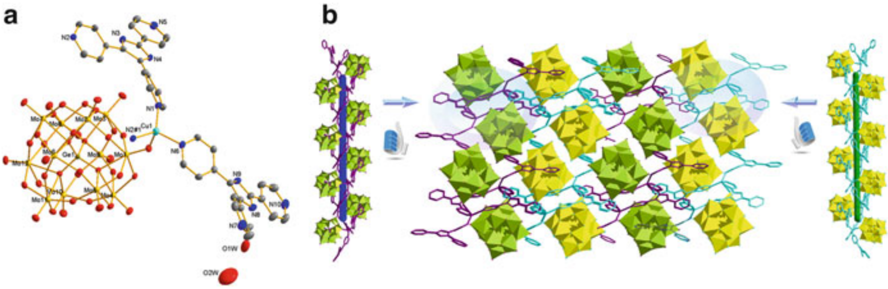

Fig. 3.24 (**a**) Coordination of the Cu(I) ions bonded to the Keggin cluster prepared by Zhou et al. which forms chains; (**b**) view of the one-dimensional left- and right-hand helical chain formed by heteropolyacid clusters (Reprinted with permission from Ref. [148]. Copyright 2014, Elsevier)

Sheng et al. have synthesized the Keggin $K_6ZrW_{11}O_{39}Sn{\cdot}12H_2O$ ($ZrW_{11}Sn$), which can be activated by sunlight. This solid is active in the decolouration of some dyes, i.e. Acid Brilliant Scarlet 3R, Reactive Red 24 and Reactive Black 5 with natural sunlight irradiation [147]. Unfortunately, the mechanism of the degradative process has not been fully explained, and the homogeneous decomposition of the dyes cannot be entirely ruled out.

Very recently Zhou et al. used twisted rigid ligands to synthetize compounds based on Keggin clusters with left- and right-handed helical chains [148] (see Fig. 3.24). Helical compounds based on HPAs have attracted attention because of their attractive structural features and potential applications, for instance, in asymmetrical catalysis. The chains are further extended to three-dimensional supramolecular structures by hydrogen bonds. The methylene blue dye has been photocatalytically bleached in the presence of this solid. Stacking of the chains leads to small pore-size and narrow pore-size distribution which are not beneficial for the photocatalytic activity.

3.7 Conclusions

To conclude the overview of the state of the art in the use of heteropolyacid Keggin clusters in heterogeneous photocatalysis for environmental applications, we can say that there is still a long way to walk through. The photocatalytic activity of heteropoly compounds (HPA) in homogeneous regime has been extensively reported along with the use of supported HPAs in thermal catalysis for acidic and redox processes. The nature of HPAs as highly soluble compounds in polar solvents hinders their use as heterogeneous photocatalysts. Consequently, an appropriate heterogeneization has been reported by many researchers in order to use them in heterogeneous reactions, in particular to carry out photocatalytic degradations of several pollutants. The preparation of supported HPAs both onto non-active and photocatalytically active oxides has been carried out obtaining materials where the nature of the HPA was maintained and where the bond between the support and the HPA was mainly electrostatic. This interaction seems to be enough strong to avoid significant leaching of the HPA. Nevertheless, the covalent bond between the HPA and the oxide surface resulted more appropriate for preventing leaching, and it has been obtained by using 'lacunary' and functionalized HPA linked to supports that could be also functionalized. The immobilized HPA acted as a photocatalyst, similarly to what observed in homogeneous regime, but the use of photocatalitically active supports appeared to be preferable than the use of non-photocatalytically active supports. Indeed, the improvement of the photocatalytic activity found by using HPA-based composites was related in the first case to the electron transfer from excited HPA to O_2 to form the final oxidant species, i.e. the hydroxyl radicals. This electron transfer can occur directly from the HPA to the O_2 or alternatively through the conduction band of photoexcited oxides. Recently, the immobilization of HPA clusters has been approached by exploring the guest–host synthesis materials where the guest HPA was incorporated in inorganic or organic supramolecular hosts. Home-tailored HPAs, different from the more well-studied Keggin and Wells–Dawson structures, represent a novelty in this field, particularly when 'heterogeneized' by using polyionic liquids. Alternative HPA structures should be rationally designed, and the engineered clusters should be used to a particular function, for instance, heterogeneous photocatalyst synthesis.

The explanation of the improvement of the photocatalytic activity of HPAs inside the host systems is still unclear. An effort to clarify the mechanism of reaction is definitively necessary.

Notably, most of the literature reports the use of dyes as model molecules to test the photocatalytic activity of heterogeneized HPAs in the visible region. The use of alternative and challenging molecules is a must in order to fully understand the mechanistic aspects of the photocatalytic heterogeneous process. It is well known that the structure of a molecule determines its function, and this reasoning can be also applied to HPA clusters.

References

1. Fujishima A, Honda K (1972) Electrochemical photolysis of water at a semiconductor electrode. Nature 238:37–38
2. Schiavello M (ed) (1998) Photocatalysis and environment. Trends and applications. Kluwer, Dordrecht
3. Chen H, Nanayakkara CE, Grassian VH (2012) Titanium oxide photocatalysis in atmospheric chemistry. Chem Rev 112:5919–5948
4. Kubacka A, Fernández-García M, Colón G (2012) Advanced nanoarchitectures for solar photocatalytic applications. Chem Rev 112:1555–1614
5. Palmisano L, Augugliaro V, Bellardita M, Di Paola A, García-López E, Loddo V, Marcì G, Palmisano G, Yurdakal S (2011) Titania photocatalyst for selective oxidations in water. ChemSusChem 4:1431–1438

6. Palmisano G, García-López EI, Marcì G, Loddo V, Yurdakal S, Augugliaro V, Palmisano L (2010) Advances in selective conversions by heterogeneous photocatalysis. Chem Commun 46:7074–7089
7. Marcì G, Addamo M, Augugliaro V, Coluccia S, García-López EI, Loddo V, Martra G, Palmisano L, Schiavello M (2003) Photocatalytic oxidation of toluene on irradiated TiO_2: comparison of degradation performance in humidified air, in water and in water containing a zwitterionic surfactant. J Photochem Photobiol A 160:105–114
8. Di Paola A, García-López EI, Marcì G, Palmisano L (2012) A survey of photocatalytic materials for environmental remediation. J Hazard Mater 211–212:3–29
9. Katsoulis DE (1998) A survey of applications of polyoxometalates. Chem Rev 98:359–387
10. Long D, Burkholder E, Cronin L (2007) Polyoxometalate clusters, nanostructures and materials: from self assembly to designer materials and devices. Chem Soc Rev 36:105–121
11. Pope MT, Müller A (1991) Polyoxometalate chemistry: an old field with new dimensions in several disciplines. Angew Chem Int Ed Engl 30:34–48
12. Pope MT (1983) Heteropoly and isopoly oxometalates. Springer, Berlin
13. Errington RJ, Wingad RL, Clegg W, Elsegood MRJ (2000) Direct bromination of Keggin fragments to give $[PW_9O_{28}Br_6]^{3-}$: a polyoxotungstate with a hexabrominated face. Angew Chem Int Ed Engl 39:3884–3886
14. Mizuno N, Misono M (1998) Heterogeneous catalysis. Chem Rev 98:199–217
15. Okuhara T, Mizuno N, Misono M (1996) Catalytic chemistry of heteropoly compounds. Adv Catal 41:113–252
16. Misono M (2001) Unique acid catalysis of heteropoly compounds (heteropolyoxometalates) in the solid state. Chem Commun 1141–1152
17. Briand LE, Baronetti GT, Thomas HJ (2003) The state of the art on Wells–Dawson heteropoly-compounds: a review of their properties and applications. Appl Catal A 256:37–50
18. Micek-Ilnicka A (2009) The role of water in the catalysis on solid heteropolyacids. J Mol Catal A 308:1–14
19. Kozhevnikov IV (2002) Catalysis for fine chemical synthesis. Vol. 2: catalysis by polyoxometalates. Wiley, Chichester
20. Anastas PT, Warner JC (1998) Green chemistry: theory and practice. Oxford University Press, New York
21. Boglio C, Lemière G, Hasenknopf B, Thorimbert S, Lacôte E, Malacria M (2006) Lanthanide complexes of the monovacant Dawson polyoxotungstate [a1-P2W17O61]10 as selective and recoverable Lewis acid catalysts. Angew Chem 118:3402–3405
22. Kozhevnikov IV (1998) Catalysis by heteropoly acids and multicomponent polyoxometalates in liquid-phase reactions. Chem Rev 98:171–198
23. Zhou Y, Chen G, Long Z, Wang J (2014) Recent advances in polyoxometalate-based heterogeneous catalytic materials for liquid-phase organic transformations. RSC Adv 4:42092–42113
24. Pope MT, Müller A (2001) Polyoxometalate chemistry from topology via self-assembly to applications. Kluwer, New York
25. Borrás-Almenar JJ, Coronado E, Müller A, Pope MT (2003) Polyoxometalate molecular science. Kluwer, Dordrecht
26. Yamase T, Pope MT (2004) Polyoxometalate chemistry for nano-composite design. Kluwer, New York
27. Hill CL (1998) Introduction: polyoxometalates multicomponent molecular vehicles to probe fundamental issues and practical problems. Chem Rev 98:1–2
28. Cronin L, Müller A (2012) From serendipity to design of polyoxometalates at the nanoscale, aesthetic beauty and applications. Chem Soc Rev 41:7333–7334
29. Omwoma S, Chen W, Tsunashima R, Song YF (2014) Recent advances on polyoxometalates intercalated layered double hydroxides: from synthetic approaches to functional material applications. Coord Chem Rev 258–259:58–71

30. Omwoma S, Gore CT, Ji Y, Hu C, Song Y (2015) Environmentally benign polyoxometalate materials. Coord Chem Rev 286:17–29
31. Hill CL (ed) (1996) Polyoxometalates in catalysis. J Mol Catal A 114:1–359
32. Hill CL (ed) (1998) Polyoxometalates multicomponent molecular vehicles to probe fundamental issues and practical problems. Chem Rev 98:1–390
33. Kiricsi I, Molnár A (eds) (2003) Heteropolyacids in catalysis. App Catal A 256:1–328
34. Guo Y, Hu C (2007) Heterogeneous photocatalysis by solid polyoxometalates. J Mol Catal A 262:136–148
35. Sivakumar R, Thomas J, Yoon M (2012) Polyoxometalate-based molecular/nano composites: advances in environmental remediation by photocatalysis and biomimetic approaches to solar energy conversion. J Photochem Photobiol C 13:277–298
36. Okuhara T, Mizuno N, Misono M (2001) Catalysis by heteropoly compounds-recent developments. Appl Catal A 222:63–77
37. Kozhevnikov IV (2007) Sustainable heterogeneous acid catalysis by heteropoly acids. J Mol Catal A 262:86–92
38. Itagaki S, Kamata K, Yamaguchi K, Mizuno N (2013) A monovacant lacunary silicotungstate as an efficient heterogeneous catalyst for dehydration of primary amides to nitriles. ChemCatChem 5:1725–1728
39. Izumi Y, Ogawa M, Urabe K (1995) Alkali metal salts and ammonium salts of Keggin-type heteropolyacids as solid acid catalysts for liquid-phase Friedel-Crafts reactions. Appl Catal A 132:127–140
40. Pizzio LR, Cáceres CV, Blanco MN (1998) Acid catalysts prepared by impregnation of tungstophosphoric acid solutions on different supports. Appl Catal A 167:283–294
41. Vazquez P, Pizzio LR, Romanelli G, Autino J, Caceres CV, Blanco MN (2002) Mo and W heteropolyacid based catalysts applied to the preparation of flavones and substituted chromones by cyclocondensation of o-hydroxyphenyl aryl 1,3-propanediones. Appl Catal A 235:233–240
42. Kozhevnikov IV, Sinnema A, Jansen RJJ, Pamin K, van Bekkum H (1994) New acid catalyst comprising heteropoly acid on a mesoporous molecular sieve MCM-41. Catal Lett 30:241–252
43. Marme F, Coudurier G, Vedrine JC (1998) Acid-type catalytic properties of heteropolyacid $H_3PW_{12}O_{40}$ supported on various porous silica-based materials. Micropor Mesopor Mater 22:151–163
44. Kim W, Kim M, Kim J, Seo G (2003) Dispersion measurement of heteropoly acid supported on KIT-1 mesoporous material. Micropor Mesopor Mater 2003(57):113–120
45. Bielanski A, Lubanska A, Pozniczek J, Micek-Ilnicka A (2003) Oxide supports for 12-tungstosilicic acid catalysts in gas phase synthesis of MTBE. Appl Catal A 238:239–250
46. Pizzio LR, Vazquez PG, Caceres CV, Blanco MN (2003) Supported Keggin type heteropolycompounds for ecofriendly reactions. Appl Catal A 256:125–139
47. Hernandez-Cortez JG, López T, Manriquez ME, Gómez R, Navarrete J (2003) Thermally induced phase transformation on 12-tungstophosphoric acid/ZrO_2 Sol–gel. J Sol–Gel Sci Technol 26:213–216
48. Bachiller-Baeza B, Anderson JA (2002) FTIR and reaction studies of styrene and toluene over silica-zirconia-supported heteropoly acid catalysts. J Catal 212:231–239
49. Jiang S, Guo Y, Wang C, Qu X, Li L (2007) One-step sol–gel preparation and enhanced photocatalytic activity of porous polyoxometalate-tantalum pentoxide nanocomposites. J Colloid Interface Sci 308:208–215
50. Mukai R, Sugiyama T, Tamon H (2003) Immobilization of heteropoly acids in the network structure of carbon gels. Appl Catal A 256:99–105
51. Hodjati S, Vaezzadeh K, Petit C, Pitchon V, Kiennemann A (2001) The mechanism of the selective NOx sorption on $H_3PW_{12}O_{40}{\cdot}6H_2O$ (HPW). Top Catal 16–17:151–155

52. Madhusudhan Rao P, Wolfson A, Kababya S, Vega S, Landau MV (2005) Immobilization of molecular $H_3PW_{12}O_{40}$ heteropolyacid catalyst in alumina-grafted silica-gel and mesostructured SBA-15 silica matrices. J Catal 232:210–225
53. Papacostantinou E (1989) Photochemistry of polyoxometalates of molybdenum and tungsten and/or vanadium. Chem Soc Rev 18:1–31
54. Park H, Choi W (2003) Photoelectrochemical investigation on electron transfer mediating behaviors of polyoxometalate in UV-illuminated suspensions of TiO_2 and Pt/TiO_2. J Phys Chem B 107:3885–3890
55. Marcì G, García-López EI, Palmisano L (2012) Comparison between catalytic and catalytic photo-assisted propene hydration by using supported heteropolyacid. Appl Catal A 421–422:70–78
56. Hiskia A, Mylonas A, Papaconstantinou E (2001) Comparison of the photoredox properties of polyoxometalates and semiconducting particles. Chem Soc Rev 30:62–69
57. Guo Y, Hu C (2007) Heterogeneous photocatalysis by solid polyoxometalates. J Mol Catal A: Chem 262:136–148
58. Guo Y, Hu C, Wang Y, Wang E, Zhou Y, Feng S (2000) Microporous polyoxometalates POMs/SiO_2: synthesis and photocatalytic degradation of aqueous organochlorine pesticides. Chem Mater 12:3501–3508
59. Guo Y, Yang Y, Hu C, Guo C, Wang E, Zhou Y, Feng S (2002) Preparation, characterization and photochemical properties of ordered macroporous hybrid silica materials based on monovacant Keggin-type polyoxometalates. J Mater Chem 12:3046–3052
60. Guo Y, Hu C, Jiang S, Guo C, Yang Y, Wang E (2002) Heterogeneous photodegradation of aqueous hydroxy butanedioic acid by microporous polyoxometalates. Appl Catal B 36:9–17
61. Guo Y, Hu C, Jiang C, Yang Y, Jiang S, Li X, Wang E (2003) Preparation and heterogeneous photocatalytic behaviors of the surface-modified porous silica materials impregnated with monosubstituted keggin units. J Catal 217:141–151
62. Winter RS, Cameron JM, Cronin L (2014) Controlling the minimal self assembly of "complex" polyoxometalate clusters. J Am Chem Soc 136:12753–12761
63. Shen H, Mao H, Ying L, Xi Q (2007) Photocatalytic selective aerobic oxidation of alcohols to aldehydes and ketones by HPW/MCM-41 in ionic liquids. J Mol Catal A 276:73–79
64. Feng C, Li Y, Liu X (2012) Photocatalytic degradation of imidacloprid by phosphotungstic acid supported on a mesoporous sieve MCM-41. Chin J Chem 30:127–132
65. Tao S, Wang Y, Yu Y, An Y, Shi W (2013) Hierarchically porous tungstophosphoric acid/silica hybrid for high performance vis-light photocatalysis. J Environ Chem Eng 1:719–727
66. Kim S, Choi W (2005) Visible-light-induced photocatalytic degradation of 4-chlorophenol and phenolic compounds in aqueous suspension of pure titania: demonstrating the existence of a surface-complex-mediated path. J Phys Chem B 109:5143–5149
67. Rochkind M, Pasternak S, Paz Y (2015) Using dyes for evaluating photocatalytic properties: a critical review. Molecules 20:88–110
68. Zhao L, Chi Y, Yuan Q, Li N, Yan W, Li X (2013) Phosphotungstic acid anchored to amino-functionalized core-shell magnetic mesoporous silica microspheres: a magnetically recoverable nanocomposite with enhanced photocatalytic activity. J Colloid Interface Sci 390:70–77
69. Li H, Gao S, Cao M, Cao R (2013) Self-assembly of polyoxometalate–thionine multilayer films on magnetic microspheres as photocatalyst for methyl orange degradation under visible light irradiation. J Colloid Interface Sci 394:434–440
70. Gamelas JAF, Evtyugina MG, Portugal I, Evtug DV (2012) New polyoxometalate-functionalized cellulosic fibre/silica hybrids for environmental applications. RSC Adv 2:831–839
71. Ozer RR, Ferry JL (2002) Photocatalytic Oxidation of Aqueous 1,2-Dichlorobenzene by Polyoxometalates Supported on the NaY Zeolite. J Phys Chem B 106:4336–4342
72. Leal Marchena C, Frenzel RA, Gomez S, Pierella LB, Pizzio LR (2013) Tungstophosphoric acid immobilized on ammonium Y and ZSM5 zeolites: Synthesis, characterization and catalytic evaluation. Appl Catal B 130–131:187–196

73. Li S, Yu X, Zhang G, Ma Y, Yao J, Keita B, Nadjo L, Zhao H (2011) Green chemical decoration of multiwalled carbon nanotubes with polyoxometalate-encapsulated gold nanoparticles: visible light photocatalytic activities. J Mater Chem 21:2282–2287
74. Marcì G, García-López E, Bellardita M, Parisi F, Colbeau-Justin C, Sorgues S, Liotta LF, Palmisano L (2013) Keggin heteropolyacid $H_3PW_{12}O_{40}$ supported on different oxides for catalytic and catalytic photo-assisted propene hydration. Phys Chem Chem Phys 15:13329–13342
75. Marcì G, García-López EI, Palmisano L (2014) Heteropolyacid-based materials as heterogeneous photocatalysts. Eur J Inorg Chem 2014:21–35
76. Weinstock IA (1998) Homogeneous-phase electron-transfer reactions of polyoxometalates. Chem Rev 98:113–170
77. Dimitrievic NM, Savic D, Micic OI, Nozik AJ (1984) Interfacial electron-transfer equilibria and flatband potentials of alpha-ferric oxide and titanium dioxide colloids studied by pulse radiolysis. J Phys Chem 88:4278–4283
78. Yoon M, Chang JA, Kim Y, Choi JR, Kim K, Lee SJ (2001) Heteropoly acid-incorporated TiO_2 colloids as novel photocatalytic systems resembling the photosynthetic reaction center. J Phys Chem B 105:2539–2545
79. Tachikawa T, Fujitsuka M, Majima T (2007) Mechanistic insight into the TiO_2 photocatalytic reactions: design of new photocatalysts. J Phys Chem C 111:5259–5275
80. Tachikawa T, Tojo S, Fujitsuka M, Majima T (2006) One-electron redox processes during polyoxometalate-mediated photocatalytic reactions of TiO_2 studied by two-color two-laser flash photolysis. Chem Eur J 12:3124–3131
81. Ozer RR, Ferry JL (2001) Investigation of the photocatalytic activity of TiO_2-polyoxometalate systems. Environ Sci Technol 35:3242–3246
82. Akid R, Darwent JR (1985) Heteropolytungstates as catalysts for the photochemical reduction of oxygen and water. J Chem Soc Dalton Trans 395–399
83. Renneke RF, Pasquali M, Hill CL (1990) Polyoxometalate systems for the catalytic selective production of nonthermodynamic alkenes from alkanes. Nature of excited-state deactivation processes and control of subsequent thermal processes in polyoxometalate photoredox chemistry. J Am Chem Soc 112:6585–6594
84. Chen C, Lei P, Ji H, Ma W, Zhao J, Hidaka H, Serpone N (2004) Photocatalysis by titanium dioxide and polyoxometalate/TiO_2 cocatalysts. Intermediates and mechanistic study. Environ Sci Technol 38:329–337
85. Yang Y, Wu Q, Guo Y, Hu C, Wang E (2005) Efficient degradation of dye pollutants on nanoporous polyoxotungstate–anatase composite under visible-light irradiation. J Mol Catal A 225:203–212
86. Li L, Wu Q, Guo Y, Hu C (2005) Nanosize and bimodal porous polyoxotungstate–anatase TiO_2 composites: preparation and photocatalytic degradation of organophosphorus pesticide using visible-light excitation. Microp Mesop Mater 87:1–9
87. Jin H, Wu Q, Pang W (2007) Photocatalytic degradation of textile dye X-3B using polyoxometalate-TiO_2 hybrid materials. J Hazard Mater 141:123–127
88. Yu X, Guo Y, Xu L, Yang X, Guo Y (2008) A novel preparation of mesoporous $Cs_xH_{3-x}PW_{12}O_{40}/TiO_2$ nanocomposites with enhanced photocatalytic activity. Colloids Surf A 316:110–118
89. Li J, Kang W, Yang X, Yu X, Xu L, Guo Y, Fang H, Zhang S (2010) Mesoporous titania-based $H_3PW_{12}O_{40}$ composite by a block copolymer surfactant-assisted templating route: preparation, characterization, and heterogeneous photocatalytic properties. Desalination 255:107–116
90. Xu L, Yang X, Guo Y, Ma F, Guo Y, Yuan X, Huo M (2010) Simulated sunlight photodegradation of aqueous phthalate esters catalyzed by the polyoxotungstate/titania nanocomposite. J Hazard Mater 178:1070–1077

91. Ma F, Shi T, Gao J, Chen L, Guo W, Guo Y, Wang S (2012) Comparison and understanding of the different simulated sunlight photocatalytic activity between the saturated and monovacant Keggin unit functionalized titania materials. Colloid Surf A 401:116–125
92. Proust A, Matt B, Villanneau R, Guillemot G, Gouzerh P, Izzet G (2012) Functionalization and post-functionalization: a step towards polyoxometalate-based materials. Chem Soc Rev 41:7605–7622
93. Lv K, Xu Y (2006) Effects of polyoxometalate and fluoride on adsorption and photocatalytic degradation of organic dye X3B on TiO_2: the difference in the production of reactive species. J Phys Chem B 110:6204–6212
94. Rengifo-Herrera JA, Blanco MN, Pizzio LR (2011) Photocatalytic bleaching of aqueous malachite green solutions by UV-A and blue-light-illuminated TiO_2 spherical nanoparticles modified with tungstophosphoric acid. Appl Catal B 110:126–132
95. Rengifo-Herrera JA, Pizzio LR, Blanco MN, Roussel C, Pulgarin C (2011) Photocatalytic discoloration of aqueous malachite green solutions by UV-illuminated TiO_2 nanoparticles under air and nitrogen atmospheres: effects of counter-ions and pH. Photochem Photobiol Sci 10:29–34
96. Blanco MN, Pizzio LR (2011) Influence of the thermal treatment on the physicochemical properties and photocatalytic degradation of 4-chlorophenol in aqueous solutions with tungstophosphoric acid-modified mesoporous titania. Appl Catal A 405:69–78
97. Ngo Biboum R, Nanseu Njiki CP, Zhang G, Kortz U, Mialane P, Dolbecq A, Mbomekalle IM, Nadjo L, Keita B (2011) High nuclearity Ni/Co polyoxometalates and colloidal TiO_2 assemblies as efficient multielectron photocatalysts under visible or sunlight irradiation. J Mater Chem 21:645–650
98. Lee H, Lee J, Lee YH, Lee J, Yoon M (2011) Formation of Ag^+-N-TiO_2 nanochains and their HPA-composites as highly visible light-sensitive photocatalysts toward two-color solar cells. J Mater Chem 221:12829–12835
99. Shi H, Zhang T, An T, Li B, Wang X (2012) Enhancement of photocatalytic activity of nano-scale TiO_2 particles co-doped by rare earth elements and heteropolyacids. J Colloid Interf Sci 380:121–127
100. Wu D, Huo P, Lu Z, Gao X, Liu X, Shi W, Yan Y (2012) Preparation of heteropolyacid/TiO_2/fly-ash-cenosphere photocatalyst for the degradation of ciprofloxacin from aqueous solutions. Appl Surf Sci 258:7008–7015
101. Feng C, Xu G, Liu X (2013) Photocatalytic degradation of imidacloprid by composite catalysts $H_3PW_{12}O_{40}$/La-TiO_2. J Rare Earths 31:41–48
102. Anandan S, Ryu S, Cho W, Yoon M (2003) Heteropolytungstic acid ($H_3PW_{12}O_{40}$)-encapsulated into the titanium-exchanged HY (TiHY) zeolite: a novel photocatalyst for photoreduction of methyl orange. J Mol Catal A 195:201–208
103. Dubey N, Rayalu SS, Labhsetwar NK, Naidu RR, Chatti RV, Devotta S (2006) Photocatalytic properties of zeolite-based materials for the photoreduction of methyl orange. Appl Catal A 303:152–157
104. Chatti R, Rayalu SS, Dubey N, Labhsetwar N, Devotta S (2007) Solar-based photoreduction of methyl orange using zeolite supported photocatalytic materials. Sol Energy Mater Sol Cells 91:180–190
105. Rengifo-Herrera JA, Blanco MN, Pizzio LR (2014) Visible light absorption of TiO_2 materials impregnated with tungstophosphoric acid ethanol–aqueous solution at different pH values. Evidence about the formation of a surface complex between Keggin anion and TiO_2 surfaces. Mater Res Bull 49:618–624
106. Rengifo-Herrera JA, Frenzel RA, Blanco MN, Pizzio LR (2014) Visible-light-absorbing mesoporous TiO_2 modified with tungstosilicic acid as photocatalyst in the photodegradation of 4-chlorophenol. J Photochem Photobiol A 289:22–30
107. Feng C, Shang H, Liu X (2014) Photocatalysis of dinitrotoluene decomposition by $H_3PW_{12}O_{40}$/TiO_2 and $H_4SiW_{12}O_{40}$/TiO_2 prepared by a modified sol-gel synthesis and solvothermal treatment method. Chin J Catal 35:168–174

108. Wang Y, Lu K, Feng C (2013) Influence of inorganic anions and organic additives on photocatalytic degradation of methyl orange with supported polyoxometalates as photocatalyst. J Rare Earths 31:360–365
109. de Souza Lourenc RER, Passoni LC, Canela MC (2014) The synergistic effect of TiO_2 and $H_5PW_{10}V_2O_{40}$ in photocatalysis as a function of the irradiation source. J Mol Catal A 392:284–289
110. Lu L, Li L, Hu T, Zhang W, Huang X, Zhang J, Liu X (2014) Preparation, characterization, and photocatalytic activity of three-dimensionally ordered macroporous hybrid monosubstituted polyoxometalate $K_5[Co(H_2O)PW_{11}O_{39}]$ amine functionalized titanium catalysts. J Mol Catal A 394:283–294
111. Navio A, Hidalgo MC, Colón G, Botta SG, Litter M (2001) Preparation and physicochemical properties of ZrO_2 and Fe/ZrO_2 prepared by a sol-gel technique. Langmuir 17:202–210
112. Qu X, Guo Y, Hu C (2007) Preparation and heterogeneous photocatalytic activity of mesoporous $H_3PW_{12}O_{40}/ZrO_2$ composites. J Mol Catal A 262:128–135
113. Jiang C, Guo Y, Hu C, Wang C, Li D (2004) Photocatalytic degradation of dye naphthol blue black in the presence of zirconia-supported Ti-substituted Keggin-type polyoxometalates. Mater Res Bull 39:251–257
114. Farhadi S, Zaidi M (2009) Polyoxometalate-zirconia (POM/ZrO_2) nanocomposite prepared by sol-gel process: a green and recyclable photocatalyst for efficient and selective aerobic oxidation of alcohols into aldehydes and ketones. Appl Catal A 354:119–126
115. Salavati H, Tavakkoli N, Hosseinpoor M (2012) Preparation and characterization of polyphosphotungstate/ZrO_2 nanocomposite and their sonocatalytic and photocatalytic activity under UV light. Ultrason Sonochem 19:546–553
116. Sayama K, Arakawa H (1994) Effect of Na_2CO_3 addition on photocatalytic decomposition of liquid water over various semiconductor catalysis. J Photochem Photobiol A 77:243–247
117. Murase T, Irie H, Hashimoto K (2004) Visible light sensitive photocatalysts, nitrogen-doped Ta_2O_5 powders. J Phys Chem B 108:15803–15807
118. Jiang S, Guo Y, Wang C, Qu X, Li L (2007) One-step sol–gel preparation and enhanced photocatalytic activity of porous polyoxometalate–tantalum pentoxide nanocomposites. J Colloid Interf Sci 308:208–215
119. Su FZ, Mathew SC, Lipner G, Fu XZ, Antonietti M, Blechert S, Wang XC (2010) mpg-C_3N_4-catalyzed selective oxidation of alcohols using O_2 and visible light. J Am Chem Soc 132:16299–16301
120. Jun YS, Park J, Lee SU, Thomas A, Hong WH, Stucky GD (2013) Three-dimensional macroscopic assemblies of low-dimensional carbon nitrides for enhanced hydrogen evolution. Angew Chem 125:11289–11293
121. Niu P, Zhang L, Liu G, Cheng H (2012) Graphene-like carbon nitride nanosheets for improved photocatalytic activities. Adv Funct Mater 224:763–4770
122. Lin Z, Wang X (2013) Nanostructure engineering and doping of conjugated carbon nitride semiconductors for hydrogen photosynthesis. Angew Chem 125:1779–1782
123. Li K, Yan L, Zeng Z, Luo S, Luo X, Liu X, Guo H, Guo Y (2014) Fabrication of H3PW12O40-doped carbon nitride nanotubes by one-step hydrothermal treatment strategy and their efficient visible-light photocatalytic activity toward representative aqueous persistent organic pollutants degradation. Appl Catal B 156–157:141–152
124. Xing X, Liu R, Yu X, Zhang G, Cao H, Yao J, Ren B, Jiang Z, Zhao H (2012) Self-assembly of CdS quantum dots with polyoxometalate encapsulated gold nanoparticles: enhanced photocatalytic activities. J Mater Chem A 1:1488–1494
125. Kornarakis I, Lykakis IN, Vordos N, Armatas GS (2014) Efficient visible-light photocatalytic activity by band alignment in mesoporous ternary polyoxometalate-Ag_2S-CdS semiconductors. Nanoscale 6:8694–8703
126. Bian ZY, Zhu YQ, Zhang JX, Ding AZ, Wang H (2014) Visible-light driven degradation of ibuprofen using abundant metal-loaded $BiVO_4$ photocatalysts. Chemosphere 117:527–531

127. Zhang J, Li C, Wang B, Cui H, Zhai J, Li Q (2013) Synthesis, characterization and photocatalytic application of H3PW12O40/BiVO4 composite photocatalyst. Sci China Chem 56:1285–1292
128. Cao M, Lin J, Lu J, You Y, Liu T, Cao R (2011) Development of a polyoxometalate-based photocatalyst assembled with cucurbit[6]uril via hydrogen bonds for azo dyes degradation. J Hazard Mater 186:948–951
129. You Y, Gao S, Yang Z, Cao M, Cao R (2012) Facile synthesis of polyoxometalate–thionine composite via direct precipitation method and its photocatalytic activity for degradation of rhodamine B under visible light. J Colloid Interface Sci 365:198–203
130. Bonchio M, Carraro M, Scorrano G, Bagno A (2004) Photooxidation in water by new hybrid molecular photocatalysts integrating an organic sensitizer with a polyoxometalate core. Adv Synth Catal 346:648–654
131. Zhou W, Cao M, Li N, Su S, Zhao X, Wang J, Li X, Hu C (2013) Ag@AgHPW as a plasmonic catalyst for visible-light photocatalytic degradation of environmentally harmful organic pollutants. Mater Res Bull 48:2308–2316
132. Zhou W, Cao M, Su S, Li N, Zhao X, Wang J, Li X, Hu C (2013) A newly-designed polyoxometalate-based plasmonic visible-light catalyst for the photodegradation of methyl blue. J Mol Catal A 371:70–76
133. Corma A, García H, Llabrés i Xamena FX (2010) Engineering metal organic frameworks for heterogeneous catalysis. Chem Rev 110:4606–4655
134. An HY, Xiao DR, Wang EB, Li YGY, Wang XL, Xu L (2005) Open-framework polar compounds: synthesis and characterization of rare-earth polyoxometalates $(C_6NO_2H_5)_2[Ln(H_2O)_5(CrMo_6H_6O_{24})]\cdot 0.5H_2O$ (Ln = Ce and La). Eur J Inorg Chem 2005:854–859
135. Sun CY, Liu SX, Liang DD, Shao KZ, Ren YH, Su ZM (2009) Highly stable crystalline catalysts based on a microporous metal-organic framework and polyoxometalates. J Am Chem Soc 131:1883–1888
136. Maksimchuk NV, Timofeeva MN, Melgunov MS, Shmakov AN, Chesalov YA, Dybtsev DN, Fedin VP, Kholdeeva OA (2008) Heterogeneous selective oxidation catalysts based on coordination polymer MIL-101 and transition metal-substituted polyoxometalates. J Catal 257:315–323
137. Dolbecq A, Dumas E, Mayer CR, Mialane P (2010) Hybrid organic-inorganic polyoxometalate compounds: from structural diversity to applications. Chem Rev 110:6009–6048
138. Marrot J, Mellot-Draznieks C, O'Keeffe M, Biboum RN, Lemaire J, Keita B, Nadjo L, Dolbecq A (2011) Polyoxometalate-Based Metal Organic Frameworks (POMOFs): structural trends, energetics, and high electrocatalytic efficiency for hydrogen evolution reaction. J Am Chem Soc 133:13363–13374
139. Zhu W, Yang XY, Li YH, Li JP, Wu D, Gao Y, Yi FY (2014) A novel porous molybdophosphate-based FeII,III-MOF showing selective dye degradation as a recyclable photocatalyst. Inorg Chem Commun 49:159–162
140. Guo J, Yang J, Liu Y, Ma J (2013) Two new polyoxometalate-templated supramolecular compounds constructed by a new tridentate ligand 2,4,6-tris[1-(4-oxidroxypyridinium)-ylmethyl]-mesitylene. Inorg Chim Acta 400:51–58
141. Liu B, Yang J, Yang G, Ma J (2013) Four new three-dimensional polyoxometalate-based metal-organic frameworks constructed from $[Mo_6O_{18}(O_3AsPh)_2]^{4-}$ polyoxoanions and copper(I)-organic fragments: syntheses, structures, electrochemistry, and photocatalysis properties. Inorg Chem 52:84–94
142. Meng B, You W, Sun X, Zhang F, Liu M (2011) A hydrotalcitelike Ce(III) coordination polymer pillared by Keggin anions: Synthesis, single crystal structure and photocatalysis. Inorg Chem Commun 14:35–37
143. Ngo Biboum R, Doungmene R, Keita B, Oliveira P, Nadjo L, Lepoittevin B, Roger P, Brisset F, Mialane P, Dolbecq A, Mbomekalle IM, Pichon C, Yin P, Liu T, Contant R

(2012) Poly(ionic liquid) and macrocyclic polyoxometalate ionic self-assemblies: new water-insoluble and visible light photosensitive catalysts. J Mater Chem 22:319–323

144. Fu Z, Zeng Y, Liu X, Song D, Liao S, Dai J (2012) Copper based metal-organic molecular ring with inserted Keggin-type polyoxometalate: a stable photofunctional host-guest molecular system. Chem Commun 48:6154–6156
145. Li T, Li Q, Yan J, Li F (2014) Photocatalytic degradation of organic dyes by La^{3+}/Ce^{3+}-$H_3PW_{12}O_{40}$ under different light irradiation. Dalton Trans 43:9061–9069
146. Xue C, Li S, Zhang L, Sha J, Zheng T, Zhang Q, Li L (2013) Hydrothermal synthesis, characterization and electrocatalytic/photocatalytic activities of new polyoxometalate based hybrid compound. J Inorg Organomet Polym 23:1468–1476
147. Sheng F, Zhu X, Wang W, Bai H, Liu J, Wang P, Zhang R, Han L, Mu J (2014) Synthesis of novel polyoxometalate $K_6ZrW_{11}O_{39}Sn\cdot 12H_2O$ and photocatalytic degradation aqueous azo dye solutions with solar irradiation. J Mol Catal A 393:232–239
148. Zhou S, Liu B, Li X, Shi T, Chen Y (2014) Two new helical compounds based on Keggin clusters and N-donor multidentate ligand: syntheses, structures and properties. J Solid State Chem 219:15–20

Chapter 4
Alternative Materials to TiO_2

Ren Su, Flemming Besenbacher, and Graham Hutchings

Abstract One of the most significant investigations on heterogeneous photocatalytic process can be dated back to the 1970s, when Fujishima and Honda showed that the TiO_2 electrode is capable of water splitting under suitable electromagnetic irradiation. Since then, TiO_2-based materials have become the dominant photocatalyst and have been investigated for decades due to their abundance, non-toxicity, and relatively high reactivity. However, the bandgap of pristine TiO_2 is larger than 3 eV, which can only absorb light that has a wavelength of less than 400 nm. Unfortunately, this portion of photons only corresponds to 4–5 % of the solar spectrum, which has limited the application of photocatalysis at an industrial scale. Moreover, the conduction band position of TiO_2 is only slightly negative relative to that of the proton reduction potential, resulting in a relatively poor reduction power for solar-to-fuel conversion. Therefore, the development of alternative photocatalysts with visible light absorption and tunable properties is essential in the application of photocatalysis techniques.

In this chapter, we will consider the most popular photocatalyst systems other than TiO_2. Their synthesis methods, characteristics, optimisations, and design will be presented. Last but not least, the design and synthesis of promoters, which play a very essential role in photocatalyst systems, will also be demonstrated at the end of this chapter.

Keywords Photocatalyst materials • Metal oxides • Perovskites • Sulphides • Nitrides • Zeolites • MOFs • Anchored systems • Promoters • Cocatalysts

---

R. Su (✉)
Syncat@Beijing, Synfuels China Co. Ltd., Leyuan South Street II, No.1, Yanqi Economic Development Zone C# Huairou District, Beijing 101407, P.R. China
e-mail: suren@synfuelschina.com.cn

F. Besenbacher
Department of Physics and Astronomy, Interdisciplinary Nanoscience Center (iNANO), Aarhus University, Gustav Wieds Vej 14, Aarhus C DK-8000, Denmark
e-mail: fbe@inano.au.dk

G. Hutchings
Cardiff Catalysis Institute, School of Chemistry, Cardiff University, Cardiff CF10 3AT, UK
e-mail: Hutch@cardiff.ac.uk

J.C. Colmenares, Y.-J. Xu (eds.), *Heterogeneous Photocatalysis*, Green Chemistry and Sustainable Technology, DOI 10.1007/978-3-662-48719-8_4

4.1 Overview and Basic Concepts

Photocatalysis can be described as the acceleration of photon-driven reactions by catalysts, where a photocatalyst absorbs photons, generates electron–hole (e^-–h^+) pairs, and then uses the e^-–h^+ pairs or corresponding radicals to react with surface-adsorbed molecules to form new compounds. Thus, a photocatalyst plays a dual role in the process: (I) absorber and (II) reactor.

Light absorption of a photocatalyst depends on the bandgap (Eg) of a material. Whilst valence band maximum (VBM) and conduction band minimum (CBM) together determine the Eg of inorganic semiconductor-based materials, the highest occupied molecular orbital (HOMO) and lowest unoccupied molecular orbital (LUMO) define the Eg of organic semiconductor photocatalysts. On the other hand, the redox potentials of photoexcited e^- and h^+ should be greater than that of the redox couple to drive the reaction from a thermodynamic perspective.

Due to the variety of redox potentials for different reactions, an all-purpose photocatalyst does not exist neither from the "absorber" nor the "reactor" aspect. Take pristine TiO_2, for example, its large bandgap and high VBM position (~3.0 eV vs. standard hydrogen electrode (SHE)) make TiO_2 extremely stable and suitable for detoxification of water and air that requires strong oxidising power, but its bandgap is too large to fully use the solar spectrum and the CBM is not ideally positioned (~ – 0.2 eV vs. SHE) for solar-to-fuel conversions. Moreover the VBM is somewhat too positive and will fully oxidise most organic compounds to CO_2, thus making it not ideal for partial oxidation reactions. However, TiO_2-based photocatalyst materials still account for 2/3 of the published papers up to 2015 due to several reasons [1]. Firstly, the global annual production of TiO_2 is ~4,700 k tons, making TiO_2 affordable from an economic aspect. Secondly, the photocatalytic performances of TiO_2-based materials are reasonably good due to the relatively long lifetime of photogenerated charge carriers compared to that of other materials [2]. Therefore, in addition to the requirement that the bandgaps should match the solar spectrum, alternative photocatalyst materials should also possess these two requirements to be considered in large-scale applications. Last but not least, the photocatalyst materials should be stable and ideally nontoxic under working conditions. This is extremely important for water or air purification applications as it will be not wise to introduce additional contaminants (e.g. CdS and PbO).

Figure 4.1 demonstrates the investigation in searching for alternative heterogeneous photocatalyst materials from the periodic table. Whilst the d0 (marked in red) and d10 (marked in black) cations are utilised to construct both crystal structures and energy structures of semiconductors together with nonmetal anions (marked in green), group 1–3 elements are often applied to build crystal structures. The combination of these three types of ions can form simple oxides, oxynitrides, nitrides, and sulphides to more complicated compounds such as perovskites, zeolites, and metal–organic frameworks (MOFs). The origin of VBM and CBM of photocatalysts depends on the building elements and their oxidation states. When

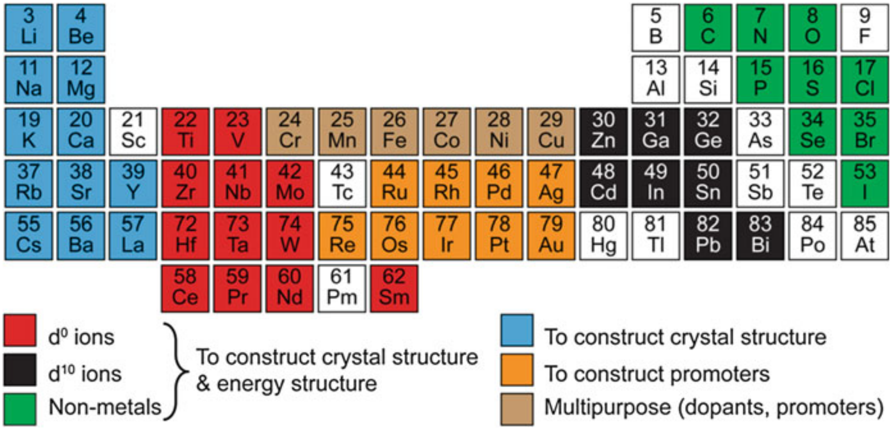

Fig. 4.1 Periodic table demonstrates the design of heterogeneous photocatalysts

d0 cations in their highest oxidation states are used to build photocatalysts along with anions, the empty d orbitals of cations and fully filled p orbitals of anions contribute to CBM and VBM in general (i.e. TiO_2, V_2O_5, and Ta_2N_5) [3]. In contrast, the VBM of photocatalysts formed by d10 cations at their highest oxidation states with anions is contributed from both the d orbitals of cations and the p orbitals of anions (i.e. ZnO and Ga_2O_3) [3]. Note that variation in the oxidation states may result in the marked changes in the electronic structures of a photocatalyst; thus, experiments combined with theoretical analysis are required to reveal the origin of band structures for complicated semiconductor photocatalysts. In order to prolong the lifetime of photogenerated charge carriers and accelerate preferred redox reactions, promoters are frequently employed to decorate the surface of photocatalysts (marked in orange in Fig. 4.1). Promoters normally do not convert photons to charge carriers but play a key role in enhancing the photocatalytic performance, especially in water splitting and selective organic transformation reactions. Although classic promoters are based on noble metal elements, recent development in oxides and nonmetal promoters (i.e. NiO, graphene, and C nanodots) has also shown great potential [4–6]. Nevertheless, there are also elements that can be used to build photocatalysts or promoters (marked in brown).

4.2 Simple Oxides and Derivatives

Metal oxides have been investigated extensively due to their relative high stability and abundance, and most combinations of metal–oxygen have been tested for photocatalysis. Based on the d orbital electron configuration of the cation, metal oxides can be divided into d0 type, d10 type, and other transition metal oxides that

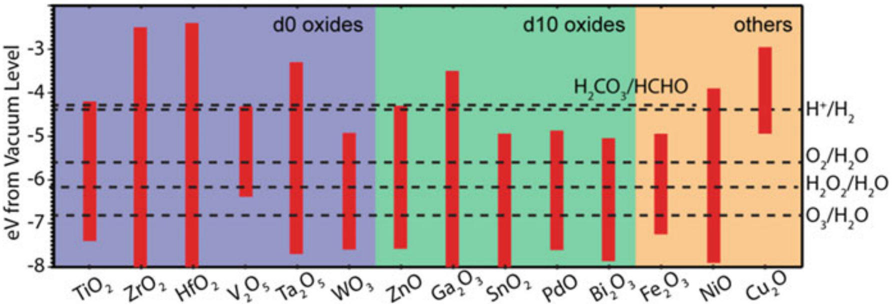

Fig. 4.2 Bandgaps and band positions of some simple metal oxides. The *dashed lines* indicate the reduction potentials of various reactions

cannot be categorised into d0 and d10 type. Figure 4.2 depicts the bandgaps and band positions of some popular oxides that have been employed as photocatalysts. Since there are several dedicated reviews and book chapters on conventional metal oxide-based photocatalysts [3, 7, 8], we will focus on some characteristic metal oxides to demonstrate the design strategy.

4.2.1 d0 Oxides

Strictly speaking, the d0 oxides consist of group 4–6 metal cations in their highest oxidation states within the corresponding oxides (see Fig. 4.1). In this case, although the group VI metal oxides (HfO_2 and ZrO_2) are considered to have excellent properties in surface charge trapping according to the density functional theory (DFT) calculations [9], their large bandgaps (6 eV for HfO_2 and 5.8 eV for ZrO_2; see Fig. 4.2) limit their application in photocatalysis. In contrast, the group V and VI metal oxides are normally characterised by moderated bandgaps, which are comparable to that of TiO_2. For example, silica-supported V_2O_5 with the addition of alkali metal ions located adjacent to the surface VO_4 species have been reported to be quite photoactive in selective oxidation of propane to propanone by oxygen at room temperature (RT) [10]. The MoO_3 supported on silica materials have been applied in photocatalytic NO reduction with CO as the oxidant at RT, yielding full conversion to N_2 and CO_2 [11]. The alkali metal ion-doped MoO_3/SiO_2 is also capable of performing metathesis reaction (propene here) at RT [10], which enables the redistribution of fragments of alkenes by the scission and regeneration of carbon–carbon double bonds. Since such reactions are very important in petroleum industry for the synthesis of higher olefins that are normally realised using metal complexes, the use of cheap heterogeneous photocatalysts is of particular interest. However, similar to the issue of pristine TiO_2 for application, further enhancement in catalytic performance and light adsorption toward visible light range is needed.

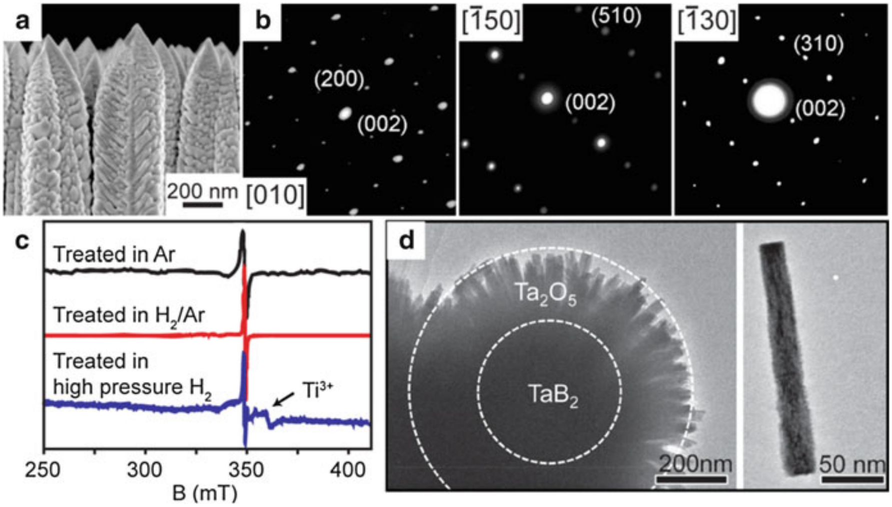

Fig. 4.3 (**a**) SEM image of *bcc* VO_2 rods grown on Si substrate; (**b**) SAED patterns of a *bcc* VO_2 rod taken with incident beam along different directions (Reprinted with permission from Ref. [12] Copyright 2008, American Chemical Society). (**c**) EPR spectra comparison of TiO_2 nanotubes treated in Ar, H_2/Ar, and high-pressure H_2 (Reprinted with permission from Ref. [13] Copyright 2014, American Chemical Society). (**d**) Cross section and side-view TEM images of core/shell TaB_2/Ta_2O_5 photocatalyst (Reprinted with permission from Ref. [14] Copyright 2014, Wiley VCH)

Several approaches have been applied to extend the light absorption and photocatalytic performance. Inspired by the bandgap difference of anatase and rutile TiO_2, enlargement/reduction of the energy gaps of materials with narrow/large bandgaps by searching different polymorph structures is a feasible strategy. For example, vanadium oxides exhibit many intermediates within the V_2O_5–V_2O_3 system that have different crystal structures and bandgaps. Whilst the tetragonal and monoclinic VO_2 exhibit metallic and semiconductive (~0.7 eV) characteristics, respectively, a recent work shows that the bcc VO_2 has a bandgap of ~2.7 eV, which is ideal for visible light-induced photocatalysis [12]. Figure 4.3a presents a SEM image of the vertically aligned VO_2 nanorods deposited on a silicon substrate via thermal oxidation. The selected area electron diffraction (SAED) along different axes indicates that the rods have a bcc structure with a lattice constant of ~0.94 nm (Fig. 4.3b). This bcc VO_2 film exhibits excellent photocatalytic H_2 evolution performance in the presence of hole scavengers.

Another strategy to extend the light absorption is by doping with other elements. Doping of nonmetal (i.e. C, N, S) or metal (i.e. Fe, Cu, Mn) elements has been extensively investigated in tuning the bandgap of d0 metal oxides (especially TiO_2). Take TiO_2, for example, whilst the bandgap can be narrowed, the photocatalytic performance under visible light irradiation is generally very poor. Even worse, a significant decrease in performance under UV irradiation is often observed. The decrease in photocatalytic performance originates from the reduced lifetime of charge carriers that recombine at the dopant (impurity) sites. Therefore, a careful control of the dopant (i.e. identity, concentration, and location) is required to achieve desirable performance. The recently developed self-doping approach provides a feasible approach for fine-tuning the bandgap whilst exhibiting reasonable performance under visible light irradiation. For example, Nb^{4+} self-doped $K_4Nb_6O_{17}$ microspheres can be synthesised via photoreduction of $K_4Nb_6O_{17}$ under deaerated conditions in the presence of hole scavengers (i.e. methanol, ethanol) [15]. Here, partial reduction of Nb^{5+} to Nb^{4+} by irradiation leads to the formation of Nb^{4+} self-doped $K_4Nb_6O_{17}$, which is responsible for the colour change from white (pristine $K_4Nb_6O_{17}$) to black. Amazingly, compared to the analogous photon-induced Ti^{3+} in deaerated TiO_2–ethanol colloidal that has a short lifetime, the Nb^{4+} self-doped $K_4Nb_6O_{17}$ exhibits an astonishing stability according to the clear signal of Nb^{4+} in electron paramagnetic resonance (EPR). Long-term photocatalytic H_2 evolution tests also prove the stability although the mechanism remains unclear.

The black TiO_2 (Ti^{3+} self-doped TiO_2) can be considered as a new material since it exhibits completely different optical properties compared to that of pristine or other doped TiO_2. Originally it has been synthesised by the hydrogenation of pristine TiO_2 under high pressure of H_2 (20 bar) at 200 °C for a long period (5 days), resulting in a disordered surface with a large amount of adsorbed H atoms [16]. - Mid-gap states that lay above the VBM but below the Fermi level are created within such a disordered surface. X-ray photoelectron spectroscopy (XPS) along with DFT calculations reveal that the mid-gap states originate from the hybridisation of O2p and Ti3d orbitals of the disordered surface layer. Although the H1s orbital coupling to the Ti atom does not influence the electronic structure, it is essential in stabilising the lattice disorders by passivating the dangling bonds. Nevertheless, these disordered surfaces can provide trapping sites for charge carriers to prolong their lifetime. Several studies have reported on the successful synthesis of black TiO_2 and applied this material for visible light-induced H_2 evolution [13, 16]. However, it is noticed that the preparation conditions influence the photoreactivity significantly. Although the high-pressure H_2-treated TiO_2 shows identical lattice space and diffraction pattern compared to that of TiO_2 annealed in air or in 1 bar pressure of Ar/H_2 due to the very low concentration of Ti^{3+} in the disordered surface layer, EPR spectra clearly demonstrate the existence of Ti^{3+} in hydrogenated TiO_2 at RT (Fig. 4.3c), which contributes to enhanced light absorption and charge trapping for a major improvement in photocatalytic performance under visible light conditions.

Tuning the charge transfer kinetics is another key issue in enhancing the photocatalytic performance. A feasible approach is to construct heterostructures to spatially separate the charge carriers. This strategy has been very successful in the case of anatase/rutile TiO_2 heterostructures and has been extended to other d0 metal oxides as well. The TEM images shown in Fig. 4.3e demonstrate the conceptual design of a Ta_2O_5-based photocatalyst, in which the Ta_2O_5 shell is directly formed from the TaB_2 core via a vapour-phase hydrothermal process. According to DFT calculations, the CBM of Ta_2O_5 lays above the Fermi level of TaB_2, enabling electron transfer from the Ta_2O_5 shell to the TaB_2 core [14].

4.2.2 d10 Metal Oxides

The d10 oxides are built from group 12–15 metal cations with oxygen (see Fig. 4.1). The hexagonal wurtzite-structured ZnO, which has a similar bandgap (~3.3 eV) and band positions compared to that of anatase TiO_2, has been extensively studied due to its high electron mobility and tunable microstructure. However, the bandgap is too large to absorb visible light and the CB potential is not suitable for solar-to-fuel conversion. It should be noted that the formation of solid solution with wurtzite GaN can reduce the bandgap of the GaN:ZnO system, which will be discussed in Sect. 4.4.2. CdO, which has a bandgap of ~2.2 eV, crystallises in a cubic rock salt lattice with octahedral Cd^{2+} and O^{2-} centres. Although it has been reported as a photocatalyst for phenol decomposition, the solubility of CdO and the toxicity of Cd^{2+} make CdO a less promising candidate.

Although the monoclinic-structured gallium oxide (β-Ga_2O_3) has a large bandgap (~4.8 eV), it has been shown to be a very efficient photocatalyst for the decomposition of aromatic compounds (i.e. benzene, toluene, and ethylbenzene) when compared to that of TiO_2 (~4 times better) [17]. Such great enhancement may originate from the more negative VBM and positive CBM of β-Ga_2O_3 compared to that of TiO_2, which increases the driving force of pollutant oxidation and oxygen reduction. However, the photocatalytic oxidation of C_2H_4 and CH_3Br does not support this simple assumption, as TiO_2 and β-Ga_2O_3 show comparable performance. Thus, a mechanistic understanding of ad-/desorption of aromatic compounds and reaction intermediates from a surface science perspective is needed to reveal the superior photocatalytic performance of β-Ga_2O_3.

Whilst β-Ga_2O_3 is the thermally stable polymorph, theoretical calculations predict that the metastable hexagonal phase (α-Ga_2O_3) has some interesting physical properties [18]. The α-Ga_2O_3 can be generated from β-Ga_2O_3 under ~9.5 GPa pressure at RT (calculated) or under ~4.4 GPa pressure at 1000 °C and retain its crystal structure under ambient condition. Due to a higher symmetry, Ga coordination number, and the packing density of α-Ga_2O_3, it exhibits a higher bulk modulus, bandgap (5.03 eV), and refractive index than that of β-Ga_2O_3. Compared to β-Ga_2O_3 that shows an isotropic optical absorption edge, the α-Ga_2O_3 exhibits an anisotropic dispersion ε_{xx} (ε_{yy}) function with respect to ε_{zz}. Recently, it has been shown that physically attaching these two polymorphs benefits the overall photocatalytic water-splitting process [19]. Figure 4.4a and b demonstrates the effects of α–β junction on the kinetics of photogenerated charge carriers by transient absorption spectroscopy and IR spectroscopy. Three types of process that involve charge carriers can be extracted by following the exponential decay of the normalised absorption at 850 nm (Fig. 4.4a). Whilst surface charge trapping (~14–32 ps) and recombination processes ($>$1000 ps) are observed for all Ga_2O_3, an ultrafast charge transfer at approximately 3 ps is only noticed for the α–β junction, indicating a more efficient charge separation at the interface of the α and β polymorphs. Moreover, transient IR spectroscopy (Fig. 4.4b) shows that the lifetime of photogenerated electrons within α–β junctions has been prolonged

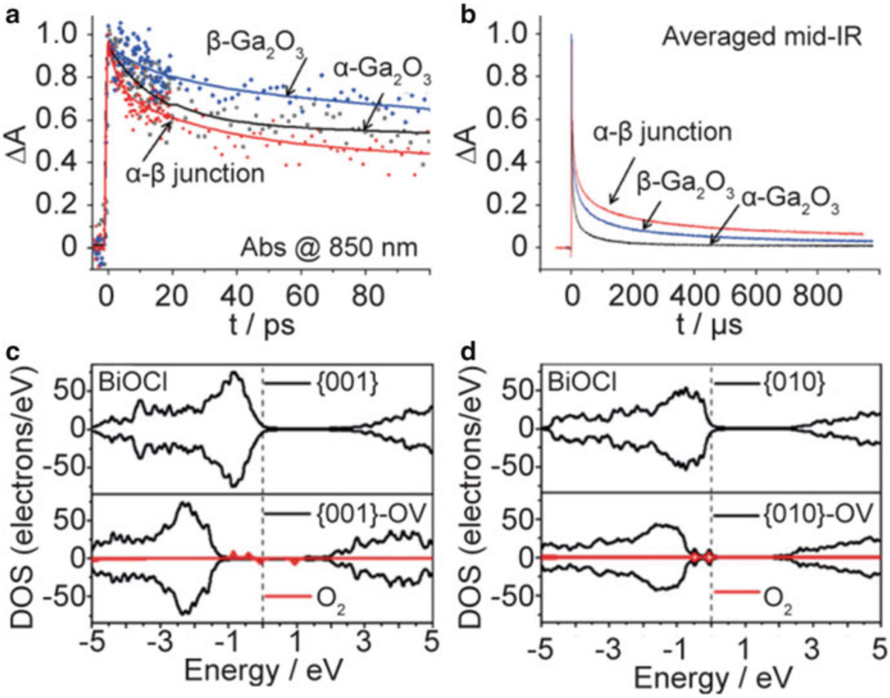

Fig. 4.4 (**a**) Normalised transient absorption spectra of Ga_2O_3 samples at 850 nm excited by a 255 nm laser. (**b**) Normalised transient averaged mid-IR absorption spectra of Ga_2O_3 samples excited by a 266 nm laser (Reprinted with permission from Ref. [19] Copyright 2012, John Wiley and Sons). (**c**) and (**d**) density of states (*DOS*) of clean BiOCl surfaces and surfaces with oxygen vacancies (*OV*) and O_2 adsorption. Positive and negative y values represent majority and minority spin states. The vertical dashed lines indicate VBM (Reprinted with permission from Ref. [20] Copyright 2013, American Chemical Society)

compared to that in either α or β phase. More importantly, the corresponding hole species within the α–β junctions are also characterised by a long lifetime, which allows migration of hole species to the surface to react with electron donors (i.e. methanol).

The extension of light absorption to solar spectrum is crucial for d10 oxides due to their large bandgaps. Doping with d0 cations has been used to reduce the bandgaps of indium oxides and bismuth oxides ($InMO_4$ and $BiMO_4$, $M = V^{5+}$, Nb^{5+}, and Ta^{5+}) [21]. Whilst the VBM still originates from the O2p orbitals, the presence of d0 cations in their highest oxidation states can insert unoccupied d orbitals to lower the conduction band potential. The bandgaps of $InMO_4$ have been gradually reduced from 3 eV (In_2O_3) to 2.6 eV, 2.5 eV, and 1.9 eV by using V^{5+}, Nb^{5+}, and Ta^{5+}, respectively. Moreover, the VBM and CBM are all suitable for water-splitting half reactions.

Bismuth oxyhalides (BiOX, X = Cl, Br, and I) have also been studied as photocatalyst materials. The tetragonal matlockite BiOX consists of [X–Bi–O–

Bi–X] slices that are stacked along the c-axis through van der Waals interlayer interactions of halogen atoms, where the Bi centre is surrounded by four O and four halogen atoms. Due to the strong intralayer covalent bonding and the weak interlayer interaction, highly anisotropic mechanical, electrical, and optical properties make the BiOX a promising photocatalyst material [22]. The bandgap of BiOX is dependent on the identity of halogen atom (3.2 eV for BiOCl, 2.7 eV for BiOBr, and 1.8 eV for BiOI). Whilst the O2p and Xnp orbital states contribute to the VBM, the Bi6p orbital states construct the CBM of BiOX. The contribution of Xns orbital states increases as a result of the increase in the atomic number of halogen atoms, thus narrowing the bandgap.

BiOX can be synthesised by various wet chemical approaches (i.e. hydrothermal and solvothermal synthesis) with thermal annealing to crystallise the precursor. The microstructure, exposed facets (orientation), and oxygen and halogen vacancies can be easily adjusted by varying the synthesis parameters for fine-tuning the electronic structure thus alternating the photocatalytic performance. Taking BiOCl as example, calculations reveal that whilst O_2 adsorbs on oxygen vacancies (OV) of (001) surface by combining with two nearest Bi atoms from the sublayer to form an end-on structure, it interacts with the OV of (010) surface by combining with two nearest Bi atoms in the outer layer and one next nearest Bi atom in sublayer, forming a complex bridge-on structure [20]. The O – O bond length on (001) and (101) surfaces is estimated to be 1.32 Å and 1.46 Å, which are close to that of $O_2^{\bullet -}$ (1.26 Å) and O_2^{2-} (1.49 Å), respectively. It is therefore considered that the oxygen activation pathway is facet-dependent on BiOCl. Figure 4.4c and d further demonstrate the facet effect of BiOCl on the oxygen activation process from density of states (DOS) calculations. Both pure BiOCl surfaces (top part of Fig. 4.4c and d) are clearly spin-paired with symmetric majority and minority states of Bi atoms; however, after OV generation and O_2 adsorption, the spin states of the BiOCl surfaces are changed. Whilst the symmetric majority and minority states of Bi atoms at VBM break up to provide donor sites for O_2 on (001) surface, the spin states of all (010) surface atom orbitals are reorganised and maintain symmetric majority and minority states (bottom part of Fig. 4.4c and d). This difference in DOS suggests magnetic moments of 0.81 μB and 0 for surface-adsorbed O_2 on (001) and (010) surfaces, which match the electron configurations of $O_2^{\bullet -}$ and O_2^{2-} very well, implying distinct O_2 activation processes on different surfaces. Nevertheless, theoretical calculations also reveal that high-energy (001) facets require surface-adsorbed protons to stabilise the dangling bonds of surface oxygen atoms, whereas the low-energy (010) facets do not require such stabilisation. Therefore, the preparation of BiOCl materials with preferred exposed surface can be achieved by adjusting the pH during wet chemical synthesis.

4.2.3 Other Transition Metal Oxides

Other transition metal oxides have also been investigated for photocatalysis applications. Iron oxides, nickel oxides, and copper oxides are among the most popular materials due to the abundance and low toxicity.

Among the known 16 types of iron oxides and hydroxides, hematite (α-Fe_2O_3) is considered as a promising photocatalyst, especially as the photoanode material for solar water splitting. Hematite crystallises in the rhombohedral lattice system, characterised by a bandgap of ~2.2 eV with a sufficient positive VBM (2.7 V vs. SHE), which is ideal for water oxidation (O_2 evolution). Although a theoretical photon conversion efficiency of ~15 % is possible for hematite, its low charge carrier mobility (10^{-2} to 10^{-1} $cm^2V^{-1}s^{-1}$) and short hole mean free path (2–4 nm) lead to rapid recombination thus very low solar light-to-current conversion efficiency. Whilst doping may be helpful in improving the charge carrier mobility, nanostructuring by means of nanotubes and porous films can effectively reduce the diffusion length thus facilitating charge carriers moving from the generation sites to surface sites before being recombined. There are numerous reports about the synthesis of nanostructured hematite (i.e. hydrothermal synthesis and anodic oxidation), where in most cases a mixture of FeO, Fe_2O_3, and Fe_3O_4 in different polymorphs coexists in the sample. Although the synthesis of high-quality pristine α-Fe_2O_3 is challenging, it is worth exploring from both fundamental and application aspects. A recent study on α-Fe_2O_3 nanotubes by anodic oxidation reveals that the purity of iron substrate significantly influences the composition of iron oxide layers (Fig. 4.5a). Whilst the thermally formed iron oxide plain layers exhibit identical composition from the XRD patterns (black curves) regardless of the iron substrate,

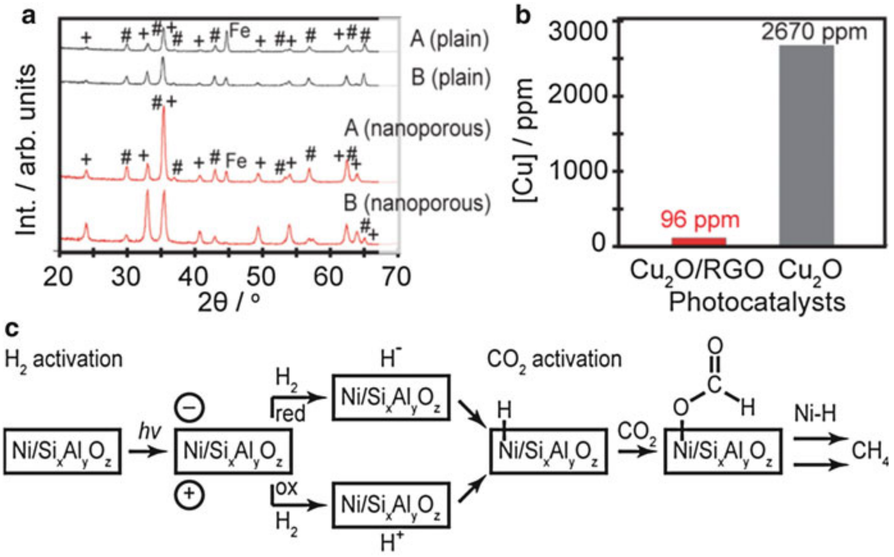

Fig. 4.5 (**a**) XRD patterns of thermally annealed plain and nanoporous oxide layers on iron foils A (Fe-99.5 %) and B (Fe-99.99 %), +: α-Fe_2O_3, #: γ-Fe_3O_4 (Reprinted with permission from Ref. [23] Copyright 2014, Wiley VCH). (**b**) Comparison of leached Cu from Cu_2O/RGO and Cu_2O (Reprinted with permission from Ref. [24] Copyright 2014, Wiley VCH). (**c**) Proposed mechanisms of CO_2 photoreduction using Ni supported on silica alumina (Ni/$SiO_2{\cdot}Al_2O_3$) (Reprinted with permission from Ref. [25] Copyright 2014, American Chemical Society)

the composition of thermally treated nanotubes from anodisation depends on the purity of the substrate (red curves). The low-purity Fe substrate (A, 99.5 %) promotes the formation of γ-Fe_3O_4, whereas the high-purity Fe substrate (B, 99.99 %) inhibits the formation of γ-Fe_3O_4 and facilitates the formation of α-Fe_2O_3. The disappearance of Fe diffraction peaks on substrate B also indicates a higher ratio of α-Fe_2O_3 due to its relative large attenuation factor than that of γ-Fe_3O_4.

The reddish copper (I) oxide is also an attractive photocatalyst. The cubic structured Cu_2O has a direct bandgap of ~2 eV with a quite negative CBM (1.5 V vs. SHE), making it a very promising material for reduction half reactions in water-splitting and artificial synthesis. Cu_2O is capable of reducing CO_2 to CO under visible light, which can be used for the Fischer–Tropsch synthesis to produce diesel. However, the stability of Cu_2O in aqueous solution is a serious issue as the free enthalpies of oxidation and reduction for Cu_2O lie within the bandgap. A simple method to improve the stability would be the creation of a thin layer (i.e. ZnO and TiO_2) to avoid direct contact of Cu_2O with water, but this may hinder the active sites thus reducing the performance. An alternative way to improve the stability but retain or even enhance the reactivity would be the formulation of a heterojunction that spatially separate the charge carriers. The reduced graphene oxide (RGO) exhibits excellent electronic properties and can thus be used to modify pristine Cu_2O [24]. Figure 4.5b compares the leaching of Cu from pristine Cu_2O and Cu_2O/RGO composite after CO_2 reduction for 3 h. Apparently the corrosion of Cu_2O can be effectively quenched with the presence of RGO. Meanwhile, a 0.5 wt% RGO also improves the CO_2 conversion rate by a factor of four. Nevertheless, since the Fermi level of RGO is only slightly more negative than the reduction potential of CO_2, searching for alternative promoters that have more negative Fermi level to maintain the large driving force of Cu_2O would be of great interest.

In contrast to the n-type semiconductors (i.e. TiO_2 and CeO_2) that oxidise CO into CO_2 in the presence of water, it is worth noting that some of the p-type semiconductors (i.e. NiO, Co_3O_4, Fe_3O_4) exhibit potentials for photoreduction of CO to hydrocarbons (mainly methane) by using H_2 or H_2O under visible light irradiations [26]. This can be considered as photocatalysed Fischer–Tropsch synthesis, and it may solve the energy crisis. Among these p-type semiconductors, NiO exhibits the best performance in CO reduction, and a quantum efficiency (QE) of 7.5 % can be reached under 450 nm irradiation when H_2 is employed. Although the cubic NiO has an optical bandgap of ~4 eV, it still can absorb some visible light due to the complicated d–d transition and oxygen vacancies from the nonstoichiometric NiO. It should also be mentioned that the formation of CH_4 exhibits an induction period, wherein graphitic carbon species are observed on the surface of p-type semiconductors. In contrast, carbon deposition has not been observed on n-type semiconductors, indicating the in situ formed surface graphitic carbon may play an important role as promoter.

Recent developments in Ni-based material have further extended its application in CO_2 photoconversion with H_2 under visible light irradiation. The starting photocatalyst, Ni supported on silica alumina ($Ni/SiO_2 \cdot Al_2O_3$), achieves an impressive CO_2 conversion (3.7 mmol) of ~95 % with a CH_4 selectivity of ~97 % in 1 h

[25]. Unfortunately the reaction mechanisms remain unclear. Since metallic Ni is highly unlikely to serve as a photocatalyst, the reduction of CO_2 cannot be induced by the CB electrons. A hypothesis proposed by Sastre et al. suggests that CO_2 conversion occurs via H_2 activation followed by CO_2 activation, where the formation of Ni – H initiates the CO_2 reduction rather than the CB electrons (Fig. 4.5c). The key process in this hypothesis is the formation of Ni–H phase via H^- with Ni^+ or H^+ with Ni^-; however, the Ni – H phase has not been observed yet. Another possible mechanism could be the formation of NiO in the beginning of the reaction. During irradiation, the visible and infrared light from the solar simulator, along with the exothermal CO_2 reduction, can heat the catalyst surface up to 150 °C, which may facilitate the oxygen uptake of supported Ni nanoparticles (NPs) from the silicate substrate. Therefore, a careful examination of the support may help unravel the reaction mechanisms.

4.3 Perovskites

Perovskite materials (ABX_3) exhibit many fascinating properties from both theoretical and application perspectives, including ferroelectricity, superconductivity, charge ordering, and spin-dependent transport. The interplay of compositional, structural, optical, and transportation properties is commonly observed in this family, making them promising candidates as photocatalysts. Perovskites are characterised by a crystal structure similar to that of calcium titanium oxide ($CaTiO_3$). Normally A and B sites are occupied by two cations with very different sizes ($d_A > d_B$), whereas X (normally O) is an anion that bonds to both. In the ideal cubic-symmetry structure, the A and B cations are 12- and sixfold coordinated in bulk and surrounded by cuboctahedron and octahedron of anions, respectively.

Alkali metal tantalates ($ATaO_3$, A = Li, Na, and K) have been employed as photocatalysts for water splitting since 2001 [27]. Varying the A site alkali cations from Li^+ to K^+ results in extension of light absorption (Fig. 4.6a) and red shifting of excitation and emission peaks (Fig. 4.6b). It is also worth noting that a reduction of the Stokes shift is observed following the increase of atomic number of the alkali number ($13.6 * 10^{-3}$ to $10.3 * 10^{-3}$ cm^{-1}), indicating that a higher energy of the excited electrons can be preserved. The variation in optical properties of $ATaO_3$ can be explained by the increasing of Ta–O–Ta bond angle (Li–Na–K: 143°–163°–180°), which reduces the bandgap and facilitates the migration of excited electrons in the crystal. The narrowing of the bandgap arises from the lowering of CBM, as the O2p orbital states contribute to VBM of all $ATaO_3$. The $NaTaO_3$ shows the optimum performance for overall water splitting with NiO as promoter, probably due to the modest bandgap and a properly aligned CBM that matches the electronic structure of NiO. However, the stability of NiO/$NaTaO_3$ in pure water remains a big issue due to the decomposition of NiO by UV light (270 nm). Further doping with La has been employed to improve stability and turned out to be very successful [4]. As shown in Fig. 4.6c, the diffraction peak of $NaTaO_3$ powders slightly shifts to

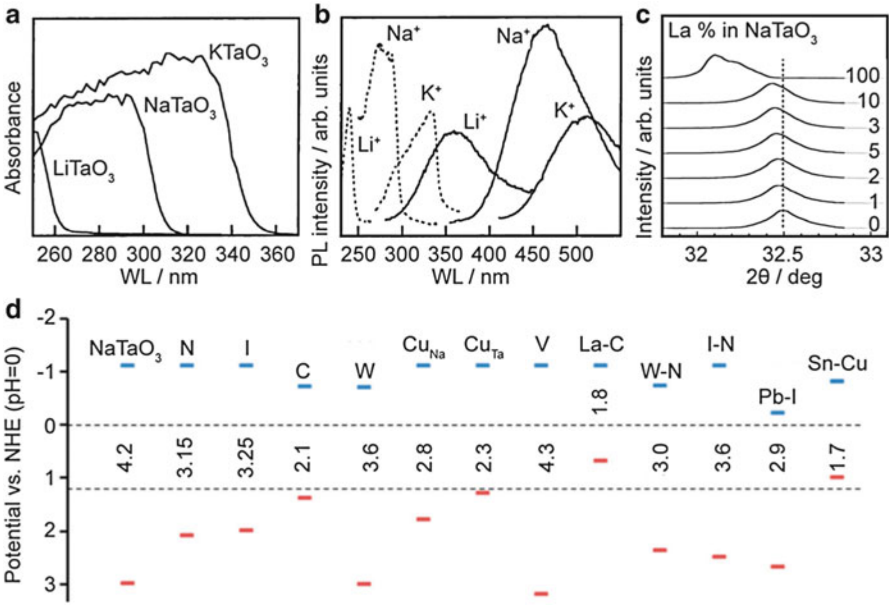

Fig. 4.6 (**a**) Absorption spectra of $ATaO_3$, (A = Li, Na, and K). (**b**) Excitation and emission spectra of $ATaO_3$ (Reprinted with permission from Ref. [27] Copyright 2001, American Chemical Society). (**c**) XRD patterns of La-doped $NaTaO_3$ (Reprinted with permission from Ref. [4] Copyright 2003, American Chemical Society). (**d**) Calculated band-edge potentials of doped and co-doped $NaTaO_3$ (Reprinted with permission from Ref. [28] Copyright 2014, The Royal Society of Chemistry. Published by the PCCP Owner Societies)

lower angles as the concentration of doped La increases. Since the ionic radii of either 12-coordinated La^{3+} (1.36 Å) or six-coordinated La^{3+} (1.032 Å) is remarkably larger than that of Ta^{5+} (0.64 Å), they are more likely to be doped into the lattice of $NaTaO_3$ by substitution of Na^+ (1.39 Å) on A sites. The doping of La results in stabilisation and nanosizing of the supported NiO, which leads to a significant enhancement in photocatalytic performance.

The main drawback of tantalate perovskites is their large bandgaps (~4.2 eV). Figure 4.5d demonstrates the calculated bandgap narrowing by various dopants. Dopants can be introduced into A, B, and X sites or co-doped at two different sites, which provides the perovskites huge opportunities for fine-tuning the band structures. Whilst introducing N and I on X sites to partially substitute O results in VBM shifting upward, doping with C on X sites significantly reduces both the potential of CBM and VBM due to the C2p–C2p excitation. However, photoexcited electrons are highly localised on the C sites and thus are not beneficial for photocatalytic reactions. Furthermore, passivated co-doping has also been proved to be an efficient strategy to narrow the bandgap whilst maintaining the ionic charge balance in a lattice. Among them, the co-doping of N–W, La–C, Cu–Sn, and Pb–I can narrow the bandgap whilst reasonable photocatalytic performances can still be obtained.

Take La–C co-doping as an example, La and C substitutes Na and O, respectively, which nullifies the dopant-induced charge imbalance. Mid-gap states that spread over 1.5 eV can be formed due to the introduction of La and C, corresponding to the bandgap narrowing.

Strontium titanates and some cobalt-based perovskites have also been used as photocatalysts for various reactions including partial oxidation (i.e. propene and benzene) and CO_2 reduction. They show relatively good photocatalytic performances under UV irradiation, but reducing the bandgaps is needed for applications. Nevertheless, the perovskite sensitizers, methylammonium lead trihalide ($CH_3NH_3PbX_3$, X: I^-, Br^-, Cl^-), which are used in solar cells could also be a promising candidate for certain photochemical reactions. It has tunable optical bandgaps between 2.3 eV and 1.6 eV depending on halide content, which ideally absorbs most of the visible light in solar spectrum. However, the methylammonium lead trihalides decompose within presence of water, which should be taken into consideration.

4.4 Sulphides and Nitrides

4.4.1 Sulphides

Metal sulphides (i.e. CdS, SnS_2, and MoS_2) usually show light absorption in visible light regions, allowing them to work as promising sensitizers in solar cells or visible light-driven photocatalysts. Among these candidates, cadmium sulphide-based materials have been extensively investigated due to their easy production and good thermal stability. It has two polymorphs, the stable hexagonal wurtzite structure and the less stable cubic zincblende structure, wherein both polymorphs Cd and S atoms have a coordination number of four. The pristine CdS is an n-type semiconductor with a direct bandgap of ~2.4 eV and CBM of −0.1 V vs. SHE, which makes it a promising photocatalyst for visible light-induced water splitting. The nanoporous CdS indeed showed excellent photocatalytic H_2 evolution performance ($QE \approx 60\ \%$) under visible light radiation conditions in the presence of Pt promoter and hole scavengers, as shown in Fig. 4.7a. Further enhancement of the QE to ~93 % can be achieved by using a combination of Pt–PdS promoters [32]. However, CdS tends to undergo photodecomposition to form toxic Cd^{2+} and S without the presence of proper hole scavengers (S^{2-} and SO_3^{2-}), which limits the application of CdS [33]. Although great efforts have been made to stabilise CdS (e.g. structure engineering by coating with thin layer of TiO_2), the catalytic performance dropped significantly.

To overcome the stability and environmental issue, sulphides with nontoxic cations have been explored. ZnS has been considered as one of the candidates. It also has two polymorphs (cubic zincblende and hexagonal wurtzite) where both Zn and S are 4-coordinated. However, the bandgaps of either polymorph are too large

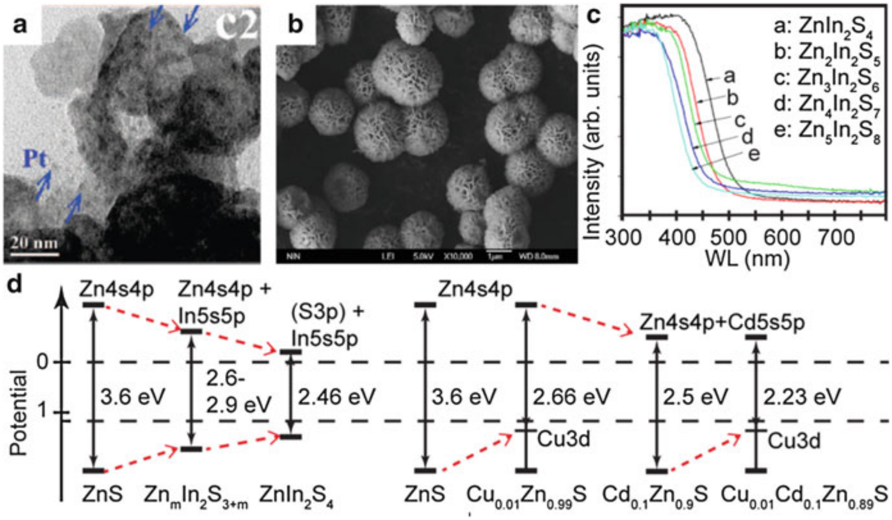

Fig. 4.7 (**a**) CdS nanosheets with Pt NPs on the surface (Reprinted with permission from Ref. [29] Copyright 2008, American Chemical Society). (**b**) SEM image of ZnIn$_2$S$_4$ prepared by hydrothermal synthesis. (**c**) Diffuse reflectance spectra of Zn$_m$In$_2$S$_{m+3}$ samples (Reprinted with permission from Ref. [30] Copyright 2010, Elsevier). (**d**) Scheme of band structure engineering of ZnS (Reprinted with permission from Ref. [30,31] Copyright 2010, Elsevier)

to absorb visible light (3.6 eV for cubic ZnS and 3.9 eV for hexagonal ZnS), which require doping of the pristine ZnS to reduce the bandgap. Figure 4.7b and c shows the SEM image of In-doped ZnS (ZnIn$_2$S$_4$) and corresponding absorption spectra. The as-synthesised Zn$_m$In$_2$S$_{3+m}$ materials generally show a flower-like microstructure with large surface area, and increasing the In concentration extends the visible light absorption range. DFT calculations reveal that whilst the VB of Zn$_m$In$_2$S$_{3+m}$ should be composed of hybrid orbitals of S3p and Zn3d, the In5s5p orbitals with Zn4s4p orbitals contribute to the formation of the CB of Zn$_m$In$_2$S$_{3+m}$ (Fig. 4.7d, left). Thus, the bandgap and the potentials of CB and VB can be tuned by varying the m value. Similarly, the addition of Cu and/or Cd can also reduce the bandgap significantly, as presented in Fig. 4.7d on the right-hand side. Whilst the hybridising of Zn4s4p with Cd5s5p orbitals reduces the CBM of ZnS, the partially filled Cu3d orbitals level up the VBM. Similar strategies have been applied to tune the electronic structures of AgInS$_2$, CuInS$_2$, and similar semiconductors to achieve visible light responses whilst maintaining good stability.

Recently, SnS$_2$ has attracted great attention. A pristine SnS$_2$ is a CdI$_2$-type layered semiconductor with a bandgap of ~2.3 eV, which is slightly smaller than that of CdS. The layered structure consists of an S–Sn–S triple layer, which is held together via van der Waals interactions. It is chemically stable in acid and neutral aqueous solution, thus can be a promising visible light-driven photocatalyst [34]. It has been applied for photocatalytic reduction of Cr^{6+} to Cr^{3+}, and the crystallite size of SnS$_2$ influences the reactivity drastically [35]. However, the deposition of Cr

$(OH)_3$ on the surface of SnS_2 causes the reduction of activity, thus making it unsuitable for recycling.

In order to harvest more visible light, transmittance and scattering of the light through the bulk and at grain boundaries need to be avoided. This calls for the synthesis of SnS_2 with minimum thickness, which has been achieved by a scalable liquid exfoliation strategy, as demonstrated in Fig. 4.8a. The freestanding, highly oriented SnS_2 thin films (Fig. 4.8b and c) display a height of ~6.1 Å as determined

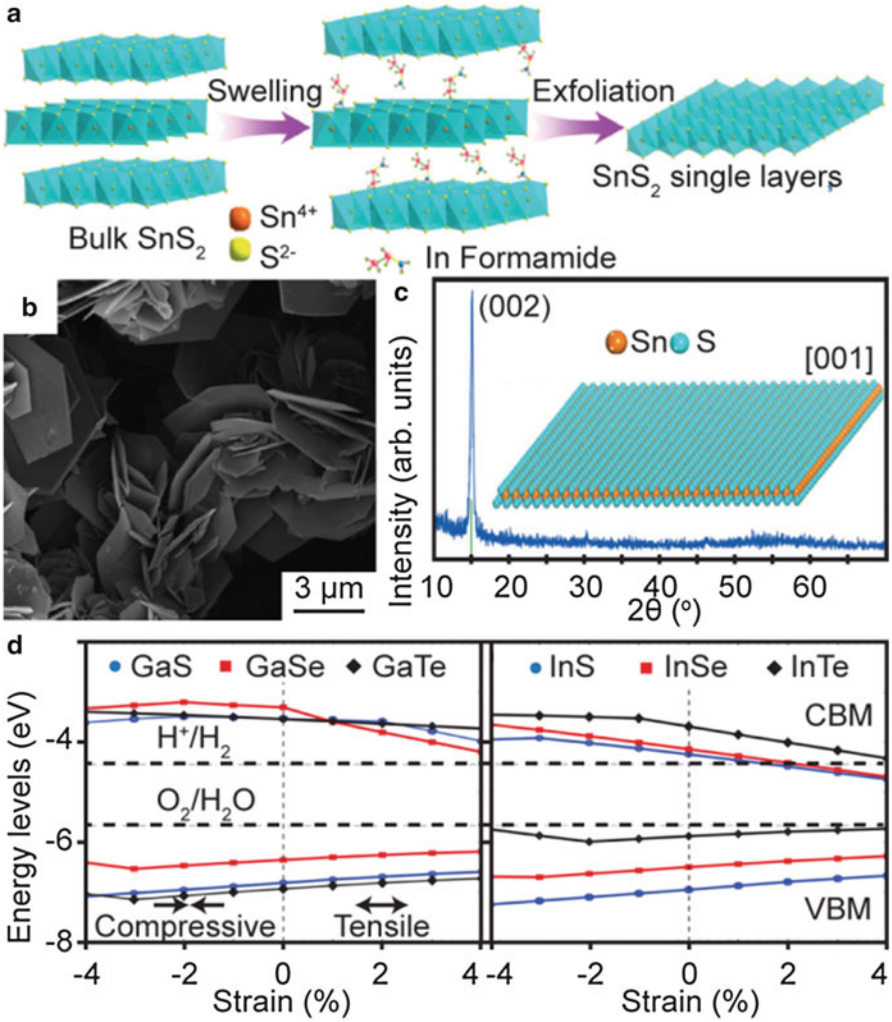

Fig. 4.8 (**a**) Scheme of exfoliation of hexagonal-layered SnS_2 into (001)-oriented freestanding SnS_2 single layers. (**b**) SEM image and (**c**) XRD patterns of the oriented SnS_2 single layers (Reprinted with permission from Ref. [36] Copyright 2012, John Wiley and Sons). (**d**) Strain effects on calculated band-edge positions of single-layer GaX and InX (Reprinted with permission from Ref. [37] Copyright 2013, American Chemical Society)

by atomic force microscopy (AFM), which agrees with theoretical thickness of a single-layered SnS_2 slab along [001] direction (5.91 Å). X-ray absorption fine structure (XAFS) analysis coupled with first-principles calculations reveals that elongation and structural disorder of surface atoms are responsible for the structural stability and increased density of states at the valence band edge. Moreover, the charge carrier density of single-layered SnS_2 shows a 40 times enhancement compared to that of bulk SnS_2 according to Mott–Schottky equation, therefore yielding a significant enhancement in incident photon-to-electron conversion efficiency (IPCE) and very stable current density during long-term test. However, one should bear in mind that the CBM of SnS_2 is not ideally aligned for water splitting (~0.7 V vs. SHE), which requires additional bias to transfer e^- to reduce H^+. Besides, the variation in the composition of SnS_x ($x = 1, 1.5, 2$) will also influence the electronic structure drastically [34]. Therefore, a careful control during synthesis is of great importance in fine-tuning the bandgap, band positions, charge carrier mobility, and density to achieve high photoactivity.

Similarly, recent development in single layer structured group III monochalcogenide (MX, M = Ga and In, X = S, Se, and, Te) materials has also attracted great attention in photocatalysis applications. These monochalcogenides synthesised via the mechanical cleavage or solvent exfoliation method exhibit bandgaps and band positions that are suitable for water splitting and CO_2 reduction under visible light irradiation [38]. Interestingly, DFT calculation reveals that the bandgaps and band positions can be further tuned by biaxial strain, as demonstrated in Fig. 4.8d. Whilst a compressive strain leads to a blue shift of the bandgap that increases driving forces for redox reactions, tensile force red shifts the bandgaps that extend the absorption of visible light. Nevertheless, the single-layered MXs are characterised by high solvation enthalpies, suggesting their stability in aqueous solution may be potentially suitable for photocatalysis.

4.4.2 Nitrides

Although metal sulphides show promising visible light absorption properties, their inherent instability and incapability in overall water splitting remain big issues for application. Therefore, metal nitrides with d10 configurations (i.e. Ge_3N_4 and GaN) have been investigated to overcome the disadvantages. The phase pure β-Ge_3N_4 has been synthesised via nitridation of GeO_2 under 1 bar NH_3 flow at 1153 K for 10 h, as shown in Fig. 4.9a. Figure 4.9b demonstrates the energy band dispersion and DOS of β-Ge_3N_4 investigated by DFT calculations. Whilst the VBM consists of N2p orbitals, the CBM is composed of hybridised Ge4s4p orbitals. The calculated bandgap of β-Ge_3N_4 is estimated to be 2.1 eV, which is smaller than that of the experimental result (3.8 eV). Unlike in metal oxides where the oxidation of water occurs from photoexcited holes in VB consisting of O2p orbitals, the N2p orbitals of β-Ge_3N_4 are responsible for generating holes to oxidise water. It should be noted

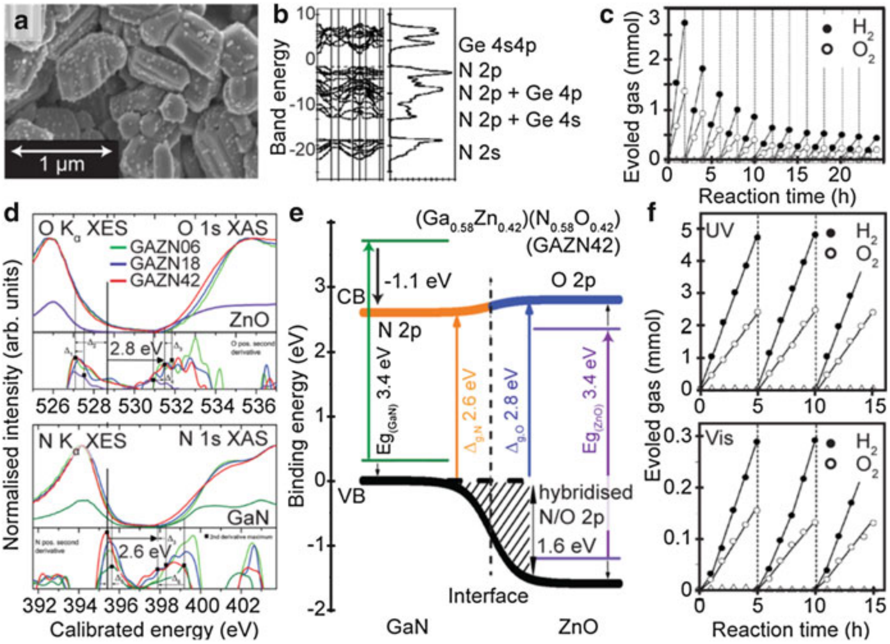

Fig. 4.9 RuO_2-loaded β-Ge_3N_4 photocatalyst: (**a**) SEM image, (**b**) electronic structure, and (**c**) overall water splitting (Reprinted with permission from Ref. [39] Copyright 2005, American Chemical Society). GaN–ZnO solid solution: (**d**) XES and XAS of ZnO–GaN samples with different compositions; (**e**) band transition scheme of $Ga_{0.58}Zn_{0.42}N_{0.58}O_{0.42}$ (Reprinted with permission from Ref. [40] Copyright 2012, American Chemical Society). (**f**) Overall water splitting under UV (*top*) and visible (*bottom*) light irradiation using RuO_2-loaded ZnO–GaN (Reprinted with permission from Ref. [41] Copyright 2005, American Chemical Society)

that the presence of RuO_2 NPs as promoter is crucial for successful photocatalytic water splitting. Whilst pristine β-Ge_3N_4 shows a negligible performance, the 1 wt% RuO_2 supported on β-Ge_3N_4 yields a maximum QE of ~ 9 % at 300 nm within the first two hours. However, the performance dropped markedly within 24 h (Fig. 4.9c), possibly due to the RuO_2–β-Ge_3N_4 interface change that hinders the interfacial charge transfer process.

In order to extend light absorption to visible range, the wurtzite-structured GaN (E_g ~ 3.4 eV) has been incorporated with wurtzite-structured ZnO (E_g ~ 3.2 eV) to form a solid solution $Ga_{1-x}Zn_xN_{1-x}O_x$ (GAZN) that can approximate desired zinc oxynitride materials. The bandgap of such solid solutions can thus be tuned by varying the Ga:Zn ratio, which has been confirmed by UV–vis diffuse reflectance spectrometry [41]. X-ray emission spectroscopy (XES) and x-ray absorption spectroscopy (XAS) of N and O reveal the electronic structure change of GaN–ZnO with different compositions, as shown in Fig. 4.9d. Both O and N CB edges are repelled to lower energies as the ZnO concentration increases, and the N CB states offset below the O CB states by 0.2 eV. The CB states of ZnO are repelled to higher orbital energy due to GaN, which shows a greater spectral weight at lower orbital energy and a higher concentration in the solid solution, thus resulting a 0.4 eV shift downward in CB onset energy from low to high Zn concentration ($x = 0.06$ to 0.42). Meanwhile, VBM remains unchanged owing to the greater energy separation of occupied N and O 2p bands. The highest-/lowest-energy local maximum of the second derivative of XES and XAS spectra can be used to estimate the energy band onset, where a 0.4 eV reduction in the bandgap of GAZN42 ($x = 0.42$) has been observed due to the reduction of conduction band onset energy. Based on XAS and XES results, reduced bandgaps of 2.6 and 2.8 eV for GaN and ZnO in the solid solution can be derived, which arise from the decrease in CB onset energy. Figure 4.9e summarises the band structure of the GaN–ZnO system, where CBM of GaN and ZnO are both shifted from the isolated precursor materials and is connected on the phase boundary. The band edges of GaN are forced to lower energy within an expanded ZnO gap caused by state repulsion.

The dual-bandgap GaN–ZnO shows quite stable photoactivity for water splitting under UV or visible light irradiation when deposited with RuO_2 as cocatalyst (Fig. 4.9f). Although the performance under visible light radiation is not satisfactory, the investigation into other methods to better control the electronic structure of GaN–ZnO could potentially be the solution. Furthermore, since such a multiple bandgap architecture (a small energy gap contained within a large one) is supposed to absorb and retain photons with higher wavelengths more efficiently, as well as increasing the available photocurrent within a semiconductor/electrolyte cell, it is theoretically possible to design VB and CB edges optimised for a range of redox reactions whilst providing desired bandgaps.

Metal nitrides with d0 electronic configuration (e.g. Ta_3N_5) have been also investigated. These stable photocatalyst show visible light absorption up to 650 nm and can easily be synthesised by nitriding the corresponding metal oxides under NH_3 flow. In contrast to CdS, these (oxy)nitrides are not toxic. DFT calculations reveal that the CBM and VBM of these materials consist of empty d orbitals of the metal and N2p orbitals, respectively, which is similar to those of d0 transition metal oxide (e.g. TiO_2). Figure 4.10a and b representatively shows the light absorption feature and band positions of Ta-related (oxy)nitrides. Gradually increasing the concentration of N extends the light absorption of the materials due to the upper shift of VBM owing to the N2p orbitals, and the complete replacement of O by N (Ta_3N_5) results in a bandgap of 2.1 eV with CBM and VBM positioned suitable for water splitting. Additionally, the addition of alkaline earth metal (Ca, Sr, and Ba) can also extend the light absorption range. Due to their promising bandgaps and band positions for visible light-induced water splitting, Ta_3N_5-based photocatalysts with various microstructures (i.e. nanoporous nonwoven cloths, mesoporous microspheres, and nanorod arrays) have been synthesised by different techniques (Fig. 4.10c–e). Both hydrogen and oxygen evolution half reactions can be realised by loading proper promoters. Unfortunately, overall water splitting has not been achieved yet. Further investigation into the kinetics of photogenerated radicals might be essential to uncover this mystery.

The recent development of nonmetal nitride, namely, the graphitic carbon nitride (g-C_3N_4) materials, has attracted huge attention due to their tunable electronic

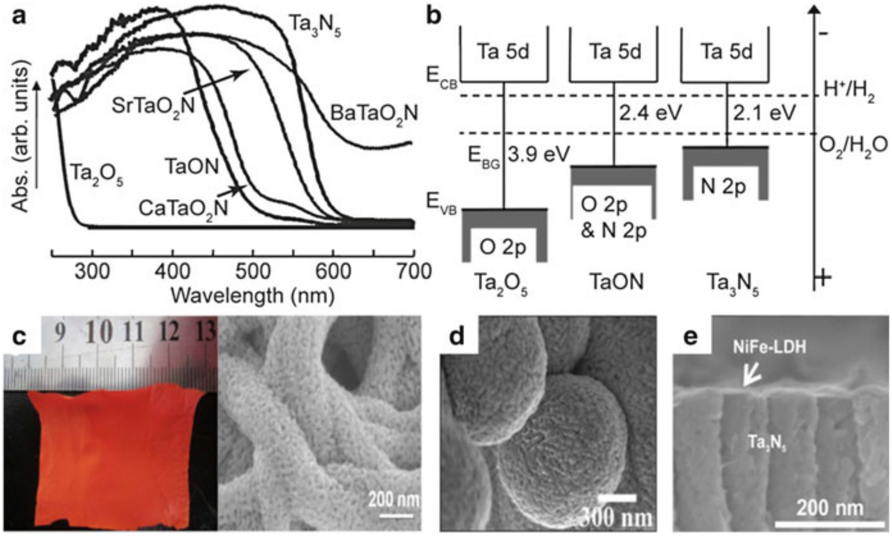

Fig. 4.10 (**a**) Absorption spectra of Ta_2O_5, TaON, Ta_3N_5, and related oxynitride (Reprinted with permission from Ref. [42] Copyright 2004, Elsevier). (**b**) Schematic band structures of Ta_2O_5, TaON, and Ta_3N_5 (Reprinted with permission from Ref. [43] Copyright 2003, American Chemical Society). (**c**–**e**) Synthesised Ta_3N_5 with different microstructures: nanofibre-fabricated cloth, mesoporous microspheres, and nanorods with NiFe promoter (Reprinted with permission from Ref. [44–46] Copyright 2014, 2013, and 2015, Nature Publishing Group, John Wiley and Sons, and American Chemical Society, respectively)

properties and chemical and thermal stability. The *g*-C_3N_4 can easily be synthesised by the polymerisation of cyanamide, dicyandiamide, or melamine, where melon (also a highly ordered polymeric C_3N_4 with pendant amino groups) will be initially formed and then comes out the less defective *g*-C_3N_4 species following further a condensation process. Figure 4.11a shows the schematic diagram of a perfect *g*-C_3N_4 species, which are formed from the tri-s-triazine (melem, C_6N_7) building blocks that are connected by planar amino groups. DFT calculation reveals that the HOMO–LUMO gaps of polymeric melon and the fully condensed *g*-C_3N_4 are ~2.6 eV (Fig. 4.11b) and 2.1 eV, which is slightly lower than that of the experimental results derived from absorption spectra (2.6–2.8 eV). Whilst the reduction potential of H^+ is positioned almost in the centre of the bandgap, the oxidation potential of water is located slightly above the HOMO, indicating a relatively small driving force for water oxidation. Since the HOMO and LUMO levels of melem originated from Np_z and Cp_z orbitals, respectively, the VBM and CBM of the *g*-C_3N_4 should also consist of Np_z and Cp_z orbitals as well.

Once the *g*-C_3N_4 photocatalyst has been loaded with appropriate promoters (i.e. Pt and Fe), it is capable of producing H_2 (in the presence of scavengers) and performing selective oxidation of benzene to phenol (in the presence of H_2O_2) under visible light radiation, as shown in Fig. 4.11c and d. The reactivity of both reactions decreases following the same tendency of light absorption decreasing. It

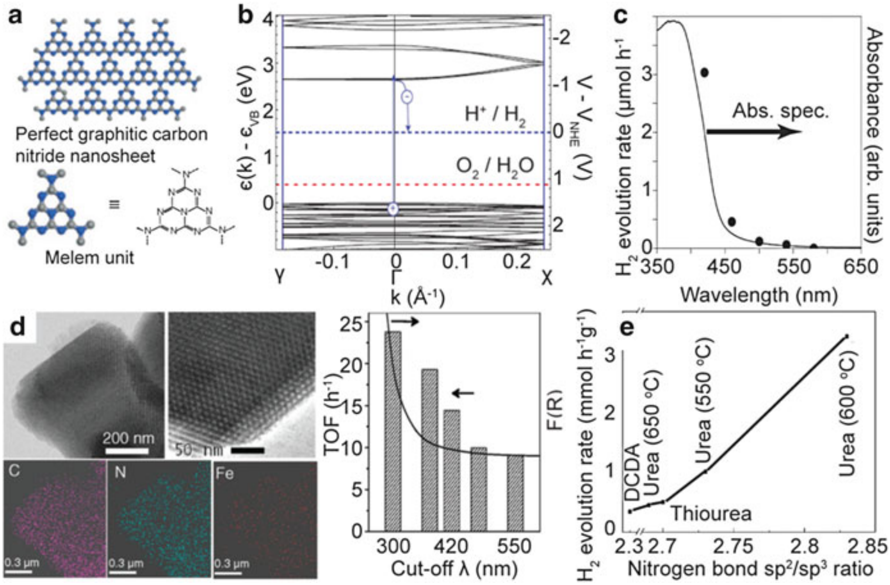

Fig. 4.11 (**a**) Structure of a perfect *g*-C_3N_4 sheet constructed from melem units. (**b**) Electronic structure of *g*-C_3N_4 (melon). (**c**) H_2 evolution rate as a function of radiation wavelength (Reprinted with permission from Ref. [47] Copyright 2008, Nature Publishing Group). (**d**) *Left*: TEM images of Fe-*g*-C_3N_4/SBA-15 and elemental mapping. *Right*: wavelength dependence of phenol production rate on Fe-*g*-C_3N_4/SBA-15 (Reprinted with permission from Ref. [48] Copyright 2009, American Chemical Society). (**e**) H_2 evolution rates as a function of N sp^2/sp^3 ratio (Reprinted with permission from Ref. [49] Copyright 2014, John Wiley and Sons)

has been shown that overall water splitting can also be achieved by using C quantum dots as promoter. This will be discussed in detail in Sect. 4.7.2.

It should be also noted that the electronic properties of *g*-C_3N_4 can be tuned by adjusting the in-plane organisation of melem and the compression of aromatic planes, which may further improve the catalytic performance of *g*-C_3N_4, as exemplarily demonstrated in Fig. 4.11e. By employing different precursors (dicyandiamide, urea, and thiourea) that contain elements other than C and N, the ratio of sp2 C–N–C bonds to sp3 H–N–$[C]_3$ and C–NH_x (amino functional groups) bonds can be adjusted. Whilst the sp2-bonded N atoms form the heptazine ring and bandgap structure, the hybridised sp3 N atoms and amino groups are responsible for the bulk and surface properties. It is therefore apparent that a lower proton concentration (higher sp2-bonded N) leads to a better performance in H_2 evolution. Since the use of an oxygen-containing precursor (urea) facilitates the removal of H in the form of formaldehyde under annealing conditions, control of the protonation and polymerisation can be realised, thus leading to a tunable activity. DFT calculations reveal that the CBM of deprotonated *g*-C_3N_4 shows a higher reduction potential than that of protonated *g*-C_3N_4, thus exhibiting a larger driving force for H_2 evolution reaction. However, one should also bear in mind that such a shift of

CBM will also result in a negative shift of the VBM, which reduces the driving force for oxygen evolution reaction that is not beneficial for overall water splitting.

4.5 Zeolites and MOFs

4.5.1 Zeolites

Zeolites have been extensively used in thermal catalysis due to their large surface area, high porosity, and the existence of acidic and basic sites. Their large surface area and pore volumes, excellent chemical and thermal stability, transparency (above 240 nm), and tunable electronic properties make zeolites good candidates as support for photocatalysts. The utilisation of zeolites in photocatalysis can be dated back to the pioneer work from Anpo et al., where Cu^{+} was anchored within cavities of ZSM-5 by ion-exchange method followed by a thermal reduction of Cu^{2+} in vacuum for photocatalytic NO reduction [50]. The porous structure of zeolite, which serves as the support, facilitates the diffusion of reactants within the pore and prolongs the interaction of reactants with anchored photocatalysts. Similarly, other transition metal ions (i.e. Ti, V, Cr) can also be anchored within the zeolite cavities via ion exchange. For example, TiO_2 can be incorporated into Y-zeolite for selective CO_2 photoreduction. The lifetime of the excited states of TiO_2–zeolite has been determined to be orders longer than that of bulk TiO_2 NPs (54 μs vs. nanosecond order), which is responsible for the significantly enhanced reactivity. It is also observed that selective reduction of CO_2 to CH_4 or CH_3OH can be realised by using different synthesis methods or loading with Pt promoter; however, the reaction mechanisms are not clear yet. Nevertheless, the photocatalysts have to be extremely small to be able to disperse within the porous structure. In the case of inorganic semiconductors, such small sizes lead to a quantum effect that causes blue shift of the bandgap, which is not ideal for the absorption of visible light.

Deposition of inorganic semiconductors on the surface of zeolite offers an alternative approach for incorporating the two parts. Such a strategy allows for the immobilisation of photocatalysts with different functions on both sides of the zeolite membrane for redox half reactions (i.e. water splitting and CO_2 reduction). Figure 4.12a presents the HRTEM image of platelike β-$Co(OH)_2$ supported on zeolite Y surface prepared by ion-exchange method [51]. With a d-spacing of 0.465 nm, the as-prepared Co species can be assigned to the [100]-oriented β-Co $(OH)_2$. Annealing of the as-synthesised β-$Co(OH)_2$/zeolite Y in air (>125 °C) leads to the formation of spinel Co_3O_4. All Co species supported on zeolite show activities for photocatalytic water oxidation using $Ru(bpy)_3{}^{2+}$ as sensitiser and $Na_2S_2O_8$ as electron acceptor, with β-$Co(OH)_2$ yielding much better performance compared to that of Co_3O_4. However, the reusability of β-$Co(OH)_2$/zeolite Y is not satisfactory, as the performance of recovered catalyst is reduced significantly

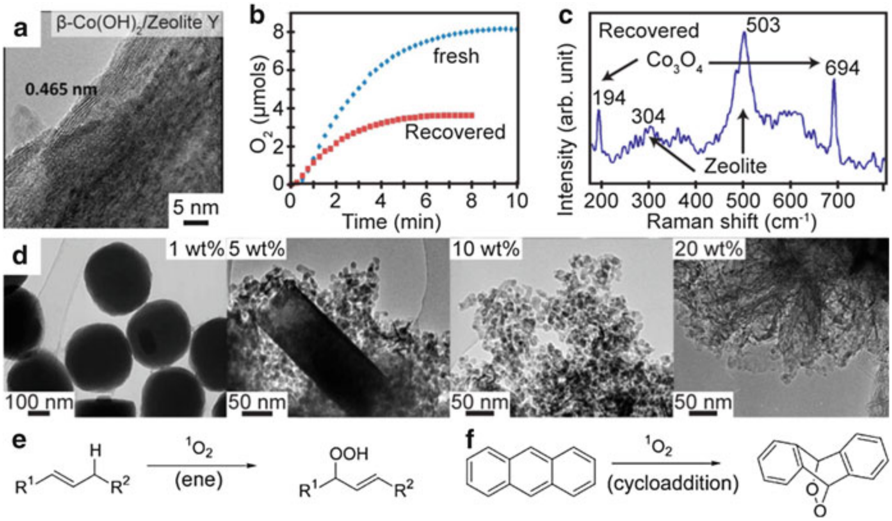

Fig. 4.12 (**a**) HRTEM image of as-prepared β-Co(OH)$_2$ supported on zeolite Y. (**b**) Photocatalytic O_2 evolution using as-prepared and recycled β-Co(OH)$_2$/zeolite Y. (**c**) Raman spectrum of the reused β-Co(OH)$_2$/zeolite Y (Reprinted with permission from Ref. [51] Copyright 2014, American Chemical Society). (**d**) TEM images of TS1 with 1, 5, 10, and 20 wt% of graphene (Reprinted with permission from Ref. [52] Copyright 2011, The Royal Society of Chemistry). (**e**) Scheme of the *ene* reaction and cycloaddition reaction

(Fig. 4.12b). Raman spectroscopy reveals that the surface of β-Co(OH)$_2$ undergoes phase transformation to form Co_3O_4 (194 and 694 cm^{-1} peaks) during irradiation, which is responsible for the drop of photocatalytic performance (Fig. 4.12c).

One disadvantage of zeolite supports is that the aluminosilicates do not absorb light in the UV–vis region; thus, they are photochemically inactive. This can be solved by incorporation of heteroatoms (normally transition metals) into the framework (i.e. titanosilicate TS-1 and EST-10 and vanadium silicate VS-2). In the case of TS-1, an absorption band at 225 nm has been observed, corresponding to the ligand-to-metal (–O–Ti≡) electron transfer at isolated Ti atoms. These zeolites show excellent photoreactivity in the decomposition of organic pollutants, CO_2 and NO reduction, and metathesis of propene. It is also possible to further improve the catalytic performance by hybridising photoreactive zeolites with graphene using a microwave-assisted solvothermal technique, as demonstrated in Fig. 4.12d. Note that the addition of graphene impacts the morphology of TS-1 remarkably. Whilst pristine TS-1 exhibits a hexagonal prism shape with a crystallite size of ~300 nm, a gradual increase in the addition of graphene reshapes the TS-1 into ellipsoidal particles (<1 wt%), rectangular plates (1–5 wt%), and finally to spherical NPs with a crystallite size of ~10 nm (>10 wt%). Such a drastic change in size results in enhanced charge transfer kinetics, thus promoting photocatalytic reactions compared to that of carbon nanotube-modified TS-1.

Although photoactive zeolites show some enhanced intrinsic performance compared to that of the bulk materials, the negative blue shift that reduces light absorption in the UV region limits their application. Therefore, harvesting light with organic sensitizers anchored within the porous structure has attracted great attention. For example, dye (e.g. eosin Y)-sensitised Ti-MCM-41 zeolite along with Pt promoters has been reported as efficient photocatalysts for hydrogen evolution reaction under visible light irradiation [53]. Another important application of zeolite is improving the selectivity of singlet oxygen photocatalyst. Singlet oxygen ($^1O_2$) reacts rapidly with alkenes and aromatic hydrocarbons via the *ene* and cycloaddition reactions (see Fig. 4.12e and f); however, such reactions normally have poor selectivity due to the highly reactive properties of $^1O_2$. The encapsulation of a $^1O_2$ photocatalyst (i.e. thionin, methylene blue, and methylene green) into zeolite X and Y not only prevents aggregation and self-quenching of these dyes that enhance the quantum yield of $^1O_2$ but, more importantly, improves the regioselectivity of *ene* and cycloaddition reactions. The regioselectivity has been rationalised as the following: alkene first forms a complex with the alkali metal ions in the zeolite super-cage, forcing the allylic methyl groups to occupy the face of the olefin that is approached by $^1O_2$. The alkali ions shift slightly to stabilise the perepoxide intermediate that is formed via $^1O_2$ reaction with alkene. Therefore, the regioselectivity originates from the steric interactions of these alkali metal ion perepoxides that govern the population of each diastereomer [54]. More details on anchored systems will be discussed in Sect. 4.6.

4.5.2 Metal–Organic Frameworks (MOFs)

MOFs are a class of crystallites that have tunable dimensions and porous structures. MOFs are built from organic linkers and metal ions or clusters, characterised by a high surface area, tunable pore size, and porosity. In contrast to zeolites that are limited by the fixed tetrahedral coordination of Si/Al and the two-coordinated oxide linkers, MOFs exhibit more diversity in coordination geometries, polytopic linkers, and ancillary ligands, making them useful in driving various catalytic reactions (i.e. Lewis acid/base reactions and asymmetric reactions). Furthermore, MOFs are typically synthesised under mild conditions, which allows for the incorporation of delicate functional groups into the framework. Theoretical calculations and optical measurements reveal that MOFs have bandgaps between 1.0 and 5.5 eV, indicating possible applications in photocatalysis (i.e. H_2 evolution, CO_2 reduction, water oxidation, and organic synthesis) [55].

The photophysical property investigation of MOF-5 by Alvaro et al. initiated the study of MOFs as photocatalysts [56]. MOF-5 can emit light with an emission maximum at 540 nm under excitation of 350 nm. Whilst the localised excited electrons have a lifetime of ~5 μs, the delocalised excited electrons have a lifetime of ~30 μs. By investigating the transient absorption spectra of the moiety (sodium terephthalate) with additional Zn^{2+} in solution, it is revealed that a ligand-to-metal

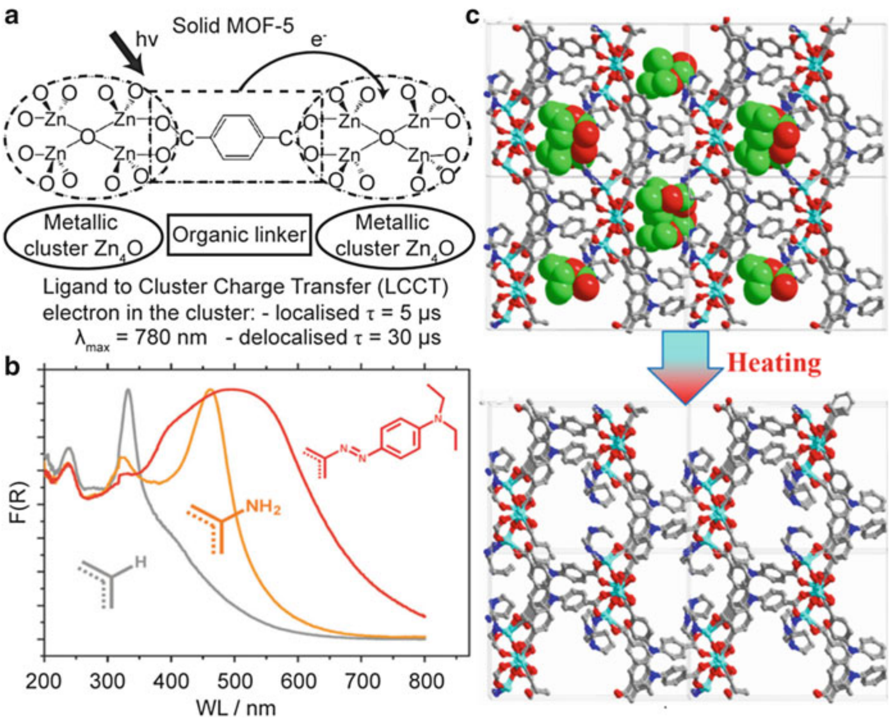

Fig. 4.13 (**a**) Photophysical processes that occur after irradiation of MOF-5 (Reprinted with permission from Ref. [56] Copyright 2007, John Wiley and Sons). (**b**) Diffuse reflectance spectra of MIL-125(Ti) (*gray*), NH_2-MIL-125(Ti) (*orange*), and MR-MIL-125(Ti) (*red*) (Reprinted with permission from Ref. [57] Copyright 2013, The Royal Society of Chemistry). (**c**) Crystal structure of the Zn – BCIP1 framework (*top*) and the simulated structure of Zn – PYI1 from thermolytic expulsion of the Boc moieties (*bottom*). The *cyan*, *red*, *blue*, *gray*, and *green* balls represent Zn, O, N, and C atoms and Boc moiety, respectively (Reprinted with permission from Ref. [58] Copyright 2012, American Chemical Society)

charge transfer (LMCT) occurs, which is responsible for the prolonged lifetime of delocalised electrons in the moiety-Zn^{2+} solution. Since MOF-5 can be considered as a periodic repetition of Zn_4O clusters in which each Zn^{2+} is coordinated to the O atoms of the moiety terephthalate, as shown in Fig. 4.13a, a ligand-to-cluster charge transfer (LCCT) process within the framework is proposed.

MOF-5 has a bandgap of ~3.4 eV with a CBM of 0.2 V vs. SHE, which is chemically stable under UV irradiation. With the intension of extending light absorption into visible region and adjusting the CBM position, NH_2-Uio-66(Zr), a Zr-containing MOF has been prepared for CO_2 reduction under visible light irradiation [59]. Whilst the CBM is governed by the redox potential of Zr^{4+}/Zr^{3+} that is more negative than that of Ti^{4+}/Ti^{3+}, the visible light absorption originates from the 2-aminoterephthalate (ATA) ligand that substitutes the benzenedicarboxylate (BDC). More recently, a significant extension of light absorption of the Ti-containing MOF

[MIL-125(Ti)] to visible region has been realised via post-synthetic modification (PSM) using antenna-like moieties, as shown in Fig. 4.13b [57]. The final visible light-active MOF, MR-MIL-125(Ti) (red curve in Fig. 4.13b), has been prepared by NH_2-MIL-125(Ti) (orange curve in Fig. 4.13b) reacting with diazonium salt followed by reacting with diethylaniline. Owing to the enhanced light absorption, the MR-MIL-125(Ti) shows impressive performance in selective photooxidation of benzyl alcohol under visible light radiation.

Nevertheless, photoactive MOFs also show unique photocatalytic properties that other materials cannot compete with, especially in organic synthesis applications. MOFs create the opportunity to combine photocatalyst with organocatalyst. One example is the chiral MOF, namely, Zn-PYI1, which exhibits high selectivity for photocatalytic asymmetric α-alkylation of aldehydes, as demonstrated in Fig. 4.13c. The Zn-PYI1 has also been synthesised via a PSM process of the parent MOF Zn-BCIP1 (top of Fig. 4.13c), which has been synthesised via solvothermal reaction from L-*N*-*tert*-butoxycarbonyl-2-(imidazole)-1-pyrrolidine (L-BCIP) [58]. The key point of the PSM process is the removal of the protective *tert*-butoxycarbonyl (Boc) moiety to expose active sites, which are likely to be the $N-H$ of pyrrolidine of the L-BCIP molecules that is located within the channels according to dye adsorption test. This has been realised by microwave irradiation in dry *N,N*-dimethylformamide solution. The activated Zn-PYI1 shows a high reaction efficiency (74 % in yield) and excellent enantioselectivity (92 % ee) in photocatalytic α-alkylation of aliphatic aldehydes compared to that of other MOFs.

4.6 Anchored Homogeneous–Heterogeneous Systems

The most well-known homogeneous systems for light-driven reactions are photosynthesis and photo-Fenton reductions. Whilst in photosynthesis chlorophylls and carotenoids serve as photosensitizers to oxidise water and reduce CO_2, Fe^{2+} and Fe^{3+} ions are used as photosensitizers and catalysts to decompose H_2O_2 and H_2O to form hydroxyl radicals for water detoxification. For homogeneous photocatalysts, every single catalytic entity acts as a single active site, which makes them intrinsically more active and selective compared to traditional heterogeneous photocatalysts. However, their disadvantages are also obvious compared to their counterparts. The syntheses of homogeneous photocatalysts are normally costly due to the complexity of the structure and utilisation of expensive precursors; most homogeneous photocatalyst systems normally suffer from short lifetimes due to the decomposition of the light-absorbing molecules; besides, since the catalyst and products are mixed in the same phase, separation and reuse of the homogeneous photocatalyst have to be considered. Therefore, anchoring a homogeneous catalyst to heterogeneous materials may provide a solution to prolong the lifetime and facilitate the recycling of the molecular catalyst.

The anchored systems can be divided into three categories depending on the functionality of the molecule. In type I, the molecule only serves as a photosensitizer, as shown in Fig. 4.14a. The role of the sensitizer molecule is exactly the same

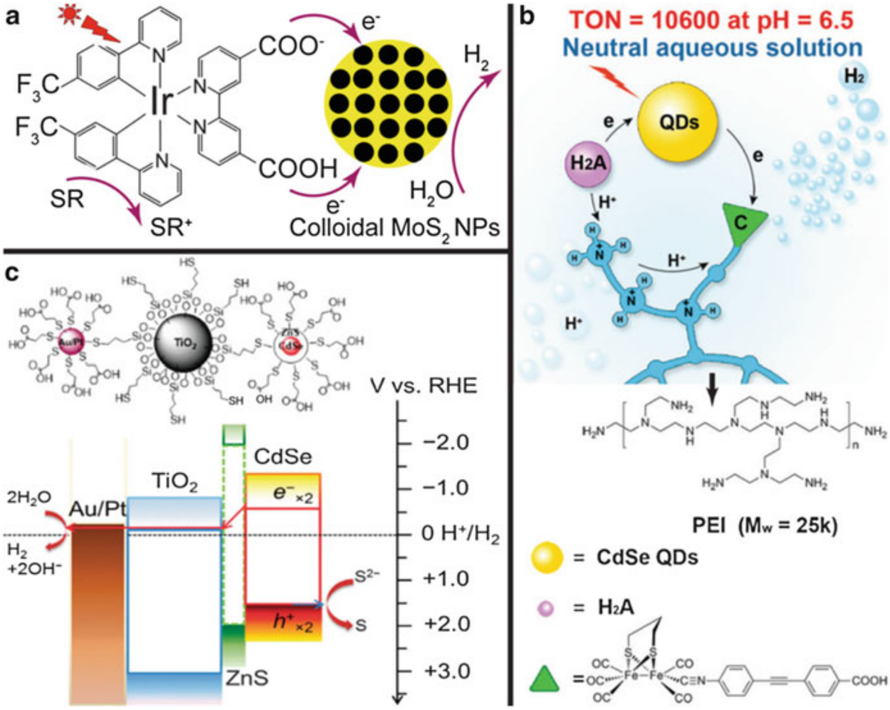

Fig. 4.14 Anchored homogeneous–heterogeneous systems. (**a**) Ir(III) complex as photosensitiser anchored on MoS_2 NPs (Reprinted with permission from Ref. [60] Copyright 2014, Nature Publishing Group). (**b**) Fe complex as catalyst anchored on CdSe QDs (Reprinted with permission from Ref. [61] Copyright 2015, John Wiley and Sons). (**c**) Core-shell CdSe–ZnS QDs and Au/Pt promoter anchored on TiO_2 surface by organic linkers (Reprinted with permission from Ref. [62] Copyright 2015, The Royal Society of Chemistry)

as that of dyes in solar cells, where the sensitizer absorbs photons and gets excited. Then, electrons are injected from the sensitizer to the CB of the semiconductor (MoS_2 here) for reduction reactions. This indicates that most of the dyes for dye-sensitised solar cells (DSSCs) can be used for this purpose with proper modification. However, such immobilisation process should not modify the intrinsic coordination and catalytic properties of the dyes. Meanwhile, sacrificial reducing agents (SRs) will donate electrons to the sensitizer molecules to complete the redox reaction. Compared to that of DSSC configuration, the only difference is that the redox reaction takes place at different sites rather than at different electrodes. Therefore, optimisation of two interfacial charge transfer kinetics (sensitizer to semiconductor and semiconductor to electron acceptor) by tuning the backbone structure of the sensitizer and surface properties of the semiconductor is the key to achieve high QE.

Type II molecules play the role as promoters in photocatalysis, as indicated in Fig. 4.14b. They (polyethylenimine (PEI)-grafted [FeFe]-hydrogenase mimic here) receive excited electrons that are generated via excitation of semiconductors (CdSe quantum dots [QDs] here) and utilise the trapped electrons for proton reduction reactions. A wide range of hydrogenase catalysts have been also used as promoters for H_2 production (i.e. [CoIII(dmgH)$_2$pyCl] and [(μ-SPh-4-NH$_2$)$_2$Fe$_2$(CO)$_6$]) and CO_2 reduction (i.e. iron(0) porphyrin and ReI(bpy)(CO)$_3$L complexes), and they have been anchored on the surfaces of various heterogeneous sensitisers (i.e. CdS, MoS_2, and ZnS) [61, 63]. In this case, charge trapping and releasing of the trapped electrons, as well as stability of the organic promoters under different reaction conditions, need to be improved.

Type III organic molecules serve as linkers to bind photocatalyst and promoters together to achieve satisfactory interfacial charge transfer kinetics. Figure 4.14c representatively demonstrates the application of 3-mercaptopropyl trimethoxysilane (MPTMS) and mercaptopropionic acid (MPA) as linkers to immobilise Au/Pt promoter and core-shell CdSe–ZnS QDs on the surface of TiO_2. Under visible light irradiation, CdSe absorb photons and generate excited electrons, which are then transferred to the Au/Pt promoter through the ZnS shell, MPA, MPTMS, TiO_2, MPTMS, and MPA chains for hydrogen evolution. This system shows QE of ~1.5–2.5 % from 400 to 575 nm in the presence of Na_2S as scavenger. Apparently, the exhaustive charge transfer chain might be the rate-limiting step for high QE. Further utilisation of dihydrolipoic acid (DHLA) to couple CdSe nanocrystals with a soluble Ni^{2+}–DHLA promoter has achieved great enhancement for proton reduction (>600,000 turnovers, ascorbic acid as electron donor) [63]. Such system yields a QE of 36 % (520 nm irradiation) with more than 360 h of lifetime.

Nevertheless, molecular photocatalysts may also serve multiple roles in photocatalytic reactions. Figure 4.15a shows the molecular structure of phosphonated Re complexes (ReP), which act as excellent sensitisers and promoters in visible light-induced CO_2 reduction when coupled with TiO_2. In this case, ReP molecules absorb photons, undergo excitation, and consume the electron donor (TEOA) to form ReP^-, which further interacts with CO_2 to form CO (Fig. 4.15c). Transient absorption spectrometry reveals that the lifetime of ReP^- can be prolonged more than one order when ReP is anchored on a TiO_2 support (Fig. 4.15b), which may be due to the formation of Re dimers as intermediates in the deactivation pathway of CO_2 reduction.

It is also worth noting that sacrificial electron donors (i.e. HA and TEOA) are used in the anchored photocatalyst systems in most cases. This provides a simple approach to evaluate the reactivity of photocatalysts; however, H_2 production and CO_2 reduction without such sacrificial electron donors are more important for industrial applications, which will be the key point in future investigations.

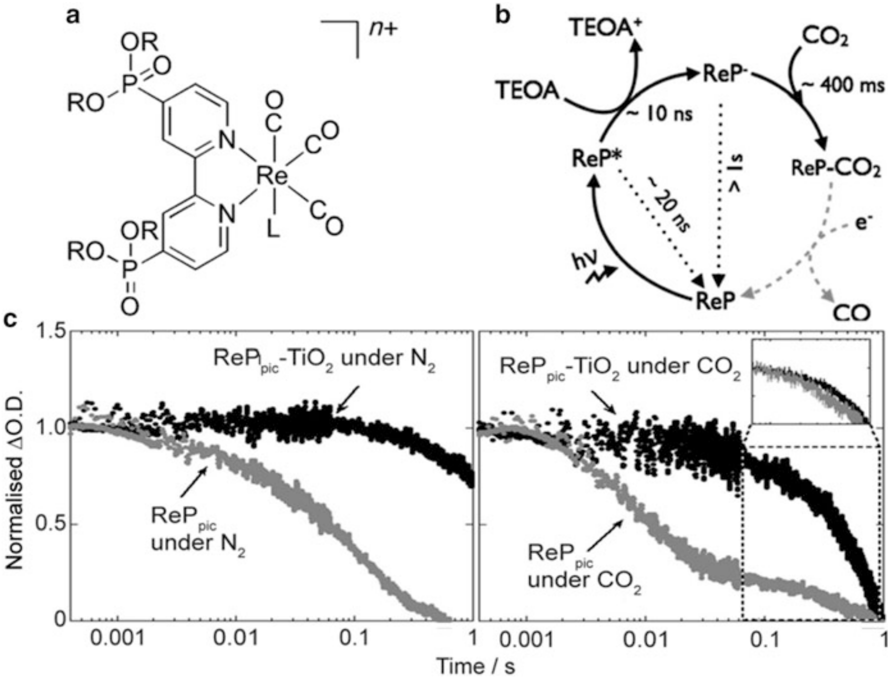

Fig. 4.15 (**a**) Molecular structure of the anchored ReP catalysts; (**b**) transient absorption at 500 nm of the reduced intermediate ReP^- after 415 nm excitation in the presence of an electron donor (TEOA, 1 M) under N_2 (*left*) and under CO_2 (*right*). (**c**) Proposed CO_2 reduction mechanisms based on transient spectrometry (Reprinted with permission from Ref. [64] Copyright 2015, John Wiley and Sons)

4.7 Promoters

As mentioned in the beginning of this chapter, a photocatalyst serves dual roles in a photocatalytic reaction, absorbing the light and using the light for catalytic reaction. However, pristine photocatalysts have generally very poor performance. Whilst the excitation of e^-–h^+ pairs via irradiation normally takes place within the femtosecond scale, the rest of the elementary steps are much slower. In the absence of an electron acceptor (A) and donor (D), surface charge trapping of e^-–h^+ pairs and recombination of e^-–h^+ pairs take place within 10–100 ns, indicating the competition between the two steps. Interfacial charge transfers that involve surface-adsorbed electron acceptors (A_{ad}) and donors (D_{ad}) generally occur within microsecond to millisecond, which are much slower compared to that of both charge trapping and recombination processes. This explains the intrinsic low QE of photocatalysis, and engineering the surface properties of the material to slow down the recombination kinetics or speed up the interfacial charge transfer are two possible approaches to improve the QE.

One effective solution that we can imagine is to transport and separate one species of the charge carriers in space. The prerequisites of this approach include (a) a physical contact of a semiconductor to another substance; (b) a driving force that transports the charge carriers from the semiconductor to the substance; and (c) only one type of charge carriers can be transferred and trapped into the other substance. Besides, it is also necessary that the trapped charge carriers in the substance can be utilised to perform reactions.

4.7.1 Noble Metal Nanoparticles (NPs)

Nanosized noble metals (i.e. Au, Pt, and Pd) are often employed for the task. Once the CBM of a semiconductor has a more negative potential than the unfilled band of the metal, the migration of e^- from semiconductor surface states to metal surface states will take place when they are in direct contact. The e^- that are trapped in the surface states of the metal NPs can be released when proper A (e.g. O_2 and Cl_2) is in presence. Meanwhile, the photogenerated holes remain at the semiconductor surface sites and are capable of performing the oxidation reactions. The advantages of metal NP-decorated photocatalysts have been further confirmed using transient spectrometry techniques by several groups. A rapid interfacial charge transfer from semiconductor photocatalyst to metal NPs was observed within the timescale of nanoseconds, which is comparable or even faster than that of the recombination kinetics. Besides these fundamental investigations, the metal NPs have also been supported on nearly all types of photocatalyst via various methods for more applied studies. Often a promotion effect can be observed when photocatalysts are coupled with metal NPs. However, there are also reports that show the presence of metal NPs decelerates the photocatalysis reactions. Recent studies by Mogyorosi and other coworkers suggest the photocatalytic efficiency of noble metal-modified photocatalysts is largely dependent on the reactant [65]. They found that the decomposition rates of oxalic and formic acid are enhanced whilst phenol decomposition rate is decreased.

Figure 4.16a illustrates the charge separation model from a thermodynamic perspective. As soon as the photoexcited electrons are trapped at the unoccupied d orbital states, the apparent Fermi level of the system will shift from E_F to E_F' due to accumulation of electrons. This is the most recognised model to explain the role of promoters. It is therefore not difficult to predict that the metal NPs, which can trap the most electrons in quantity, win the competition based on this assumption. Unfortunately, experimental results disagree with this prediction, as Au NPs can trap more electrons than Pt but show relative poor performance compared to that of Pt in photoinduced reduction reactions. Apparently, a more precise model that takes the kinetics of the trapped electrons into consideration is needed, as shown in Fig. 4.16b. In this model the kinetics of trapped electrons for redox reaction (k_{red}) and reverse trapping to the trap state of semiconductor (k_{rev}) were taken into account. These two rate constants can be extracted by in situ UV–vis spectrometry

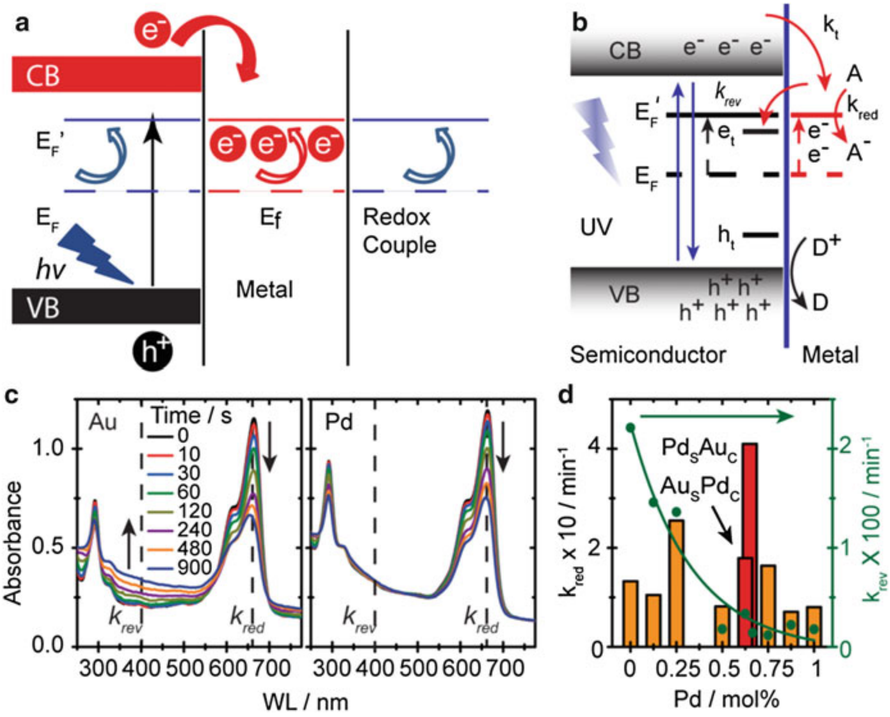

Fig. 4.16 (**a**) Charge separation model proposed (Reprinted with permission from Ref. [66] Copyright 2004, American Chemical Society). (**b**) Charge separation model with consideration of kinetics of trapped electrons. (**c**) In situ UV–vis spectra for the determination of k_{rev} and k_{red} of Au and Pd supported on TiO$_2$. (**d**) The derived k_{rev} and k_{red} of Au–Pd alloys and core-shell-structured Au–Pd NPs as promoters (Reprinted with permission from Ref. [67] Copyright 2014, American Chemical Society)

using methylene blue (MB) as probing molecule under deaerated conditions, where one MB react with two electrons to get bleached ($E^0_{MB/MB^{2-}} = 0.01$ V vs. SHE), as shown in Fig. 4.16c.

Recent investigations have also discovered that the metal NPs not only serve as an electron sink but are also involved in photocatalytic reactions. It has been found that in photocatalytic decomposition of phenol, the presence of metal on TiO$_2$ can mediate the formation of undesired phenolic intermediates (hydroquinone and benzoquinone) that consume the photogenerated radicals inefficiently [68]. Li et al. found out that tuning the chemical composition of Pt NPs to PtO NPs can accelerate the reduction of proton to molecular hydrogen whilst suppressing the reoxidation of the as-generated H$_2$ by O$_2$ (Fig. 4.17a). The reoxidation of H$_2$ under dark conditions is negligible when using PtO NPs as promoter, as indicated by dashed circles in Fig 4.17b. DFT calculation reveals that the adsorption and dissociation of both O$_2$ and H$_2$ on Pt NPs are much easier than that of PtO NPs, as shown in Fig. 4.17c.

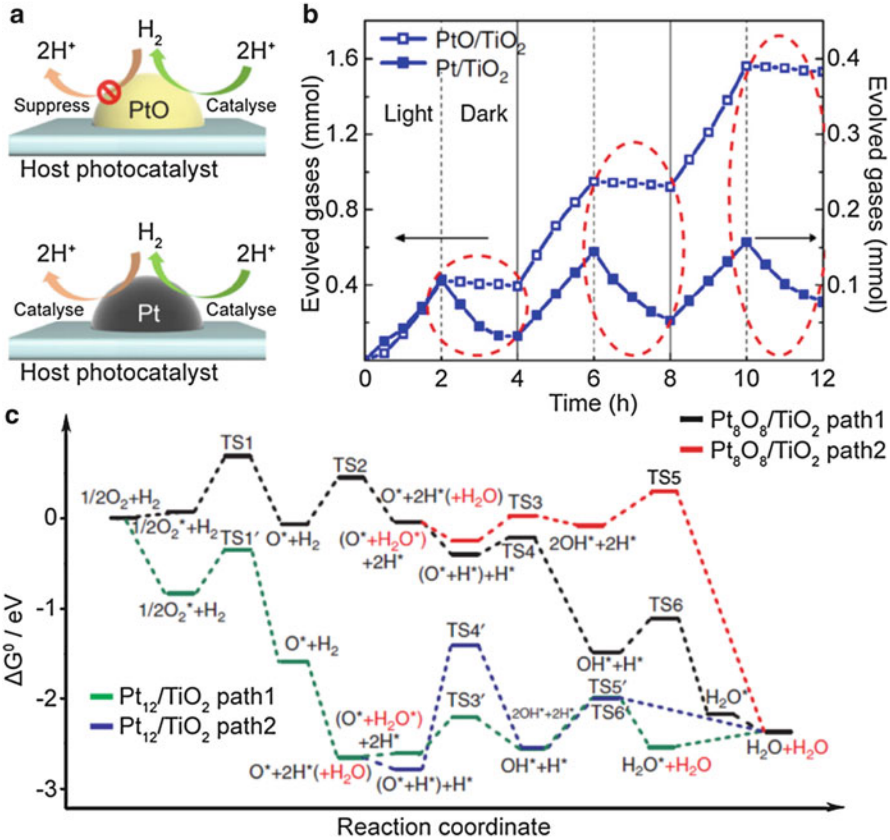

Fig. 4.17 (**a**) Photocatalytic hydrogen production using PtO or Pt as promoter; (**b**) proposed reaction mechanism of PtO and Pt as promoter; (**c**) standard Gibbs free energy profile of H_2 reacting with O_2 on Pt_8O_8/TiO_2 and Pt_{12}/TiO_2 surfaces in gas phase (Reprinted with permission from Ref. [69] Copyright 2013, Nature Publishing Group)

It is also worth noting that some of the noble metal NPs (i.e. Au, Ag, and Cu) show characteristic absorption in visible light regions, which can be used for photocatalysis. This phenomenon originates from the surface plasmon oscillations of free electrons, which result from the generation of a dipole in the metal NPs due to electromagnetic radiations. Since the incident light couples with electrons, polarised light can be used to control the distribution of the delocalised electrons and alter the Mulliken term symbol for the irreducible representation. Nevertheless, these NPs can also be used to manipulate light absorption on nanoscale by tuning the geometry, size, and spacing of the NPs.

In photocatalysis, these plasmonic NPs are normally coupled with semiconductor for various photocatalytic reactions (i.e. H_2 production, selective oxidation, and Suzuki coupling reactions) under visible light irradiation. Note in these cases that the metal NPs play the role of "absorber" and partially as "reactor," whereas the

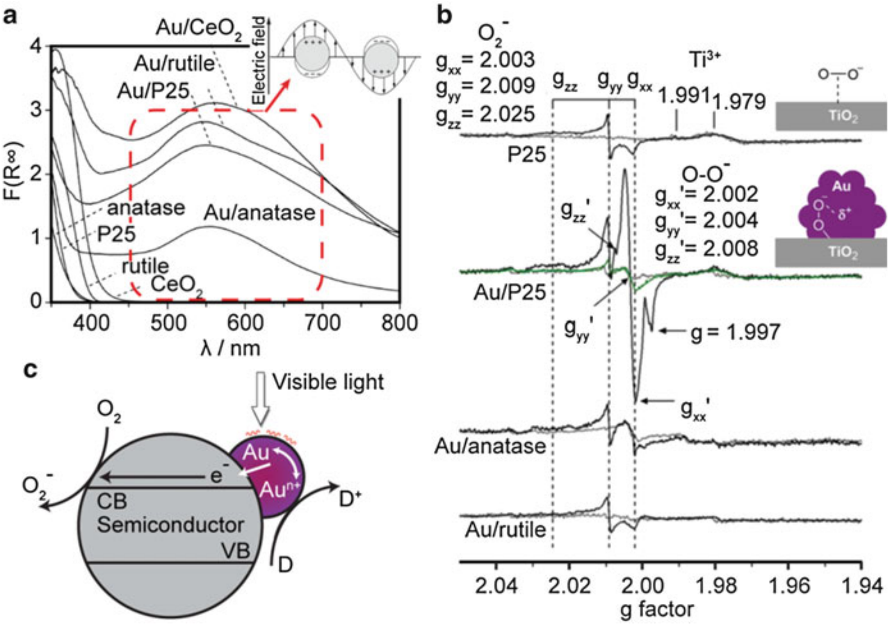

Fig. 4.18 (**a**) Visible light absorption of Au NPs supported on different photocatalysts originating from surface plasmon oscillations of Au; (**b**) EPR spectra of Au NPs supported on TiO_2 with different polymorph compositions; (**c**) the proposed charge transfer based on EPR analysis (Reprinted with permission from Ref. [70] Copyright 2012, American Chemical Society)

semiconductor separates the charge carriers (electrons) and partially works as a "reactor." Figure 4.18 demonstrates the mechanisms using Au/TiO_2 systems. The surface plasmonic band of Au results in visible light absorption in the range of 450–700 nm (Fig. 4.18a); however, such absorption does not guarantee the interfacial charge transfer to the TiO_2 support and further to the surface-adsorbed O_2, as shown in Fig. 4.18b. It works only when Aeroxide® TiO_2 P25 (Degussa P25), a mixture of anatase and rutile, is used, where a significant amount of O_2^- has been created under visible light irradiation. Thus, the charge transfer mechanisms in such systems are not as simple as the one presented in Fig. 4.18c. Nevertheless, one should also bear in mind that the efficiency in light adsorption of the plasmonic NPs needs to be considered from an application perspective, as the metal loadings are normally very low (<5 wt%).

4.7.2 Oxides and Nonmetal NPs

Noble metal NPs are excellent promoters, but their high cost might limit large-scale applications. Therefore, oxides and nonmetal promoters have been developed, mainly for the purpose of water splitting and CO_2 reduction.

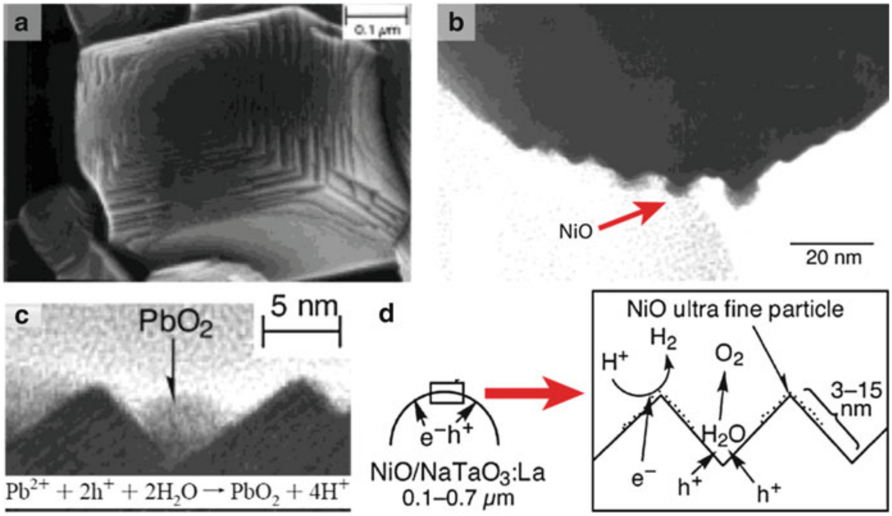

Fig. 4.19 (**a**) SEM image of a 2 wt% La-doped $NaTaO_3$; (**b**) TEM image of 0.5 wt% NiO deposited on La-doped $NaTaO_3$; (**c**) TEM image of photodeposited PdO_2 on La-doped $NaTaO_3$; (**d**) proposed photocatalytic water-splitting mechanisms of NiO/$NaTaO_3$:La (Reprinted with permission from Ref. [4] Copyright 2003, American Chemical Society)

In the case of photocatalytic water-splitting process, both hydrogen and oxygen should evolve on the surface of the photocatalyst. This requires different sites on the material to serve as photo-anode and photo-cathode. For hydrogen evolution, NiO are considered as a promising promoter for proton reduction. Kato et al. reported the photocatalytic water splitting over alkali (Li, Na, K) tantalate [4]. It was observed that naked alkali tantalate shows very low QE for hydrogen evolution (<1 %) upon irradiation ($\lambda < 270$ nm). Interestingly, a huge enhancement (AQE = 20 % at 270 nm irradiation) is noticed when NiO NPs are supported on the surface of tantalate. Further investigations into NiO-modified La-doped $NaTaO_3$ photocatalyst shows an impressive AQE of 56 % at 270 nm (Fig. 4.19a and b). Based on the photodeposition of Pb^{2+}, it is found that the oxidation sites are located at the grooves of the step, as shown in Fig. 4.19c. Therefore, it is supposed that whilst the reduction of proton takes place at the edges where ultrafine NiO NPs are located, the oxidation of water is located at the grooves of the step, respectively, as illustrated in Fig. 4.19d.

Meanwhile, RuO_x, Ir_2O_x, and CoO_x have been extensively applied as promoters for oxidation half reactions. Figure 4.20a shows the effect of promoter identities on photocatalytic O_2 evolution on $Zn_{2-x}GeO_{4-x-3y}N_{2y}$ (ZGON) semiconductor. Whilst the presence of ZnO in the system presents a higher O_2 evolution activity due to the formation of solid solution-phase junction, the addition of IrO_x can further enhance the activity. The O_2 evolution can also be enhanced by the deposition of IrO_x, CoO_x, and RuO_x promoters on ZGON without ZnO, and CoO_x exhibits the highest performance. Deposition of these promoters is also effective for enhancing the H_2

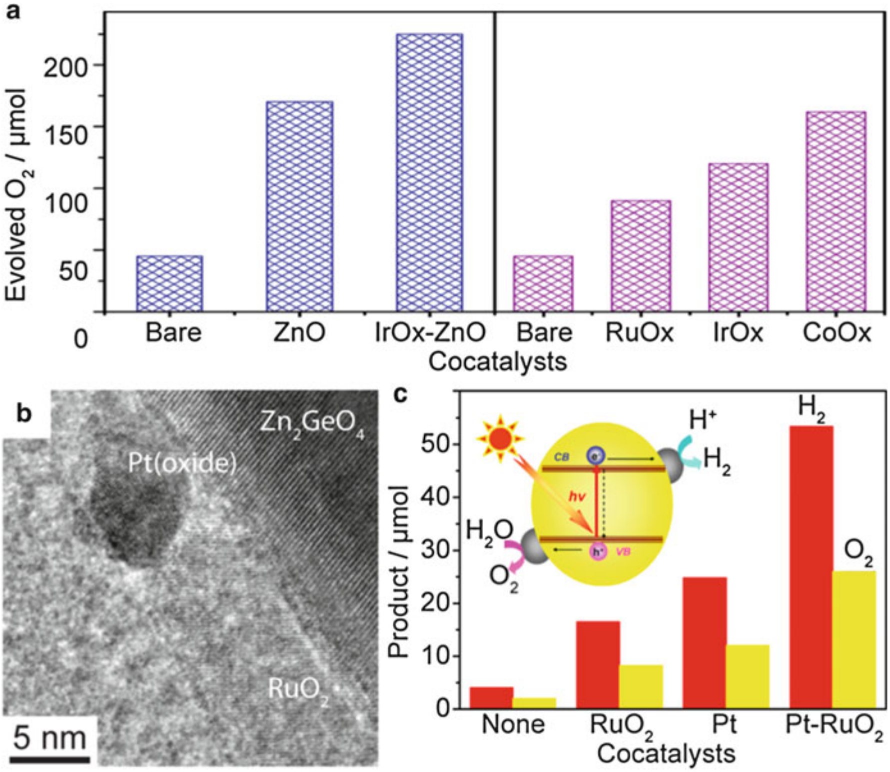

Fig. 4.20 (**a**) Photocatalytic activities of O_2 evolution on $Zn_{2-x}GeO_{4-x-3y}N_{2y}$ loaded with various cocatalysts (Reprinted with permission from Ref. [71] Copyright 2013, American Chemical Society). (**b**) HRTEM image of Pt and RuO_2 on Zn_2GeO_4 photocatalyst and (**c**) photocatalytic water splitting using RuO_2, Pt, and Pt–RuO_2 promoters (Reprinted with permission from Ref. [71,72] Copyright 2010 and 2013, Springer Publishing Company and American Chemical Society)

evolution reaction. Very recently, the development of inexpensive promoters, such as boron oxynitride ($B_2O_{3-x}N_x$) and cobalt phosphate (CoPi) nanoclusters, has been found to be also effective [71].

In order to realise overall water splitting, both reduction and oxidation promoters are simultaneously required. Figure 4.20b illustrates PtO_x and RuO_2 NPs co-deposited on a Zn_2GeO_4 photocatalyst as hydrogen evolution reaction and oxygen evolution reaction promoters, respectively. Only a significant enhancement of water splitting can be achieved when both promoters are present, as shown in Fig. 4.20c.

Carbon-related promoters, including C nanotubes (CNT), graphite, and graphene (GR), have been also considered as promising candidates due to their abundance and their unique microstructure and electronic structure. It has been found that in gas-phase benzene oxidation, the addition of 0.5 % GR not only improves the photocatalytic performance but also enhances the long-term stability

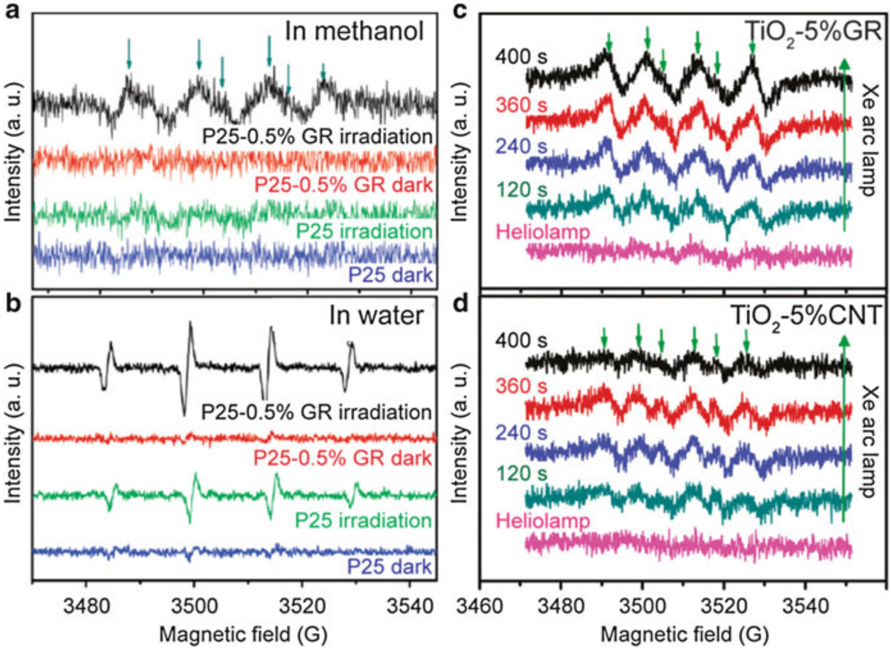

Fig. 4.21 EPR spectra of radicals trapped by DMPO in P25 and P25 + 0.5 % GR dispersions. (**a**) DMPO-$O_2^{-\bullet}$ formed in irradiated methanol dispersions; (**b**) DMPO-$^{\bullet}$OH formed in irradiated aqueous dispersions (Reprinted with permission from Ref. [73] Copyright 2010, American Chemical Society). (**c**) and (**d**), EPR spectra of superoxide radical species trapped by DMPO in TiO_2-5 % GR and TiO_2-5 % CNT dispersions in BTF solvent under visible light irradiation (Reprinted with permission from Ref. [5] Copyright 2011, American Chemical Society)

of pristine TiO_2. Further EPR analysis reveals that the presence of GR can effectively separate the photogenerated charge carriers, utilising them to generate extra $O_2^{-\bullet}$ and $^{\bullet}$OH radicals compared to that of pristine TiO_2, as shown in Fig. 4.21a and b. Carbon-based promoters have also been employed in selective alcohol oxidation reactions for the synthesis of corresponding aldehydes. The EPR analysis suggests that identical radical species ($O_2^{-\bullet}$.) have been generated under irradiation regardless of the structural difference of C promoters (GR and CNT), indicating CR and CNT play the same role in the reaction, as shown in Fig. 4.21c and d. However, the intensity of radicals depends on the structure of C promoters, where more radicals can be generated when using GR as promoter. This phenomenon suggests that a sufficient and intimate interfacial contact between GR and the photocatalyst support is the key in improving the selective organic transformation.

Recently, it has also been found that carbon nanodots exhibit unique catalytic properties when coupled with carbon nitride for pure water splitting [6]. It has been found that the presence of C nanodots facilitates the formation and decomposition of H_2O_2 ($2e^-$ process) whilst inhibiting direct water splitting ($4e^-$ process), thus resulting in a magnificent QE of 16 % under 420 nm irradiation condition and 2 %

overall solar energy conversion efficiency. This reaction mechanism is confirmed by rotating ring-disc electrode (RRDE) analysis, which proves that a two-electron transfer process takes place under different irradiation conditions. Besides, photocurrent measurements demonstrate that whilst the C_3N_4 shows a rapid decrease of photocurrent, the C nanodots supported on C_3N_4 only shows current oscillations between 190 and 240 nA, indicating that the presence of C nanodots accelerates the generation and decomposition of H_2O_2 that may adsorb and poison pristine C_3N_4.

It is apparent that the synthesis of promoters and the decoration of photocatalysts are of great importance to gear up the photocatalytic performance; thus, mechanistic understanding is the key for rational design of highly efficient promoters. There are some promising progresses in this topic based on model catalyst systems. However, these results only help the design to some extent due to the complexity of real photocatalytic systems. This calls for investigations by various in situ and *in operando* techniques on well-defined real photocatalyst systems to explore (i) electronic and geometric structural effect of promoters on photocatalyst; (ii) thermodynamics, kinetics, and identities of charge carriers; and (iii) stability of promoter-modified photocatalysts. With in-depth understandings of the above-mentioned points, hopefully new ideas and modelling will be derived to guide the design of novel promoters.

4.8 Concluding Remarks and Perspectives

In this chapter we reviewed the most promising photocatalyst materials as alternative to TiO_2 based on their design, synthesis, characterisation, and applications. The search for new photocatalyst materials has mainly focused on (i) reduction of the optical bandgaps and (ii) improving reaction efficiency and selectivity. Whilst doping, strain force, and employing organic sensitizer can be used to adjust the bandgap of photocatalysts, surface and/or interface modification is a common strategy for enhancing the efficiency and selectivity of photocatalytic reactions. Nevertheless, zeolites, MOFs, and anchored systems with unique structural and electronic properties may extend the application of photocatalysis to other catalytic reactions.

Whilst the holy grail of photocatalysis is centred on the design of novel materials that can absorb visible light and perform reactions efficiently, such a task relies on a thorough understanding of the whole photocatalytic process from light absorption, to charge carrier generation and separation, to radical formation, to charge recombination, to chemical reactions on the surface. Part of these elementary steps has been modelled and investigated under simplified conditions, bringing new ideas to the design of new photocatalyst materials (i.e. Black TiO_2, C_3N_4). However, a rational modelling of the full image of photocatalysis under real conditions is still missing, limiting the development of next-generation photocatalyst. Due to the complexity of photocatalytic processes, there is no doubt that the combination of modelling, calculations, time-resolved spectrometry analysis, radical chemistry, and surface science approaches, ideally in situ and *in operando*, is needed to understand photocatalysis from both thermodynamic and kinetic aspects. Thankfully such research strategies are being recognised by more and more researchers; thus, a promising future of photocatalysis should be expected.

References

1. Web of Knowledge (2015) http://apps.webofknowledge.com
2. Hoffmann MR, Martin ST, Choi WY, Bahnemann DW (1995) Environmental applications of semiconductor photocatalysis. Chem Rev 95:69–96
3. Kudo A, Miseki Y (2009) Heterogeneous photocatalyst materials for water splitting. Chem Soc Rev 38:253–278
4. Kato H, Asakura K, Kudo A (2003) Highly efficient water splitting into H_2 and O_2 over lanthanum-doped $NaTaO_3$ photocatalysts with high crystallinity and surface nanostructure. J Am Chem Soc 125:3082–3089
5. Zhang Y, Tang Z-R, Fu X, Xu Y-J (2011) Engineering the unique 2D Mat of graphene to achieve graphene-TiO_2 nanocomposite for photocatalytic selective transformation: what advantage does graphene have over its forebear carbon nanotube? ACS Nano 5:7426–7435
6. Liu J, Liu Y, Liu N et al (2015) Metal-free efficient photocatalyst for stable visible water splitting via a two-electron pathway. Science 347:970–974
7. Bak T, Nowotny J, Rekas M, Sorrell CC (2002) Photo-electrochemical hydrogen generation from water using solar energy. Materials-related aspects. Int J Hydrog Energy 27:991–1022
8. Ameen S, Akhtar MS, Seo H-K, Shin HS (2014) Metal oxide semiconductors and their nanocomposites application towards photovoltaic and photocatalytic. In: Tiwari A, Valyukh S (eds) Advanced energy materials. Wiley, Hoboken. doi:10.1002/9781118904923.ch3
9. Wolf MJ, McKenna KP, Shluger AL (2012) Hole trapping at surfaces of m-ZrO_2 and m-HfO_2 nanocrystals. J Phys Chem C 116:25888–25897
10. Takenaka S, Tanaka T, Funabiki T, Yoshida S (1998) Effect of alkali-metal ion addition to silica-supported molybdenum oxide on photocatalysis photooxidation of propane and propene, and photo-assisted metathesis of propene. J Chem Soc Faraday Trans 94:695–700
11. Subbotina IR, Shelimov BN, Kazansky VB, Lisachenko AA, Che M, Coluccia S (1999) Selective photocatalytic reduction of nitric oxide by carbon monoxide over silica-supported molybdenum oxide catalysts. J Catal 184:390–395
12. Wang Y, Zhang Z, Zhu Y et al (2008) Nanostructured VO_2 photocatalysts for hydrogen production. ACS Nano 2:1492–1496
13. Liu N, Schneider C, Freitag D et al (2014) Black TiO_2 nanotubes: cocatalyst-free open-circuit hydrogen generation. Nano Lett 14:3309–3313
14. Yang Y, Sun C, Wang L et al (2014) Constructing a metallic/semiconducting TaB_2/Ta_2O_5 core/shell heterostructure for photocatalytic hydrogen evolution. Adv Energy Mater 4:14057–14064
15. Zhou C, Zhao Y, Shang L et al (2014) Facile preparation of black Nb^{4+} self-doped $K_4Nb_6O_{17}$ microspheres with high solar absorption and enhanced photocatalytic activity. Chem Commun 50:9554–9556
16. Chen XB, Liu L, Yu PY, Mao SS (2011) Increasing solar absorption for photocatalysis with black hydrogenated titanium dioxide nanocrystals. Science 331:746–750
17. Hou Y, Wang X, Wu L, Ding Z, Fu X (2006) Efficient decomposition of benzene over a β-Ga_2O_3 photocatalyst under ambient conditions. Environ Sci Technol 40:5799–5803
18. He H, Orlando R, Blanco MA et al (2006) First-principles study of the structural, electronic, and optical properties of Ga_2O_3 in its monoclinic and hexagonal phases. Phys Rev B 74:195123

19. Wang X, Xu Q, Li M et al (2012) Photocatalytic overall water splitting promoted by an α–β phase junction on Ga_2O_3. Angew Chem Int Ed 51:13089–13092
20. Zhao K, Zhang L, Wang J, Li Q, He W, Yin JJ (2013) Surface structure-dependent molecular oxygen activation of BiOCl single-crystalline nanosheets. J Am Chem Soc 135:15750–15753
21. Ye J, Zou Z, Arakawa H et al (2002) Correlation of crystal and electronic structures with photophysical properties of water splitting photocatalysts $InMO_4$ ($M = V^{5+}$, Nb^{5+}, Ta^{5+}). J Photochem Photobiol A 148:79–83
22. Ye L, Su Y, Jin X, Xie H, Zhang C (2014) Recent advances in BiOX (X = Cl, Br and I) photocatalysts: synthesis, modification, facet effects and mechanisms. Environ Sci Nano 1:90–112
23. Lee C-Y, Wang L, Kado Y, Killian MS, Schmuki P (2014) Anodic nanotubular/porous hematite photoanode for solar water splitting: substantial effect of iron substrate purity. ChemSusChem 7:934–940
24. An X, Li K, Tang J (2014) Cu_2O/reduced graphene oxide composites for the photocatalytic conversion of CO_2. ChemSusChem 7:1086–1093
25. Sastre F, Puga AV, Liu L, Corma A, García H (2014) Complete photocatalytic reduction of CO_2 to methane by H_2 under solar light irradiation. J Am Chem Soc 136:6798–6801
26. Sastre F, Corma A, García H (2013) Visible-light photocatalytic conversion of carbon monoxide to methane by nickel(II) oxide. Angew Chem Int Ed 52:12983–12987
27. Kato H, Kudo A (2001) Water splitting into H_2 and O_2 on alkali tantalate photocatalysts $ATaO_3$ (a = Li, Na, and K). J Phys Chem B 105:4285–4292
28. Kanhere P, Shenai P, Chakraborty S, Ahuja R, Zheng J, Chen Z (2014) Mono- and Co-doped $NaTaO_3$ for visible light photocatalysis. Phys Chem Chem Phys 16:16085–16094
29. Bao N, Shen L, Takata T, Domen K (2007) Self-templated synthesis of nanoporous CdS nanostructures for highly efficient photocatalytic hydrogen production under visible light. Chem Mater 20:110–117
30. Shen S, Zhao L, Guo L (2010) $Zn_mIn_2S_{3+m}$ (m = 1–5, integer): a new series of visible-light-driven photocatalysts for splitting water to hydrogen. Int J Hydrog Energy 35:10148–10154
31. Liu G, Zhao L, Ma L, Guo L (2008) Photocatalytic H_2 evolution under visible light irradiation on a novel $Cd_xCu_yZn_{1-x-y}S$ catalyst. Catal Commun 9:126–130
32. Yan H, Yang J, Ma G et al (2009) Visible-light-driven hydrogen production with extremely high quantum efficiency on Pt–PdS/CdS photocatalyst. J Catal 266:165–168
33. Daskalaki VM, Antoniadou M, Puma GL, Kondarides DI, Lianos P (2010) Solar light-responsive Pt/CdS/TiO_2 photocatalysts for hydrogen production and simultaneous degradation of inorganic or organic sacrificial agents in wastewater. Environ Sci Technol 44:7200–7205
34. Burton LA, Colombara D, Abellon RD et al (2013) Synthesis, characterization, and electronic structure of single-crystal SnS, Sn_2S_3, and SnS_2. Chem Mater 25:4908–4916
35. Zhang YC, Li J, Zhang M, Dionysiou DD (2011) Size-tunable hydrothermal synthesis of SnS_2 nanocrystals with high performance in visible light-driven photocatalytic reduction of aqueous Cr(VI). Environ Sci Technol 45:9324–9331
36. Sun Y, Cheng H, Gao S et al (2012) Freestanding tin disulfide single-layers realizing efficient visible-light water splitting. Angew Chem Int Ed 51:8727–8731
37. Zhuang HL, Hennig RG (2013) Single-layer group-III monochalcogenide photocatalysts for water splitting. Chem Mater 25:3232–3238
38. Hu P, Wang L, Yoon M et al (2013) Highly responsive ultrathin GaS nanosheet photodetectors on rigid and flexible substrates. Nano Lett 13:1649–1654
39. Sato J, Saito N, Yamada Y et al (2005) RuO_2-loaded β-Ge_3N_4 as a non-oxide photocatalyst for overall water splitting. J Am Chem Soc 127:4150–4151
40. McDermott EJ, Kurmaev EZ, Boyko TD et al (2012) Structural and band Gap investigation of GaN:ZnO heterojunction solid solution photocatalyst probed by soft X-ray spectroscopy. J Phys Chem C 116:7694–7700
41. Maeda K, Takata T, Hara M et al (2005) GaN:ZnO solid solution as a photocatalyst for visible-light-driven overall water splitting. J Am Chem Soc 127:8286–8287

42. Yamasita D, Takata T, Hara M, Kondo JN, Domen K (2004) Recent progress of visible-light-driven heterogeneous photocatalysts for overall water splitting. Solid State Ionics 172:591–595
43. Chun W-J, Ishikawa A, Fujisawa H et al (2003) Conduction and valence band positions of Ta_2O_5, TaON, and Ta_3N_5 by UPS and electrochemical methods. J Phys Chem B 107:1798–1803
44. Li S, Zhang L, Wang H et al (2014) Ta_3N_5-Pt nonwoven cloth with hierarchical nanopores as efficient and easily recyclable macroscale photocatalysts. Sci Rep 4:3978
45. Cao J, Ren L, Li N, Hu C, Cao M (2013) Mesoporous Ta_3N_5 microspheres prepared from a high-surface-area, microporous, amorphous precursor and their visible-light-driven photocatalytic activity. Chem Eur J 19:12619–12623
46. Wang L, Dionigi F, Nguyen NT et al (2015) Tantalum nitride nanorod arrays: introducing Ni–Fe layered double hydroxides as a cocatalyst strongly stabilizing photoanodes in water splitting. Chem Mater 27:2360–2366
47. Wang X, Maeda K, Thomas A et al (2009) A metal-free polymeric photocatalyst for hydrogen production from water under visible light. Nat Mater 8:76–80
48. Chen X, Zhang J, Fu X, Antonietti M, Wang X (2009) Fe-g-C_3N_4-catalyzed oxidation of benzene to phenol using hydrogen peroxide and visible light. J Am Chem Soc 131:11658–11659
49. Martin DJ, Qiu K, Shevlin SA et al (2014) Highly efficient photocatalytic H_2 evolution from water using visible light and structure-controlled graphitic carbon nitride. Angew Chem Int Ed 53:9240–9245
50. Anpo M, Shioya Y, Yamashita H et al (1994) Preparation and characterization of the $Cu+$/ZSM-5 catalyst and its reaction with NO under UV irradiation at 275 K. In situ photoluminescence, EPR, and FT-IR investigations. J Phys Chem 98:5744–5750
51. Del Pilar-Albaladejo J, Dutta PK (2014) Topotactic transformation of zeolite supported cobalt (II) hydroxide to oxide and comparison of photocatalytic oxygen evolution. ACS Catal 4:9–15
52. Ren Z, Kim E, Pattinson SW et al (2012) Hybridizing photoactive zeolites with graphene: a powerful strategy towards superior photocatalytic properties. Chem Sci 3:209–216
53. Li Q, Jin Z, Peng Z, Li Y, Li S, Lu G (2007) High-efficient photocatalytic hydrogen evolution on eosin Y-sensitized $Ti - MCM41$ zeolite under visible-light irradiation. J Phys Chem C 111:8237–8241
54. Corma A, Garcia H (2004) Zeolite-based photocatalysts. Chem Commun 13:1443–1459
55. Wang J-L, Wang C, Lin W (2012) Metal–organic frameworks for light harvesting and photocatalysis. ACS Catal 2:2630–2640
56. Alvaro M, Carbonell E, Ferrer B, Llabrés i Xamena FX, Garcia H (2007) Semiconductor behavior of a metal-organic f(MOF). Chem Eur J 13:5106–5112
57. Nasalevich MA, Goesten MG, Savenije TJ, Kapteijn F, Gascon J (2013) Enhancing optical absorption of metal-organic frameworks for improved visible light photocatalysis. Chem Commun 49:10575–10577
58. Wu P, He C, Wang J et al (2012) Photoactive chiral metal–organic frameworks for light-driven asymmetric α-alkylation of aldehydes. J Am Chem Soc 134:14991–14999
59. Sun D, Fu Y, Liu W et al (2013) Studies on photocatalytic CO_2 reduction over NH_2-Uio-66 (Zr) and its derivatives: towards a better understanding of photocatalysis on metal–organic frameworks. Chem Eur J 19:14279–14285
60. Yuan Y-J, Yu Z-T, Liu X-J, Cai J-G, Guan Z-J, Zou Z-G (2014) Hydrogen photogeneration promoted by efficient electron transfer from iridium sensitizers to colloidal MoS_2 catalysts. Sci Rep 4:4045
61. Liang W-J, Wang F, Wen M et al (2015) Branched polyethylenimine improves hydrogen photoproduction from a CdSe quantum Dot/[FeFe]-hydrogenase mimic system in neutral aqueous solutions. Chem Eur J 21:3187–3192

62. Yu W, Noureldine D, Isimjan T et al (2015) Nano-design of quantum dot-based photocatalysts for hydrogen generation using advanced surface molecular chemistry. Phys Chem Chem Phys 17:1001–1009
63. Han ZJ, Qiu F, Eisenberg R, Holland PL, Krauss TD (2012) Photogeneration of H_2 in water using semiconductor nanocrystals and a nickel catalyst. Science 338:1321–1324
64. Windle CD, Pastor E, Reynal A et al (2015) Improving the photocatalytic reduction of CO_2 to CO through immobilisation of a molecular Re catalyst on TiO_2. Chem Eur J 21:3746–3754
65. Mogyorosi K, Kmetyko A, Czirbus N, Vereb G, Sipos P, Dombi A (2009) Comparison of the substrate dependent performance of Pt-, Au- and Ag-doped TiO_2 photocatalysts in H_2 production and in decomposition of various organics. React Kinet Catal Lett 98:215–225
66. Subramanian V, Wolf EE, Kamat PV (2004) Catalysis with TiO_2/gold nanocomposites. Effect of metal particle size on the fermi level equilibration. J Am Chem Soc 126:4943–4950
67. Su R, Tiruvalam R, Logsdail AJ et al (2014) Designer titania-supported Au-Pd nanoparticles for efficient photocatalytic hydrogen production. ACS Nano 8:3490–3497
68. Su R, Tiruvalam R, He Q et al (2012) Promotion of phenol photodecomposition over TiO_2 using Au, Pd, and Au–Pd nanoparticles. ACS Nano 6:6284–6292
69. Li YH, Xing J, Chen ZJ et al (2013) Unidirectional suppression of hydrogen oxidation on oxidized platinum clusters. Nat Commun 4:2500–2504
70. Tsukamoto D, Shiraishi Y, Sugano Y, Ichikawa S, Tanaka S, Hirai T (2012) Gold nanoparticles located at the interface of anatase/rutile TiO_2 particles as active plasmonic photocatalysts for aerobic oxidation. J Am Chem Soc 134:6309–6315
71. Yang J, Wang D, Han H, Li C (2013) Roles of cocatalysts in photocatalysis and photoelectrocatalysis. Acc Chem Res 46:1900–1909
72. Ma B, Wen F, Jiang H, Yang J, Ying P, Li C (2010) The synergistic effects of two Co-catalysts on Zn_2GeO_4 on photocatalytic water splitting. Catal Lett 134:78–86
73. Zhang Y, Tang Z-R, Fu X, Xu Y-J (2010) TiO_2 – graphene nanocomposites for Gas-phase photocatalytic degradation of volatile aromatic pollutant: is TiO_2 – graphene truly different from other TiO_2 – carbon composite materials? ACS Nano 4:7303–7314

Chapter 5
1D TiO_2 Nanotube-Based Photocatalysts

Fang-Xing Xiao and Bin Liu

Abstract In this chapter, the latest developments of one-dimensional semiconductors, typically TiO_2 nanotube arrays (TNTAs) in the photocatalysis, are reviewed including the modification strategies for preparing TNTA-based photocatalysts, diverse photocatalytic applications of TNTA-based hybrid nanostructures in a myriad of fields, and a perspective on future challenges regarding the design and improvement of TNTAs for photocatalysis.

Keywords One dimensional • TiO_2 nanotube arrays • Photocatalysis • Photoelectrochemical

5.1 Introduction

In recent years, sustainable developments of human being are retarded by increasingly serious environmental pollution and depletion of fossil fuel resources [1]. To surmount these obstacles, various technologies have been extensively developed to reduce the environmental and energy crisis by conventional techniques including adsorption, precipitation, and osmosis [2]. Although intense endeavors have been made to impede the deterioration of these two crises, it is still challenging to develop an efficient and green technique to control and reduce the pollution growth. Photocatalysis, as a novel route to achieve deep mineralization of organic pollutants toward carbon dioxide and water under light irradiation, has attracted enormous attention on account of its great efficiency and promising potential applications [3]. Among various semiconductors, TiO_2 has been determined as the most widely used photocatalyst for versatile photocatalytic applications such as hydrogen production, CO_2 reduction, selective organic transformation, and nonselective organic oxidation, owing to its environmental friendliness, stable chemical and physical properties, nontoxicity, and durability [4, 5].

Up to date, a large variety of TiO_2 nanostructures have been prepared for photocatalytic investigations which mainly include nanoparticles, nanowires,

---

F.-X. Xiao • B. Liu (✉)
School of Chemical and Biomedical Engineering, Nanyang Technological University,
62 Nanyang Drive, Singapore 637459, Singapore
e-mail: liubin@ntu.edu.sg

J.C. Colmenares, Y.-J. Xu (eds.), *Heterogeneous Photocatalysis*, Green Chemistry
and Sustainable Technology, DOI 10.1007/978-3-662-48719-8_5

nanorods, nanosheets, and nanotubes [6]. Among which, TiO_2 nanotube arrays (TNTAs) growing vertically from Ti foil afforded by electrochemical anodization can serve as an ideal platform for exploring new photocatalysts [7]. The structural advantages of TNTAs predominantly center on the following several aspects. Firstly, one-dimensional geometry of TNTAs with smooth surface is beneficial for efficient charge transfer, thus providing significantly shorter carrier-diffusion paths along the tube walls and minimizing the charge losses arising from electron hopping between nanoparticles in comparison with corresponding bulk TiO_2 nanoparticles [8]. Secondly, owing to direct growth property of TNTAs on Ti substrate, it is convenient to separate the TNTA-based photocatalysts from reaction systems for recycling reactions, thus reducing tedious recovery procedures for practical applications [9]. Despite the developments of TNTAs in the field of heterogeneous photocatalysis during the past few years, two intrinsic drawbacks still remarkably retard their potential applications. Specifically, wide bandgap of TNTAs (i.e., 3.2 eV) requires UV light irradiation to trigger the photocatalytic reactions, which accounts for only a small fraction of (ca. 5 %) solar spectrum in comparison with visible light (52 %) and infrared light (43 %). Additionally, fast recombination of photogenerated electron–hole charge carriers over TNTAs substantially reduces the efficiency of photocatalytic reactions. In this regard, it is highly desirable to shift the optical response of TNTAs toward visible or even infrared region in conjunction with high separation efficiency of photoexcited charge carriers for boosting the photocatalytic performances of TNTA-based photocatalysts. To this end, various strategies have therefore been developed to conquer the disadvantage of TNTAs including metal or nonmetal element doping [10, 11], noble metal deposition [12], sensitization with narrow-bandgap semiconductors [13], and formation of p–n heterojunction [14], just named a few, which will be specifically elucidated in the following parts.

In this chapter, we primarily focus on the state-of-the-art developments of TiO_2 nanotube with an emphasis on the TNTA-based nanocomposites, the content of which primarily contains basic introduction of TNTAs, preparation of varieties of TNTA-based heterostructures, and their diverse photocatalytic applications in a myriad of fields. Finally, a perspective on future challenges regarding the design and improvement of TNTAs for photocatalysis is afforded. It is hoped that this chapter could provide enriched information on the potential applications of TiO_2 nanotube-based nanocomposites as multifunctional photocatalysts.

5.2 Basic Introduction of TNTAs

The fabrication of TNTAs via anodic oxidation of titanium foil in a fluoride-based solution was firstly reported in 2001 by Grimes and co-workers [15]. Since then, precise control over the nanotube morphology, length, pore size, and wall thickness has been the focus of many studies [16, 17]. It has been well established that electrolyte composition plays an imperative role in determining the architecture

Scheme 5.1 Experimental setup for preparing the TNTAs

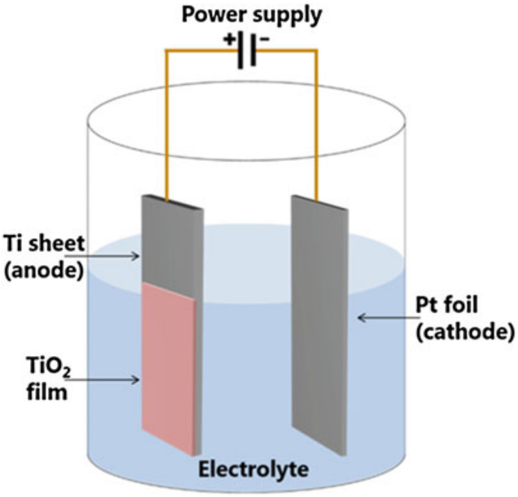

and chemical composition of nanotube arrays. In particular, the formation rate of TNTAs can be tuned by electrolyte composition and its pH value.

The key process responsible for anodic preparation of TNTAs mainly includes the following four processes: (1) oxide growth on the metal surface owing to the interaction of metal with O^{2-} or OH^- ions. The in situ formed anions during the formation of an initial oxide layer can migrate through the oxide layer approaching the metal/oxide interface where they react with the metal [18]. (2) Ti^{4+} migrated from the metal at the interface will be rapidly released under an exerted external electric field and move toward the oxide/electrolyte interface. (3) The third process is the field-assisted dissolution of the oxide at the oxide/electrolyte interface [19]. The Ti–O bond is weakened under applied electric field giving rise to dissolution of the Ti^{4+} which dissolves into the electrolyte and interacts with the free O^{2-} anions at the interface [20, 21]. (4) Chemical dissolution of titania in the HF electrolyte also takes place during the anodization process. Based on the above mechanism, highly ordered and self-aligned TNTAs were thus prepared. The experimental setup for preparing TNTAs was illustrated in Scheme 5.1.

5.3 TNTA-Based Photocatalysts

5.3.1 *TNTAs with Nonmetal Element Doping*

Vertically oriented TNTAs have been regarded as an ideal candidate for photocatalytic applications, such as water splitting to produce H_2 and photocatalytic degradation of organic dye pollutants, owing to their high catalyst/electrolyte interface area, electrolyte percolation, and remarkably enhanced separation of photogenerated electron–hole charged careers [22]. Nonetheless, the applications of TNTAs were retarded by the wide bandgap (E_g) energy (ca. 3.2 eV) of TiO_2 which can only be excited by UV light irradiation. Hence, it is essential to shift the photoresponse of TiO_2 from UV region to visible scope which may significantly promote the photocatalytic and photoelectrochemical properties of TiO_2-based nanomaterials [23]. To this end, modification of the electronic structure of TNTAs with nonmetal element doping to narrow its bandgap energy has provided a convenient way to solve the disadvantage of TiO_2, most of which centers on carbon [24], nitrogen [25, 26], phosphorus–fluorine [27], and nitrogen–fluorine–iodine doping [28], which result in remarkably enhanced visible-light-driven photocatalytic performances of the materials.

N-doped TNTA nanocomposites have been fabricated for photocatalytic explorations under visible light irradiation [29]. The N-modified TNTAs can be prepared by annealing TNTAs in a urea atmosphere or by anodization in nitrogen-containing electrolytes [30]. The N-implanted TNTAs have been well demonstrated to be the most efficient visible-light-driven photocatalyst among various nonmetal element-doped TNTAs since the nitrogen p states placed just above the valence band maximum of TiO_2 may contribute to the bandgap narrowing without substantial increase of the charge career recombination.

Sulfur doping can also facilitate similar bandgap narrowing; nevertheless, the ionic radius of sulfur was found to be too large to be introduced into TiO_2 lattice as proved by larger formation energy need for the substitution of sulfur than that need for the substitution of N. For example, Tang and Li fabricated S-doped TNTAs by annealing TNTAs in a H_2S atmosphere, and the result showed that sulfur-modified TNTAs demonstrate more pronounced response over the visible light scope leading to significantly enhanced photoelectrochemical signals [31]. Carbon-doped TNTAs were fabricated by oxidation of TNTAs in a burning flame [32] or in CO gas flow [33] or under an argon and acetylene gas mixture flow [34], which endows TNTAs with improved photocatalytic performances under visible light irradiation.

Boron doping was also found to reinforce the visible-light-driven photocatalytic activities, as reported by Lu and co-workers [35] who prepared B-doped TNTAs via chemical vapor deposition approach, in which trimethyl borate was used as boron source and N_2 as carrier gas. It was found that UV–vis spectra of B-doped TNTA nanostructures exhibited a relatively small absorption edge shift toward visible region (385–405 nm) when compared with the large shift observed in N-doping and C-doping TNTAs [36].

5.3.2 TNTAs with Metal Element Doping

Another efficient way to extend the photoresponse of TiO_2 to visible region is doping of TiO_2 with transitional metal ions or rare early metal ions [37, 38]. Extrinsic energy levels in the bandgap of TiO_2 can be formed by incorporation of metal ions into TiO_2 lattice, which may greatly influence the transfer of photogenerated electrons and holes. Generally, doped metal ions locate near TiO_2 surface to facilitate charge transferring in which the energy level of metal ion reduction should be less negative than the conduction band edge of TiO_2 and the energy level of metal oxidation should be less positive than the valence band edge of TiO_2. Noteworthily, there exists the optimum concentration for metal ion doping, above which the photoactivity decreases owing to recombination of charge carriers in the site of metal ion [39, 40]. With respect to the fabrication of metal ion-doped TNTAs, it is essential to develop applicable approach to efficiently introduce metal ions into TNTAs without changing the vertically oriented morphology of TNTAs. For instance, Zn-doped TNTAs were achieved by immersing TNTAs in Zn-containing solution followed by calcination, as carried out by Yang and co-workers [41]. Zr-doped TNTAs can be fabricated via an electrochemical strategy based on their similar atomic radii (Ti, 2 Å; Zr, 2.16 Å) and belonging to both IV B elements and tetravalentine (+4) elements. W-doped TNTAs were prepared by anodization of tungsten titanium foil, and the red shift of the absorbance edge and a reduction in bandgap (0.14 eV) result in enhanced photocurrent density in comparison with blank TNTAs [42]. Alternatively, Cr-doped TNTAs attained by ion implantation exhibited a significant enhancement in photocurrent response within both UV and visible regions [43].

Few works involving the preparation of Fe-doped TNTAs have been reported, except that Sun and co-workers [44] prepared Fe^{3+}-doped TNTAs by anodization of Ti foil in HF-aqueous electrolyte containing ferric nitrate. Similarly, Li and co-workers [45] prepared Fe-doped TNTAs by anodization of Ti foil in F^- containing aqueous electrolytes of ferrous sulfate. It was found that the Fe-doped TNTAs demonstrate enhanced photocurrent response as compared with blank TNTAs.

5.3.3 TNTA/Noble Metal Nanocomposites

It has been ascertained that modification of TNTAs with noble metal nanoparticles (NPs) renders TNTA/metal nanocomposites efficient photocatalysts leading to significantly enhanced photocatalytic and photoelectrochemical performances [46]. Up to now, TiO_2 has been deposited with various metal NPs such as Pt [47, 48], Au [49, 50], Pd [51], Ag [52, 53], and Co–Ag–Pt [54]. Deposition of metal NPs on the TNTA substrate is beneficial for retarding the recombination of photoexcited electron and hole charge carriers, in which metal NPs can serve as "electron reservoirs" for capturing the photogenerated electrons, thus giving rise to improved photocatalytic performances. For example, with respect to Ag-loaded TNTA nanocomposites, the conduction band (CB) of TiO_2 is lower than the Fermi level of metallic Ag which allows for the transport of photogenerated electrons from CB of TiO_2 to Ag forming a Schottky barrier between TNTAs and Ag NPs [55, 56]. The photogenerated electrons trapped by Ag NPs could be transferred to the adsorbed oxygen on the Ag surface resulting in O_2^- active species which favor the photocatalytic process. Simultaneously, holes collected in the valence band of TiO_2 could react with water to yield hydroxyl radicals which oxidize pollutants to CO_2 and water, thereby fulfilling the whole photocatalytic cycle.

On the other hand, with regard to the preparation of metal/TNTA nanocomposites, the challenges of synthetically controlling the monodispersivity and homogeneous site distribution of metal NPs on the TNTAs still met with limited success. In particular, uniform deposition of metal NPs on the interior surfaces of TNTAs has been evidenced to be rather difficult than that on the outer surface [57]. Meanwhile, conventional synthetic methods such as complicated photoreduction [58–60] or chemical reduced approach [61] continued to plague the fabrication of well-defined metal/TNTA nanomaterials owing to poor repeatability. Therefore, achieving monodispersed deposition of metal NPs on the TNTAs is highly desirable. To this end, a facile, precisely controlled, and repeatable layer-by-layer (LBL) assembly route was developed to fabricate hierarchically ordered metal/TNTA heterostructures, M/TNTAs (M = Au, Ag, Pt). It was found that the tailor-made metal (Au, Ag, Pt) colloidal NPs were uniformly deposited on the TNTAs through the self-assembly monolayer (SAM) of LBL buildup, as shown in Fig. 5.1, which is afforded by substantial electrostatic attractive interaction between metal NPs and polyelectrolytes. Moreover, photoactivity of these well-defined heterostructures can be tuned by deposition cycles in the LBL process

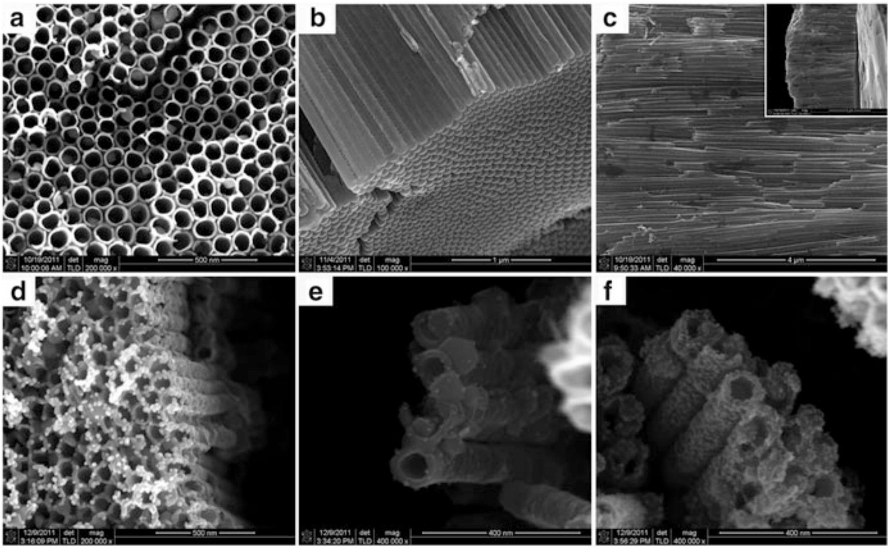

Fig. 5.1 (**a**) Panoramic, (**b**) bottom, and (**c**) magnified cross-sectional SEM images of TNT substrate post-treated by calcination at 450 °C in air for 3 h with corresponding overall cross-sectional view in the inset of (**c**). Top-view SEM images of (**d**) Au/TNT, (**e**) Ag/TNT, and (**f**) Pt/TNT hybrid nanostructures prepared via LBL assembly method (Reprinted with the permission from Ref. [62]. Copyright 2012, American Chemical Society)

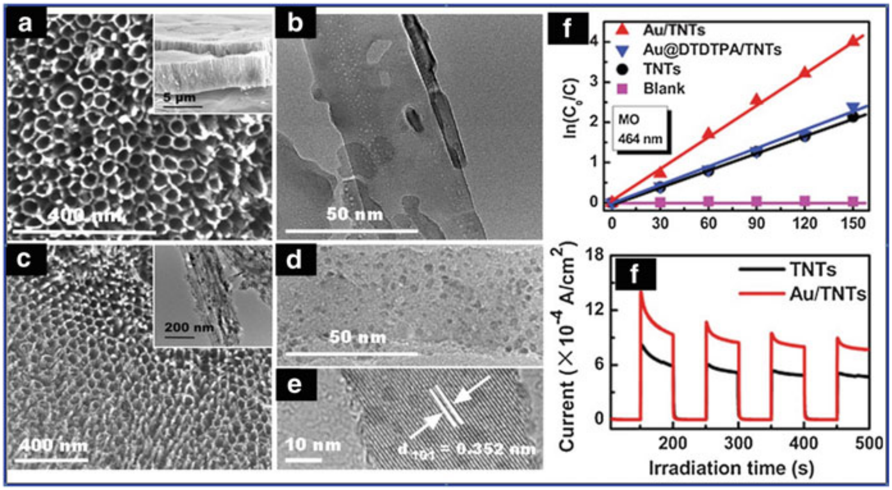

Fig. 5.2 (**a**) Panoramic SEM and (**b–c**) TEM views of blank TNTs with cross-sectional image in the inset of (**a**), (**d**) SEM and (**e**) TEM views of the Au/TNT heterostructure. (**f**) Photocatalytic performances of TNT, Au@DTDTPA/TNT, and Au/TNT heterostructure and (**g**) transient photocurrent response of TNT and Au/TNT heterostructure in 0.1 M Na$_2$SO$_4$ aqueous solution under UV light irradiation (365 ± 15 nm). The potential of the working electrode was set at 0.0 V versus the Pt counter electrode (Reprinted with permission from Ref. [64]. Copyright 2012, Royal Society of Chemistry)

[62, 63]. Apart from the LBL assembly approach, another facile and green deposition strategy was also developed to achieve the preparation of Au/TNTAs, in which the negatively charged surface ligands of Au NPs were used as linking medium to facilitate the uniform deposition of Au NPs on the positively charged TNTA framework, as shown in Fig. 5.2 [64]. The as-assembled Au/TNTA heterostructure demonstrates significantly enhanced photocatalytic performances under UV light irradiation in comparison with blank TNTAs, for which Au NP deposited intimately on the TNTA substrate is speculated to serve as "electron trap" leading to enhanced separation of photogenerated electron–hole pairs. In another similar work, a facile self-assembly approach based on chemical bonding was developed to synthesize Au/TNTA binary nanostructures, in which Au NPs capped with dodecanethiol (DDT) linker were tethered to the interior and exterior surfaces of TNTAs via 3-mercaptopropionic acid (MPA) molecular which possesses bifunctional groups, as shown in Fig. 5.3. The ensemble of results indicated that the Au/TNTA nanocomposite obtained via the self-assembly approach exhibits significantly enhanced photocatalytic performance as compared to the counterparts of blank TNTAs, P25 particulate film, flat anodic TiO$_2$ layer (FTL), and Au/FTL owing to the well-dispersed deposition of Au on the TNTA matrix, in which Au components play crucial roles as "electron reservoirs" and, simultaneously, the conducting Ti substrate beneath the nanotubes is conducive to electron transport, thus concurrently reinforcing the separation of photogenerated electron–hole pairs.

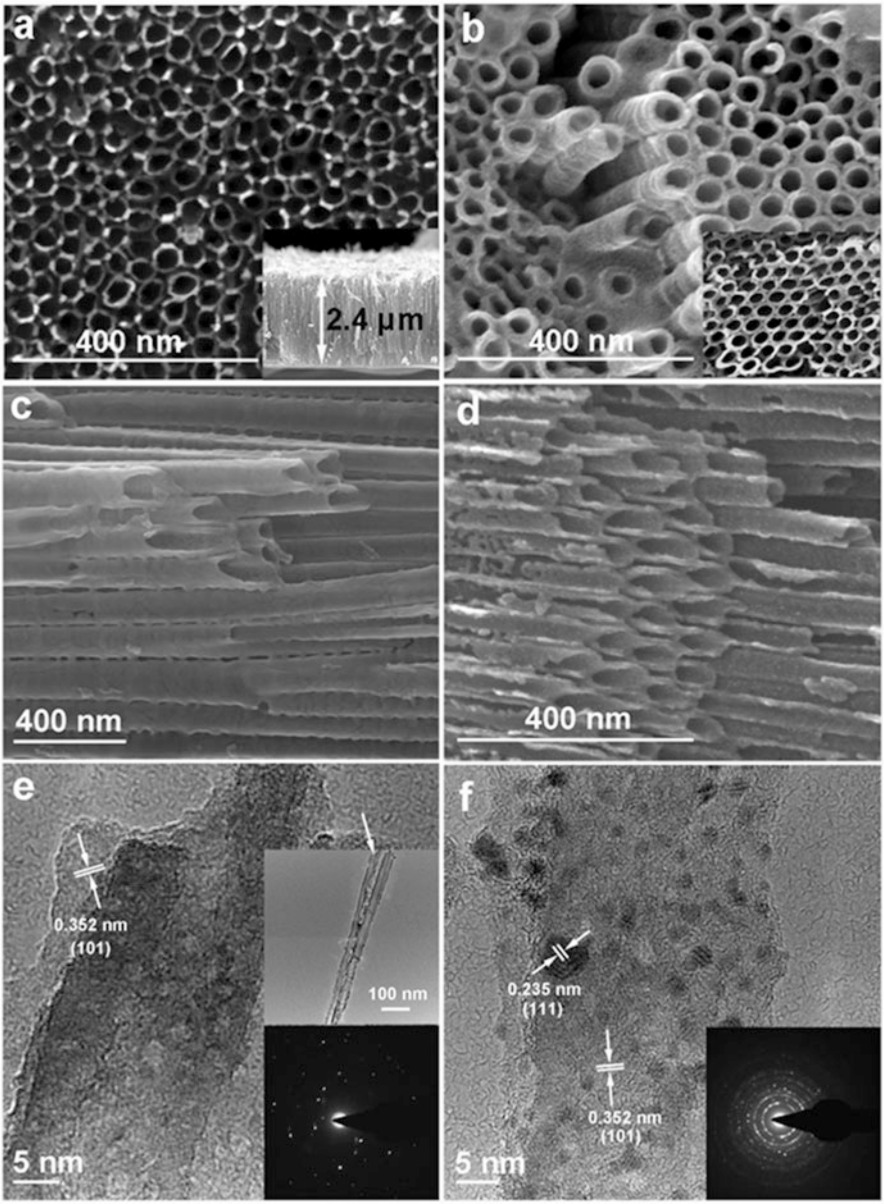

Fig. 5.3 Typical panoramic SEM views of (**a**) vertically oriented TNTAs post-treated with calcination at 450 °C in air for 3 h with cross-sectional image in the inset and (**b**) Au/TNTAs (1.14 wt%) with additional detailed image in the inset; magnified cross-sectional SEM images of (**c**) TNTAs and (**d**) Au/TNTAs; HRTEM images of (**e**) TNTAs and (**f**) Au/TNTAs with corresponding SAED patterns in the inset (Reprinted with permission from Ref. [91]. Copyright 2012, Royal Society of Chemistry)

This work affords a facile and efficient strategy to prepare a large variety of metal/TNTA nanocomposites via similar surface modification.

5.3.4 TNTA/Plasmonic Metal or Metal Cluster Nanocomposites

In recent years, plasmonic energy conversion was proposed as a promising route to conventional electron–hole separation in semiconductors [65]. The key to utilize the plasmonic effect of metal component in photocatalysis is the controlled spatial distribution of monodispersed metal NPs on the semiconductor matrix. Till now, there have been some promising results on the applications of plasmonic effect to enhance the photoactivities of TNTAs, such as visible-light-driven Ag/AgCl/TNTA nanocomposite [66]. In such a ternary heterostructure, a new surface-plasmon-induced photocatalytic mechanism was presented for the remarkably enhanced photocatalytic performance of Ag/AgCl/TNTA nanocomposite, in which Ag NPs with a mean diameter of 20 nm were speculated to be photoexcited owing to plasmonic resonance, followed by the transfer of photogenerated electrons from Ag NPs to the conduction band of TiO_2 and, simultaneously, the transfer of compensative electrons from electron donor (Cl^-) to the Ag NPs, thereby resulting in pronouncedly enhanced photoactivities of the ternary nanostructure [67].

Besides, a new class of nanomaterial-metal cluster, consisting of precise number of metal atoms protected by thiolate ligands, has recently emerged as a novel photosensitizer to extend the photoactivity of TiO_2. In striking contrast to conventional bulk metallic NPs, metal clusters exhibit (e.g., Au_x clusters) several distinct properties, such as unique atom-packing mode, strong electron energy quantization induced by the ultra-small cluster size, sizable bandgap, and controllable catalytic properties. More recently, glutathione-capped Au_x clusters and highly ordered nanoporous layer-covered TNTAs (NP-TNTAs) were employed as nanobuilding blocks for the construction of well-defined Au_x/NP-TNTA heterostructures via a facile electrostatic self-assembly strategy. Versatile photocatalytic performances of the Au_x/NP-TNTA heterostructure which acts as a model catalyst, including photocatalytic oxidation of organic pollutants, photocatalytic reduction of aromatic nitro compounds, and photoelectrochemical (PEC) water splitting under simulated solar light irradiation, were systematically exploited [68]. It was found that synergistic interaction stemming from monodisperse coverage of Au_x clusters on NP-TNTAs in combination with hierarchical nanostructure of NP-TNTAs reinforces light absorption of Au_x/NP-TNTA heterostructure especially within visible region, hence contributing to the significantly enhanced photocatalytic and PEC water splitting performances.

5.3.5 TNTA/Semiconductor Nanocomposites

A formidable challenge still remains in reducing the quick recombination rate of photogenerated electron–hole pairs over TiO_2. Although transformation of TiO_2 morphology to nanotubular structure may open a convenient avenue to improve the photocatalytic efficiency, it cannot tackle the central issue of photocatalysis [69]. Therefore, various research activities have devoted to reinforcing the photocatalytic properties by synthesizing TNTA/semiconductor hybrid nanostructures [70, 71]. For example, nanosized judicious coupling of TiO_2 and ZnO has been well established to remarkably enhance the separation efficiency of photoexcited charge carriers due to the formation of heterojunction structure between them [72, 73], thereby boosting quantum efficiency and photostability of the hybrid photocatalyst [74, 75].

Inspired by this, combined with structural advantages of vertically aligned TNTA framework (e.g., high specific surface area and excellent chemical stability) as starting nanobuilding blocks, hierarchical ordered ZnO/TNTA composite photocatalysts with promising photocatalytic performances could be attained. Numerous chemical, electrochemical, and physical approaches have been developed to fabricate the ZnO/TNTA hybrid nanomaterials, including template-assisted strategy [76–78], hydrothermal method [79, 80], electrodeposition approach [81], and filtered cathodic-vacuum-arc technique [82]. Besides, Xiao et al have developed an efficient one-step pyrolysis route to fabricate 1D hierarchical ZnO/TNTA heterostructures, by which in situ formed ZnO nanocrystals were uniformly grafted on the framework of TNTAs [83]. The results show that enhanced separation of electron–hole pairs and improved photostability of the ZnO/TNTA heterostructures were achieved. The morphologies of the hierarchical nanostructures of ZnO/TNTA heterostructure were illustrated in Fig. 5.4.

In another work, spatially hierarchically ordered ZnO nanorod (NR)-decorated NP-TNTA (ZnO NR/NP-TNTA) nanocomposites have been prepared by an efficient, two-step anodization route combined with an electrochemical deposition strategy, by which monodispersed one-dimensional (1D) ZnO NRs were uniformly grown on the framework of NP-TNTA substrate, as shown in Fig. 5.5 [84]. It was found that the ZnO NR/NP-TNTA heterostructure exhibits significantly enhanced photocatalytic and photoelectrocatalytic performances, along with favorable photostability toward degradation of organic pollutants under UV light irradiation, as compared to the single-component counterparts. The remarkably enhanced photoactivity of ZnO NR/NP-TNTA heterostructure is ascribed to the intimate interfacial integration between ZnO NR and NP-TNTA substrate imparted by the unique spatially branched hierarchical structure, thereby contributing to the efficient transfer and separation of photogenerated electron–hole charge carriers.

Moreover, many other narrow-bandgap semiconductors have also been used to sensitize the NP-TNTAs, for example, a hierarchically ordered CdSe/NP-TNTA hybrid nanostructure was fabricated through a facile electrochemical deposition strategy, by which the CdSe ingredients, consisting of clusters of quantum dots (QDs), were uniformly assembled on the inner and outer surfaces of the NP-TNTA framework, as revealed by Fig. 5.6 [85]. It was demonstrated that the as-prepared

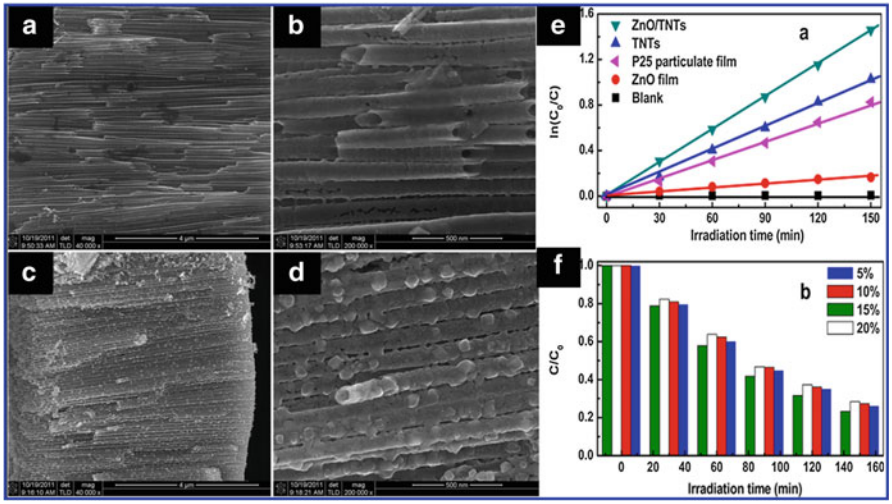

Fig. 5.4 Panoramic views of (**a**) TNTs fabricated via two-step anodization approach and the as-prepared (**b**) ZnO/TNT heterostructure; cross-sectional images of (**c** and **e**) TNT and (**d** and **f**) ZnO/TNT heterostructure (15 %); (**e**) photocatalytic activities of TNT, ZnO film, and ZnO/TNT heterostructure (15 %), and P25 particulate film for photodegradation of RhB aqueous solution under ambient conditions. (**f**) Photocatalytic performance of the ZnO/TNT heterostructure with varied deposition percentage of $Zn(NO_3)_2$ precursor in ethanol aqueous solution (Reprinted with the permission from Ref. [83]. Copyright 2012, American Chemical Society)

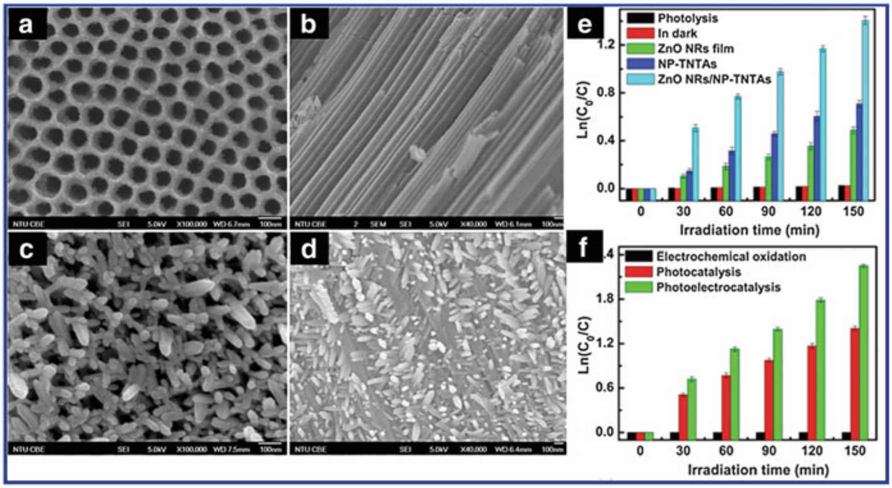

Fig. 5.5 Panoramic FESEM images of (**a**) NP-TNTA and (**c**) spatially branched hierarchical ZnO NR/NP-TNTA heterostructure, and cross-sectional images of (**b**) NP-TNTA and (**d**) ZnO NR/NP-TNTA heterostructure. (**e**) Photocatalytic performances of blank NP-TNTAs, pure ZnO NR film, and spatially branched hierarchical ZnO NR/NP-TNTA heterostructure toward degradation of RhB under UV light irradiation (365 ± 15 nm), (**f**) photocatalytic and photoelectrocatalytic activities of ZnO NR/NP-TNTA heterostructure under UV light irradiation (365 ± 15 nm) (Reprinted with permission from Ref. [84]. Copyright 2014, Royal Society of Chemistry)

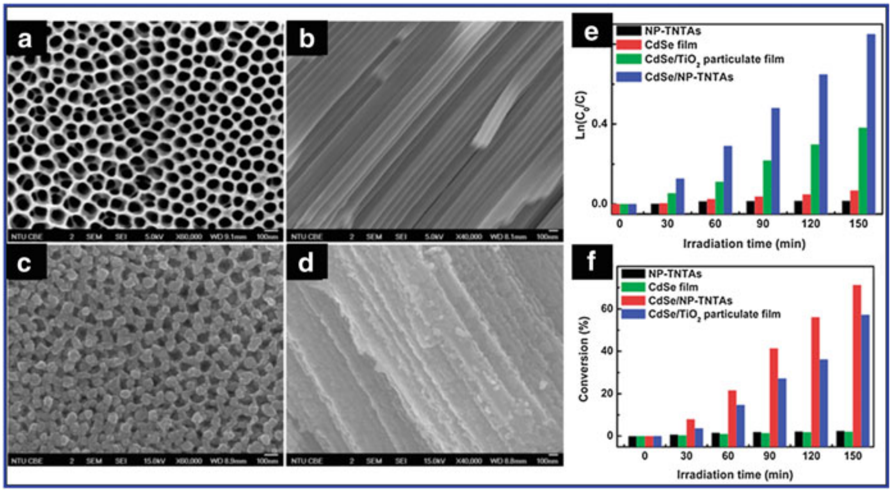

Fig. 5.6 FESEM images of (**a** and **b**) NP-TNTA and (**c** and **d**) CdSe/NP-TNTA heterostructure prepared via electrochemical deposition with deposition time of 1600s. (**e**) Photocatalytic performances of different samples and (**f**) photocatalytic reduction of 4-NA over different samples under visible light irradiation ($\lambda > 420$ nm) with the addition of ammonium formate as quencher for photogenerated holes and N_2 purge under ambient conditions (Reprinted with permission from Ref. [85]. Copyright 2014, Royal Society of Chemistry)

CdSe/NP-TNTA heterostructure could serve as an efficient photoanode for photoelectrochemical water splitting, and, moreover, it could also be used as a multifunctional photocatalyst for photoredox applications, including photocatalytic oxidation of organic dye pollutants and selective reduction of aromatic nitro compounds under visible light irradiation. Similarly, tailor-made negatively charged CdS QDs were evenly deposited on a hierarchical framework of NP-TNTAs by modulating surface charge properties of constituents, as displayed in Fig. 5.7. It has been demonstrated that the CdS/NP-TNTA hybrid nanostructures exhibit promising visible-light-driven photoactivity toward photooxidation of organic dye pollutants and photocatalytic reduction of nitrophenol derivatives as a result of monodisperse deposition of CdS QDs on the well-defined NP-TNTA scaffold [86].

5.4 Photocatalytic Applications of TNTA-Based Nanocomposites

5.4.1 *Nonselective Degradation of Organic Dye Pollutants*

Nonselective photocatalysis has been extensively investigated owing to its great significance to environmental remediation [5, 87–89], by which contaminants are mineralized to less toxic inorganic compounds, such as water, carbon dioxide, and

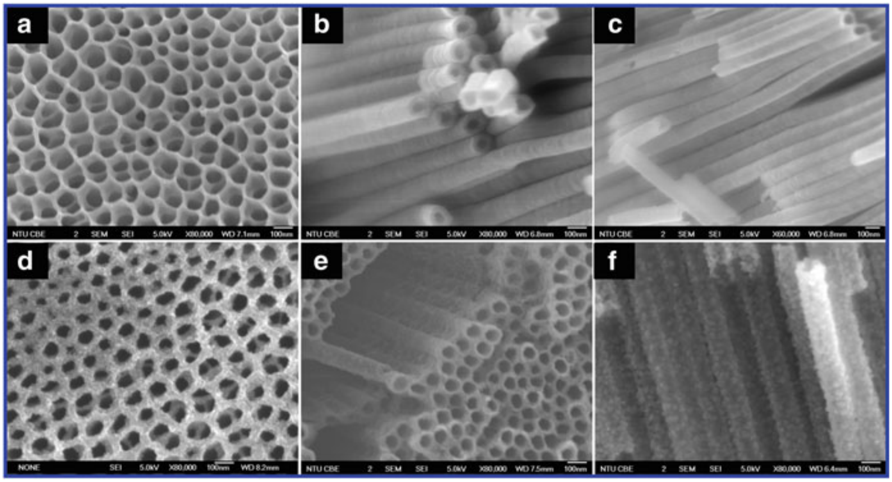

Fig. 5.7 Panoramic FESEM images of (**a**) NP-TNTAs and (**d**) CdS QD/NP-TNTAs and cross-sectional FESEM images of (**b** and **c**) NP-TNTAs, (**e** and **f**) CdS QD/NP-TNTA heterostructure (Reprinted with permission from Ref. [86]. Copyright 2013, Royal Society of Chemistry)

salts [90]. A series of 1D noble metal/TiO_2 nanocomposites (with mean diameter of 14.7, 6.3, and 3.1 nm for Au, Ag, and Pt, respectively.) have been prepared via a facile and easily accessible electrostatic self-assembly approach by tuning surface charge properties of the hierarchically ordered TNTAs, as shown in Fig. 5.8 [62–64, 91]. These 1D hybrid nanostructures exhibited substantially enhanced photocatalytic performances toward degradation of organic dye pollutants owing to the Schottky barrier effect of noble metal NPs, which provides a new strategy to design highly ordered metal/1D semiconductor binary nanocomposites based on electrostatic interaction.

5.4.2 *Selective Organic Transformation*

Selective organic transformation is of great industrial importance owing to the extensive use of organics in diverse applications. In particular, photocatalytic selective organic transformation is a green and promising technique, exhibiting intrinsic merits including mild reaction conditions and the possibility to reduce the generation of undesired by-products. More recently, TNTAs modified with ultra-small Au_x clusters has been utilized as an efficient photocatalyst for selective reduction of a series of aromatic nitro compounds to corresponding amino compounds under simulated solar light irradiation [68]. It was speculated that the photogenerated electrons photoexcited from the HOMO (highest occupied molecular orbital) to LUMO (lowest unoccupied molecular orbital) of Au_x clusters under simulated solar light irradiation transfer to the conduction band of TiO_2 which

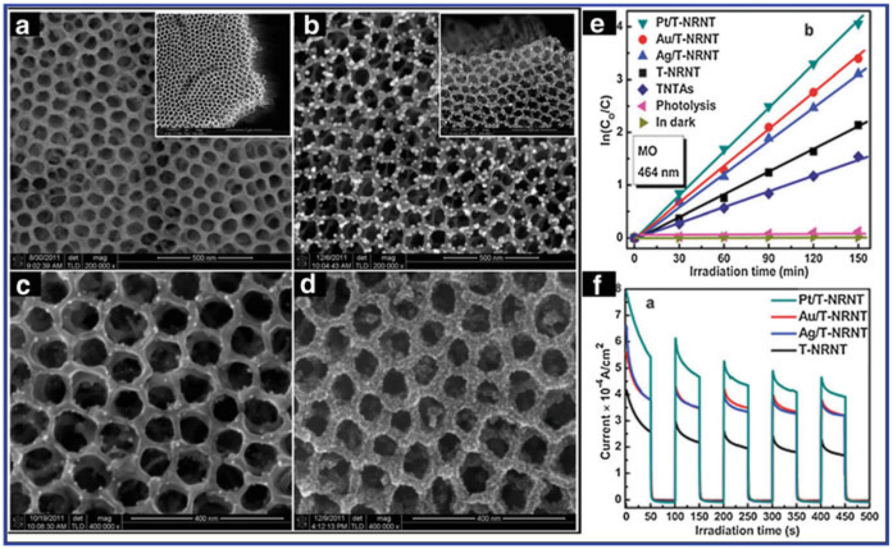

Fig. 5.8 (**a**) Panoramic view of T-NRNT attained via the 2nd anodization with cross-sectional view in the inset, (**b**) high-resolution images of Au/T-NRNT with cross-sectional view in the inset, (**c**) Ag/T-NRNT, and (**d**) Pt/T-NRNT fabricated via a LBL self-assembly approach. (**e**) Photocatalytic performances of M/T-NRNT (M = Au, Ag, Pt) and (**f**) transient photocurrent responses of T-NRNT and M/T-NRNT (M = Au, Ag, Pt) heterostructures in 0.1 M Na_2SO_4 aqueous solution under UV light irradiation (365 ± 15 nm) (Reprinted with permission from Ref. [63]. Copyright 2012, Royal Society of Chemistry)

reduces the nitro compounds absorbed on the scaffold of TNTAs to amino compounds, as clearly displayed in Fig. 5.9. Noteworthily, the selective photocatalytic reactions were performed in a N_2 atmosphere, and photogenerated holes were completely quenched by hole scavengers; thus all photoinduced electrons in the reaction system were involved in the selective photoreduction reactions. Similar organic transformation reactions were also observed on the CdS QDs/NP-TNTAs which demonstrated significantly enhanced photoreduction performances under visible light irradiation in comparison with blank NP-TNTAs [86].

5.4.3 *CO_2 Reduction*

Solar-energy-driven conversion of CO_2 into hydrocarbon fuels can simultaneously generate chemical fuels to meet energy demand and mitigate rising CO_2 levels. Thus far, diverse ranges of 1D nanostructures have been used for photoreduction of CO_2 into chemical fuels [92–94], among which TNTAs were found to efficiently convert CO_2 and water vapor into methane and other hydrocarbons under outdoor sunlight irradiation [92]. Specifically, Shankar's group demonstrated an approach that is able to achieve high-rate sunlight-driven conversion of diluted CO_2 to light

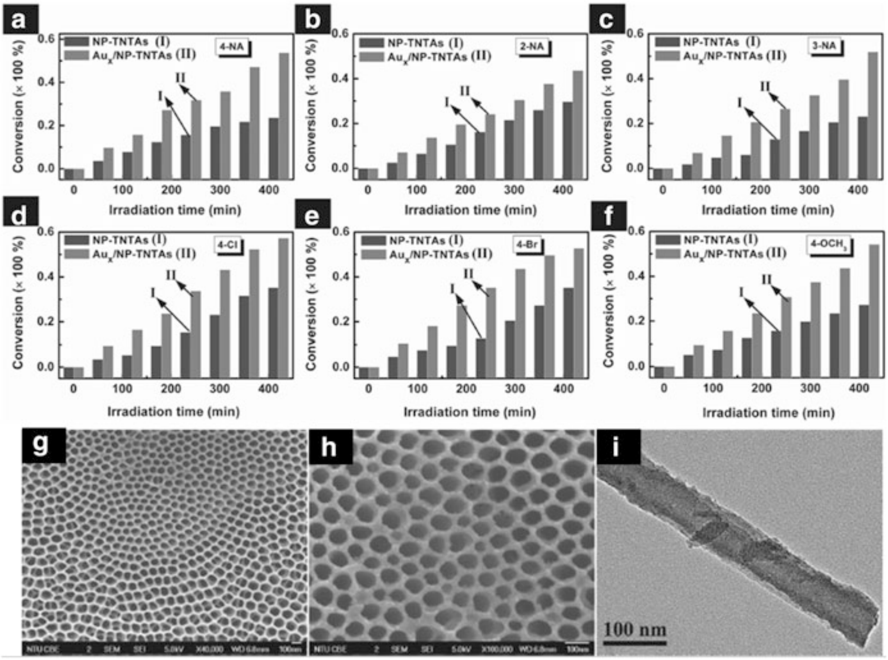

Fig. 5.9 Photocatalytic reduction of substituted aromatic nitro compounds over blank NP-TNTA and Au$_x$/NP-TNTA heterostructure (with dipping time for 96 h) under simulated solar light irradiation, with the addition of ammonium formate as quencher for photogenerated holes and N_2 purge under ambient conditions: (**a**) 4-nitroaniline (4-NA), (**b**) 3-nitroaniline (3-NA), (**c**) 2-nitroaniline (2-NA), (**d**) 1-chloro-4-nitrobenzene (4-Cl), (**e**) 1-bromo-4-nitrobenzene (4-Br), and (**f**) 4-nitroanisole (4-OCH_3). (**g** and **h**) Panoramic FESEM images of Au$_x$/NP-TNTA heterostructure. (**i**) Low-magnified TEM image of Au$_x$/NP-TNTA heterostructure (Reproduced from Ref. [68] by permission of John Wiley & Sons, Ltd)

hydrocarbons in which an optimized combination of a Cu–Pt coating and modulated-diameter TiO_2 nanotube was used as photocatalyst. Their results showed that at least fourfold improvement in CO_2 conversion rates over prior art using a catalyst consisting of coaxial Cu–Pt bimetallic shells supported on a periodically modulated double-walled TNTA (PMTiNT) core. Under AM 1.5 one-sun illumination, a hydrocarbon production rate of 3.51 mL g^{-1} h^{-1} or 574 nmol cm^{-2} h^{-1} using 99.9 % CO_2 was attained, as shown in Fig. 5.10. Moreover, the periodic modulation of the diameters of the TNTAs increased the surface area and improved the utilization of light, while the bimetallic coating increased catalyst activity and specificity [92]. In another work, nitrogen-doped TNTAs were used for photocatalytic conversion of CO_2 and water vapor to hydrogen fuels. Using outdoor global AM 1.5 sunlight (100 mW/cm^2), a hydrocarbon production rate of 111 ppm cm^{-2} h^{-1}, or $\approx$ 160 μL/(g h), was obtained when the nanotube arrays were loaded with both Cu and Pt nanoparticles [95, 96]. This work suggested that high-rate photocatalytic conversion of CO_2 can be achieved using sunlight and

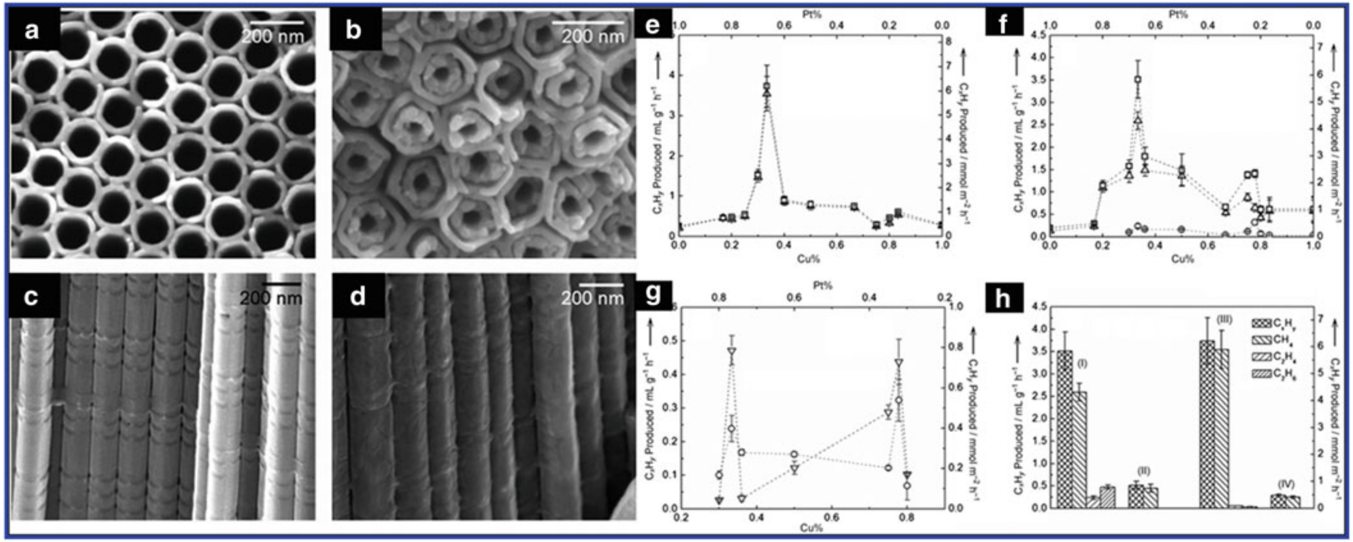

Fig. 5.10 (**a** and **b**) Plan-view and (**c** and **d**) cross-sectional SEM images of the as-prepared PMTiNT platform (**a** and **c**) and Cu–Pt loaded nanotubes (**b** and **d**). (**e** and **f**) Plots of hydrocarbon (□), CH_4 (△), and C_2H_4 (○) solar-driven generation rates against fraction of Cu in Cu–Pt bimetallic system using 0.998 % (**e**) and 99.9 % (**f**) CO_2. (**g**) Comparison of the C_2H_4 (○) and C_2H_6 (▽) solar-driven generation rates against fraction of Cu in the Cu–Pt bimetallic system using 99.9 % CO_2. (**h**) Comparison of hydrocarbon generation activities of $Cu_{0.33}$–$Pt_{0.67}$ nanotube-loaded PMTiNTs (I, III) and regular TiNTs (II, IV) using 99.9 % (I, II) and 0.998% (III, IV) CO_2 (Reproduced from Ref. [92] by permission of John Wiley & Sons, Ltd)

high-surface-area TNTAs, with a nanotube wall thickness less than or in the range of the minority carrier-diffusion length, in combination with co-catalyst nanoparticles coated on the nanotube array surface. These two works open new avenues for carbon recycling using renewable sources.

5.4.4 Photoelectrochemical (PEC) Water Splitting

The aligned porosity, crystallinity, and oriented nature of the nanotubular structure make TNTAs an ideal candidate for promising PEC applications. The intrinsic configuration of TNTAs affords significantly shorter carrier-diffusion paths along the nanotube wall and minimizes the occurrence of charge losses arising from the electron hopping between nanoparticles [97, 98]. Moreover, the freestanding TNTAs are grown vertically on Ti substrate which can be directly used as photoelectrodes. In the past few years, construction of TNTA-based photoelectrode for PEC water splitting has been gaining continuous interest. For example, a visible-light-responsive plasmonic photocatalytic composite photoelectrode was constructed by rationally selecting Au nanocrystals (20 nm) and assembling them onto TNTA-based photonic crystal substrate with a pore diameter of 200 nm (Fig. 5.11) [99]. The rational design of the composite materials remarkably increased the SPR intensity of Au and consequently promoted the hot-electron

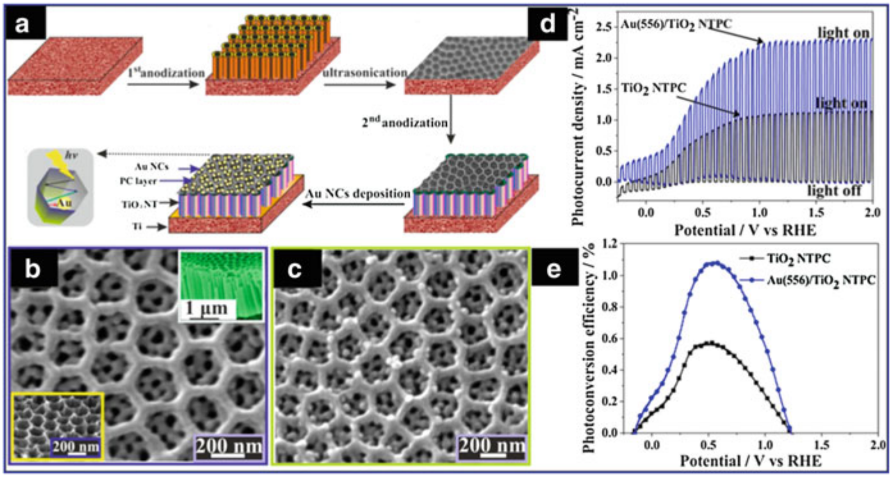

Fig. 5.11 (**a**) Schematic diagram showing the fabrication procedure for Au/TiO_2 nanotube photonic crystals (NTPC). (**b**) SEM images of TiO_2 NTPC, top right inset shows a cross-sectional view and bottom left inset shows high magnification of tilt 15° cross-sectional view of top PC layer, and (**c**) SEM image of Au/TiO_2 NTPC. (**d**) Linear-sweep voltammograms of the samples under chopped AM 1.5G irradiation with a scan rate of 5 mV/s, and (**e**) photoconversion efficiency as a function of applied potential (Reprinted with the permission from Ref. [99]. Copyright 2013, American Chemical Society)

injection from Au nanocrystals into CB of TiO_2, thus resulting in substantially enhanced PEC water splitting performances under visible light irradiation ($\lambda > 420$ nm). In another work, TNTAs modified with palladium quantum dots (Pd QDs, 3.3 ± 0.7 nm) demonstrated substantially increased monochromatic incident photon-to-electron conversion efficiency (IPCE) of nearly 100 % at $\lambda = 330$ nm [100]. It was speculated that the synergistic interaction between nanotubular structure of TNTAs and uniformly dispersed Pd QDs facilitated the charge transfer of photogenerated electrons from TNTAs to Pd QDs and, simultaneously, the high activity of Pd QDs acting as catalytic centers contributed to the high-efficiency PEC hydrogen production. Apart from TNTAs, multicomponent nanotube arrays such as vertically oriented Ti–Pd mixed oxynitride nanotube arrays [101], Ti–Fe–O nanotube arrays [102], Ti–Nb–Zr–O mixed oxide nanotube arrays [103], and Ta_3N_5 nanotube arrays [104] have also been studied for PEC water splitting under simulated solar light or visible light irradiation.

5.5 Conclusions

In summary, TNTA-based nanostructures have emerged as promising photocatalysts for utilizing solar energy in the field of photocatalysis owing to their structural advantages including high surface-to-volume ratios and unique nanotube array structures. This chapter briefly introduces the state-of-the-art developments of TNTAs which mainly concentrate on the modification strategies and photocatalytic applications of TNTA-based nanocomposites. These judiciously modified TNTA nanostructures exhibit improved UV and visible light absorption, thus harvesting an increased portion of solar spectrum and reducing the recombination of photogenerated electron–hole pairs. Future research efforts may be directed to fabricate TNTAs of different chemical compositions with good chemical and physical stabilities to absorb a broader solar spectrum, especially the infrared region which accounts for a large portion of the solar spectrum. It is anticipated that TNTA-based hybrid nanostructures could afford more versatile potential applications in a myriad of fields.

References

1. Liu C, Dasgupta NP, Yang P (2014) Semiconductor nanowires for artificial photosynthesis. Chem Mater 26:415–422
2. Wang M, Ioccozia J, Sun L et al (2014) Inorganic-modified semiconductor TiO_2 nanotube arrays for photocatalysis. Energy Environ Sci 7:2182–2202
3. Fujishima A, Honda K (1972) Electrochemical photolysis of water at a semiconductor electrode. Nature 238:37–38
4. Zhang Y, Zhang N, Tang Z-R et al (2012) Visible-light-driven oxidation of primary C–H bonds over CdS with dual co-catalysts graphene and TiO_2. Chem Sci 3:2812–2822

5. Zhang Y, Tang Z-R, Fu X et al (2010) TiO_2-graphene nanocomposites for gas-phase photocatalytic degradation of volatile aromatic pollutant: is TiO_2-graphene truly different from other TiO_2-carbon composite materials? ACS Nano 4:7303–7314
6. Hochbaum AI, Chen R, Delgado RD et al (2008) Enhanced thermoelectric performance of rough silicon nanowires. Nature 451:163–167
7. Zhang Z, Yu Y, Hedhili MN (2012) Microwave-assisted self-doping of TiO_2 photonic crystal for efficient photoelectrochemical water splitting. ACS Appl Mater Interfaces 4:990–996
8. Zhu K, Vinzant TB, Neale NR et al (2007) Removing structural disorder from oriented TiO_2 nanotube arrays: reducing the dimensionality of transport and recombination in dye-sensitized solar cells. Nano Lett 7:3739–3746
9. Albu SP, Ghicov A, Macak JM et al (2007) Self-organized, free-standing TiO_2 nanotube membrane for flow-through photocatalytic applications. Nano Lett 7:1286–1289
10. Asahi R, Morikawa T, Ohwaki T et al (2001) Visible-light photocatalysis in nitrogen-doped titanium oxides. Science 293:269–271
11. Qin WP, Zhang DS, Zhao D et al (2010) Near-infrared photocatalysis based on YF_3:Yb^{3+}, Tm^{3+}/TiO_2 core/shell nanoparticles. Chem Commun 46:2304–2306
12. Wu Y, Liu H, Zhang J et al (2009) Enhanced photocatalytic activity of nitrogen-doped titania by deposited with gold. J Phys Chem C 113:14689–14695
13. Wang CL, Sun L, Yun H et al (2009) Sonoelectrochemical synthesis of highly photoelectrochemically active TiO_2 nanotubes by incorporating CdS nanoparticles. Nanotechnology 20:295601–295606
14. Wang M, Sun L, Lin Z et al (2013) p–n Heterojunction photoelectrodes composed of Cu_2O-loaded TiO_2 nanotube arrays with enhanced photoelectrochemical and photoelectrocatalytic activities. Energy Environ Sci 6:1211–1220
15. Gong D, Grimes CA, Varghese OK et al (2001) Titanium oxide nanotube arrays prepared by anodic oxidation. J Mater Res 16:3331–3334
16. Cai Q, Paulose M, Varghese OK et al (2005) The effect of electrolyte composition on the fabrication of self-organized titanium oxide nanotube arrays by anodic oxidation. J Mater Res 20:230–235
17. Mor GK, Shankar K, Paulose M et al (2005) Enhanced photocleavage of water using titania nanotube arrays. Nano Lett 5:191–195
18. Parkhutik VP, Shershulsky VI (1992) Theoretical modelling of porous oxide growth on aluminium. J Phys D Appl Phys 25:1258–1263
19. Macdonald DD (1993) On the formation of voids in anodic oxide films on aluminum. J Electrochem Soc 140:27–30
20. Thompson GE (1997) Porous anodic alumina: fabrication, characterization and applications. Thin Solid Films 297:192–201
21. Siejka J, Ortega C (1977) An O^{18} study of field-assisted pore formation in compact anodic oxide films on aluminum. J Electrochem Soc 124:883–891
22. Roy P, Berger S, Schmuki P (2011) TiO_2 nanotubes: synthesis and applications. Angew Chem 50:2904–2940
23. Mohamed AE, Kasemphaibulsuk N, Rohani S et al (2010) Fabrication of titania nanotube arrays in viscous electrolytes. J Nanosci Nanotechnol 10:1998–2008
24. Xu C, Shaban YA, Ingler WB et al (2007) Nanotube enhanced photoresponse of carbon modified (CM)-n-TiO_2 for efficient water splitting. Sol Energy Mater Sol Cells 91:938–943
25. Vitiello RP, Macak JM, Ghicov A et al (2006) N-doping of anodic TiO_2 nanotubes using heat treatment in ammonia. Electrochem Commun 8:544–548
26. Geng J, Yang D, Zhu J et al (2009) Nitrogen-doped TiO_2 nanotubes with enhanced photocatalytic activity synthesized by a facile wet chemistry method. Mater Res Bull 2009 (44):146–150
27. Chen X, Zhang X, Su Y et al (2008) Preparation of visible-light responsive P F-codoped TiO_2 nanotubes. Appl Surf Sci 254:6693–6696

28. Lei L, Su Y, Zhou M (2007) Fabrication of multi-non-metal-doped TiO_2 nanotubes by anodization in mixed acid electrolyte. Mater Res Bull 42:2230–2236
29. Beranek R, Macak JM, Gartner M et al (2009) Enhanced visible light photocurrent generation at surface-modified TiO_2 nanotubes. Electrochim Acta 54:2640–2646
30. Su Y, Zhang X, Zhou M et al (2008) Preparation of high efficient photoelectrode of N–F-codoped TiO_2 nanotubes. J Photochem Photobiol A Chem 194:152–160
31. Tang X, Li D (2008) Sulfur-doped highly ordered TiO_2 nanotubular arrays with visible light response. J Phys Chem C 112:5405–5409
32. Shankar K, Paulose M, Mor GK et al (2005) A study on the spectral photoresponse and photoelectrochemical properties of flame-annealed titania nanotube-arrays. J Phys D Appl Phys 38:3543–3549
33. Park JH, Kim S, Bard AJ (2006) Novel carbon-doped TiO_2 nanotube arrays with high aspect ratios for efficient solar water splitting. Nano Lett 6:24–28
34. Lee HH, Shin SL et al (2008) Effect of gas pressure on Al coatings by cold gas dynamic spray. Mater Lett 62:1579–1581
35. Lu N, Quan X, Li JY et al (2007) Fabrication of boron-doped TiO_2 nanotube array electrode and investigation of its photoelectrochemical capability. J Phys Chem C 111:11836–11842
36. Su Y, Chen S, Quan X et al (2008) A silicon-doped TiO_2 nanotube arrays electrode with enhanced photoelectrocatalytic activity. Appl Surf Sci 255:2167–2172
37. Choi W, Termin A, Hoffmann MR (1994) The role of metal ion dopants in quantum-sized TiO_2: correlation between photoreactivity and charge carrier recombination dynamics. J Phys Chem C 98:13669–13679
38. Dvoranova D, Brezova V, Mazur AM (2002) Investigations of metal-doped titanium dioxide photocatalysts. Appl Catal, B 37:91–105
39. Tu YF, Huang SY, Sang JP (2010) Preparation of Fe-doped TiO_2 nanotube arrays and their photocatalytic activities under visible light. Mater Res Bull 45:224–229
40. Tu YF, Huang SY, Sang JP (2009) Synthesis and photocatalytic properties of Sn-doped TiO_2 nanotube arrays. J Alloys Compd 482:382–387
41. Yang Y, Wang X, Li L (2010) Zinc-doped TiO_2 nanotube arrays. Key Eng Mater 434:446–447
42. Zhao J, Wang X, Kang Y et al (2008) Photoelectrochemical activities of W-doped titania nanotube arrays fabricated by anodization. IEEE Photon Technol Lett 20:1213–1215
43. Ghicov A, Schmidt B, Kunze J et al (2007) Photoresponse in the visible range from Cr doped TiO_2 nanotubes. Chem Phys Lett 433:323–326
44. Sun L, Li J, Wang CL et al (2009) An electrochemical strategy of doping Fe^{3+} into TiO_2 nanotube array films for enhancement in photocatalytic activity. Sol Energy Mater Sol Cells 93:1875–1880
45. Li J, Yun H, Lin CJ (2008) Investigations on the Fe-doped TiO_2 nanotube arrays as a photoanode for cathodic protection of stainless steel. ECS Trans 3:1–9
46. Zhu BL, Guo Q, Huang XL et al (2006) Characterization and catalytic performance of TiO_2 nanotubes-supported gold and copper particles. J Mol Catal A Chem 249:211–217
47. Mussy JPG, Macpherson JV, Delplancke JL (2003) Characterisation and behaviour of Ti/TiO_2/noble metal anodes. Electrochim Acta 2003(48):1131–1141
48. Ikuma Y, Bessho H (2007) Effect of Pt concentration on the production of hydrogen by a TiO_2 photocatalyst. Int J Hydrog Energy 32:2689–2692
49. Furube A, Du L, Hara K et al (2008) Ultrafast plasmon-induced electron transfer from gold nanodots into TiO_2 nanoparticles. J Am Chem Soc 129:14852–14853
50. Milsom EV, Novak J, Oyama M et al (2007) Electrocatalytic oxidation of nitric oxide at TiO_2–Au nanocomposite film electrodes. Electrochem Commun 9:436–442
51. Lee JH, Choi HS, Lee JH et al (2009) Fabrication of titania nanotubular film with metal nanoparticles. J Cryst Growth 311:638–641
52. Sun L, Li J, Wang C et al (2009) Ultrasound aided photochemical synthesis of Ag loaded TiO_2 nanotube arrays to enhance photocatalytic activity. J Hazard Mater 171:1045–1050

53. He BL, Dong B, Li HL (2007) Preparation and electrochemical properties of Ag-modified TiO_2 nanotube anode material for lithium-ion battery. Electrochem Commun 9:425–430
54. Yang L, He D, Cai Q et al (2007) Fabrication and catalytic properties of Co-Ag-Pt nanoparticle-decorated titania nanotube arrays. J Phys Chem C 111:8214–8217
55. Yu J, Xiong J, Cheng B et al (2005) Fabrication and characterization of Ag–TiO_2 multiphase nanocomposite thin films with enhanced photocatalytic activity. Appl Catal B Environ 60:211–221
56. Subramanian V, Wolf E, Kamat PV (2001) Semiconductor-metal composite nanostructures. To what extent do metal nanoparticles improve the photocatalytic activity of TiO_2 films? J Phys Chem B 105:11439–11446
57. Seabold JA, Shankar K, Wilke RHT et al (2008) Photoelectrochemical properties of heterojunction CdTe/TiO_2 electrodes constructed using highly ordered TiO_2 nanotube arrays. Chem Mater 20:5266–5273
58. Paramasivam I, Macak JM, Ghicov A (2007) Enhanced photochromism of Ag loaded self-organized TiO_2 nanotube layers. Chem Phys Lett 445:233–237
59. Paramasivam I, Macak JM, Schmuki P et al (2008) Photocatalytic activity of TiO_2 nanotube layers loaded with Ag and Au nanoparticles. Electrochem Commun 0:71–75
60. Song YY, Gao ZD, Schmuki P (2011) Highly uniform Pt nanoparticle decoration on TiO_2 nanotube arrays: a refreshable platform for methanol electrooxidation. Electrochem Commun 13:290–293
61. Macak JM, Schmidt-Stein F, Schmuki P (2007) Efficient oxygen reduction on layers of ordered TiO_2 nanotubes loaded with Au nanoparticles. Electrochem Commun 9:1783–1787
62. Xiao F (2012) Layer-by-layer self-assembly construction of highly ordered metal-TiO_2 nanotube arrays heterostructures (M/TNTs, $M = Au, Ag, Pt$) with tunable catalytic activities. J Phys Chem C 116:16487–16498
63. Xiao F (2012) An efficient layer-by-layer self-assembly of metal-TiO_2 nanoring/nanotube heterostructures, M/T-NRNT ($M = Au, Ag, Pt$), for versatile catalytic applications. Chem Commun 48:6538–6540
64. Xiao F-X (2012) A novel route for self-assembly of gold nanoparticle-TiO_2 nanotube array (Au/TNTs) heterostructure for versatile catalytic applications: pinpoint position via hierarchically dendritic ligand. RSC Adv 2:12699–12701
65. Clavero C (2014) Plasmon-induced hot-electron generation at nanoparticle/metal-oxide interfaces for photovoltaic and photocatalytic devices. Nat Photonics 8:95–103
66. Yu J, Dai G, Huang B (2009) Fabrication and characterization of visible-light-driven plasmonic photocatalyst Ag/AgCl/TiO_2 nanotube arrays. J Phys Chem C 113:16394–16401
67. Wu F, Hu X, Fan J et al (2013) Photocatalytic activity of Ag/TiO_2 nanotube arrays enhanced by surface plasmon resonance and application in hydrogen evolution by water splitting. Plasmonics 2013(8):501–508
68. Xiao F-X, Hung S-F, Miao J et al (2014) Metal-cluster decorated TiO_2 nanotube arrays: a composite heterostructure toward versatile photocatalytic and photoelectrochemical applications. Small 11:554–567
69. Ghicov A, Macak JM, Tsuchiya H et al (2006) Ion implantation and annealing for an efficient N-doping of TiO_2 nanotubes. Nano Lett 6:1080–1082
70. Jiang Y, Wu M, Wu X et al (2009) Low-temperature hydrothermal synthesis of flower-like ZnO microstructure and nanorod array on nanoporous TiO_2 film. Mater Lett 63:275–278
71. Liu Z, Zhang X, Nishimoto S et al (2008) Highly ordered TiO_2 nanotube arrays with controllable length for photoelectrocatalytic degradation of phenol. J Phys Chem C 112:253–259
72. Kostedt WL, Ismail AA, Mazyck DW (2008) Impact of heat treatment and composition of ZnO-TiO_2 nanoparticles for photocatalytic oxidation of an azo dye. Ind Eng Chem Res 47:1483–1487

73. Liao DL, Badour CA, Liao BQ (2008) Preparation of nanosized TiO_2/ZnO composite catalyst and its photocatalytic activity for degradation of methyl orange. J Photochem Photobiol A Chem 194:11–19
74. Yu H, Zhang Z, Han M et al (2005) A general low-temperature route for large-scale fabrication of highly oriented ZnO nanorod/nanotube arrays. J Am Chem Soc 127:2378–2379
75. Yu QJ, Fu WY, Yu CL et al (2007) Fabrication and optical properties of large-scale ZnO nanotube bundles via a simple solution route. J Phys Chem C 111:17521–17526
76. Qiu J, Jin Z, Liu Z et al (2007) Fabrication of TiO_2 nanotube film by well-aligned ZnO nanorod array film and sol–gel process. Thin Solid Films 515:2897–2902
77. Qiu J, Yu W, Gao X, Li X (2006) Sol–gel assisted ZnO nanorod array template to synthesize TiO_2 nanotube arrays. Nanotechnology 17:4695–4698
78. Thitima R, Takashi S, Susumu Y (2008) Photovoltaic performance of hybrid solar cell with TiO_2 nanotubes arrays fabricated through liquid deposition using ZnO template. Sol Energy Mater Sol Cells 92:1445–1449
79. Kim SS, Na SI, Nah YC (2011) TiO_2 nanotubes decorated with ZnO rod-like nanostructures for efficient dye-sensitized solar cells. Electrochim Acta 58:503–509
80. Benkara S, Zerkout S (2010) Preparation and characterization of ZnO nanorods grown into aligned TiO_2 nanotube array. J Mater Environ Sci 1:173–188
81. Zhang Z, Yuan Y, Liang L et al (2008) Preparation and photoelectrocatalytic activity of ZnO nanorods embedded in highly ordered TiO_2 nanotube arrays electrode for azo dye degradation. J Hazard Mater 158:517–526
82. Yang HY, Yu SF, Lau SP et al (2009) Direct growth of ZnO nanocrystals onto the surface of porous TiO_2 nanotube arrays for highly efficient and recyclable photocatalysts. Small 5:2260–2264
83. Xiao F (2012) Construction of highly ordered ZnO–TiO_2 nanotube arrays (ZnO/TNTs) heterostructure forphotocatalytic application. ACS Appl Mater Interface 4:7055–7063
84. Xiao F-X, Hung S-F, Tao HB et al (2014) Spatially branched hierarchical ZnO nanorod-TiO_2 nanotube array heterostructures for versatile photocatalytic and photoelectrocatalytic applications: towards intimate integration of 1D-1D hybrid nanostructures. Nanoscale 6:14950–14961
85. Xiao F-X, Miao J, Wang H-Y et al (2014) Electrochemical construction of hierarchically ordered CdSe-sensitized TiO_2 nanotube arrays: towards versatile photoelectrochemical water splitting and photoredox applications. Nanoscale 6:6727–6737
86. Xiao F-X, Miao J, Wang H-Y et al (2013) Self-assembly of hierarchically ordered CdS quantum dots-sensitized TiO2 nanotube array heterostructure as efficient visible light photocatalyst for photoredox applications. J Mater Chem A 1:12229–12238
87. Zhang Y, Tang Z-R, Fu X et al (2011) Self-assembly of hierarchically ordered CdS quantum dots–TiO_2 nanotube array heterostructures as efficient visible light photocatalysts for photoredox applications. Appl Catal B 106:445–452
88. Zhang N, Ciriminna R, Pagliaro M et al (2014) Nanochemistry-derived Bi_2WO_6 nanostructures: Towards production of sustainable chemicals and fuels induced by visible light. Chem Soc Rev 43:5276–5287
89. Weng B, Liu S, Tang Z-R et al (2014) One-dimensional nanostructure based materials for versatile photocatalytic applications. RSC Adv 4:12685–12700
90. Fujishima A, Rao TN, Tryk DA (2000) Titanium dioxide photocatalysis. J Photochem Photobiol C 1:1–21
91. Xiao F (2012) Self-assembly preparation of gold nanoparticles-TiO_2 nanotube arrays binary hybrid nanocomposites for photocatalytic applications. J Mater Chem 22:7819–7830
92. Zhang X, Han F, Shi B et al (2012) Photocatalytic conversion of diluted CO_2 into light hydrocarbons using periodically modulated multiwalled nanotube arrays. Angew Chem Int Ed 51:12732–12735

93. Li X, Liu H, Luo D et al (2012) Adsorption of CO_2 on heterostructure $CdS(Bi_2S_3)/TiO_2$ nanotube photocatalysts and their photocatalytic activities in the reduction of CO_2 to methanol under visible light irradiation. Chem Eng J 180:151–158
94. Feng X, Sloppy JD, LaTempa TJ et al (2011) Synthesis and deposition of ultrafine Pt nanoparticles within high aspect ratio TiO_2 nanotube arrays: application to the photocatalytic reduction of carbon dioxide. J Mater Chem 21:13429–13433
95. Varghese OK, Paulose M, LaTempa TJ et al (2009) High-rate solar photocatalytic conversion of CO_2 and water vapor to hydrocarbon fuels. Nano Lett 9:731–737
96. Roy SC, Varghese OK, Paulose M et al (2010) Toward solar fuels: photocatalytic conversion of carbon dioxide to hydrocarbons. ACS Nano 4:1259–1278
97. Beranek R, Tsuchiya H, Sugishima T et al (2005) Enhancement and limits of the photoelectrochemical response from anodic TiO_2 nanotubes. Appl Phys Lett 87:243114–243116
98. Roy P, Berger S, Schmuki P (2011) TiO_2 nanotubes: synthesis and applications. Angew Chem Int Ed 50:2904–2939
99. Zhang Z, Zhang L, Hedhili MN et al (2013) Plasmonic gold nanocrystals coupled with photonic crystal seamlessly on TiO_2 nanotube photoelectrodes for efficient visible light photoelectrochemical water splitting. Nano Lett 13:14–20. http://pubs.acs.org/doi/abs/10.1021/nl3029202
100. Ye M, Gong J, Lai Y et al (2012) High-efficiency photoelectrocatalytic hydrogen generation enabled by palladium quantum dots-sensitized TiO_2 nanotube arrays. J Am Chem Soc 134:15720–15723
101. Allam NK, Poncheri AJ, EI-Sayed MA et al (2011) Vertically oriented Ti–Pd mixed oxynitride nanotube arrays for enhanced photoelectrochemical water splitting. ACS Nano 5:5056–5066
102. Mor GK, Prakasam HE, Varghese OK et al (2007) Vertically oriented Ti-Fe-O nanotube array films: toward a useful material architecture for solar spectrum water photoelectrolysis. Nano Lett 7:2356–2364
103. Allam NK, Alamgir F, EI-Sayed MA (2010) Enhanced photoassisted water electrolysis using vertically oriented anodically fabricated Ti−Nb−Zr−O mixed oxide nanotube arrays. ACS Nano 4:5819–5826
104. Feng X, LaTempa T, Basham JI et al (2010) Ta_3N_5 nanotube arrays for visible light water photoelectrolysis. Nano Lett 2010(10):948–952

Chapter 6
Water Splitting By Photocatalytic Reduction

Xin Li and Jiaguo Yu

Abstract Water splitting by photocatalytic reduction is considered to be one of the most promising solutions to solve both the worldwide energy shortage and environmental pollution problems. Metal sulfide semiconductor photocatalysts as an important kind of photocatalysts have gained extensive interest in the field of photocatalytic H_2 evolution due to their superior photocatalytic activity under visible light irradiation. This chapter summarizes the integration and optimization of highly efficient metal sulfide-based semiconductors from a system engineering perspective. To achieve the optimum efficiency, several typical system integration strategies such as loading co-catalysts onto nanoscale metal sulfides, forming doped or nanosized solid solutions, developing core/shell and intercalated semiconductors, fabricating hybrid or multi-junction photocatalysts, and exploring new mechanisms beyond heterojunctions are outlined and discussed in detail. Further research should focus on the investigation of mechanism, the development of highly efficient co-catalysts and semiconductors, as well as the construction of multi-junction photocatalysts with high H_2-evolution activity. In this chapter, we not only provide a summary of system integration strategies of metal sulfides for solar water splitting but also may provide some potential opportunities for designing other types of heterogeneous photocatalysts used in solar water splitting.

Keywords Heterogeneous photocatalysts • Water splitting • Hydrogen production • Artificial photosynthesis • Photocatalytic water reduction

6.1 Introduction

It has been widely recognized that the shortage of energy supply and the disastrous environmental pollution are two main challenges within the next 50 years (see Fig. 6.1) [1,2]. According to estimation, nonrenewable fossil fuels including coal,

X. Li
College of Materials and Energy, South China Agricultural University, Guangzhou 510642, China

J. Yu (✉)
State Key Laboratory of Advanced Technology for Material Synthesis and Processing,
Wuhan University of Technology, Wuhan 430070, China
e-mail: jiaguoyu@yahoo.com

J.C. Colmenares, Y.-J. Xu (eds.), *Heterogeneous Photocatalysis*, Green Chemistry and Sustainable Technology, DOI 10.1007/978-3-662-48719-8_6

Fig. 6.1 The top ten problems mankind will face during the next 50 years according to Nobel laureate Richard Smalley

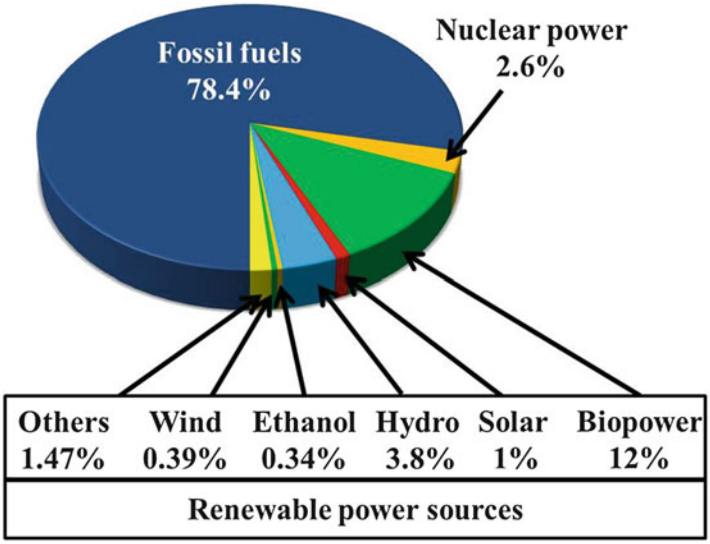

Fig. 6.2 World total primary energy supply 2004, shares of 11.2 billion tons of oil equivalent, or 470 EJ

oil, and gas account for ~80 % of the total global energy supply, as depicted in Fig. 6.2 [3]. Because of the depletion of fossil fuels, the serious environmental problems accompanying their combustion, and the rapid increase in the world total primary energy consumption, there is an urgent need to find clean, renewable, cheap, and sustainable energy sources to replace fossil fuels and satisfy the increased energy demands [4, 5]. During the past 40 years, some promising concepts based on methanol, ethanol, and hydrogen economics have been suggested [3, 6–8]. Among them, the carbon-free H_2, as one of the most attractive fuels in the future, has caused widespread concerns by scientists recently since it is environmentally friendly, economic, and green [9–11]. However, at present, hydrogen is mainly generated from fossil fuels by steam reforming of natural gas or the high-energy consumption process [12]. Thus, from the sustainability viewpoint, it is highly expected that hydrogen can be produced by a sustainable way, especially, using a source of renewable energy [11, 13].

Fortunately, the solar energy is safe, abundant, free, and clean [14, 15]. Thus, to effectively address the world energy problems, the efficient and inexpensive conversion of solar energy into fuels such as hydrogen has long been considered as one of the most desirable approaches to solve both solar energy store and green production of hydrogen fuel since Fujishima and Honda firstly discovered the photoelectrochemical (PEC) water splitting by using TiO_2 as a photoelectrode in 1972 [16]. The photocatalytic water splitting into H_2 and O_2 using solar energy and semiconductors is usually called artificial photosynthesis (APS) because these reactions are similar to those in the natural photosynthesis [5]. Typically, the APS is composed of H_2-evolution reaction (HER, photocatalytic water reduction) and O_2-evolution reaction (OER, photocatalytic water oxidation). It is known that the OER is quite complicated, which requires a four-electron oxidation of two water molecules coupled with the removal of four protons to form a relatively weak oxygen–oxygen bond [15]. Whereas, the two-electron HER is simpler and easier, which yields the desirable product of H_2. Thus, considerable efforts have been devoted to the study about water splitting by photocatalytic reduction.

So far, various heterogeneous [17–23] and homogeneous [24, 25] photocatalysts have been successfully explored and extensively applied in photocatalytic hydrogen production by water splitting over the past 40 years. Due to its simplicity and potential broad applications [20, 23, 26], the heterogeneous photocatalytic hydrogen generation has attracted more attention. In recent years, some major advances have also been made in the heterogeneous photocatalysts for water splitting by photocatalytic reduction, and many excellent reviews have been available [17–23]. More importantly, various visible light-driven photocatalysts (such as metal oxides [27–30], (oxy)sulfides [31–34], (oxy)nitrides [35–38], and metal-free C_3N_4 [39–43] and SiC [44–49]) have been found to achieve hydrogen production from photocatalytic water reduction in recent years. Among them, metal sulfide semiconductor materials have been considered as a type of promising candidate for photocatalytic water reduction due to their superior H_2-evolution activities under visible light irradiation. As compared to other kinds of photocatalysts, metal sulfides generally exhibit higher quantum efficiency (>30 %) for H_2 evolution at 420 nm. So far, the highest H_2-evolution quantum efficiency (about 93 % at 420 nm) has also been achieved in the Pt–PdS–CdS photocatalyst systems [50]. Recently, many great achievements in engineering heterogeneous metal sulfides for photocatalytic water reduction have been made, and a series of novel metal sulfides with the outstanding photocatalytic H_2-production performances have emerged. Although there are also several reviews or chapters regarding metal sulfide semiconductors for photocatalytic hydrogen production [33, 51], most of them paid particular attention to summarizing the advances on the basis of different isolated engineering strategies such as the composition or structure modification of metal sulfides and the construction of heterostructured semiconductors. However, from a systems engineering perspective, the overall H_2-evolution activities and stabilities of metal sulfide semiconductors are determined by the synergistic effect of all factors including co-catalyst, composition, structure, sacrificial reagent, and so on. So far, there is still no comprehensive review or chapter focusing on the integration and optimization of metal sulfide H_2-evolution photocatalysts through combining various types of engineering strategies (e.g., nanostructured design, earth-abundant co-catalyst loading, and heterojunction construction). Thus, in this chapter, we firstly systematically analyze the important factors influencing the H_2-evolution activity/stability of metal sulfides, then focus on the integration and optimization of metal sulfide-based semiconductors for water splitting by photocatalytic reduction. Through studying the systematic design of highly efficient metal sulfide semiconductors, it may open a new opportunity for developing highly effective and practical photocatalysts for photocatalytic H_2 evolution from water reduction, guided by a series of systems integration strategies.

6.2 Fundamentals in Photocatalytic Water Splitting

The multielectron water-splitting reaction is a typical uphill reaction ($\Delta G = 237.2$ kJ/mol, Eq. 6.1), which is composed of two half-reactions, the hydrogen evolution reaction (HER, Eq. 6.2) and oxygen evolution reaction (OER, Eq. 6.3). Clearly, hydrogen can be produced by photocatalytic water reduction. In terms of this reaction, solar energy can be transferred into chemical energy (H_2) during water splitting. It should be noted that the water oxidation (Eq. 6.3) as an accompany reaction is inevitable in the overall water-splitting systems. However, it can be suppressed in the presence of sacrificial reagents.

$$\begin{aligned} H_2O(l) \rightarrow H_2(g) + 1/2O_2(g), \Delta G &= 237.2 \ \text{KJ/mol} \Delta E^0 \\ &= 1.23\text{V} \end{aligned} \tag{6.1}$$

$$2H^+ + 2e^- \rightarrow H_2(g) \quad \Delta E^0 = -0.41\text{V} \tag{6.2}$$

$$2\ H_2O(l) \rightarrow O_2(g) + 4H^+ + 4e^- \quad \Delta E^0 = +0.82\text{V} \tag{6.3}$$

The fundamental principle for photocatalytic hydrogen production by water splitting has been extensively discussed in many excellent reviews [18–23, 52, 53], which was shown in Fig. 6.3. As depicted in Fig. 6.3, the electrons can be excited from the valence band (VB) to the conduction band (CB) of the semiconductor under light irradiation of suitable wavelengths, leaving holes in the VB. These electrons and holes can then transfer to the surface reaction sites of the photocatalysts and initiate the HER and OER, respectively. Therefore, to

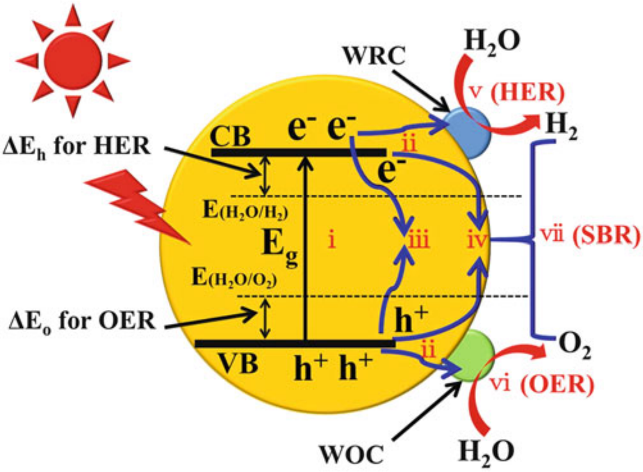

Fig. 6.3 Fundamental principle of semiconductor-based photocatalytic water splitting for hydrogen generation. *CB* conduction band; *VB* valence band; E_g bandgap; *OER* oxygen evolution reaction; *HER* hydrogen evolution reaction; *WRC* water reduction co-catalysts; *WOC* water oxidation co-catalysts; *SBR* surface back reaction; ΔE_o and ΔE_h kinetic overpotentials for OER and HER, respectively

achieve water reduction, the bottoms of the CB must be located at a more negative potential than the reduction potential of H^+ to H_2 (−0.41 V vs NHE at pH 7). Furthermore, the reduction potentials of water and CB levels of semiconductors at different pH values could be generally calculated according to Nernstian relation, i.e., shifting up by −0.059 V as the pH increases by 1, which has been reviewed on other reviews or articles [22, 54, 55].

Based on these parameters, it is clear that a good H_2-evolution photocatalyst must have suitable CB positions for water splitting by photocatalytic reduction. The band positions for a series of semiconductors and the redox potentials of water splitting in solution at pH = 7 are presented in Fig. 6.4. As shown in Fig. 6.4, the CB levels of most metal sulfides are much higher than the reduction potentials of water at pH 7. Therefore, in theory, these metal sulfides are capable of reducing water during the photocatalytic process. However, it is should be noted from Fig. 6.4 that the VB levels of most metal sulfides are also close to the water oxidation potentials, suggesting their weak water oxidation kinetics and strong photocorrosion. Therefore, sacrificial reagents are usually used to enhance the stabilities of these metal sulfides during photocatalytic water reduction.

In addition, the main processes in the overall photocatalytic water-splitting reaction are illustrated in Figs. 6.3 and 6.5. As shown in Fig. 6.3, overall water splitting on a semiconductor photocatalyst occurs in the following steps: (i) the generation of excited charge carriers (electron-hole pairs) in the semiconductor particles by light absorption; (ii) the separation of photoexcited carriers and their migration to the surface without recombination; (iii) the recombination of the excited charge carriers in the bulk; (iv), the recombination of the excited charge

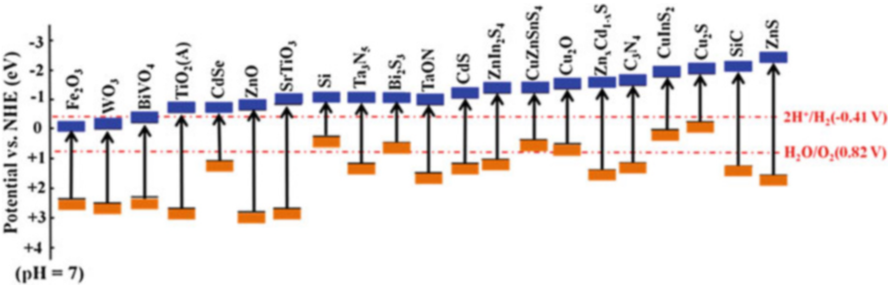

Fig. 6.4 Band positions for a series of semiconductors and the redox potentials of water splitting in solution at pH = 7

carriers on the surface; (v) and (vi) the trap of excited charge carriers on the surface by water oxidation and reduction co-catalysts and the driven surface chemical reactions; and (vii) the undesirable surface back reaction (SBR). For metal sulfides, the step (vii) does not take place due to the introduction of sacrificial reagents. Other six processes occur in unit cells, bulk phases, and surface phases, respectively. Thus, these processes can be divided into three stages, which are given in Fig. 6.5. It is clear that the overall efficiency for solar water splitting strongly depends on the balance of thermodynamics and kinetics of all processes in the three stages, which is influenced by the bulk and surface properties and electronic structure of a photocatalyst. Since most of metal sulfides have narrower bandgaps as compared to other kinds of semiconductors (see Fig. 6.4), the processes in the bulk and surface phases seem to be more important for enhancing the overall photocatalytic efficiency under visible light irradiation.

The important factors influencing the overall efficiency of metal sulfides for solar water reduction and the corresponding measures for enhancing their activities and stabilities are also summarized in Fig. 6.5. As shown in Fig. 6.5, to achieve these aims, some important factors influencing the overall efficiency of metal sulfides for solar water reduction should be comprehensively taken into account, such as improving the stability by sacrificial reagents, developing earth-abundant co-catalysts for H_2 evolution, designing nanoscale metal sulfides, and forming metal sulfide solid solutions for water splitting. Clearly, the processes in the bulk and surface phases must be synergistically optimized, thus the integration and optimization of metal sulfide-based semiconductors play key roles in achieving their high overall efficiency. The possible measures for enhancing their activities and stabilities, including loading co-catalysts onto nanoscale metal sulfides, forming doped or nanosized solid solutions, developing core/shell and intercalated semiconductors, fabricating hybrid or multi-junction photocatalysts, and exploring new mechanisms beyond heterojunctions, will be discussed in detail in the following sections.

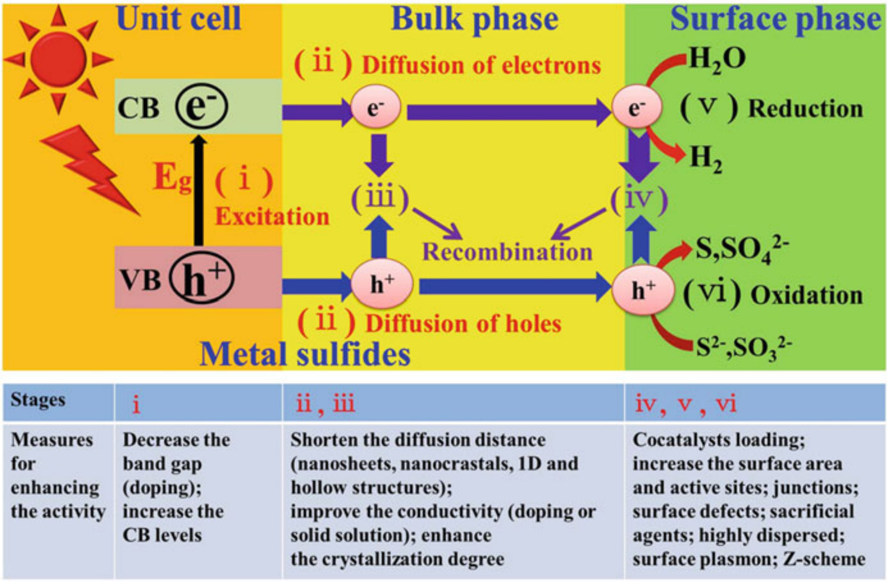

Stages	i	ii , iii	iv , v , vi
Measures for enhancing the activity	Decrease the band gap (doping); increase the CB levels	Shorten the diffusion distance (nanosheets, nanocrastals, 1D and hollow structures); improve the conductivity (doping or solid solution); enhance the crystallization degree	Cocatalysts loading; increase the surface area and active sites; junctions; surface defects; sacrificial agents; highly dispersed; surface plasmon; Z-scheme

Fig. 6.5 The stages in solar water splitting over metal sulfide and the corresponding measures for enhancing their activities and stabilities

6.3 Integration and Optimization of Metal Sulfide-Based Semiconductors

6.3.1 Loading Co-catalysts onto Nanoscale Metal Sulfides

In general, co-catalysts on the surface of metal sulfides could not only serve as surface electron traps to enhance the separation of the photogenerated electron–hole pairs but also provide surface reaction sites and decrease the activation energy for H_2 evolution, thus significantly improving the photocatalytic activity and selectivity for water reduction [22, 56, 57]. Meanwhile, as compared to the conventional bulk counterparts, semiconductor nanosized photocatalysts usually exhibit higher surface area, greater optical absorption, faster bulk diffusion, and less bulk recombination, thus improving transport properties and tunable electronic structure [58, 59] and allowing faster capture of the photogenerated charge carriers by solution species. All these factors are beneficial for solar H_2 fuel generation. Therefore, the coupling of co-catalysts and nanoscale metal sulfides can make full use of the advantages of nanostructured co-catalysts and semiconductors. As a result, loading co-catalysts onto nanoscale metal sulfides has become an integrated strategy to enhance the overall efficiencies of metal sulfide semiconductors for the photocatalytic water reduction.

In 1981, Graetzel and his coworkers demonstrated the first successful example on loading both Pt and RuO_2 co-catalysts onto CdS colloidal NCs for the cleavage of H_2O and H_2S [17, 60]. Since then, the coupling of appropriate electrocatalysts and metal sulfide NCs, as the most promising and simplest means for photocatalytic water splitting, has received a great deal of attention in the past decade. Some famous co-catalyst-loaded metal sulfides and their corresponding H_2-production activities have been summarized in Table 6.1. As shown in Table 6.1, Li's group successfully prepared CdS NPs with dual co-catalysts Pt (as a reduction co-catalyst) and PdS (as an oxidation co-catalyst), achieving the highest quantum yield of about 93 % in the presence of sacrificial reagents under visible light irradiation [50]. Here, the oxidation co-catalyst PdS also plays an important role in protecting CdS from photocorrosion due to the favorable hole transfer from CdS to PdS. This interesting result further verified that the synergistic effect of dual co-catalysts not only can greatly enhance the photocatalytic activity of CdS NPs for H_2 evolution but also can improve their stability [50]. So far, various H_2-evolution co-catalysts (e.g., Pt [61–69], Pt_3Co [70], Ni [71–76], NiS [77–80], NiS_2 [81], Ni_2P [82], NiO [83], CoO_x [84, 85], $Co(OH)_2$ [86], $Ni(OH)_2$ [79, 87, 88], Co_2P [89], MoS_2 [90, 91], WC [92], WS_2 [93], graphene [94–97], and CuS [98–100]) have been widely employed to enhance the photocatalytic H_2-production activity of nanoscale metal sulfides.

Among them, noble metals such as Pt and Au are the most widely used H_2-evolution co-catalysts. It is noted that many novel 1D CdS NRs and NWs, which have been successfully prepared by the solvothermal method, exhibit significantly enhanced photocatalytic H_2-production activity, due to the unique physical and chemical properties of 1D nanostructures [61, 64, 87, 101–105]. Interestingly, the H_2-production activity of 1D CdS NRs could be greatly enhanced through a very low Pt loading [101], which is strongly related to their nanoscale size and high dispersion of Pt clusters [64, 104]. Meanwhile, it was demonstrated that the enhanced H_2-evolution activities were achieved over Pt-loaded multiarmed CdS NRs and porous CdS nanosheet-based flowers [63, 65]. Furthermore, plasmonic Au as co-catalyst and sensitizer has been coupled with semiconductors to improve their H_2-evolution activity [69, 106–109]. Recently, an asymmetric Au–CdS plasmonic photocatalyst exhibited a much higher activity under visible light irradiation than the samples with a symmetrical core–shell structure due to improved localized surface plasmon resonance (LSPR) effects through controlling the fine structural configuration [106]. The results highlighted that the load of plasmonic metals in semiconductors played a critical role in achieving extremely strong local electric near fields. Therefore, it is expected that the H_2-evolution activity of metal sulfides with different nanostructures could be further improved through the loading of precisely controlled single noble metal and alloy NPs or the codecoration of different kinds of metal NPs [110–113].

However, the scarcity and high cost of noble metal-based H_2-evolution co-catalysts limit their practical applications in photocatalytic water reduction. Thereby, much attention has focused on the development and application of earth-abundant metal-based H_2-evolution co-catalysts. For instance, the earth-abundant Mo-, Co-, Ni-, and Cu-based co-catalysts have been successfully developed and

Table 6.1 Some famous co-catalyst-loaded metal sulfides for their H_2-production activities

Photocatalyst	Co-catalyst	Light source	Sacrificial reagent	Activity (μmol g^{-1} h^{-1})	AQY (%)	Ref. (year)
CdSe-seeded CdS nanorods (NRs)	Pt	300 W Xe	2-propanol	40,000	20(450 nm)	[61] (2010)
CdS nanostructures	Pt	>420 nm	$Na_2S + Na_2SO_3$	27,333	60(420 nm)	[62] (2007)
Multiarmed CdS NRs	Pt	≥420 nm	Lactic acid	24,200	51(420 nm)	[63] (2012)
Single-crystal CdS nanowires (NWs)	Pt	>420 nm	Lactic acid	18,625	61.7(420 nm)	[64] (2013)
Porous CdS nanosheet-based flowers	Pt	>420 nm	Lactic acid	9374	24.7(420 nm)	[65] (2013)
CdS nanocrystals (NCs)	Pt_3Co	≥420 nm	Lactic acid	15,890		[70] (2013)
Heterodimer Au/CdS NCs	Au	≥400 nm	$Na_2S + Na_2SO_3$	7300		[106] (2014)
CdS nanoclusters	RGO+ Pt	≥420 nm	Lactic acid	56,000	22.5(420 nm)	[94] (2011)
CdS	RGO+ Pt	≥420 nm	Lactic acid	29,861	50.7(420 nm)	[200] (2013)
CdS	Graphene + MoS_2	≥420 nm	Lactic acid	9000	28.1(420 nm)	[133] (2014)
CdS	RGO + MoS_2	UV–vis lamp	Lactic acid	6857		[134] (2014)
CdS nanoparticles (NPs)	Pt + PdS	>420 nm	H_2S-diethanolamine	~94,000	30 (420 nm)	[225] (2008)
CdS NPs	Pt + PdS	≥420 nm	$Na_2S + Na_2SO_3$	29,232	93 (420 nm)	[50] (2009)
CdS NRs	Co_3O_4	300 W Xe, ≥400 nm	$Na_2S + Na_2SO_3$	236		[84] (2015)
CdS NRs	$Co(OH)_2$	500 W Xe	Ethanol	61		[86] (2014)
CdS/TiO_2 NPs	CoO_x	300 W Xe, ≥400 nm	$Na_2S + Na_2SO_3$	660		[85] (2014)
CdS NPs	CoS	300 W Xe, ≥420 nm	Lactic acid	1050		[77] (2010)
CdS	MoS_2	300 W Xe, ≥420 nm	Lactic acid	~5400		[90] (2008)

(continued)

Table 6.1 (continued)

Photocatalyst	Co-catalyst	Light source	Sacrificial reagent	Activity (μmol g^{-1} h^{-1})	AQY (%)	Ref. (year)
CdSe-seeded CdS NRs	MoS_3	≥450 nm)	Triethanolamine	100,000	10(450 nm)	[226] (2011)
CdS NPs	WS_2	300 W Xe, ≥420 nm	Lactic acid	~4200	5.0(420 nm)	[93] (2011)
CdS NPs	WC	500 W Hg 420 nm	$Na_2S + Na_2SO_3$	1400		[92] (2008)
CdS NPs	NiS	300 W Xe, ≥420 nm	Lactic acid	7266	51.3(420 nm)	[77] (2010)
CdS NRs	NiS	300 W Xe, ≥420 nm	$Na_2S + Na_2SO_3$	1131	6.1(420 nm)	[78] (2013)
CdS NPs	NiO_X	300 W Xe, >400 nm	Methanol	5402	8.6(400 nm)	[83] (2014)
CdS NPs	Ni@C	≥420 nm	$Na_2S + Na_2SO_3$	6227	20.5(420 nm)	[227] (2013)
CdS NRs	$Ni(OH)_2$	≥420 nm	Triethanolamine	5084	28(420 nm)	[87] (2011)
CdS NRs	CuS	500 W Xe,	$Na_2S + Na_2SO_3$	332		[228] (2013)
CdS–titanate hybrid colloids	Ni	≥420 nm	Ethanol	11,038	21 (420 nm)	[71] (2013)
Nih-CdSe/CdS	$NiCl_2$	>400 nm	2-propanol	153,000	11.2(410 nm)	[229] (2013)
ZnS	CuS	≥420 nm	$Na_2S + Na_2SO_3$	4147	20 (420 nm)	[98] (2011)
$Zn_{0.5}Cd_{0.5}S$	CuS	≥420 nm	$Na_2S + Na_2SO_3$	4638.5	20.9(420 nm)	[99] (2013)
CdS QDs-$ZnIn_2S_4$	RGO+ Pt	≥420 nm	$Na_2S + Na_2SO_3$	27,000	56(420 nm)	[230] (2013)
$Zn_{0.8}Cd_{0.2}S$	RGO	AM1.5	$Na_2S + Na_2SO_3$	1824	23.4(420 nm)	[132] (2012)
$Zn_{0.8}Cd_{0.2}S$	$Ni(OH)_2$	≥420 nm	Triethanolamine	7160	29.5(420 nm)	[79] (2014)
$Zn_{0.8}Cd_{0.2}S$	NiS	≥420 nm	Triethanolamine	2507		[79] (2014)
$Zn_{0.8}Cd_{0.2}S$	Ni	≥420 nm	Triethanolamine	3242		[79] (2014)
$Zn_{0.2}Cd_{0.8}S$ NPs	MoS_2	≥420 nm	$Na_2S + Na_2SO_3$	420		[114] (2013)
$Zn_{0.5}Cd_{0.5}S$	RGO	≥400 nm	$Na_2S + Na_2SO_3$	21,200	19.8(420 nm)	[95] (2014)

$Zn_{0.5}Cd_{0.5}S$	NiS + RGO	AM-1.5	$Na_2S + Na_2SO_3$	7510	31.1(420 nm)	[80] (2014)
$Cd_{0.1}Zn_{0.9}S$	MWCNTs	≥420 nm	$Na_2S + Na_2SO_3$	1563.2	7.9(420 nm)	[130] (2012)
$ZnIn_2S_4$ microspheres	Pt	≥420 nm	$Na_2S + Na_2SO_3$	8420	34.3(420 nm)	[66] (2011)
Hierarchical $ZnIn_2S_4$	Pt	≥420 nm	$Na_2S + Na_2SO_3$	1150		[67] (2013)
$ZnIn_2S_4$	MoS_2	≥420 nm	$Na_2S + Na_2SO_3$	3060		[91] (2014)
$ZnIn_2S_4$ microspheres	MWCNTs	>420 nm		6840	23.3(420 nm)	[131] (2012)
$(Zn_{0.95}Cu_{0.05})_{0.5}Cd_{0.5}S$ NCs	Pt	≥420 nm	$Na_2S + Na_2SO_3$	3633	31.8(420 nm)	[231] (2008)
CdS QDs(3 wt%)-$ZnIn_2S_4$	RGO+ Pt	≥420 nm	$Na_2S + Na_2SO_3$	27,000		[230] (2013)
$ZnIn_2S_4$ microspheres	Pt + carbon QDs	≥400 nm	Triethanolamine	1032.2	2.2(420 nm)	[129] (2014)
Cu (0.5 wt%)-doped $ZnIn_2S_4$ microspheres	Pt	≥430 nm	$Na_2S + Na_2SO_3$	757.5	14.2(420 nm)	[232] (2008)
ZnS–$CuInS_2$–$AgInS_2$	Ru	AM-1.5	$Na_2S + K_2SO_3$	7677	7.4 (440–520 nm)	[32] (2005)
$Cu_{0.02}In_{0.3}ZnS_{1.47}$	RGO	800 W Xe, ≥420 nm	$Na_2S + Na_2SO_3$	3800		[96] (2013)
$CuIn_{0.3}Ga_{0.7}S_2$	Pt	300 W Xe	$Na_2S + Na_2SO_3$	1728		[68] (2014)
Cu_2ZnSnS_4 (CZTS)	Pt	300 W Xe	$Na_2S + Na_2SO_3$	1020		[69] (2014)
Au/CZTS core/shell NPs	Au	150 W Xe	$Na_2S + Na_2SO_3$	102		[107] (2014)

$$\text{AQY (apparent quantum yields, \%)} = \frac{N\text{umber of reacted electrons}}{N\text{umber of incident photons}} \times 100 = \frac{N\text{umber of evolved hydrogen molecules} \times 2}{N\text{umber of incident photons}} \times 100\,[22]$$

applied in enhancing the photocatalytic H_2-evolution activity over metal sulfides under visible light irradiation. For example, Li et al. found that a 36 times enhancement in activity for HER was achieved through the loading of MoS_2 onto CdS by an impregnation–sulfidation method due to the formation of heterojunction [90]. It was also demonstrated that $ZnIn_2S_4$ and $Zn_{0.2}Cd_{0.8}S$ loaded by MoS_2 can display obviously improved H_2-production activities, which are 10 and 210 times of that over bare samples under similar condition, respectively [91, 114]. Similarly, NiS and $Ni(OH)_2$ as co-catalysts have been found to efficiently enhance the H_2-evolution activities of CdS and $Zn_xCd_{1-x}S$ with different nanostructures [77–80, 87, 115]. Moreover, $Ni(OH)_2$ and NiS as H_2-generation co-catalysts have also been extended to the photocatalytic applications of water splitting over other types of semiconductors such as $g\text{-}C_3N_4$ and TiO_2 [116–120]. In the future, people are also expected to further enhance the activity of these earth-abundant co-catalysts through doping or optimizing their nanostructures [121, 122]. At this point, the explosive research on electrocatalytic water reduction may provide new insights into potential co-catalysts for photocatalytic water reduction [123].

In addition, the earth-abundant hydrogenases, biomimetic complexes, and graphene have also been extensively utilized as H_2-evolution co-catalysts of nanoscale metal sulfides. For example, the *Clostridium* acetobutylicum [FeFe]-hydrogenase I (CaI) could greatly enhance the H_2-evolution activity of CdS NRs [124], which were ascribed to the improved kinetics of electron transfer (ET) between light-absorbing CdS NRs and the [FeFe]-hydrogenase [125]. Recently, Li and his coworkers successfully demonstrated that the H_2-evolution activity of a ZnS semiconductor in water and DMF could be greatly improved by loading an $[Fe_2S_2]$ hydrogenase mimic ($[(\mu\text{-SPh-4-NH}_2)2Fe_2(CO)_6]$) as co-catalyst for H_2 evolution [126]. Furthermore, cobaloximes and Ni-based molecules were also extensively used to couple with the CdS semiconductors to construct the highly efficient composite system [127, 128]. In addition, earth-abundant carbon-based nanomaterials such as carbon quantum dots (QDs) [129], multiwalled carbon nanotubes (MWCNTs) [130, 131], and reduced graphene oxide (RGO) [95, 96, 132] have proven to be good co-catalysts for photocatalytic water reduction. For example, Yu and his coworkers found that a 4.5-fold enhancement in the photocatalytic H_2-evolution rate over $Zn_{0.8}Cd_{0.2}S$ could be achieved by loading 0.25 wt% RGO as co-catalysts [132], which is even higher than that of 1 wt% Pt-loaded $Zn_{0.8}Cd_{0.2}S$. It is believed that the introduction of RGO as a promising co-catalyst could effectively promote the transfer and separation of charge carriers, and increase the surface active sites of water reduction, thus leading to the greatly enhanced H_2-evolution rate. Surprisingly, the hybrid co-catalysts of RGO and Pt NPs could lead to a 4.87-fold enhancement in the H_2-evolution rate of CdS nanoclusters, due to the synergetic effects between graphene and supported co-catalysts such as Pt (see Fig. 6.6) [94]. In contrast, there are few reports about the preparation of the 2D–2D hybrid co-catalysts such as MoS_2–graphene and their applications in photocatalytic H_2 evolution [133–136]. Thus, anchoring suitable co-catalysts on graphene as composite co-catalysts may represent a promising direction to construct highly efficient H_2-evolution co-catalysts for nanoscale metal sulfides, deserving more attention in future studies [80, 137].

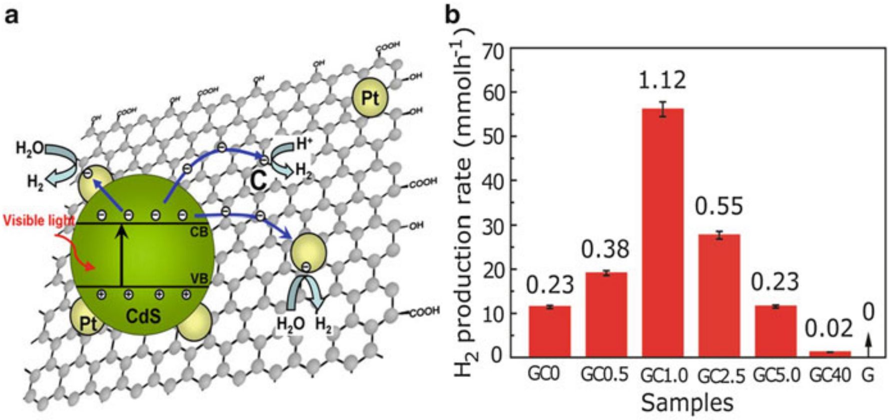

Fig. 6.6 (**a**) Schematic illustration for the separation and transfer of charge carriers in the graphene–CdS system under visible light, (**b**) comparison of the visible light photocatalytic activity of different samples (Reprinted with permission from Ref. [94]. Copyright 2011, American Chemical Society)

6.3.2 Forming Doped or Nanosized Metal Sulfide Solid Solutions

On the one hand, the forming solid solutions have been proven to be an effective strategy for enhancing transfer and separation efficiency of carriers and achieving improved photocatalytic H_2-production activity. The solid solutions not only can continuously tune the bandgap energy and CB potentials of multicomponent metal sulfide semiconductors via control of constituent stoichiometries [37, 138] but also can achieve high chemical stability, carrier mobility, and long carrier lifetime [59]. To date, a great variety of multicomponent metal sulfide semiconductors, such as $(AgIn)_xZn_{2(1-x)}S_2$ [31], $ZnS-CuInS_2-AgInS_2$ [32], $AgInZn_7S_9$ [139], $Zn_{1-x}Cu_xS$ [140, 141], $CdIn_2S_4$ [142], $Zn_xCd_{1-x}S$ [80, 95, 132, 143, 144], and $ZnIn_2S_4$ [33], have been available in photocatalytic water splitting. On the other hand, proper dopants not only can enhance the adsorption of visible light due to the formation of intermediate energy levels but also enhance the separation efficiency of photogenerated electron–hole pairs [20, 22, 145, 146]. Thus, the photocatalytic activity of doped semiconductor is significantly improved. As a result, forming doped or nanosized metal sulfide solid solutions could lead to a further improvement in the H_2-evolution activity of metal sulfide solid solutions due to the integrative effect of different engineering strategies; some representative results are summarized in Table 6.2.

To further enhance the visible light utilization of the metal sulfide solid solutions for hydrogen evolution, doping of metal sulfide solid solution with transition or alkaline metal ions has been extensively explored recently. As shown in Table 6.2, the metal sulfide solid solutions doped by Cu [147, 148], Ni [149, 150], Ag [151], Sn [152], and Bi [153] ions have been found to exhibit higher photocatalytic

Table 6.2 Comparison of some doped or nanosized metal sulfide solid solutions for their H_2-production activities

Photocatalyst	Light source	Sacrificial reagent	Activity (μmol g^{-1} h^{-1})	AQY (%)	Ref. (year)
CdS–ZnS core–shell	>400 nm	Na_2S + Na_2SO_3	792		[174] (2014)
$Zn_{0.5}Cd_{0.5}S$ NPs	≥400 nm	Na_2S + Na_2SO_3	7420	9.6 (420 nm)	[143] (2013)
$Cd_{0.5}Zn_{0.5}S$ anisotropic NRs	≥430 nm	Na_2S + Na_2SO_3	25,800	62(425 nm)	[157] (2013)
Twinned $Cd_{0.5}Zn_{0.5}S$ NCs	≥430 nm	Na_2S + Na_2SO_3	17,900	43(425 nm)	[156] (2011)
Cu_2ZnSnS_4 nanosheets	500 W Xe	Na_2S + Na_2SO_3	1500		[233] (2012)
Cu_3SnS_4 microspheres	300 W Xe	Na_2S + Na_2SO_3	1100	3.9 (420 nm)	[160] (2013)
$Mn_{0.24}Cd_{0.76}S$ NPs	≥420 nm	Na_2S + Na_2SO_3	10 900	9.5 (420 nm)	[234] (2014)
Ni(4 %)–$Cd_{0.1}Zn_{0.9}S$	≥420 nm	Na_2S + Na_2SO_3	404	14.36 (420 nm)	[149] (2012)
Ni(4 %)–$Zn_{0.4}Cd_{0.6}S$	≥420 nm	Na_2S + Na_2SO_3	18,820	22.8 (420 nm)	[150] (2012)
Bi(0.10 mol%)–$Cd_{0.5}Zn_{0.5}S$	≥420 nm	Na_2S + Na_2SO_3	559	9.71 (420 nm)	[153] (2012)
$Zn_{0.5}Cd_{0.5}S$ NRs	≥420 nm	Na_2S + Na_2SO_3	10,970	30.4 (420 nm)	[235] (2011)
1D cubic $Cd_{0.8}Zn_{0.2}S$ NWs	>400 nm	Na_2S + Na_2SO_3	157		[236] (2015)
$(CuIn)_{0.2}Zn_{1.6}S_2$ NCs	>420 nm	Na_2S + Na_2SO_3	984		[237] (2012)
$CdIn_2S_4$	≥420 nm	KOH (H_2S)	6960	17.1 (500 nm)	[142] (2006)
$Cd_{0.1}Sn_{0.01}Zn_{0.88}S$	500 W Hg	Na_2S + Na_2SO_3	17,600		[152] (2011)
Cu(5 %)-doped $Cd_{0.1}Zn_{0.9}S$	500 W Xe	Na_2S + Na_2SO_3	21,850		[147] (2012)
Cu(1 %)/$In_{1.4}Zn_{0.9}S_3$	≥420 nm	Na_2S + Na_2SO_3	4380		[148] (2013)
La(1.0 wt%)/$ZnIn_2S_4$	>420 nm	Na_2S + Na_2SO_3	583.4	8.83 (420 nm)	[238] (2015)
$Cd_{0.8}Zn_{0.2}S$	>430	Na_2S + Na_2SO_3	850	10.23 (420 nm)	[239] (2007)
Ba-doped $Cd_{0.8}Zn_{0.2}S$ NPs	>430	Na_2S + Na_2SO_3	700	17.4 (425 nm)	[154] (2011)
Sr-doped CdS · ZnS NPs	>430	Na_2S + Na_2SO_3	500		[155] (2010)

(continued)

Table 6.2 (continued)

Photocatalyst	Light source	Sacrificial reagent	Activity (μmol g^{-1} h^{-1})	AQY (%)	Ref. (year)
Ag–$ZnIn_{1.5}S_{3.2575}$ + Ru	≥420 nm	Na_2S + Na_2SO_3	3200		[151] (2014)
$Cd_{0.44}Zn_{0.56}S$	≥420 nm	Na_2S + Na_2SO_3	2640		[240] (2010)
$Cd_{0.8}Zn_{0.2}S$/SBA-15	≥420 nm	Na_2S + Na_2SO_3	972		[165] (2012)
$Cd_{0.8}Zn_{0.2}S$/SBA-16	≥420 nm	Na_2S + Na_2SO_3	1420		[166] (2013)
Hierarchical $Cd_{0.2}Zn_{0.8}S$	≥420 nm	Na_2S + Na_2SO_3	1800		[241] (2013)
$Cd_{0.57}Zn_{0.43}S$ nanospheres	≥420 nm	Na_2S + Na_2SO_3	1766.4		[242] (2014)

activity for hydrogen production than the undoped ones. It is believed that the impurity levels in the forbidden band created by doping can enhance the visible light response and accommodate the photogenerated charge carriers, thus leading to the enhanced hydrogen evolution. More interestingly, Guo and his coworkers verified that the alkaline metal ion doping (such as Ba and Sr) could be used to dramatically enhance the photocatalytic activities of $Cd_{1-x}Zn_xS$ NCs [154, 155]. It is suggested that the alkaline metal ions on the surface are beneficial for the separation and migration of photoinduced carriers, thus resulting in the improved photocatalytic activities. Consequently, as a potential modification strategy, transition or alkaline metal ion doping deserves more attention in optimizing the performances of metal sulfide semiconductors for water splitting.

Besides doping, constructing nanosized metal sulfide solid solutions has also been found to be an effective strategy to improve photocatalytic activity for water splitting, due to efficient separation and fast transport of the photogenerated carriers achieved by unique nanosized structures. For example, Guo's group constructed the spherical $Cd_{0.5}Zn_{0.5}S$ photocatalysts by precipitate–hydrothermal method ($Cd_{0.5}Zn_{0.5}S$–PH, see Fig. 6.7a, b). The results revealed that the existence of twin structure in solid solutions can significantly improve the transport and separation of charge carriers, thus achieving an extremely high visible light H_2-evolution rate of 1.79 mmol h^{-1} without noble metal co-catalysts, with an extremely high AQY (= 43 %) at 425 nm [156]. It is believed that the "back to back" potential with an anisotropy in photocatalysts can efficiently suppressed the recombination of photogenerated electrons and holes, thus boosting the photocatalytic activity (see Fig. 6.7c). More interestingly, they also found that an AQY of 62 % for solar hydrogen evolution can be achieved over a twin-induced one-dimensional $Cd_{0.5}Zn_{0.5}S$ NR homojunctions, without noble metal loading, because of the efficient transport and separation of photogenerated charge carriers [157]. The results further indicated that the construction of photocatalyst with long-range ordered homojunctions at the

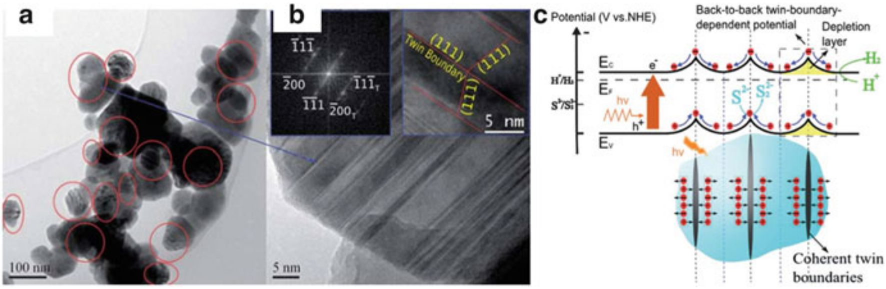

Fig. 6.7 (**a**) TEM images of the $Zn_{0.5}Cd_{0.5}S$–PH solid solution (The unique nanotwin structures are marked in *red circles*); (**b**) HRTEM image at the area of *red circle*; (**c**) the migration of free charges and photocatalytic hydrogen production from aqueous solution over nanotwin $Cd_{0.5}Zn_{0.5}S$-PH crystals (Reprinted with permission from Ref. [156]. Copyright 2011, Royal Society of Chemistry)

nanoscale is a powerful strategy to enhance the photocatalytic activity and stability for water splitting. In another example, Zhang and his coworkers developed two-dimensional (2D) porous $Zn_{0.5}Cd_{0.5}S$ nanosheets through the intermediates of the inorganic–organic hybrid semiconductor sheets (see Fig. 6.8a) [158]. The as-prepared porous nanosheets exhibit the highest H_2-production rate, 1.67 $mmolh^{-1}g^{-1}$, which was 2.5 times higher than that over the $Zn_{0.5}Cd_{0.5}S$ solid solution NRs (see Fig. 6.8b). Thus, the development of sulfide solid solution nanosheets represents a promising direction to enhance their photocatalytic H_2-evolution activity.

In addition, the 3D hierarchical metal sulfide solid solution microspheres such as nanoflowers have attracted much attention and been widely applied in the fields of photocatalytic H_2 evolution. For example, the reported 3D flowerlike metal sulfide nanostructures such as $CuInS_2$ [159], $ZnIn_2S_4$ microspheres [66, 131], CdS [65], Cu_3SnS_4 [160], and $AgGa_{1-x}In_xS_2$ [160] exhibited enhanced photocatalytic activity for photocatalytic hydrogen generation from water splitting. It was demonstrated that flowerlike morphology is important for the excellent photocatalytic activity and stability because of enhanced visible light harvesting and promoted charge separation. In addition, the combined effects of several factors including large surface area, more accessible reaction sites in mesopores, and the suitable bandgap size and band positions are also beneficial for the enhancement in the photoactivity of the hierarchical nanoflowers.

In general, most of doped or nanosized metal sulfide solid solutions could be synthesized by soft chemistry routes; however, their low surface areas seriously limit the enhancements in activity. The preparation of high surface area samples with mesoporous structures and exposed surface sites is still a great challenge and highly desired [161]. At this end, research efforts should be directed at constructing 2D nanosheets and nanoporous structures of metal sulfide solid solutions [158, 162–164]. In addition, the surface areas of metal sulfide solid solutions can be enhanced by loading them into the porous materials such as microporous and mesoporous silicas [165–167].

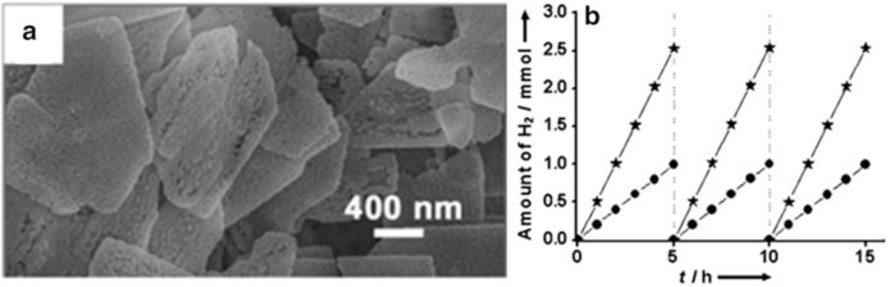

Fig. 6.8 (**a**) SEM image of the nanoporous $Zn_{0.5}Cd_{0.5}S$ nanosheets, (**b**) time course of evolved H_2 under irradiation of visible light for the as-prepared $Zn_{0.5}Cd_{0.5}S$ porous nanosheets (★) and $Zn_{0.5}Cd_{0.5}S$ NRs (●) (Reprinted with permission from Ref. [158]. Copyright 2012, WILEY-VCH Verlag GmbH & Co. KGaA Weinheim)

6.3.3 Developing Core/Shell and Intercalated Semiconductors

Recently, core–shell nanocomposite photocatalysts as highly integrated systems have also drawn much attention due to their unique properties and promising applications in environmental and clean energy areas [168–171]. Generally, the shell layers could tune the light transmission capacity, enhance adsorption capacity of reactants, and favor the separation of photogenerated charge carriers [168, 170]. More importantly, the stability of metal sulfides can also be enhanced greatly by the loading of shell layers due to the significant passivation effects [171, 172]. All these factors are favorable for photoactivity enhancement of metal sulfides in the water splitting.

The hierarchical core–shell metal sulfide nanoarchitectures present an important candidate for the application in photocatalytic H_2 evolution. For instance, the enhanced H_2-evolution activity was observed in the core–shell structured CdSe/CdS [173] or CdS/ZnS [172, 174] system due to the passivation effects of shell layer. Recently, Cheng et al. demonstrated that the mesoporous ZnS shell in the hierarchical CdS–ZnS core–shell particles can promote the unique spatial distribution of the photoexcited charge carriers and thus greatly enhance the hydrogen evolution rate, which is 169 and 56 times higher than those of ZnS and CdS under visible light, respectively [174]. Moreover, the core–shell particles exhibit excellent photocatalytic stability over 60 h. For this core/shell system, the mesoporous shell and spatial separation of photoexcited charge carriers on the interface of core and shell are responsible for the enhanced activity and stability in the photocatalytic hydrogen evolution from water under visible light (as Fig. 6.9) [174]. Here, it is believed that the acceptor states above the VB of ZnS such as zinc vacancies (V_{Zn}) and interstitial sulfur (I_S) may be beneficial for the transfer of photoexcited holes from the CdS core to the ZnS shell, thus leading to the enhanced photocatalytic stability. Therefore, as an efficient strategy, surface passivation should be taken into

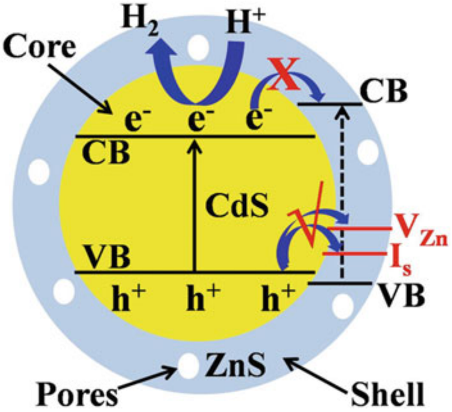

Fig. 6.9 Band structure alignments of the CdS–ZnS core–shell structure and schematic of the photoexcited charge carrier distribution

consideration seriously in optimizing the stability and activity of metal sulfide photocatalysts for water splitting.

Besides 0D core–shell nanoheterostructures, 1D core–shell metal sulfides also deserve more attention [175]. For example, Zhang et al. constructed novel CdS/g-C_3N_4 core/shell NWs with different g-C_3N_4 contents by a combined solvothermal and chemisorption method (see Fig. 6.10a–c) [176]. An optimal photocatalytic activity of up to 4152 μmol h^{-1} g^{-1} could be achieved at the g-C_3N_4 content of 2 wt%. Furthermore, a CdS/g–C_3N_4 core/shell configuration also exhibits excellent photostability. It is believed that the well-matched band energy alignment between g-C_3N_4 and CdS could achieve the synergic effect, which can effectively accelerate the transfer of corrosive holes in CdS to robust C_3N_4, thus greatly enhancing the photocatalytic activity and photostability of CdS [176].

Recently, Amirav et al. constructed a multicomponent 1D core–shell nanoheterostructure for photocatalytic hydrogen production, which is composed of a Pt-tipped CdS rod with an embedded CdSe seed [61]. In such a three-component structure (see Fig. 6.11), the holes will be confined to the CdSe core, while electrons are transferred to the Pt due to their matching energy band, thus achieving significantly increased hydrogen production activity due to the efficient separation of holes and electrons. An apparent quantum yield of 20 % at 450 nm could be obtained by tuning the length of CdS rod and the size of an embedded CdSe seed [61]. In another novel system using 3-mercaptopropionic acid (MPA) as the sacrificial hole acceptor, an internal quantum yield of 13.6 ± 1.0 % was estimated for CdSe/CdS dot-in-rod NRs [177].

In addition, constructing intercalated metal sulfide semiconductors has also been considered as a promising strategy to improve their photocatalytic stability and photoactivity. For example, Shangguan et al. demonstrated that the photocatalytic activities of CdS-intercalated metal oxides for hydrogen evolution were much higher than those of CdS alone or a physical mixture between them [178, 179]. Other metal sulfides have also been widely intercalated into the interlayers of some lamellar compounds such as double hydroxide and titanium- and

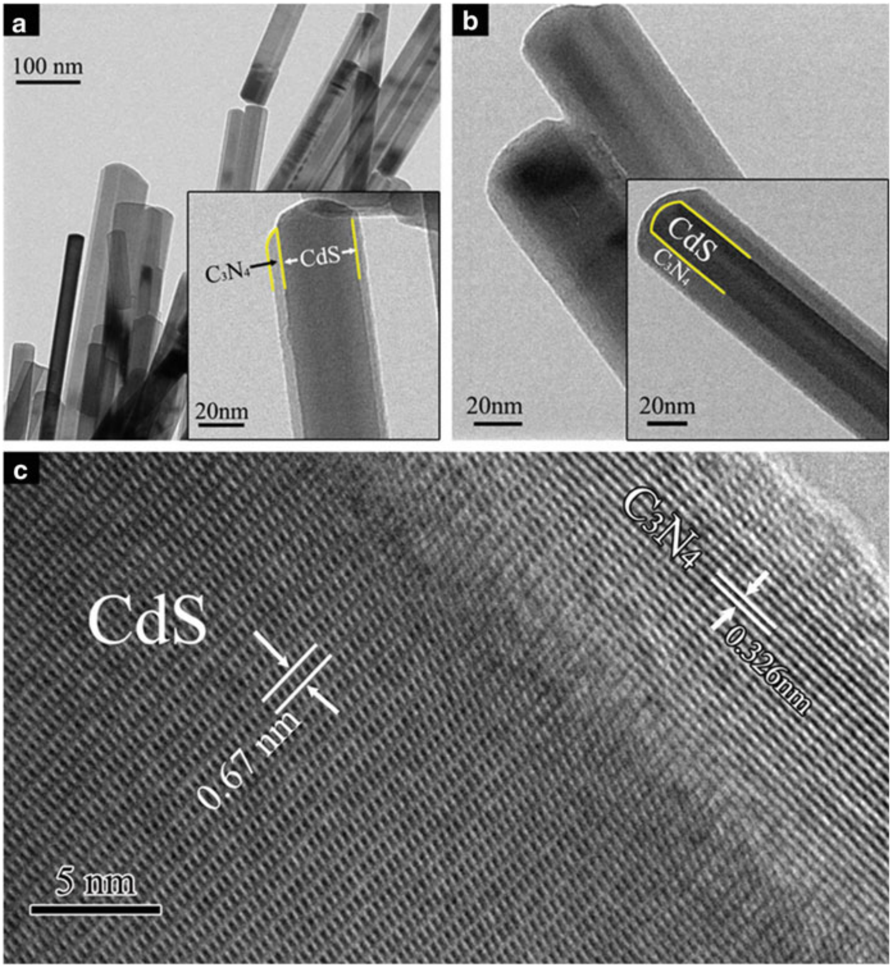

Fig. 6.10 TEM (**a**, **b**) and HRTEM (**c**) images of CdS/g–C_3N_4 core/shell NWs CN2 (**a**) and CN_4 (**b**, **c**) fabricated via a two-step self-assembly procedure. A given amount of g-C_3N_4 was grounded to fine powder and then added into 25 mL methanol. After ultrasonically treated for 30 min, bulk g-C_3N_4 was exfoliated into thin sheets and disintegrated into a homogeneous suspension. Then, CdS NWs were dispersed in the suspension and stirred at room temperature for 24 h. The residual methanol was removed by a stream of nitrogen. The obtained yellow solid was collected and dried in a vacuum oven at 60 °C. The nominal weight ratios of g-C_3N_4 to CdS were 2 and 4 wt%, and the samples were labeled as CN_2 and CN_4, respectively (Reprinted with permission from Ref. [176]. Copyright 2013,American Chemical Society)

niobium-based lamellar perovskite [180–182]. Typically, the photogenerated electrons from nanosized metal sulfides could be quickly transferred to the layered materials, which could efficiently suppress the recombination of photogenerated charge carriers, thus leading to significantly enhancing the stability and activity of sulfides.

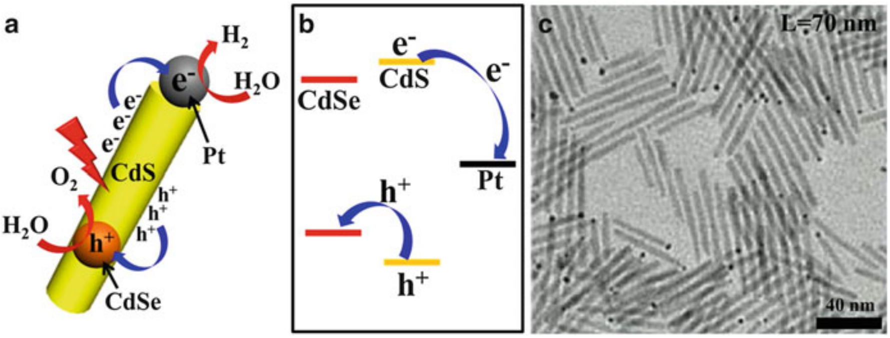

Fig. 6.11 An illustration of the multicomponent nanoheterostructures (**a**) and their energy band diagram (**b**); (**c**) TEM images of Pt-tipped seeded rods with an average length of 70 nm (Reprinted with permission from Ref. [61]. Copyright 2010,American Chemical Society)

6.3.4 Fabricating Hybrid or Multi-junction Photocatalysts

The integration of metal sulfide and other nanomaterials with different dimensions to form hybrid or multi-junction photocatalysts has been proven to be a powerful strategy for achieving enhanced photocatalytic H_2-production performance under visible irradiation. So far, many low-dimensional hybrid photocatalysts such as 0D–1D [183–185], 0D–2D [186–189], 1D–1D [190], 1D–2D [191–197], and 2D–2D [163, 164, 198, 199] have been constructed and applied in environmental and clean energy areas. Here, we focus on the 0D–2D and 2D–2D hybrids and multi-junction photocatalysts.

In general, the hybrids of 0D NPs and 2D nanosheets could efficiently suppress the aggregation and overgrowth of NPs, increase the surface area and the number of surface active sites, and reduce the bulk recombination of photogenerated e^-–h^+ pairs, thus greatly improving the photoactivity of 0D–2D hybrids. For example, the hybrids of CdS NCs or quantum dots with the 2D graphene [94, 200], g-C_3N_4 [201], MoS_2 [200, 202, 203], TiO_2 [204, 205], and titanate nanosheets [206] exhibited greatly promoted H_2-evolution activity due to the enhanced transfer and separation rate of photogenerated charge carriers. Furthermore, Zhang et al. also demonstrated that H_2-evolution rates of $Zn_xCd_{1-x}S$ could be greatly enhanced by coupling with the 2D graphene [80, 132]. Especially, when NiS was further introduced into the binary $Zn_xCd_{1-x}S$/RGO nanocomposites, ternary hybrids will be constructed (as Fig. 6.12a). As a result, the ternary nanocomposites exhibited a greatly enhanced solar photocatalytic H_2-production activity due to the positive synergetic effect of NiS and RGO over $Zn_xCd_{1-x}S$ (as Fig. 6.12a, b). It is believed that the creation of p–n junction region between NiS and CdS could efficiently achieve the transport of photogenerated holes from CdS to NiS, thus inhibiting the serious photocorrosion of CdS. This result implies that constructing multi-junction photocatalysts based on 0D–2D hybrids is also a promising direction to enhance the photocatalytic activity of metal sulfides [94, 136, 200].

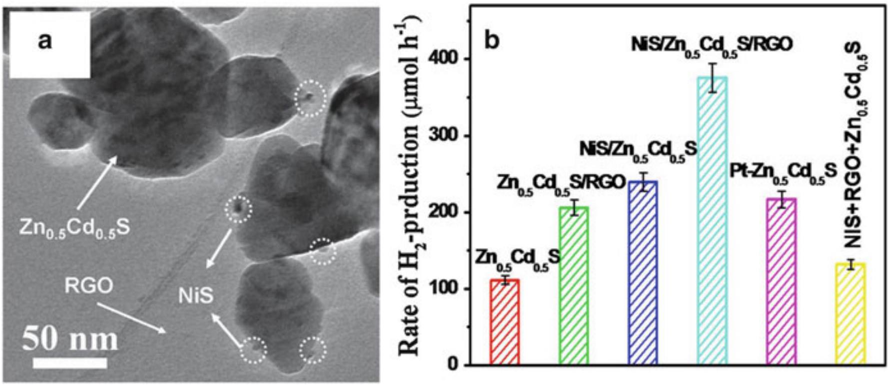

Fig. 6.12 (**a**) TEM image of the NiS/Zn0.5Cd0.5S/RGO composite, (**b**) comparison of the photocatalytic H_2-production activity under simulated solar irradiation over different samples (Reprinted with permission from Ref. [80]. Copyright 2014, WILEY-VCH Verlag GmbH & Co. KGaA Weinheim)

Besides 0D–2D hybrids, the hybrids between 2D and 2D nanosheets are also promising candidates for conducting high-performance photocatalysts for photocatalytic hydrogen evolution from water splitting due to their excellent properties. The unique 2D layered composite photocatalysts have many advantages such as increased contact surface, highly exposed active edge sites, and enhanced electron and hole transfer rate [207, 208]. For example, the efficient MoS_2–g-C_3N_4 composite photocatalyst with facet coupling could be constructed by in situ sulfidation or impregnation method, since MoS_2 co-catalysts and g-C_3N_4 semiconductors have similar 2D layered structures and matching energy band positions (see Fig. 6.13a, b) [208, 209]. It was found that the H_2-evolution activity of 0.5 wt% MoS_2/g-C_3N_4 was better than that over 0.5 wt% Pt/mpg-CN under the same reaction conditions [208], suggesting that 2D–2D coupling played an important role in promoting the photoactivity of MoS_2/g-C_3N_4. Recently, the 2D–2D junctions between MoS_2 and reduced graphene oxide (RGO) was extensively investigated; thus it is expected that the highly efficient multi-junction photocatalysts based on MoS_2–RGO 2D–2D hybrid could be deeply developed and applied in the photocatalytic H_2-evolution reaction [133, 134, 191, 210, 211].

6.3.5 Exploring New Mechanisms Beyond Heterojunctions

It is known that forming heterojunctions between CdS and other semiconductors such as TiO_2 and C_3N_4 could efficiently promote the separation of photogenerated charge carriers, thus significantly enhancing the photocatalytic activities in environmental and clean energy areas [176, 185, 212–214]. Recently, a new and interesting concept of an all-solid-state Z-scheme composed of a CdS/Au/TiO_2 nanojunction was first presented by Tada et al., in which the CdS (reduction site),

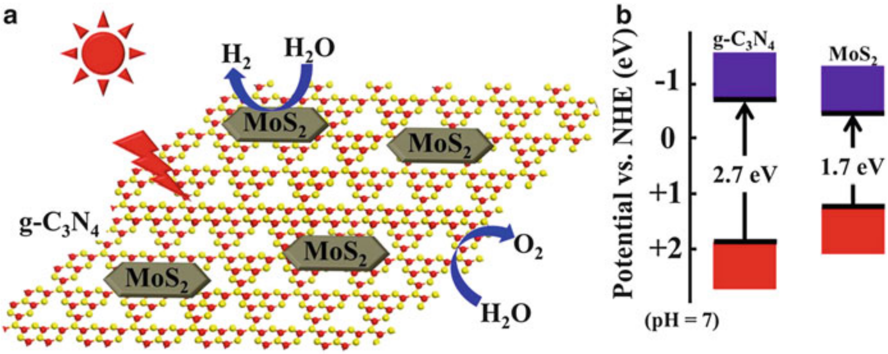

Fig. 6.13 (**a**) The structural model of the MoS_2/g-C_3N_4 layered junctions, (**b**) band energy diagrams for g-C_3N_4 and thin MoS_2

Fig. 6.14 Schematic diagram of electron transfer of the all-solid-state Z-scheme CdS–Au–TiO_2 system

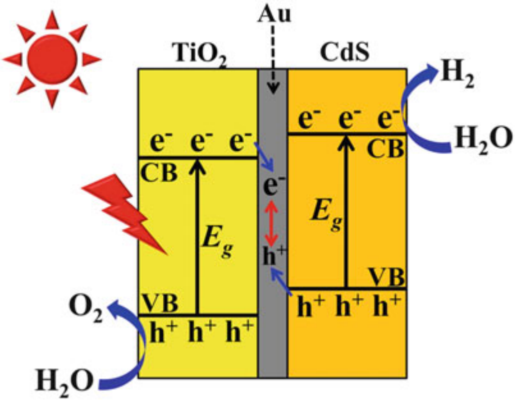

TiO_2 (oxidation site), and the interconnect Au are spatially fixed [215]. This three-component system exhibits a high photocatalytic activity, far exceeding those of the single- and two-component systems, as a result of vectorial electron transfer driven by the two-step excitation of TiO_2 and CdS. The proposed energy diagram is shown in Fig. 6.14. Similarly, an improved CdS/Au/$TiO_{1.96}C_{0.04}$ solid-state Z-scheme system was developed, and the H_2-evolution activity over it was about 4 times higher than that of CdS/Au/TiO_2 under visible light irradiation [216]. In another example, the plasmonic Au was introduced into the interface between TiO_2 and CdS, thus leading to the formation of the interfacial Schottky barrier, which greatly increases the transfer lifetime of charge carriers, reduces the trap-state Auger rate, suppresses the long-timescale back transfer, and partially compensates the negative effects of the surface trap states [217]. More importantly, in these Z-scheme photocatalysts, the photogenerated holes from CdS could efficiently recombine with the electrons from TiO_2 with low reduction ability, leaving the high-energy electrons of CdS for water reduction. Consequently, the enhanced photocatalytic activity and stability could be obtained in the Z-scheme systems.

Besides CdS/Au/TiO_2 systems, other Z-scheme photocatalysts such as sulfide/graphene/TiO_2 [218], CdS/ZnO [219–222], CdS/SiC [223], and CdS/WO_3 [224] have also been successfully constructed, all of which exhibited great enhancements in the photocatalytic H_2-evolution activity. As compared to the semiconductor heterostructures, more powerful photogenerated electrons and holes in the direct Z-scheme systems are used to perform the photocatalytic H_2 and O_2 evolution, respectively, thus achieving enhanced activities for solar water splitting [22]. In the future, the stability and activity of semiconductors in Z-scheme water-splitting systems should be further improved by loading suitable co-catalysts.

6.4 Conclusion and Prospective

In summary, this review highlights the integrated systems for the modification of heterogeneous metal sulfide photocatalysts used in the fields of solar water splitting. Over the past decade, many different design strategies for the integration of systems listed above have been successfully designed and applied in enhancing efficiencies of heterogeneous photocatalysts for solar water splitting. Although some significant advances have been achieved in the recent years, the H_2-evolution rates of the metal sulfides are rather low and are far from practical application. Therefore, many underlying mechanisms limiting the activity of metal sulfides still need to be clarified in the future.

The new, cheap, robust, efficient, and stable metal sulfide photocatalysts and co-catalysts should be further designed and developed in the near future. Although the $Cd_{1-x}Zn_xS$ solid solution photocatalysts seem to be very promising, their poor stability, high toxicity, and complicated synthesis methods should be further improved. Meanwhile, new photocatalysts with good visible light absorption (1.8–2.4 eV), especially for the solid solutions, should be further designed and developed. For co-catalysts, the earth-abundant co-catalysts (such as MoS_2, CuS_x, WS_2 and NiS) have proven to be efficient in the photocatalytic and photoelectrocatalytic performance, which are also favorable for the mechanism study of solar water splitting. The electrocatalysts for H_2 and O_2 evolution can serve as co-catalysts for water splitting, which should be deeply studied and developed.

Many sulfide photocatalysts generally suffer from photocorrosion in aqueous electrolytes due to the oxidation of themselves by photogenerated holes, which is one of the most fundamental problems that limit the lifetime of all nonoxide photocatalysts. Therefore, the photostability of the semiconductor should be carefully improved to prevent corrosion in the practical application. Thus, highly efficient sacrificial agents should be further developed. New modification strategies to enhance their stabilities and new co-catalysts are still highly expected. However, the systems using sacrificial reagents cannot achieve overall water splitting. It is a great challenge to achieve the overall water splitting and separating water oxidation and reduction processes on the surface of semiconductor nanoparticles. At this point, the Z-scheme water-splitting photocatalysts seem to be a more promising strategy among various other routes due to the separation of the two half-reactions. In addition, the multi-junction photocatalysts should be paid more attention because the combination of different engineering strategies theoretically has the ability to give a higher optimum photocatalytic efficiency and stability.

Besides experimental investigations, the first-principle DFT calculations are also encouraged since they can reveal the actual interaction mechanism at molecular levels. It is believed that substantial breakthroughs will be achieved when photocatalyst materials are well designed and photocatalysis mechanism will be deeply addressed in the near future through more fundamental interdisciplinary researches, including chemistry, energy, environment, physics, materials, and engineering.

Acknowledgment J. Yu would like to thank the 973 program (2013CB632402), and NSFC (51272199, 51320105001 and 21433007) and X. Li would like to thank NSFC (20906034), and industry and research collaborative innovation major projects of Guangzhou (201508020098) and the State Key Laboratory of Advanced Technology for Material Synthesis and Processing (Wuhan University of Technology) (2015-KF-7) for their support.

References

1. Gratzel M (2005) Mesoscopic solar cells for electricity and hydrogen production from sunlight. Chem Lett 34:8–13
2. Gratzel M (2001) Photoelectrochemical cells. Nature 414:338–344
3. Goldemberg J (2007) Ethanol for a sustainable energy future. Science 315:808–810
4. Marszewski M, Cao S, Yu J, Jaroniec M (2015) Semiconductor-based photocatalytic CO_2 conversion. Mater Horiz 2:261–278
5. Li X, Wen J, Low J, Fang Y, Yu J (2014) Design and fabrication of semiconductor photocatalyst for photocatalytic reduction of CO_2 to solar fuel. Sci China Mater 57:70–100
6. Olah GA (2005) Beyond oil and gas: the methanol economy. Angew Chem Int Ed 44:2636–2639
7. Balat M, Balat H (2009) Recent trends in global production and utilization of bio-ethanol fuel. Appl Energy 86:2273–2282
8. Barreto L, Makihira A, Riahi K (2003) The hydrogen economy in the 21st century: a sustainable development scenario. Int J Hydrog Energy 28:267–284
9. Turner JA (2004) Sustainable hydrogen production. Science 305:972–974
10. Schlapbach L, Zuttel A (2001) Hydrogen-storage materials for mobile applications. Nature 414:353–358
11. Turner JA (1999) A realizable renewable energy future. Science 285:687–689
12. Navarro RM, Peña MA, Fierro JLG (2007) Hydrogen production reactions from carbon feedstocks: fossil fuels and biomass. Chem Rev 107:3952–3991
13. Nielsen M, Alberico E, Baumann W, Drexler HJ, Junge H, Gladiali S, Beller M (2013) Low-temperature aqueous-phase methanol dehydrogenation to hydrogen and carbon dioxide. Nature 495:85–89
14. Lewis NS, Nocera DG (2006) Powering the planet: chemical challenges in solar energy utilization. Proc Natl Acad Sci U S A 103:15729–15735

15. Kanan MW, Nocera DG (2008) In situ formation of an oxygen-evolving catalyst in neutral water containing phosphate and Co2+. Science 321:1072–1075
16. Fujishima A, Honda K (1972) Electrochemical photolysis of water at a semiconductor electrode. Nature 238:37–38
17. Grätzel M (1981) Artificial photosynthesis: water cleavage into hydrogen and oxygen by visible light. Acc Chem Res 14:376–384
18. Chen X, Shen S, Guo L, Mao SS (2010) Semiconductor-based photocatalytic hydrogen generation. Chem Rev 110:6503–6570
19. Hisatomi T, Kubota J, Domen K (2014) Recent advances in semiconductors for photocatalytic and photoelectrochemical water splitting. Chem Soc Rev 43:7520–7535
20. Kudo A, Miseki Y (2009) Heterogeneous photocatalyst materials for water splitting. Chem Soc Rev 38:253–278
21. Osterloh FE (2007) Inorganic materials as catalysts for photochemical splitting of water. Chem Mater 20:35–54
22. Li X, Yu J, Low J, Fang Y, Xiao J, Chen X (2015) Engineering heterogeneous semiconductors for solar water splitting. J Mater Chem A 3:2485–2534
23. Maeda K, Domen K (2007) New non-oxide photocatalysts designed for overall water splitting under visible light. J Phys Chem C 111:7851–7861
24. Esswein AJ, Nocera DG (2007) Hydrogen production by molecular photocatalysis. Chem Rev 107:4022–4047
25. Han Z, Qiu F, Eisenberg R, Holland PL, Krauss TD (2012) Robust photogeneration of H_2 in water using semiconductor nanocrystals and a nickel catalyst. Science 338:1321–1324
26. Bard AJ, Fox MA (1995) Artificial photosynthesis: solar splitting of water to hydrogen and oxygen. Acc Chem Res 28:141–145
27. Kato H, Asakura K, Kudo A (2003) Highly efficient water splitting into H-2 and O-2 over lanthanum-doped $NaTaO_3$ photocatalysts with high crystallinity and surface nanostructure. J Am Chem Soc 125:3082–3089
28. Ni M, Leung MKH, Leung DYC, Sumathy K (2007) A review and recent developments in photocatalytic water-splitting using TiO_2 for hydrogen production. Renew Sustain Energy Rev 11:401–425
29. Chen XB, Liu L, Yu PY, Mao SS (2011) Increasing solar absorption for photocatalysis with black hydrogenated titanium dioxide nanocrystals. Science 331:746–750
30. Xiang Q, Yu J, Wang W, Jaroniec M (2011) Nitrogen self-doped nanosized TiO_2 sheets with exposed {001} facets for enhanced visible-light photocatalytic activity. Chem Commun 47:6906–6908
31. Tsuji I, Kato H, Kobayashi H, Kudo A (2004) Photocatalytic H-2 evolution reaction from aqueous solutions over band structure-controlled $(AgIn)(x)Zn_2(1-x)S_2$ solid solution photocatalysts with visible-light response and their surface nanostructures. J Am Chem Soc 126:13406–13413
32. Tsuji I, Kato H, Kudo A (2005) Visible-light-induced H-2 evolution from an aqueous solution containing sulfide and sulfite over a ZnS-CuInS2-AgInS2 solid-solution photocatalyst. Angew Chem Int Ed 44:3565–3568
33. Zhang K, Guo L (2013) Metal sulphide semiconductors for photocatalytic hydrogen production. Catal Sci Technol 3:1672–1690
34. Ishikawa A, Takata T, Kondo JN, Hara M, Kobayashi H, Domen K (2002) Oxysulfide $Sm_2Ti_2S_2O_5$ as a stable photocatalyst for water oxidation and reduction under visible light irradiation ($\lambda \leq 650$ nm). J Am Chem Soc 124:13547–13553
35. Hitoki G, Ishikawa A, Takata T, Kondo JN, Hara M, Domen K (2002) Ta3N5 as a novel visible light-driven photocatalyst ($\lambda < 600$ nm). Chem Lett 31:736–737
36. Hitoki G, Takata T, Kondo JN, Hara M, Kobayashi H, Domen K (2002) An oxynitride, TaON, as an efficient water oxidation photocatalyst under visible light irradiation ([small lambda] [less-than-or-equal] 500 nm). Chem Commun 38:1698–1699

37. Maeda K, Takata T, Hara M, Saito N, Inoue Y, Kobayashi H, Domen K (2005) GaN:ZnO solid solution as a photocatalyst for visible-light-driven overall water splitting. J Am Chem Soc 127:8286–8287
38. Maeda K, Teramura K, Lu DL, Takata T, Saito N, Inoue Y, Domen K (2006) Photocatalyst releasing hydrogen from water – enhancing catalytic performance holds promise for hydrogen production by water splitting in sunlight. Nature 440:295–295
39. Wang Y, Wang X, Antonietti M (2012) Polymeric graphitic carbon nitride as a heterogeneous organocatalyst: from photochemistry to multipurpose catalysis to sustainable chemistry. Angew Chem Int Ed 51:68–89
40. Sun J, Zhang J, Zhang M, Antonietti M, Fu X, Wang X (2012) Bioinspired hollow semiconductor nanospheres as photosynthetic nanoparticles. Nat Commun 3:1139
41. Wang X, Maeda K, Thomas A, Takanabe K, Xin G, Carlsson J, Domen K, Antonietti M (2009) A metal-free polymeric photocatalyst for hydrogen production from water under visible light. Nat Mater 8:76–80
42. Cao S, Low J, Yu J, Jaroniec M (2015) Polymeric photocatalysts based on graphitic carbon nitride. Adv Mater 27:2150–2176
43. Liu J, Liu Y, Liu N, Han Y, Zhang X, Huang H, Lifshitz Y, Lee S-T, Zhong J, Kang Z (2015) Metal-free efficient photocatalyst for stable visible water splitting via a two-electron pathway. Science 347:970–974
44. Zhou X, Li X, Gao Q, Yuan J, Wen J, Fang Y, Liu W, Zhang S, Liu Y (2015) Metal-free carbon nanotube-SiC nanowire heterostructures with enhanced photocatalytic H_2 evolution under visible light irradiation. Catal Sci Technol 5:2798–2806
45. Zhou X, Liu Y, Li X, Gao Q, Liu X, Fang Y (2014) Topological morphology conversion towards SnO_2/SiC hollow sphere nanochains with efficient photocatalytic hydrogen evolution. Chem Commun 50:1070–1073
46. Hao J-Y, Wang Y-Y, Tong X-L, Jin G-Q, Guo X-Y (2012) Photocatalytic hydrogen production over modified SiC nanowires under visible light irradiation. Int J Hydrog Energy 37:15038–15044
47. Hao JY, Wang YY, Tong XL, Jin GQ, Guo XY (2013) SiC nanomaterials with different morphologies for photocatalytic hydrogen production under visible light irradiation. Catal Today 212:220–224
48. Wang Y, Guo X, Dong L, Jin G, Wang Y, Guo X-Y (2013) Enhanced photocatalytic performance of chemically bonded SiC-graphene composites for visible-light-driven overall water splitting. Int J Hydrog Energy 38:12733–12738
49. Zhou X, Gao Q, Li X, Liu Y, Zhang S, Fang Y, Li J (2015) Ultra-thin SiC layers covered graphene nanosheets as advanced photocatalysts for hydrogen evolution. J Mater Chem A 3:10999–11005
50. Yan H, Yang J, Ma G, Wu G, Zong X, Lei Z, Shi J, Li C (2009) Visible-light-driven hydrogen production with extremely high quantum efficiency on Pt-PdS/CdS photocatalyst. J Catal 266:165–168
51. Sheng H, Yu L, Jian-Hua Y, Ying Y (2013) CdS-based semiconductor photocatalysts for hydrogen production from water splitting under solar light. Nanotechnol Sustain Energy (Am Chem Soc) 1140:219–241
52. Bard AJ (1980) Photoelectrochemistry. Science 207:139–144
53. Bard AJ (1982) Design of semiconductor photoelectrochemical systems for solar energy conversion. J Phys Chem 86:172–177
54. Chen SY, Wang LW (2012) Thermodynamic oxidation and reduction potentials of photocatalytic semiconductors in aqueous solution. Chem Mater 24:3659–3666
55. Xu Y, Schoonen MAA (2000) The absolute energy positions of conduction and valence bands of selected semiconducting minerals. Am Mineral 85:543–556
56. Yang J, Wang D, Han H, Li C (2013) Roles of cocatalysts in photocatalysis and photoelectrocatalysis. Acc Chem Res 46:1900–1909

57. Ran J, Zhang J, Yu J, Jaroniec M, Qiao SZ (2014) Earth-abundant cocatalysts for semiconductor-based photocatalytic water splitting. Chem Soc Rev 43:7787–7812
58. Chen X, Li C, Gratzel M, Kostecki R, Mao SS (2012) Nanomaterials for renewable energy production and storage. Chem Soc Rev 41:7909–7937
59. Osterloh FE (2013) Inorganic nanostructures for photoelectrochemical and photocatalytic water splitting. Chem Soc Rev 42:2294–2320
60. Kalyanasundaram K, Borgarello E, Duonghong D, Grätzel M (1981) Cleavage of water by visible-light irradiation of colloidal CdS solutions; inhibition of photocorrosion by RuO_2. Angew Chem Int Ed 20:987–988
61. Amirav L, Alivisatos AP (2010) Photocatalytic hydrogen production with tunable nanorod heterostructures. J Phys Chem Lett 1:1051–1054
62. Bao N, Shen L, Takata T, Domen K (2007) Self-templated synthesis of nanoporous CdS nanostructures for highly efficient photocatalytic hydrogen production under visible light. Chem Mater 20:110–117
63. Yu J, Yu Y, Cheng B (2012) Enhanced visible-light photocatalytic H-2-production performance of multi-armed CdS nanorods. RSC Adv 2:11829–11835
64. Jin J, Yu J, Liu G, Wong PK (2013) Single crystal CdS nanowires with high visible-light photocatalytic H_2-production performance. J Mater Chem A 1:10927–10934
65. Xiang Q, Cheng B, Yu J (2013) Hierarchical porous CdS nanosheet-assembled flowers with enhanced visible-light photocatalytic H-2-production performance. Appl Catal B Environ 138:299–303
66. Chai B, Peng T, Zeng P, Zhang X, Liu X (2011) Template-free hydrothermal synthesis of $ZnIn2S_4$ floriated microsphere as an efficient photocatalyst for H_2 production under visible-light irradiation. J Phys Chem C 115:6149–6155
67. Shang L, Zhou C, Bian T, Yu H, Wu L-Z, Tung C-H, Zhang T (2013) Facile synthesis of hierarchical $ZnIn_2S_4$ submicrospheres composed of ultrathin mesoporous nanosheets as a highly efficient visible-light-driven photocatalyst for H-2 production. J Mater Chem A 1:4552–4558
68. Yu X, An X, Shavel A, Ibanez M, Cabot A (2014) The effect of the Ga content on the photocatalytic hydrogen evolution of CuIn1-xGaxS2 nanocrystals. J Mater Chem A 2:12317–12322
69. Yu X, Shavel A, An X, Luo Z, Ibáñez M, Cabot A (2014) Cu_2ZnSnS_4-Pt and Cu_2ZnSnS_4-Au heterostructured nanoparticles for photocatalytic water splitting and pollutant degradation. J Am Chem Soc 136:9236–9239
70. Hu Z, Yu JC (2013) Pt_3Co-loaded CdS and TiO_2 for photocatalytic hydrogen evolution from water. J Mater Chem A 1:12221–12228
71. Cao-Thang D, Minh-Hao P, Kleitz F, Trong-On D (2013) Design of water-soluble CdS-titanate-nickel nanocomposites for photocatalytic hydrogen production under sunlight. J Mater Chem A 1:13308–13313
72. Cao S, Wang C-J, Lv X-J, Chen Y, Fu W-F (2015) A highly efficient photocatalytic H-2 evolution system using colloidal CdS nanorods and nickel nanoparticles in water under visible light irradiation. Appl Catal B Environ 162:381–391
73. Chen S, Chen X, Jiang Q, Yuan J, Lin C, Shangguan W (2014) Promotion effect of nickel loaded on CdS for photocatalytic H-2 production in lactic acid solution. Appl Surf Sci 316:590–594
74. Wang H, Chen W, Zhang J, Huang CP, Mao LQ (2015) Nickel nanoparticles modified CdS – a potential photocatalyst for hydrogen production through water splitting under visible light irradiation. Int J Hydrog Energy 40:340–345
75. Li X, Wang H, Chu T, Li D, Mao L (2014) Synthesis and peferentially loading of nickel nanoparticle on CdS surface and its photocatalytic performance for hydrogen evolution under visible light. Mater Res Bull 57:254–259

76. Simon T, Bouchonville N, Berr MJ, Vaneski A, Adrovic A, Volbers D, Wyrwich R, Doblinger M, Susha AS, Rogach AL et al (2014) Redox shuttle mechanism enhances photocatalytic H_2 generation on Ni-decorated CdS nanorods. Nat Mater 13:1013–1018
77. Zhang W, Wang Y, Wang Z, Zhong Z, Xu R (2010) Highly efficient and noble metal-free NiS/CdS photocatalysts for H_2 evolution from lactic acid sacrificial solution under visible light. Chem Commun 46:7631–7633
78. Zhang J, Qiao SZ, Qi L, Yu J (2013) Fabrication of NiS modified CdS nanorod p-n junction photocatalysts with enhanced visible-light photocatalytic H-2-production activity. Phys Chem Chem Phys 15:12088–12094
79. Ran J, Zhang J, Yu J, Qiao SZ (2014) Enhanced visible-light photocatalytic H_2 production by ZnxCd1-xS modified with earth-abundant nickel-based cocatalysts. ChemSusChem 7:3426–3434
80. Zhang J, Qi L, Ran J, Yu J, Qiao SZ (2014) Ternary NiS/ZnxCd1-xS/reduced graphene oxide nanocomposites for enhanced solar photocatalytic H_2-production activity. Adv Energy Mater 4:1301925
81. Yuan Y-P, Cao S-W, Yin L-S, Xu L, Xue C (2013) NiS_2 Co-catalyst decoration on $CdLa_2S_4$ nanocrystals for efficient photocatalytic hydrogen generation under visible light irradiation. Int J Hydrog Energy 38:7218–7223
82. Cao S, Chen Y, Wang C-J, He P, Fu W-F (2014) Highly efficient photocatalytic hydrogen evolution by nickel phosphide nanoparticles from aqueous solution. Chem Commun 50:10427–10429
83. Chen X, Chen W, Gao H, Yang Y, Shangguan W (2014) In situ photodeposition of NiOx on CdS for hydrogen production under visible light: enhanced activity by controlling solution environment. Appl Catal B Environ 152:68–72
84. Yuan J, Wen J, Gao Q, Chen S, Li J, Li X, Fang Y (2015) Amorphous Co_3O_4 modified CdS nanorods with enhanced visible-light photocatalytic H-2-production activity. Dalton Trans 44:1680–1689
85. Yan Z, Wu H, Han A, Yu X, Du P (2014) Noble metal-free cobalt oxide (CoOx) nanoparticles loaded on titanium dioxide/cadmium sulfide composite for enhanced photocatalytic hydrogen production from water. Int J Hydrog Energy 39:13353–13360
86. Zhang LJ, Zheng R, Li S, Liu BK, Wang DJ, Wang LL, Xie TF (2014) Enhanced photocatalytic H_2 generation on cadmium sulfide nanorods with cobalt hydroxide as cocatalyst and insights into their photogenerated charge transfer properties. ACS Appl Mater Interfaces 6:13406–13412
87. Ran J, Yu J, Jaroniec M (2011) $Ni(OH)_2$ modified CdS nanorods for highly efficient visible-light-driven photocatalytic H_2 generation. Green Chem 13:2708–2713
88. Yan Z, Yu X, Han A, Xu P, Du P (2014) Noble-metal-free Ni(OH)(2)-modified CdS/reduced graphene oxide nanocomposite with enhanced photocatalytic activity for hydrogen production under visible light irradiation. J Phys Chem C 118:22896–22903
89. Cao S, Chen Y, Hou C-C, Lv X-J, Fu W-F (2015) Cobalt phosphide as a highly active non-precious metal cocatalyst for photocatalytic hydrogen production under visible light irradiation. J Mater Chem A 3:6096–6101
90. Zong X, Yan H, Wu G, Ma G, Wen F, Wang L, Li C (2008) Enhancement of photocatalytic H-2 evolution on CdS by loading MOS_2 as cocatalyst under visible light irradiation. J Am Chem Soc 130:7176–7176
91. Wei L, Chen Y, Lin Y, Wu H, Yuan R, Li Z (2014) MoS_2 as non-noble-metal co-catalyst for photocatalytic hydrogen evolution over hexagonal $ZnIn_2S_4$ under visible light irradiations. Appl Catal B Environ 144:521–527
92. Jang JS, Ham DJ, Lakshminarasimhan N, Choi WY, Lee JS (2008) Role of platinum-like tungsten carbide as cocatalyst of CdS photocatalyst for hydrogen production under visible light irradiation. Appl Catal A Gen 346:149–154
93. Zong X, Han J, Ma G, Yan H, Wu G, Li C (2011) Photocatalytic H-2 evolution on CdS loaded with WS_2 as cocatalyst under visible light irradiation. J Phys Chem C 115:12202–12208

94. Li Q, Guo B, Yu J, Ran J, Zhang B, Yan H, Gong JR (2011) Highly efficient visible-light-driven photocatalytic hydrogen production of Cds-cluster-decorated graphene nanosheets. J Am Chem Soc 133:10878–10884
95. Li Q, Meng H, Yu J, Xiao W, Zheng Y, Wang J (2014) Enhanced photocatalytic hydrogen-production performance of graphene-ZnxCd1-xS composites by using an organic S source. Chem Eur J 20:1176–1185
96. Tang X, Tay Q, Chen Z, Chen Y, Goh GKL, Xue J (2013) CuInZnS-decorated graphene nanosheets for highly efficient visible-light-driven photocatalytic hydrogen production. J Mater Chem A 1:6359–6365
97. Li Q, Li X, Wageh S, Al-Ghamdi AA, Yu J (2015) CdS/graphene nanocomposite photocatalysts. Adv Energy Mater, n/a–n/a
98. Zhang J, Yu J, Zhang Y, Li Q, Gong JR (2011) Visible light photocatalytic H-2-production activity of CuS/ZnS porous nanosheets based on photoinduced interfacial charge transfer. Nano Lett 11:4774–4779
99. Zhang J, Xu Q, Qiao SZ, Yu J (2013) Enhanced visible-light hydrogen-production activity of copper-modified ZnxCd1-xS. ChemSusChem 6:2009–2015
100. Yu J, Zhang J, Liu S (2010) Ion-exchange synthesis and enhanced visible-light photoactivity of CuS/ZnS nanocomposite hollow spheres. J Phys Chem C 114:13642–13649
101. Li Y, Hu Y, Peng S, Lu G, Li S (2009) Synthesis of CdS nanorods by an ethylenediamine assisted hydrothermal method for photocatalytic hydrogen evolution. J Phys Chem C 113:9352–9358
102. Berr MJ, Vaneski A, Mauser C, Fischbach S, Susha AS, Rogach AL, Jäckel F, Feldmann J (2012) Delayed photoelectron transfer in Pt-decorated CdS nanorods under hydrogen generation conditions. Small 8:291–297
103. Berr MJ, Wagner P, Fischbach S, Vaneski A, Schneider J, Susha AS, Rogach AL, Jäckel F, Feldmann J (2012) Hole scavenger redox potentials determine quantum efficiency and stability of Pt-decorated CdS nanorods for photocatalytic hydrogen generation. Appl Phys Lett 100:223903
104. Berr M, Vaneski A, Susha AS, Rodríguez-Fernández J, Döblinger M, Jäckel F, Rogach AL, Feldmann J (2010) Colloidal CdS nanorods decorated with subnanometer sized Pt clusters for photocatalytic hydrogen generation. Appl Phys Lett 97:093108
105. Yu J, Yu Y, Zhou P, Xiao W, Cheng B (2014) Morphology-dependent photocatalytic H-2-production activity of CdS. Appl Catal B Environ 156:184–191
106. Zhao Q, Ji M, Qian H, Dai B, Weng L, Gui J, Zhang J, Ouyang M, Zhu H (2014) Controlling structural symmetry of a hybrid nanostructure and its effect on efficient photocatalytic hydrogen evolution. Adv Mater 26:1387–1392
107. Sarina S, Zhu H-Y, Xiao Q, Jaatinen E, Jia J, Huang Y, Zheng Z, Wu H (2014) Viable photocatalysts under solar-spectrum irradiation: nonplasmonic metal nanoparticles. Angew Chem Int Ed 53:2935–2940
108. Wang Y, Yu J, Xiao W, Li Q (2014) Microwave-assisted hydrothermal synthesis of graphene based Au-TiO_2 photocatalysts for efficient visible-light hydrogen production. J Mater Chem A 2:3847–3855
109. Zhang J, Wang Y, Zhang J, Lin Z, Huang F, Yu J (2012) Enhanced photocatalytic hydrogen production activities of Au-loaded ZnS flowers. ACS Appl Mater Interfaces 5:1031–1037
110. Zhang Z, Wang Z, Cao S-W, Xue C (2013) Au/Pt nanoparticle-decorated TiO_2 nanofibers with plasmon-enhanced photocatalytic activities for solar-to-fuel conversion. J Phys Chem C 117:25939–25947
111. Jang JS, Choi SH, Kim HG, Lee JS (2008) Location and state of Pt in platinized CdS/TiO_2 photocatalysts for hydrogen production from water under visible light. J Phys Chem C 112:17200–17205
112. Cui E, Lu G (2013) Modulating photogenerated electron transfer and hydrogen production rate by controlling surface potential energy on a selectively exposed Pt facet on Pt/TiO_2 for enhancing hydrogen production. J Phys Chem C 117:26415–26425

113. Wang Y, Wang Y, Xu R (2013) Photochemical deposition of Pt on CdS for H-2 evolution from water: markedly enhanced activity by controlling Pt reduction environment. J Phys Chem C 117:783–790
114. Nguyen M, Tran PD, Pramana SS, Lee RL, Batabyal SK, Mathews N, Wong LH, Graetzel M (2013) In situ photo-assisted deposition of MoS2 electrocatalyst onto zinc cadmium sulphide nanoparticle surfaces to construct an efficient photocatalyst for hydrogen generation. Nanoscale 5:1479–1482
115. Wang Q, Yun G, Bai Y, An N, Chen Y, Wang R, Lei Z, Shangguan W (2014) CuS, NiS as co-catalyst for enhanced photocatalytic hydrogen evolution over TiO_2. Int J Hydrogen Energy 39:13421–13428
116. Yu J, Hai Y, Cheng B (2011) Enhanced photocatalytic H_2-production activity of TiO_2 by Ni $(OH)_2$ cluster modification. J Phys Chem C 115:4953–4958
117. Yu J, Wang S, Cheng B, Lin Z, Huang F (2013) Noble metal-free Ni(OH)(2)-g-C_3N_4 composite photocatalyst with enhanced visible-light photocatalytic H-2-production activity. Catal Sci Technol 3:1782–1789
118. Zhang L, Tian B, Chen F, Zhang J (2012) Nickel sulfide as co-catalyst on nanostructured TiO_2 for photocatalytic hydrogen evolution. Int J Hydrog Energy 37:17060–17067
119. Hong J, Wang Y, Wang Y, Zhang W, Xu R (2013) Noble-metal-free NiS/C3N4 for efficient photocatalytic hydrogen evolution from water. ChemSusChem 6:2263–2268
120. Chen Z, Sun P, Fan B, Zhang Z, Fang X (2014) In situ template-free ion-exchange process to prepare visible-light-active g-C_3N_4/NiS hybrid photocatalysts with enhanced hydrogen evolution activity. J Phys Chem C 118:7801–7807
121. Tran PD, Nguyen M, Pramana SS, Bhattacharjee A, Chiam SY, Fize J, Field MJ, Artero V, Wong LH, Loo J et al (2012) Copper molybdenum sulfide: a new efficient electrocatalyst for hydrogen production from water. Energy Environ Sci 5:8912–8916
122. Tran PD, Chiam SY, Boix PP, Ren Y, Pramana SS, Fize J, Artero V, Barber J (2013) Novel cobalt/nickel-tungsten-sulfide catalysts for electrocatalytic hydrogen generation from water. Energy Environ Sci 6:2452–2459
123. Walter MG, Warren EL, McKone JR, Boettcher SW, Mi Q, Santori EA, Lewis NS (2010) Solar water splitting cells. Chem Rev 110:6446–6473
124. Brown KA, Wilker MB, Boehm M, Dukovic G, King PW (2012) Characterization of photochemical processes for H_2 production by CdS nanorod–[FeFe] hydrogenase complexes. J Am Chem Soc 134:5627–5636
125. Wilker MB, Shinopoulos KE, Brown KA, Mulder DW, King PW, Dukovic G (2014) Electron transfer kinetics in CdS nanorod–[FeFe]-hydrogenase complexes and implications for photochemical H_2 generation. J Am Chem Soc 136:4316–4324
126. Wen F, Wang X, Huang L, Ma G, Yang J, Li C (2012) A hybrid photocatalytic system comprising ZnS as light harvester and an $[Fe_2S_2]$ hydrogenase mimic as hydrogen evolution catalyst. ChemSusChem 5:849–853
127. Wen F, Yang J, Zong X, Ma B, Wang D, Li C (2011) Photocatalytic H-2 production on hybrid catalyst system composed of inorganic semiconductor and cobaloximes catalysts. J Catal 281:318–324
128. Wen F, Li C (2013) Hybrid artificial photosynthetic systems comprising semiconductors as light harvesters and biomimetic complexes as molecular cocatalysts. Acc Chem Res 46:2355–2364
129. Lounis SD, Runnerstrom EL, Bergerud A, Nordlund D, Milliron DJ (2014) Influence of dopant distribution on the plasmonic properties of indium tin oxide nanocrystals. J Am Chem Soc 136:7110–7116
130. Yu J, Yang B, Cheng B (2012) Noble-metal-free carbon nanotube-Cd0.1Zn0.9S composites for high visible-light photocatalytic H-2-production performance. Nanoscale 4:2670–2677
131. Chai B, Peng T, Zeng P, Zhang X (2012) Preparation of a MWCNTs/$ZnIn_2S_4$ composite and its enhanced photocatalytic hydrogen production under visible-light irradiation. Dalton Trans 41:1179–1186

132. Zhang J, Yu J, Jaroniec M, Gong JR (2012) Noble metal-free reduced graphene oxide-ZnxCd1-xS nanocomposite with enhanced solar photocatalytic H-2-production performance. Nano Lett 12:4584–4589
133. Chang K, Mei Z, Wang T, Kang Q, Ouyang S, Ye J (2014) MoS2/graphene cocatalyst for efficient photocatalytic H_2 evolution under visible light irradiation. ACS Nano 8:7078–7087
134. Jia T, Kolpin A, Ma C, Chan RC-T, Kwok W-M, Tsang SCE (2014) A graphene dispersed CdS-MoS_2 nanocrystal ensemble for cooperative photocatalytic hydrogen production from water. Chem Commun 50:1185–1188
135. Lang D, Shen T, Xiang Q (2015) Roles of MoS_2 and graphene as cocatalysts in the enhanced visible-light photocatalytic H_2 production activity of multiarmed CdS nanorods. ChemCatChem 7:943–951
136. Zhu B, Lin B, Zhou Y, Sun P, Yao Q, Chen Y, Gao B (2014) Enhanced photocatalytic H-2 evolution on ZnS loaded with graphene and MoS_2 nanosheets as cocatalysts. J Mater Chem A 2:3819–3827
137. Lightcap IV, Kosel TH, Kamat PV (2010) Anchoring semiconductor and metal nanoparticles on a two-dimensional catalyst Mat. storing and shuttling electrons with reduced graphene oxide. Nano Lett 10:577–583
138. Wang D, Kako T, Ye J (2008) Efficient photocatalytic decomposition of acetaldehyde over a solid-solution perovskite (Ag0.75Sr0.25)(Nb0.75Ti0.25)O_3 under visible-light irradiation. J Am Chem Soc 130:2724–2725
139. Kudo A, Tsuji I, Kato H (2002) $AgInZn_7S_9$ solid solution photocatalyst for H-2 evolution from aqueous solutions under visible light irradiation. Chem Commun 38:1958–1959
140. Kudo A, Sekizawa M (1999) Photocatalytic H_2 evolution under visible light irradiation on Zn1-x Cu x S solid solution. Catal Lett 58:241–243
141. Arai T, Senda S-I, Sato Y, Takahashi H, Shinoda K, Jeyadevan B, Tohji K (2008) Cu-doped ZnS hollow particle with high activity for hydrogen generation from alkaline sulfide solution under visible light. Chem Mater 20:1997–2000
142. Kale BB, Baeg JO, Lee SM, Chang H, Moon SJ, Lee CW (2006) $CdIn_2S_4$ nanotubes and “Marigold” nanostructures: a visible-light photocatalyst. Adv Funct Mater 16:1349–1354
143. Li Q, Meng H, Zhou P, Zheng Y, Wang J, Yu J, Gong J (2013) Zn1-xCdxS solid solutions with controlled bandgap and enhanced visible-light photocatalytic H-2-production activity. ACS Catal 3:882–889
144. Yu J, Zhang J, Jaroniec M (2010) Preparation and enhanced visible-light photocatalytic H-2-production activity of CdS quantum dots-sensitized Zn1-xCdxS solid solution. Green Chem 12:1611–1614
145. Zhang J, Liu S, Yu J, Jaroniec M (2011) A simple cation exchange approach to Bi-doped ZnS hollow spheres with enhanced UV and visible-light photocatalytic H-2-production activity. J Mater Chem 21:14655–14662
146. Huang S, Lin Y, Yang J, Li X, Zhang J, Yu J, Shi H, Wang W, Yu Y (2013) Enhanced photocatalytic activity and stability of semiconductor by Ag doping and simultaneous deposition: the case of CdS. RSC Adv 3:20782–20792
147. Kimi M, Yuliati L, Shamsuddin M (2012) Preparation of Cu-doped Cd0.1Zn0.9S solid solution by hydrothermal method and its enhanced activity for hydrogen production under visible light irradiation. J Photochem Photobiol A 230:15–22
148. Li F, Chen G, Luo J, Huang Q, Luo Y, Meng Q, Li D (2013) Band engineering of Cu2+ doped In2xZn3(1-x)S3 solid solution with high photocatalytic activity for H-2 production under visible light. Catal Sci Technol 3:1993–1999
149. Zhang X, Jing D, Guo L (2010) Effects of anions on the photocatalytic H-2 production performance of hydrothermally synthesized Ni-doped Cd0.1Zn0.9S photocatalysts. Int J Hydrog Energy 35:7051–7057
150. Wang Y, Wu J, Zheng J, Jiang R, Xu R (2012) Ni^{2+} – doped ZnxCd1-xS photocatalysts from single-source precursors for efficient solar hydrogen production under visible light irradiation. Catal Sci Technol 2:581–588

151. Li F, Luo J, Chen G, Fan Y, Huang Q, Luo Y, Li D, Meng Q (2014) Hydrothermal synthesis of zinc indium sulfide microspheres with Ag+ doping for enhanced H-2 production by photocatalytic water splitting under visible light. Catal Sci Technol 4:1144–1150
152. Kimi M, Yuliati L, Shamsuddin M (2011) Photocatalytic hydrogen production under visible light over Cd0.1SnxZn0.9-2xS solid solution photocatalysts. Int J Hydrog Energy 36:9453–9461
153. Peng S, An R, Li Y, Lu G, Li S (2012) Remarkable enhancement of photocatalytic hydrogen evolution over Cd0.5Zn0.5S by bismuth-doping. Int J Hydrog Energy 37:1366–1374
154. Zhang K, Zhou Z, Guo L (2011) Alkaline earth metal as a novel dopant for chalcogenide solid solution: improvement of photocatalytic efficiency of Cd1-xZnxS by barium surface doping. Int J Hydrog Energy 36:9469–9478
155. Zhang K, Jing D, Chen Q, Guo L (2010) Influence of Sr-doping on the photocatalytic activities of CdS-ZnS solid solution photocatalysts. Int J Hydrog Energy 35:2048–2057
156. Liu M, Wang L, Lu G, Yao X, Guo L (2011) Twins in Cd1-xZnxS solid solution: highly efficient photocatalyst for hydrogen generation from water. Energy Environ Sci 4:1372–1378
157. Liu M, Jing D, Zhou Z, Guo L (2013) Twin-induced one-dimensional homojunctions yield high quantum efficiency for solar hydrogen generation. Nat Commun 4:2278
158. Yu Y, Zhang J, Wu X, Zhao W, Zhang B (2012) Nanoporous single-crystal-like CdxZn1-xS nanosheets fabricated by the cation-exchange reaction of inorganic–organic hybrid ZnS-amine with cadmium ions. Angew Chem Int Ed 51:897–900
159. Zheng L, Xu Y, Song Y, Wu C, Zhang M, Xie Y (2009) Nearly monodisperse $CuInS_2$ hierarchical microarchitectures for photocatalytic H_2 evolution under visible light. Inorg Chem 48:4003–4009
160. Chen F, Zai J, Xu M, Qian X (2013) 3D-hierarchical Cu_3SnS_4 flowerlike microspheres: controlled synthesis, formation mechanism and photocatalytic activity for H-2 evolution from water. J Mater Chem A 1:4316–4323
161. Yonemoto BT, Hutchings GS, Jiao F (2014) A general synthetic approach for ordered mesoporous metal sulfides. J Am Chem Soc 136:8895–8898
162. Chen J, Xin F, Yin X, Xiang T, Wang Y (2015) Synthesis of hexagonal and cubic $ZnIn_2S_4$ nanosheets for the photocatalytic reduction of CO_2 with methanol. RSC Adv 5:3833–3839
163. Tian G, Chen Y, Ren Z, Tian C, Pan K, Zhou W, Wang J, Fu H (2014) Enhanced photocatalytic hydrogen evolution over hierarchical composites of $ZnIn_2S_4$ nanosheets grown on MoS_2 slices. Chem Asian J 9:1291–1297
164. Zhou J, Tian GH, Chen YJ, Meng XY, Shi YH, Cao XR, Pan K, Fu HG (2013) In situ controlled growth of $ZnIn_2S_4$ nanosheets on reduced graphene oxide for enhanced photocatalytic hydrogen production performance. Chem Commun 49:2237–2239
165. Macias-Sanchez SA, Nava R, Hernandez-Morales V, Acosta-Silva YJ, Gomez-Herrera L, Pawelec B, Al-Zahrani SM, Navarro RM, Fierro JLG (2012) Cd1-xZnxS solid solutions supported on ordered mesoporous silica (SBA-15): structural features and photocatalytic activity under visible light. Int J Hydrog Energy 37:9948–9958
166. Macias-Sanchez SA, Nava R, Hernandez-Morales V, Acosta-Silva YJ, Pawelec B, Al-Zahrani SM, Navarro RM, Fierro JLG (2013) Cd1-xZnxS supported on SBA-16 as photocatalysts for water splitting under visible light: influence of Zn concentration. Int J Hydrog Energy 38:11799–11810
167. Ryu SY, Balcerski W, Lee TK, Hoffmann MR (2007) Photocatalytic production of hydrogen from water with visible light using hybrid catalysts of CdS attached to microporous and mesoporous silicas. J Phys Chem C 111:18195–18203
168. Chen Z, Xu Y-J (2013) Ultrathin TiO_2 layer coated-CdS spheres core–shell nanocomposite with enhanced visible-light photoactivity. ACS Appl Mater Interfaces 5:13353–13363
169. Zhang N, Liu S, Fu X, Xu Y-J (2011) Synthesis of $M@TiO_2$ ($M = Au$, Pd, Pt) core-shell nanocomposites with tunable photoreactivity. J Phys Chem C 115:9136–9145
170. Zhang N, Liu S, Xu Y-J (2012) Recent progress on metal core@semiconductor shell nanocomposites as a promising type of photocatalyst. Nanoscale 4:2227–2238

171. Liu S, Zhang N, Tang Z-R, Xu Y-J (2012) Synthesis of one-dimensional CdS@TiO_2 core-shell nanocomposites photocatalyst for selective redox: the dual role of TiO_2 shell. ACS Appl Mater Interfaces 4:6378–6385
172. Huang L, Wang X, Yang J, Liu G, Han J, Li C (2013) Dual cocatalysts loaded type I CdS/ZnS core/shell nanocrystals as effective and stable photocatalysts for H_2 evolution. J Phys Chem C 117:11584–11591
173. Thibert A, Frame FA, Busby E, Holmes MA, Osterloh FE, Larsen DS (2011) Sequestering high-energy electrons to facilitate photocatalytic hydrogen generation in CdSe/CdS nanocrystals. J Phys Chem Lett 2:2688–2694
174. Xie YP, Yu ZB, Liu G, Ma XL, Cheng H-M (2014) CdS-mesoporous ZnS core-shell particles for efficient and stable photocatalytic hydrogen evolution under visible light. Energy Environ Sci 7:1895–1901
175. Long L, Yu X, Wu L, Li J, Li X (2014) Nano-CdS confined within titanate nanotubes for efficient photocatalytic hydrogen production under visible light illumination. Nanotechnology 25:035603
176. Zhang J, Wang Y, Jin J, Zhang J, Lin Z, Huang F, Yu J (2013) Efficient visible-light photocatalytic hydrogen evolution and enhanced photostability of core/shell CdS/g-C_3N_4 nanowires. ACS Appl Mater Interfaces 5:10317–10324
177. Zhu H, Song N, Lv H, Hill CL, Lian T (2012) Near unity quantum yield of light-driven redox mediator reduction and efficient H_2 generation using colloidal nanorod heterostructures. J Am Chem Soc 134:11701–11708
178. Shangguan W, Yoshida A (2001) Synthesis and photocatalytic properties of CdS-intercalated metal oxides. Sol Energy Mater Sol Cells 69:189–194
179. Shangguan WF, Yoshida A (2002) Photocatalytic hydrogen evolution from water on nanocomposites incorporating cadmium sulfide into the interlayer. J Phys Chem B 106:12227–12230
180. Cui W, Liu Y, Liu L, Hu J, Liang Y (2012) Microwave-assisted synthesis of CdS intercalated $K_4Nb_6O_{17}$ and its photocatalytic activity for hydrogen production. Appl Catal A Gen 417:111–118
181. Wei Y, Zhang X, Xu J, Wang J, Huang Y, Fan L, Wu J (2014) Enhancement of photocatalytic activity from $HCa_2TaxNb_3\text{-}xO_{10}$ ($x = 0, 1$), co-intercalated with sulfides particles. Appl Catal B Environ 147:920–928
182. Zhang G, Lin B, Yang W, Jiang S, Yao Q, Chen Y, Gao B (2015) Highly efficient photocatalytic hydrogen generation by incorporating CdS into ZnCr-layered double hydroxide interlayer. RSC Adv 5:5823–5829
183. Banerjee S, Mohapatra SK, Das PP, Misra M (2008) Synthesis of coupled semiconductor by filling 1D TiO_2 nanotubes with CdS. Chem Mater 20:6784–6791
184. Kim YK, Park H (2011) Light-harvesting multi-walled carbon nanotubes and CdS hybrids: application to photocatalytic hydrogen production from water. Energy Environ Sci 4:685–694
185. Li X, Liu H, Luo D, Li J, Huang Y, Li H, Fang Y, Xu Y, Zhu L (2012) Adsorption of CO_2 on heterostructure CdS(Bi_2S_3)/TiO_2 nanotube photocatalysts and their photocatalytic activities in the reduction of CO_2 to methanol under visible light irradiation. Chem Eng J 180:151–158
186. Yang M-Q, Weng B, Xu Y-J (2013) Improving the visible light photoactivity of In_2S_3-graphene nanocomposite via a simple surface charge modification approach. Langmuir 29:10549–10558
187. Chen Z, Liu S, Yang M-Q, Xu Y-J (2013) Synthesis of uniform CdS nanospheres/graphene hybrid nanocomposites and their application as visible light photocatalyst for selective reduction of nitro organics in water. ACS Appl Mater Interfaces 5:4309–4319
188. Zhang N, Zhang Y, Pan X, Fu X, Liu S, Xu Y-J (2011) Assembly of CdS nanoparticles on the two-dimensional graphene scaffold as visible-light-driven photocatalyst for selective organic transformation under ambient conditions. J Phys Chem C 115:23501–23511

189. Zhang N, Yang M-Q, Tang Z-R, Xu Y-J (2013) CdS-graphene nanocomposites as visible light photocatalyst for redox reactions in water: a green route for selective transformation and environmental remediation. J Catal 303:60–69
190. Weng B, Liu S, Zhang N, Tang Z-R, Xu Y-J (2014) A simple yet efficient visible-light-driven CdS nanowires-carbon nanotube 1D-1D nanocomposite photocatalyst. J Catal 309:146–155
191. Liu M, Li F, Sun Z, Ma L, Xu L, Wang Y (2014) Noble-metal-free photocatalysts MoS2-graphene/CdS mixed nanoparticles/nanorods morphology with high visible light efficiency for H-2 evolution. Chem Commun 50:11004–11007
192. Yu J, Jin J, Cheng B, Jaroniec M (2014) A noble metal-free reduced graphene oxide-CdS nanorod composite for the enhanced visible-light photocatalytic reduction of CO_2 to solar fuel. J Mater Chem A 2:3407–3416
193. Liu S, Chen Z, Zhang N, Tang Z-R, Xu Y-J (2013) An efficient self-assembly of CdS nanowires-reduced graphene oxide nanocomposites for selective reduction of nitro organics under visible light irradiation. J Phys Chem C 117:8251–8261
194. Liu S, Weng B, Tang Z-R, Xu Y-J (2015) Constructing one-dimensional silver nanowire-doped reduced graphene oxide integrated with CdS nanowire network hybrid structures toward artificial photosynthesis. Nanoscale 7:861–866
195. Zhu T, Wu HB, Wang Y, Xu R, Lou XW (2012) Formation of 1D hierarchical structures composed of Ni_3S_2 nanosheets on CNTs backbone for supercapacitors and photocatalytic H_2 production. Adv Energy Mater 2:1497–1502
196. Han B, Liu S, Xu Y-J, Tang Z-R (2015) 1D CdS nanowire-2D $BiVO_4$ nanosheet heterostructures toward photocatalytic selective fine-chemical synthesis. RSC Adv 5:16476–16483
197. Han C, Chen Z, Zhang N, Colmenares JC, Xu Y-J (2015) Hierarchically CdS decorated 1D ZnO nanorods-2D graphene hybrids: low temperature synthesis and enhanced photocatalytic performance. Adv Funct Mater 25:221–229
198. An X, Yu JC, Tang J (2014) Biomolecule-assisted fabrication of copper doped SnS_2 nanosheet-reduced graphene oxide junctions with enhanced visible-light photocatalytic activity. J Mater Chem A 2:1000–1005
199. Tang Z-R, Yu Q, Xu Y-J (2014) Toward improving the photocatalytic activity of $BiVO_4$-graphene 2D-2D composites under visible light by the addition of mediator. RSC Adv 4:58448–58452
200. Fang Z, Wang Y, Song J, Sun Y, Zhou J, Xu R, Duan H (2013) Immobilizing CdS quantum dots and dendritic Pt nanocrystals on thiolated graphene nanosheets toward highly efficient photocatalytic H-2 evolution. Nanoscale 5:9830–9838
201. Cao S-W, Yuan Y-P, Fang J, Shahjamali MM, Boey FYC, Barber J, Loo SCJ, Xue C (2013) In-situ growth of CdS quantum dots on g-C3N4 nanosheets for highly efficient photocatalytic hydrogen generation under visible light irradiation. Int J Hydrog Energy 38:1258–1266
202. Zhang J, Zhu Z, Feng X (2014) Construction of two-dimensional MoS2/CdS p-n nanohybrids for highly efficient photocatalytic hydrogen evolution. Chem Eur J 20:10632–10635
203. Chen J, Wu X-J, Yin L, Li B, Hong X, Fan Z, Chen B, Xue C, Zhang H (2015) One-pot synthesis of CdS nanocrystals hybridized with single-layer transition-metal dichalcogenide nanosheets for efficient photocatalytic hydrogen evolution. Angew Chem Int Ed 54:1210–1214
204. Qi L, Yu J, Jaroniec M (2011) Preparation and enhanced visible-light photocatalytic H-2-production activity of CdS-sensitized Pt/TiO_2 nanosheets with exposed (001) facets. Phys Chem Chem Phys 13:8915–8923
205. Zhang J, Zhu Z, Tang Y, Muellen K, Feng X (2014) Titania nanosheet-mediated construction of a two-dimensional titania/cadmium sulfide heterostructure for high hydrogen evolution activity. Adv Mater 26:734–738
206. Kim HN, Kim TW, Kim IY, Hwang S-J (2011) Cocatalyst-free photocatalysts for efficient visible-light-induced H-2 production: porous assemblies of CdS quantum dots and layered titanate nanosheets. Adv Funct Mater 21:3111–3118

207. Low J, Cao S, Yu J, Wageh S (2014) Two-dimensional layered composite photocatalysts. Chem Commun 50:10768–10777
208. Hou Y, Laursen AB, Zhang J, Zhang G, Zhu Y, Wang X, Dahl S, Chorkendorff I (2013) Layered nanojunctions for hydrogen-evolution catalysis. Angew Chem Int Ed 52:3621–3625
209. Ge L, Han C, Xiao X, Guo L (2013) Synthesis and characterization of composite visible light active photocatalysts MoS_2-g-C_3N_4 with enhanced hydrogen evolution activity. Int J Hydrog Energy 38:6960–6969
210. Xiang Q, Yu J, Jaroniec M (2012) Synergetic effect of MoS_2 and graphene as cocatalysts for enhanced photocatalytic H-2 production activity of TiO_2 nanoparticles. J Am Chem Soc 134:6575–6578
211. Li Y, Wang H, Peng S (2014) Tunable photodeposition of MoS_2 onto a composite of reduced graphene oxide and CdS for synergic photocatalytic hydrogen generation. J Phys Chem C 118:19842–19848
212. Li X, Xia T, Xu C, Murowchick J, Chen X (2014) Synthesis and photoactivity of nanostructured CdS-TiO_2 composite catalysts. Catal Today 225:64–73
213. Ge L, Zuo F, Liu J, Ma Q, Wang C, Sun D, Bartels L, Feng P (2012) Synthesis and efficient visible light photocatalytic hydrogen evolution of polymeric g-C3N4 coupled with CdS quantum dots. J Phys Chem C 116:13708–13714
214. Fu J, Chang B, Tian Y, Xi F, Dong X (2013) Novel C3N4-CdS composite photocatalysts with organic–inorganic heterojunctions: in situ synthesis, exceptional activity, high stability and photocatalytic mechanism. J Mater Chem A 1:3083–3090
215. Tada H, Mitsui T, Kiyonaga T, Akita T, Tanaka K (2006) All-solid-state Z-scheme in CdS-Au-TiO_2 three-component nanojunction system. Nat Mater 5:782–786
216. Yun HJ, Lee H, Kim ND, Lee DM, Yu S, Yi J (2011) A combination of two visible-light responsive photocatalysts for achieving the Z-scheme in the solid state. ACS Nano 5:4084–4090
217. Li J, Cushing SK, Zheng P, Senty T, Meng F, Bristow AD, Manivannan A, Wu N (2014) Solar hydrogen generation by a CdS-Au-TiO_2 sandwich nanorod array enhanced with Au nanoparticle as electron relay and plasmonic photosensitizer. J Am Chem Soc 136:8438–8449
218. Iwashina K, Iwase A, Ng YH, Amal R, Kudo A (2015) Z-schematic water splitting into H-2 and O-2 using metal sulfide as a hydrogen-evolving photocatalyst and reduced graphene oxide as a solid-state electron mediator. J Am Chem Soc 137:604–607
219. Wang X, Liu G, Chen Z-G, Li F, Wang L, Lu GQ, Cheng H-M (2009) Enhanced photocatalytic hydrogen evolution by prolonging the lifetime of carriers in ZnO/CdS heterostructures. Chem Commun 45:3452–3454
220. Wang X, Liu G, Wang L, Chen Z-G, Lu GQ, Cheng H-M (2012) ZnO-CdS@Cd heterostructure for effective photocatalytic hydrogen generation. Adv Energy Mater 2:42–46
221. Yu ZB, Xie YP, Liu G, Lu GQ, Ma XL, Cheng H-M (2013) Self-assembled CdS/Au/ZnO heterostructure induced by surface polar charges for efficient photocatalytic hydrogen evolution. J Mater Chem A 1:2773–2776
222. Wang X, Yin L, Liu G (2014) Light irradiation-assisted synthesis of ZnO-CdS/reduced graphene oxide heterostructured sheets for efficient photocatalytic H-2 evolution. Chem Commun 50:3460–3463
223. Peng Y, Guo Z, Yang J, Wang D, Yuan W (2014) Enhanced photocatalytic H-2 evolution over micro-SiC by coupling with CdS under visible light irradiation. J Mater Chem A 2:6296–6300
224. Zhang LJ, Li S, Liu BK, Wang DJ, Xie TF (2014) Highly efficient CdS/WO_3 photocatalysts: Z-scheme photocatalytic mechanism for their enhanced photocatalytic H-2 evolution under visible light. ACS Catal 4:3724–3729
225. Ma G, Yan H, Shi J, Zong X, Lei Z, Li C (2008) Direct splitting of H(2)S into H(2) and S on CdS-based photocatalyst under visible light irradiation. J Catal 260:134–140

226. Tang ML, Grauer DC, Lassalle-Kaiser B, Yachandra VK, Amirav L, Long JR, Yano J, Alivisatos AP (2011) Structural and electronic study of an amorphous MoS_3 hydrogen-generation catalyst on a quantum-controlled photosensitizer. Angew Chem Int Ed 50:10203–10207
227. Peng T, Zhang X, Zeng P, Li K, Zhang X, Li X (2013) Carbon encapsulation strategy of Ni co-catalyst: Highly efficient and stable Ni@C/CdS nanocomposite photocatalyst for hydrogen production under visible light. J Catal 303:156–163
228. Zhang LJ, Xie TF, Wang DJ, Li S, Wang LL, Chen LP, Lu YC (2013) Noble-metal-free CuS/CdS composites for photocatalytic H-2 evolution and its photogenerated charge transfer properties. Int J Hydrog Energy 38:11811–11817
229. Li Z-J, Wang J-J, Li X-B, Fan X-B, Meng Q-Y, Feng K, Chen B, Tung C-H, Wu L-Z (2013) An exceptional artificial photocatalyst, Nih-CdSe/CdS core/shell hybrid, made in situ from CdSe quantum dots and nickel salts for efficient hydrogen evolution. Adv Mater 25:6613–6618
230. Hou J, Yang C, Cheng H, Wang Z, Jiao S, Zhu H (2013) Ternary 3D architectures of CdS QDs/graphene/$ZnIn_2S_4$ heterostructures for efficient photocatalytic H-2 production. Phys Chem Chem Phys 15:15660–15668
231. Zhang W, Zhong Z, Wang Y, Xu R (2008) Doped solid solution: (Zn0.95Cu0.05)(1-x)CdxS nanocrystals with high activity for H-2 evolution from aqueous solutions under visible light. J Phys Chem C 112:17635–17642
232. Shen S, Zhao L, Zhou Z, Guo L (2008) Enhanced photocatalytic hydrogen evolution over Cu-doped $ZnIn_2S_4$ under visible light irradiation. J Phys Chem C 112:16148–16155
233. Wang L, Wang W, Sun S (2012) A simple template-free synthesis of ultrathin Cu_2ZnSnS_4 nanosheets for highly stable photocatalytic H-2 evolution. J Mater Chem 22:6553–6555
234. Liu M, Zhang L, He X, Zhang B, Song H, Li S, You W (2014) L-Cystine-assisted hydrothermal synthesis of Mn1-xCdxS solid solutions with hexagonal wurtzite structure for efficient photocatalytic hydrogen evolution under visible light irradiation. J Mater Chem A 2:4619–4626
235. Wang Y, Wu J, Zheng J, Xu R (2011) Highly active ZnxCd1-xS photocatalysts containing earth abundant elements only for H_2 production from water under visible light. Catal Sci Technol 1:940–947
236. Han Z, Chen G, Li C, Yu Y, Zhou Y (2015) Preparation of 1D cubic Cd0.8Zn0.2S solid-solution nanowires using levelling effect of TGA and improved photocatalytic H-2-production activity. J Mater Chem A 3:1696–1702
237. Xu M, Zai J, Yuan Y, Qian X (2012) Band gap-tunable (CuIn)(x)Zn_2(1-x)S_2 solid solutions: preparation and efficient photocatalytic hydrogen production from water under visible light without noble metals. J Mater Chem 22:23929–23934
238. Tian F, Zhu RS, Song KL, Ouyang F, Cao G (2015) The effects of amount of La on the photocatalytic performance of $ZnIn_2S_4$ for hydrogen generation under visible light. Int J Hydrog Energy 40:2141–2148
239. Zhang K, Jing D, Xing C, Guo L (2007) Significantly improved photocatalytic hydrogen production activity over Cd1-xZnxS photocatalysts prepared by a novel thermal sulfuration method. Int J Hydrog Energy 32:4685–4691
240. Wang L, Wang W, Shang M, Yin W, Sun S, Zhang L (2010) Enhanced photocatalytic hydrogen evolution under visible light over Cd1-xZnxS solid solution with cubic zinc blend phase. Int J Hydrog Energy 35:19–25
241. Wang J, Li B, Chen J, Li L, Zhao J, Zhu Z (2013) Hierarchical assemblies of CdxZn1-xS complex architectures and their enhanced visible-light photocatalytic activities for H-2-production. J Alloys Compd 578:571–576
242. Zhou H, Liu Q, Liu W, Ge J, Lan M, Wang C, Geng J, Wang P (2014) Template-free preparation of volvox-like CdxZn1-xS nanospheres with cubic phase for efficient photocatalytic hydrogen production. Chem Asian J 9:811–818

Chapter 7
Photoreactor Design Aspects and Modeling of Light

**Paweł Mazierski, Beata Bajorowicz, Ewelina Grabowska,
and Adriana Zaleska-Medynska**

Abstract Geometry of the photoreactors depends mainly on the application as well as on the available irradiation source. Additionally, the following factors also need to be considered during the design of photoreactors: (1) type and particle size of the photocatalyst; (2) distribution of the photocatalyst (fixed or suspended); (3) type, content, and distribution of pollutants; (4) mass transfer; (5) fluid dynamics (laminar or turbulent flow); (6) temperature control; (7) reaction mechanism; and (8) reaction kinetics. This chapter deals with the general classification and description of photoreactors used for reaction carried out in the gas and liquid phase. Different types of photoreactors are described in relation to their applications.

Keywords Heterogeneous photocatalysis • Photoreactors • Solar-driven photoreactors • Wastewater treatment • Water disinfection • Air treatment

7.1 Introduction

Since heterogeneous photocatalysis has become an important area of research, it has been applied to various environmental problems including air, water, and wastewater treatment [1], destruction of microorganisms such as bacteria and viruses (disinfection processes) [2, 3], inactivation of cancer cells [4, 5], energy production (hydrogen generation by water splitting, biomass conversion, as well as CO_2 conversion into useful hydrocarbons) [6–12], remediation of oil spills [13], and chemical synthesis [14]. Nevertheless, the accomplishment of the photocatalytic processes at required scale stipulates the use of a photoreactor, a device which allows to contact photons, a photocatalyst, and reactants, as well as to collect the reaction products. In this regard, there are two critical factors and major challenges in the design of photoreactors: (1) how to provide the efficient illumination of the photocatalyst (for a high activity, a large area has to be illuminated) and (2) how to adapt photoreactors for utilization of irradiation provided by

---

P. Mazierski • B. Bajorowicz • E. Grabowska • A. Zaleska-Medynska (✉)
Department of Environmental Engineering, University of Gdansk, ul. Wita Stwosza 63,
80-308 Gdańsk, Poland
e-mail: adriana.zaleska@ug.edu.pl

J.C. Colmenares, Y.-J. Xu (eds.), *Heterogeneous Photocatalysis*, Green Chemistry
and Sustainable Technology, DOI 10.1007/978-3-662-48719-8_7

different sources. Due to the fact that scaling up of photocatalytic reactors is a difficult and complex process, there are some additional factors that also need to be considered, such as the (1) type and particle size of the photocatalyst; (2) distribution of the photocatalyst (fixed or suspended); (3) type, content, and distribution of pollutants; (4) mass transfer; (5) fluid dynamics (laminar or turbulent flow); (6) temperature control; (7) reaction mechanism; and (8) reaction kinetics.

The design of reactor geometry and selection of a photocatalytic reactor depend on the experimental conditions and the specific application. Moreover, the design of large-scale photoreactors must take into account the capacity, ruggedness, reliability, and ease of use. Figure 7.1 illustrates the main types of reactors used for air and wastewater treatment, water splitting, and CO_2, glycerol, and biomass photoconversion. In the liquid phase, the photocatalyst particles are usually suspended in a fluid phase, although other reactor configurations have also been proposed such as packed and fluidized beds with an immobilized photocatalyst. In gas-phase photocatalysis, the most common photoreactors are tubular, annular, and flat-plate types.

Regarding the photocatalyst structural configuration, thin-film powder layer and/or fluidized bed, coated wall-parallel, and honeycomb/foam monolithic reactors are probably the most representative. For photochemical water splitting, batch-type photoreactor is most frequently used configuration in lab-scale investigations. In the case of solar photoreactor systems, there are two of the major design issues: (i) whether to use a suspended or a supported photocatalyst and (ii) whether to use concentrated or non-concentrated sunlight.

The most popular reactors are (1) parabolic trough reactors (PTRs), (2) compound parabolic collecting reactors (CPCRs), and (3) non-concentrating flat-plate reactors which are the double-skin sheet reactor (DSSR).

In addition, it is necessary to pay attention to:

- The type of irradiation: photoreactors can be irradiated using artificial UV light, UV polychromatic lamps, or solar radiation
- The position of the irradiation source: immersed light source, external light source, and distributed light sources such as reflectors or optical fibers

This review deals with the general classification and description of photoreactors used for reaction carried out in the gas and liquid phase. Different types of photoreactors are described in relation to their applications.

7.2 Gas-Phase Photoreactors

Photocatalytic gas-phase reactor should contain two parts: (i) the reactor structure and (ii) source of light. Ideally, the structure of a photocatalytic reactor for air purification should have (i) light source irradiating directly on the photocatalyst surface, (ii) high specific surface area of photocatalyst, and (iii) high mass transfer, low pressure drop, and long residential time. Many types of photocatalytic reactors

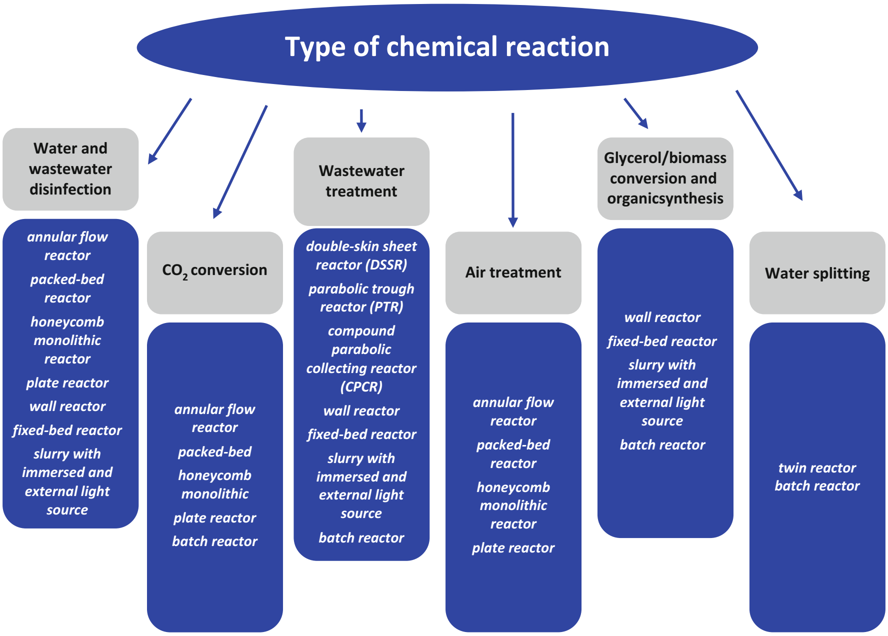

Fig. 7.1 Main types of photoreactors depending on the application

are designed. Annular, plate, slurry, honeycomb monolith, packed bed, and fluidized bed reactors are the most popular, but in the literature, other types are also described: powder layer reactor, with aerosol generator, with optical fibers, and others. However, most of the studies are only based on laboratory scale. Therefore, one of the challenges in the development of photocatalysis for environmental application is the design of efficient reactor that can be used to large-scale commercial application.

7.2.1 *Reactors for Photocatalytic Degradation of Volatile Organic Compounds (VOCs)*

Generally, the annular reactors are composed of two or more concentric cylindrical tubes mostly made of Pyrex glass. The photocatalyst is coated on the inner wall of the outer cylindrical tubes. The light source is located at the central part of the cylindrical tube. The photocatalyst film coated on the wall of the surface should be thin enough to let all the photocatalyst be irradiated by the light source. Furthermore, source of light can be located outside the reactor, and then thin film of the photocatalyst is coated on the surface of two or more concentric cylindrical tubes. The airflow is provided along the axial direction through the annulus between the lamp and the tube. Figure 7.2a shows one of the types of the annular reactor.

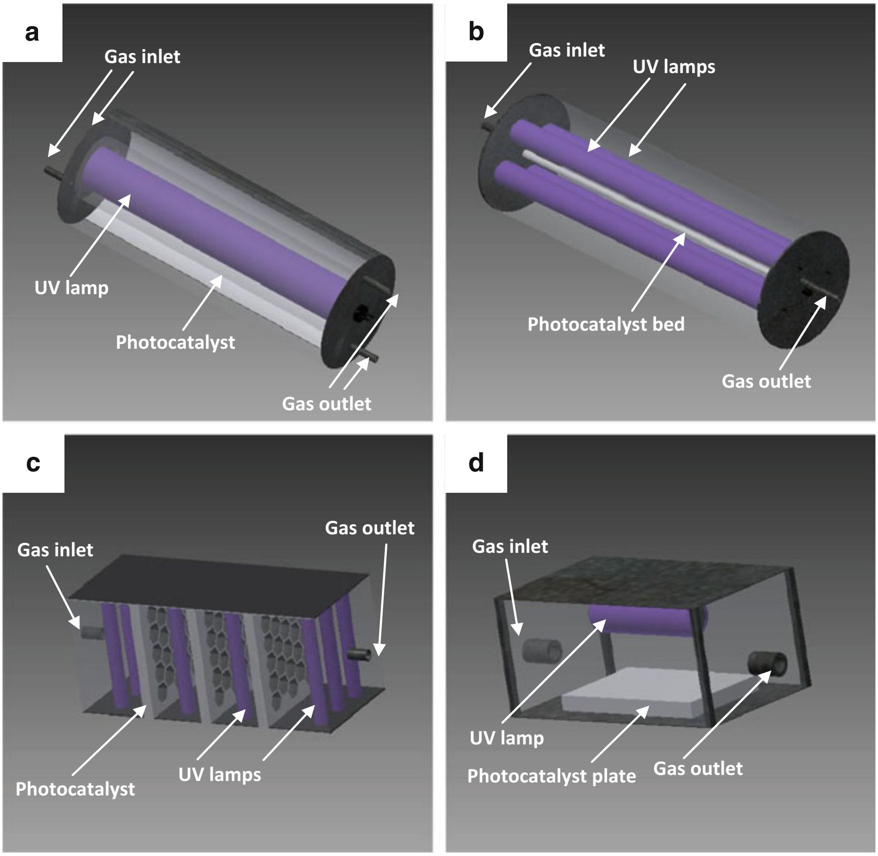

Fig. 7.2 Main types of reactors used for air treatment (**a**) annular, (**b**) packed bed, (**c**) honeycomb monolith, and (**d**) plate

Different types of the annular reactors have been used by several research groups for photocatalytic degradation of volatile organic compounds [15–19].

Tomasic et al. used the annular fixed bed photocatalytic reactor (total volume of the reactor was 0.485 dm^3) to study the degradation of toluene in the gas phase [15]. The P25-TiO_2 thin film was coated on the internal glass surface of the outer tube of the annular reactor. Fluorescent blacklight blue lamp was placed in the central part of the reactor. Tomasic et al. used mathematical models of the photocatalytic reactor (1D model and 2D models based on ideal flow and laminar flow conditions) to understand complex reaction pathways and the reactor's limitation. The obtained models were verified by comparing the computer simulation data with the experimental results. It was found out that photocatalytic reaction carried out in the annular photocatalytic reactor was mainly limited by the interphase mass transfer. Imoberdorf et al. studied the performance of single and multi-annular photocatalytic wall reactor configurations by using a two-dimensional, reaction–diffusion–convection model and reliable intrinsic reaction kinetics for the photocatalytic degradation of perchloroethylene [16]. The effect of (i) the reactor volume, (ii) the photocatalytic surface area, and (iii) the annulus width on photocatalytic degradation of perchloroethylene in single annular reactor was studied. In the case of multi-annular reactor configurations, the effect on the reactor conversion of (i) the type of flow pattern and (ii) the thickness distribution of TiO_2 films was investigated. It was found that the performance of reactors was strongly influenced by external diffusive resistances; single- and multi-annular photocatalytic reactors present high values of reactor irradiation incidence and photocatalyst irradiation absorption efficiencies. Vincent et al. investigated the photocatalytic oxidation of gaseous 1-propanol by using annular reactor (total volume was 0.0664 dm^3) [17]. The fiberglass support impregnated of P25-TiO_2 was placed between two Pyrex glass tubes. The fiberglass support area exposed to UV irradiation was 0.36 dm^2. 18 W fluorescent tube used as a source of light was located in the center of the reactor. The influence of kinetic parameters such as pollutant concentration, incident light irradiance, contact time, and humidity content has been studied. The authors concluded that the reactor efficiency could be improved in order to reduce the by-product concentrations with other experimental conditions (such as a higher contact time) [17].

The plate reactor, shown in Fig. 7.2d, is the simplest type of photoreactor used for photocatalytic degradation of volatile organic compounds. There are two basic types of plate reactors – with inner and outer source of irradiation. The typical form of this reactor is square or rectangular box, made of different materials (such as stainless steel, plexiglass, or polycarbonate), that is resistant to UV light. Photocatalyst samples used in plate reactors are in the form of powders or flat shape located at the bottom of the reactor. In the case of the plate reactors with inner source of irradiation, a lamp is placed at the upper part of the reactor. In the second one, reactors are equipped with a quartz or borosilicate window, which allows the light passage from lamp into the photocatalyst sample. The advantages of the plate reactor are small pressure drop, the possibility of obtaining large reaction rates, and simplicity. However, the major disadvantage of this type of reactor is the smaller reaction area. Salvado-Estivill et al. used a two-dimensional (2D) analysis of a flat-plate reactor for photocatalytic oxidation of trichloroethylene (TCE) in gas phase under different experimental conditions [20]. The reactor was made of stainless steel (75 mm wide and 600 mm long). A glass plate coated with the photocatalyst (P25-TiO_2) was placed 270 mm from the inlet of the reactor and 170 mm from the outlet. The plate reactor was irradiated by blacklight blue fluorescent lamps. It was found that a two-dimensional model of a flat-plate photocatalytic reactor was shown to approximate closely the experimental results of the photocatalytic oxidation of trichloroethylene. Demeestere et al. used flat-plate reactor to study the photocatalytic degradation kinetics of gaseous trichloroethylene [21]. The reactor was made of stainless steel, with two photocatalyst (P25–TiO_2)-coated glass plates located in the reactor. 18 W blacklight blue lamp used as a source of light was placed over the reactor. The effect of trichloroethylene inlet concentrations (100–500 ppmv), gas residence times (2.5–60.3 s), and relative humidity (0–62 %) has been investigated. The authors concluded that a trimolecular Langmuir–Hinshelwood model could not fit the experimental results adequately. Therefore, a new kinetic model has been developed, which was based on linear trichloroethylene adsorption–desorption equilibrium and first-order reaction kinetics. Mo et al. studied the by-products during photocatalytic degradation of toluene in a plate reactor [22]. The reactor was made of stainless steel, which two photocatalyst (P25–TiO_2)-coated glass plates located in the reactor. The UVC lamps (Philips Hg lamps) were used to irradiate the photocatalyst plate from the top of the reactor through a quartz glass. It was found that acetaldehyde, methanol, acetone, benzaldehyde, formic acid, ethanol, and acetic acid were the main by-products in the gas-phase toluene degradation.

The packed bed reactors are simple, easy-constructing, and efficient reactor. This type of reactor consists of cylindrical tube made of Pyrex glass, metal, or others. The photocatalyst is located in the central part of the reactor. The source of light can be placed inside or outside reactors. Arabatzis et al. proposed a new packed bed reactor for photocatalytic degradation of volatile organic compounds (VOCs) (see Fig. 7.2b) [23]. The form of this reactor was a cylindrical container made of metal. This container was used to concentrate the emitted light energy from the irradiation source (Sylvania F15w T8/BLBlue lamps). The porous photocatalyst was located on the outer wall of the central glass tube. This reactor has been optimized using theoretical prediction of the conversion factor as a function of the volume, reaction, and molecular feed. Ibhadon et al. presented theoretical study and kinetic modeling of a new packed bed photocatalytic reactor [24]. These results have been confirmed by experimental study on the degradation of benzene, toluene, and xylene. A cylindrical metal container was used to concentrate emitted light energy from four irradiation sources (Sylvania F15WT8/BLBlue lamps). In the central part of cylindrical metal container transparent to UV light, glass tube was located. This tube was filled with the porous P25–TiO_2 photocatalyst. It was found that theoretical and experimental conversion factor was similar and amounted to 96.7 % and 95 %, respectively. This study showed efficient way to design and optimize a packed bed photocatalytic reactor for degradation of VOCs. Fu et al. studied the effect of reaction temperature and water vapor content on the photocatalytic degradation of ethylene using packed bed reactor [25]. The reactor was made of Pyrex tube and was illuminated by four fluorescent UV bulbs. The tube with the bulbs was placed in an insulated cylindrical glass container. It was found that the reaction temperature has a strong influence on the rate of photocatalytic degradation of ethylene under UV light and TiO_2 or Pt/TiO_2 used as photocatalysts. The cause of enhanced photoactivity which was observed at increased reaction temperatures may be due to an enhanced desorption of water from both types of photocatalysts at higher operating temperatures.

Honeycomb monolith reactors are commonly used in automobile exhaust emission control and for NO_x reduction in power-plant flue gases by catalytic reduction, but they also can be used for photocatalytic reactions in the gas phase (see Fig. 7.2c). This type of reactors contains certain number of channels of circular or square cross section. The photocatalyst is coated onto the inner walls of channels as a thin film. The irradiation source is located in front of the channels. Wang et al. used honeycomb monolith reactor for modeling of formaldehyde photocatalytic degradation using computational fluid dynamics [26]. It was found that distance between the monolith and lamp should be decreased when the number of lamps increases to achieve an optimal configuration. The choice of an optimal number of lamps depends on the flow rate over the monolith. Taranto et al. used an aluminum honeycomb monolith reactor, coated with a thin film of P25–TiO_2 for methane and toluene degradation in the gas phase [27]. As the irradiation source, low-pressure mercury lamps were used. Different types of honeycomb monolith reactors have been used by several research groups for photocatalytic degradation of volatile organic compounds [28, 29].

Fluidized bed reactors are made of transparent container; the treated airstreams pass through container filled with the photocatalyst bed. The light source is located outside of the reactor. The photocatalyst has good contact with the treated airstreams. Fluidized bed reactors can be used to treating fairly high airstreams. Palma et al. used fluidized bed reactor for the intensification of gas-phase photocatalytic oxidative dehydrogenation of cyclohexane [30]. UV irradiation was provided by a two ultraviolet-light-emitting diode (UV-LED) modules located in front of the Pyrex windows. A mathematical modeling was based on Langmuir–Hinshelwood (LH)-type kinetic model. It was found that proposed mathematical model describes the performance of the photocatalytic fluidized bed reactor well for all operating conditions. Hajaghazadeh et al. studied the photocatalytic oxidation of methyl ethyl ketone under UVA light in a fluidized bed reactor [31]. The reactor was made of two parallel quartz windows incorporated in a stainless steel frame. 40 UVA-LEDs were used as an irradiation source and were located in the contact with reactor's quartz windows. Commercial TiO_2 such as P25, PC50, and PC500 was used as a photocatalyst. It was found that the photocatalytic activity depends on the surface area of the photocatalyst.

The batch reactor is the simple type of photoreactors used for VOC degradation. Typically, the batch reactor consists of a chamber made of Pyrex glass. The photocatalyst is located in the lower part of the chamber. The irradiation source is located outside the reactor. Amama et al. used cylindrical batch reactor for photocatalytic degradation of trichloroethylene [32]. The reactor (total volume 0.11 dm^3) was made of Pyrex glass. TiO_2 coated on glass fiber cloth by sol–gel process was used as a photocatalyst and illuminated by eight symmetrically arranged fluorescent blacklight lamps which were located at a fixed distance from the reactor. The authors suggested that photocatalytic degradation of trichloroethylene to carbon dioxide did not occur in the gas phase but mainly at the surface of TiO_2. Additionally, it was found that mineralization yield of trichloroethylene and by-product formation could be affected by pretreatment step of TiO_2, such as preillumination, prehydroxylation, and prechlorination of photocatalyst surface.

Debono et al. used batch reactor for photocatalytic oxidation of decane at ppb levels [33]. This reactor consisted of a Pyrex glass chamber (total volume 120 dm^3) was illuminated by nine PL-L-40 Philips UV lamps. The photocatalyst used for experiments (TiO_2–P25) was placed in the lower part of the reactor chamber. It was found that formaldehyde, acetaldehyde, and propanal were the main by-products formed in the gas phase during photocatalytic degradation of decane. Moreover, the amounts of these compounds were linearly dependent on the initial decane concentration.

To conclude, many types of photocatalytic reactors for photocatalytic degradation of VOCs have been designed. More examples of reactors are compiled in Table 7.1. The kinetic reaction and mass transfer rate are two of the main

Table 7.1 Reactors used for photocatalytic degradation of volatile organic compounds

Type of the reactor	Material of the reactor	Irradiation source	Photocatalyst	Model of VOCs	Ref.
Annular	Material not claimed	12 W low-pressure Hg lamp	TiO_2 – immobilized in the internal surface of the cylindrical tube	Methyl tert-butyl ether	[34]
				Mixture of benzene, toluene, ethylbenzene, m-, o-, and p-xylene	[35]
				C_5–C_7 alkanes	[36]
	Pyrex reactor made of two coaxial tubes	8 W blacklight lamp	Aeroxide TiO_2P25	Methyl ethyl ketone	[37]
	Two concentric Pyrex tubes	80 W Philips UVA lamp	Glass fiber tissue coated with colloidal silica and TiO_2 nanoparticles.	Isovaleraldehyde	[38]
	Material not claimed	18 W low-pressure Hg lamp	TiO_2 was coated onto the internal glass surface of reactor using dip-coating method	Benzene, toluene, ethylbenzene, and m-xylene	[39]
	Material not claimed	11 W low-pressure Hg lamp	TiO_2, TiO_2/Pt, TiO_2/Fe, TiO_2/Ce- based on P25 and isopropoxide prepared using dip-coating method	Benzene, toluene, ethylbenzene, and m-xylene	[40]
	Open tubular reactors made of Pyrex glass	4 W UVC lamp (Sankyo Denki G4T5)	Commercial P25	Dimethyl sulfide	[41]
	Pyrex glass	6 W UV lamp (Sylvania F6WBLT-6)	Platinum-doped TiO_2, painted on a Pyrex tube	Toluene	[42]
	Pyrex reactor made of two coaxial tubes	24 W solar light-simulating lamp (Philips DeLuxe pro LTJHo)	Commercial P25	Diethyl sulfide	[43]

(continued)

Table 7.1 (continued)

Type of the reactor	Material of the reactor	Irradiation source	Photocatalyst	Model of VOCs	Ref.
Batch	Stainless steel	700 W medium-pressure Hg lamp	Mixed TiO_2 and SiO_2, deposited on the cellulose and synthetic fibers bound	Acetone and 2-butanone	[44]
	Cylindrical Pyrex reactor equipped with a septum	1500 W high-pressure Xe lamp	$Y_xSr_{1-x}TiO_3$	2-Propanol and propene	[45]
	280 cm^3 glass flask	1000 W high-pressure Hg lamp	Multiphase CdS/TiO_2	Ethanol	[46]
	Quartz light window and columnar stainless steel chamber	8 W UVB lamp	Ag and Pt deposited on P25, TiO_2 prepared using sol–gel method	Trichloroethylene, chloroform, dichloromethane, toluene, benzene, carbon tetrachloride	[47]
	120 dm^3 Pyrex chamber	Nine PL-L-40 Phillips UV lamps	TiO_2 powder is sieved on a circular Pyrex plate	Limonene	[48]
	Closed stainless steel reactor with the volume of 105 dm^3	10 W germicidal lamps	TiO_2/Sr_2CeO_4	Benzene	[49]
	Cylindrical bottle with silicon/Teflon Septum	Four blacklight lamps (4 W)	TiO_2 film	2,4,6-Trichloroanisole	[50]
	Cylindrical Pyrex glass reactor	8 symmetrically arranged fluorescent blacklight (160 W)	TiO_2 coated on glass fiber cloth	Trichloroethylene	[51]
	Material not claimed	500 W Xe lamp	TiO_2 nanoparticles	Toluene	[52]
	Reactor made of Pyrex glass, upper part of the reactor was sealed with a Teflon lid	6 W germicidal lamp	TiO_2 coated on the Pyrex glass tube	Trichloroethylene, acetone, methanol, and toluene	[53]
	Closed stainless steel reactor with a volume of 105 dm^3	10 W blacklight lamps	TiO_2 loaded on $Bi_{12}TiO_{20}$	Benzene	[54]

(continued)

Table 7.1 (continued)

Type of the reactor	Material of the reactor	Irradiation source	Photocatalyst	Model of VOCs	Ref.
Optical fiber	Pyrex tube with fused silica optical fibers	500 W UV lamp	TiO_2 coated on the fused silica optical fibers	Benzene	[55]
	Pieces of optical fiber	300 W Xe arc lamp	Quartz fibers coated with TiO_2 layer	Acetone	[56]
Fixed bed	Tubular quartz reactor	Four 4W UV lamps	$BiPO_4$	Benzene	[57]
	Material not claimed	Two 8 W UV lamps	TiO_2 nanoparticles	Hexane, methanol	[58]
	Made of glass tube	Four 6 W UVA lamps	TiO_2 and F-TiO_2 nanoparticles were prepared using sol–gel method	Acetaldehyde and ethanol	[59]
	Rectangle quartz reactor	500 W Xe arc lamp equipped with a UV cutoff filter	Bi_2WO_6-coated carbon microspheres, N-doped TiO_2	Benzene	[60]
Fluidized bed	Made of glass	15 W UVC lamp	TiO_2 coated on the γ-Al_2O_3	Methyl ethyl ketone	[61]
	Concentric double-pipe structure made of Pyrex glass tube	25 W UV lamp	Commercial P25	Cyclohexane	[62]
	Quartz glass tube	10 W and 8 W germicidal white light UV lamps	TiO_2 coated on the silica gel	Trichloroethylene	[63]
Plate	Made of glass	Two germicidal UV lamps	Commercial P25 coated on the glass plate	Vinyl chloride	[64]
	Made of aluminum	Monochromatic germicidal lamps or blacklight lamps	Composite sol–gel TiO_2 and commercial P25 coated on the glass plate	Trichloroethylene and toluene	[65]

parameters having influence for performance of a photocatalytic reactor. Other influencing factors of the reactor efficiency include light of source and intensity, contaminant concentration, humidity, temperature, surface area, and activity of photocatalyst.

7.2.2 Reactors for Photocatalytic Degradation of Inorganic Pollutants

There are various photocatalytic reactors used for oxidation of inorganic pollutants in the gas phase [66–69]. Soylu et al. used flow reactor for photocatalytic oxidation of NO_x [70]. TiO_2–Al_2O_3 photocatalyst was placed on polymethyl methacrylate (PMMA) sample holder inside the reactor. The irradiation was provided by 8 W UVA lamps located outside the reactor. It was found out that TiO_2–Al_2O_3 photocatalyst showed remarkable photocatalytic NO_x oxidation and storage performance in relation to the TiO_2–P25. Dong et al. used flow reactor for photocatalytic NO removal on BiOI surface under the influence of visible light [71]. Photoreactor (4.5 dm^3) was in the form of rectangular box, made of stainless steel, and covered with quartz glass. Testing BiOI film on sample dish was located in the middle of the reactor. A LED lamp was vertically located outside the reactor above the sample dish. Wang et al. used continuous flow reactor for the oxidation of NO from a gaseous phase [72]. Photoreactor was made of Pyrex glass with "Z" type and was irradiated by one 125 W Hg arc lamp located outside the reactor. The volume of the reactor was 340 dm^3. The reactor and source of light were set in a hollow chamber which was coated with tinfoil. Various surfaces platinized TiO_2 were placed in the bottom part of the reactor. Portela et al. used continuous flow flat reactor for photocatalytic oxidation of H_2S [73]. Various photocatalysts were coated on the glass plates. The reactor with a top borosilicate glass window was irradiated by two 8 W UVA lamps. Sheng et al. used continuous flow reactor for photocatalytic oxidation of NO [74]. The woven glass fabric immobilized with photocatalyst was placed into reactor with a "Z" type, made of cylindrical Pyrex glass. 125 W Hg arc lamp used as an irradiation source was located outside the reactor.

Several research groups used fixed bed reactor for photocatalytic oxidation of NO_x, SO_2, and H_2S in the gas phase [75–78]. Liu et al. used fixed bed reactor made of double concentric quartz tubes for oxidation of NO_x and SO_2 [75]. 125 W high-pressure mercury lamp was located in the center of inner tube and was used as an irradiation source. The reactor was placed inside a black box. Cu doped titanium dioxide supported by multi-walled carbon nanotubes was placed in the outer tube. Ou et al. studied photocatalytic oxidation of NO under the influence of visible light using a fixed bed continuous flow reactor [77]. This reactor was made of tubular quartz. The 350 W Xe lamp was vertically placed, parallel with the reactor. The photocatalyst powder (g-C_3N_4/$BiVO_4$) was mixed with silica sand and packed in the reactor. The photocatalytic activity test showed that the maximum conversion of NO was 40 % when the concentration of NO was about 400 ppm under the visible light irradiation Wang et al. used bed reactor for photocatalytic decomposition of H_2S under the influence of visible light [78]. These experiments were carried out in a glass tubular reactor. The 100 W lamp was located outside the reactor. A shutter window was located between the lamp and the reactor to remove UV radiation.

Lafjah et al. studied photocatalytic oxidation of H_2S in the gas phase using single pass annular Pyrex reactor [79]. This reactor was made of two coaxial tubes, between which the contaminated air was passed through. The irradiation source (8 W blacklight tube) was located inside the internal tube. The photocatalyst powder was placed on the inner surface of the external tube. Tellez et al. used annular reactor for photocatalytic oxidation of H_2S [37, 80]. This type of annular reactor has been described previously.

The plate reactors are often used for photocatalytic oxidation of NO_x in the gas phase [81–86]. These types of reactors were described in the previous subsection. Ao et al. studied photocatalytic oxidation of NO_2 using plate reactor with inner source of irradiation (6 W UV lamp) [81]. The reactor's surface was coated by a Teflon film. TiO_2 powder was coated on the glass fiber filter. Moreover, the plate reactor made of stainless steel with inner source of irradiation was used by Chen et al. for photocatalytic oxidation of NO_x [60, 82]. Yu et al. used plate reactor with outer source of irradiation for removal of NO [83]. This reactor was made of non-adsorbing plastic material. Top of the reactor was covered with a borosilicate plate. The photocatalyst was illuminated by 25 W cool daylight lamps. Other types of the reactors used for photocatalytic oxidation of inorganic pollutants were described elsewhere [87, 88].

7.2.3 Reactors for Photocatalytic Inactivation of Bacteria

Lin et al. used reactor with the commercial TiO_2 filter for photocatalytic inactivation of *Bacillus subtilis* and *Penicillium citrinum* [89]. 8 W fluorescent blacklight lamp was placed above the surface of the filter and glass slide. Photocatalyst-coated filter and irradiation source were located inside the chamber. The spore suspensions of bacteria were dropped directly onto the center part of the TiO_2 filter. TiO_2 filter had a large pore size about 500 μm. Chotigawin et al. used photocatalytic HEPA filter for microorganism disinfection [90]. Two photocatalytic HEPA filters were located into the closed loop chamber side by side. The photocatalyst was irradiated by five 36 W UVA lamps. The photocatalytic filters were made by dip coating a HEPA filter in a P25–TiO_2 slurry. *S. epidermidis*, *B. subtilis*, *A. niger*, *and P. citrinum* were used as the model of microorganism. Vohra et al. investigated the disinfection effectiveness of commercial titanium dioxide coated on the fabric filters for *Bacillus cereus*, *Staphylococcus aureus*, *Escherichia coli*, *Aspergillus niger*, and *MS2 bacteriophage* inactivation [91]. These experiments were carried out in the recirculation duct. The form of this reactor is rectangular in cross section while the lower duct portion is circular.

Keller et al. used the photocatalytic reactor which is a Vigreux-like Pyrex tubular reactor for photocatalytic inactivation of *Escherichia coli* as the model bacteria in airstream [92]. This reactor was made of Pyrex glass. Four 8 W blacklight tubes were located outside the reactor. The photocatalyst was coated on the inside of the tube. This technical solution of the reactor allowed better contact between the solid photocatalyst and flowing bacterial contamination. The reactor consisted of an aerosol generator and a bacterial cultivation medium.

Guo et al. studied photocatalytic inactivation of *Escherichia coli* K12 placed in Petri dish irradiated by two 8 W fluorescent lamps [93]. It was found, that photocatalytic inactivation of microorganism by TiO_2, based on generation of reactive oxygen species (ROS), are followed by action of the generated ROS on the target organism. It was stated that photocatalytic inactivation of bacteria involved oxidative damage of cell walls, membranes, enzymes, and nucleic acids by ROS. Modesto et al. used plate reactor for inactivation of bacteria in the gas phase [94]. *Escherichia coli*, *Bacillus subtilis*, and *Staphylococcus aureus* were used as the model of bacteria. The reactor was made of wooden medium density fiber (MDF) plates of 15 mm thickness. Six glass plates coated with the photocatalyst were located at the lateral walls of the chamber. Four 4 W blacklight lamps were located along the chamber. The suspension of microorganisms in the airstream passed through the reactor. TiO_2, Ag–TiO_2, Pd–TiO_2, and Fe–TiO_2 were used as photocatalysts.

7.2.4 Reactors for Photocatalytic CO_2 Conversion

Photocatalytic CO_2 conversion is carried out in two major system types: (i) two phases and (ii) three phases. Two-phase systems include (i) gas photocatalyst and (ii) liquid photocatalyst. Table 7.2 shows various types of reactors that can be applied for photocatalytic CO_2 conversion in two-phase and three-phase system. It could be concluded that the convective mass transfer rate of CO_2, reaction rate, and surface area of the photocatalyst are the main factors for efficient photocatalytic CO_2 conversion.

Zhao et al. studied photocatalytic reduction of CO_2 in fixed bed reactor [100]. Gas mixture of CO_2, H_2O, and methanol was introduced into a cylindrical reactor made of stainless steel and quartz window. Ag/TiO_2 photocatalyst was coated on the glass fiber filter and placed at the bottom of the reactor. A 150 W solar simulator was located outside the reactor. The same reactor has been used by Liu et al. for photocatalytic reduction of CO_2 in the presence of Cu/TiO_2

Table 7.2 Various types of reactors used for photocatalytic CO_2 conversion in two-phase and three-phase systems

Type of the reactor	Type of CO_2 conversion systems	Ref.
Slurry	Three	[95–97]
Fixed bed	Two	[98, 99]
	Three	[100]
Annular	Two	[101, 102]
Optical fiber	Two	[103–105]
	Three	[106]
Honeycomb monolith	Two	[107]
	Three	[108]

photocatalyst [98]. Shi et al. used fixed bed reactor for photocatalytic conversion of CH_4 and CO_2 to acetone production [109]. The experiments were carried out in a continuous flow quartz fixed bed reactor. A 125 W ultrahigh pressure mercury lamp was located in the center part of the reactor. The photocatalyst bed was placed along the reactor's wall. Cu/CdS–TiO_2/SiO_2 was used as the photocatalyst. Wang et al. used fixed bed reactor for CO_2 reduction with H_2O under simulated solar irradiation [99, 110]. This reactor was made of a stainless steel with the volume of 1.5 dm^3. Photocatalyst powder was placed on the stainless steel omentum located in the center of the reactor. A 300 W Xe arc lamp was put at the top of the quartz window. A moist glass wool was placed between the bottom of the reactor and photocatalyst. The bottom of glass wool support was moisturized of deionized water.

Ola et al. used honeycomb monolith reactor for CO_2 conversion using Pd and Rh–TiO_2 photocatalyst under the influence of ultraviolet irradiation [107]. The optical fibers were uniformly distributed in the monolith and located into a cylindrical reactor made of Pyrex glass. The irradiation was carried out by the high-pressure mercury lamp through the quartz window. The reactor was covered in aluminum foil and located in the gloved box. The experiments were also carried out in the slurry batch annular reactor to comparison quantum efficiency. It was found that the quantum efficiency of the monolith reactor was 23.5 times higher than that of the slurry batch annular reactor due to the high surface area of the monolith and the elimination of uneven light distribution via the optical fibers. Tahir and Amin used microchannel monolith reactor for photocatalytic CO_2 reduction [111, 112]. The reactor was made of a stainless steel cylindrical vessel with a total volume of 0.15 dm^3. The monolith has been coated with photocatalyst and located in the center of the cylindrical reactor, equipped with a quartz window for passing light irradiations from 200 W mercury lamp. The reactor was fitted with heating and cooling jacket to adjust the reactor temperature. The photocatalytic experiment was carried out in a microchannel monolith photoreactor, and its performance was compared with a cell-type photoreactor. It was found that the quantum efficiency achieved in the cell-type reactor was much lower compared to the microchannel monolith reactor due to higher illuminated surface area, higher photon energy consumption, and better utilization of monolith reactor volume.

Nguyen et al. used continuous circular reactor made of Pyrex glass with a quartz window for reduction of CO_2 over ruthenium dye-sensitized TiO_2 metal-doped photocatalysts under concentrated natural sunlight [113]. Photocatalyst was coated on the optical fibers. High-pressure Hg lamp or concentrated natural sunlight was used as the irradiation source. The concentrated natural sunlight was collected by using a solar concentrator and transmitted via an optical cable and focused on the window of the reactor. Wu and Lin used optical fiber reactor for photocatalytic reduction of CO_2 to methanol [104]. Photocatalysts coated on 120 fibers with 16 cm long were located into the reactor. Both sides of the reactor were sealed using O-rings and illuminated from the quartz window of one side by an Hg lamp. The reactor was covered using aluminum foil to avoid the light from the outside during the reaction. Wu et al. studied this same optical fiber reactor for CO_2 reduction using TiO_2, Cu/TiO_2, and Ag/TiO_2 films coated on 216 fibers as photocatalysts [103].

7.3 Liquid-Phase Photoreactors

There are many types of reactors that can be used in the liquid-phase photocatalytic reactions. The selection usually depends on the experimental conditions and the application. Different water contaminants, ranging from hazardous contaminants of pesticides, herbicides, and detergents to pathogens, viruses, coliforms, etc., can be effectively removed in liquid-phase photoreactors. Table 7.3 summarizes various model compounds and microorganisms commonly used in the photocatalytic reactions. Examples of these various photocatalytic degradation processes and inactivation of the microorganisms will be considered in the following sections.

Liquid-phase heterogeneous photoreactors can be generally divided into three main groups based on their design characteristic such as [114–116]:

1. State of the photocatalyst: reactors with suspended photocatalyst particles (slurry) and reactors with photocatalyst immobilized on the inert surfaces
2. Type of illuminations: artificial light or solar light
3. Position of the irradiation source: external light source, immersed light sources, and distributed light sources (such as reflectors or optical fibers)

While fundamental principles of the photocatalytic processes are relatively well understood, the design and modeling of photocatalytic reactors still require consideration. It is particularly essential in the case of scaled reactors processing large volumes of water and using high levels of irradiation [115, 117].

Table 7.3 Overview of model compounds and microorganisms used for photocatalytic applications

Application	Model compound/microorganism
Photocatalytic degradation of organic pollutants	Methyleneblue [118]; methyl orange [119]; rhodamine B [120], phenol [121]; 4-nitrophenol [122]; trichloroethylene [123]; Congo red [124], chlorophenol [125], tetracycline [126], atrazine [127]
Photocatalytic inactivation of microorganisms	*E. coli* [128]; *Enterococci* [129]; *Bacillus subtilis* [130], *Pseudomonas aeruginosa* [131], *Klebsiella faecal* [132], *Pseudomonas fluorescens*, *Macrococcus caseolyticus* [133], *Salmonella typhimurium* [134], *Bacillus stearothermophilus* [135]

7.3.1 State of the Photocatalyst

7.3.1.1 Slurry Reactors

Slurry reactors are the most common and conventional reactors in photocatalytic technology [136]. In a slurry system, the catalysts are suspended in the liquid phase with the help of mechanical or gas-promoted agitation.

These show the largest photocatalytic activity compared with the immobilized photocatalyst and provide a high total surface area of photocatalyst per unit volume which is one of the most important factors configuring a photoreactor. However, these reactors require an additional downstream separation unit for the recovery of photocatalyst particles [116, 137]. Table 7.4 summarizes the advantages and disadvantages of both slurry and immobilized systems.

The effects of operational parameters on the photocatalytic slurry reactors are systematically investigated to achieve optimum reactor design for more effective photocatalytic water treatment process [115]. Nishio et al. examined the influence of light intensity, initial dye concentration, photocatalyst loading, and initial solution pH on the decolorization rate of Orange II in an external UV light irradiation slurry photoreactor using zinc oxide (ZnO) as a semiconductor photocatalyst. The experiments were performed in a Pyrex glass cylindrical reactor of 0.08 m inside diameter and 0.55 m height. The working volume was 2 dm^3. Around the cylindrical photoreactor were located three 15 W near UV fluorescent lamps (352 nm) and

Table 7.4 The advantages and disadvantages of slurry and immobilized-type reactors [115, 116, 138, 139]

Slurry reactors		Immobilized reactors
Advantages	High total surface area of photocatalyst per unit volume; Simple construction; Potentially lower capital required for a large-scale slurry reactor; Excellent heat transfer performance; Lower catalyst amount than the fixed bed reactor; Well mixed catalyst suspension; Feasibility for large capacity; Low pressure drop; Online removal and addition of catalyst; Limited mass transfer	Continuous operation; Not requiring catalyst recovery; Improved removal organic pollutant from water while using adsorptive materials
Disadvantages	The separation of product and catalyst; Catalyst attrition; Important light scattering and particle; adsorption in the particle suspended; medium	Low surface-area-to-volume ratios; Inherent inefficiencies introduced by light absorption and light scattering in the particle suspension medium; Significant pressure drop; Catalyst fouling or catalyst washout; Mass transfer limitation

externally irradiated the solution. The distance between the lamp and the photoreactor surface was 0.025 m. The photocatalytic reactor as well as lamps was totally covered with an aluminum foil. It was observed that the dye removal efficiency increased as initial pollutant concentration decreased and UV light intensity increased. The highest efficiency was achieved for ZnO concentration being around 1000 mg/dm^3 and pH was around 7.7 [140]. McCullagh presented a novel photoreactor based on a slurry continuous flow reactor configuration for methylene blue (MB) photodegradation in the presence of TiO_2 photocatalyst. This configuration combines the high surface area contact of photocatalyst with pollutant of a slurry reactor and also provides a high illumination of photocatalyst. Moreover, on the inside wall of the reactor vessel, reactor has a unique array of weir-like baffles which continuously remove catalyst from aqueous, enabling the catalyst to be exposed to UV irradiation as the reactor vessel rotates perpendicular to the light source. Experimental results indicated that developed novel reactor configuration exhibited a high UV light penetration characteristic as well as very effective mass transfer rate [141]. In another study, Subramanian et al. reported phenol degradation studies in an annular slurry reactor under various operating and design conditions. The photoreactor had concentric transparent acrylic stationary outer cylinder and inner cylinder rotating at specified revolutions per minute. Authors studied the influence of pollutant concentration (10–50 mg/dm^3), inner cylinder rotation speed (0–50 rpm), catalyst loading (0–8 g/dm^3), annular gap width (7.5, 17.5, and 32.5 mm), as well as mode of illumination: continuous or periodic on the photocatalytic performance. It was clearly demonstrated that the performance of the reactor was improving with the increased content of catalyst, but controlled periodic illumination had no significant influence on reactor efficiency over the regular continuous irradiation. Moreover, rotation of the inner cylinder was necessary only in the case of high gap width configuration at high catalyst loadings [142].

Wang et al. investigated photocatalytic disinfection of gram-negative *Pseudomonas fluorescens* and gram-positive *Macrococcus caseolyticus* spoilage bacteria under various conditions. The reactor system consisted of a magnetic stirrer, a black UV light lamp, and a baker which was exposed to the irradiation from the top. The light intensity was measured using a digital light intensity meter. It was demonstrated that increased photocatalyst contents and UVA light intensity resulted in increased microorganisms killing. Moreover, effectiveness of suspended photocatalyst depended on the initial bacterial population – nano-TiO_2 was more effective against *M. caseolyticus* than *Pseudomonas fluorescens* bacteria [133].

For the photocatalytic reduction of CO_2, in 1979, Inoue et al. introduced a slurry reactor in which catalysts were suspended in water [143]. Until 2000, slurry-type reactors were widely considered for reduction of CO_2 under UV or visible irradiation. On the other hand, Tahir and Amin suggested that this type of reactor is not efficient for enhancing the photocatalytic activity due to the low surface area and complicated separation process required to isolate the miniature catalyst grains [144]. Furthermore, one of the limitations for CO_2 photoreduction in the liquid phase is due to its low solubility in water. Therefore, Rossetti et al. developed an innovative concept of photoreactor, allowing to operate under high pressure (up to

20 bar). The proposed stainless steel reactor was effectively employed to improve CO_2 solubility in a liquid solvent even at high temperature. The suspension was saturated with CO_2 at various temperature and pressure and then irradiated with a 125 W medium-pressure Hg vapor lamp (range of emission: 254–364 nm). The results showed a strong dependence of product distribution on temperature and pressure. An increase of pressure caused increase in CO_2 concentration in the liquid phase and preferred the formation of liquid fuels such as CH_3OH and HCOOH [145].

Priya et al. developed two slurry photocatalytic reactors: batch reactor (BR) (see Fig. 7.3d) and batch-recycle reactor with continuous supply of inert gas (BRRwCG) and compared their performance in the process of hydrogen production. The photoreactors of capacity 300 m leach were made of plexiglass material which was transparent to the solar light. The photocatalytic powders were kept suspended using magnetic stirrer in the BR and gas bubbling and recycling of the suspension in the BRRwCG. The higher generation of hydrogen was observed in the case of BRRwCG due to the recycling of solution and continuous purging of inert gas, enabling the fast desorption of products [146].

7.3.1.2 Immobilized Reactor

Photocatalytic reactors with immobilized photocatalyst are those in which the photocatalyst is fixed to support by physical surface forces or chemical bonds. These reactors extend the benefit of not requiring catalyst recovery and permit the continuous operation [114, 137].

Typical photocatalyst supports are:

- Sand [147]
- Polymer films [148]
- Alumina [149]
- Glass beads [150]
- Zeolite [151]
- Activated carbon [152]
- Silica gel [153, 154]
- Stainless steel [155, 156]
- Carbon fiber [157]

Recently, Li et al. designed novel double-cylindrical-shell (DCS) photoreactor for degradation of rhodamine B (RhB) and methyl orange (MO). The photoreactor was developed by immobilizing TiO_2-coated silica gel beads on the outside surface of interior quartz glass tube of the DCS reactor. In order to optimize designed photocatalytic reactor, the operational parameters such as flow rate, initial concentration, and repetitive operation for the degradation of dye were studied. The developed novel reactor exhibited higher efficiency, lower energy consumption, and better repetitive operation performance for the degradation of RhB and MO as compared with reported slurry and thin-film photoreactors [158]. Behnajady

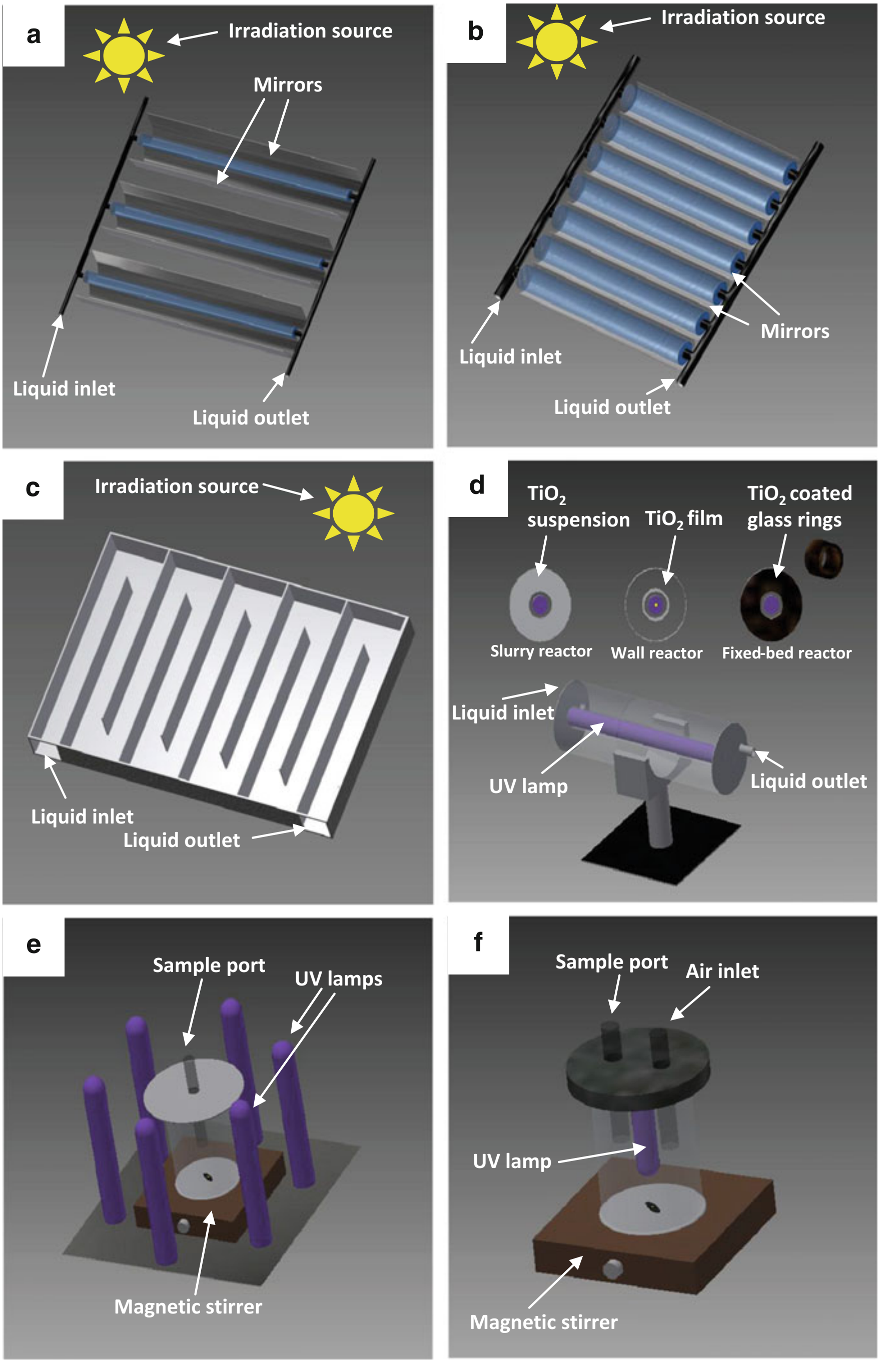

Fig. 7.3 Main types of photoreactors used for water and wastewater treatment (irradiated by sun or UV lamps): (**a**) compound parabolic collector (CPC); (**b**) parabolic trough reactors (PTR); (**c**) double-skin sheet reactor (DSSR); (**d**) slurry, wall, fixed bed reactor; (**e**) batch reactor with outer source of irradiation; and (**f**) batch reactor with inner source of irradiation

et al. described the construction and performance of a continuous flow photoreactor with immobilized TiO_2 on glass plates for photodegradation of C.I. Acid Red 27 (AR27). The photocatalytic reactor consisted of four quartz tubes connected through means of polyethylene tubes from the top to the bottom. Three glass plates loaded with TiO_2–P25 were put into the quartz tubes. Four low-pressure mercury UV lamps were placed in front of the quartz tubes. The results showed that removal efficiency of AR27 increased linearly with increasing the light intensity, but it decreased when the flow rate increased [159].

The reports about photocatalytic disinfection of water commonly use slurry photoreactor, reaching a high efficiency to inactivate microorganisms. However, some efforts have been also concentrated on using immobilized systems, usually exhibiting to be less active and requiring more irradiation time as compared with suspended systems [160, 161]. Grieken et al. developed wall and fixed bed reactors for inactivation of *Escherichia coli*. TiO_2 photocatalyst was immobilized in an annular reactor in two different ways: on the inner reactor wall and on the surface of glass rings used in packed fixed bed reactor. The effect of the increase in the TiO_2 layer thickness has been evaluated, and the results have been compared with those obtained for increasing concentrations of TiO_2 slurries (see Fig. 7.3d). Although immobilized systems were less photoactive than slurry system, they exhibited a higher resistance to the inhibition by organic matter, leading to comparable irradiation time to obtain microorganism concentration below detection limit in wastewater [162].

Hsu et al. immobilized S-doped ZnO nanorods on stainless steel mesh as novel hierarchical photocatalysts for water splitting to hydrogen production. Polymer additive enabled the growth of nanorods on the total surface of wire mesh. The surface texture and photocatalytic hydrogen production performance from salt water under UV light irradiation in a reactor loaded with these photocatalysts were tested. The highest evolution rate was achieved due to increased surface area of the hierarchical immobilized photocatalyst, enhanced light trapping, as well as liquid flow among wire meshes [163].

7.3.2 Type of Irradiation

7.3.2.1 Artificial Light

One of the most challenging parameters in the design of photoreactors is the appropriate illumination of catalyst. Therefore, the important aspects in design consideration for photocatalytic reactors are light wavelength, light intensity, as well as type of irradiation source [115]. There are main types of artificial irradiation sources including: (i) arc lamps, (ii) fluorescent lamps, (iii) incandescent lamps, (iv) lasers, and (v) light-emitting diodes (LEDs). Arc lamps are often named according to the gas contained in the bulb, including neon, argon, xenon, krypton,

Table 7.5 Overview of artificially illuminated liquid-phase photoreactor

Configuration	Catalyst	Light source	Application	Ref.
Labyrinth flow bubble photoreactor	Suspended	Tubular UV lamp (365 nm)	Methyl orange degradation	[165]
Carberry photoreactor	Immobilized	Low-pressure mercury (355 nm)	4-Chlorophenol degradation	[166]
Twin reactor	Suspended	500 W halogen lamp	Hydrogen production	[167]
Batch-recycle reactors	Suspended	Hg-Xe UV lamp	Hydrogen production	[168]
Batch annular reactor	Suspended	9 W Hg lamp	CO_2 photoreduction	[169]
Tubular reactor	Immobilized	Low-pressure mercury lamp	Pollutant degradation	[170]
Fluidized bed reactor	Immobilized	Low-pressure mercury vapor UV lamp	Hydrogen production	[171]

sodium, metal halide, and mercury. Additionally, mercury lamps can be grouped in low, medium, and high-pressure mercury lamp categories [164] (Table 7.5).

Swarnalatha et al. studied photocatalytic oxidation of 2,6-dinitrophenol using different catalysts: TiO_2, TiO_2–P25, CdS, WO_3, and ZnO. The annular-flow photocatalytic reactor used in this research was a cylindrical plastic vessel, in which the mercury lamp is surrounded by a quartz glass tube to belay it from direct contact with an aqueous solution flowing by an annulus between the inner surface of the vessel and the outer surface of the quartz glass tube. It was demonstrated that aqueous TiO_2–P25 suspension exhibited the highest efficiency in photocatalytic degradation at the wavelength of 254 nm using an annular-flow-type reactor equipped with an 8 W low-pressure mercury lamp. Moreover, the effect of irradiation time and pH on the efficiency of degradation was investigated. The pollutant degradation in the presence of P25 was found to incrementally increase with increasing irradiation time at an optimum pH of 8. Complete degradation of the 2,6-dinitrophenol occurred after 3 h of irradiation [172]. In another study, Han et al. investigated photocatalytic degradation of p-chlorobenzoic acid (p-CBA) in aqueous solution using two kinds of low-pressure mercury lamps: UV lamp emitted at 254 nm and the vacuum UV lamp emitted at both 254 nm and 185 nm. The lamp was put in the center of the photocatalytic reactor with quartz tube protection (outer diameter 25 mm). Oxygen or air was used as a bubbling gas which was implemented to the reactor through a porous glass plate with a flow rate of 200 cm^3/min. It could be seen that degradation of p-chlorobenzoic acid was more effective in the presence of vacuum UV lamp than in the case of UV lamp when the same power lamps were used in research [173].

Chen et al. investigated photocatalytic disinfection of *Escherichia coli* K12 using natural sphalerite (NS) as a photocatalyst under various spectra and intensities of visible light emitted by LEDs. The photocatalytic test was performed in the reactor equipped with 16 LED lights and compared with results obtained for two other visible light sources such as fluorescent tube and xenon lamp. Moreover, photocatalytic disinfection of microorganisms was compared under various single spectra: blue, green, yellow, and red color LEDs. It was shown that the most effective wavelength ranges for photocatalytic inactivation of bacteria are 440–490 and 570–620 nm. Moreover, a positive dependence was observed between the disinfection efficiency and the visible light intensity. The results showed also that NS caused complete inactivation of *E. coli* within 8 h irradiation using white LEDs [174]. In another study, Benabbou et al. examined photocatalytic inactivation of *Escherichia coli* K12. The disinfection experiments were carried out in a Pyrex reactor in which an HPK 125 W lamp emitting in the 200–400 nm range was used as irradiation source. Moreover, various optical filters were used to modify lamp emission spectrum. The light intensity was controlled by grids with various sizes of mesh, which were put on the lamp. The effect of different types of UV light, including UVA, UVB, and UVC was also examined, and modification of the light radiation intensity was discussed. It was found that the addition of photocatalyst at low concentration improved the inactivation of bacteria in the presence of UVA and UVB, but negative effect was noted under UVC. Furthermore, the photocatalytic efficiency increased as a function of light intensity, no matter the experimental conditions [175].

Kočí et al. studied the effect of reactor geometry on the photocatalytic reduction of CO_2 using ZnS nanoparticles deposited on montmorillonite as a catalyst. The photocatalytic experiments were performed in two homemade batch annular reactors with three quartz tubes of various diameters: 3.5, 4.0, and 4.5 cm. The photocatalyst was suspended in NaOH solutions, and after saturation by CO_2, the suspension was illuminated using UV 8 W Hg lamp (254 nm). It was demonstrated that for both reactors, the highest activity of the photocatalytic reduction was obtained in a configuration where the lamp touched the surface of the liquid in the reactor and the configuration of the reactor was not annular. Moreover, it was suggested that one of the most important factors in the slurry reactors is appropriate mixing but its implementation is difficult in apparatus of annular configuration [102].

Hernández-Gordillo et al. investigated photocatalytic activity of CdS photocatalyst for the hydrogen production from either methanol–water or sulfide/sulfite solution in the presence of blue light energy. The photocatalytic tests were performed in a glass homemade photoreactor without any cooling system. The solution was irradiated using blue light emitted by LED lamps of very low power (3 W) which were placed in appropriate positions to allow complete illumination of the suspended catalysts. It was shown that the amount of hydrogen generated linearly increased as a function of the number of LED lamps, achieving to a hydrogen production of 9.54 μmol/h. This study suggested that the hydrogen production depended very strongly on the lamp intensity [176]. In another study, Gomathisankar et al. investigated photocatalytic hydrogen production from aqueous methanol solution using Cu-deposited ZnO photocatalyst. The photocatalytic test was carried out in the Pyrex column vessel reactor. The spout of vessel was hermetic closed with septum and aluminum insulating. The optical filter

($\lambda > 400$ nm) was used for the visible light irradiation. A xenon lamp (500 W) was located on the side of the photoreactor and used as a light source. The light intensity was controlled by a UV radiometer equipped with a sensor of 320–410 nm wavelengths. It was demonstrated that Cu-deposited ZnO had the response to the visible light for the hydrogen production. Furthermore, under the optimal conditions, the photoactivity was about 130 times higher than those showed for bare ZnO photocatalyst [177].

7.3.2.2 Solar Light

The implementation of solar photocatalytic reactors has occurred concurrently with advances in the design of solar thermal collectors. There are specific constraints for the design of solar photocatalytic reactors such as [178, 179]:

- The wastewater must be exposed to ultraviolet solar radiation; therefore, the collector must be made of UV transparent materials.
- Temperature negligible affected the photocatalytic process, so no insulation is required.
- Construction should be economical and efficient with a low pressure drop.

Solar photocatalytic reactors can be divided into concentrating and non-concentrating (one sun) systems depending on received irradiation [180]. - Non-concentrating solar reactors use intensities equal or lesser than natural solar irradiation, while concentrating solar reactors require intensities that surpass irradiations equivalent to one sun [116].

In the concentrating design, solar radiation is collected in a photocatalytic reactor by a reflecting surface, and because of this, for the same light-harvesting area, the reactor volume is smaller than in the case of non-concentrating system [180]. The most promising type of concentrating solar reactor is parabolic trough collector (PTC) which is demonstrated to be efficient for wastewater treatment. PTCs consist of platform that has one or two motors controlled by single- or dual-axis solar tracking system that maintain the collector aperture plane perpendicular to incoming solar radiation (see Fig. 7.3b) [181].

Non-concentrating photoreactors have no moving parts or solar tracking devices (see Fig. 7.3c). This kind of reactor does not concentrate radiation, and because of this, efficiency is not limited by factors connected with reflection, concentration, or solar tracking. In this system, optical efficiency is higher as compared with concentrating reactors. Moreover, non-concentrating system can utilize the diffuse and direct portion of the solar UVA [182]. One-sun collectors are usually cheaper than PTCs because their elements are simpler, and the surface required for their installation is smaller [178].

Compound parabolic collectors (CPCs) belong to the most promising photocatalytic solar reactors which combine the advantages of parabolic trough concentrator and non-concentrating system [178]. CPCs are low-concentration static collectors with reflective surface and can be designed for any given reactor shape (see Fig. 7.3a) [182]. The CPC reflectors are usually made from polished aluminum because of its high reflectivity in the UV range and high resistance to the environmental conditions. Pipes and valves are manufactured from polyethylene; photoreactor tube is made of borosilicate 25 glass due to high transmission in the UV range of its material. Water flows through the borosilicate tubes to a tank by a centrifugal pump, allowing a turbulent regime inside the photocatalytic reactor [183].

Zayani et al. investigated performances of solar pilot plant for photocatalytic removal of azo dye used as a model pollutant. Experiments were carried out in thin-film fixed bed reactor with an illuminated area of 25 m^2. Effect of important operating parameters including flow rate, catalyst loading, and initial dye concentration on photocatalytic treatment kinetic was examined for optimization which will be necessary in designing large-scale photoreactors. Furthermore, the photodegradation kinetic of total organic carbon (TOC) was discussed in terms of Langmuir–Hinshelwood model [184]. Xu et al. developed novel optical fiber reactor (OFR) in which side-glowing optical fibers (SOFs) were used as light transmission medium as well as photocatalyst supporter. The SOF was made up of quartz core with a silicon cover which can emanate light from side surface more uniformly and transmit light for longer distance. Furthermore, SOF was flexible and can be entwined into any shapes. It was demonstrated that novel reactor can collect solar light efficiency while occupying smaller surface as compared with traditional solar collectors. It was observed that 79 % of 4-chlorophenol decomposed under sunlight irradiation during 8 h [185].

Vidal et al. presented the first pilot-plant study about solar photocatalysis for bacterial inactivation. Researchers constructed a new low-cost compound parabolic concentrator (CPC) prototype containing: solar collector (Pyrex photoreactor tubes, aluminum reflective surface), flowmeter, pump, sensors (pH, O, T, UV radiation), pipes, fittings, and tanks (PVC). This solar photoreactor has an area of 4.5 m^2 and it was tilted at local latitude to maximize the available solar irradiation. It was observed 5-log reduction for *E. coli* and *Enterococcus faecalis* (initial concentration: 10^2–10^4 CFU/cm^3) after 30 min of solar irradiation (solar UV value: 25 W/m^2) [186]. In another study, McLoughlin et al. compared three different solar collectors for the disinfection of water heavily contaminated with *Escherichia coli*. It was demonstrated that three lab-scale solar photoreactors which were constructed using Pyrex tubing and aluminum reflectors of compound parabolic, parabolic, and V-groove profiles all enhance the effect of natural solar irradiation. Among these three collector shapes, compound parabolic reflector promoted the most efficient inactivation of bacteria. Moreover, researchers carried out the tests to assess the improvement to disinfection which could be achieved using TiO_2-coated Pyrex rods fixed within the reactors. However, this solution caused only a slight improvement in performance of the compound parabolic reactor and no enhancement to overall disinfection performance in either the parabolic and V-groove reactors [187]. Alrousan et al. carried out solar photocatalytic disinfection of water using compound parabolic collector and P25 immobilized on borosilicate glass tube. Researchers tested several photoreactor configurations such as (1) borosilicate glass tubes (1.5 m in length) of diameter 50 mm dip coated with TiO_2–P25, (2) uncoated 50 mm borosilicate glass tubes, (3) 32 mm borosilicate glass tube externally dip coated with TiO_2, and (4) uncoated 32 mm borosilicate glass tube.

Each configuration was examined using one tube and one CPC mirror, with an irradiated surface of 0.2 m^2 and a total volume of treated water of 7 dm^3 The most effective configuration was the concentric tube arrangement with CPC [188].

In spite of the still insufficient efficiency of direct photocatalytic water splitting, there are few trials in large-scale application of hydrogen photoreactors in the literature [189]. Jing et al. developed CPC-based solar reactor for photocatalytic hydrogen production that consisted of solar collector, Pyrex photoreactor tubes, reflective surface, and flow meter; fitting, pipes, and tanks; and pump and sensors. The photocatalytic performance was investigated for various design parameters such as tube radius, flow velocity, photocatalyst, as well as sacrificial agent concentrations. In optimal conditions, this photoreactor had higher hydrogen rate per unit volume than in the case of lab-scale reactor which could be caused by the design of tubular reactor properly illuminated by CPC on one side [190]. In another study, Villa et al. tested the simultaneous photocatalytic hydrogen production under direct solar irradiation at pilot-plant scale. The experiments were performed in a compound parabolic collector (CPC) composed of Pyrex glass tube placed on the fixed platform. A centrifugal pump with a flow rate of 20 dm^3/min enabled the recirculation of the aqueous slurry from the tank to the tubes of the photoreactor. The hydrogen was generated from aqueous solutions of formic acid, glycerol, as well as a real wastewater. The highest hydrogen production was obtained with aqueous solution of formic acid after 5 h of irradiation. However, the tests with real wastewater gave moderate amount of hydrogen, suggesting the possible use of such waters for hydrogen production in the future [191].

7.3.3 Position of the Irradiation Source

The arrangement of light source is another important aspect of photocatalytic reactor design. In the case of immersed-type reactor configuration, the lamp is placed inside the unit (see Fig. 7.3e). In external-type reactor, the lamp is located outside the reactor (see Fig. 7.3f). Light has to pass through reactor wall to get the water body. In this kind of reactor, the light intensity and evenness of UV fluence rate (UV-FR) are usually lower than that in the other two types for the same power consumption [192, 193]. Another type is the distributed reactor where light is transported from the source to the photocatalytic reactor using reflectors or light guides [194]. The distributive-type reactor usually is characterized by higher and more uniform irradiation inside the reactor than the external-type reactor.

Effects of different lamp arrangements on photocatalytic reactor performance have not been well studied. Recently, Xu et al. used computational fluid dynamics (CFD) simulation software FLUENT to simulate microorganism particle motion in various UV water disinfection reactors. The influence of lamp arrangements on the UV-FR field and log reduction of different UV water disinfection photoreactors were studied under various flow rates and constant UV dosage. In the experiment, direction, number, and orientation of lamps were diverged. The results showed that overall effects on the reactor log reduction were complex. Higher water flow rate reduced “barrier” effect in reactors with multiple lamps, lowering log reduction. This study provided new approach for understanding the effect of lamp arrangement on the performance of photodisinfection reactor [193]. Palmisano et al. performed the validation of a two-dimensional model describing the behavior of a batch cylindrical photoreactor, externally irradiated by 1–6 UV fluorescent lamps coupled with a modified Langmuir–Hinshelwood kinetics. Experimental runs were performed at different 4-nitrophenol concentration, Degussa TiO_2–P25 amounts, and under various irradiation configurations. The proposed model allows to determine the behavior of the photoreactor in a wide range of operating conditions: various catalyst and substrate loadings as well as radiations have been applied [195]. Moreover, in the literature, there are a few other reports about models for externally irradiated cylindrical reactors [196, 197].

7.4 Light Modeling

Most of the work in the field of design and modeling of photoreactors was done by Cassano and Alfano [16, 180, 198, 199]. In the case of photoreactor modeling, three main components should be considered: (1) thermal energy balance, (2) multicomponent mass conservation, and (3) photon balance (radiation energy). Balance of photons should be considered independently from the thermal energy balance since the energy useful in photochemical processes is generally negligible. The radiation energy used in the most majority of photochemical processes can be attributed to a range of wavelengths between 200 and 600 nm. *Local volumetric rate of energy absorption* (LVREA), defined as the rate of the radiation-activated step and proportional to the absorbed energy, was preliminarily introduced by Irazoqui et al. [200]. The LVREA depends on the photon distribution in the reaction space. To begin any photochemical reactions, absorption of a photon by a molecule resulted in formation of an excited state is a necessary step. Following absorption of radiation, a few pathways, different from the desired reaction, could be predicted, such as (1) a different, parallel reaction, (2) phosphorescence, (3) fluorescence, (4) deactivation by chemical quenching, etc. In a single-photon absorption process, the rate of radiation-activated step is proportional to the rate of energy absorbed (LVREA). The proportionality constant is the primary reaction quantum yield, defined as:

$$\Phi_{prim,\ v} = \frac{numbermolec_{prim}}{numberphoto_{v}absorb.}$$

where:

$numbermolec_{prim}$ is the number of molecules following the expected path in the primary process.

$numberphot_{v}$ *absorb.* is the number of absorbed quanta of radiation.

In most cases, radiation may be arriving at one point inside a photochemical reactor from all directions in space. For a photochemical reaction to take place, this radiation has to be absorbed by an elementary reacting volume described as spectral incident radiation (G_v expressed in W/m^2):

$$G_v = \int_{\Omega} I_v d\Omega$$

where:

I_v is the spectral specific intensity (W/m$^2 \cdot$ sr).
Ω is the unit direction vector (coincides with the axis of an elementary cone of solid angle $d\Omega$).

Thus, to evaluate the LVREA in the case of polychromatic radiation, we have to know the spectral intensity at each point inside the reactor, according to the following equation [198]:

$$e^a = \int_{v1}^{v2}\int_{\theta1}^{\theta2}\int_{\phi1}^{\phi2} \kappa_v I_v \sin\theta d\phi d\theta dv$$

where:
(θ_1, θ_2) and (Φ_1, Φ_2) are the integration limit that define the space from which radiation arrives at the point of incidence.

7.5 Conclusions

Gas- and liquid-phase photoreactors discussed in this chapter specify the diversity in photocatalytic reactor design along with their potential applications. The following conclusions could be pointed based on the current state of the art in this field:

1. Photoreactors could be generally classified into three main groups based on their design characteristics such as (*i*) *state of the photocatalyst*, reactors with suspended photocatalyst particles (slurry) and reactors with photocatalyst immobilized on the inert surfaces; (*ii*) type of illuminations, artificial light or solar light; and (*iii*) position of the irradiation source, external light source, immersed light sources, and distributed light sources (such as reflectors or optical fibers).
2. Solar-driven large-scale photoreactors are mainly used for water/wastewater treatment and disinfection.
3. Local volumetric rate of energy absorption (LVREA) is defined as the rate of the radiation-activated step in the photochemical reaction and depended on the photon distribution in the reaction space.

Table 7.6 Summary of the principal advantages and disadvantages of gas- and liquid-phase photoreactors

Type of the photoreactor	Advantages	Disadvantages
Liquid-phase photoreactors	Feasibility for large capacity; Very good heat transfer performance; More efficient removal of organic pollutants from water while using adsorptive material	Inherent inefficiencies introduced by light absorption or scattering in the particle suspension medium; Photocatalyst attrition; Possible photocatalyst fouling or washout
Gas phase photoreactors	Relatively low levels of radiation intensity needed to perform reaction; Small amount of photons adsorbed by air and sufficient electron scavengers; Photocatalyst in a form of thin layer – there is no separation of product and photocatalyst; Higher quantum yield of photocatalytic reaction (comparing to liquid phase)	Pollutant adsorption on the walls of the reactor

The advantages and disadvantages of liquid- and gas-phase photoreactors are briefly summarized in Table 7.6.

The industrial application of photocatalytic processes is still limited due to the high cost of UV irradiation light as well as the problem with separation and reusing of photocatalysts after reaction. It could be also assumed that quantum yield in gas-phase reaction is much higher than that one in liquid-phase reaction due to lower light scattering. Therefore, solar-driven or low-powered UV lamp-irradiated (e.g., light-emitting diodes) photoreactors are crucial for broader-scale application of photocatalytic processes. Moreover, the future prospect of photocatalysis cannot rely only on the design of the photoreactors but also on the development of more effective photocatalysts. Photocatalysts used during the processes must achieve greater conversion efficiencies at lower irradiation energies. Finally, visible light-absorbing materials will be the most important component in wide-scale technology.

References

1. Fujishima A, Zhang X (2006) Titanium dioxide photocatalysis: present situation and future approaches. C R Chim 9:750–760
2. Ireland JC, Klostermann P, Rice EW, Clark RM (1993) Inactivation of Escherichia coli by titanium dioxide photocatalytic oxidation. Appl Environ Microbiol 59:1668–1670
3. McCullagh C, Robertson JM, Bahnemann DW, Robertson PK (2007) The application of TiO_2 photocatalysis for disinfection of water contaminated with pathogenic micro-organisms: a review. Res Chem Intermed 33:359–375

4. Cai R, Hashimoto K, Kubota Y, Fujishima A (1992) Increment of photocatalytic killing of cancer cells using TiO_2 with the aid of superoxide dismutase. Chem Lett 21:427–430
5. Cai R, Kubota Y, Shuin T, Sakai H, Hashimoto K, Fujishima A (1992) Induction of cytotoxicity by photoexcited TiO_2 particles. Cancer Res 52:2346–2348
6. Borgarello E, Kiwi J, Pelizzetti E, Visca M, Grätzel M (1981) Photochemical cleavage of water by photocatalysis. Nature 289:158–160
7. Li C, Xi Z, Fang W, Xing M, Zhang J (2015) Enhanced photocatalytic hydrogen evolution activity of $CuInS_2$ loaded TiO_2 under solar light irradiation. J Solid State Chem 226:94–100
8. Wang H, Chen W, Zhang J, Huang C, Mao L (2015) Nickel nanoparticles modified CdS–A potential photocatalyst for hydrogen production through water splitting under visible light irradiation. Int J Hydrog Energy 40:340–345
9. Wang Z, Teramura K, Hosokawa S, Tanaka T (2015) Photocatalytic conversion of CO_2 in water over Ag-modified La_2 Ti_2 O_7. Appl Catal Environ 163:241–247
10. Lee C-W, Kourounioti RA, Wu JC, Murchie E, Maroto-Valer M, Jensen OE, Huang C-W, Ruban A (2014) Photocatalytic conversion of CO_2 to hydrocarbons by light-harvesting complex assisted Rh-doped TiO_2 photocatalyst. J CO_2 Utils 5:33–40
11. Chong R, Li J, Ma Y, Zhang B, Han H, Li C (2014) Selective conversion of aqueous glucose to value-added sugar aldose on TiO_2-based photocatalysts. J Catal 314:101–108
12. Gu Q, Long J, Fan L, Chen L, Zhao L, Lin H, Wang X (2013) Single-site Sn-grafted Ru/TiO_2 photocatalysts for biomass reforming: synergistic effect of dual co-catalysts and molecular mechanism. J Catal 303:141–155
13. Nair M, Luo Z, Heller A (1993) Rates of photocatalytic oxidation of crude oil on salt water on buoyant, cenosphereattached titanium dioxide. Ind Eng Chem Res 32:2318–2323
14. Yoon TP, Ischay MA, Du J (2010) Visible light photocatalysis as a greener approach to photochemical synthesis. Nat Chem 2:527–532
15. Tomašić V, Jović F, Gomzi Z (2008) Photocatalytic oxidation of toluene in the gas phase: modelling an annular photocatalytic reactor. Catal Today 137:350–356
16. Imoberdorf GE, Cassano AE, Irazoqui HA, Alfano OM (2007) Optimal design and modeling of annular photocatalytic wall reactors. Catal Today 129:118–126
17. Vincent G, Marquaire P-M, Zahraa O (2009) Photocatalytic degradation of gaseous 1-propanol using an annular reactor: kinetic modelling and pathways. J Hazard Mater 161:1173–1181
18. Vincent G, Marquaire P-M, Zahraa O (2008) Abatement of volatile organic compounds using an annular photocatalytic reactor: study of gaseous acetone. J Photochem Photobiol A 197:177–189
19. Imoberdorf G, Irazoqui H, Cassano A, Alfano O. Modelling of a multi-annular photoreactor for the degradation of perchloroethylene in gas phase
20. Salvadó-Estivill I, Brucato A, Li Puma G (2007) Two-dimensional modeling of a flat-plate photocatalytic reactor for oxidation of indoor air pollutants. Ind Eng Chem Res 46:7489–7496
21. Demeestere K, De Visscher A, Dewulf J, Van Leeuwen M, Van Langenhove H (2004) A new kinetic model for titanium dioxide mediated heterogeneous photocatalytic degradation of trichloroethylene in gas-phase. Appl Catal Environ 54:261–274
22. Mo J, Zhang Y, Xu Q, Zhu Y, Lamson JJ, Zhao R (2009) Determination and risk assessment of by-products resulting from photocatalytic oxidation of toluene. Appl Catal Environ 89:570–576
23. Arabatzis I, Spyrellis N, Loizos Z, Falaras P (2005) Design and theoretical study of a packed bed photoreactor. J Mater Process Technol 161:224–228
24. Ibhadon A, Arabatzis I, Falaras P, Tsoukleris D (2007) The design and photoreaction kinetic modeling of a gasphase titania foam packed bed reactor. Chem Eng J 133:317–323
25. Fu X, Clark LA, Zeltner WA, Anderson MA (1996) Effects of reaction temperature and water vapor content on the heterogeneous photocatalytic oxidation of ethylene. J Photochem Photobiol A 97:181–186

26. Wang X, Tan X, Yu T (2014) Modeling of formaldehyde photocatalytic degradation in a honeycomb monolith reactor using computational fluid dynamics. Ind Eng Chem Res 53:18402–18410
27. Taranto J, Frochot D, Pichat P (2009) Photocatalytic air purification: comparative efficacy and pressure drop of a TiO_2-coated thin mesh and a honeycomb monolith at high air velocities using a 0.4 m 3 close-loop reactor. Sep Purif Technol 67:187–193
28. Wei D, Vanderspurt T, Hay S, Schmidt W, Obee T, Wei D, H. VT, O HS, R SW, N OT (2005) Bifunctional layered photocatalyst/thermocatalyst for improving indoor air quality
29. Wei D, Obee TN, Hay SO, Vanderspurt TH, Schmidt WR, Sangiovanni JJ (2007) C. Corporation, oxidation impurities in air; applying ultraviolet radiation to oxidation catalyst; activation
30. Palma V, Sannino D, Vaiano V, Ciambelli P (2010) Fluidized-bed reactor for the intensification of gas-phase photocatalytic oxidative dehydrogenation of cyclohexane. Ind Eng Chem Res 49:10279–10286
31. Hajaghazadeh M, Vaiano V, Sannino D, Kakooei H, Sotudeh-Gharebagh R, Ciambelli P (2014) Heterogeneous photocatalytic oxidation of methyl ethyl ketone under UV-A light in an LED-fluidized bed reactor. Catal Today 230:79–84
32. Amama PB, Itoh K, Murabayashi M (2002) Gas-phase photocatalytic degradation of trichloroethylene on pretreated TiO_2. Appl Catal Environ 37:321–330
33. Debono O, Thévenet F, Gravejat P, Hequet V, Raillard C, Le Coq L, Locoge N (2013) Gas phase photocatalyticoxidation of decane at ppb levels: removal kinetics, reaction intermediates and carbon mass balance. J Photochem Photobiol A 258:17–29
34. Boulamanti AK, Philippopoulos CJ (2008) Photocatalytic degradation of methyl tert-butyl ether in the gas-phase: a kinetic study. J Hazard Mater 160:83–87
35. Boulamanti AK, Korologos CA, Philippopoulos CJ (2008) The rate of photocatalytic oxidation of aromatic volatile organic compounds in the gas-phase. Atmos Environ 42:7844–7850
36. Boulamanti AK, Philippopoulos CJ (2009) Photocatalytic degradation of C_5–C_7 alkanes in the gas–phase. Atmos Environ 43:3168–3174
37. Alonso-Tellez A, Masson R, Robert D, Keller N, Keller V (2012) Comparison of Hombikat UV100 and P_{25} TiO_2 performance in gas-phase photocatalytic oxidation reactions. J Photochem Photobiol A 250:58–65
38. Assadi AA, Palau J, Bouzaza A, Wolbert D (2013) Modeling of a continuous photocatalytic reactor for isovaleraldehyde oxidation: effect of different operating parameters and chemical degradation pathway. Chem Eng Res Des 91:1307–1316
39. Korologos CA, Philippopoulos CJ, Poulopoulos SG (2011) The effect of water presence on the photocatalytic oxidation of benzene, toluene, ethylbenzene and m-xylene in the gas-phase. Atmos Environ 45:7089–7095
40. Korologos CA, Nikolaki MD, Zerva CN, Philippopoulos CJ, Poulopoulos SG (2012) Photocatalytic oxidation of benzene, toluene, ethylbenzene and m-xylene in the gas-phase over TiO_2-based catalysts. J Photochem Photobiol A 244:24–31
41. Lee DM, Yun HJ, Yu S, Yun SJ, Lee SY, Kang SH, Yi J (2012) Design of an efficient photocatalytic reactor for the decomposition of gaseous organic contaminants in air. Chem Eng J 187:203–209
42. Colón G, Maicu M, Hidalgo M, Navío J, Kubacka A, Fernández-García M (2010) Gas phase photocatalytic oxidation of toluene using highly active Pt doped TiO_2. J Mol Catal A 320:14–18
43. Grandcolas M, Cottineau T, Louvet A, Keller N, Keller V (2013) Solar light-activated photocatalytic degradation of gas phase diethylsulfide on WO_3-modified TiO_2 nanotubes. Appl Catal Environ 138:128–140
44. Raillard C, Hequet V, Le Cloirec P, Legrand J (2004) Kinetic study of ketones photocatalytic oxidation in gas phase using TiO_2-containing paper: effect of water vapor. J Photochem Photobiol A 163:425–431

45. García-López E, Marcì G, Megna B, Parisi F, Armelao L, Trovarelli A, Boaro M, Palmisano L (2015) $SrTiO_3$- based perovskites: preparation, characterization and photocatalytic activity in gas–solid regime under simulated solar irradiation. J Catal 321:13–22
46. Kozlova EA, Kozhevnikova NS, Cherepanova SV, Lyubina TP, Gerasimov EY, Kaichev VV, Vorontsov AV, Tsybulya SV, Rempel AA, Parmon VN (2012) Photocatalytic oxidation of ethanol vapors under visible light on CdS–TiO_2 nanocatalyst. J Photochem Photobiol A 250:103–109
47. Zuo G-M, Cheng Z-X, Chen H, Li G-W, Miao T (2006) Study on photocatalytic degradation of several volatile organic compounds. J Hazard Mater 128:158–163
48. Ourrad H, Thevenet F, Gaudion V, Riffault V (2015) Limonene photocatalytic oxidation at ppb levels: assessment of gas phase reaction intermediates and secondary organic aerosol heterogeneous formation. Appl Catal Environ 168:183–194
49. Zhong J, Wang J, Tao L, Gong M, Zhimin L, Chen Y (2007) Photocatalytic degradation of gaseous benzene over TiO_2/Sr_2 CeO_4: kinetic model and degradation mechanisms. J Hazard Mater 139:323–331
50. Vlachos P, Stathatos E, Lyberatos G, Lianos P (2008) Gas-phase photocatalytic degradation of 2, 4, 6- trichloroanisole in the presence of a nanocrystalline Titania film. Applications to the treatment of cork stoppers. Catal Commun 9:1987–1990
51. Amama PB, Itoh K, Murabayashi M (2004) Photocatalytic degradation of trichloroethylene in dry and humid atmospheres: role of gas-phase reactions. J Mol Catal A 217:109–115
52. Inaba R, Fukahori T, Hamamoto M, Ohno T (2006) Synthesis of nanosized TiO_2 particles in reverse micellesystems and their photocatalytic activity for degradation of toluene in gas phase. J Mol Catal A 260:247–254
53. Kim SB, Hwang HT, Hong SC (2002) Photocatalytic degradation of volatile organic compounds at the gas–solid interface of a TiO_2 photocatalyst. Chemosphere 48:437–444
54. Lin T, Pi Z, Gong MC, Zhong JB, Wang JL, Chen YQ (2007) Gas-phase photocatalytic oxidation of benzene over titanium dioxide loaded on Bi_{12} TiO_20. Chin Chem Lett 18:241–243
55. Wang W, Ku Y, Ma C, Jeng F (2005) Modeling of the photocatalytic decomposition of gaseous benzene in a TiO_2 coated optical fiber photoreactor. J Appl Electrochem 35:709–714
56. Choi W, Ko JY, Park H, Chung JS (2001) Investigation on TiO_2-coated optical fibers for gas-phase photocatalytic oxidation of acetone. Appl Catal Environ 31:209–220
57. Long B, Huang J, Wang X (2012) Photocatalytic degradation of benzene in gas phase by nanostructured $BiPO_4$ catalysts. Prog Nat Sci 22:644–653
58. Wu C, Yue Y, Deng X, Hua W, Gao Z (2004) Investigation on the synergetic effect between anatase and rutile nanoparticles in gas-phase photocatalytic oxidations. Catal Today 93:863–869
59. Jiang Y, Amal R (2013) Selective synthesis of TiO_2-based nanoparticles with highly active surface sites for gasphase photocatalytic oxidation. Appl Catal Environ 138:260–267
60. Chen Y, Cao X, Kuang J, Chen Z, Chen J, Lin B (2010) The gas-phase photocatalytic mineralization of benzene over visible-light-driven Bi_2WO_6@C microspheres. Catal Commun 12:247–250
61. Dashliborun AM, Sotudeh-Gharebagh R, Hajaghazadeh M, Kakooei H, Afshar S (2013) Modeling of the photocatalytic degradation of methyl ethyl ketone in a fluidized bed reactor of nano-TiO_2/γ-Al_2 O_3 particles. Chem Eng J 226:59–67
62. Geng Q, Wang Q, Zhang Y, Wang L, Wang H (2013) Photocatalytic degradation intrinsic kinetics of gaseous cyclohexane in a fluidized bed photocatalytic reactor. Res Chem Intermed 39:1711–1726
63. Lim TH, Kim SD (2004) Photo-degradation characteristics of TCE (trichloroethylene) in an annulus fluidized bed photoreactor. Korean J Chem Eng 21:905–909
64. Mohseni M, Taghipour F (2004) Experimental and CFD analysis of photocatalytic gas phase vinyl chloride (VC) oxidation. Chem Eng Sci 59:1601–1609

65. Keshmiri M, Troczynski T, Mohseni M (2006) Oxidation of gas phase trichloroethylene and toluene using composite sol–gel TiO_2 photocatalytic coatings. J Hazard Mater 128:130–137
66. Ou M, Dong F, Zhang W, Wu Z (2014) Efficient visible light photocatalytic oxidation of NO in air with band-gap tailored $(BiO)_2$ CO_3–BiOI solid solutions. Chem Eng J 255:650–658
67. Polat M, Soylu AM, Erdogan DA, Erguven H, Vovk EI, Ozensoy E (2015) Influence of the sol–gel preparation method on the photocatalytic NO oxidation performance of TiO_2/Al_2O_3 binary oxides. Catal Today 241:25–32
68. Sugrañez R, Álvarez J, Cruz-Yusta M, Mármol I, Morales J, Vila J, Sánchez L (2013) Enhanced photocatalytic degradation of NO_x gases by regulating the microstructure of mortar cement modified with titanium dioxide. Build Environ 69:55–63
69. Menéndez-Flores VM, Bahnemann DW, Ohno T (2011) Visible light photocatalytic activities of S-doped TiO_2-Fe^{3+} in aqueous and gas phase. Appl Catal Environ 103:99–108
70. Soylu AM, Polat M, Erdogan DA, Say Z, Yıldırım C, Birer Ö, Ozensoy E (2014) TiO_2–Al_2O_3 binary mixed oxide surfaces for photocatalytic NO_x abatement. Appl Surf Sci 318:142–149
71. Dong G, Ho W, Zhang L (2015) Photocatalytic NO removal on BiOI surface: the change from nonselective oxidation to selective oxidation. Appl Catal Environ 168:490–496
72. Wang H, Wu Z, Liu Y, Wang Y (2009) Influences of various Pt dopants over surface platinized TiO_2 on the photocatalytic oxidation of nitric oxide. Chemosphere 74:773–778
73. Portela R, Suárez S, Rasmussen S, Arconada N, Castro Y, Durán A, Ávila P, Coronado J, Sánchez B (2010) Photocatalytic-based strategies for H_2S elimination. Catal Today 151:64–70
74. Sheng Z, Wu Z, Liu Y, Wang H (2008) Gas-phase photocatalytic oxidation of NO over palladium modified TiO_2 catalysts. Catal Commun 9:1941–1944
75. Liu H, Yu X, Yang H (2014) The integrated photocatalytic removal of SO_2 and NO using Cu doped titaniumdioxide supported by multi-walled carbon nanotubes. Chem Eng J 243:465–472
76. Signoretto M, Ghedini E, Trevisan V, Bianchi C, Ongaro M, Cruciani G (2010) TiO_2–MCM-41 for the photocatalytic abatement of NO_x in gas phase. Appl Catal Environ 95:130–136
77. Ou M, Zhong Q, Zhang S, Yu L (2015) Ultrasound assisted synthesis of heterogeneous gC_3 $N_4/BiVO_4$ composites and their visible-light-induced photocatalytic oxidation of NO in gas phase. J Alloys Compd 626:401–409
78. Wang Z, Ci X, Dai H, Yin L, Shi H (2012) One-step synthesis of highly active Ti-containing Cr-modified MCM-48 mesoporous material and the photocatalytic performance for decomposition of H_2S under visible light. Appl Surf Sci 258:8258–8263
79. Lafjah M, Mayoufi A, Schaal E, Djafri F, Bengueddach A, Keller N, Keller V (2014) TiO_2 nanorods for gas phase photocatalytic applications. Catal Today 235:193–200
80. Alonso-Tellez A, Robert D, Keller N, Keller V (2012) A parametric study of the UV-A photocatalytic oxidation of H_2S over TiO_2. Appl Catal Environ 115:209–218
81. Ao C, Lee S, Mak C, Chan L (2003) Photodegradation of volatile organic compounds (VOCs) and NO for indoor air purification using TiO_2: promotion versus inhibition effect of NO. Appl Catal Environ 42:119–129
82. Chen M, Liu Y (2010) NO_x removal from vehicle emissions by functionality surface of asphalt road. J Hazard Mater 174:375–379
83. Yu Q, Brouwers H (2009) Indoor air purification using heterogeneous photocatalytic oxidation. Part I: experimental study. Appl Catal B 92:454–461
84. Nguyen NH, Bai H (2014) Photocatalytic removal of NO and NO_2 using titania nanotubes synthesized by hydrothermal method. J Environ Sci 26:1180–1187
85. Hüsken G, Hunger M, Brouwers H (2009) Experimental study of photocatalytic concrete products for air purification. Build Environ 44:2463–2474
86. Toma F-L, Bertrand G, Chwa SO, Meunier C, Klein D, Coddet C (2006) Comparative study on the photocatalytic decomposition of nitrogen oxides using TiO_2 coatings prepared by conventional plasma spraying and suspension plasma spraying. Surf Coat Technol 200:5855–5862

87. Krishnan P, Zhang M-H, Cheng Y, Riang DT, Liya EY (2013) Photocatalytic degradation of SO_2 using TiO_2- containing silicate as a building coating material. Construct Build Mater 43:197–202
88. Martinez T, Bertron A, Ringot E, Escadeillas G (2011) Degradation of NO using photocatalytic coatings applied to different substrates. Build Environ 46:1808–1816
89. Lin C-Y, Li C-S (2003) Inactivation of microorganisms on the photocatalytic surfaces in air. Aerosol Sci Technol 37:939–946
90. Chotigawin R, Sribenjalux P, Supothina S, Johns J, Charerntanyarak L, Chuaybamroong P (2010) Airborne microorganism disinfection by photocatalytic HEPA filter. Environment Asia 3:1–7
91. Vohra A, Goswami D, Deshpande D, Block S (2006) Enhanced photocatalytic disinfection of indoor air. Appl Catal Environ 64:57–65
92. Keller V, Keller N, Ledoux MJ, Lett M-C (2005) Biological agent inactivation in a flowing air stream by photocatalysis. Chem Commun 23:2918–2920
93. Guo M-Z, Ling T-C, Poon C-S (2012) TiO_2-based self-compacting glass mortar: comparison of photocatalytic nitrogen oxide removal and bacteria inactivation. Build Environ 53:1–6
94. Modesto O, Hammer P, Nogueira RFP (2013) Gas phase photocatalytic bacteria inactivation using metal modified TiO_2 catalysts. J Photochem Photobiol A 253:38–44
95. Slamet HWN, Purnama E, Riyani K, Gunlazuardi J (2009) Effect of copper species in a photocatalytic synthesis of methanol from carbon dioxide over copper-doped titania catalysts. World Appl Sci J 6:112–122
96. Wang Q, Wu W, Chen J, Chu G, Ma K, Zou H (2012) Novel synthesis of ZnPc/TiO_2 composite particles and carbon dioxide photo-catalytic reduction efficiency study under simulated solar radiation conditions. Colloids Surf A Physicochem Eng Asp 409:118–125
97. Lee W-H, Liao C-H, Tsai M-F, Huang C-W, Wu JC (2013) A novel twin reactor for CO_2 photoreduction to mimic artificial photosynthesis. Appl Catal Environ 132:445–451
98. Liu L, Gao F, Zhao H, Li Y (2013) Tailoring Cu valence and oxygen vacancy in Cu/TiO_2 catalysts for enhanced CO_2 photoreduction efficiency. Appl Catal Environ 134:349–358
99. Wang Y, Li B, Zhang C, Cui L, Kang S, Li X, Zhou L (2013) Ordered mesoporous CeO_2-TiO_2 composites: highly efficient photocatalysts for the reduction of CO_2 with H_2O under simulated solar irradiation. Appl Catal Environ 130:277–284
100. Zhao C, Krall A, Zhao H, Zhang Q, Li Y (2012) Ultrasonic spray pyrolysis synthesis of Ag/TiO_2 nanocomposite photocatalysts for simultaneous H_2 production and CO_2 reduction. Int J Hydrog Energy 37:9967–9976
101. Kočí K, Matějka V, Kovář P, Lacný Z, Obalová L (2011) Comparison of the pure TiO_2 and kaolinite/TiO_2 composite as catalyst for CO_2 photocatalytic reduction. Catal Today 161:105–109
102. Kočí K, Reli M, Kozák O, Lacný Z, Plachá D, Praus P, Obalová L (2011) Influence of reactor geometry on the yield of CO_2 photocatalytic reduction. Catal Today 176:212–214
103. Wu JC, Wu T-H, Chu T, Huang H, Tsai D (2008) Application of optical-fiber photoreactor for CO_2 photocatalytic reduction. Top Catal 47:131–136
104. Wu J, Lin H-M (2005) Photo reduction of CO_2 to methanol via TiO_2 photocatalyst. Int J Photoenergy 7:115–119
105. Zhao Z-H, Fan J-M, Wang Z-Z (2007) Photo-catalytic CO_2 reduction using sol–gel derived titania-supported zinc-phthalocyanine. J Clean Prod 15:1894–1897
106. Guan G, Kida T, Harada T, Isayama M, Yoshida A (2003) Photoreduction of carbon dioxide with water over $K_2Ti_6O_{13}$ photocatalyst combined with Cu/ZnO catalyst under concentrated sunlight. Appl Catal Gen 249:11–18
107. Ola O, Maroto-Valer M, Liu D, Mackintosh S, Lee C-W, Wu JC (2012) Performance comparison of CO_2 conversion in slurry and monolith photoreactors using Pd and Rh-TiO_2 catalyst under ultraviolet irradiation. Appl Catal Environ 126:172–179

108. Liou P-Y, Chen S-C, Wu JC, Liu D, Mackintosh S, Maroto-Valer M, Linforth R (2011) Photocatalytic CO_2 reduction using an internally illuminated monolith photoreactor. Energy Environ Sci 4:1487–1494
109. Shi D, Feng Y, Zhong S (2004) Photocatalytic conversion of CH_4 and CO_2 to oxygenated compounds over Cu/CdS–TiO_2/SiO_2 catalyst. Catal Today 98:505–509
110. Wang Y, Wang F, Chen Y, Zhang D, Li B, Kang S, Li X, Cui L (2014) Enhanced photocatalytic performance of ordered mesoporous Fe-doped CeO_2 catalysts for the reduction of CO_2 with H_2O under simulated solar irradiation. Appl Catal Environ 147:602–609
111. Tahir M, Amin NS (2013) Photocatalytic CO_2 reduction and kinetic study over In/TiO_2 nanoparticles supported microchannel monolith photoreactor. Appl Catal Gen 467:483–496
112. Tahir M, Amin NS (2013) Photocatalytic CO_2 reduction with H_2O vapors using montmorillonite/TiO_2 supported microchannel monolith photoreactor. Chem Eng J 230:314–327
113. Nguyen T-V, Wu JC, Chiou C-H (2008) Photoreduction of CO_2 over ruthenium dye-sensitized TiO_2-based catalysts under concentrated natural sunlight. Catal Commun 9:2073–2076
114. McCullagh C, Skillen N, Adams M, Robertson PK (2011) Photocatalytic reactors for environmental remediation: a review. J Chem Technol Biotechnol 86:1002–1017
115. Chong MN, Jin B, Chow CWK, Saint C (2010) Recent developments in photocatalytic water treatment technology: a review. Water Res 44:2997–3027
116. De Lasa H, Serrano B, Salaices M (2005) Photocatalytic reaction engineering. Springer, New york
117. Ibhadon A, Fitzpatrick P (2013) Heterogeneous photocatalysis: recent advances and applications. Catalysts 3:189–218
118. Wetchakun N, Chainet S, Phanichphant S, Wetchakun K (2015) Efficient photocatalytic degradation of methylene blue over $BiVO_4$/TiO_2 nanocomposites. Ceram Int 41:5999–6004
119. Zhang L, Zhang J, Zhang W, Liu J, Zhong H, Zhao Y (2015) Photocatalytic activity of attapulgite–BiOCl–TiO_2 toward degradation of methyl orange under UV and visible light irradiation. Mater Res Bull 66:109–114
120. Xu W, Fang J, Chen Y, Lu S, Zhou G, Zhu X, Fang Z (2015) Novel heterostructured Bi_2S_3/$Bi_2Sn_2O_7$ with highlyvisible light photocatalytic activity for the removal of rhodamine B. Mater Chem Phys 154:30–37
121. Kunduz S, Soylu GSP (2015) Highly active $BiVO_4$ nanoparticles: the enhanced photocatalytic properties under natural sunlight for removal of phenol from wastewater. Sep Purif Technol 141:221–228
122. Chen J, Zhang H, Liu P, Li Y, Liu X, Li G, Wong PK, An T, Zhao H (2015) Cross-linked $ZnIn_2S_4$/rGO composite photocatalyst for sunlight-driven photocatalytic degradation of 4-nitrophenol. Appl Catal Environ 168–169:266–273
123. Lee D-S, Park S-J (2015) Water-mediated modulation of TiO_2 decorated with graphene for photocatalytic degradation of trichloroethylene. Curr Appl Phys 15:144–148
124. Habibi MH, Rahmati MH (2015) The effect of operational parameters on the photocatalytic degradation of Congo red organic dye using ZnO–CdS core–shell nano-structure coated on glass by Doctor Blade method. Spectrochim Acta A Mol Biomol Spectrosc 137:160–164
125. Yamazaki S, Yamate T, Adachi K (2013) Photocatalytic activity of aqueous WO_3 sol for the degradation of Orange II and 4-chlorophenol. Appl Catal Gen 454:30–36
126. Yan X, Wang X, Gu W, Wu M, Yan Y, Hu B, Che G, Han D, Yang J, Fan W, Shi W (2015) Single-crystalline $AgIn(MoO_4)_2$ nanosheets grafted Ag/AgBr composites with enhanced plasmonic photocatalytic activity for degradation of tetracycline under visible light. Appl Catal Environ 164:297–304
127. Zhang Y, Han C, Nadagouda MN, Dionysiou DD (2015) The fabrication of innovative single crystal N, Fcodoped titanium dioxide nanowires with enhanced photocatalytic activity for degradation of atrazine. Appl Catal B 168–169:550–558
128. Sun B, Qiao Z, Hai Fan SK, Ai S (2013) Facile synthesis of silver sulfide/bismuth sulfide nanocomposites for photocatalytic inactivation of Escherichia coli under solar light irradiation. Mater Lett 91:142–145

129. Lydakis-Simantiris N, Riga D, Katsivela E, Mantzavinos D, Xekoukoulotakis NP (2010) Disinfection of spring water and secondary treated municipal wastewater by TiO_2 photocatalysis. Desalination 250:351–355
130. Zacarías SM, Satuf ML, Vaccari MC, Alfano OM (2015) Photocatalytic inactivation of bacterial spores using TiO_2 films with silver deposits. Chem Eng J 266:133–140
131. Wang J, Li C, Zhuang H, Zhang J (2013) Photocatalytic degradation of methylene blue and inactivation of Gramnegative bacteria by TiO_2 nanoparticles in aqueous suspension. Food Control 34:372–377
132. Vijay M, Ramachandran K, Ananthapadmanabhan PV, Nalini B, Pillai BC, Bondioli F, Manivannan A, Narendhirakannan RT (2013) Photocatalytic inactivation of Gram-positive and Gram-negative bacteria by reactive plasma processed nanocrystalline TiO_2 powder. Curr Appl Phys 13:510–516
133. Wang J, Zhuang H, Hinton A Jr, Bowker B, Zhang J (2014) Photocatalytic disinfection of spoilage bacteria Pseudomonas fluorescens and Macrococcus caseolyticus by nano-TiO_2. LWT – Food Sci Technol 59:1009–1017
134. Long M, Wang J, Zhuang H, Zhang Y, Wu H, Zhang J (2014) Performance and mechanism of standard nano- TiO_2 (P-25) in photocatalytic disinfection of foodborne microorganisms – Salmonella typhimurium and Listeria monocytogenes. Food Control 39:68–74
135. Berberidou C, Paspaltsis I, Pavlidou E, Sklaviadis T, Poulios I (2012) Heterogenous photocatalytic inactivation of B. stearothermophilus endospores in aqueous suspensions under artificial and solar irradiation. Appl Catal Environ 125:375–382
136. Schrank SG, José HJ, Moreira RFPM (2002) Simultaneous photocatalytic Cr(VI) reduction and dye oxidation in a TiO_2 slurry reactor. J Photochem Photobiol A 147:71–76
137. Umar M, Aziz HA (2013) Organic pollutants - monitoring, risk and treatment. InTech, Rijeka
138. Wang T, Wang J, Jin Y (2007) Slurry reactors for gas-to-liquid processes: a review. Ind Eng Chem Res 46:5824–5847
139. Sivaiah M, Majumder SK (2013) Hydrodynamics and mixing characteristics in an ejector-induced downflow slurry bubble column (EIDSBC). Chem Eng J 225:720–733
140. Nishio J, Tokumura M, Znad HT, Kawase Y (2006) Photocatalytic decolorization of azo-dye with zinc oxide powder in an external UV light irradiation slurry photoreactor. J Hazard Mater 138:106–115
141. McCullagh C, Robertson PKJ, Adams M, Pollard PM, Mohammed A (2010) Development of a slurry continuous flow reactor for photocatalytic treatment of industrial waste water. J Photochem Photobiol A 211:42–46
142. Subramanian M, Kannan A (2010) Photocatalytic degradation of phenol in a rotating annular reactor. Chem Eng Sci 65:2727–2740
143. Inoue T, Fujishima A, Konishi S, Honda K (1979) Photoelectrocatalytic reduction of carbon dioxide in aqueous suspensions of semiconductor powders. Nature 277:637–638
144. Tahir M, Amin NS (2013) Advances in visible light responsive titanium oxide-based photocatalysts for CO_2 conversion to hydrocarbon fuels. Energy Convers Manag 76:194–214
145. Rossetti I, Villa A, Pirola C, Prati L, Ramis G (2014) A novel high-pressure photoreactor for CO_2 photoconversion to fuels. RSC Adv 4:28883–28885
146. Priya R, Kanmani S (2009) Batch slurry photocatalytic reactors for the generation of hydrogen from sulfide and sulfite waste streams under solar irradiation. Solar Energy 83:1802–1805
147. Matthews RW (1991) Photooxidative degradation of coloured organics in water using supported catalysts. TiO_2 on sand. Water Res 25:1169–1176
148. Dhananjeyan MR, Kiwi J, Thampi KR (2000) Photocatalytic performance of TiO_2 and Fe_2O_3 immobilized on derivatized polymer films for mineralisation of pollutants. Chem Commun 15:1443–1444
149. Wang X, Shi F, Huang W, Fan C (2012) Synthesis of high quality TiO_2 membranes on alumina supports and their photocatalytic activity. Thin Solid Films 520:2488–2492

150. Sakthivel S, Shankar MV, Palanichamy M, Arabindoo B, Murugesan V (2002) Photocatalytic decomposition of leather dye: comparative study of TiO_2 supported on alumina and glass beads. J Photochem Photobiol A 148:153–159
151. Khatamian M, Hashemian S, Yavari A, Saket M (2012) Preparation of metal ion (Fe^{3+} and Ni^{2+}) doped TiO_2 nanoparticles supported on ZSM-5 zeolite and investigation of its photocatalytic activity. Mate Sci Eng 177:1623–1627
152. Li Y, Zhou X, Chen W, Li L, Zen M, Qin S, Sun S (2012) Photodecolorization of Rhodamine B on tungstendoped TiO_2/activated carbon under visible-light irradiation. J Hazard Mater 227–228:25–33
153. Zhang Y, Crittenden JC, Hand DW, Perram DL (1994) Fixed-bed photocatalysts for solar decontamination of water. Environ Sci Technol 35:435–442
154. Li D, Zhua Q, Hana C, Yanga Y, Jiangb W, Zhang Z (2015) Photocatalytic degradation of recalcitrant organic pollutants in water using a novel cylindrical multi-column photoreactor packed with TiO_2-coated silica gel beads. J Hazard Mater 285:398–408
155. Ahmed MH, Keyes TE, Byrne JA, Blackledge CW, Hamilton JW (2011) Adsorption and photocatalytic degradation of human serum albumin on TiO_2 and Ag–TiO_2 films. J Photochem Photobiol A 222:123–131
156. Pan JH, Lei Z, Lee WI, Xiong Z, Wang Q, Zhao XS (2011) Mesoporous TiO_2 photocatalytic films on stainless steel for water decontamination. Catal Sci Technol 2:147–155
157. Wang B, Karthikeyan R, Lu X-Y, Xuan J, Leung MK (2013) High photocatalytic activity of immobilized TiO_2 nanorods on carbonized cotton fibers. J Hazard Mater 263:659–669
158. Li D, Zheng H, Wang Q, Wang X, Jiang W, Zhang Z, Yang Y (2014) A novel double-cylindrical-shell photoreactor immobilized with monolayer TiO_2-coated silica gel beads for photocatalytic degradation of Rhodamine B and methyl orange in aqueous solution. Sep Purif Technol 123:130–138
159. Behnajady MA, Modirshahla N, Daneshvar N, Rabbani M (2007) Photocatalytic degradation of an azo dye in a tubular continuous-flow photoreactor with immobilized TiO_2 on glass plates. Chem Eng J 127:167–176
160. Faure M, Gerardin F, Andréa J-C, Ponsa M-N, Zahraa O (2011) Study of photocatalytic damages induced on E. coli by different photocatalytic supports (various types and TiO_2 configurations). J Photochem Photobiol A 222:323–329
161. Pablos C, Van Grieken R, Marugán J, Moreno B (2011) Photocatalytic inactivation of bacteria in a fixed-bedreactor: mechanistic insights by epifluorescence microscopy. Catal Today 161:133–139
162. Van Grieken R, Marugan J, Sordo C, Pablos C (2009) Comparison of the photocatalytic disinfection of E. coli suspensions in slurry, wall and fixed-bed reactors. Catal Today 144:48–54
163. Hsu M-H, Chang C-J (2014) S-doped ZnO nanorods on stainless-steel wire mesh as immobilized hierarchical photocatalysts for photocatalytic H_2 production. Int J Hydrog Energy 39:16524–16533
164. Augugliaro V, Loddo V, Pagliaro M, Palmisano G, Palmisano L (2010) Clean by light irradiation. RSC Publishing, Cambridge
165. Hao X-g, Li H-h, Zhang Z-l, Fan C-m, Liu S-b, Sun Y-p (2009) Modeling and experimentation of a novel labyrinth bubble photoreactor for degradation of organic pollutant. Chem Eng Res Des 87:1604–1611
166. Cernigoj U, Stangar UL, Trebse P (2007) Evaluation of a novel Carberry type photoreactor for the degradation of organic pollutants in water. J Photochem Photobiol A 188:169–176
167. Lo C-C, Huang C-W, Liao C-H, Wu JCS (2010) Novel twin reactor for separate evolution of hydrogen and oxygen in photocatalytic water splitting. Int J Hydrog Energy 35:1523–1529
168. Oralli E, Dincer I, Naterer GF (2011) Solar photocatalytic reactor performance for hydrogen production from incident ultraviolet radiation. Int J Hydrog Energy 36:9446–9452

169. Xiong Z, Zhao Y, Zhang J, Zheng C (2015) Efficient photocatalytic reduction of CO_2 into liquid products over cerium doped titania nanoparticles synthesized by a sol–gel auto-ignited method. Fuel Process Technol 135:6–13
170. Wang J, Yang C, Wang C, Han W, Zhu W (2014) Photolytic and photocatalytic degradation of micro pollutants in a tubular reactor and the reaction kinetic models. Sep Purif Technol 122:105–111
171. Reilly K, Taghipour F, Wilkinson DP (2012) Photocatalytic hydrogen production in a UV-irradiated fluidized bed reactor. Energy Procedia 29:513–521
172. Swarnalatha B, Anjaneyulu Y (2004) Studies on the heterogeneous photocatalytic oxidation of 2,6-dinitrophenol in aqueous TiO_2 suspension. J Mol Catal A 223:161–165
173. Han W, Zhang P, Zhu W, Yin J, Li L (2004) Photocatalysis of p-chlorobenzoic acid in aqueous solution under irradiation of 254 nm and 185 nm UV light. Water Res 38:4197–4203
174. Chen Y, Lu A, Li Y, Yip HY, An T, Li G, Jin P, Wonga P-K (2011) Photocatalytic inactivation of Escherichia coli by natural sphalerite suspension: effect of spectrum, wavelength and intensity of visible light. Chemosphere 84:1276–1281
175. Benabbou AK, Derriche Z, Felix C, Lejeune P, Guillard C (2007) Photocatalytic inactivation of Escherischia coli: effect of concentration of TiO_2 and microorganism, nature, and intensity of UV irradiation. Appl Catal Environ 76:257–263
176. Hernández-Gordillo A, Tzompantzi F, Oros-Ruiz S, Torres-Martinez LM, Gómez R (2014) Enhanced blue-light photocatalytic H_2 production using CdS nanofiber. Catal Commun 45:139–143
177. Gomathisankar P, Hachisuka K, Katsumata H, Suzuki T, Funasaka K, Kaneco S (2013) Enhanced photocatalytic hydrogen production from aqueous methanol solution using ZnO with simultaneous photodeposition of Cu. Int J Hydrog Energy 38:11840–11846
178. Gálvez JB, Rodríguez SM (2003) Solar detoxification. UNESCO Publishing, Paris
179. Spasiano D, Marotta R, Malato S, Fernandez-Ibanez P, Di Somma I (2015) Solar photocatalysis: materials, reactors, some commercial, and pre-industrialized applications. A comprehensive approach. Appl Catal B 170–171:90–123
180. Alfano OM, Bahnemann D, Cassano AE, Dillert R, Goslich R (2000) Photocatalysis in water environments using artificial and solar light. Catal Today 58:199–230
181. Tanveer M, Guyer GT (2013) Solar assisted photo degradation of wastewater by compound parabolic collectors: review of design and operational parameters. Renew Sustain Energy Rev 24:534–543
182. Malato S, Fernandez-Ibanez P, Maldonado MI, Blanco J, Gernjak W (2009) Decontamination and disinfection of water by solar photocatalysis: recent overview and trends. Catal Today 147:1–59
183. Keane DA, McGuigan KG, Ibáñez PF, Polo-López MI, Byrne JA, Dunlop PSM, O'Shea K, Dionysiou DD, Pillai SC (2014) Solar photocatalysis for water disinfection: materials and reactor design. Catal Sci Technol 4:1211–1226
184. Zayani G, Bousselmi L, Mhenni F, Ghrabi A (2009) Solar photocatalytic degradation of commercial textile azo dyes: performance of pilot plant scale thin film fixed-bed reactor. Desalination 246:344–352
185. Xu J, Ao Y, Fu D, Lin J, Lin Y, Shen X, Yuan C, Yin Z (2008) Photocatalytic activity on TiO_2-coated side-glowing optical fiber reactor under solar light. J Photochem Photobiol A 199:165–169
186. Vidal A, Dıaz AI, El Hraiki A, Romero M, Muguruza I, Senhaji F, González J (1999) Solar photocatalysis for detoxification and disinfection of contaminated water: pilot plant studies. Catal Today 54:283–290
187. McLoughlin OA, Kehoe SC, McGuigan KG, Duffy EF, Al Touati F, Gernjak W, Alberola IO, Rodrıguez SM, Gill LW (2004) Solar disinfection of contaminated water: a comparison of three small-scale reactors. Sol Energy 77:657–664

188. Alrousan DMA, Polo-López MI, Dunlop PSM, Fernández-Ibánez P, Byrne JA (2012) Solar photocatalytic disinfection of water with immobilised titanium dioxide in re-circulating flow CPC reactors. Appl Catal Environ 128:126–134
189. Xing Z, Zong X, Pan J, Wang L (2013) On the engineering part of solar hydrogen production from water splitting: photoreactor design. Chem Eng Sci 104:125–146
190. Jing D, Guo L, Zhao L, Zhang X, Liu H, Li M, Shen S, Liu G, Hu X, Zhang X, Zhang K, Ma L, Guo P (2010) Efficient solar hydrogen production by photocatalytic water splitting: from fundamental study to pilot demonstration. Int J Hydrog Energy 35:7087–7097
191. Villa K, Domenech X, Malato S, Maldonado MI, Peral J (2013) Heterogeneous photocatalytic hydrogen generation in a solar pilot plant. Int J Hydrog Energy 38:12718–12724
192. Malato S, Blanco J, Alarcon DC, Maldonado MI, Fernandez-Ibanez P, Gernjak W (2007) Photocatalytic decontamination and disinfection of water with solar collectors. Catal Today 122:137–149
193. Xu C, Rangaiah GP, Zhao XS (2015) A computational study of the effect of lamp arrangements on the performance of ultraviolet water disinfection reactors. Chem Eng Sci 122:299–306
194. Ray AK, Beenackers AACM (1998) Development of a new photocatalytic reactor for water purification. Catal Today 40:73–83
195. Palmisano G, Loddo V, Augugliaro V, Bellardita M, Camera Roda G, Parrino F (2015) Validation of a twodimensional modeling of an externally irradiated slurry photoreactor. Chem Eng J 262:490–498
196. Tokumura M, Znad HT, Kawase Y (2006) Modeling of an external light irradiation slurry photoreactor: UV light or sunlight-photoassisted Fenton discoloration of azo-dye Orange II with natural mineral tourmaline powder. Chem Eng Sci 61:6361–6371
197. Palmisano G, Loddo V, Augugliaro V (2013) Two-dimensional modeling of an externally irradiated slurry photoreactor. Int J Chem React Eng 11
198. Cassano AE, Martin CA, Brandi RJ, Alfano OM (1995) Photoreactor analysis and design: fundamentals and applications. Ind Eng Chem Res 34:2155–2201
199. Pozzo RL, Brandi RJ, Giombi JL, Baltanás MA, Cassano AE (2005) Design of fluidized bed photoreactors: optical properties of photocatalytic composites of titania CVD-coated onto quartz sand. Chem Eng Sci 60:2785–2794
200. Irazoqui HA, Cerdá J, Cassano AE (1976) The radiation field for the point and line source approximations and the three-dimensional source models: applications to photoreactions. Chem Eng J 11:27–37

Chapter 8
Solar–Chemical Energy Conversion by Photocatalysis

Lan Yuan, Nan Zhang, Yi-Jun Xu, and Juan Carlos Colmenares

Abstract With the late but fast development, photocatalytic selective organic transformation has been recognized to be a promising alternative to traditional organic synthesis because it features unique advantages of being able to employ mild reaction conditions and avoid environmentally detrimental heavy metal catalysts as well as strong chemical oxidants or reducing agents. Moreover, it can facilitate the design of short and efficient reaction sequences, minimizing side processes and leading to high selectivity. This chapter provides an overview of the basic principles and evaluation methods of photocatalytic selective organic transformations. Recent progress on photocatalytic selective oxidation, reduction, and coupling reactions is represented based on selected examples. Besides, the future research challenges are concisely discussed.

Keywords Photocatalytic • Organic synthesis • Selective oxidation • Selective reduction • Coupling reactions

8.1 Introduction

Since the Industrial Age beginning with the invention of the steam engine in the 1760s, human beings have been exploiting fossil resources for energy and development. However, after more than 150 years' exploitation and utilization, expected depletion of the fossil fuel reserves has emphasized the issue of energy and environmental

---

L. Yuan • N. Zhang
State Key Laboratory of Photocatalysis on Energy and Environment, College of Chemistry,
Fuzhou University, Fuzhou 350002, China

College of Chemistry, New Campus, Fuzhou University, Fuzhou 350108, People's Republic of
China

Y.-J. Xu (✉)
State Key Laboratory of Photocatalysis on Energy and Environment, Fuzhou University,
Industry Road 523, Fuzhou 350002, China
e-mail: yjxu@fzu.edu.cn

J.C. Colmenares (✉)
Institute of Physical Chemistry, Polish Academy of Sciences, ul. Kasprzaka 44/52, 01-224,
Warsaw, Poland
e-mail: jcarloscolmenares@ichf.edu.pl

J.C. Colmenares, Y.-J. Xu (eds.), *Heterogeneous Photocatalysis*, Green Chemistry
and Sustainable Technology, DOI 10.1007/978-3-662-48719-8_8

sustainability [1–6]. Heterogeneous photocatalysis by semiconductors, as a green technology, has received intense attention and been widely applied to environmental remediation and solar–chemical conversion for further energy supplies, including photodegradation of organic contaminants, photocatalytic CO_2 reduction for value-added chemicals, and water splitting for H_2 production [1, 2, 7–25].

The application of photocatalysis in selective organic transformations is not common at first because semiconductor photocatalysis has long been considered as "nonselective" processes, especially in aqueous media [26]. Nevertheless, many researchers have devoted efforts to this subject and have clarified that several reactions can proceed highly efficiently and selectively in various heterogeneous photocatalytic systems [26–32]. Following that, photocatalytic selective organic transformations have received growing interest and been recognized as an alternative to conventional synthetic routes for synthesis of fine chemicals through the selection of appropriate semiconductors and control of the reaction conditions [26, 27, 33–37]. Compared to traditional synthesis methods [34, 38–40], photocatalytic organic synthesis features several unique advantages: (i) it is driven by sunlight as a completely renewable source of energy; (ii) it can go on under milder conditions (room temperature and atmospheric pressure) and avoid environmentally detrimental heavy metal catalysts as well as strong chemical oxidants or reducing agents; (iii) it can facilitate the design of short and efficient reaction sequences, minimizing side processes and leading to high selectivity [29, 32–34, 38–42].

With the late but fast development, photocatalytic selective organic transformations have been considered to play a major role in promoting the evolution of twenty-first-century chemistry by replacing environmentally hazardous processes with environmental friendly and energy-efficient routes, allowing maximization of the quantity of raw material that ends up in the final product [26–34, 41, 43, 44]. To date, several organic transformation reactions are promoted with high selectivity and efficiency on various photocatalytic systems [26, 29–34, 38–41, 43–45]. This chapter will provide an overview of the basic principles and evaluation methods of photocatalytic selective organic transformations, following which recent progress in the significant examples of photocatalytic processes employed for synthetic purposes will be represented, including selective oxidation, reduction, and coupling reactions. In addition, the future research challenges will be concisely discussed.

8.2 Main Process and Basic Principles for Photocatalytic Selective Organic Transformations

In general, semiconductor-based photocatalytic process involves three main steps, as shown in Fig. 8.1, and the conversion of light into chemical energy by selective organic transformations can be described as $A + D = A_{red} + D_{ox}$. The optimization of every step plays an important role in boosting the photocatalytic efficiency.

Specifically, (i) upon light irradiation, the photocatalyst absorbs supra-bandgap photons ($\geq$Eg, Eq. 8.1), and photoexcited electron (e^-) and hole (h^+) pairs are produced in the CB and the VB, respectively (Eqs. 8.2 and 8.3). In this step, the

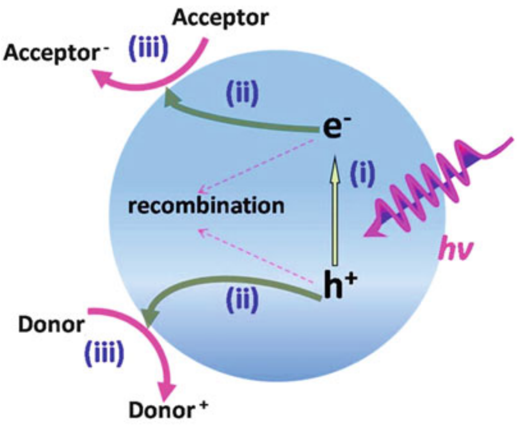

Fig. 8.1 Schematic illustration of semiconductor-based photocatalytic processes

light absorption range and coefficient of photocatalyst should be increased to maximize the light harvesting and thus to harness more photons. In addition, since UV light only accounts for about 4 % of solar spectrum, it is highly desired for a photocatalyst with a narrow bandgap to utilize visible light, which occupies about 43 % of solar light [10, 46]. (ii) The photogenerated electrons and holes are separated and migrated to catalytically active sites at semiconductor surface (or recombined). Typically, photogenerated electron–hole pairs have a recombination time on the order of 10^{-9} s, while the chemical interaction with adsorbed species has a longer time of 10^{-8}–10^{-3} s [46]. Therefore, in this step, accelerating the separation and migration of the photoexcited electrons and holes to avoid their recombination is fundamentally important. (iii) An efficient charge separation of the electron–hole pairs allows the respective oxidation and reduction reactions on the particle surface (Eqs. 8.4 and 8.5).

However, undesirable reactions might occur. On one hand, efficient back electron transfer between the primary redox products (Eq. 8.6) will prevent in most cases successive reactions to generate the final redox products. In this regard, efficient photocatalytic systems that can inhibit charge recombination as well as photocatalysts with proper electronic band structure for visible light harvesting and redox reactions are needed.

$$\text{Band gap}\ (eV) = \frac{1240}{\lambda(nm)} \tag{8.1}$$

$$\mathrm{PC} + \mathrm{h}\nu\,(\geq \mathrm{Eg}) \rightarrow \mathrm{h}^{+} + \mathrm{e}^{-} \tag{8.2}$$

$$\mathrm{h}^{+} - \mathrm{e}^{-} \rightarrow \mathrm{h}^{+}_{\mathrm{VB}} + \mathrm{e}^{-}{}_{\mathrm{CB}} \tag{8.3}$$

$$\mathrm{A} \rightarrow \mathrm{A}^{\bullet-} \rightarrow \mathrm{A}_{\mathrm{red}} \tag{8.4}$$

$$\mathrm{D} \rightarrow \mathrm{D}^{\bullet+} \rightarrow \mathrm{D}_{\mathrm{OX}} \tag{8.5}$$

$$A_{red} + D_{ox} \rightarrow A + D \tag{8.6}$$

$$e^{-} + O_2 \rightarrow O_2^{\bullet -} \tag{8.7}$$

$$h^{+} + OH^{-}\ (\text{or HO}) \rightarrow \bullet OH \tag{8.8}$$

On the other hand, under most circumstances, molecular oxygen (O_2) usually functions as an electron acceptor by interacting with the photogenerated electrons on the CB of the photocatalyst, thus forming reactive oxygen species (ROS), superoxide radicals ($O_2^{\cdot -}$), an oxidizing agent (Eq. 8.7). In contrast, the holes on the VB react with surface hydroxyl groups or water molecules adsorbed on the surface of the photocatalyst and produce hydroxyl radicals, a different type of ROS acting as a strong oxidizing agent (Eq. 8.8). The ROS are highly nonselective oxidants and can degrade or completely oxidize the organic compounds all the way to the deep oxidation products to CO_2 and H_2O. Therefore, photocatalytic selective organic transformation to the desirable products by partially oxidizations is often hard to accomplish without the use of a proper electron or hole scavenger. Thus, using appropriate substrates and employing appropriate reaction conditions are of great importance for promoting selective organic transformations. That is, the type of electron–hole scavenger, the photocatalyst, the wavelength and the intensity of light used for irradiation, and the type of reactant and solvent all should be carefully chosen to achieve desired products.

8.3 Efficiency Evaluation of Photocatalytic Selective Organic Transformations

8.3.1 Light-Based Measures

The overall quantum yield and (apparent) quantum yield of photocatalytic process are defined in Eqs. 8.9 and 8.10, respectively:

$$\text{Overall quantum yield } (\%) = \frac{\text{Number of reacted electrons}}{\text{Number of absorbed photons}} \times 100\% \tag{8.9}$$

$$\text{(Apparent) quantum yield } (\%) = \frac{\text{Number of reacted electrons}}{\text{Number of incident photons}} \times 100\% \tag{8.10}$$

Based on the two equations, it is estimated that the apparent quantum yield should be smaller than the total quantum yield because not all the incident photons can be absorbed. However, this method is not often applied to evaluate selective organic transformations since the “number of reacted electrons” for these selective redox reactions is often difficult to be exactly determined, particularly for selective oxidation reactions, due to the relatively complex reaction process and mechanisms. For example, regarding selective oxidation reactions, both the photogenerated holes and O_2 or activated oxygen (e.g., $\bullet O_2^-$ obtained by accepting the photogenerated electrons) can play the role in oxidizing the substrates.

8.3.2 *Product-Based Measures*

The most widely employed measure to evaluate the activity of photocatalytic selective organic transformations is the conversion, yield, and selectivity of the organic compounds transformed to target product. The definitions are as follows:

$$\begin{aligned}&\text{conversion}(\%) \ = [(C_0 - C_r)/C_0] \times 100\\&\text{yield}(\%) = C_P/C_0 \times 100\\&\text{selectivity}(\%) \ = [C_P(C_0 - C_r)] \times 100\end{aligned}$$

where C_0 is the initial concentration of reactant and C_r and C_p are the concentration of reactant and product at a certain time after the photocatalytic reaction, respectively.

8.4 Photooxidation of Organic Substrates

Oxidation processes play an important role in the production of a wide range of chemicals, where traditional industrial oxidation processes always need stringent reaction conditions and strong oxidants such as mineral acids, chromates, permanganate, hydrogen peroxide, etc [3, 28, 35, 47, 48]. Photooxidation can be cogitated as a possible alternative approach to overcome the harsh conditions as well as the questions of toxicity and corrosiveness.

8.4.1 *Hydroxylation of Benzene*

Phenol is an important industrial chemical because of its wide usage, ranging from disinfectant, precursor of phenolic resins to preservative for pharmaceutical aid [27, 49–56]. Different from the industrial production of phenol from benzene by the multistep cumene process under high temperature and pressure [57], photocatalytic hydroxylation of benzene to phenol can be realized via direct electrophilic addition of hydroxyl radicals (•OH) under mild reaction conditions, since •OH can be generated through the reaction of the photogenerated holes from semiconductor photocatalysts with surface –OH groups or adsorbed H_2O molecules. However, the product selectivity is often low since •OH is highly reactive and nonselective with hydroxylated phenols being further oxidized and mineralized. For example, the

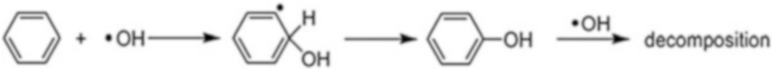

Scheme 8.1 Photocatalytic oxidation of benzene to phenol and subsequent decomposition of phenol on TiO_2 (Reproduced with permission [26]. Copyright 2008 Elsevier)

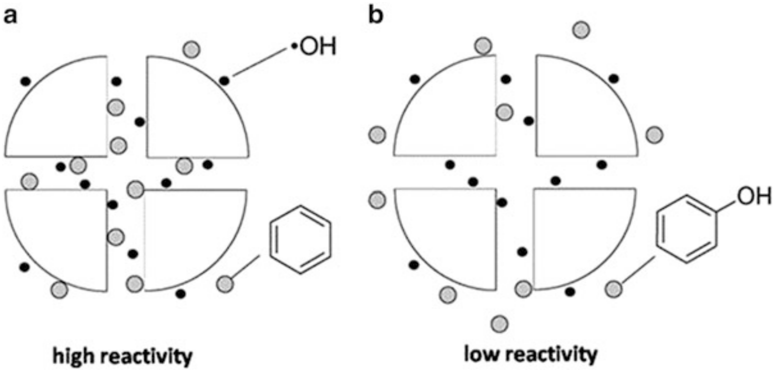

Fig. 8.2 Schematic representation of the reactivity difference between (**a**) benzene and (**b**) phenol on *m*TiO_2 (Reproduced with permission [26]. Copyright 2008 Elsevier)

photocatalytic oxidation of benzene to phenol with TiO_2 in aqueous media has been performed by many researchers [51–54, 56]. As shown in Scheme 8.1, the phenol produced by direct hydroxylation of benzene via an electrophilic addition of •OH radical formed on the TiO_2 surface can be sequentially decomposed by further reaction with •OH radicals [58–60] and results in a low phenol selectivity.

Therefore, efforts have been devoted to lower the affinity of phenol on the catalyst surface and thus reduce the possibility of further decomposition and improve the selectivity of phenol. For example, Skirmish's group has reported a system of mesoporous TiO_2 particles (*m*TiO_2) with high phenol selectivity ($>80\ \%$) [56]. It is suggested that mesopores on the catalyst are the crucial factor for selective phenol production. As schematically shown in Fig. 8.2, benzene is a hydrophobic molecule and adsorbed well on the inner *m*TiO_2 surface, while hydrophilic phenol is scarcely adsorbed. The •OH radicals formed inside the pores scarcely diffuse out of the pores of *m*TiO_2 since they are deactivated rapidly in a near-diffusion controlled rate [27]. Therefore, they efficiently react with the well-adsorbed benzene, whereas less adsorbed phenol scarcely enters the pores and cannot react with them. In this way, further decomposition of phenol is effectively suppressed and high phenol selectivity is obtained.

Similarly, Choi's group later has reported a method for entrapping titanium oxide nanoparticles into hydrophobically modified mesocellular siliceous foam (MCF), which serves as an efficient photocatalyst for the selective hydroxylation of benzene to phenol. As shown in Fig. 8.3, the interior of the hydrophobically modified MCF (by surface organo-grafting with silylation agent) provides a

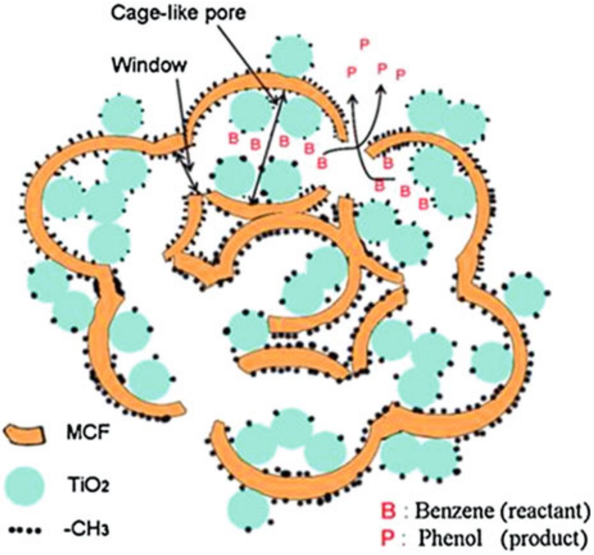

Fig. 8.3 Titanium oxide entrapped in the cage-like mesopores of hydrophobically modified mesocellular siliceous foam (MCF) for the hydroxylation of benzene (Reprinted with permission [51]. Copyright 2011 Elsevier)

hydrophobic environment where the reactant benzene molecules are preferentially attracted into mesopores, whereas the hydrophilic product phenol molecules are rapidly released out of the pores before they undergo further oxidative degradation within the MCF cages. Ultimately, the phenol selectivity is significantly enhanced [51].

In addition to the method of enhancing the catalytic performance of photocatalysts toward hydroxylation of benzene through improving their adsorption and desorption toward reactants and products specificity, efforts in terms of visible light harvesting have been devoted. For example, Huang and co-workers have prepared M@TiO_2 (M = Au, Pt, Ag) composites for direct oxidation of benzene to phenol in aqueous phenol under visible light irradiation, where Au@TiO_2 with a content of 2 wt% Au exhibits a high yield (63 %) and selectivity (91 %), as shown in Fig. 8.4a. The high photocatalytic activity for the composite is attributed to the enhanced visible light absorption as well as the strongest surface plasmon resonance (SPR) effect (Fig. 8.4b) [52]. Notably, the yield and selectivity of the phenol formation are increased with initially added phenol (ranging from 0 to 18,000 ppm) in water. As schematically shown in Fig. 8.4c, it is proposed that the initially added phenol is partially ionized into phenoxy anions and protons, and the SPR effect allows the electron transfer from the Au nanoparticle (NP) to the TiO_2 particle to which it is attached. Compared with benzene, the phenoxy anions are preferred to adsorb on electron-depleted Au NPs due to the opposite charges. Then, the electron-depleted Au NPs under visible light irradiation will oxidize phenoxy anions into phenoxy free radicals, which in turn oxidize benzene to phenol, thus becoming phenoxy anions again. Finally, O_2 dissolved in the solution is reduced by the electrons from the conduction band minimum (CBM) of TiO_2. Increasing the

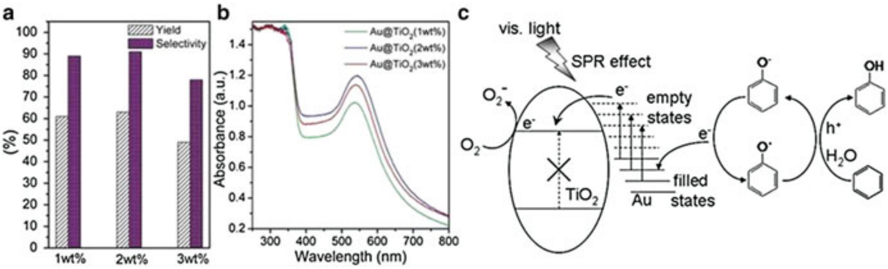

Fig. 8.4 (**a**) Visible light-induced catalytic oxidation of benzene with Au@TiO$_2$-microsphere composites with 1–3 wt% of Au. (**b**) UV/Vis diffuse-reflectance spectra of Au@TiO$_2$-microsphere composites. (**c**) Proposed mechanism for the photooxidation benzene into phenol in the presence of phenol under visible light irradiation (Reprinted with permission [52]. Copyright 2011 Royal Society of Chemistry)

amount of initially added phenol will generate more phenoxy anions in water, which can lead to more phenoxy free radicals under visible light irradiation, thereby enhancing the oxidation of benzene.

Besides, Chen and co-workers have reported that Fe ion-modified porous graphitic carbon nitride (Fe-g-C_3N_4) is active for the direct oxidation of benzene to phenol in the presence of H_2O_2 at mild conditions (60 °C, 4 h) in both the presence (with a yield of 4.8 % based on benzene) and absence (with a yield of 1.8 % based on benzene) of visible light irradiation [55]. The enhanced yield of phenol with light irradiation is explained as that the surface-bound -Fe^{3+} can capture the photoinduced electrons, resulting in -Fe^{2+} to bind and reduce H_2O_2 to produce •OH, which is able to oxidize benzene to phenol. Moreover, when loading the Fe-g-C_3N_4 into the mesoporous system of SBA-15, the yield can be further improved to ~12 %, demonstrating that the activity is related to the exposure of the Fe-g-C_3N_4 surface structure and the increased surface active sites for benzene activation.

8.4.2 *Oxidation of Alcohols*

Selective oxidation of alcohols to carbonyls is a kind of rather important reactions both in industrial and laboratory synthesis since the products such as aldehydes and ketone derivatives are widely utilized in the fragrance, confectionary, and pharmaceutical industries [42, 61–63]. To date, photocatalytic selective oxidation of alcohols to the corresponding aldehydes and ketones has been performed both in liquid phase and gas phase. Since gas-phase reactions need high temperature, liquid-phase reactions are more appealing in the view of green chemistry. Moreover, its selectivity can be significantly improved by the deployment of organic solvent and visible light harvesting.

By weak bonding surface complexation of heteroatom (X = O, S, or N)-containing substrates, metal oxides (such as Nb_2O_5 and TiO_2) could

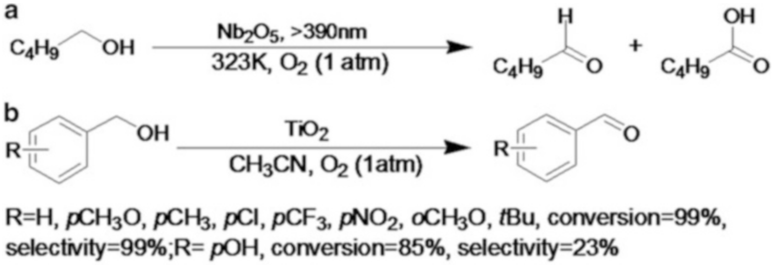

Scheme 8.2 (**a**) Photooxidation of 1-pentanol with Nb_2O_5 [64]. (**b**) Photooxidation of benzyl alcohol with various substitution groups with TiO_2 in CH_3CN [65, 66]

straightforwardly serve as the platform for visible light-induced organic reactions. For example, Shishido and co-workers have reported that the photooxidation of 1-pentanol can proceed over Nb_2O_5 under light irradiation (>390 nm), as shown in Scheme 8.2a [64]. The mechanism is proposed that alcohol is adsorbed onto Nb_2O_5 as an alcoholate species in the dark, which can be activated by visible light and transfer electrons to the conduction band reducing Nb^{5+} to Nb^{4+}, resulting in the formation of the alcoholate species and a hydroxy group. And then the alcoholate species can be photoactivated to generate an alkenyl radical, which subsequently is converted to a carbonyl compound and desorbed, with the reduced Nb^{4+} sites reoxidized via the reaction with molecular oxygen.

Likewise, the oxidation of alcohols to corresponding carbonyl compounds with O_2 on anatase TiO_2 has been achieved under visible light irradiation (Scheme 8.2b) [65, 66]. It is proposed that the surface complexes formed by the interaction of the $–CH_2OH$ group or possibly the phenyl ring of benzyl alcohol with the surface –OH group can induce absorption in the visible region [66]. Upon visible light irradiation, the surface complex is photoexcited to form holes (h^+) and electrons (e^-), and the holes can abstract hydrogen atoms from the $–CH_2OH$ group of benzyl alcohol. Subsequently, the photoinduced benzyl alcoholic radicals may automatically release another electron to form benzaldehyde due to the current-doubling effect. Excellent conversion of 99 % and selectivity of 99 % are achieved for a series of substituted benzyl alcohols except when the substituent is –OH. This is because the substituted –OH group provides extra coordination sites for interacting with TiO_2, consequently leading to the destruction of the phenyl ring [67]. This mechanism is also applicable to rutile TiO_2 nanorods, which have been used for aerobic oxidation of benzyl alcohols to benzaldehydes, yielding a high selectivity of 99 % under visible light irradiation [68].

Localized surface plasmon resonance (SPR) arising from a resonant oscillation of free electrons coupled by light has been extensively studied and combined with semiconductors as promising heterogeneous photocatalysts because of their strong light absorption in the visible region. Tsukamoto et al. have prepared Au/TiO_2 via the deposition–precipitation method from H_4AuCl_4 and TiO_2 (Degussa, P25), which shows enhanced activity toward selective aerobic oxidation of alcohols relative to the reaction in the dark at room temperature [69]. It is proposed that

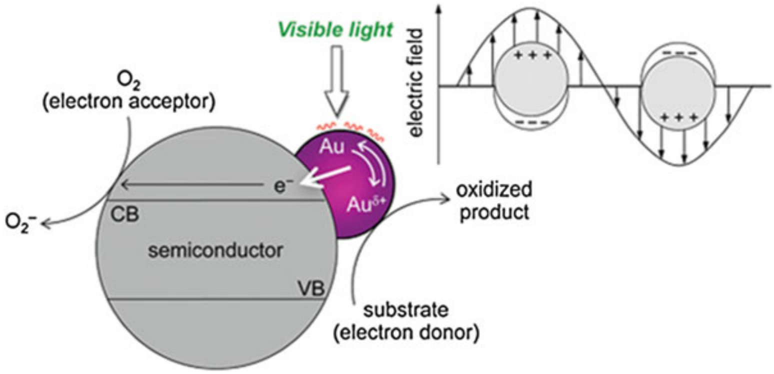

Scheme 8.3 Proposed mechanism for visible light-driven aerobic oxidation by Au particles supported on semiconductor particles (Reprinted with permission [69]. Copyright 2012 American Chemical Society)

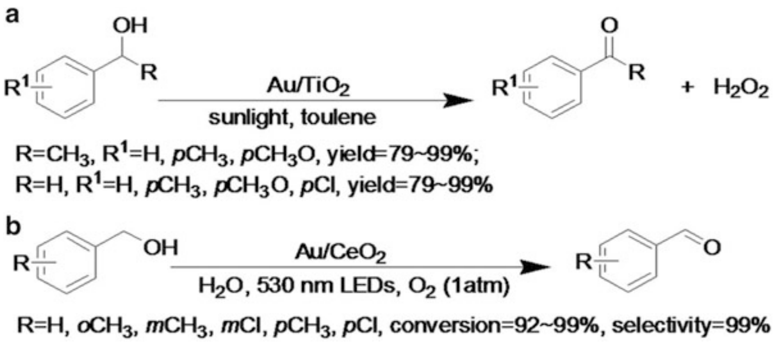

Scheme 8.4 (**a**) Aerobic oxidation of alcohols with Au/TiO_2 in toluene under the irradiation of natural sunlight [69]. (**b**) Photooxidation of alcohols with various substitution groups with Au/CeO_2 [70]

for visible light-driven aerobic oxidation, as depicted in Scheme 8.3, plasmonic photocatalyst might oxidize a substrate (electron donor) on the Au surface, while e^- is consumed by the reduction of O_2 (electron acceptor) on the semiconductor surface. Besides, it is found that the catalyst architecture is critical for the activity, i.e., small Au particles ($d_{Au} < 5$ nm) loaded on P25 are necessary and Au particles located at the anatase/rutile interface behave as the active sites, facilitating efficient e^- transfer to TiO_2 and successful aerobic oxidation under sunlight irradiation, as shown in Scheme 8.4a. Apart from TiO_2, Kominami's group has prepared Au/CeO_2 by photochemical deposition of H_4AuCl_4 on CeO_2 in the presence of citric acid as the reducing agent, which presents the maximum absorption around 550 nm, in agreement with the SPR of Au NPs [70]. When exposed to 530 nm LED irradiation,

Table 8.1 Selective oxidation of a range of alcohols over the TiO_2-5 % GR photocatalyst under the visible light irradiation ($\lambda > 400$ nm) for 20 h (Reprinted with permission [72]. Copyright 2011 American Chemical Society)

Entry	Substrate	Product	Conversion (%)	Yield (%)	Selectivity (%)
1	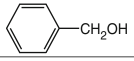	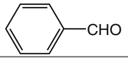	62	62	100
2	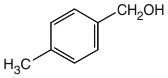	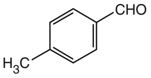	70	70	100
3	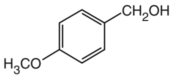	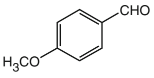	80	80	100
4	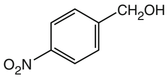	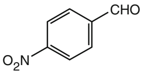	74	73	99
5	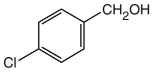	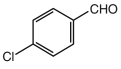	45	43	96
6	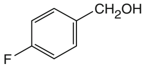	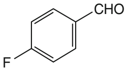	84	76	91
7	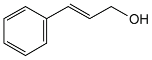	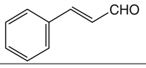	50	46	92
8	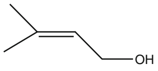	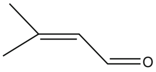	41	37	90

benzyl alcohols can be stoichiometrically oxidized to corresponding benzaldehydes with O_2 in water, as displayed in Scheme 8.4b.

Our group has found that the introduction of graphene (GR) into semiconductors leads to enhanced performance for aerobic oxidation of various benzylic alcohols with different substituents and allylic alcohols [71–74]. As displayed in Table 8.1, GR-TiO_2 composite has been fabricated via a two-step wet chemistry approach, using graphene oxide (GO) and TiF_4 as the precursors of GR and TiO_2, respectively [72]. It is proposed that the superior and easily accessible "structure-directing" role of GO, the intimate interfacial contact between GR and TiO_2, and the better separation of the photogenerated carriers of GR-TiO_2 play a synergistic role in leading to the enhanced photocatalytic performance. Similarly, the introduction of GR into CdS substrate can also influence the morphology and structure, enhance the visible light absorption intensity, and improve the lifetime and transfer of photogenerated electron–hole pairs over the CdS–GR, leading to enhanced photocatalytic performance toward photocatalytic selective oxidation of benzylic and allylic alcohols, as shown in Fig. 8.5a [75]. In addition, it has been found the intimate interfacial interaction between CdS and GR can inhibit the photocorrosion of CdS during the photocatalytic reactions effectively.

In addition to the dual-ingredient hybrid systems, we have also constructed ternary nanocomposites with further improved photocatalytic performances toward catalytic selective oxidation of alcohols, as shown in Fig. 8.5b [74]. Based on our previous CdS–GR composite with lamellar structure, TiO_2 nanoparticles can be uniformly carpeted on the surface of the CdS–GR by an in situ growth strategy [74]. The enhanced photocatalytic performance of ternary CdS–GR–TiO_2 hybrids can be ascribed to the combined interaction of larger surface area, the intimate interfacial contact among them, and two possible routes for electron transfer in the system [74]. The photogenerated electrons can transfer to the graphene nanosheets and TiO_2 simultaneously, which contributes to promoting the interfacial charge transfer rate and lengthening the lifetime of photogenerated electron–hole pairs, consequently resulting in the enhanced photoactivity.

Recently, our group has reported the transfer efficiency of photogenerated charge carriers across the interface between graphene (GR) and semiconductor CdS can be further improved by introducing a small amount of metal ions (M = Ca^{2+}, Cr^{3+}, Mn^{2+}, Fe^{2+}, Co^{2+}, Ni^{2+}, Cu^{2+}, and Zn^{2+}) as "mediator" into their interfacial layer matrix [73]. The photoactivity of GR–M–CdS for aerobic oxidation of alcohol is significantly improved (Fig. 8.5c) because the metal ions introduced can optimize the atomic charge carrier transfer pathway across the interface between GR and the semiconductor as well as drive a balance between the positive effect of GR on retarding the recombination of electron–hole pairs photogenerated from semiconductor and the negative "shielding effect" of GR resulting from the high weight addition of GR. Inspired by this, Pd has been selected as a typical noble metal to investigate whether it can play the similar role to metal ions as the interfacial mediator between GR and CdS. It is found that the ternary CdS–(GR–Pd)

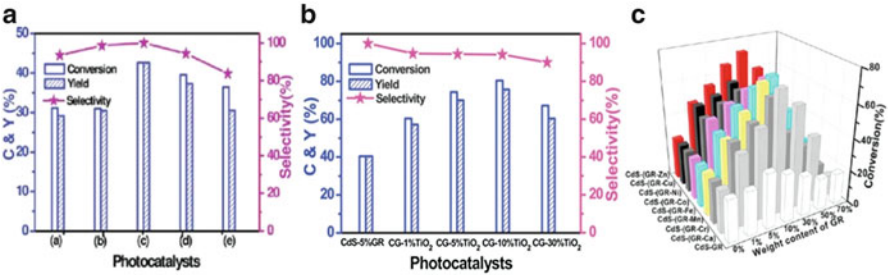

Fig. 8.5 (**a**) Photocatalytic selective oxidation of benzyl alcohol to benzaldehyde under the visible light irradiation over the as-prepared samples: (*a*) blank CdS; (*b*) CdS-1 % GR; (*c*) CdS-5 % GR; (*d*) CdS-10 % GR; and (*e*) CdS-30 % GR nanocomposites (Note: C and Y is short for conversion and yield. Reprinted with permission [75]. Copyright 2011 American Chemical Society). (**b**) CdS–GR–TiO_2 nanocomposites (Note: CG is short for CdS-5 % GR; GR–M–CdS nanocomposites. Reprinted with permission [74]. Copyright 2012 American Chemical Society). (**c**) Photocatalytic performance of blank CdS, CdS–GR, and CdS–(GR–M) (M = Ca^{2+}, Cr^{3+}, Mn^{2+}, Fe^{2+}, Co^{2+}, Ni^{2+}, Cu^{2+}, and Zn^{2+}) nanocomposites with different weight addition ratios of GR for photocatalytic selective oxidation of benzyl alcohol under visible light ($\lambda > 420$ nm) for 2 h (Reprinted with permission [73]. Copyright 2014 American Chemical Society)

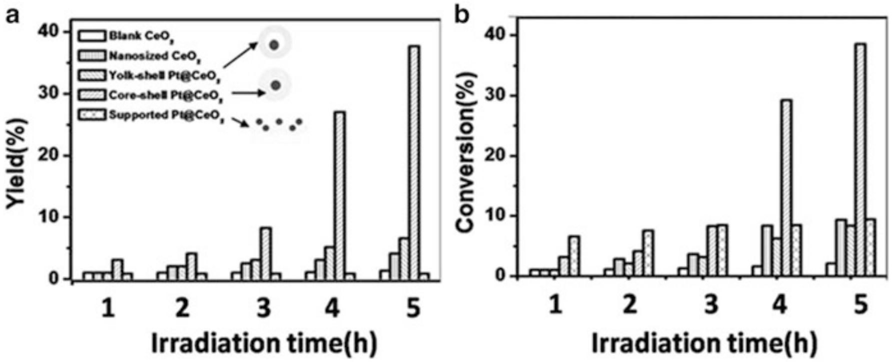

Fig. 8.6 The yield (**a**) and conversion (**b**) of photocatalytic selective oxidation of benzyl alcohol to benzaldehyde over the core–shell Pt/CeO_2, yolk–shell Pt/CeO_2, supported Pt/CeO_2, nanosized CeO_2 powder, and blank CeO_2 under the irradiation of visible light ($\lambda > 420$ nm) at room temperature and ambient atmosphere (Reprinted with permission [77]. Copyright 2011 Royal Society of Chemistry)

nanocomposite shows significantly enhanced visible light photocatalytic activity as compared to both blank CdS and the optimum binary CdS–GR, which verifies Pd can also play as the interfacial mediator to optimize and improve the spatial charge carrier separation and transfer across the interfacial domain between GR and CdS upon visible light irradiation [76].

Since optimizing the structure of the photocatalysts also has significant impact on the photocatalysts' performance, our group has synthesized the Pt/CeO_2 nanocomposite in an aqueous phase with tunable core–shell and yolk–shell structure via a facile and green template-free hydrothermal approach toward selective oxidation of benzyl alcohol [77]. The yield of benzaldehyde obtained over core–shell Pt/CeO_2 is ca. 9, 27, and 39 times higher than that of nanosized CeO_2, blank CeO_2, and supported Pt/CeO_2, respectively (Fig. 8.6), which can be ascribed to the advantageous core–shell structure, where Pt core can trap/store the photogenerated electrons to prolong the lifetime of charge carriers, hence improving the efficiency toward photocatalytic redox process. As for the yolk–shell structure, the interfacial contact between the Pt core and CeO_2 shell is quite loose, and thus the role of Pt core has decreased markedly, resulting in lower photocatalytic activity.

In addition, Pd@CeO_2 semiconductor nanocomposite with "plum-pudding" structure has been fabricated via a facile low-temperature hydrothermal reaction of polyvinylpyrrolidone (PVP)-capped Pd colloidal particles and cerium chloride precursor followed by a calcination process in air, as shown in Fig. 8.7a [78]. This unique nanostructure endows the Pd@CeO_2 nanocomposite with enhanced activity and selectivity toward the visible light-driven oxidation of various benzylic alcohols to corresponding aldehydes using dioxygen as oxidant at room temperature and ambient pressure compared with a supported Pd/CeO_2 nanocomposite and nanosized CeO_2 powder (Fig. 8.7b, c), which is ascribed to the unique structure assembly of multi-Pd core@CeO_2 shell nanocomposite. First, the uniform structure

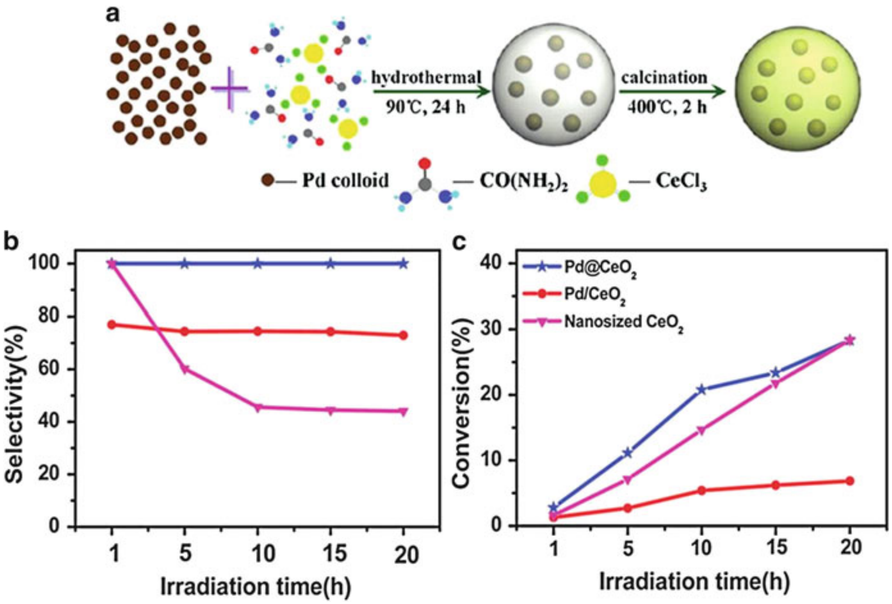

Fig. 8.7 Overall flowchart for fabrication of the multi-Pd core@CeO_2 shell semiconductor nanocomposite (**a**); time-online photocatalytic selective oxidation of benzyl alcohol to benzaldehyde over the multi-Pd core@ CeO_2 shell nanocomposite, supported Pd/CeO_2, and commercial CeO_2 nanosized powder under the irradiation of visible light ($\lambda > 420$ nm) under ambient conditions, selectivity (**b**); conversion (**c**) (Reprinted with permission [78]. Copyright 2011 American Chemical Society)

composition, i.e., the evenly dispersed Pd cores are spatially encapsulated by the CeO_2 shell, provides a homogeneous environment for photocatalytic reaction. Second, the multi-Pd core@CeO_2 shell nanostructure can significantly increase the surface area compared with the supported counterpart. Third, the "three-dimensional" intimate contact between the evenly dispersed Pd core and CeO_2 shell maximizes the metal–support interaction, which facilitates the interfacial charge transfer process.

Notably, aiming to give validity to targeted reactions for a fast screening of catalysts for photocatalytic transformations, Colmenares and co-workers have synthesized 24 different titania-based systems (either alone or modified with metals) through the sol–gel process varying the precursor (titanium isopropoxide or tetrachloride) and the aging (magnetic stirring, ultrasounds, microwave, or reflux) conditions. They are tested for liquid-phase selective photooxidation of 2-butenol (crotyl alcohol) to 2-butenal (crotonaldehyde) and gas-phase selective photooxidation of 2-propanol to acetone [61]. It is found that both test reactions (despite having very different reactant/catalyst ratio and contact times) show quite similar results in terms of influence of the precursor and the metals. That is, taking titanium isopropoxide as the precursor of titanium leads to better results than titanium tetrachloride and the presence of iron, palladium, or zinc is detrimental

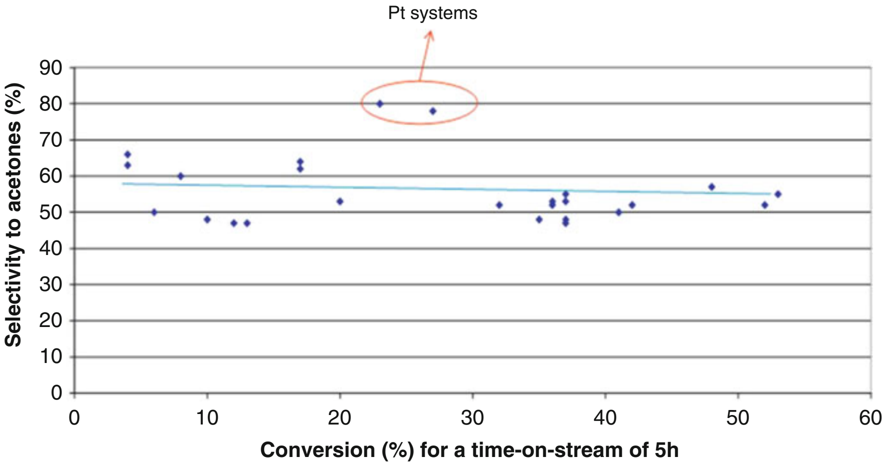

Fig. 8.8 Dependence of selectivity to acetone on 2-propanol conversion for all the titania-based systems used in the present study. Highlighted values correspond to platinum-containing titania (Reprinted with permission [61]. Copyright 2012 Elsevier)

to activity, whereas zirconium and especially gold can improve the results as compared to pure titania. Especially, for 2-propanol transformation into acetone, platinum-containing catalyst shows quite high selectivity values to acetone (in the 78–80 % range at 22–28 % conversion), suggesting that this test reaction is more sensitive to platinum, as shown in Fig. 8.8.

8.4.3 Oxidation of Saturated Primary C–H Bonds

The selective oxidation of stable alkyl aromatics such as toluene to commercial chemicals, including benzaldehyde, benzyl alcohol, benzoic acid, and benzyl benzoate with molecular oxygen, has important applications in fine chemicals and pharmaceutical production [79]. However, selective oxidation of C–H bonds with environmentally benign oxygen is often very difficult to control due to the abundance and inertness of C–H bonds in organic substrates. On the other hand, in thermal heterogeneous catalysis, the activation of saturated sp^3 C–H bonds often requires transition metal nanoparticles as a catalyst and relatively harsh reaction conditions. The rapid progress in selective transformation by heterogeneous photocatalysis presents the possibility of the selective activation of saturated sp^3 C–H bonds using molecular oxygen as a benign oxidant and visible light under ambient conditions [80, 81].

Zhu and co-workers have devised a new class of photocatalysts, metal hydroxide nanoparticles grafted with alcohols, which can efficiently oxidize alkyl aromatic compounds with O_2 using visible or ultraviolet light or even sunlight to generate the corresponding aldehydes, alcohols, and acids at ambient temperatures and give very

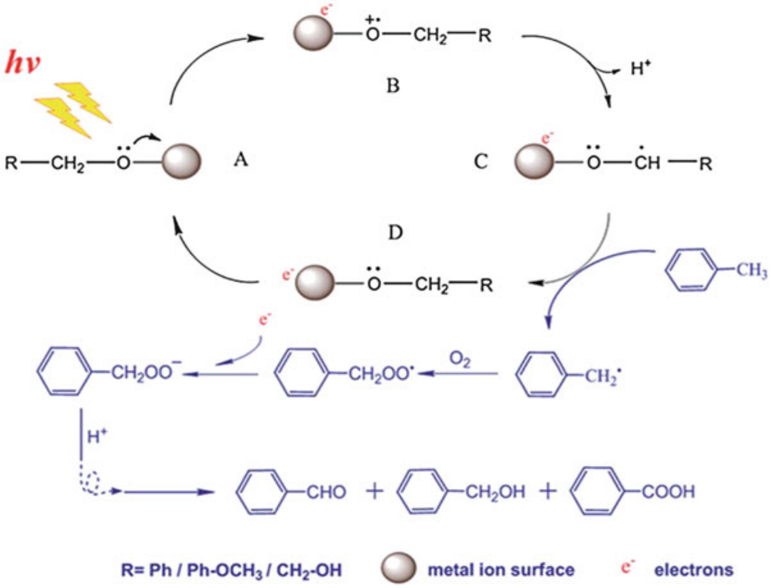

Scheme 8.5 Proposed pathways of the reaction mechanism for the selective oxidization of alkyl aromatics (Reprinted with permission [81]. Copyright 2012 Royal Society of Chemistry)

little overoxidation [81]. For example, toluene can be oxidized with a 23 % conversion after a 48 h exposure to sunlight with 85 % of the product being benzaldehyde and only a trace of CO_2. A tentative free radical mechanism is proposed, as shown in Scheme 8.5. The surface complexes catalyze the selective oxidation by an efficient mechanism that employs light absorption by the complexes to yield highly reactive surface radicals (−O–C–H–R), and these surface radicals initiate the aerobic oxidation of the organic molecules in contact with them. Moreover, the oxidation ability of the photocatalysts can be tuned through selection of the metal element and the alcohols grafted.

Our group has reported a cubic phase CdS semiconductor with specific sheet structure morphology synthesized by a simple room temperature method, which is able to be used as a visible light-driven photocatalyst for the selective oxidation of saturated primary C–H bonds in alkyl aromatics with high activity and selectivity using molecular oxygen as a benign oxidant and benzotrifluoride as the solvent under ambient conditions [82]. The superior photocatalytic performance of CdS is attributed to its unique structure assembly of specific sheet morphology with cubic phase, high surface area, and efficient separation of photogenerated charge carriers upon visible light irradiation. This work strongly suggests that tuning the microscopic structure and composition in diverse respects, e.g., size, shape, phase, crystallinity, or morphology, continues to be a very versatile, feasible, and general strategy to adjust the photocatalytic performance of a specific semiconductor photocatalyst with tunable photoactivity.

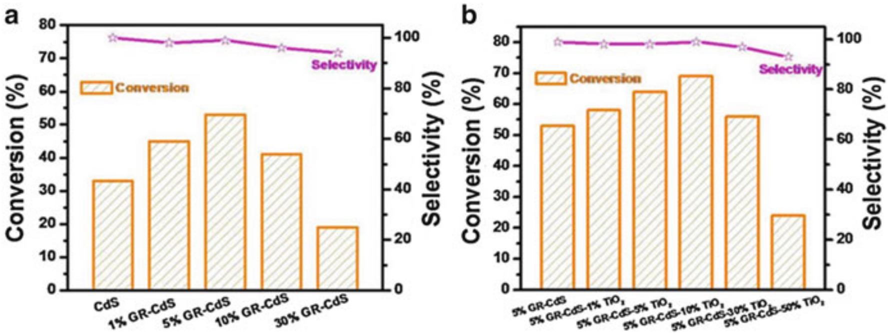

Fig. 8.9 Photocatalytic selective oxidation of toluene to benzaldehyde under visible light irradiation of 10 h over the as-prepared GR–CdS composites and blank CdS (**a**) and over GR–CdS–TiO_2 composites (**b**) (Reprinted with permission [83]. Copyright 2013 Nature Publishing Group)

Considering the fact that there is still a need to improve the photocatalytic performance of CdS for selective oxidation of C–H bonds, we later have designed and synthesized ternary GR–CdS–TiO_2 composites with an intimate spatial integration and sheetlike structure, which is afforded by assembling two co-catalysts, graphene and TiO_2, into the semiconductor CdS matrix with specific morphology as a visible light harvester [83]. As shown in Fig. 8.9, under visible light irradiation of 10 h, 53 % conversion of toluene is achieved over the optimal 5 % GR–CdS composite, which is much higher than 33 % conversion over the blank-CdS photocatalyst with the selectivity still maintained as high as 99 % (Fig. 8.9a). With the addition of second co-catalyst TiO_2, the photoactivity toward aerobic oxidation of C–H in toluene is further enhanced as compared to the binary 5% GR–CdS composite (Fig. 8.9b). It is proposed that the co-catalysts are able to cooperate with the light harvester to facilitate the charge separation/transfer and lengthen the lifetime of photogenerated electron–hole pairs, thereby resulting in an enhanced overall photocatalytic performance. This work demonstrates a wide, promising scope of adopting co-catalyst strategy to design more efficient semiconductor-based photocatalyst toward selective activation of C–H bonds using solar light and molecular oxygen.

8.4.4 Epoxidation of Alkenes

The epoxidation of alkene is another type of reaction of industrial importance. However, since alkenes lack the suitable coordination sites present in heteroatom substrates, the weak adsorbed alkene substrates are unable to interact with TiO_2 directly to induce visible light absorbance. Thus, the deployment of H_2O_2 as the terminal oxidant is needed to form active surface complex through the interplay between H_2O_2 and TiO_2. As early as 2001, it is reported that 1-decene can be converted to 1,2-epoxydecane on TiO_2 powder using molecular oxygen as the

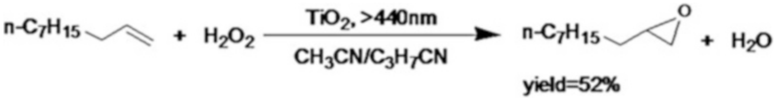

Scheme 8.6 Epoxidation of 1-decen to 1,2-epoxydecane with TiO_2 in CH_3CN/C_3H_7CN [84]

Scheme 8.7 Epoxidation of ethylene to ethylene oxide (**a**) [85] and propylene to propylene oxide (**b**) [86]

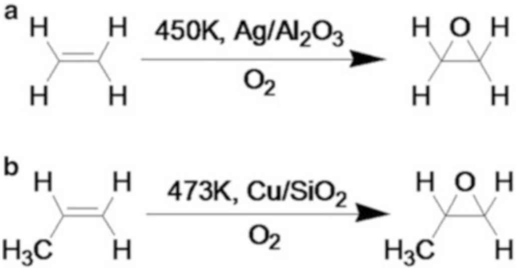

oxygen source under UV light irradiation [84]. For rutile TiO_2 powders, the rate of epoxide generation can be significantly increased by addition of hydrogen peroxide (Scheme 8.6). In this case, the reaction can occur under visible light as well as UV light. The selectivity of the production of 1, 2-epoxydecane is higher under visible light than under UV light, due to the formation of Ti-η^2-peroxide species on the surface of rutile TiO_2 upon treatment with H_2O_2, which can induce visible light absorbance [84].

With regard to the plasmonic photocatalysts, Linic and co-workers have found that Ag nanocubes of ~60 nm edge length supported on α-Al_2O_3 can be used for selective oxidation of ethylene to ethylene oxide (Scheme 8.7a) [85]. At 450 K, with the introduction of visible light into the system, the steady-state oxidation rate shows a fourfold increase relative to that driven by thermal energy only. And it is verified that the dissociation of molecular O_2 on silver to form adsorbed atomic oxygen controls the reaction rates. Later, they reported that Cu nanoparticles (NPs) with an average size of 41 nm supported on the inert SiO_2 (Cu/SiO_2) can tune the selectivity for the light-driven epoxidation of propylene to propylene oxide (Scheme 8.7b) [86]. The selectivity enhancement by Xe lamp irradiation is attributed to the localized SPR of Cu NPs which weakens the Cu–O bond, thereby prompting the reduction of Cu_2O to Cu^0.

Our group has reported an organic dye-like macromolecular “photosensitizer” role of graphene (GR) in wide-bandgap ZnS semiconductors for aerobic epoxidation of alkenes, including styrene, cyclohexene, and cyclooctene by visible light [87]. In this study, the assembly of nanosized ZnS particles on the two-dimensional platform of GR with an intimate interfacial contact has been prepared by a facile two-step wet chemistry process. Although the introduction of GR into the substrate of ZnS is not able to narrow the bandgap of ZnS to visible light region, the as-prepared ZnS–GR exhibits visible light photoactivity toward visible light irradiation ($\lambda > 420$ nm). Different from previous studies on GR–semiconductor photocatalysts, where GR is claimed to behave as an electron reservoir to capture and shuttle the electrons photogenerated from the semiconductor, it is proposed that the GR in the ZnS–GR nanocomposites is serving as an organic dye-like macromolecular "photosensitizer." Under visible light irradiation, GR is excited from the ground state to the excited state GR* and then injects electrons into the conduction band of ZnS, ultimately leading to visible light photoactivity.

8.4.5 Sulfoxidation of Thioethers

The sulfoxidation of sulfides is important organic transformations in many fields, including pharmaceuticals, fossil fuel desulfurization, industrial wastewater treatment, and chemical warfare agent disposal [47, 88]. However, the over-sulfoxidation of sulfides into sulfone is the main side reaction, and efforts should be devoted to achieve selective sulfoxidation [89]. Photocatalytic sulfoxidation using molecular oxygen as the terminal oxidant turns out to be more advantageous toward achieving sustainable chemistry. Although the mechanism of sulfoxidation by molecular oxygen via photochemical irradiation has been investigated in physical chemistry [90–94], the applications are just beginning to be reported recently [48, 95–98].

Yao's group has reported a metal-free aerobic selective sulfoxidation photosensitized by Rose Bengal (an organic dye) or solid-supported Rose Bengal, utilizing visible light as the driving force and molecular oxygen as the oxidant (Scheme 8.8) [97]. With the assistance of a catalytic amount of hydrochloric acid, Rose Bengal appears to be the most efficient and selective catalyst toward the selective sulfoxidation of thioanisole, compared to the metal complex photoredox catalysts. A series of other thioethers have been subjected to the optimized reaction conditions, verifying the generality of this reaction. In addition, Rose Bengal is readily accessible and inexpensive, and with the use of a solid-support catalyst, the workup procedure can be significantly improved. Moreover, a 50 mmol scale reaction has been carried out in an Erlenmeyer flask under sunlight on the roof of the chemistry building and demonstrated that the reaction is practical and scalable.

Apart from various organic photocatalysts, our group has reported a spatially branched hierarchical system composed of inorganic photocatalysts, CdS/ZnO nanocomposites (CZ), and its photoactivity toward sulfoxidation of thioanisole has been tested (Fig. 8.10) [99]. The conversion for thioanisole and yield for

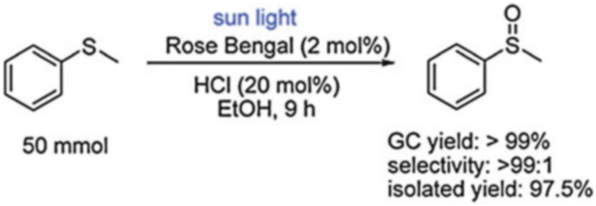

Scheme 8.8 Selective sulfoxidation of thioanisole under sunlight with Rose Bengal (Reprinted with permission [97]. Copyright 2013 Royal Society of Chemistry)

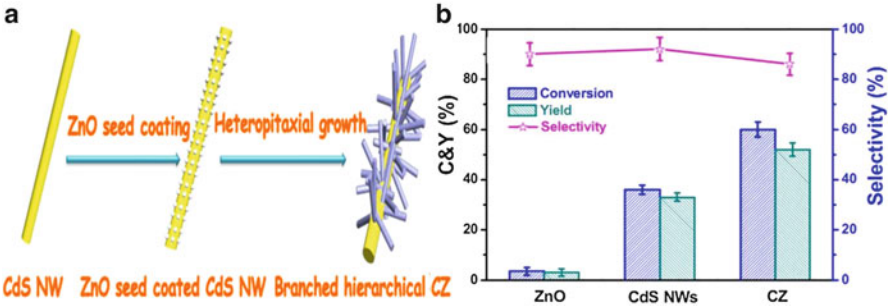

Fig. 8.10 (**a**) Schematic illustration for synthesis of branched hierarchical CZ nanocomposites and (**b**) photocatalytic performance of CdS NWs, blank ZnO, and branched hierarchical CZ nanocomposites for selective oxidation of thioanisole (Reprinted with permission [99]. Copyright 2014 Royal Society of Chemistry)

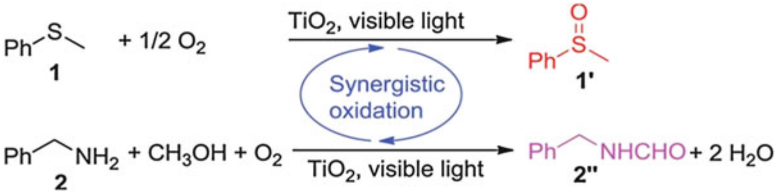

Scheme 8.9 The synergistic aerobic oxidation of two substrates, sulfide **1** and amine **2**, occurs simultaneously on the surface of TiO_2 under visible light irradiation (Reprinted with permission [95]. Copyright 2015 Royal Society of Chemistry)

methylsulfinylbenzene are about 60 % and 52 % over the branched hierarchical CZ, respectively, which are much higher than the values obtained over CdS NWs (conversion 36 % and yield 33 %) and blank ZnO (conversion 3.5 % and yield 3 %). The enhanced photoactivities can be ascribed to the branched hierarchical structure of CZ nanocomposites, which can not only increase the light harvesting efficiency but also boost charge separation and faster charge transport and collection. Additionally, under light irradiation, the branched hierarchical CZ nanocomposites are thought to generate a "Z-scheme" system [7] to drive the photocatalytic processes.

Recently, Zhao and co-workers have achieved the selective oxidation of thioanisole with TiO_2 photocatalyst under visible light irradiation by combining the aerobic oxidation of sulfide and the aerobic oxidative formylation of amine with methanol through the synergistic interplay of reactants and catalyst (Scheme 8.9) [95]. In contrast, attempts to perform these two reactions individually are not successful. The mechanism for the selective synergistic aerobic oxidation of thioanisole **1** and benzylamine **2** has been proposed and demonstrated in Scheme 8.10. The adsorption of benzylamine on TiO_2 leads to the formation of surface complex **a**, which shows activity under visible light irradiation, facilitating

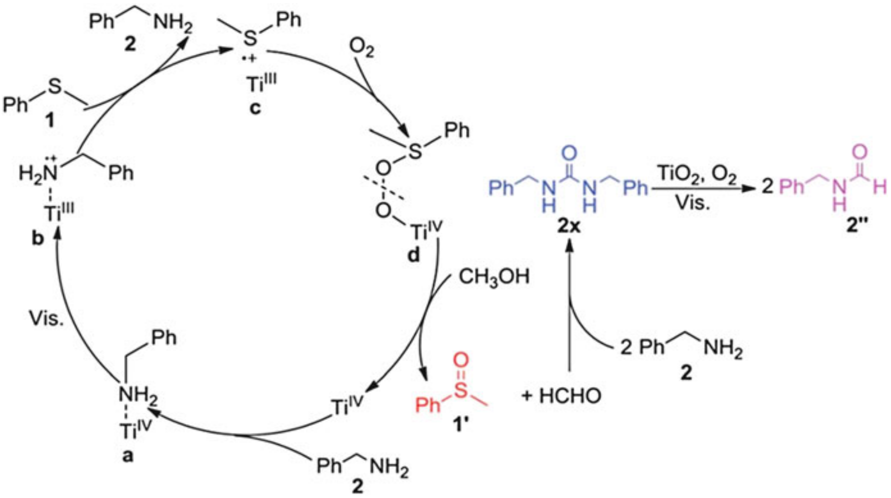

Scheme 8.10 Proposed mechanism for the synergistic selective oxidation of thioanisole **1** and benzylamine **2** with O_2 on TiO_2 under visible light irradiation (Reprinted with permission [95]. Copyright 2015 Royal Society of Chemistry)

electron transfer from the adsorbed benzylamine to TiO_2, and thus a series of reactions are initiated. During the whole stage, the addition of redox player, CH_3OH, is required to associate the two reactions. It is expected that more synergistic redox reactions can be achieved by judiciously selecting a pair of substrates and an appropriate solvent.

8.5 Photoreduction of Nitroaromatics

Photocatalytic reduction has also been studied as extensively as oxidation reactions since it is generally safer than the conventional methods, which always employ dangerous reducing agents such as hydrogen and carbon monoxide [28, 38]. Among the photocatalytic reductions, nitroaromatics reduction has been studied most extensively since amino compounds have been widely applied in the industrial synthesis of dyes, biologically active compounds, pharmaceuticals, rubber chemicals, and photographic and agricultural chemicals [73, 100–102]. In the transformation process, the removal of O_2 from the reaction mixture by purging N_2 and adding hole scavenger acting as electron donors can effectively improve the reaction rates and selectivities.

As early as 1997, Brezova et al. have reported that 4-nitrophenol can be successfully reduced to 4-aminophenol in various alcohols (methanol, ethanol, 1-propanol, 2-propanol, 1-butanol, and 2-butanol) with TiO_2 (Degussa P25) under UV irradiation [103]. The best yield of 92 % has been obtained after 20 min

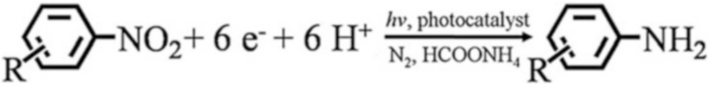

Scheme 8.11 Photocatalytic reduction of nitro compounds to amino compounds in water with the addition of ammonium formate ($HCOONH_4$) for quenching photogenerated holes under N_2 atmosphere

irradiation ($\lambda = 365$ nm) of 4-nitrophenol in methanol suspensions. It is proposed that the photoreduction rate is significantly affected by the solvent parameters, such as viscosity, polarity, and polarizability. For example, increase in the polarity parameter leads to better stabilization of the charged intermediate and accelerates the photocatalytic reduction.

Xu et al. have prepared GR-modified TiO_2 hybrids by electrostatic assembly, and its photocatalytic reduction of nitroaromatics to the corresponding aminoaromatics is examined under UV light irradiation [104]. When the dosage of GO is about 1.0 %, almost all of the 4-nitrophenol is converted, and the yield rate of 4-aminophenol achieves around 95 % with $H_2C_2O_4$ as hole scavenger under N_2 purge. The results indicate that the addition of GR can effectively minimize the recombination of photogenerated charge carriers derived from the irradiated TiO_2 and better encourage these separated electrons to participate in the reactions. In addition, it is found that different hole scavengers lead to discrepant reduction efficiency. Therefore, to adjust and optimize such photocatalytic reduction reactions is of great importance to improve its reduction ability.

Our group has fabricated various GR-based nanocomposites such as CdS nanowire/GR [100], CdS nanosphere/GR [105], In_2S_3/GR [102], $ZnIn_2S_4$/GR [106], TiO_2/CdS nanowire/GR [107], GR–M–CdS (M = Ca^{2+}, Cr^{3+}, Mn^{2+}, Fe^{2+}, Co^{2+}, Ni^{2+}, Cu^{2+}, and Zn^{2+}) [73], GR–Pd–CdS [76], and hierarchical CdS–ZnO–GR hybrids [108]. It is found that their photoactivities for reduction of nitro compounds to amino compounds with ammonium formate ($HCOONH_4$) for hole scavenger in N_2 atmosphere (Scheme 8.11) under visible light irradiation are all remarkably enhanced as compared to the blank semiconductors [73, 100–102, 106, 107]. It has been concluded that the selective reduction efficiency can be driven by appropriate introduction of GR into the matrix of pure semiconductor, which can boost the transfer and prolong the lifetime of the electrons photoexcited from the semiconductor due to the tighter connection between GR and the semiconductor, as well as the optimization of the atomic charge carrier transfer pathway across the interface between GR and the semiconductor.

In addition, our group has designed a Pd/CeO_2 hollow core–shell nanocomposite (Pd@hCeO_2) composed of tiny Pd nanoparticle (NP) cores encapsulated within CeO_2 hollow shells, as shown in Fig. 8.11a [109]. As compared to supported Pd/CeO_2 and commercial CeO_2, the as-prepared Pd@hCeO_2 demonstrates improved photoactivity toward selective reduction of aromatic nitro compounds under visible light irradiation with the addition of ammonium oxalate as quencher for photogenerated holes and N_2 purge at room temperature (Table 8.2). It is

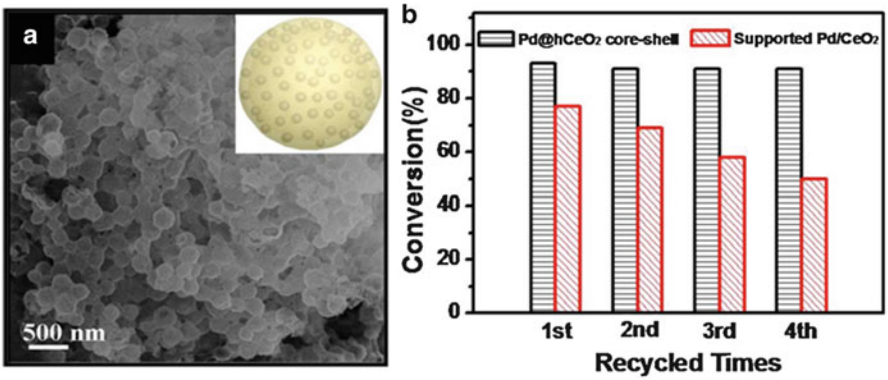

Fig. 8.11 (**a**) Typical SEM images of Pd@hCeO_2 core–shell nanocomposite. (**b**) Stability testing of photocatalytic activity of supported Pd/CeO_2 and Pd@hCeO_2 core–shell nanocomposites for reduction of 4-nitrophenol under visible light irradiation ($\lambda > 420$ nm) for 6 h (Reprinted with permission [109]. Copyright 2013 American Chemical Society)

recognized that the CeO_2 shell acts as the primary active component to give photogenerated electron–hole pairs, while the Pd nanoparticle cores with low-lying Fermi level serve as an electron reservoir to prolong the lifetime of the charge carriers. The three-dimensional interfacial contact between Pd cores and hollow CeO_2 shells facilitates the efficient charge carrier transfer, thereby leading to the enhanced fate of photogenerated electron–hole pairs from CeO_2. In particular, the core–shell strategy efficiently prevents the aggregation of Pd NPs in the high-temperature calcination process and the leaching of Pd NPs for the catalytic reaction in a liquid phase, which is not able to be achieved for traditional supported Pd/CeO_2 catalyst. As shown in Fig. 8.11b, the core–shell Pd@hCeO_2 almost does not have the loss of photoactivity during the recycled activity testing on reused samples, whereas the significant loss of photoactivity is clearly observed for supported Pd/CeO_2, due to the significant leaching of Pd nanoparticles in supported Pd/CeO_2.

8.6 Coupling Reactions

The photoinduced charge separation occurring on the surface of photocatalysts creates both a reduction center and an oxidation center. This unique feature allows multistep reactions on a single photocatalyst: intermediates generated from one reaction center could be the substrates at another center. The integrated use of both reaction centers could therefore complete a sophisticated multistep synthesis in "one-pot" reaction, i.e., the coupling reactions.

Table 8.2 Photocatalytic reduction of substituted aromatic nitro compounds over Pd@hCeO_2 core–shell nanocomposite, supported Pd/CeO_2, and commercial CeO_2 aqueous suspension under visible light irradiation ($\lambda > 420$ nm) with the addition of ammonium oxalate as quencher for photogenerated holes and N_2 purge at room temperature (Reprinted with permission [109]. Copyright 2013 American Chemical Society)

Entry	Substrate	t/[h]	Conversion (%)		
			Pd@hCeO_2	Pd/CeO_2	CeO_2
1	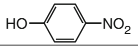	6	93	77	19
2	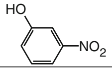	6	87	69	16
3	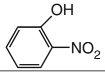	6	99	81	22
4	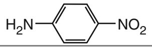	6	64	44	13
5	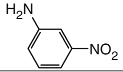	6	50	35	8
6	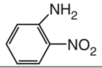	6	43	22	6
7	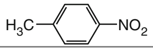	4	96	75	14
8	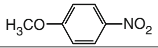	6	84	55	11
9	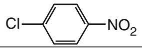	4	92	75	17
10	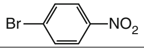	4	94	73	15

8.6.1 C–N Coupling

Various kinds of organic compounds can be synthesized through C–N coupling reactions [110–112]. For example, Ohtani and co-workers have found that photoirradiation to an aqueous solution containing primary amines in the presence of a powdered mixture of TiO_2 with Pt black (Pt/TiO_2 catalyst) gives rise to the corresponding secondary amines via C–N coupling reaction (Scheme 8.12a) [113]. L-Pipecolinic acid has been achieved by the cyclization reaction through photoirradiation of a deaerated aqueous suspension of TiO_2 containing L-lysine (Scheme 8.12b). This reaction involves a single-electron transfer from the terminal amino group of L-pipecolinic acid to h^+ on the TiO_2 surface and subsequent removal of the amino group, leading to intramolecular C–N coupling to form an imine, which is then reduced to form the L-pipecolinic acid. The highest selectivity (77 %) and conversion of L-lysine (90 %) have been achieved [110].

The C–N coupling reaction also can proceed between amines and alcohols. For example, photoirradiation to an alcohol solution containing primary or secondary amines with Pt/TiO_2 can produce the corresponding secondary or tertiary amines [114, 115]. In these reactions, alcohols are oxidized by h^+ formed on the catalyst

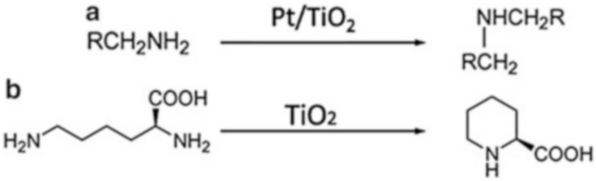

Scheme 8.12 (**a**) Photocatalytic transformation of primary amines to secondary amines via C–N coupling reaction on Pt/TiO_2 [113]. (**b**) Photocatalytic transformation of L-lysine to L-pipecolinic acid via C–N coupling reaction on TiO_2 [110]

surface to the corresponding aldehydes or ketones, which then could couple with amine to form an imine. In addition, imines can also be produced by reacting alkynes with amines to hydro-amination products with Au nanoparticles supported on nitrogen-doped TiO_2 (Au/TiO_2–N), which serves as the visible light plasmonic photocatalyst [116]. The presence of Ti^{3+} of TiO_2, arising from nitrogen doping, provides more coordination sites for the alkyne, thereby prompting a better performance than that of pure TiO_2 (Scheme 8.13a). Through a similar reaction, propargyl-amines have been produced by a one-pot synthesis procedure with the introduction of aldehyde to the amine and alkyne mixture, on the catalyst Au/ZnO under 530 nm LED irradiation (Scheme 8.13b) [117]. The high yields of propargyl-amines result from the interaction of alkyne with the ZnO support. Therefore, the use of plasmonic photocatalysts can also be employed to manipulate the oxidative condensation of amine with aldehyde under visible light irradiation.

8.6.2 C–C Coupling

Heterocyclic bases can easily be functionalized via C–C coupling by the reaction with amides or ethers. For example, Caronna and co-workers have found that with the addition of H_2SO_4 and H_2O_2, heterocyclic bases can react with amide to produce the corresponding amide-functionalized heterocycles (Scheme 8.14) [118]. It is considered that during these reactions, amide first reacts with •OH radical formed on the TiO_2 surface to form amide radical via hydrogen abstraction, which then attacks the heterocyclic bases and produces the C–C coupling products. The additional H_2SO_4 and H_2O_2 can accelerate the amide radical formation.

Subsequently, it is reported by the same group that the reactions between various heterocyclic bases and ethers can be induced by sunlight, and various kinds of heterocycle-ether conjugates are formed in liquid–solid heterogeneous system in the presence of TiO_2 (Scheme 8.15) [119]. The derivatives obtained with trioxane may give an easy entry to heterocyclic aldehydes. It is considered that in these reactions, the α-oxyalkyl radical is generated by hydrogen abstraction from the α-carbon of the ethers or by electron transfer from the oxygen atom of the ethers, which then is claimed to attack the heterocyclic bases to form the heterocycle-ether conjugates.

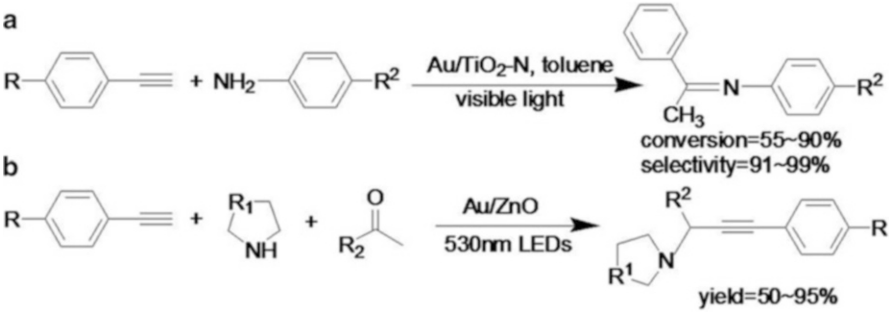

Scheme 8.13 Photocatalytic C–N coupling reactions between alkynes with amines (Reprinted with permission [33]. Copyright 2014 Royal Society of Chemistry)

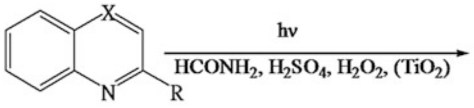

(1) X = CH, R = H

(2) X = CH, R = CH_3

(3) X = C-CH_3, R = H

(4) X = N, R = H

(5) X = CH, R = $CONH_2$

(6) X = C-$CONH_2$, R = CH_3

(7) X = C-CH_3, R= $CONH_2$

(8) X = N, R = $CONH_2$

Scheme 8.14 Photocatalytic reactions of heterocyclic bases and formamide in aqueous solution with TiO_2 (Reprinted with permission [118]. Copyright 2003 Royal Society of Chemistry)

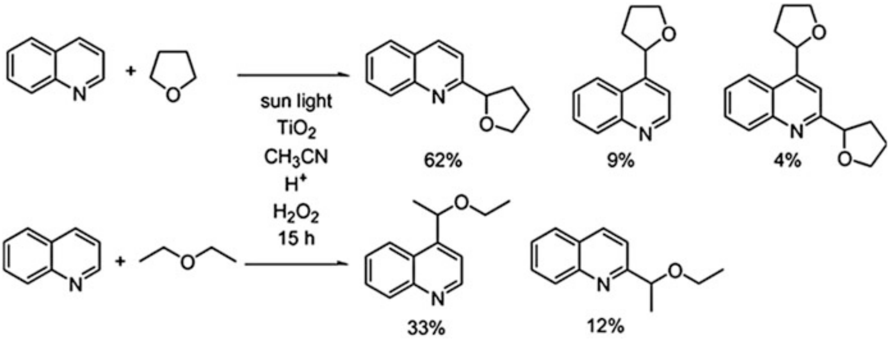

Scheme 8.15 Photocatalytic functionalization of heterocyclic base with ethers by TiO_2 (Reprinted with permission [26]. Copyright 2008 Elsevier)

In addition, other nucleophiles have also been incorporated into the activated substrates adjacent to N-atom, enabling even more complicated functionalization under visible light irradiation on P25 TiO_2. Using P25 as a photocatalyst, new C–C

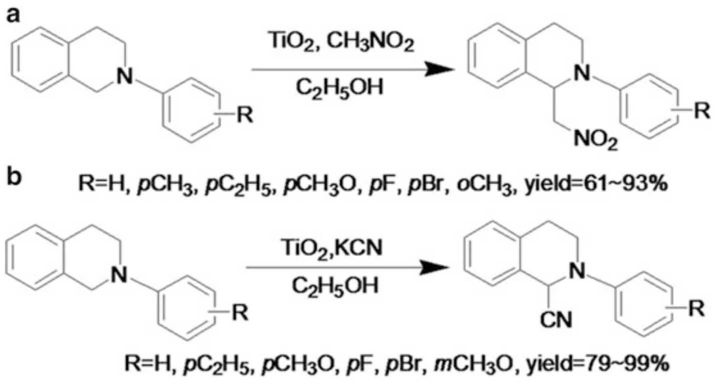

Scheme 8.16 C–C coupling of a variety of N-aryltetrahydroisoquinolines with CH_3NO_2 and KCN over TiO_2 (Reprinted with permission [33]. Copyright 2014 Royal Society of Chemistry)

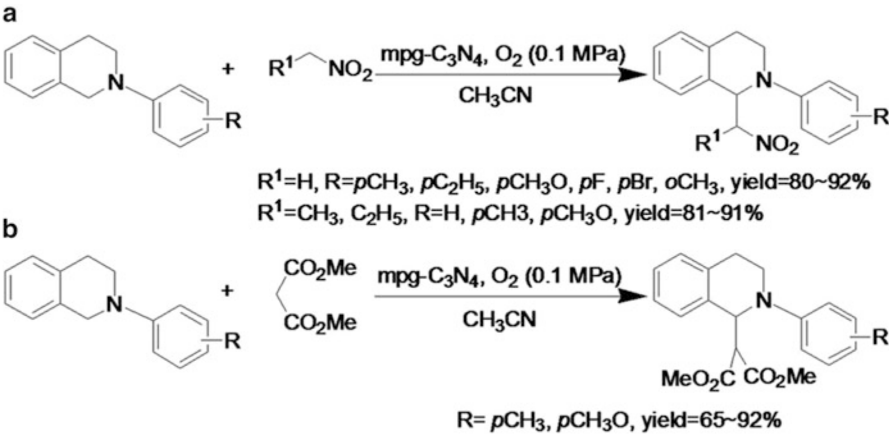

Scheme 8.17 C–C coupling of a variety of N-aryltetrahydroisoquinolines with nitroalkanes and dimethyl malonate over mpg-C_3N_4 (Reprinted with permission [33]. Copyright 2014 Royal Society of Chemistry)

bonds were successfully constructed under the mild visible light irradiation of an 11 W fluorescent lamp [120]. As shown in Scheme 8.16, both CH_3NO_2 and KCN are able to act as the nucleophile to facilitate the formation of different C–C bonds to afford different tetrahydroisoquinoline derivatives in good to excellent yields [120].

Besides, Möhlmann and co-workers have operated mpg-C_3N_4 as a visible light photocatalyst to functionalize the benzylic C–H adjacent to N-atoms with a suitable nucleophile, using 0.1 MPa of O_2 as the oxidant, without the assistance of an additional additive. Under the visible light irradiation, a variety of N-aryltetrahydroisoquinolines could be connected with nitroalkanes and dimethyl malonate to construct new C–C bonds, as shown in Scheme 8.17 [121].

8.7 Conclusion

Selective organic transformation plays an important role in the synthesis of various commodity chemicals closely linked to our daily lives. In comparison to conventional methods, photocatalytic organic transformations possess several inherent advantages, including benign environmental impacts and employment of mild reaction conditions. It is offering an alternative "green" route for the production of organics. However, despite significant progress made in this area of research as reviewed above, typical challenges still exist and need to be resolved before it is more viable for large-scale practical applications. In this regard, more exciting discoveries of efficient photocatalysts and more precise deployment of the reaction conditions are required to be conceived in the pursuit of higher conversion and higher selectivity for photocatalytic organic transformations in a practical scale-up manner. More investigations are needed to deepen our understanding of the photoinduced interfacial charge carrier transfer processes and optimized photocatalytic reactor design, which can help effectively promote the development and implementation of rapid global spread of organic synthesis by semiconductor-based photocatalysis. Hopefully, because many organic reactions are thermodynamic downhill exothermic reactions, thus we believe that the prospect of photocatalytic organic transformations in practical application is more available.

Acknowledgments The support from the Key Project of National Natural Science Foundation of China (U1463204), the National Natural Science Foundation of China (20903023 and 21173045), the Award Program for Minjiang Scholar Professorship, the Natural Science Foundation of Fujian Province for Distinguished Young Investigator Grant (2012 J06003), the Independent Research Project of State Key Laboratory of Photocatalysis on Energy and Environment (NO. 2014A05), the first Program of Fujian Province for Top Creative Young Talents, and the Program for Returned High-Level Overseas Chinese Scholars of Fujian province is kindly acknowledged.

References

1. Ran J, Zhang J, Yu J, Jaroniec M, Qiao SZ (2014) Earth-abundant cocatalysts for semiconductor-based photocatalytic water splitting. Chem Soc Rev 43(22):7787–7812
2. Yang J, Wang D, Han H, Li C (2013) Roles of cocatalysts in photocatalysis and photoelectrocatalysis. Acc Chem Res 46(8):1900–1909
3. Chen X, Shen S, Guo L, Mao SS (2010) Semiconductor-based photocatalytic hydrogen generation. Chem Rev 110(11):6503–6570
4. Navarro Yerga RM, Álvarez Galván MC, Del Valle F, Villoria de la Mano JA, Fierro JL (2009) Water splitting on semiconductor catalysts under visible-light irradiation. Chemsuschem 2(6):471–485
5. Stott PA, Tett S, Jones G, Allen M, Mitchell J, Jenkins G (2000) External control of 20th century temperature by natural and anthropogenic forcings. Science 290(5499):2133–2137
6. Herzog HJ (2001) Peer reviewed: what future for carbon capture and sequestration? Environ Sci Technol 35(7):148A–153A
7. Zhou P, Yu J, Jaroniec M (2014) All-solid-state Z-scheme photocatalytic systems. Adv Mater 26(29):4920–4935

8. Wang C, Astruc D (2014) Nanogold plasmonic photocatalysis for organic synthesis and clean energy conversion. Chem Soc Rev 43(20):7188–7216
9. Tong H, Ouyang S, Bi Y, Umezawa N, Oshikiri M, Ye J (2012) Nano-photocatalytic materials: possibilities and challenges. Adv Mater 24(2):229–251
10. Shen S, Shi J, Guo P, Guo L (2011) Visible-light-driven photocatalytic water splitting on nanostructured semiconducting materials. Int J Nanotechnol 8(6):523–591
11. Maeda K (2011) Photocatalytic water splitting using semiconductor particles: history and recent developments. J Photochem Photobiol C 12(4):237–268
12. Langer R, Leitus G, Ben-David Y, Milstein D (2011) Efficient hydrogenation of ketones catalyzed by an iron pincer complex. Angew Chem 123(9):2168–2172
13. Navarro RM, Alvarez-Galvan MC, Villoria de la Mano JA, Al-Zahrani SM, Fierro JLG (2010) A framework for visible-light water splitting. Energy Environ Sci 3(12):1865–1882
14. Maeda K, Domen K (2010) Photocatalytic water splitting: recent progress and future challenges. J Phys Chem Lett 1(18):2655–2661
15. Tu W, Zhou Y, Zou Z (2014) Photocatalytic conversion of CO_2 into renewable hydrocarbon fuels: state-of-the-art accomplishment, challenges, and prospects. Adv Mater 26 (27):4607–4626
16. Liu L, Li Y (2014) Understanding the reaction mechanism of photocatalytic reduction of CO_2 with H_2O on TiO_2-based photocatalysts: a review. Aerosol Air Qual Res 14(2):453–469
17. Li K, An X, Park KH, Khraisheh M, Tang J (2014) A critical review of CO_2 photoconversion: catalysts and reactors. Catal Today 224:3–12
18. Izumi Y (2013) Recent advances in the photocatalytic conversion of carbon dioxide to fuels with water and/or hydrogen using solar energy and beyond. Coord Chem Rev 257 (1):171–186
19. Habisreutinger SN, Schmidt-Mende L, Stolarczyk JK (2013) Photocatalytic reduction of CO_2 on TiO_2 and other semiconductors. Angew Chem Int Ed 52(29):7372–7408
20. Mori K, Yamashita H, Anpo M (2012) Photocatalytic reduction of CO_2 with H_2O on various titanium oxide photocatalysts. RSC Adv 2(8):3165–3172
21. Liu G, Wang K, Hoivik N, Jakobsen H (2012) Progress on free-standing and flow-through TiO_2 nanotube membranes. Sol Energy Mater Sol Cells 98:24–38
22. Yui T, Tamaki Y, Sekizawa K, Ishitani O (2011) Photocatalytic reduction of CO_2: from molecules to semiconductors. Photocatal 303:151–184
23. Wu C, Zhou Y, Zou Z (2011) Research progress in photocatalytic conversion of CO_2 to hydrocarbons. Chin J Catal 32(10):1565–1572
24. Roy SC, Varghese OK, Paulose M, Grimes CA (2010) Toward solar fuels: photocatalytic conversion of carbon dioxide to hydrocarbons. ACS Nano 4(3):1259–1278
25. Jiang Z, Xiao T, Kuznetsov V, Edwards P (2010) Turning carbon dioxide into fuel. Philos Trans R Soc A Math Phys Eng Sci 368(1923):3343–3364
26. Shiraishi Y, Hirai T (2008) Selective organic transformations on titanium oxide-based photocatalysts. J Photochem Photobiol C 9(4):157–170
27. Lawless D, Serpone N, Meisel D (1991) Role of hydroxyl radicals and trapped holes in photocatalysis. A pulse radiolysis study. J Phys Chem 95(13):5166–5170
28. Fox MA, Dulay MT (1993) Heterogeneous photocatalysis. Chem Rev 93(1):341–357
29. Palmisano G, Augugliaro V, Pagliaro M, Palmisano L (2007) Photocatalysis: a promising route for 21st century organic chemistry. Chem Commun 33:3425–3437
30. Protti S, Fagnoni M (2009) The sunny side of chemistry: green synthesis by solar light. Photochem Photobiol Sci 8(11):1499–1516
31. Ravelli D, Dondi D, Fagnoni M, Albini A (2009) Photocatalysis. A multi-faceted concept for green chemistry. Chem Soc Rev 38(7):1999–2011
32. Palmisano G, García-López E, Marcì G, Loddo V, Yurdakal S, Augugliaro V, Palmisano L (2010) Advances in selective conversions by heterogeneous photocatalysis. Chem Commun 46(38):7074–7089

33. Lang X, Chen X, Zhao J (2014) Heterogeneous visible light photocatalysis for selective organic transformations. Chem Soc Rev 43(1):473–486
34. Yang M-Q, Xu Y-J (2013) Selective photoredox using graphene-based composite photocatalysts. Phys Chem Chem Phys 15(44):19102–19118
35. Colmenares JC, Luque R (2014) Heterogeneous photocatalytic nanomaterials: prospects and challenges in selective transformations of biomass-derived compounds. Chem Soc Rev 43 (3):765–778
36. Colmenares JC, Magdziarz A, Bielejewska A (2011) High-value chemicals obtained from selective photo-oxidation of glucose in the presence of nanostructured titanium photocatalysts. Bioresour Technol 102(24):11254–11257
37. Colmenares JC, Luque R, Campelo JM, Colmenares F, Karpiński Z, Romero AA (2009) Nanostructured photocatalysts and their applications in the photocatalytic transformation of lignocellulosic biomass: an overview. Materials 2(4):2228–2258
38. Zhang N, Zhang Y, Xu Y-J (2012) Recent progress on graphene-based photocatalysts: current status and future perspectives. Nanoscale 4(19):5792–5814
39. Zhang N, Liu S, Xu Y-J (2012) Recent progress on metal core@semiconductor shell nanocomposites as a promising type of photocatalyst. Nanoscale 4(7):2227–2238
40. Weng B, Liu S, Tang Z-R, Xu Y-J (2014) One-dimensional nanostructure based materials for versatile photocatalytic applications. RSC Adv 4(25):12685–12700
41. Liu S, Zhang N, Tang Z-R, Xu Y-J (2012) Synthesis of one-dimensional CdS@TiO_2 core-shell nanocomposites photocatalyst for selective redox: the dual role of TiO_2 shell. ACS Appl Mater Interfaces 4(11):6378–6385
42. Zhang M, Wang Q, Chen C, Zang L, Ma W, Zhao J (2009) Oxygen atom transfer in the photocatalytic oxidation of alcohols by TiO_2: oxygen isotope studies. Angew Chem Int Ed 48 (33):6081–6084
43. Qu Y, Duan X (2013) Progress, challenge and perspective of heterogeneous photocatalysts. Chem Soc Rev 42(7):2568–2580
44. Kisch H (2013) Semiconductor photocatalysis-mechanistic and synthetic aspects. Angew Chem Int Ed 52(3):812–847
45. Yang M-Q, Zhang N, Pagliaro M, Xu Y-J (2014) Artificial photosynthesis over graphene–semiconductor composites. Are we getting better? Chem Soc Rev 43(24):8240–8254
46. Fan W, Zhang Q, Wang Y (2013) Semiconductor-based nanocomposites for photocatalytic H_2 production and CO_2 conversion. Phys Chem Chem Phys 15(8):2632–2649
47. Caron S, Dugger RW, Ruggeri SG, Ragan JA, Ripin DHB (2006) Large-scale oxidations in the pharmaceutical industry. Chem Rev 106(7):2943–2989
48. Fukuzumi S, Kishi T, Kotani H, Lee Y-M, Nam W (2011) Highly efficient photocatalytic oxygenation reactions using water as an oxygen source. Nat Chem 3(1):38–41
49. Ohkubo K, Kobayashi T, Fukuzumi S (2011) Direct oxygenation of benzene to phenol using quinolinium ions as homogeneous photocatalysts. Angew Chem 123(37):8811–8814
50. Ye X, Cui Y, Qiu X, Wang X (2014) Selective oxidation of benzene to phenol by Fe-CN/TS-1 catalysts under visible light irradiation. Appl Catal B 152:383–389
51. Zhang G, Yi J, Shim J, Lee J, Choi W (2011) Photocatalytic hydroxylation of benzene to phenol over titanium oxide entrapped into hydrophobically modified siliceous foam. Appl Catal B 102(1):132–139
52. Zheng Z, Huang B, Qin X, Zhang X, Dai Y, Whangbo M-H (2011) Facile in situ synthesis of visible-light plasmonic photocatalysts M@TiO_2 (M = Au, Pt, Ag) and evaluation of their photocatalytic oxidation of benzene to phenol. J Mater Chem 21(25):9079–9087
53. Chen J, Eberlein L, Langford CH (2002) Pathways of phenol and benzene photooxidation using TiO_2 supported on a zeolite. J Photochem Photobiol A: Chem 148(1):183–189
54. Bui TD, Kimura A, Ikeda S, Matsumura M (2010) Determination of oxygen sources for oxidation of benzene on TiO_2 photocatalysts in aqueous solutions containing molecular oxygen. J Am Chem Soc 132(24):8453–8458

55. Chen X, Zhang J, Fu X, Antonietti M, Wang X (2009) Fe-g-C_3N_4-catalyzed oxidation of benzene to phenol using hydrogen peroxide and visible light. J Am Chem Soc 131 (33):11658–11659
56. Shiraishi Y, Saito N, Hirai T (2005) Adsorption-driven photocatalytic activity of mesoporous titanium dioxide. J Am Chem Soc 127(37):12820–12822
57. Herron N, Tolman CA (1987) A highly selective zeolite catalyst for hydrocarbon oxidation. A completely inorganic mimic of the alkane. omega.-hydroxylases. J Am Chem Soc 109 (9):2837–2839
58. Izumi I, Dunn WW, Wilbourn KO, Fan F-RF, Bard AJ (1980) Heterogeneous photocatalytic oxidation of hydrocarbons on platinized titanium dioxide powders. J Phys Chem 84 (24):3207–3210
59. Fujihira M, Satoh Y, Osa T (1981) Heterogeneous photocatalytic oxidation of aromatic compounds on TiO_2. Nature 293:206–208
60. Shimizu K-I, Kaneko T, Fujishima T, Kodama T, Yoshida H, Kitayama Y (2002) Selective oxidation of liquid hydrocarbons over photoirradiated TiO_2 pillared clays. Appl Catal A Gen 225(1):185–191
61. López-Tenllado FJ, Marinas A, Urbano FJ, Colmenares JC, Hidalgo MC, Marinas JM, Moreno JM (2012) Selective photooxidation of alcohols as test reaction for photocatalytic activity. Appl Catal B 128:150–158
62. Lykakis IN, Tanielian C, Seghrouchni R, Orfanopoulos M (2007) Mechanism of decatungstate photocatalyzed oxygenation of aromatic alcohols: part II. Kinetic isotope effects studies. J Mol Catal A: Chem 262(1):176–184
63. Tanaka A, Hashimoto K, Kominami H (2012) Preparation of Au/CeO2 exhibiting strong surface plasmon resonance effective for selective or chemoselective oxidation of alcohols to aldehydes or ketones in aqueous suspensions under irradiation by green light. J Am Chem Soc 134(35):14526–14533
64. Shishido T, Miyatake T, Teramura K, Hitomi Y, Yamashita H, Tanaka T (2009) Mechanism of photooxidation of alcohol over Nb_2O_5. J Phys Chem C 113(43):18713–18718
65. Higashimoto S, Kitao N, Yoshida N, Sakura T, Azuma M, Ohue H, Sakata Y (2009) Selective photocatalytic oxidation of benzyl alcohol and its derivatives into corresponding aldehydes by molecular oxygen on titanium dioxide under visible light irradiation. J Catal 266 (2):279–285
66. Higashimoto S, Suetsugu N, Azuma M, Ohue H, Sakata Y (2010) Efficient and selective oxidation of benzylic alcohol by O_2 into corresponding aldehydes on a TiO_2 photocatalyst under visible light irradiation: effect of phenyl-ring substitution on the photocatalytic activity. J Catal 274(1):76–83
67. Higashimoto S, Okada K, Azuma M, Ohue H, Terai T, Sakata Y (2012) Characteristics of the charge transfer surface complex on titanium (IV) dioxide for the visible light induced chemoselective oxidation of benzyl alcohol. RSC Adv 2(2):669–676
68. Li C-J, Xu G-R, Zhang B, Gong JR (2012) High selectivity in visible-light-driven partial photocatalytic oxidation of benzyl alcohol into benzaldehyde over single-crystalline rutile TiO_2 nanorods. Appl Catal B 115:201–208
69. Tsukamoto D, Shiraishi Y, Sugano Y, Ichikawa S, Tanaka S, Hirai T (2012) Gold nanoparticles located at the interface of anatase/rutile TiO_2 particles as active plasmonic photocatalysts for aerobic oxidation. J Am Chem Soc 134(14):6309–6315
70. Tanaka A, Hashimoto K, Kominami H (2011) Selective photocatalytic oxidation of aromatic alcohols to aldehydes in an aqueous suspension of gold nanoparticles supported on cerium (iv) oxide under irradiation of green light. Chem Commun 47(37):10446–10448
71. Li X, Weng B, Zhang N, Xu Y-J (2014) In situ synthesis of hierarchical In_2S_3-graphene nanocomposite photocatalyst for selective oxidation. RSC Adv 4(110):64484–64493
72. Zhang Y, Tang Z-R, Fu X, Xu Y-J (2011) Engineering the unique 2D mat of graphene to achieve graphene-TiO_2 nanocomposite for photocatalytic selective transformation: what

advantage does graphene have over its forebear carbon nanotube? ACS Nano 5 (9):7426–7435

73. Zhang N, Yang M-Q, Tang Z-R, Xu Y-J (2014) Toward improving the graphene-semiconductor composite photoactivity via the addition of metal ions as generic interfacial mediator. ACS Nano 8(1):623–633
74. Zhang N, Zhang Y, Pan X, Yang M-Q, Xu Y-J (2012) Constructing ternary CdS-graphene-TiO_2 hybrids on the flatland of graphene oxide with enhanced visible-light photoactivity for selective transformation. J Phys Chem C 116(34):18023–18031
75. Zhang N, Zhang Y, Pan X, Fu X, Liu S, Xu Y-J (2011) Assembly of CdS nanoparticles on the two-dimensional graphene scaffold as visible-light-driven photocatalyst for selective organic transformation under ambient conditions. J Phys Chem C 115(47):23501–23511
76. Han C, Yang M-Q, Zhang N, Xu Y-J (2014) Enhancing the visible light photocatalytic performance of ternary CdS-(graphene-Pd) nanocomposites via a facile interfacial mediator and co-catalyst strategy. J Mater Chem A 2(45):19156–19166
77. Zhang N, Fu X, Xu Y-J (2011) A facile and green approach to synthesize Pt@CeO_2 nanocomposite with tunable core-shell and yolk-shell structure and its application as a visible light photocatalyst. J Mater Chem 21(22):8152–8158
78. Zhang N, Liu S, Fu X, Xu Y-J (2011) A simple strategy for fabrication of “Plum-Pudding” type Pd@CeO_2 semiconductor nanocomposite as a visible-light-driven photocatalyst for selective oxidation. J Phys Chem C 115(46):22901–22909
79. Kesavan L, Tiruvalam R, Ab Rahim MH, bin Saiman MI, Enache DI, Jenkins RL, Dimitratos N, Lopez-Sanchez JA, Taylor SH, Knight DW (2011) Solvent-free oxidation of primary carbon-hydrogen bonds in toluene using Au-Pd alloy nanoparticles. Science 331 (6014):195–199
80. Yuan R, Fan S, Zhou H, Ding Z, Lin S, Li Z, Zhang Z, Xu C, Wu L, Wang X (2013) Chlorine-radical-mediated photocatalytic activation of C–H bonds with visible light. Angew Chem 125 (3):1069–1073
81. Sarina S, Zhu H, Zheng Z, Bottle S, Chang J, Ke X, Zhao J-C, Huang Y, Sutrisno A, Willans M (2012) Driving selective aerobic oxidation of alkyl aromatics by sunlight on alcohol grafted metal hydroxides. Chem Sci 3(6):2138–2146
82. Zhang Y, Zhang N, Tang Z-R, Xu Y-J (2012) Transforming CdS into an efficient visible light photocatalyst for selective oxidation of saturated primary C–H bonds under ambient conditions. Chem Sci 3(9):2812–2822
83. Yang M-Q, Zhang Y, Zhang N, Tang Z-R, Xu Y-J (2013) Visible-light-driven oxidation of primary C–H bonds over CdS with dual Co-catalysts graphene and TiO_2. Sci Rep 3:3314
84. Ohno T, Masaki Y, Hirayama S, Matsumura M (2001) TiO_2-photocatalyzed epoxidation of 1-decene by H_2O_2 under visible light. J Catal 204(1):163–168
85. Christopher P, Xin H, Linic S (2011) Visible-light-enhanced catalytic oxidation reactions on plasmonic silver nanostructures. Nat Chem 3(6):467–472
86. Marimuthu A, Zhang J, Linic S (2013) Tuning selectivity in propylene epoxidation by plasmon mediated photo-switching of Cu oxidation state. Science 339(6127):1590–1593
87. Zhang Y, Zhang N, Tang Z-R, Xu Y-J (2012) Graphene transforms wide band gap ZnS to VIS photocatalyst. -Macromolecular Photosensitizer. ACS Nano 6(11):9777–9789
88. Otsuki S, Nonaka T, Takashima N, Qian W, Ishihara A, Imai T, Kabe T (2000) Oxidative desulfurization of light gas oil and vacuum gas oil by oxidation and solvent extraction. Energ Fuel 14(6):1232–1239
89. Wojaczynska E, Wojaczynski J (2010) Enantioselective synthesis of sulfoxides: 2000–2009. Chem Rev 110(7):4303–4356
90. Bonesi SM, Fagnoni M, Albini A (2008) Biaryl formation involving carbon-based leaving groups: why not? Angew Chem Int Ed 47(52):10022–10025
91. Baciocchi E, Giacco TD, Elisei F, Gerini MF, Guerra M, Lapi A, Liberali P (2003) Electron transfer and singlet oxygen mechanisms in the photooxygenation of dibutyl sulfide and thioanisole in MeCN sensitized by N-methylquinolinium tetrafluoborate and

9, 10-dicyanoanthracene. The probable involvement of a thiadioxirane intermediate in electron transfer photooxygenations. J Am Chem Soc 125(52):16444–16454

92. Liang J, Gu C, Kacher M, Foote CS (1983) Chemistry of singlet oxygen. 45. Mechanism of the photooxidation of sulfides. J Am Chem Soc 105(14):4717–4721
93. Nahm K, Foote CS (1989) Trimethyl phosphite traps intermediates in the reaction of singlet oxygen (102) and diethyl sulfide. J Am Chem Soc 111(5):1909–1910
94. Nahm K, Li Y, Evanseck JD, Houk K, Foote CS (1993) Structures and energies of intermediates in the reactions of singlet oxygen with organic phosphines and sulfides. J Am Chem Soc 115(11):4879–4884
95. Lang X, Leow WR, Zhao J, Chen X (2015) Synergistic photocatalytic aerobic oxidation of sulfides and amines on TiO_2 under visible-light irradiation. Chem Sci 6(2):1075–1082
96. Company A, Sabenya G, González-Béjar M, Gómez L, Clémancey M, Blondin G, Jasniewski AJ, Puri M, Browne WR, Latour J-M (2014) Triggering the generation of an iron (IV)-oxo compound and its reactivity toward sulfides by RuII photocatalysis. J Am Chem Soc 136 (12):4624–4633
97. Gu X, Li X, Chai Y, Yang Q, Li P, Yao Y (2013) A simple metal-free catalytic sulfoxidation under visible light and air. Green Chem 15(2):357–361
98. Li X-H, Chen J-S, Wang X, Sun J, Antonietti M (2011) Metal-free activation of dioxygen by graphene/g-C_3N_4 nanocomposites: functional dyads for selective oxidation of saturated hydrocarbons. J Am Chem Soc 133(21):8074–8077
99. Liu S, Yang M-Q, Tang Z-R, Xu Y-J (2014) A nanotree-like CdS/ZnO nanocomposite with spatially branched hierarchical structure for photocatalytic fine-chemical synthesis. Nanoscale 6(13):7193–7198
100. Liu S, Chen Z, Zhang N, Tang Z-R, Xu Y-J (2013) An efficient self-assembly of CdS nanowires-reduced graphene oxide nanocomposites for selective reduction of nitro organics under visible light irradiation. J Phys Chem C 117(16):8251–8261
101. Yang M-Q, Pan X, Zhang N, Xu Y-J (2013) A facile one-step way to anchor noble metal (Au, Ag, Pd) nanoparticles on a reduced graphene oxide mat with catalytic activity for selective reduction of nitroaromatic compounds. CrystEngComm 15(34):6819–6828
102. Yang M-Q, Weng B, Xu Y-J (2013) Improving the visible light photoactivity of In_2S_3-graphene nanocomposite via a simple surface charge modification approach. Langmuir 29(33):10549–10558
103. Brezova V, Blažková A, Šurina I, Havlinova B (1997) Solvent effect on the photocatalytic reduction of 4-nitrophenol in titanium dioxide suspensions. J Photochem Photobiol A: Chem 107(1):233–237
104. Xu C, Yuan Y, Yuan R, Fu X (2013) Enhanced photocatalytic performances of TiO_2-graphene hybrids on nitro-aromatics reduction to amino-aromatics. RSC Adv 3 (39):18002–18008
105. Chen Z, Liu S, Yang M-Q, Xu Y-J (2013) Synthesis of uniform CdS nanospheres/graphene hybrid nanocomposites and their application as visible light photocatalyst for selective reduction of nitro organics in water. ACS Appl Mater Interfaces 5(10):4309–4319
106. Yuan L, Yang M-Q, Xu Y-J (2014) A low-temperature and one-step method for fabricating ZnIn2S4-GR nanocomposites with enhanced visible light photoactivity. J Mater Chem A 2 (35):14401–14412
107. Liu S, Yang M-Q, Xu Y-J (2014) Surface charge promotes the synthesis of large, flat structured graphene-(CdS nanowire)-TiO_2 nanocomposites as versatile visible light photocatalysts. J Mater Chem A 2(2):430–440
108. Han C, Chen Z, Zhang N, Colmenares JC, Xu Y-J (2015) Hierarchically CdS decorated 1D ZnO nanorods-2D graphene hybrids: low temperature synthesis and enhanced photocatalytic performance. Adv Funct Mater 25(2):221–229
109. Zhang N, Xu Y-J (2013) Aggregation- and leaching-resistant, reusable, and multifunctional Pd@CeO_2 as a robust nanocatalyst achieved by a hollow core-shell strategy. Chem Mater 25(9):1979–1988

110. Ohtani B, Tsuru S, Nishimoto S, Kagiya T, Izawa K (1990) Photocatalytic one-step syntheses of cyclic imino acids by aqueous semiconductor suspensions. J Org Chem 55(21):5551–5553
111. Ohtani B, Kawaguchi J, Kozawa M, Nakaoka Y, Nosaka Y, Nishimoto S (1995) Effect of platinum loading on the photocatalytic activity of cadmium(II) sulfide particles suspended in aqueous amino acid solutions. J Photochem Photobiol A: Chem 90(1):75–80
112. Ohtani B, Iwai K, Kominami H, Matsuura T, Kera Y, Nishimoto S-i (1995) Titanium (IV) oxide photocatalyst of ultra-high activity for selective N-cyclization of an amino acid in aqueous suspensions. Chem Phys Lett 242(3):315–319
113. Nishimoto S, Ohtani B, Yoshikawa T, Kagiya T (1983) Photocatalytic conversion of primary amines to secondary amines and cyclization of polymethylene-α, ω-diamines by an aqueous suspension of titanium (IV) oxide/platinum. J Am Chem Soc 105(24):7180–7182
114. Ohtani B, Osaki H, Nishimoto S, Kagiya T (1986) A novel photocatalytic process of amine N-alkylation by platinized semiconductor particles suspended in alcohols. J Am Chem Soc 108(2):308–310
115. Ohtani B, Goto Y, Nishimoto S-I, Inui T (1996) Photocatalytic transfer hydrogenation of Schiff bases with propan-2-ol by suspended semiconductor particles loaded with platinum deposits. J Chem Soc, Faraday Trans 92(21):4291–4295
116. Zhao J, Zheng Z, Bottle S, Chou A, Sarina S, Zhu H (2013) Highly efficient and selective photocatalytic hydroamination of alkynes by supported gold nanoparticles using visible light at ambient temperature. Chem Commun 49(26):2676–2678
117. Gonzalez-Bejar M, Peters K, Hallett-Tapley GL, Grenier M, Scaiano JC (2013) Rapid one-pot propargylamine synthesis by plasmon mediated catalysis with gold nanoparticles on ZnO under ambient conditions. Chem Commun 49(17):1732–1734
118. Caronna T, Gambarotti C, Palmisano L, Punta C, Recupero F (2003) Sunlight induced functionalisation of some heterocyclic bases in the presence of polycrystalline TiO_2. Chem Commun 18:2350–2351
119. Caronna T, Gambarotti C, Palmisano L, Punta C, Recupero F (2005) Sunlight-induced reactions of some heterocyclic bases with ethers in the presence of TiO_2: a green route for the synthesis of heterocyclic aldehydes. J Photochem Photobiol A: Chem 171(3):237–242
120. Rueping M, Zoller J, Fabry DC, Poscharny K, Koenigs RM, Weirich TE, Mayer J (2012) Light-mediated heterogeneous cross dehydrogenative coupling reactions: metal oxides as efficient, recyclable, photoredox catalysts in C–C bond forming reactions. Chem –Eur J 18 (12):3478–3481
121. Möhlmann L, Baar M, Rieß J, Antonietti M, Wang X, Blechert S (2012) Carbon nitride-catalyzed photoredox C–C bond formation with N-aryltetrahydroisoquinolines. Adv Synth Catal 354(10):1909–1913

Chapter 9
Synthetic Applications of Titanium(IV) Oxide-Based Photocatalysts

Kazuya Imamura and Hiroshi Kominami

Abstract In this chapter, several photocatalytic conversions of organic compounds over titanium(IV) oxide (TiO_2)-based photocatalyst are described. After short summary of photocatalytic conversions of organic compounds, mainly reduction, six topics are introduced. (1) Photocatalytic reduction of nitrobenzenes to anilines in water, green solvent, is reported. (2) In photocatalytic reduction of benzonitrile to benzylamine as a new photocatalytic reduction, palladium-loaded TiO_2 (Pd–TiO_2) exhibits excellent catalytic performance. (3) Pd–TiO_2 is also effective for photocatalytic hydrogenation of alkenes as new photocatalytic reduction. (4) Nitro compounds having other reducible groups are chemoselectively reduced to amino compounds over bare TiO_2 photocatalyst without reduction of the reducible groups. (5) In photocatalytic conversion of nitrobenzene in 2-propanol suspensions of TiO_2, aniline and acetone are simultaneously produced almost stoichiometrically. (6) Benzaldehyde and dihydrogen are simultaneously produced with a molar ratio of 1:1 from benzyl alcohol in acetonitrile suspensions of platinum-loaded TiO_2 under deaerated conditions. This reaction is introduced as example of high atom efficiency system.

Keywords Photocatalyst • Titanium(IV) oxide • Reduction • Chemoselective • Stoichiometry

9.1 Introduction

9.1.1 Advantages of TiO_2 for Organic Synthesis

In 1972, Fujishima and Honda succeeded in electro-photo-assisted water splitting using a titanium(IV) oxide (TiO_2) photoanode in combination with a platinum

---

K. Imamura
Department of Applied Chemistry, Faculty of Engineering, Oita University, Dannoharu 700, Oita 870-1192, Japan

H. Kominami (✉)
Department of Applied Chemistry, Faculty of Science and Engineering, Kinki University, Kowakae, Higashiosaka, Osaka 577-8502, Japan
e-mail: hiro@apch.kindai.ac.jp

J.C. Colmenares, Y.-J. Xu (eds.), *Heterogeneous Photocatalysis*, Green Chemistry and Sustainable Technology, DOI 10.1007/978-3-662-48719-8_9

(Pt) counter electrode in an electrolyte aqueous solution, a phenomenon known as the Fujishima–Honda effect [1]. During the 1980s and early 1990s, several papers about photocatalytic reactions of organic compounds began to appear, and information on the mechanism accumulated [2]. Application of photocatalysis of TiO_2 particles to organic synthesis is attractive because of the following reasons: (1) Since both oxidation and reduction occur on the surface of TiO_2 particles, reactions such as electrolytic organic synthesis are expected without an electrolyte and electrical wiring, both of which are requisites in conventional electrolyses. Furthermore, these redox reactions by electrons and positive holes leave no by-product that originates in the reductant and oxidant, whereas conventional redox reagents such as permanganate or lithium aluminum hydride leave manganese ion or aluminum hydroxide after oxidation and reduction, respectively. (2) A photocatalytic reaction proceeds at room temperature and under atmospheric pressure. (3) Since light is indispensable for a photocatalytic reaction, the reactions can be easily controlled by the intensity of light and finally can be stopped by turning the light source off. (4) By simple filtration or centrifugation, a TiO_2 photocatalyst is easily separated from the reaction mixture after the reaction and reused. (5) In addition, TiO_2 has been used for a long time as a common inorganic material such as a pigment and UV absorber because it is inexpensive and not toxic for humans and the environment. Since the abovementioned characteristics of photocatalysis satisfy almost all of the 12 proposed requirements for green chemistry [3], organic synthesis of various compounds using photocatalysis has recently been studied [2, 4–10].

9.1.2 Photocatalytic Reductive Conversions

Most of the applications of TiO_2 photocatalysis to organic synthesis are oxidation reactions such as oxidative dehydrogenation and oxygenation. Dehydrogenation reactions, such as conversion of a hydroxy group to a carbonyl group, have been reported by several researchers because aldehydes or ketones formed are precursors in the synthesis of valuable organic compounds such as drugs, vitamins, or fragrances. In these reactions, a substrate is oxidized with positive holes and electrons are trapped by dioxygen (O_2). Applications of photocatalytic reduction have been less frequently reported, whereas total or partial oxidation of organic compounds has been extensively studied. When photocatalytic reduction is applied, removal of O_2 in the system is necessary to improve reduction efficiency because O_2 competes kinetically with substrates in trapping photogenerated conduction band (CB) electrons. Active oxygen species generated by trapping electrons oxidize the substrate and/or products. Therefore, it is difficult to control the photocatalytic reduction system. In the 1990s, an electron-trap reagent in photocatalysis and reduction of mineral ion were reported. Methyl viologen dication has a much lower reduction potential than most organic substrates by virtue of its double positive charge. Muzyka and Fox used methyl viologen dication as an electron trap in heterogeneous photocatalysis of TiO_2 under deaerated conditions [11]. Reductive detoxification of ions such as nitrogen oxides has been reported, especially since 2000. In 1998, Li and Wasgestian reported photocatalytic reduction of nitrate ion (NO_3^-) in an aqueous suspension of bare TiO_2 [12]. After this report, many researchers have studied reduction of NO_3^-. However, reduction products of NO_3^- were mainly ammonia (NH_3) or nitrite ion (NO_2^-) in all of those studies. From the point of view of eco-friendly production of chemicals, NO_3^- should be selectively reduced to nontoxic dinitrogen (N_2). In our laboratory, NO_2^- was photocatalytically reduced to N_2 in an aqueous suspension of two kinds of TiO_2 particles loaded with palladium and silver (Pd–TiO_2 and Ag–TiO_2) in the presence of sodium oxalate as a hole scavenger [13]. Photocatalytic reduction of organic compounds is more difficult than reduction of ions because most of the organic substrates are decomposed by positive holes. Therefore, oxidation of a reduction substrate and/or reoxidation of products must be avoided. As photocatalytic reduction of organic compounds, reduction of a carbonyl group [14–17] and a nitro group [18–25] has been reported. One of the major photocatalytic reductions for organic synthesis with TiO_2 is reduction of nitrobenzenes. Primary alcohols such as methanol or ethanol have been used as both a solvent and a sacrificial reagent for photocatalytic reduction of nitrobenzene to aniline. In this case, yield of aniline decreased with a long reaction time because aldehydes formed as the oxidized species of primary alcohols react with aniline or intermediates (such as nitroso compounds and hydroxylamines) [26]. In addition, reoxidation of aniline that has been formed occurs. As mentioned above, photocatalytic reduction for organic synthesis is difficult to control, and thus there have been few reports of a photocatalytic reduction system such as reduction of nitrobenzene. Here, various photocatalytic conversions, mainly reduction, are described.

9.2 Photocatalytic Reduction of Nitrobenzenes in Aqueous Suspensions of TiO_2 in the Presence of “Greener” Hole Scavengers

Photocatalytic reduction of nitrobenzenes has been well studied in photocatalytic reductions because reduction (hydrogenation) of nitrobenzenes to corresponding aminobenzenes is an important reaction in industrial chemistry. This reduction has been industrially achieved by hydrogenation over a metal (thermo)catalyst such as nickel (Ni) or copper (Cu) under high pressure of dihydrogen (H_2) and high temperature. Since a photocatalytic reaction proceeds under mild conditions, reduction of nitrobenzenes by photocatalysts has attracted attention. Also from the point of view of eco-friendly production of chemicals, formation of aldehydes is unfavorable and a “greener” sacrificial reagent that is converted to a nontoxic compound is preferable. The use of a large excess of a hole scavenger gives a large amount of wastes containing oxidative products of the hole scavenger, which often causes problem for the photocatalytic system. Formic acid (FA) is "greener" sacrificial reagents because they are easily oxidized and converted into carbon dioxide (CO_2), which is separated from the solvent under acidic conditions [27, 28]. It is obvious that water is the "greenest" among all solvents.

9.2.1 Photocatalytic Reduction of m-*Nitrobenzenesulfonic Acid in the Presence of Formic Acid Under Deaerated Conditions*

Figure 9.1 shows photocatalytic reduction of *m*-nitrobenzenesulfonic acid (*m*-NBS) in an aqueous suspension of TiO_2 powder in the presence of FA under deaerated conditions. Reduction of a nitro group to an amino group consists of several steps as shown in Eq. 9.1:

$$R - NO_2 \rightarrow R - NO \rightarrow R - NH(OH) \rightarrow R - NH_2 \qquad (9.1)$$

m-Nitrosobenzenesulfonic acid (*m*-NSBS) was not detected as an intermediate with high-performance liquid chromatography, while a small amount of *m*-hydroxylaminesulfonic acid (*m*-PHAS) was detected as well as the final reduced product, *m*-aminobenzenesulfonic acid (*m*-ABS). The time course of summation of the amounts of *m*-NBS, *m*-PHAS, and *m*-ABS is also shown in Fig. 9.1, indicating that a satisfactory material balance was kept during the course of reaction. The amount of *m*-NBS monotonously decreased with photoirradiation time, and *m*-NBS was almost completely consumed by the photoirradiation for 60 min. A small amount of *m*-PHAS was formed in the early stage, and then *m*-PHAS was gradually

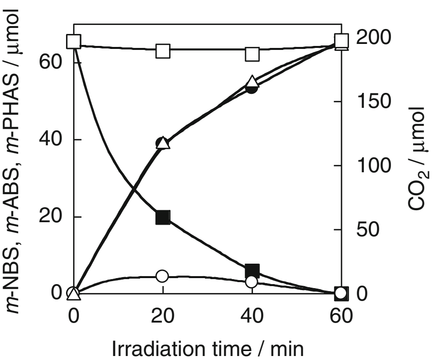

Fig. 9.1 Time courses of *m*-NBS (*closed squares*), *m*-ABS (*closed circles*), *m*-PHAS (*open circles*), and CO_2 (*open triangles*) and summation of *m*-NBS, *m*-ABS, and *m*-PHAS (*open squares*) in an aqueous suspension of TiO_2 (50 mg) in the presence of FA (200 µmol) as a hole scavenger under deaerated conditions (Reproduced from Ref. [28] with permission from the PCCP Owner Societies)

consumed with prolonged irradiation time. The amount of *m*-ABS increased with irradiation time, and *m*-ABS was obtained almost quantitatively (>99 % yield) after photoirradiation for 60 min, indicating that no side reaction(s) of *m*-NBS and/or intermediates occurred in the present system.

The high yield of *m*-ABS also indicates that neither reaction of the benzene ring nor reoxidation of the amino group of *m*-ABS occurred in the present system. Behavior of *m*-PHAS intermediate in the photocatalytic reduction of *m*-NBS in the presence of FA suggests that the rate of *m*-PHAS formation was slightly larger than the rate of *m*-PHAS reduction under the present conditions.

The time course of CO_2 formation is also shown in Fig. 9.1. As the oxidized product, CO_2 could be liberated in the gas phase because of the acidic condition of this reaction system (pH = 1.84), and 195 μmol of CO_2 was formed by photoirradiation for 60 min. As shown in Eq. 9.2, FA scavenges two holes and, therefore, two photogenerated electrons can be used for reduction of *m*-NBS:

$$\mathrm{HCOOH} + 2(\mathrm{e}^- - \mathrm{h}^+) \rightarrow \mathrm{CO_2} + 2\mathrm{H}^+ + 2\mathrm{e}^- \qquad (9.2)$$

Assuming that all of the CO_2 originated from FA, efficiency of FA utilization as a hole scavenger (EUH) was calculated by using Eq. 9.3, and the time course of EUH is shown in Fig. 9.2:

$$\mathrm{EUH} = (4n_{m-\mathrm{PHAS}} + 6n_{m-\mathrm{ABS}})/2n_{\mathrm{CO2}} \times 100, \qquad (9.3)$$

where $n_{m\text{-PHAS}}$, $n_{m\text{-ABS}}$, and n_{CO2} are the amounts of *m*-PHAS, *m*-ABS, and CO_2 formed, respectively. One hundred percent of EUH means that redox balance was preserved in the formation of *m*-PHAS, *m*-ABS, and CO_2 in the photocatalytic reaction. The high level of EUH continuing for 60 min indicates that FA worked effectively as a hole scavenger in the photocatalytic reduction of *m*-NBS to *m*-ABS. Therefore, stoichiometry of the photocatalytic reaction in the presence of FA is shown in Eq. 9.4.

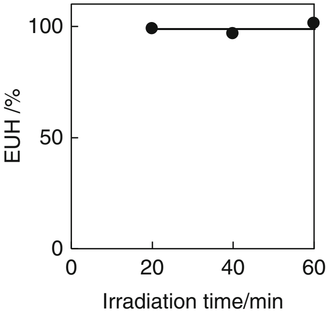

Fig. 9.2 Time course of EUH in photocatalytic reduction of *m*-NBS to *m*-ABS. Data shown in Fig. 9.1 were used for calculation (Reproduced from Ref. [28] with permission from the PCCP Owner Societies)

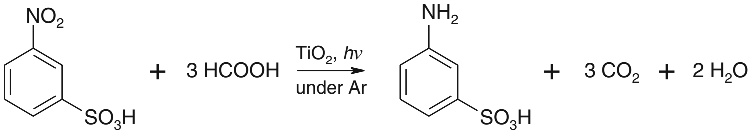

(9.4)

After 60-min photoirradiation, FA was almost completely converted to CO_2 and *m*-ABS was obtained with >99 % yield. Therefore, only *m*-ABS was present in the aqueous phase after 60 min. Since it is not necessary to remove the hole scavenger (FA), carbonate ion generated by oxidation of FA, unreacted substrate (*m*-NBS), intermediates (*m*-NSBS and *m*-PHAS), and by-product(s), it can be concluded that this photoreaction system is a "green" reduction process.

9.2.2 Effect of Physical Properties of TiO_2 Samples on Photocatalytic Reduction of m-*NBS*

In order to determine the effect of *m*-NBS adsorption on the TiO_2 surface on yield of *m*-ABS, photocatalytic reduction of *m*-NBS to *m*-ABS using TiO_2 samples with various specific surface areas was examined. Preparation of TiO_2 samples consists of two steps, i.e., synthesis of anatase-type TiO_2 by the HyCOM method [29] and post-calcination of the product at various temperatures up to 1273 K. Highly crystallized HyCOM-TiO_2 exhibited high thermal stability. Therefore, the physical properties could be controlled in a wide range by changing the calcination temperature. Figure 9.3 shows the effect of specific surface area of HyCOM-TiO_2 samples on yields of *m*-ABS in aqueous suspensions of various HyCOM-TiO_2 samples (50 mg) under deaerated conditions after 30 min of photoirradiation. A linear correlation between them was observed, indicating that the specific surface area of TiO_2 is one of the decisive factors determining photocatalytic activity.

Figure 9.4 shows the effect of specific surface area of HyCOM-TiO_2 samples on the amount of *m*-NBS adsorbed on TiO_2 (100 mg) under the same conditions as those used for the photocatalytic reaction. A linear correlation between them was observed, indicating that density of *m*-NBS adsorbed on the TiO_2 surface, i.e., the amount of *m*-NBS adsorbed per unit surface area of HyCOM-TiO_2 samples, was almost constant regardless of total surface area of TiO_2. Figure 9.5 shows the correlation between amount of *m*-NBS adsorbed on HyCOM-TiO_2 samples and yield of *m*-ABS after 30-min photoirradiation. An almost linear correlation between them was observed. Therefore, a large surface area of TiO_2 causing a large amount of adsorption of *m*-NBS is an important factor for high yield of *m*-ABS in photocatalytic reduction of *m*-NBS. However, the use of commercial TiO_2 (Ishihara, ST-01) having a surface area of *ca*. 300 $m^2\ g^{-1}$ resulted in low yield (36.0 μmol) and low mass balance, suggesting that a very large surface area negatively affects photocatalytic reduction of *m*-NBS. Further photoirradiation (60 min) to the ST-01 system resulted in an increase in *m*-ABS yield (53.4 μmol);

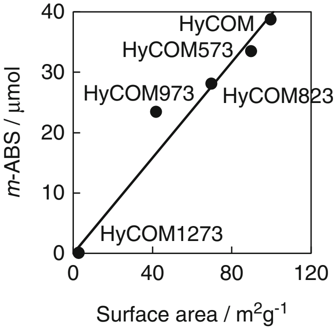

Fig. 9.3 Effect of specific surface area of HyCOM-TiO_2 samples (50 mg) on *m*-ABS yields in aqueous suspensions containing FA (200 µmol) under deaerated conditions after 30 min of photoirradiation. Values after "HyCOM" indicate temperatures of calcination of as-synthesized HyCOM-TiO_2 (Reproduced from Ref. [28] with permission from the PCCP Owner Societies)

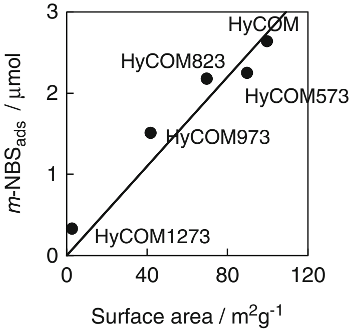

Fig. 9.4 Effect of specific surface area of HyCOM-TiO_2 samples (100 mg) on amount of *m*-NBS (5 µmol) adsorbed on the surface. Conditions other than the amounts of TiO_2 samples and *m*-NBS were the same as those for the photocatalytic reaction shown in Fig. 9.3 (Reproduced from Ref. [28] with permission from the PCCP Owner Societies)

Fig. 9.5 Correlation between amount of *m*-NBS adsorbed on TiO_2 surface and *m*-ABS yield after 30 min of photoirradiation (Reproduced from Ref. [28] with permission from the PCCP Owner Societies)

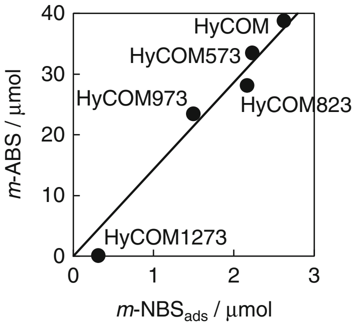

however, the amount of remaining *m*-NBS was only 1.2 μmol, suggesting that *m*-NBS or an intermediate(s) is strongly adsorbed on the surface of ST-01.

9.2.3 *Photocatalytic Reduction of* m-*NBS in the Presence of FA Under Air*

Figure 9.6 shows the time courses of the amounts of *m*-NBS remaining and the reduced products (*m*-PHAS and *m*-ABS) in the photocatalytic reaction under an artificial air condition (O_2:$N_2 = 1$:4). The amount of *m*-NBS monotonously decreased with time, and *m*-NBS was almost completely consumed after photoirradiation for 60 min as well as in the case of absence of O_2. An almost quantitative yield (99 %) of *m*-ABS was obtained after 60-min photoirradiation. It should be noted that photocatalytic reduction of *m*-NBS to *m*-ABS in the presence of FA proceeded even in the presence of O_2. Since O_2 generally competes with the substrate to be reduced in scavenging e^- and causes side reaction(s) such as oxidation of the substrate, the presence of O_2 must be avoided for effective and selective reduction of the substrate by e^-. Almost quantitative formation of *m*-ABS also shows that neither reaction of the benzene ring nor reoxidation of the amino group of *m*-ABS occurred even in the presence of O_2. The fact that photocatalytic reduction of *m*-NBS to *m*-ABS proceeded almost quantitatively under air is significant for practical use of photocatalytic reduction because no gas-phase control is required. The amount of *m*-PHAS formed in the early stage was slightly larger than that in the case under deaerated conditions, and *m*-PHAS was gradually consumed by extension of photoirradiation time. These results indicate that the rate of reduction of *m*-PHAS to *m*-ABS was smaller than that under deaerated conditions since O_2 competed with *m*-PHAS. The time course of summation of the amounts of *m*-NBS, *m*-PHAS, and *m*-ABS is also shown in Fig. 9.6. The summation was almost constant during the reaction for 60 min as was the case during reaction under deaerated conditions (Fig. 9.1). The time course of CO_2 formation is also shown in Fig. 9.6. In the presence of O_2, fruitless consumption of FA may occur in addition to consumption of FA as a sacrifice reagent for *m*-NBS reduction. Along with photoirradiation time, CO_2 was evolved and 202 μmol of CO_2 was formed after 60 min. This value was only slightly larger than that of stoichiometry in the reductive formation of *m*-ABS (195 μmol = 3 × 65 μmol) shown in Eq. 9.4, indicating that FA was used almost selectively and effectively as the sacrifice reagent for *m*-NBS reduction even in the presence of O_2.

Figure 9.7 shows the time course of EUH in the reduction of *m*-NBS to *m*-ABS under aerated conditions. The value of EUH at 10 min was 93 % and the value of EUH did not decrease with prolongation of reaction time (with increase in *m*-ABS formation). The high EUH as well as the high yield of *m*-ABS under air is significant for practical use of photocatalytic reduction. There are several reasons for the high value of EUH in *m*-NBS reduction in the presence of O_2. The one

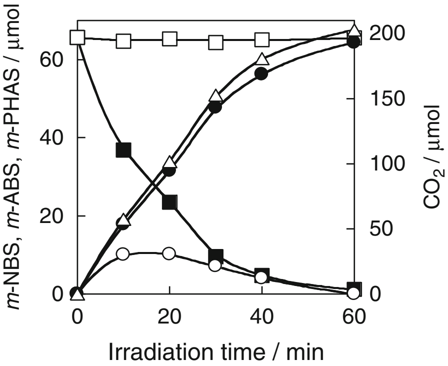

Fig. 9.6 Time courses of *m*-NBS (*closed squares*), *m*-ABS (*closed circles*), *m*-PHAS (*open circles*), and CO_2 (*open triangles*) and summation of *m*-NBS, *m*-ABS, and *m*-PHAS (*open squares*) in an aqueous suspension of TiO_2 (50 mg) containing FA (200 µmol) as a hole scavenger under air (Reproduced from Ref. [28] with permission from the PCCP Owner Societies)

Fig. 9.7 Time course of EUH in photocatalytic reduction of *m*-NBS to *m*-ABS. Data shown in Fig. 9.6 were used for calculation (Reproduced from Ref. [28] with permission from the PCCP Owner Societies)

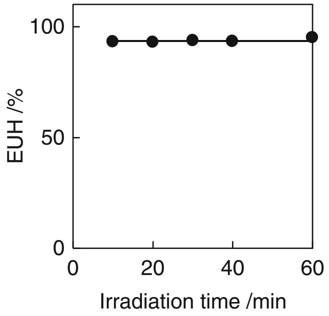

reason is that FA works effectively as a hole scavenger preventing the oxidation of *m*-NBS and the reoxidation of *m*-ABS. Other reasons are that *m*-NBS is more reducible than O_2 and protons and that positively charged products having a $-NH_3^+$ group are eliminated from the TiO_2 surface in acidic conditions.

9.3 Photocatalytic Reduction of Benzonitrile

As applications of photocatalytic reduction to organic synthesis with TiO_2, reduction of a carbonyl group [14–17] and a nitro group [18–25] have been reported. On the other hand, loading of an appropriate metal co-catalyst enables reduction of substrates that cannot be reduced by bare TiO_2. The purpose of a co-catalyst is to decrease activation energy. For example, Pt-loaded TiO_2 reduces protons (H^+) to H_2, whereas it is impossible to reduce H^+ with bare TiO_2. Therefore, various new photocatalytic organic syntheses using a TiO_2 photocatalyst can be achieved if an appropriate co-catalyst is loaded.

Recently, photocatalytic reduction of benzonitrile (PhCN) to benzylamine ($BnNH_2$) using oxalic acid (OA) as a hole scavenger has been achieved as a new photocatalytic reduction system (Eq. 9.5) [30]. Primary amines produced by reduction (hydrogenation) of corresponding nitriles are important compounds as intermediates of chemical products, and reduction of a cyano group is an important reaction in fine chemicals [31–34]. This reduction has been achieved by catalytic hydrogenation using a metal catalyst such as Ni, cobalt, ruthenium (Ru), or palladium (Pd) supported on a suitable material. Since these reactions require high pressure of H_2 and high temperature, more mild conditions are favored. In addition, it is difficult to produce primary amines selectively by catalytic hydrogenation of corresponding nitriles because there are many reaction pathways in hydrogenation of nitriles [33].

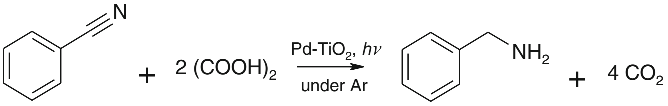

(9.5)

9.3.1 Effect of Metal Loaded

Figure 9.8 shows effects of metal co-catalysts (0.3 wt%) on the production of $BnNH_2$, H_2, and CO_2 in the photocatalytic reduction of PhCN after photoirradiation for 60 min. When bare (metal-free) TiO_2 was used as the photocatalyst, only a small amount of CO_2 was evolved and the color of TiO_2 became blue, indicating that Ti^{4+} in TiO_2 was reduced to Ti^{3+}. These results showed that positive holes oxidized oxalic acid to give CO_2, while photogenerated electrons in the conduction band (CB) of TiO_2 did not reduce PhCN. Almost the same results were obtained when gold (Au), silver (Ag), or Cu was loaded on TiO_2 as a co-catalyst. Relatively large amounts of H_2 and CO_2 were evolved when Pt was loaded on TiO_2.

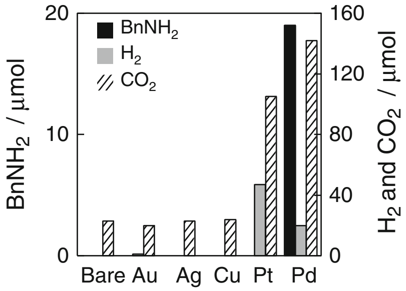

Fig. 9.8 Effects of metals loaded on TiO_2 (MT-150A, Tayca) on photocatalytic reduction of PhCN (50 µmol) to $BnNH_2$ in 0.1 mol dm^{-3} aqueous hydrochloric acid suspensions (5 cm^3) under deaerated conditions in the presence of oxalic acid (200 µmol) for 60-min photoirradiation (Reproduced from Ref. [30] with permission from the Royal Society of Chemistry)

However, no $BnNH_2$ was produced. The ratio of H_2 and CO_2 evolved was about 1:2, indicating that only fruitless decomposition of oxalic acid occurred over Pt-loaded TiO_2 as shown in Eq. 9.6:

$$(COOH)_2 \rightarrow H_2 + 2CO_2 \tag{9.6}$$

In contrast to these metal-loaded TiO_2 samples, $BnNH_2$ was obtained when Pd-loaded TiO_2 (Pd–TiO_2) was used as a photocatalyst. As far as we know, this is the first report on photocatalytic reduction (hydrogenation) of a cyano group (C≡N triple bond) to primary amine. Since the reduction potential of PhCN is believed to be much higher than the potential of the CB of TiO_2, formation of $BnNH_2$ indicates that the applicability of photocatalytic reduction is not limited by the CB position of semiconductor photocatalysts. Supported Pd nanoparticles are often used for catalytic hydrogenation of a cyano group with H_2 as a hydrogen source, in which an activated hydrogen species (H–Pd) formed by dissociative adsorption of H_2 on the surface of Pd reacts with the cyano group [35]. Similarly, H–Pd formed in the photocatalytic process probably reacts with the cyano group under the present conditions.

9.3.2 *Effect of Solvents and Hole Scavengers*

Figure 9.9 shows effects of solvents and hole scavengers on the photocatalytic reduction of PhCN to $BnNH_2$. The highest $BnNH_2$ yield was obtained when

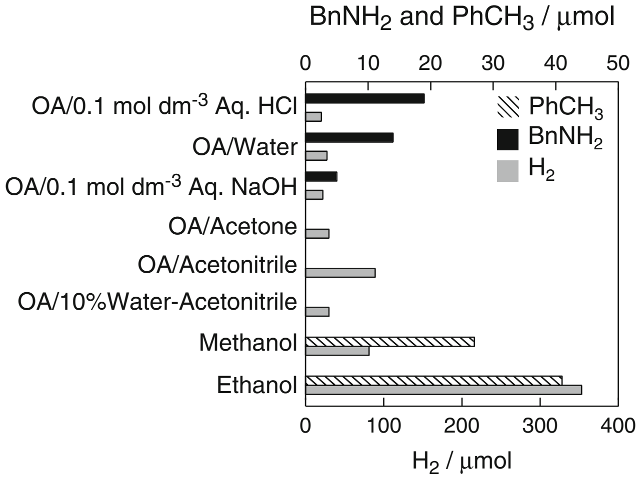

Fig. 9.9 Effects of solvents and hole scavengers on photocatalytic reduction of PhCN to $BnNH_2$ over Pd–TiO_2 for 60-min irradiation (Reproduced from Ref. [30] with permission from the Royal Society of Chemistry)

hydrochloric acid (HCl) solution and water were used. The yield drastically decreased in sodium hydroxide (NaOH) solution. As shown in Eq. 9.5, four hydrogen atoms (protons) are incorporated into $BnNH_2$. These protons were provided by oxalic acid in an acidic condition. In basic conditions, protons were consumed by the base, resulting in a low yield of $BnNH_2$. These results indicate that the concentration of H^+ is one of the important factors controlling the yield of $BnNH_2$. A small amount of toluene ($PhCH_3$) was formed as a by-product; however, quantitative analysis could not be performed because of the very low solubility of $PhCH_3$ in water. When acetone and acetonitrile were used as aprotic solvents instead of water, no reduction of PhCN occurred and a small amount of H_2 was evolved. These results indicate that only splitting of oxalic acid (Eq. 9.6) occurred in acetone and acetonitrile solvents. It has often been reported that addition of water to acetonitrile improved the reaction rates [36, 37]. However, no effect of water addition was observed in this system. Alcohols, especially methanol and ethanol, have been used as solvents and hole scavengers in photocatalytic reduction [2, 4, 5]. In alcoholic systems, no $BnNH_2$ was produced, while $PhCH_3$ was formed as the reduced product of PhCN together with a large amount of H_2, indicating that dehydrogenation of alcohols vigorously occurred and deep hydrogenation of PhCN induced elimination of nitrogen atoms.

There are several pathways involving the generation of $PhCH_3$ in catalytic hydrogenation of PhCN [35]. Sugano et al. reported that benzonitriles were converted to corresponding toluenes and triethylamine over a Pd–TiO_2 photocatalyst in mixtures of ethanol and hexane, producing no $BnNH_2$ [38]. They proposed that, when alcohols are used as hole scavengers, $BnNH_2$ reacts with aldehydes and thus formed imines intermediates are hydrogenated to amines. Hydrogenolysis of amines produces $PhCH_3$. In this study, aldehydes or other reactive species were not formed in reaction mixtures because the oxalic acid used as a hole scavenger is converted to CO_2 and removed from the liquid phase under an acidic condition. Acidic conditions have two roles: maintenance of a sufficient proton concentration and CO_2 isolation. From the results shown in Fig. 9.9, it is clear that the combination of acidic conditions and oxalic acid as a hole scavenger is essential for reduction of PhCN to $BnNH_2$.

9.3.3 Time Course of Photocatalytic Reduction of PhCN over Pd–TiO_2 in Water Containing Oxalic Acid as Hole Scavenger

Figure 9.10 shows time courses of photocatalytic reduction of PhCN. The amount of PhCN monotonously decreased along with photoirradiation time, and PhCN was almost completely consumed after 30 min, while $BnNH_2$ was obtained in 74 % yield. Assuming that all of the CO_2 originated in oxalic acid, the efficiency of

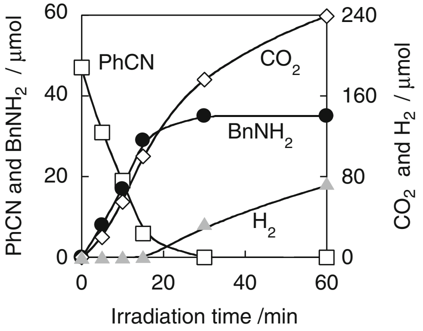

Fig. 9.10 Time courses of amounts of PhCN remaining (*squares*), $BnNH_2$ formed (*circles*), CO_2 evolved (*diamonds*), and H_2 evolved (*triangles*) in 0.1 mol dm^{-3} aqueous HCl suspensions of Pd–TiO_2 in the presence of oxalic acid (Reproduced from Ref. [30] with permission from the Royal Society of Chemistry)

utilizing oxalic acid as a hole scavenger (EUH) was calculated to be 80 % by using Eq. 9.7:

$$\mathrm{EUH} = \frac{4 \times \text{Amount of BnNH}_2 \text{ formed}}{\text{Amount of CO}_2 \text{ evolved}} \times 100 \tag{9.7}$$

The value of EUH indicates that the electrons donated by oxidization of oxalic acid were efficiently used for reduction of PhCN to $BnNH_2$. After consumption of PhCN, H_2 was formed, indicating that reduction of PhCN and protons competed and that the Pd co-catalyst predominantly reduced PhCN. We also noted that the $BnNH_2$ formed was not converted to other compounds under excessive photoirradiation. In photocatalytic reduction of nitrobenzenes to aminobenzenes in acidic aqueous solutions, aminobenzenes were not reoxidized under excessive photoirradiation because the protonated forms of aminobenzenes were eliminated from the protonated surface of TiO_2 [27, 28]. Therefore, in the present system, $BnNH_2$ was also protonated in the acidic aqueous suspension, and the protonated form was eliminated from the TiO_2 surface, escaping from further conversion.

9.4 Photocatalytic Hydrogenation of Alkenes to Alkanes in Alcoholic Suspensions of Palladium-Loaded Titanium(IV) Oxide Without the Use of Hydrogen Gas

In Sect. 9.3, we reported photocatalytic reduction (hydrogenation) of a cyano group (benzonitrile) to an amino group (benzylamine) using Pd–TiO_2 even though the reduction potential of benzonitrile is higher than the potential of the CB of TiO_2, indicating that the applicability of photocatalytic reduction is not limited by the CB position of semiconductor photocatalysts. Therefore, a new photocatalytic reduction can be developed if metal co-catalysts are introduced on photocatalysts.

Hydrogenation is one of the important processes in petroleum chemistry, industrial chemistry, food chemistry, and fine chemistry [39, 40]. However, these (thermo)catalytic systems require a high temperature and reducing reagents such as H_2 gas. Hydrogenation of alkenes to alkanes would be more attractive if the reaction occurs without the use of H_2 at room temperature. In this section, we explored a new photocatalytic reduction system other than reduction of nitrobenzenes, carbonyl compounds, and nitriles, and we found that photocatalytic hydrogenation of a C=C double bond to a C–C bond occurred in alcoholic suspensions of TiO_2 with metal co-catalysts at room temperature without the use of H_2. Here we briefly report (1) the effect of metal co-catalysts on hydrogenation of styrene to ethylbenzene as a model reaction of hydrogenation of a C=C double bond to a C–C bond, (2) the stoichiometry and characteristics of the reaction, and (3) the applicability of the photocatalytic hydrogenation of alkenes to alkanes [41].

9.4.1 *Effect of Metal Co-catalyst on Photocatalytic Hydrogenation of Styrene*

Figure 9.11 shows effects of metal co-catalysts on production of ethylbenzene in photocatalytic hydrogenation of styrene in methanol solutions after 30-min photoirradiation. When bare TiO_2 was used as the photocatalyst, no reaction of styrene occurred and the color of TiO_2 became blue, indicating that Ti^{4+} in TiO_2 was reduced to Ti^{3+} by photogenerated electrons. This result means that positive holes oxidized methanol, while photogenerated electrons in the CB of TiO_2 did not reduce styrene. Almost the same results were obtained when Au, Ag, Cu, and Ru were loaded on TiO_2 as co-catalysts. These results (no hydrogenation of styrene) can be explained by the reduction potential of styrene being more negative than that of the CB of TiO_2. Since the half-wave reduction potential of the system was reported to be −2.4 V versus SHE, a high voltage is required for electrochemical reduction (hydrogenation) of styrene. In contrast to these metal-loaded TiO_2

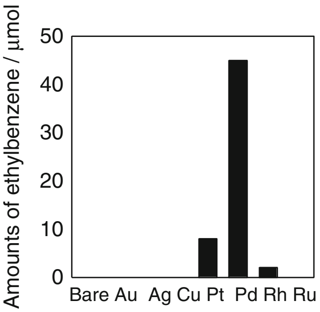

Fig. 9.11 Effects of metals (0.1 wt%) loaded on the TiO_2 surface on photocatalytic reduction of styrene (45 μmol) to ethylbenzene in methanolic suspensions (5 cm^3) under deaerated conditions for 30-min photoirradiation at 298 K (Reproduced from Ref. [41] with permission from the Royal Society of Chemistry)

samples, when Pd-, Pt-, and rhodium-loaded TiO_2 photocatalysts (Pd–TiO_2, Pt–TiO_2, and Rh–TiO_2) were used, styrene was hydrogenated and ethylbenzene was obtained without the use of H_2. Pd–TiO_2 showed a much higher ethylbenzene yield than those of the other photocatalysts, and styrene was hydrogenated to ethylbenzene almost stoichiometrically after 30 min. Since supported Pd nanoparticles are often used for catalytic hydrogenation of a C=C double bond with H_2 as a hydrogen source, it could be considered that ethylbenzene was formed thermocatalytically. However, two blank reactions at 298 K without light irradiation and without Pd–TiO_2 produced no ethylbenzene, indicating that ethylbenzene was formed photocatalytically. As far as we know, this is the first report on hydrogenation of a C=C double bond by using a TiO_2 photocatalyst.

9.4.2 Photocatalytic Hydrogenation of Styrene to Ethylbenzene over Pd–TiO_2

Figure 9.12a shows time courses of styrene remaining, ethylbenzene formed, and acetone formed in 2-propanol suspensions of 0.1 wt% Pd–TiO_2 without the use of H_2. Just after photoirradiation, styrene monotonously decreased, while ethylbenzene and acetone were formed as the reduction (hydrogenation) product of styrene and the oxidation product of 2-propanol, respectively. After 25-min photoirradiation, styrene was almost completely consumed and ethylbenzene was obtained in a high yield (98 %). Styrene was hydrogenated as follows. Methanol was oxidized with two positive holes to form formaldehyde and protons (H^+). Thus, formed H^+ were reduced with electrons in the CB to form active hydrogen species on metal co-catalyst. Styrene was reduced with the H species to ethylbenzene. It should be noted that H_2 was formed only after consumption of styrene. Formation of H_2 means that H^+ in the reaction system were reduced. Therefore, reduction (hydrogenation) of styrene occurred selectively under the present conditions. Material balance (MB) calculated by using Eq. 9.8 is shown in Fig. 9.12b:

$$\mathrm{MB} = \frac{n(\text{styrene}) + n(\text{ethylbenzene})}{n_0(\text{styrene})}, \tag{9.8}$$

where n(styrene) and n(ethylbenzene) are the amounts of styrene and ethylbenzene after photoirradiation, respectively, and n_0(styrene) is the initial amount of styrene. The high yield of ethylbenzene and the value of MB close to unity indicate that only hydrogenation of styrene to ethylbenzene occurred, i.e., neither polymerization of styrene, cracking of ethylbenzene, nor hydrogenation of the aromatic ring occurred. To evaluate the redox property and competitive reduction of styrene and H^+ by

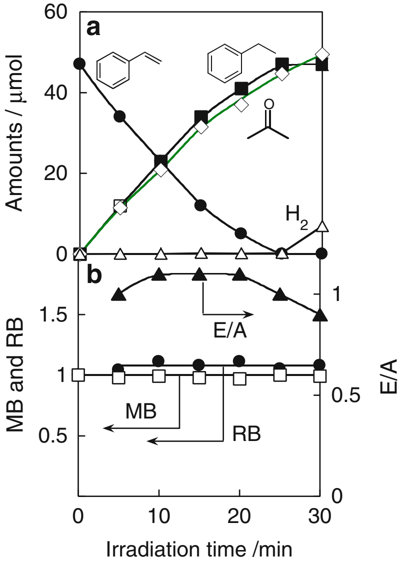

Fig. 9.12 Time courses of (**a**) amounts of styrene remaining (*closed circles*), ethylbenzene formed (*closed squares*), acetone formed (*open diamonds*), and H_2 (*open triangles*) and (**b**) MB (*left axis*, *open squares*), RB (*left axis*, *closed circles*), and E/A (*right axis*, *closed triangles*) in 2-propanolic suspensions of 0.1 wt% Pd–TiO_2 (50 mg) under deaerated condition at 298 K (Reproduced from Ref. [41] with permission from the Royal Society of Chemistry)

photogenerated electrons, new indicators, i.e., redox balance (RB) and selectivity for ethylbenzene production (ethylbenzene/acetone, E/A), were calculated from Eqs. 9.9 to 9.10, respectively, and are shown in Fig. 9.12b:

$$\mathrm{RB} = \frac{2 \times \text{amount of ethylbenzene} + 2 \times \text{amount of } \mathrm{H_2}}{2 \times \text{amount of acetone}} \tag{9.9}$$

$$\mathrm{E/A} = \frac{2 \times \text{amount of ethylbenzene}}{2 \times \text{amount of acetone}} \tag{9.10}$$

The value of RB close to unity was preserved in all of the reaction, indicating that electrons were used only for reduction of styrene (to ethylbenzene) and H^+ (to H_2) and that holes were consumed only for oxidation of 2-propanol (to acetone). Therefore, only a desired main reaction (Eq. 9.11) and a side reaction (Eq. 9.12) occurred in the present photocatalytic reaction system. Therefore, we can conclude that photocatalytic hydrogenation of styrene to ethylbenzene along with 2-propanol oxidation to acetone occurred over Pd–TiO_2 without the use of H_2. However, the value of E/A slightly higher than unity suggests that a small amount of acetone was consumed by a photocatalytic reaction.

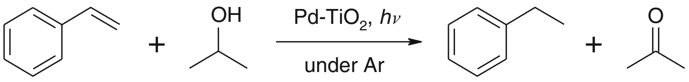

(9.11)

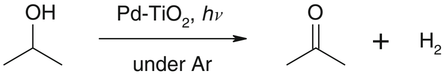

(9.12)

9.4.3 Applicability of the Photocatalytic Hydrogenation of Alkenes

Applicability of the photocatalytic hydrogenation of alkenes to alkanes was investigated using various aromatic or aliphatic alkenes, and Table 9.1 shows results of the photocatalytic hydrogenation in methanolic suspensions of Pd–TiO_2 particles under deaerated conditions. Hydrogenation reaction proceeded in all cases, and high yield was obtained.

In thermocatalytic process, H_2 is dissociatively adsorbed on Pd surface, and thus formed H species (as H–Pd) are incorporated into a C=C double bond. Based on the mechanism of thermocatalytic hydrogenation over Pd catalyst, the mechanism of photocatalytic hydrogenation without the use of H_2 can be considered as follows: (1) H^+ are reduced by photogenerated electrons on Pd surface to give active H species (probably as H–Pd) and (2) this active H species on Pd are inserted into a C=C double bond, resulting in ethylbenzene formation. The active species formed in thermocatalytic and photocatalytic reactions would be essentially same because H_2 was evolved after consumption of styrene (Fig. 9.12a). It is apparent that H species photocatalytically formed on Pd are very active for hydrogenation of alkenes.

Table 9.1 Photocatalytic hydrogenation of various alkenes to alkanes in methanolic suspensions of 0.1 wt% Pd–TiO_2 for 30-min photoirradiation (Reproduced from Ref. [41] with permission from the Royal Society of Chemistry)

Entries	Substances	Products	Yield
1	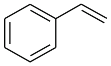	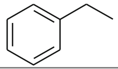	>99
2[a]	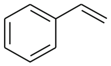	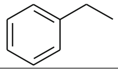	98
3	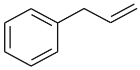	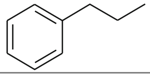	98
4	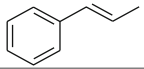	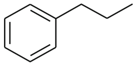	92
5	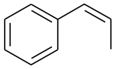	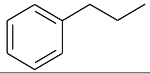	>99
6	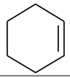	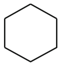	93
7	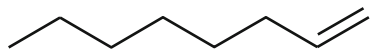	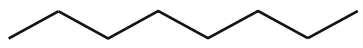	98

[a] 2-Propanol was used as solvent

9.5 Chemoselective Reduction of Nitrobenzenes to Aminobenzenes Having Reducible Groups by Titanium(IV) Oxide Photocatalyst Under Gas- and Metal-Free Conditions

Aminobenzenes synthesized by reduction of corresponding nitrobenzenes are important compounds as intermediates of agrochemicals, medicines, dyes, and various useful compounds. However, it is difficult to selectively reduce the nitro group of nitrobenzenes having other reducible groups such as a vinyl group [42]. Catalytic hydrogenation over a metal catalyst such as Ni or Cu is the main method for reduction of a nitro group. However, this method cannot be applied for selective reduction of the nitro group of nitrobenzenes having a vinyl group because both the nitro and vinyl groups are reduced. Chemoselective reduction of the nitro group is achieved by using a large excess of a reducing agent such as tin (Sn) [43], zinc (Zn) [44], iron (Fe) [45], or sodium hydrosulfite [46]. However, these reaction systems give harmful wastes. Although catalytic chemoselective reduction of nitrobenzenes is important, there have been only a few reports on chemoselective reduction of a nitro group in the presence of C–C bonds [47–49] and their yields were low. Recently, chemoselective reduction of *m*-nitrostyrene (NS) to *m*-aminostyrene (AS) has been achieved by many researchers [42, 50–60]. However, these (thermo)catalytic systems require precious metals, high temperature, and high pressure of reducing reagents such as H_2 and carbon monoxide (CO). Reduction of NS to AS would be more attractive if reducing reagents other than gaseous H_2 and CO are applied, and the reaction is catalyzed by common elements having a simple component and structure under mild conditions such as room temperature and atmospheric pressure.

In this section, we examined the photocatalytic reduction of nitrobenzenes having other reducible groups using a simple photocatalyst, TiO_2, in the presence of oxalic acid as a hole scavenger at room temperature and atmospheric pressure, and we found that only the nitro group was chemoselectively reduced to an amino group and that aminobenzenes with reducible groups were obtained in high yields without using precious metals or high-pressure gaseous reducing reagents [37].

9.5.1 Photocatalytic Chemoselective Reduction of NS to AS in 10 Vol% Water–Acetonitrile Suspension of TiO_2

Figure 9.13 shows time courses of the amounts of NS remaining and AS formed in the photocatalytic reduction of NS in a 10 % (v/v) water–acetonitrile suspension of TiO_2. The amount of NS monotonously decreased along with photoirradiation time, and NS was almost completely consumed after 2 h, while AS was obtained in a high

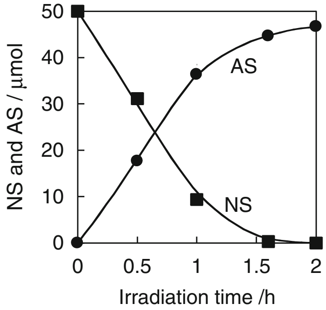

Fig. 9.13 Time courses of amount of NS remaining (*squares*) and amount of AS formed (*circles*) in a 10 %water–acetonitrile suspension of TiO_2 (50 mg) in the presence of oxalic acid (200 µmol) as a hole scavenger under deaerated conditions (Reproduced from Ref. [37] with permission from the Royal Society of Chemistry)

yield (93 %). The high yield of AS indicates that none of the reaction of the benzene ring, reduction of the vinyl group, or reoxidation of the amino group of AS occurred in the present system. It is notable that there are no reports on photocatalytic chemoselective reduction of a nitro group having a C=C double bond. Equation 9.13 shows the probable stoichiometry of photocatalytic chemoselective reduction of NS to AS in the presence of oxalic acid.

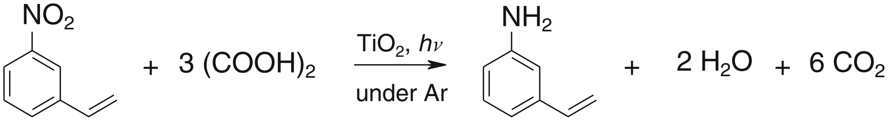

(9.13)

The present photocatalytic reduction required no co-catalyst such as a precious metal and occurred under conditions (298 K, atmospheric pressure, and H_2-free) milder than those of thermocatalytic systems. The value of apparent quantum efficiency (AQE) at 366 nm is calculated from the ratio of the amount of AS, and the amount of photons irradiated using Eq. 9.14 reached 15 %:

$$\text{AQE} = (6 \times \text{amount of AS} \,/\, \text{number of incident photons}) \times 100 \qquad (9.14)$$

For comparison, AQE for photocatalytic H_2 formation from 2-propanol (200 µmol) in an aqueous suspension of platinized TiO_2 was also examined and determined to be 4.1 % under the same irradiation conditions. This reaction has often been used as a model reaction to evaluate the activity of a photocatalyst for H_2 evolution. The value of AQE in the present reaction larger than that of 2-propanol dehydrogenation shows that oxalic acid efficiently works as hole scavenger for photocatalytic reduction of NS to AS.

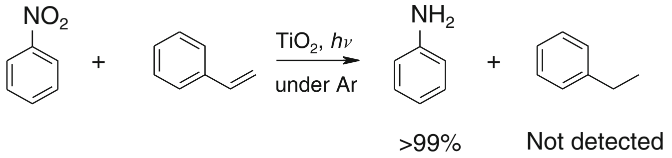

Scheme 9.1 Intermolecular competitive reaction of nitrobenzene and styrene in an acetonitrile suspension of TiO_2 in the presence of oxalic acid as a hole scavenger

9.5.2 Intermolecular Chemoselective Reduction of Nitrobenzene and Styrene

The high chemoselectivity of this method for reduction of NS was further investigated in the intermolecular competitive reaction of nitrobenzene and styrene. As expected, nitrobenzene (50 μmol) was reduced to give aniline (50 μmol) with over >99 % yield, while styrene (49 μmol) was not reduced at all as shown in Scheme 9.1. These results clearly demonstrate that the photocatalytic system showed complete chemoselectivity for the nitro group in the presence of inter- and intramolecular vinyl groups. The selectivity between a nitro group and a vinyl group can be explained electrochemically, i.e., reduction potential of the CB of the TiO_2 and substrates. The half-wave reduction potential of styrene (−2.41 V) [61] is more negative than the potential of TiO_2 CB (−0.3 V), while the half-wave reduction potential of nitrobenzene (0.16 V) [62] is more positive [63].

9.5.3 Applicability

Applicability of the photocatalytic chemoselective reduction was investigated using various nitro compounds having other reducible groups (chloro-, bromo-, carboxyl, and acetyl groups), and Table 9.2 shows results of the photocatalytic chemoselective reduction of various nitrobenzenes in acetonitrile suspension of TiO_2 particles under deaerated conditions. Only the nitro group of these compounds was chemoselectively reduced even in the presence of chloro, bromo, carboxyl, and acetyl groups, resulting in the formation of corresponding amino compounds with high yields. These results indicate wide applicability of this photocatalytic method for chemoselective reduction of a nitro group to an amino group without using protecting process, precious metals, and H_2. When *o*-acetylnitrobenzene was used as substrate (entry 8), the selectivity was low even at low conversion, suggesting that intermediate(s) and/or *o*-acetylaminobenzene easily converted to by-product(s) under photoirradiation.

Table 9.2 Photocatalytic chemoselective reduction of various nitrobenzenes to corresponding aminobenzenes (Reproduced from Ref. [37] with permission from the Royal Society of Chemistry)

Entries	Substrates	Products	Time/h	Conv./%	Sel./%
1	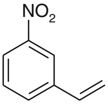	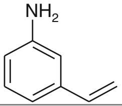	6	>99	88
2	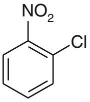	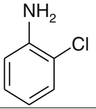	2	>99	>99
3	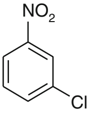	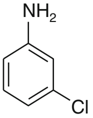	2	>99	95
4	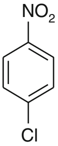	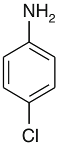	2	>99	54
5	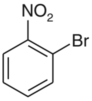	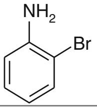	2	>99	>99
6	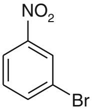	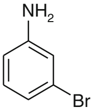	2	>99	>99
7	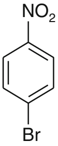	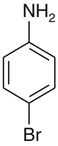	2	>99	88
8	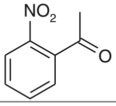	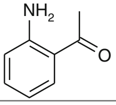	2	>99	15
9	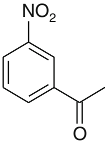	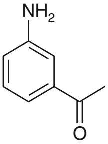	2	>99	91
10	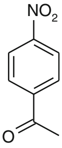	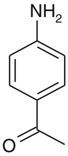	2	>99	88

(continued)

Table 9.2 (continued)

Entries	Substrates	Products	Time/h	Conv./%	Sel./%
11	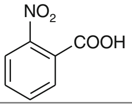	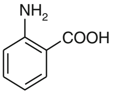	2	>99	98
12	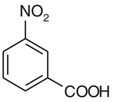	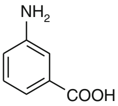	2	>99	>99
13	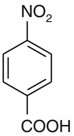	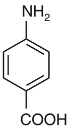	2	>99	98

9.6 Stoichiometric Production of Aminobenzenes and Ketones by Photocatalytic Reduction of Nitrobenzenes in Secondary Alcoholic Suspension of Titanium(IV) Oxide Under Metal-Free Conditions

In the photocatalytic reduction of nitrobenzenes, positive holes in the valence band were effectively removed by formic acid and oxalic acid. These hole scavengers are "greener" sacrificial reagents because they are easily oxidized into CO_2, and thus formed CO_2 molecules are removed from the liquid phase in the presence of organic acids. The photocatalytic reduction of nitrobenzenes would be more attractive if positive holes are utilized for synthesis of valuable compounds, not for fruitless degradation or mineralization. Utilization of positive holes enables simultaneous production of two valuable reduced and oxidized compounds. In the case of reduction of nitrobenzene using oxalic acid (Eq. 9.15), atom efficiency (AE) [64], which is defined in Eq. 9.16, is calculated to be 23.7 %:

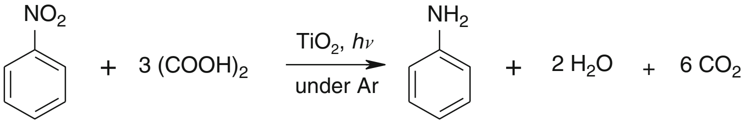

$$\text{Atom efficiency (\%)} = \frac{\text{(molecular weight of the desired product)}}{\text{(sum total of molecular weights of all substances produced)}} \times 100 \tag{9.15}$$

$$\text{Atom efficiency }(\%) = \frac{(\text{molecular weight of the desired product})}{(\text{sum total of molecular weights of all substances produced})} \times 100 \tag{9.16}$$

The photocatalytic reduction of nitrobenzenes to anilines using oxalic acid or formic acid is “green” from the viewpoint of practical operation for reasons stated above; however, the atom efficiency of the reaction is not high because positive holes are consumed only for mineralization of the hole scavengers and large amounts of CO_2 (six times larger than the amount of aminobenzenes) and water (twice the amount of aminobenzenes) are formed. Therefore, atom efficiency should increase if positive holes are utilized for production of valuable compounds, not for fruitless mineralization, during the reduction of nitrobenzenes by photogenerated electrons. In this section, photocatalytic reduction of nitrobenzenes to aminobenzenes in secondary alcohols was examined. Secondary alcohols are regarded as a model raw material of carbonyl compounds and work as hole scavengers and solvents. Since carbonyl compounds such as aldehydes and ketones are precursors for many drugs, vitamins, and fragrances, selective oxidation of alcohols to carbonyl compounds is one of the most important transformations in industrial and fundamental chemistry [65, 66]. Therefore, several photocatalytic methods for selective oxidation of alcohols to corresponding carbonyl compounds have been reported [67–74]. Here we report (1) stoichiometry of products, i.e., anilines and carbonyl compounds, in the photocatalytic reaction, (2) chemoselective reduction of nitrobenzene having reducible groups such as *m*-nitrostyrene to *m*-aminostyrene, and (3) effects of the presence of O_2 and type of TiO_2 on nitrobenzene formation [75].

9.6.1 Stoichiometric Production of Aniline and Acetone in Photocatalytic Reaction of Nitrobenzene in 2-Propanol Suspension of TiO_2 Under Deaerated Conditions

Photocatalytic reaction of nitrobenzene in a 2-propanol suspension of rutile-type TiO_2 (Tayca, MT-150A) with irradiation of UV light was examined under deaerated conditions. Expected stoichiometry of this reaction is shown in Eq. 9.17, and AE of this reaction is calculated to be 88.1 %, in which acetone is regarded as a desired product.

Fig. 9.14 Time courses of amounts of nitrobenzene remaining (*squares*), aniline formed (*circles*), and acetone formed (*diamonds*) and RB of aniline and acetone (*triangles*) in photocatalytic reaction of nitrobenzene in 2-propanol suspensions of TiO_2 under deaerated conditions (Reprinted from Ref. [75], Copyright 2013, with permission from Elsevier)

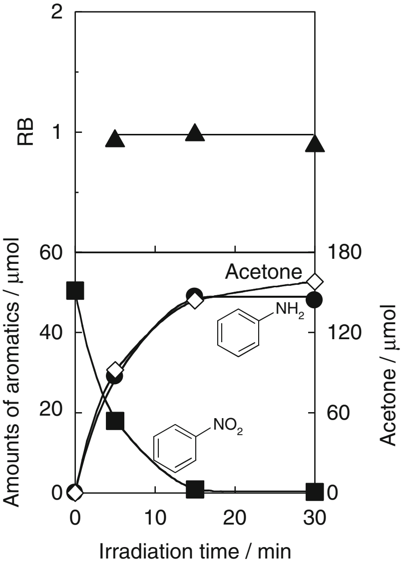

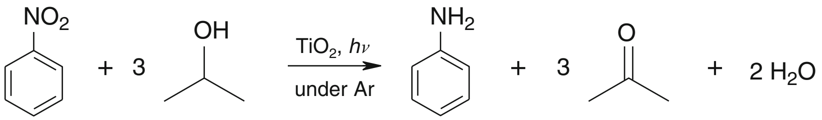

(9.17)

The value was larger than that of reduction of nitrobenzene with oxalic acid (Eq. 9.15) because no CO_2 was formed in the reduction in 2-propanol (Eq. 9.17). Figure 9.14 shows time courses of nitrobenzene remaining, aniline formed, and acetone formed in a 2-propanol suspension of TiO_2 (Tayca, MT-150A) for 30-min photoirradiation under deaerated conditions. Just after photoirradiation, nitrobenzene monotonously decreased, while aniline and acetone were formed as the reduction product of nitrobenzene and the oxidation product of 2-propanol, respectively. After 15-min photoirradiation, nitrobenzene was almost completely consumed and aniline was obtained in a high yield (98 %). We noted that the aniline that had been formed was not reoxidized even by excessive photoirradiation after complete consumption of nitrobenzene. This result indicates that no reoxidation of aniline by holes occurred in the presence of a large excess of 2-propanol. After nitrobenzene had been consumed, a small amount of acetone was formed and the color of TiO_2 became blue, indicating that a part of Ti^{4+} in TiO_2 was reduced to Ti^{3+} along with oxidation of 2-propanol to acetone. To evaluate stoichiometry of the reaction in the present conditions, a new indicator, i.e., redox balance (RB), was used. Since reduction of nitrobenzene to aniline and oxidation of 2-propanol to acetone require six electrons and two holes, respectively, RB was calculated in Eq. 9.18 and values of RB are also shown in Fig. 9.14:

$$\mathrm{RB} = \frac{6 \times \text{amount of aniline}}{2 \times \text{amount of acetone}} \tag{9.18}$$

The values of RB were almost unity at 5 and 15 min, indicating that the reaction proceeded stoichiometrically according to Eq. 9.17, i.e., generated electrons and holes were selectively used only for reduction of nitrobenzene to aniline and oxidation of 2-propanol to acetone, respectively. Due to the formation of a small amount of acetone, the value of RB was slightly decreased at 30 min. From the ratio of the amount of aniline and the amount of photons irradiated (Eq. 9.19), AQE was calculated to be 89 % at 10-min irradiation by UV-LED:

$$\mathrm{AQE}(\%) = \frac{6 \times \text{amount of aniline}}{\text{number of incident photons}} \times 100 \tag{9.19}$$

9.6.2 Chemoselective Reduction of Nitrobenzenes to Anilines Having Reducible Groups in 2-Propanol Suspension of TiO_2 Under Deaerated Conditions

Photocatalytic stoichiometric formation of aniline and acetone was expanded to chemoselective reduction of nitrobenzenes to aminobenzenes having reducible groups (vinyl, chloro, and bromo groups) along with oxidation of 2-propanol to acetone. Figure 9.15 shows time courses of *m*-nitrostyrene (NS) remaining, *m*-aminostyrene (AS) formed, and acetone formed in a 2-propanol suspension of TiO_2 for 30-min photoirradiation under deaerated conditions.

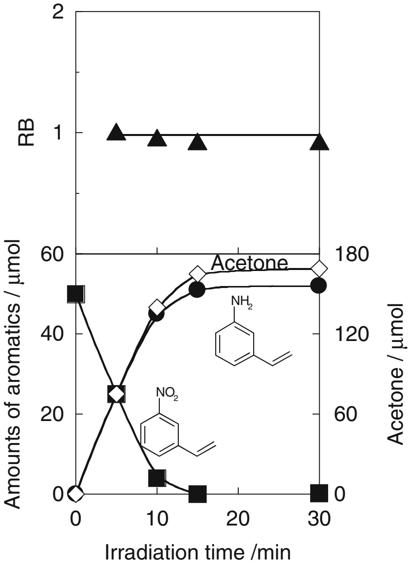

Fig. 9.15 Time courses of amounts of NS remaining (*squares*), AS formed (*circles*), and acetone formed (*diamonds*) and RB of AS and acetone (*triangles*) in photocatalytic reaction of NS in 2-propanol suspensions of TiO_2 under deaerated conditions (Reprinted from Ref. [75], Copyright 2013, with permission from Elsevier)

Just after photoirradiation, the amount of NS monotonously decreased and NS was almost completely consumed after 15 min, while AS was obtained in a high yield (>99 %) as the reduction product of NS. Other reduced products (nitroethylbenzene and aminoethylbenzene) were not formed. Equation 9.20 shows the expected stoichiometry of photocatalytic simultaneous formation of AS and acetone by reduction of NS and oxidation of 2-propanol under the present conditions.

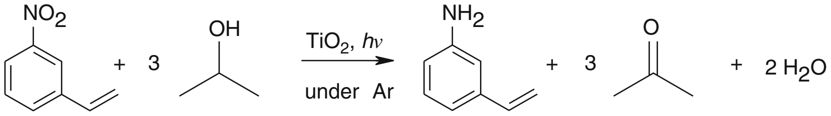

(9.20)

After NS had been consumed, a small amount of acetone was formed and the color of TiO_2 became blue as in the case of nitrobenzene, indicating that a part of Ti^{4+} in TiO_2 was reduced to Ti^{3+}. However, Ti^{3+} species was easily oxidized to Ti^{4+} because the color became white after exposing the suspension to air. The values of RB were almost unity at 5 and 10 min, indicating that the reaction proceeded stoichiometrically according to Eq. 9.20, i.e., generated electrons and holes were selectively used only for reduction of NS to AS and oxidation of 2-propanol to acetone, respectively.

Applicability of the stoichiometric chemoselective reduction was investigated using nitro compounds having other reducible groups (chloro and bromo groups), and Table 9.3 shows results of the photocatalytic chemoselective reduction of these nitrobenzenes in a 2-propanol suspension of TiO_2 particles under deaerated conditions. Only the nitro group of these compounds was chemoselectively reduced even in the presence of chloro and bromo groups, resulting in the formation of

Table 9.3 Photocatalytic chemoselective reduction of nitrobenzenes to corresponding anilines in 2-propanol suspensions of TiO_2 and redox balance of anilines and acetone under deaerated conditions[a] (Reprinted from Ref. [75], Copyright 2013, with permission from Elsevier)

Substrate	Product	Conv./%	Sel./%	RB[b]
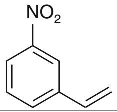	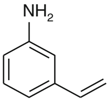	92	98	0.96
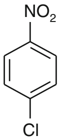	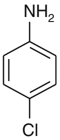	>99	82	0.84
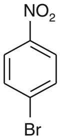	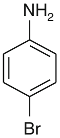	86	>99	0.94

[a]Nitrobenzenes, 50 μmol; 2-propanol, 5 cm^3; TiO_2, MT-150A (50 mg); photoirradiation, 10 min

[b]Redox balance defined as [3 × (amount of aminobenzene)/(amount of acetone)]

corresponding amino compounds with high yields. Since the values of RB were close to unity, stoichiometric reduction of nitrobenzenes and oxidation of 2-propanol occurred under the present conditions. These results indicate wide applicability of this photocatalytic method for chemoselective reduction of a nitro group to an amino group and stoichiometric formation of acetone without using precious metals and H_2. The reaction tendency of *p*-chloronitrobenzene was slightly different from that of *p*-bromonitrobenzene, i.e., *p*-chloronitrobenzene exhibited high conversion and low selectivity while *p*-bromonitrobenzene exhibited low conversion and high selectivity. It is difficult to explain these results because by-product(s) was not determined in this reaction condition. Change in the reaction condition might be required to discuss the effect of halogen on the reaction rate and selectivity.

9.6.3 Stoichiometric Production of Aniline and Acetone in Photocatalytic Reaction of Nitrobenzene in 2-Propanol Suspension of TiO_2 Under Air

When photocatalytic reaction is applied for reduction of a substrate, oxygen is generally removed from the reaction system because oxygen always acts as strong acceptor of photogenerated electrons and decreases the efficiency of photocatalytic reduction in the target. To remove the negative effect of O_2, photocatalytic reduction has been performed under vacuum or under inert gases such as nitrogen and argon. However, removal of O_2 by vacuuming or replacing with these gases requires great care and consumes a large amount of energy. Reactions under air, i.e., reactions free from any additional operations, are most favorable from the viewpoint of practical application. In this study, photocatalytic reaction of nitrobenzene in a 2-propanol suspension of TiO_2 was carried out under air to examine whether stoichiometric production of aniline and acetone was achieved or not, and the results are shown in Fig. 9.16. As well as results under deaerated conditions (Fig. 9.14), just after photoirradiation, nitrobenzene decreased monotonously, while aniline was formed and the yield of aniline reached 96 %, indicating that reduction of nitrobenzene occurred even in the presence of O_2 and the rate was almost the same in the absence of O_2. It should be noted that no aniline was reoxidized with prolonged photoirradiation even in the presence of O_2. Since the yield of acetone was larger than that of aniline and the value of RB was smaller than unity, fruitless oxidation of 2-propanol with O_2 (Eq. 9.21) partly occurred.

(9.21)

From the results in the presence of O_2, it can be concluded that (1) reduction of nitrobenzene (electron trapping by nitrobenzene) was hardly affected by the presence of O_2 and (2) electron trapping by O_2 occurred additionally and, therefore, the yield of acetone increased.

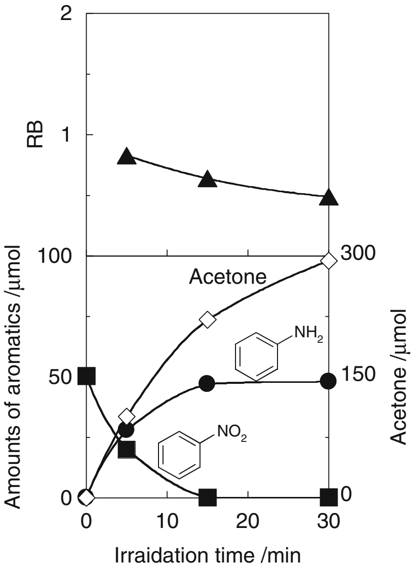

Fig. 9.16 Time courses of amounts of nitrobenzene remaining (*squares*), aniline formed (*circles*), and acetone formed (*diamonds*) and RB of aniline and acetone (*triangles*) in photocatalytic reaction of nitrobenzene in 2-propanol suspensions of TiO_2 under air (Reprinted from Ref. [75], Copyright 2013, with permission from Elsevier)

9.7 Simultaneous Production of Aromatic Aldehydes and Dihydrogen by Photocatalytic Dehydrogenation of Liquid Alcohols over Metal-Loaded Titanium (IV) Oxide Under Oxidant- and Solvent-Free Conditions

Since carbonyl compounds such as aldehydes and ketones are precursors for many drugs, vitamins, and fragrances, selective oxidation of alcohols to carbonyl compounds is one of the most important transformations in industrial chemistry. In particular, the oxidation of primary alcohols to aldehydes is a fundamentally important laboratory and commercial procedure [76–81]. Aromatic aldehydes are valuable as intermediates for both perfumes and medicines [80, 81]. Although there are many methods for oxidation of alcohols to aldehydes, these methods are generally carried out at a high temperature and high pressure by employing stoichiometric oxygen donors (such as chromate and permanganate) [82–85]. Since large amounts of wastes containing heavy metal are formed along with the products, atom efficiency, which is defined as Eq. 9.16, of these methods is very low.

A catalytic process is favorable especially in an oxidation of alcohols to corresponding carbonyl groups using molecular oxygen (O_2) as oxidant instead of stoichiometric oxygen donors. Since only water (H_2O) is formed as the by-product when O_2 is used, atom efficiency is much higher than that of oxidations using stoichiometric oxygen donors. A catalytic process for selective oxidation of various alcohols to corresponding aldehydes under mild conditions, i.e., low temperature and nearly atmospheric pressure, has recently been reported [86]. Since a photocatalytic reaction proceeds at room temperature and under atmospheric pressure, application of photocatalytic reactions to organic synthesis has attracted attention in terms of green chemistry. Recently, photocatalytic partial oxidations of benzyl alcohol with O_2 have been reported [68, 70, 87–90]. However, atom efficiency in these photocatalytic methods never reaches 100 % because a stoichiometric amount of H_2O is formed as a by-product. Formation of aldehydes by simple dehydrogenation of corresponding alcohols would be more attractive because this reaction also gives H_2, which is an alternative energy carrier [90]. Atom efficiency of simple dehydrogenation is higher than that of oxidative dehydrogenation. For example, atom efficiencies in the formation of benzaldehyde (PhCHO) from benzyl alcohol (BnOH) (Eqs. 9.22 and 9.23) are 85.5 % and 98.1 %, respectively.

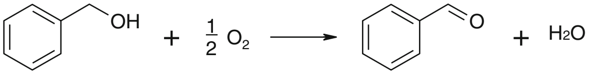

(9.22)

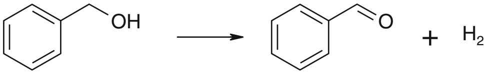

(9.23)

If H_2 is counted as a valuable product, the atom efficiency of Eq. 9.23 becomes 100 %, i.e., zero emission, yielding no useless product, is achieved by oxidant-free dehydrogenation of benzyl alcohol. However, it is generally difficult to eliminate hydrogen of alcohols as H_2 because Gibbs free energy change (ΔG) is positive and is much larger than that of oxidative dehydrogenation, yielding liquid H_2O. Nevertheless, if oxidant-free dehydrogenation is carried out in liquid phase, one of the products, i.e., H_2, is removed from the liquid phase due to the small solubility to alcohols, and a thermodynamic equilibrium is never achieved. Therefore, continuous dehydrogenation just before consumption of alcohols is expected in a liquid-phase reaction.

It has been reported that Pt–TiO_2 produced H_2 from aliphatic alcohols such as methanol, ethanol, and propanol to give corresponding aldehydes or ketones [91, 92]. Dehydrogenation of these alcohols, especially methanol, has also been used to investigate whether newly developed photocatalysts have the potential to produce H_2 or not. However, as far as we know about photocatalytic dehydrogenation of aromatic alcohols along with H_2 formation, only limited paper has been reported, although partial oxidation of benzyl alcohols to corresponding benzaldehydes in the presence of an oxidant has been reported. In this section, we examined simultaneous formation of aromatic aldehydes and H_2 by photocatalytic dehydrogenation of liquid alcohols under oxidant-free conditions at room temperature [93].

9.7.1 Photocatalytic Dehydrogenation of BnOH in an Aqueous Suspension of Pt–TiO$_2$

Figure 9.17 shows time courses of the amounts of BnOH remaining, PhCHO formed, and H_2 evolved in the photocatalytic dehydrogenation of BnOH in an acetonitrile suspension of Pt–TiO$_2$. The amount of BnOH monotonously decreased along with photoirradiation time and was almost completely consumed after 1 h, while PhCHO and H_2 were obtained in high yields (99 % and 95 %, respectively), indicating that dehydrogenation of BnOH shown in Eq. 9.23 occurred completely free from thermodynamical restraint.

Material balance (MB) and redox balance (RB) in Fig. 9.17 were calculated by using Eqs. 9.24 and 9.25, respectively, and are shown in Fig. 9.17:

$$\mathrm{MB}(\%) = (n(\mathrm{PhCHO}) + n(\mathrm{BnOH}))/n_0(\mathrm{BnOH}) \times 100 \tag{9.24}$$

$$\mathrm{RB} = n(\mathrm{H_2})/n(\mathrm{PhCHO}) \tag{9.25}$$

where n(PhCHO), n(BnOH), and $n(H_2)$ are the amounts of PhCHO, BnOH, and H_2 observed after photoirradiation, respectively, and n_0(BnOH) is the initial amount of BnOH. After 60-min photoirradiation, MB and RB were determined to be 99 % and 0.93, respectively. The high yield of PhCHO and the value of MB close to unity indicate that only dehydrogenation of BnOH to PhCHO shown in Eq. 9.23 occurred, i.e., neither a side reaction nor a successive reaction consuming BnOH and PhCHO occurred. Re-reduction of PhCHO to BnOH was not observed under the present conditions, although Kohtani et al. reported that PhCHO was reduced to

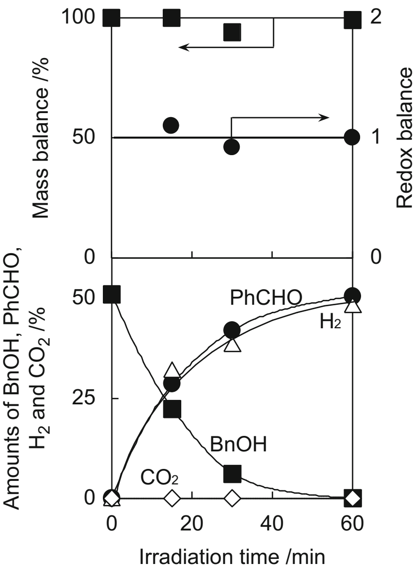

Fig. 9.17 Time courses of BnOH remaining, PhCHO formed, and H_2 and CO_2 evolved in an acetonitrile suspension of Pt–TiO$_2$ under a deaerated condition (Reprinted from Ref. [93], Copyright 2013, with permission from Elsevier)

BnOH by photocatalysis of TiO_2 in the presence of a hole scavenger such as an excess of ethanol [17]. These results indicate that photogenerated electrons were injected into the Pt co-catalyst loaded and selectively used for reduction of H^+ to form H_2. The value of RB close to unity together with MB = *ca.* 100 % indicates both that H_2 was formed from BnOH and that H_2 was quantitatively separated from the liquid phase. Self-separation of H_2 from the reaction system is indispensable to achieve complete conversion of BnOH free from thermodynamic restraint and is also practically important because no energy and process are required to separate H_2.

From the ratio of the amount of PhCHO and the amount of photons irradiated (Eq. 9.26), AQE was calculated to be 38 % at 30-min irradiation in Fig. 9.17, indicating that dehydrogenation of BnOH occurred very effectively under the deaerated conditions:

$$\mathrm{AQE}(\%) = \begin{array}{l}(2 \times \text{amount of PhCHO/number of incident photons}) \\ \times 100.\end{array} \tag{9.26}$$

To investigate the high selectivity of PhCHO in the present reaction condition, reaction of PhCHO in an acetonitrile suspension of Pt–TiO_2 was carried out under the same irradiation condition. Benzaldehyde conversion and H_2 yield were much smaller (7.6 % and 2 μmol, respectively, for 1 h) than BnOH conversion and H_2 yield (>99 % and 48 μmol, respectively, for 1 h), indicating that the reactivity of PhCHO was much smaller than that of BnOH in this condition. The smaller reactivity was attributed to the high selectivity of PhCHO in the photocatalytic oxidation of BnOH in an acetonitrile suspension of Pt–TiO_2. Photocatalytic oxidation of aldehyde under a deaerated condition is generally calculated in Eq. 9.27:

$$\mathrm{R-CHO + H_2O \rightarrow R-COOH + H_2} \tag{9.27}$$

Water is indispensable for oxidation of aldehyde to carboxylic acid. However, the present photocatalytic reaction was performed in a water-free acetonitrile suspension of Pt–TiO_2. Since no water formed as shown in Eq. 9.23, the water-free condition was preserved during the whole reaction. Therefore, we can conclude that water-free and oxygen-free conditions strongly contributed to the high selectivity of PhCHO in the photocatalytic oxidation of BnOH.

9.7.2 Durability and Reactions at High Concentrations

It is important for green chemistry to recover a photocatalyst and reuse it many times without special treatment such as calcination. To examine the durability of the Pt–TiO_2 photocatalyst in this reaction system, the Pt–TiO_2 photocatalyst was used repeatedly. After 60-min reaction in an acetonitrile suspension of Pt–TiO_2, Pt–TiO_2 particles were recovered by simple filtration from the reaction mixture and

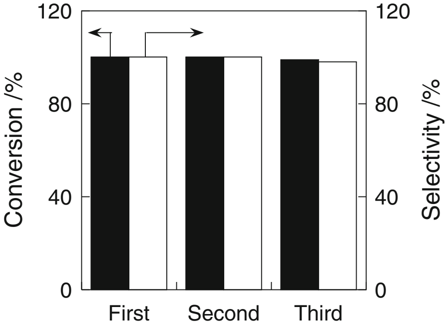

Fig. 9.18 Durability of Pt–TiO_2 in photocatalytic dehydrogenation of BnOH for 1-h irradiation (Reprinted from Ref. [93], Copyright 2013, with permission from Elsevier)

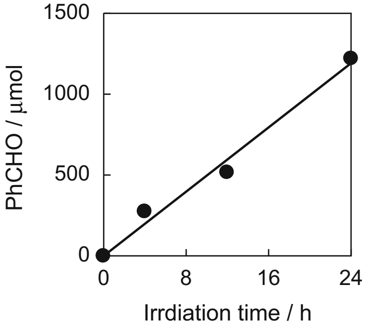

Fig. 9.19 Photocatalytic dehydrogenation of BnOH to PhCHO in a BnOH suspension of Pt–TiO_2 (Reprinted from Ref. [93], Copyright 2013, with permission from Elsevier)

were reused. Figure 9.18 shows that the Pt–TiO_2 photocatalyst was reusable without notable loss of activity.

Since reactions without the use of a solvent are more favorable from the point of view of green chemistry, photocatalytic solvent-free dehydrogenation of BnOH was also examined. The reaction was very simple, i.e., only Pt–TiO_2 particles were suspended in 5 cm^3 of BnOH and the mixture was photoirradiated under argon. Results are shown in Fig. 9.19. The amount of PhCHO increased linearly along with photoirradiation, and the PhCHO yield reached 1220 μmol after 24-h photoirradiation. Under the solvent-free condition, AQE was calculated to be 31 % after 4-h irradiation of Fig. 9.19.

In the solvent-free system, the amount of H_2 evolved was not determined because H_2 was continuously purged from the reactor (test tube) to prevent a large increase in internal pressure. These results include two important points: the first point is that photocatalytic dehydrogenation of BnOH occurred without loss of activity in the BnOH solvent as well as the acetonitrile solvent, and the second point is that high efficiency (reaction rate and AQE) was obtained compared with condition of a low concentration of BnOH.

9.8 Conclusions

Various new photocatalytic conversions, mainly reductions, were introduced in this chapter. We use oxalic acid and formic acid as greener hole scavengers. *m*-Nitrobenzenesulfonic acid was almost quantitatively converted into *m*-aminobenzenesulfonic acid, and a high yield of *m*-aminobenzenesulfonic acid was achieved even when the reaction was performed in the presence of oxygen. In this reaction system, adsorption ability of TiO_2 toward *m*-nitrobenzenesulfonic acid is important for effective production of *m*-aminobenzenesulfonic acid. Photocatalytic reduction can be applied to chemoselective reduction of various nitro compounds having other reducible groups to corresponding aminobenzenes. Loading of Pd co-catalyst expands possibility of TiO_2 photocatalysts: we achieved photocatalytic reduction (hydrogenation) of alkenes and cyano compounds as new hydrogen (H_2)-free reaction systems. Over Pd co-catalyst, H^+ originated from solvent was reduced, resulting in the formation of H–Pd active species, which have more negative potential than the conduction band (CB) of TiO_2. Use of alcohols enables us to simultaneously produce two valuable reduced and oxidized compounds. For example, in photocatalytic reaction in 2-propanol, nitrobenzene was quantitatively converted into aniline with an almost stoichiometric amount of acetone as an oxidation product of 2-propanol. Photocatalytic simultaneous production of reduced and oxidized compounds can be applied for alcohol dehydrogenation system, in which benzaldehyde and H_2 were simultaneously produced from benzyl alcohol over Pt–TiO_2 photocatalyst.

As described above, this chapter provides a new strategy for designing a photocatalytic reaction system. Photoirradiated TiO_2 shows sharp chemoselectivity in the reduction of functional groups, and the chemoselectivity is explained by the relative position of reduction potential of the functional groups and CB of TiO_2. One may think that substrates applied for photocatalytic reduction are limited because the position of CB of TiO_2 is positive to reduction potentials of most of organic compounds. Possibility of photocatalytic reduction is expanded by using catalysis of metal particles loaded on TiO_2. Compounds having multi-bonding with higher reduction potential can be reduced over Pd–TiO_2 photocatalyst. In this case, H species having strong reduction power are photocatalytically formed on Pd nanoparticles. Since there are many candidates for co-catalysts, various photocatalytic reductions would be further developed.

References

1. Fujishima A, Honda K (1972) Electrochemical photolysis of water at a semiconductor electrode. Nature 238:37–38
2. Fox MA, Dulay MT (1993) Heterogeneous photocatalysis. Chem Rev 93:341–357
3. Anastas PT, Warner JC (1998) Green chemistry: theory and practice. Oxford University Press, Oxford

4. Palmisano G, Augugliaro V, Pagliarob M, Palmisano L (2007) Photocatalysis: a promising route for 21st century organic chemistry. Chem Commun 3425–3437
5. Palmisano G, García-López E, Marcí G, Loddo V, Yurdakal S, Augugliaro V, Palmisano L (2010) Advances in selective conversions by heterogeneous photocatalysis. Chem Commun 46:7074–7089
6. Ohtani B, Pal B, Ikeda S (2003) Photocatalytic organic syntheses: selective cyclization of amino acids in aqueous suspensions. Catal Surv Asia 7:165–176
7. Ohtani B (1994) Organic syntheses by semiconductor photocatalytic reaction. Trends Photochem Photobiol 3:531–539
8. Kisch H (1994) Preparative photoreactions catalyzed by semiconductor powders. J Prakt Chem 336:635–648
9. Kisch H, Lindner W (2001) Synthesen durch halbleiter-photokatalyse: Solare chemie. Chem Unserer Zeit 35:250–257
10. Ohtani B, Ohno T (2002) Photocatalytic organic syntheses by using semiconductor particles. In: Kaneko M, Okura I (eds) Photocatalysis science and technology. Kodansha-Springer, Tokyo, p 186
11. Muzyka JL, Fox MA (1991) Oxidative photocatalysis in the absence of oxygen: methyl viologen as an electron trap in the TiO_2-mediated photocatalysis of the Diels-Alder dimerization of 2,4-dimethyl-1,3-pentadiene. J Photochem Photobiol A Chem 57:27–39
12. Li Y, Wasgestian F (1998) Photocatalytic reduction of nitrate ions on TiO_2 by oxalic acid. J Photochem Photobiol A Chem 112:255–259
13. Gekko H, Hashimoto K, Kominami H (2012) Photocatalytic reduction of nitrite to dinitrogen in aqueous suspensions of metal-loaded titanium(IV) oxide in the presence of a hole scavenger: an ensemble effect of silver and palladium co-catalysts. Phys Chem Chem Phys 14:7965–7970
14. Joyce-Pruden C, Pross JK, Li Y (1992) Photoinduced reduction of aldehydes on titanium dioxide. J Org Chem 57:5087–5091
15. Park JW, Hong MJ, Park KK (2001) Photochemical reduction of 1,2-diketones in the presence of TiO_2. Bull Korean Chem Soc 22:1213–1216
16. Matsushita Y, Kumada S, Wakabayashi K, Sakeda K, Ichimura T (2006) Photocatalytic reduction in microreactors. Chem Lett 35:410–411
17. Kohtani S, Yoshioka E, Saito K, Kudo A, Miyabe H (2010) Photocatalytic hydrogenation of acetophenone derivatives and diaryl ketones on polycrystalline titanium dioxide. Catal Commun 11:1049–1053
18. Mahdavi F, Bruton TC, Li Y (1993) Photoinduced reduction of nitro compounds on semiconductor particles. J Org Chem 58:744–746
19. Ferry JL, Glaze WH (1998) Photocatalytic reduction of nitro organics over illuminated titanium dioxide: role of the TiO2 surface. Langmuir 14:3551–3555
20. Makarova OV, Rajh T, Thurnauer MC, Martin A, Kemme PA, Cropek D (2000) Surface modification of TiO_2 nanoparticles for photochemical reduction of nitrobenzene. Environ Sci Technol 34:4797–4803
21. Brezová V, Tarábek P, Dvoranová D, Staško A, Biskupič S (2003) EPR study of photoinduced reduction of nitroso compounds in titanium dioxide suspensions. J Photochem Photobiol A Chem 155:179–198
22. Tada H, Ishida T, Takao A, Ito S (2004) Drastic enhancement of TiO_2-photocatalyzed reduction of nitrobenzene by loading Ag clusters. Langmuir 20:7898–7900
23. Zhang T, You L, Zhang Y (2006) Photocatalytic reduction of *p*-chloronitrobenzene on illuminated nano-titanium dioxide particles. Dyes Pigm 68:95–100
24. Flores SO, Rios-Bernij O, Valenzuela MA, Córdova I, Gómez R, Gutiérrez R (2007) Photocatalytic reduction of nitrobenzene over titanium dioxide: by-product identification and possible pathways. Top Catal 44:507–511
25. Chen S, Zhang H, Yu X, Liu W (2010) Photocatalytic reduction of nitrobenzene by titanium dioxide powder. Chin J Chem 28:21–26

26. Hakki A, Dillert R, Bahnemann D (2009) Photocatalytic conversion of nitroaromatic compounds in the presence of TiO_2. Catal Today 144:154–159
27. Kominami H, Iwasaki S, Maeda T, Imamura K, Hashimoto K, Kera Y, Ohtani B (2009) Chem Lett 38:410–411
28. Imamura K, Iwasaki S, Maeda T, Hashimoto K, Ohtani B, Kominami H (2011) Photocatalytic reduction of nitrobenzenes to aminobenzenes in aqueous suspensions of titanium(IV) oxide in the presence of hole scavengers under deaerated and aerated conditions. Phys Chem Chem Phys 13:5114–5119
29. Kominami H, Kohno M, Takada Y, Inoue M, Inui T, Kera Y (1999) Hydrolysis of titanium alkoxide in organic solvent at high temperatures: a new synthetic method for nanosized, thermally stable titanium(IV) oxide. Ind Eng Chem Res 38:3925–3931
30. Imamura K, Yoshikawa T, Nakanishi K, Hashimoto K, Kominami H (2013) Photocatalytic reduction of benzonitrile to benzylamine in aqueous suspensions of palladium-loaded titanium (IV) oxide. Chem Commun 49:10911–10913
31. Nishimura S (2001) Handbook of heterogeneous catalytic hydrogenation for organic synthesis. Wiley, New York, pp 254–285
32. Bellefon C, Fouilloux P (1994) Homogeneous and heterogeneous hydrogenation of nitriles in a liquid phase: chemical, mechanistic, and catalytic aspects. Catal Rev Sci Eng 36:459–506
33. Volf J, Pasek J (1986) Catalytic hydrogenation. Elsevier, Amsterdam, p 105
34. Gomez S, Peters JA, Maschmeyer T (2002) The reductive amination of aldehydes and ketones and the hydrogenation of nitriles: mechanistic aspects and selectivity control. Adv Synth Catal 344:1037–1057
35. Bakker JJW, Neut AG, Kreutzer MT, Moulijn JA, Kapteijn F (2010) Catalyst performance changes induced by palladium phase transformation in the hydrogenation of benzonitrile. J Catal 274:176–191
36. Ohno T, Masaki Y, Hirayama S, Matsumura M (2001) TiO_2-photocatalyzed epoxidation of 1-decene by H_2O_2 under visible light. J Catal 204:163–168
37. Imamura K, Hashimoto K, Kominami H (2012) Chemoselective reduction of nitrobenzenes to aminobenzenes having reducible groups by a titanium(IV) oxide photocatalyst under gas- and metal-free conditions. Chem Commun 48:4356–4358
38. Sugano Y, Fujiwara K, Shiraishi Y, Ichikawa S, Hirai T (2013) Photocatalytic hydrodenitrogenation of aromatic cyanides on TiO_2 loaded with Pd nanoparticles. Catal Sci Technol 3:1718–1724
39. Corvaisier F, Schuurman Y, Fecant A, Thomazeau C, Raybaud P, Toulhoat H, Farrusseng D (2013) Periodic trends in the selective hydrogenation of styrene over silica supported metal catalysts. J Catal 307:352–361
40. Dahlén A, Nilsson Å, Hilmersson G (2006) Estimating the limiting reducing power of SmI_2/H_2O/Amine and YbI_2/H_2O/Amine by efficient reduction of unsaturated hydrocarbons. J Org Chem 71:1576–1580
41. Imamura K, Okubo Y, Ito T, Tanaka A, Hashimoto K, Kominami H (2014) Photocatalytic hydrogenation of alkenes to alkanes in alcoholic suspensions of palladium-loaded titanium (IV) oxide without the use of hydrogen gas. RSC Adv 4:19883–19886
42. Blaser HU, Steiner H, Studer M (2009) Selective catalytic hydrogenation of functionalized nitroarenes: an update. ChemCatChem 1:210–221
43. Butera J, Bagli J (1991) WO Patent 91/09023
44. Burawoy A, Critchley JP (1959) Electronic spectra of organic molecules and their interpretation -V: effect of terminal groups containing multiple bonds on the K-bands of conjugated systems. Tetrahedron 5:340–351
45. Suchy M, Winternitz P, Zeller M (1991) WO Patent 91/02278
46. Kovar RF, Armond FE (1976) US Patent 3, 975, 444
47. Braden R, Knupfer H, Hartung S (1977) US Patetnt 4 002673 and 4 051177
48. Onopchenko A, Sabourin ET, Selwitz CM (1979) Selective catalytic hydrogenation of aromatic nitro groups in the presence of acetylenes. Synthesis of (3-aminophenyl)acetylene via

hydrogenation of dimethylcarbinol substituted (3-nitrophenyl)acetylene over heterogeneous metallic ruthenium catalyst. J Org Chem 44:1233–1236

49. Saha A, Ranu B (2008) Highly chemoselective reduction of aromatic nitro compounds by copper nanoparticles/ammonium formate. J Org Chem 73:6867–6870
50. Blaser HU, Studer M (1999) The role of catalysis for the clean production of fine chemicals. Appl Catal A Gen 189:191–204
51. Corma A, Serna P (2006) Chemoselective hydrogenation of nitro compounds with supported gold catalysts. Science 313:332–334
52. Corma A, Serna P, Concepción P, Calvino JJ (2008) Transforming nonselective into chemoselective metal catalysts for the hydrogenation of substituted nitroaromatics. J Am Chem Soc 130:8748–8753
53. Serna P, Concepción P, Corma A (2009) Design of highly active and chemoselective bimetallic gold–platinum hydrogenation catalysts through kinetic and isotopic studies. J Catal 265:19–25
54. Shimizu K, Miyamoto Y, Kawasaki T, Taji T, Tai Y, Satsuma A (2009) Chemoselective hydrogenation of nitroaromatics by supported gold catalysts: mechanistic reasons of size- and support-dependent activity and selectivity. J Phys Chem C 113:17803–17810
55. Shimizu K, Miyamoto Y, Satsuma A (2010) Size- and support-dependent silver cluster catalysis for chemoselective hydrogenation of nitroaromatics. J Catal 270:86–94
56. Shimizu K, Satsuma A (2011) Silver cluster catalysts for green organic synthesis. J Jpn Petrol Inst 54:347–360
57. Mikami Y, Noujima A, Mitsudome T, Mizugaki T, Jitsukawa K, Kaneda K (2010) Highly chemoselective reduction of nitroaromatic compounds using a hydrotalcite-supported silver-nanoparticle catalyst under a CO atmosphere. Chem Lett 39:223–225
58. Kaneda K, Kuwahara H, Imanaka T (1994) Chemoselective reduction of nitro groups in the presence of olefinic, ester, and halogeno functions using a reducing agent of CO and H_2O catalyzed by Rh carbonyl clusters. J Mol Catal 88:L267–L270
59. Reis PM, Royo B (2009) Chemoselective hydrogenation of nitroarenes and deoxygenation of pyridine N-oxides with H_2 catalyzed by MoO_2Cl_2. Tetrahedron Lett 50:949–952
60. Mitsudome T, Mikami Y, Matoba M, Mizugaki T, Jitsukawa K, Kaneda K (2012) Design of a silver-cerium dioxide core-shell nanocomposite catalyst for chemoselective reduction reactions. Angew Chem Int Ed 51:136–139
61. Ruoff RS, Kadish KM, Boulas P, Chen ECM (1995) Relationship between the electron affinities and half-wave reduction potentials of fullerenes, aromatic hydrocarbons, and metal complexes. J Phys Chem 99:8843–8850
62. Fan LJ, Wang C, Chang SC, Yang Y (1999) Reaction of nitrobenzene on gold single-crystal electrodes: surface crystallographic orientation dependence. J Electroanal Chem 477:111–120
63. Shiraishi Y, Togawa Y, Tsukamoto D, Tanaka S, Hirai T (2012) ACS Catal 2:2475–248
64. Trost BM (1991) The atom economy – a search for synthetic efficiency. Science 254:1471–1477
65. Tidwell TT (1990) Oxidation of alcohols to carbonyl compounds via alkoxysulfonium ylides: the moffatt, swern, and related oxidations. Org React 39:297–555
66. Hayashi M, Kawabata H (2006) Environmentally benign oxidation of alcohols using transition metal catalysts. In: Gerard FL (ed) Advances in chemistry research. Nova, New York, pp 45–62
67. Augugliaro V, Caronna T, Loddo V, Marci G, Palmisano G, Palmisano L, Yurdakal S (2008) Oxidation of aromatic alcohols in irradiated aqueous suspensions of commercial and home-prepared rutile TiO_2: a selectivity study. Chem Eur J 14:4640–4646
68. Yurdakal S, Palmisano G, Loddo V, Alagoz O, Augugliaro V, Palmisano L (2009) Selective photocatalytic oxidation of 4-substituted aromatic alcohols in water with rutile TiO_2 prepared at room temperature. Green Chem 11:510–516

69. Zhang M, Wang Q, Chen CC, Zang L, Ma WH, Zhao JC (2009) Oxygen atom transfer in the photocatalytic oxidation of alcohols by TiO_2: oxygen isotope studies. Angew Chem Int Ed 48:6081–6084
70. Higashimoto S, Kitao N, Yoshida N, Sakura T, Azuma M, Ohue H, Sakata Y (2009) Selective photocatalytic oxidation of benzyl alcohol and its derivatives into corresponding aldehydes by molecular oxygen on titanium dioxide under visible light irradiation. J Catal 266:279–285
71. Augugliaro V, Palmisano L (2010) Green oxidation of alcohols to carbonyl compounds by heterogeneous photocatalysis. ChemSusChem 3:1135–1138
72. Tsukamoto D, Ikeda M, Shiraishi Y, Hara T, Ichikuni N, Tanaka S, Hirai T (2011) Selective photocatalytic oxidation of alcohols to aldehydes in water by TiO_2 partially coated with WO_3. Chem Eur J 17:9816–9824
73. Furukawa S, Shishido T, Teramura K, Tanaka T (2012) Photocatalytic oxidation of alcohols over TiO_2 covered with Nb_2O_5. ACS Catal 2:175–179
74. Tanaka A, Hashimoto K, Kominami H (2012) Preparation of Au/CeO_2 exhibiting strong surface plasmon resonance effective for selective or chemoselective oxidation of alcohols to aldehydes or ketones in aqueous suspensions under irradiation by green light. J Am Chem Soc 134:14526–14533
75. Imamura K, Yoshikawa T, Hashimoto K, Kominami H (2013) Stoichiometric production of aminobenzenes and ketones by photocatalytic reduction of nitrobenzenes in secondary alcoholic suspension of titanium(IV) oxide under metal-free conditions. Appl Catal B Environ 134–135:193–197
76. Brink G, Arends IWCE, Sheldon RA (2000) Green, catalytic oxidation of alcohols in water. Science 287:1636–1639
77. Vazylyev M, Sloboda-Rozner D, Haimov A, Maayan G, Neumann R (2005) Strategies for oxidation catalyzed by polyoxometalates at the interface of homogeneous and heterogeneous catalysis. Top Catal 34:93–99
78. Pagliaro M, Campestrini S, Ciriminna R (2005) Ru-based oxidation catalysis. Chem Soc Rev 34:837–845
79. Mori K, Hara T, Mizugaki T, Ebitani K, Kaneda K (2004) Hydroxyapatite-supported palladium nanoclusters: a highly active heterogeneous catalyst for selective oxidation of alcohols by use of molecular oxygen. J Am Chem Soc 126:10657–10666
80. Markó IE, Giles PR, Tsukazaki M, Brown SM, Urch CJ (1996) Copper-catalyzed oxidation of alcohols to aldehydes and ketones: an efficient, aerobic alternative. Science 274:2044–2066
81. Schultz MJ, Adler RS, Zierkiewicz W, Privalov T, Sigman MS (2005) Using mechanistic and computational studies to explain ligand effects in the palladium-catalyzed aerobic oxidation of alcohols. J Am Chem Soc 127:8499–8507
82. Pillai UR, Sahle-Demessie E (2003) Oxidation of alcohols over Fe^{3+}/montmorillonite-K10 using hydrogen peroxide. Appl Catal A 245:103–109
83. Griffith WP, Joliffe JM (1991) Ruthenium and osmium carboxylato oxo complexes as organic oxidants. Stud Surf Sci Catal 66:395–400
84. Lee DG, Spitzer UA (1970) Aqueous dichromate oxidation of primary alcohols. J Org Chem 35:3589–3590
85. Menger FM, Lee C (1981) Synthetically useful oxidations at solid sodium permanganate surfaces. Tetrahedron Lett 22:1655–1656
86. Enache DI, Edwards JK, Landon P, Solsona-Espriu B, Carley AF, Herzing AA, Watanabe M, Kiely CJ, Knight DW, Hutchings GJ (2006) Solvent-free oxidation of primary alcohols to aldehydes using Au-Pd/TiO_2 catalysts. Science 311:362–365
87. Pillai UR, Sahle-Demessie E (2002) Selective oxidation of alcohols in gas phase using light-activated titanium dioxide. J Catal 211:434–444
88. Mohamed OS, Gaber AEM, Abdel-Wahab AA (2002) Photocatalytic oxidation of selected aryl alcohols in acetonitrile. J Photochem Photobiol A Chem 148:205–210

89. Farhadi S, Afshari M, Maleki M, Badazadeh Z (2005) Photocatalytic oxidation of primary and secondary benzylic alcohols to carbonyl compounds catalyzed by $H_3PW_{12}O_{40}/SiO_2$ under an O_2 atmosphere. Tetrahedron Lett 46:8483–8486
90. Tanaka A, Sakaguchi S, Hashimoto K, Kominami H (2012) Preparation of Au/TiO_2 exhibiting strong surface plasmon resonance effective for photoinduced hydrogen formation from organic and inorganic compounds under irradiation of visible light. Catal Sci Technol 2:907–909
91. Teratani S, Nakamichi J, Taya K, Tanaka K (1982) Photocatalytic dehydrogenation of 2-propanol over TiO_2 and metal/TiO_2 powders. Bull Chem Soc Jpn 55:1688–1690
92. Ohtani B, Iwai K, Nishimoto S, Sato S (1997) Role of platinum deposits on titanium(IV) oxide particles: structural and kinetic analyses of photocatalytic reaction in aqueous alcohol and amino acid solutions. J Phys Chem B 101:3349–3359
93. Imamura K, Tsukahara H, Hamamichi K, Seto N, Hashimoto K, Kominami H (2013) Simultaneous production of aromatic aldehydes and dihydrogen by photocatalytic dehydrogenation of liquid alcohols over metal-loaded titanium(IV) oxide under oxidant- and solvent-free conditions. Appl Catal A Gen 450:28–33

Chapter 10
Fundamentals of TiO_2 Photocatalysis. Consequences for Some Environmental Applications

Pierre Pichat

Abstract This chapter considers the fundamental phenomena occurring when TiO_2 is excited by photons. The focus is first on the formation and fate of the charges generated by the excitation. Then, the roles in photocatalytic reactions of water and oxygen which are almost always present are presented and discussed; the effects of adding ozone or hydrogen peroxide are also briefly indicated. Regarding the photocatalytic degradation of organic compounds – which is involved in potential applications such as self-cleaning materials and air or water purification – the following issues are examined: the hole-induced and hydroxyl radical-induced pathways and the predictability of the nature of the intermediate products. Some of the material aspects of photocatalysis are dealt with through (1) the influence of the structural and textural characteristics of pristine TiO_2, (2) the effects of modifying TiO_2 by metal deposits or ion doping, and (3) the basic outcomes of combining TiO_2 with either another oxide (insulating or semiconducting) or a supplementary adsorbent of high surface area. Conclusions are drawn from these fundamental topics about the applicability of TiO_2 photocatalysis.

Keywords Active species • Basic pathways • Charge carriers • Environmental applications • Modified TiO_2 • Photocatalysis • TiO_2

10.1 Introduction

The objective of this chapter is to provide for the readers of the book some of the main basic concepts of TiO_2 photocatalysis.

The first broad topic considers the formation, transport, recombination, and transfer of charge carriers, including the dynamics aspects. These phenomena are evidently crucial because they govern the occurrence and rates of photocatalytic reactions. Among the reactants to which the charges can be transferred, water and

---

P. Pichat (✉)
Photocatalyse et Environnement, CNRS/Ecole Centrale de Lyon (STMS), 69134 Ecully CEDEX, France
e-mail: pichat@ec-lyon.fr

J.C. Colmenares, Y.-J. Xu (eds.), *Heterogeneous Photocatalysis*, Green Chemistry and Sustainable Technology, DOI 10.1007/978-3-662-48719-8_10

oxygen are especially examined because of both their ubiquity and their determining roles in photocatalytic reactions. The focus is then on the basic pathways of photocatalytic degradation of organic compounds and the predictability of the nature of the intermediate products. These issues can provide fundamental information on the nature and the roles of the reactive species. They should help to optimize the operational conditions. They are obviously essential for self-cleaning materials [1] and air [2, 3] or water purification [4], which, until now, are the main applications of TiO_2 photocatalysis at the commercial or demonstration stages. The last broad topic presents and discusses the photocatalytic effects of the main characteristics of pristine TiO_2, the modifications of TiO_2 by metal deposits or doping, and the combination of TiO_2 with another oxide (either insulating or semiconducting) or with a high-surface-area adsorbent, such as activated carbon, a zeolite, or a clay. This diverse topic tries to encompass the key ideas upon which the principal efforts have been based to improve the efficiency of photocatalysts for various applications.

For each subject, the author's opinion is presented about the practical consequences for the photocatalytic removal of organic compounds or, in the case of TiO_2 with metal deposits, for hydrogen formation.

This chapter deals with TiO_2-based photocatalysts only, given their preeminence and also the limitation of space. However, much of the basic information is also relevant to other n-type semiconductor oxides.

The references cited are not intended to be comprehensive but solely to provide some highlights and examples illustrating the diverse points in order to orient the readers. The author apologizes in advance to the numerous scientists whose studies are uncited.

10.2 Formation and Fate of Charge Carriers Generated by Photon Excitation of TiO_2

10.2.1 Absorption of Photons

Electrons pertaining to an isolated atom occupy discrete energy levels. In a crystal, each of these energy levels is split into as many energy levels as there are atoms. Consequently, the resulting energy levels are very close to one another, forming a continuous band of energies. In a conductor (e.g., a metal), the highest energy band is half filled and the corresponding electrons need only a small amount of energy to be raised into the empty part of the band (which explains the electric conductivity at room temperature). By contrast, in insulators and semiconductors, valence electrons completely fill a band thus called the valence band (VB), whereas the next higher-energy band, termed the conduction band (CB), is empty, at least at 0 K. In a perfect crystal, the energy band separating the highest level of the valence band from the lowest level of the conduction band is forbidden. Its width is referred to as

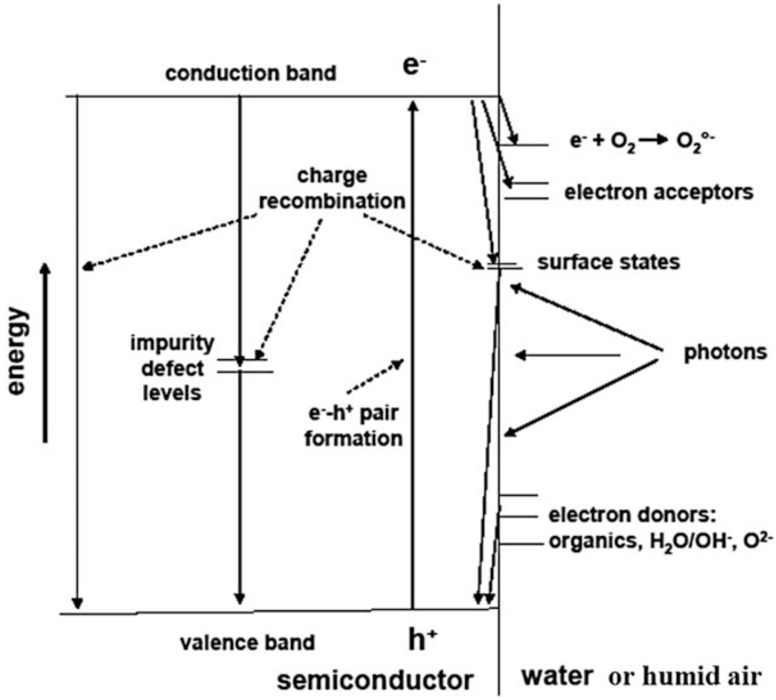

Fig. 10.1 Scheme illustrating the main electron transfers resulting from bandgap excitation of an n-type semiconductor like TiO_2. Band bending near the surface is not shown

the bandgap. It is smaller for semiconductors (viz., <ca. 4 eV) than for insulators, in accordance with the names of these materials.

The absorption by a semiconductor of photons having an energy at least equal to that of the bandgap promotes electrons from the VB (where electron vacancies or electron deficiencies or holes are thus formally created) to the CB (Fig. 10.1). This bandgap irradiation of semiconductors is the step that triggers the course of photocatalytic redox events. Therefore, this step must be considered thoroughly. Several phenomena can intervene; some of them are mentioned in the following paragraph.

Firstly, for tiny particles, the change in absorptivity due to surface states arising from lattice truncation and dangling bonds may become significant. For instance, the absorption edge can be displaced [5]. Secondly, some adsorbates are able to form charge-transfer complexes with the photocatalyst surface (Fig. 10.2) [6, 7]. Excitation of these complexes, which may occur with sub-bandgap irradiation, can generate additional charge carriers not expected in the absence of these particular adsorbates. Thirdly, when diluted suspensions of powder TiO_2 are used, e.g., in water purification, the primary particles can form aggregates and agglomerates in spite of stirring and/or flow and even ultrasound pretreatment. These changes in particle size deeply modify the absorption and scattering of photons.

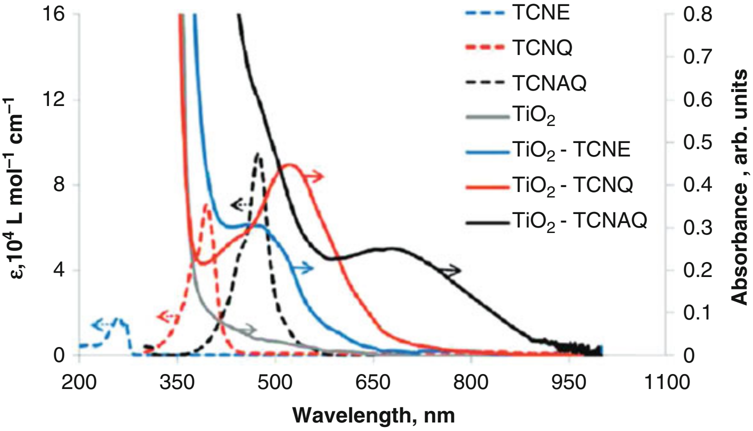

Fig. 10.2 Absorption spectra of tetracyanoethylene (TCNE), 7,7,8,8-tetracyanoquinodimethane (TCNQ), and 11,11,12,12-tetracyanonaphtho-2,6-quinodimethane (TCNAQ) in solution with or without anatase mesoporous films (the solvent was acetonitrile for TCNE and TCNQ and acetone for TCNAQ). The absorption shifts were attributed to interfacial charge-transfer transition from the chemisorbed molecule to the CB of TiO_2 (Reprinted with the permission from Ref. [6]. Copyright 2011 American Chemical Society)

In a given slurry reactor, this can mean that the same amount of photons is absorbed over a different path length (Fig. 10.3), that is, by a lower number of primary particles, if the actual particles are smaller. On the other hand, the recombination of charge carriers being predominantly confined within primary particles is not much affected by aggregation and agglomeration. Accordingly, because of the shorter path length for complete absorption when the particles are better dispersed, the absorption of a high number of photons by each of only some of the primary particles can be less effective than the absorption of a lower number of photons by each of a higher number of primary particles. In other words, the optical change arising from aggregation and agglomeration can reverse the photocatalytic effect expected from finer actual particles for other causes. This has been elegantly shown and discussed by Egerton [8]. The net effect obviously depends on the incident radiant flux. It has been shown to also depend on the reactant: the occurrence of smaller actual particles can matter more for a reactant, like dichloroacetate [8], possibly because its removal has been thought to be favored by close contact with the photocatalyst [9], which could counterbalance the attenuation of the incident beam over a shorter distance (Fig. 10.3).

In practice, one should be aware that TiO_2 modifications by, for instance, sintering, doping, or metal deposition, can change the degree of aggregation of the particles. Consequently, the comparisons of photocatalytic rates before and after these modifications can be affected by this factor in combination with the expected effects (see Sect. 10.6). Control experiments are therefore necessary to differentiate the modification effects according to the conditions of the photocatalytic reactions.

10.2.2 Charge Thermalization

If the photons used to excite TiO_2 have an energy higher than that of the bandgap, electrons with an energy higher than that of the CB bottom are generated; correspondingly, holes with an energy lower than that of the VB top are also generated. A strong coupling of these "hot" charges with phonon modes may lead to thermalization even at room temperature, that is, the excess energy of these charges with respect to their respective band edges is dissipated. This can occur very rapidly; for example, a ~300 fs value was reported [10] for electron thermalization in the case of Evonik/Degussa TiO_2 P-25 (which is used as a kind of reference to comparatively evaluate the photocatalytic efficiency, even though variations have been observed according to the P-25 batch).

However, trapping or direct transfer to adsorbates taking place before thermalization of "hot" charges has been mentioned on the basis of convincing experiments (Fig. 10.4) [11, 12], presumably because these events can sometimes be faster than thermalization [13]. A transfer to adsorbates of the phonon energy, which would be increased by thermalization, has also been suggested [12] and thought to possibly be capable of producing chemical changes. A strong interaction of adsorbates with the TiO_2 surface, such as in the cases of 2-hydroxybenzoic acid [11] and methanol

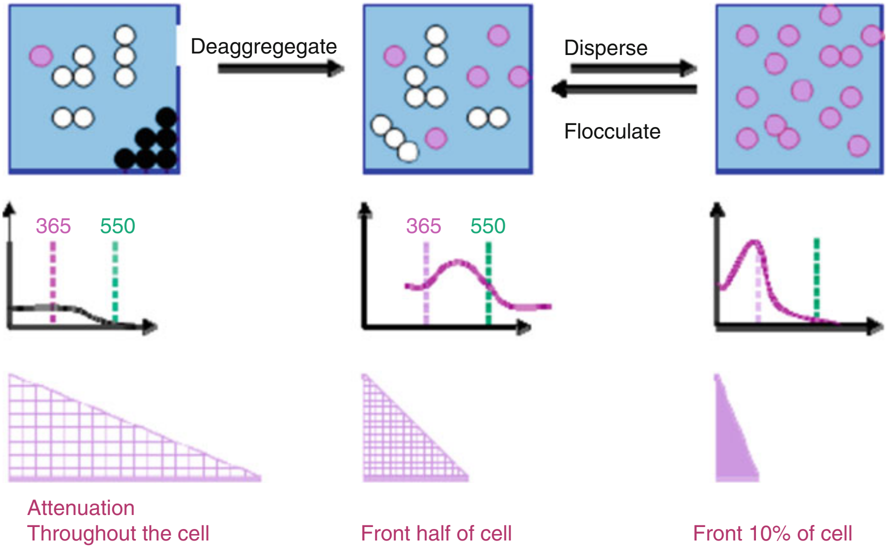

Fig. 10.3 A schematic depiction of the effects of increased UV absorption in relation to the dispersion of the TiO_2 particles. The second and third rows illustrate qualitative changes in, respectively, the transmission spectrum and the attenuation of the incident UV beam as the particle dispersion is altered in the way shown in the top row (Reprinted from Ref. [8])

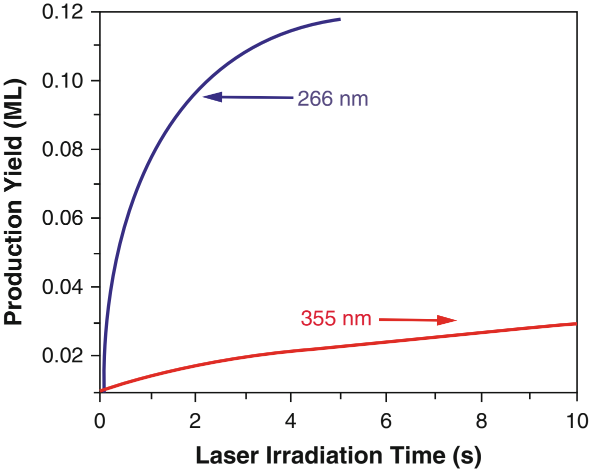

Fig. 10.4 Wavelength effect at equal irradiance upon the formation of water from a 0.5 ML methanol-covered rutile (110) surface (Reprinted with the permission from Ref. [12]. Copyright 2013 American Chemical Society)

(with respect to aliphatic alcohols with long chains) [12], should obviously be favorable to these transfers of charge or energy.

In practice, fast charge thermalization and energy dissipation to the lattice could mean that in many cases, nevertheless, no benefit for increasing the rates of photocatalytic reactions can be expected from using excitation energies in excess of the bandgap, in spite of the more reductive or more oxidative power of the charge carriers generated initially.

10.2.3 Transport to the Surface, Trapping, Detrapping, and Recombination of Charges

As was clearly summarized by Henderson [13], the key factors in slowing down the transport of charges to the surface are structural disorders, barriers at grain boundaries, the succession of trapping and detrapping events, and electrostatics depending on the charge concentration per particle (which is related to the irradiance and the particle size). The relative importance of these factors has been discussed [13, 14]. However, it seems that no clear guidance regarding TiO_2 synthesis has been derived.

On the other hand, it has been estimated that the drift velocity of holes would be higher than that of electrons: values of ~4×10^4 cm/s [15] against ~4×10^3 cm/s [16] were calculated. On this kinetics basis, it seems that direct hole transfers to OH^- ions, H_2O, and other adsorbates, provided they are thermodynamically possible [17, 18], should be regarded as key phenomena in photocatalytic reactions.

Timescales of 50–200 fs were reported for hole trapping, while electron trapping would occur within subps [13].

Regarding photocatalytic reaction rates, trapping is obviously favorable if (1) it helps charge separation (which is not always the case); (2) it permits storage of charges; and (3) the trap sites are close to sites enabling transfer to adsorbates.

Electron energy would be decreased by a fraction of eV up to 1 eV (or ~96.5 kJ/mol) on trapping [19, 20]. According to the value of this decrease, the corresponding mid-gap states will be called shallow or deep traps. For a given sample, this energy range depends on the structural and textural heterogeneities. Adsorbates are believed to sometimes have an influence [21], inasmuch as trapping is supposed to occur mainly at surfaces or at subsurface sites.

In the case of TiO_2, Ti^{4+} cations are expected to be the electron traps, giving rise, nominally, to Ti^{3+} cations. The location of the most favorable Ti^{4+} cations as trap sites has been investigated [22]. Clearly, the surface irregularities and the coverage in OH groups intervene. In particular, Ti^{4+}-OH^- species were suggested to be preferred traps [23]. *In practice*, this means that these characteristics should be considered when trying to prepare more efficient photocatalysts.

It has been assessed that around 10 % of the Ti^{4+} cations can act as electron traps [24]. The number of trapped electrons would be on the order of 0.1–3 nm^{-2} [19, 25]. This is comparable to the average coverage of TiO_2 by OH groups. However, at room temperature, because of thermally activated detrapping and charge recombination, the capacity in trapped electrons would be around one per nanoparticle on average [26, 27].

In the absence of an electron scavenger, such as O_2, the lifetimes of trapped electrons can be very long [19, 23, 28, 29], illustrating that electron trapping can effectively hinder charge recombination. In other words, if the access of O_2 is considerably restricted, the photogenerated electrons can be kept in traps, and their effect can show even after the end of irradiation, at least in extreme cases. For instance, a post-UV irradiation antibacterial effect of TiO_2 incorporated in a resin used as a dental adhesive was attributed to a retarded exposure of the TiO_2 particles to O_2 because of the resin [30].

Undercoordinated oxygen anions are thought to be hole traps at the surface or close to it [13, 14, 31–33]. These traps would nominally correspond to Ti^{4+}-O^- species where the O atom does not carry an OH group.

It is agreed that the recombination of photoproduced charges is very predominantly non-radiative [13]. Its rate increases with increasing density in structural and textural defects and thus varies markedly.

Consequently, *in practice*, a high degree of crystallinity should be a favorable factor in photocatalysis (see Sect. 10.5.1). As one would expect, the recombination rate increases as a function of the irradiance, i.e., the number of e^-/h^+ pairs formed. This underlines that increasing the irradiance could be an inappropriate means of improving the rate of photocatalytic reactions on a cost basis.

10.2.4 Electron Transfer From or To Adsorbates

In the case of TiO_2, the dynamics of hole transfer has been studied for several adsorbates, e.g., anions (SCN^- [34, 35], I^- [26]), various alcohols [36, 37], carbohydrates [37], and 4-phenylbenzoic acid [38]. The timescales were found to span from ~100 fs to ~100 ns, depending on the adsorbate and the conditions. These timescales suggest that direct oxidation of molecules via holes can be an efficient pathway in photocatalysis.

By contrast, because of the lack of molecules spectroscopically responding to the attachment of an electron on ns–fs timescales, the dynamic studies of electron transfer to adsorbates have been limited to the methyl viologen divalent cation [39]. Consequently, it is not clear to which extent the conclusion drawn from the measurements using methyl viologen, that is, transfers involving trapped rather than free electrons, is valid for other types of adsorbates, in particular for O_2 and alkyl halides [40] which are the main molecules of interest for direct electron transfer in photocatalysis.

10.3 Roles of H_2O, O_2, O_3, and H_2O_2 in TiO_2 Photocatalysis

10.3.1 Roles of Water

Water can obviously act as a solvent and thus displace the most soluble intermediate products from the adsorbed phase to the solution phase depending on their partition coefficient. When photocatalysis is employed as a purification technique, this effect can free the surface, thus allowing for the adsorption of new amounts of the initial pollutants, which is positive if the main goal is the removal of these pollutants. By contrast, if some intermediate products must also be eliminated, e.g., because of their toxicity, this effect can be detrimental. Additionally, it can delay mineralization or at least the break down of intermediate products to smaller molecules that could be more easily removed by a subsequent, non-photocatalytic treatment.

Water can also act as a reactant with organic radicals generated by primary photocatalytic events. Incorporation of ^{18}O from $H_2{}^{18}O$ into the products could be an indication of this role provided that isotopic exchange of $H_2{}^{18}O$ with $Ti^{16}O_2$ does not occur [41, 42].

It has also been suggested that water molecules allow the moving of protons from site to site on the surface and also the moving of O atoms along and across bridging O rows [13, 14, 43].

Water easily adsorbs on TiO_2 as on some other solid oxides. Its O atom is prone to form a dative bond and its H atoms to participate in hydrogen bonds. For instance, for an undefected anatase (101) surface, the computed adsorption would correspond to the rigid structure in which the O atom is linked to an

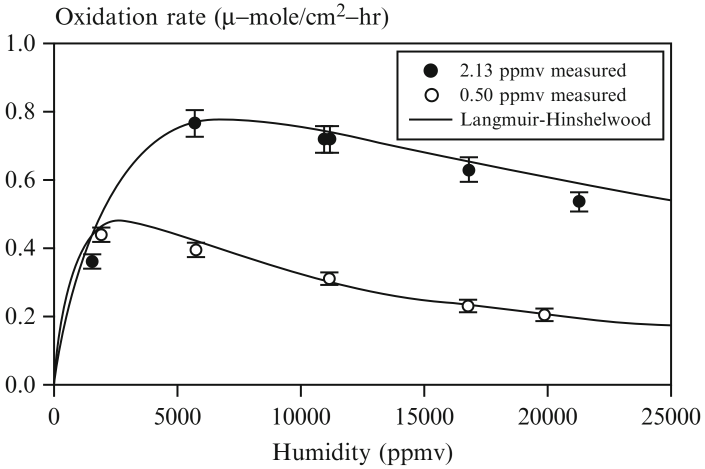

Fig. 10.5 Removal rate of toluene in synthetic air (12 cm/s face velocity) against humidity. Alumina reticulate wash coated with P-25; photon (250–350 nm) power: 33 mW/cm^2 at the photocatalyst surface (Reprinted with the permission from Ref. [44]. Copyright 1995 American Chemical Society)

undercoordinated surface Ti atom and the H atoms form H-bonds with two bridging O atoms of TiO_2 [14]. The percentage of surface atoms bonded to water molecules can be very high. Experimentally, it was established long ago that H_2O can be dissociated upon adsorption and thus supplies surface OH groups. Calculations have shown that H_2O dissociation strongly depends on the exposed facet, the water coverage, and the degree of TiO_2 reduction [14]. The direct reactions of holes with adsorbed H_2O and surface OH basic groups, nominally OH^-, have been suggested for years to be important mechanisms that generate hydroxyl radicals upon TiO_2 photoexcitation. However, it has been questioned whether these direct reactions could occur because of the respective energy levels of h^+, H_2O, and OH^- [17]. Consequently, indirect reactions involving, in addition to these species, particular surface sites such as 3-coordinate O anions and 5-coordinate Ti cations that provide proper energy conditions have been suggested for allowing hole-induced generation of hydroxyl radicals [18].

From the practical viewpoint, concerning self-cleaning materials [1] and ambient air purification [2, 3], humidity is a varying factor that can significantly modify the efficiency of these applications over time as is shown, for example, in Fig. 10.5 from Ref. [44].

10.3.2 Roles of Oxygen

When TiO_2 is immersed in liquid water or exposed to humid air – which is the case for most applications – the well-organized network of water molecules near the

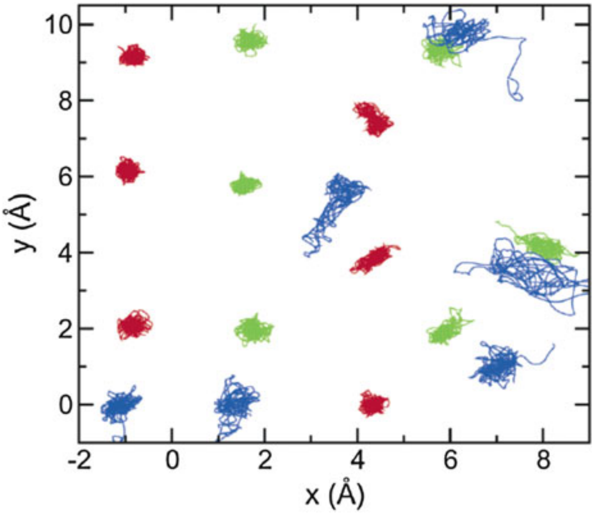

Fig. 10.6 Simulated trajectory plots illustrating that the mobility of water molecules on the anatase 101 plane at 160 K is lower in the first and second layers relative to the third layer (which corresponds to plots of significantly greater areas) (Reprinted with the permission from Ref. [45]. Copyright 2004 American Chemical Society)

TiO_2 surface (Fig. 10.6) tends to hinder the approach of O_2 molecules to the surface because the hydrogen bonds are stronger in this network than in bulk water [14, 45, 46], which makes it more difficult for O_2 molecules to form van der Waals bonds [47].

In practice, these limitations mean that the photocatalytic reactors used for water or air purification should be conceived to maximize the contact between air and TiO_2 [48].

The reaction of electrophilic O_2 with photoproduced electrons has been established long ago, principally by use of EPR, to give rise to the superoxide radical anion, $O_2^{\bullet -}$ (Eq. 10.1):

$$O_2 + e^- \rightarrow O_2^{\bullet -} \tag{10.1}$$

Other EPR signals were attributed to the ozonide radical anion, $O_3^{\bullet -}$ [49]. This latter species was assumed to result from the reaction of O_2 with a hole trapped at a surface O^{2-} anion (Eq. 10.2):

$$O^{2-} + h^+ \rightarrow O^{\bullet -}; O^{\bullet -} + O_2 \rightarrow O_3^{\bullet -}. \tag{10.2}$$

Its formation may depend on the existence of particular surface characteristics, since it has not been found on all TiO_2 samples. Moreover, $O_3^{\bullet -}$ has not been reported to be involved in photocatalytic oxidations, at least in the absence of ozone (see Sect. 10.3.3). Equations 10.1 and 10.2 tentatively suggest that O_2 could react with both types of photoproduced charge carriers; however, the electrophilicity of O_2 makes Eq. 10.1 much more probable than Eq. 10.2. Infrared bands recorded when TiO_2 was bandgap irradiated in dry air were attributed to peroxide species, $O_2^{\bullet 2-}$ [50], which are slowly transformed in superoxide (Eq. 10.3):

$$O_2^{\bullet 2-} + O_2 \rightarrow 2O_2^{\bullet -} \tag{10.3}$$

Furthermore, calculations have shown that a significant energy barrier must be overcome for the reverse reaction of Eq. 10.3, that is, to add an electron to superoxide [14]. This means that $O_2^{\bullet 2-}$ cannot be a major species in photocatalytic reactions.

Consequently, $O_2^{\bullet -}$ is the principal species to be considered as resulting from the interaction of O_2 with photoexcited TiO_2. It is often mentioned on lists of active oxygen species formed in photocatalysis. But it must not because it is poorly reactive per se toward most molecules [51]. It is also very instable; its EPR signal is detectable at low temperature (measurements are commonly performed at 77 K) but not at room temperature.

The fates of superoxide can be either productive or nonproductive regarding photocatalytic reactions. Firstly, it is supposed to yield $^{\bullet}OH$ radicals via the following Eqs. 10.1, 10.2, 10.3, and 10.4:

$$O_2^{\bullet -} + H^+ \rightarrow HO_2^{\bullet} \tag{10.4}$$

$$2\,HO_2^{\bullet} \rightarrow H_2O_2 + O_2 \tag{10.5}$$

$$H_2O_2 + e^- \rightarrow {}^{\bullet}OH + OH^- \tag{10.6}$$

$$H_2O_2 + O_2^{\bullet -} \rightarrow {}^{\bullet}OH + OH^- + O_2 \tag{10.7}$$

Equation 10.5 involves the encounter of two radicals, which means that its probability of occurring should be low. Equation 10.6 corresponds to the scavenging of a second electron in competition with Eq. 10.1. As O_2 is readily available in most potential applications of photocatalysis (air and water purification, self-cleaning materials), whereas H_2O_2 is a reaction product, Eq. 10.1 should be favored. Indeed, the addition of catalase, an enzyme which catalyzes the following overall reaction (Eq. 10.8):

$$2\,H_2O_2 \rightarrow 2\,H_2O + O_2 \tag{10.8}$$

caused a relatively moderate effect on the removal rate of 1,2-dimethoxybenzene in a P-25 aqueous suspension [52]. In other words, the low probability of these reactions (particularly, Eqs. 10.5 and 10.6) indicates that forming $^{\bullet}OH$ radicals through this pathway is not expected to be efficient.

Secondly, the radical anion superoxide has been suggested to react with organic radical cations arising from the reaction of holes with electron-rich molecules, such as aromatics carrying electron-donating substituents. Although this reaction involves instable species, its involvement was substantiated by use of Cu, Zn-superoxide dismutase (SOD) which catalyzes the following overall reaction (Eq. 10.9):

$$2\,O_2^{\bullet -} + 2\,H^+ \rightarrow O_2 + H_2O_2. \tag{10.9}$$

The test molecules were 1,2-dimethoxybenzene [52] and benzo[b]pyridine (or quinoline) [53] in TiO_2 aqueous suspensions. Added SOD markedly decreased the removal rates of these molecules and furthermore changed the distribution of the intermediate products. In particular, in the case of quinoline [53], it was very detrimental to the formation of the intermediate products attributed to the reaction of the quinolinium radical cation with superoxide. In addition, control experiments showed that the SOD effect was not due to a competition between SOD and the test molecules [52].

Thirdly, the reaction of the radical anion superoxide with a hole has been thought to produce, intermediately, singlet molecular oxygen [47, 54, 55], $^1O_2$, an active oxidizing entity (Eq. 10.10):

$$O_2^{\bullet -} + h^+ \rightarrow {}^1O_2 \rightarrow O_2 + \text{energy} \tag{10.10}$$

However, given the instability of singlet molecular oxygen, it is usually considered that scavenging of holes by $O_2^{\bullet -}$ yields mostly triplet molecular oxygen directly, the energy release between the singlet and triplet being about 1 eV (or ~96.5 kJ/mol). This pathway nominally corresponds to the recombination of the photogenerated charge carriers via O_2, which is by essence counterproductive to effect photocatalytic reactions.

In fact, reaction of $O_2^{\bullet -}$ with a hole, nominally $O^{\bullet -}$, has been suggested to cause oxygen isotope exchange (OIE) between gaseous $^{18}O_2$ and photoexcited $Ti^{16}O_2$ [47]. This suggestion was based on the lowering of the bond strengths in surface Ti^{4+}-$^{16}O^{2-}$ and in $^{18}O_2$, which would arise from scavenging of holes or electrons, respectively. These lower bond strengths were thought to permit both (1) easier removal of a ^{16}O atom from Ti^{4+}-$^{16}O^{\bullet -}$ because the decrease charge of $O^{\bullet -}$ with respect to O^{2-} should weaken the interaction with the neighboring Ti^{4+} and (2) splitting of $^{18}O_2$ and $^{18}O^{16}O$ because the added electron in $^{18}O_2^{\bullet -}$ and $^{18}O^{16}O^{\bullet -}$ is located in an antibonding orbital. Indeed, an increase in O–O bond length from ~0.122 nm for gaseous O_2 to ~0.137 nm for free $O_2^{\bullet -}$ [56] and ~0.133 nm for $O_2^{\bullet -}$ adsorbed on TiO_2 [57] has been reported. On the other hand, the removal of ^{16}O atoms is evidently favored for the ^{16}O atoms that are coordinatively unsaturated. Accordingly, OIE can be considered as a method for probing the lability of surface O atoms [47, 58, 59].

The comparison of the OIE rate with gas-phase methanol removal rate has shown that sintering of TiO_2 at various temperatures caused more pronounced decreases in efficiency for OIE [59]. This difference was interpreted by considering that, unlike OIE, the formation of methanal from methanol does not require abstraction of oxygen atoms from TiO_2 whose possibility was impaired by

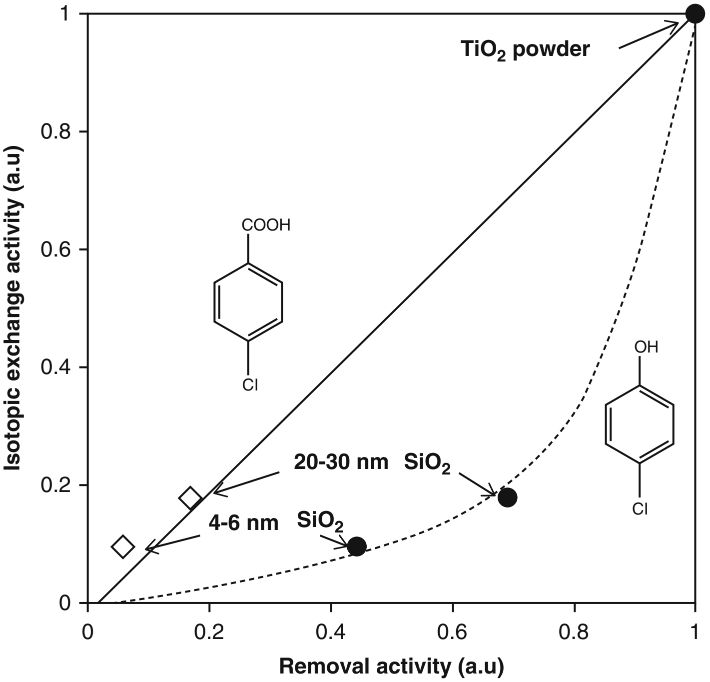

Fig. 10.7 Comparative plots of the rates of gaseous $^{18}O_2$ isotopic exchange with $Ti^{16}O_2$ and 4-chlorobenzoic acid or 4-chlorophenol photocatalytic removal in water for TiO_2 (Cristal/Millennium PC 50) as a powder or in a coating, containing 50 wt% of SiO_2 (particle size as indicated), on a fiber glass tissue (Reprinted from Ref. [9]. Copyright 2007, with permission from Elsevier)

sintering. A similar comparison between naked P-25 and P-25 onto which 2–8 wt% Se was deposited allowed one to infer that the selenate ions were preferentially adsorbed, and subsequently reduced, on surface irregularities, thus drastically decreasing and even suppressing the availability of labile surface O atoms needed for OIE [58]. Also, a comparison of aqueous-phase removal rates of 4-chlorophenol or 4-chlorobenzoic acid with the OIE rate for powder or coated TiO_2, with all values normalized (Fig. 10.7), led to the conclusion that 4-chlorobenzoic acid is more favored by access to the TiO_2 surface than is 4-chlorophenol [9]; however, this last comparison must be regarded as semiquantitative because the reactions were performed under very different conditions (aqueous phase vs. gas phase).

Regarding the question of the involvement of surface O atoms in photocatalytic oxidations, a study [60] of the products of the photocatalytic oxidation of CH_3Cl by $^{18}O_2$ on the 110 face of a $Ti^{16}O_2$ rutile single crystal showed that CO contained only ^{18}O, and HCHO was predominantly labeled with ^{18}O. This incorporation of ^{18}O could not come from a significant replacement of surface ^{16}O by surface ^{18}O as a result of OIE. Indeed, it has been reported that OIE was not observed in the presence of methylpropane (or isobutane) over a layer of powder TiO_2 [47]. These observations may mean that holes and superoxide preferentially form hydroxyl radicals (through, respectively, the oxidative and reductive pathways), which then react with the organic, rather than interacting together to effect OIE as mentioned in the next-to-last paragraph, which requires the lability of O atoms.

These conclusions have been supported by a study of the oxidation of adsorbed HCOOH in either O_2 or He [41]. Only about 3.7 % of surface O atoms of P-25 coated on Pyrex glass were calculated to be incorporated in the products of HCOOH.

In addition to scavenging electrons, molecular oxygen can also react with alkyl radicals or, more generally, organic radicals thought to be formed by H abstraction, yielding peroxyl radicals, $RO_2^\bullet$ [61–63]. The following equations have been proposed for the photocatalytic transformations of aliphatic alkyl radicals:

$$\begin{aligned}&RH + {}^\bullet OH \rightarrow R^\bullet + H_2O\\&R^\bullet + O_2 \rightarrow RO_2^\bullet\end{aligned}$$

On the basis of data provided by radiochemists, $RO_2^\bullet$ radicals may yield alkyl radicals, $R^\bullet$, and alkoxy radicals, $RO^\bullet$:

$$\begin{aligned}&RO_2^\bullet + RH \rightarrow ROOH + R^\bullet\\&ROOH \rightarrow RO^\bullet + {}^\bullet OH\\&2\,RO_2^\bullet \rightarrow 2\,RO^\bullet + O_2\end{aligned}$$

Depending on the chemical structure of the $RO^\bullet$ radical (hereafter, $RCH_2O^\bullet$ is shown as an example), the following reactions are suggested to take place:

$$\begin{aligned}&RCH_2O^\bullet \rightarrow RCHO + H^\bullet \quad \text{(according to the stability of } RCH_2O^\bullet\text{)}\\&RCH_2O^\bullet + O_2 \rightarrow RCHO + HO_2^\bullet\\&RCH_2O^\bullet + RH \rightarrow RCH_2OH + R^\bullet\end{aligned}$$

The last reaction is less probable than the next to last because it involves the initial pollutants and their intermediate products whose concentrations are much lower than that of O_2.

In the case of benzene rings, a hydroxyl radical is supposed to be added to the ring, the resulting hydroxycyclohexadienyl radical adding dioxygen and eliminating a hydroperoxyl radical. The same organic radical is also supposed to be formed by initial hole attack of the ring, followed by water addition and deprotonation (see Sect. 10.4.1) [48, 55].

10.3.3 Effect of Adding Ozone

With the electron affinity of O_3 (2.1 eV) being much higher than that of O_2 (0.44 eV), it was thought that adding O_3 in pure O_2 or in air could be a means of boosting the scavenging of the electrons, that have been photopromoted to the CB, either directly

$$e^- + O_3 \rightarrow O^{\bullet -} + O_2$$

or indirectly

$$O_2^{\bullet -} + O_3 \rightarrow O_2 + O_3^{\bullet -}$$

The radical anion $O_3^{\bullet -}$ is more unstable than O_3 and can presumably split easily at the surface of TiO_2:

$$O_3^{\bullet -} \rightarrow O^{\bullet -} + O_2$$

It might also react with adsorbed water:

$$O_3^{\bullet -} + H_2O \rightarrow {}^{\bullet}OH + OH^- + O_2$$

Furthermore, the increase in the scavenging rate of photogenerated electrons due the presence of ozone should decrease the recombination rate of electrons and holes and thus augment the formation rate of hydroxyl radicals from basic OH surface groups and adsorbed water molecules (see Sect. 10.3.1).

Through all these mechanisms, very oxidizing species, viz., $O^{\bullet -}$ and ${}^{\bullet}OH$, would be generated. Accordingly, the photocatalytic rates for removal and mineralization of organic pollutants in air and water should be increased as has been demonstrated for both gas-phase and aqueous-phase TiO_2 photocatalysis using non-photoexcited ozone.

However, O_3 can also scavenge hydroxyl radicals:

$$O_3 + {}^{\bullet}OH \rightarrow O_2 + HO_2^{\bullet}$$

thereby restraining the favorable effect (Fig. 10.8) [64].

In practice, because ozone is used in some industrial processes, TiO_2 photocatalysis could be of interest for exploiting the presence of ozone to eliminate and mineralize pollutants at higher rates while removing excess ozone. If ozone is not employed on-site for other purposes, the cost of its generation for only improving the photocatalytic rates can be prohibitive; the interest of adding it in a photocatalytic purification process will then depend on the case and regulations. Besides, in the particular situation when gaseous effluents are treated by nonthermal (or cold) plasma (which implies that the concentrations of pollutants are high enough to allow this homogeneous method to be cost-effective), the ozone formed by the plasma could appropriately be used to complete the purification in a photocatalytic reactor located behind the plasma reactor [65].

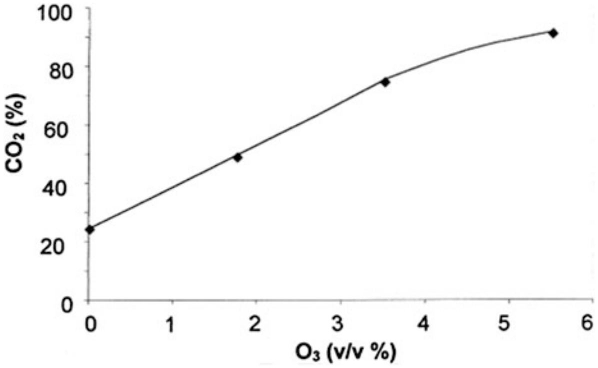

Fig. 10.8 Stationary-state percentages (relative to total mineralization) of CO_2 formed from n-octane (130 pppv) over UV-irradiated TiO_2 in flowing O_2 (24 L/h) containing various volumic percentages of O_3 (Reprinted from Ref. [64]. Copyright 2000, with permission from Elsevier)

10.3.4 Effect of Adding Hydrogen Peroxide

Adding H_2O_2 to the water to be photocatalytically treated can be a means of increasing O_2 concentration at the TiO_2 surface because H_2O_2dismutates to H_2O and O_2 over UV-irradiated TiO2 [66]. H_2O_2 can also scavenge electrons, as its electron affinity is close to that of O_2 [67], forming $^{\bullet}OH$ radicals and decreasing the recombination rate of charge carriers (Eq. 10.3) However, H_2O_2 can also consume hydroxyl radicals, which is counterproductive:

$$^{\bullet}OH + H_2O_2 \rightarrow H_2O + HO_2^{\bullet}.$$

From the practical viewpoint, the net effect depends on the type of water, the TiO_2 specimen, and other experimental conditions, especially the added amount of H_2O_2 [52]. Reported beneficial effects are less than one order of magnitude. Some companies, such as Purifics ES Inc. (www.purifics.com), have reported employing H_2O_2, though only in a few cases, as an additive in their photocatalytic process of water purification.

10.4 Removal of Organic Matter

The removal of organic compounds is at the basis of the photocatalytic applications for self-cleaning materials [1] and water [4] and air [2, 3, 47] purification. The activation and elimination of microorganisms [68, 69] is also relevant to this topic, since microorganisms are made of organic matter. However, the particular aspects regarding microorganisms have been thought to be beyond the scope of this chapter. Obtaining a clean TiO_2 coating by removing organic compounds has also been demonstrated to be at least a precondition to the phenomenon of superhydrophilicity [70] which also contributes to the self-cleaning properties of glass, even though additional interpretations have been advanced to explain the reversibility of this phenomenon [71].

10.4.1 $^{\bullet}$OH-Mediated Versus h^+-Mediated Pathways

It is generally admitted that in photocatalysis, chemical compounds are initially attacked mainly by either $^{\bullet}$OH radicals or holes. The latter attack type, which is also called single-electron transfer (SET), necessarily occurs at the surface. The former attack type could also take place in the water layers close to the surface when the photocatalyst is exposed to liquid water or humid air. This possibility is based on diverse reasoning [9, 47, 55, 72, 73].

Regarding the influence of the characteristics of TiO_2 upon directing initial attacks to either $^{\bullet}$OH or h^+, a surface with a high density of coordinatively unsaturated O^{2-} ions should favor hole trapping and possibly facilitate hole transfer to adsorbed compounds. Simultaneously, surface irregularities are also a favorable factor to increase the adsorbed quantity of some molecules and hence hole transfer to these molecules. Conversely, as aforementioned, these irregularities can also act as recombination sites of photoproduced charges. *In practice*, the choice or design of a photocatalyst for a given case will always need trials.

Whether the initial attack occurs preferentially with $^{\bullet}$OH radicals or holes depends on the nature of the molecules and chemical moieties.

For benzene derivatives, both attack types can give rise to the same intermediate organic radical (Fig. 10.9), so that they cannot be distinguished (see Sect. 10.3.2) [48, 55]. However, they can be distinguished in the case of molecules that yield different primary products through the two pathways. For that, the following molecules have been proposed: benzo[b]pyridine (or quinoline) [53]; 4-methoxy-1,3-benzenediol (or 4-methoxyresorcinol) [74]; and 1-(4-methoxyphenyl)-2,2-dimethylpropan-1-ol (or 1-anisylneopentanol) [74]. Additionally, comparison of the photocatalytic primary products of these molecules with those resulting from processes, such as photo-Fenton, generating only $^{\bullet}$OH radicals has also been employed to determine the preferential pathway [53].

For carboxylic acids, easy adsorption via the carboxylic group, if it is not sterically hindered, should favor the SET pathway. In the case of alcohols,

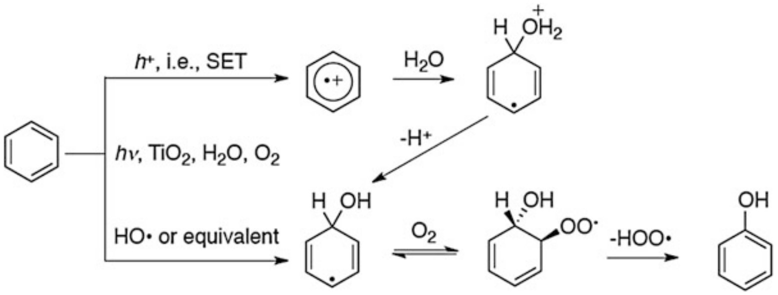

Fig. 10.9 Postulated mechanisms of the photocatalytic transformation of a benzene ring through hole-induced or hydroxyl radical-induced initial attacks (Adapted from Ref. [55] by permission of John Wiley & Sons Ltd)

scavenging of holes by methanol has been derived from time-resolved photoconductivity measurements [59] and is also in line with the interpretation of current doubling observed with this alcohol. However, alcohols can also react with $^{\bullet}$OH radicals. In that respect, the use of alcohols as $^{\bullet}$OH scavengers to evidence the role of $^{\bullet}$OH radicals in the photocatalytic oxidation of other compounds can be questioned. Nevertheless, 2-methylpropan-2-ol (or tertiobutanol) might be employed to this purpose, at least at concentrations similar to that of the studied compound, because of the steric hindrance of the alcohol OH group limiting the adsorbed amount and hence the SET pathway [55].

Alkanes are poorly adsorbed, and the alkyl parts of molecules containing chemical groups susceptible to form bonds with the photocatalyst surface are oriented away from the surface. Accordingly, alkanes and alkyl parts [63] are thought to be prone to react with $^{\bullet}$OH radicals rather than directly with holes.

From the practical viewpoint, it is obvious that in the case of water photocatalytic treatment, assuring as good as possible aeration enables both the formation of $^{\bullet}$OH radicals through the route starting by O_2 reduction and the necessary supply of molecular oxygen that acts as a reactant to transform organic radicals (see Sect. 10.3.2).

10.4.2 Types of Intermediate Products of Photocatalytic Degradation

Identifying and quantitating the primary intermediate products that are formed from the initial pollutants (as checked via thorough analyses of the fluid to be treated) are essential in the efficiency evaluation. To assist this evaluation, the numerous papers reporting which intermediate products are produced from the many molecules whose photocatalytic degradation has been investigated are of course very important, at least in the cases where identification was correctly performed and as comprehensive as possible. For example, it has been shown that benzene rings are degraded through ring hydroxylation, OH substitution, ring opening, and oxidation of the alkyl groups present in the substituents. When the degradation is prolonged, oxidation products containing alcohol, carbonyl, and carboxyl groups are expected to be formed from the primary intermediate products. Most often, acetate and formate ions correspond to the major fraction of compounds in the last stages of the degradation [48].

Formation of intermediate products resulting from coupling of organic radicals has been observed; however, that was in laboratory experiments for initial pollutant concentrations much higher than those usually expected in waters to be treated [48]. Therefore, these counterproductive products should normally not be a problem in practice.

The formation of Cl^- ions from Cl atoms directly attached to aromatic rings occurs relatively easily. Mineralization of organic N atoms present in either substituents or in aromatic rings leads to both ammonium and nitrate ions depending mainly on the oxidation number of N in the initial compound, though the occurrence of reductive steps has been reported [40]. The C-N = N-C groups, where N is at the oxidation number −1, are oxidized to N_2, known as one of the best leaving group, as it is the case with other oxidation methods [75].

From a practical viewpoint, it is possible to predict which will be the intermediate products of given pollutants on the basis of both the photocatalysis literature and common knowledge in organic chemistry. These predictions should help both to look for specific intermediate products and to optimize the operational conditions.

10.5 Effects of Structural/Textural Characteristics of Pristine TiO_2 upon the Photocatalytic Efficiency

10.5.1 Effect of Crystallinity

As aforementioned, increased crystallinity should induce higher photocatalytic efficiency (Fig. 10.10 from reference [76]) because the surface dangling bonds and the distorted lattice are thought to behave as recombination centers and traps of

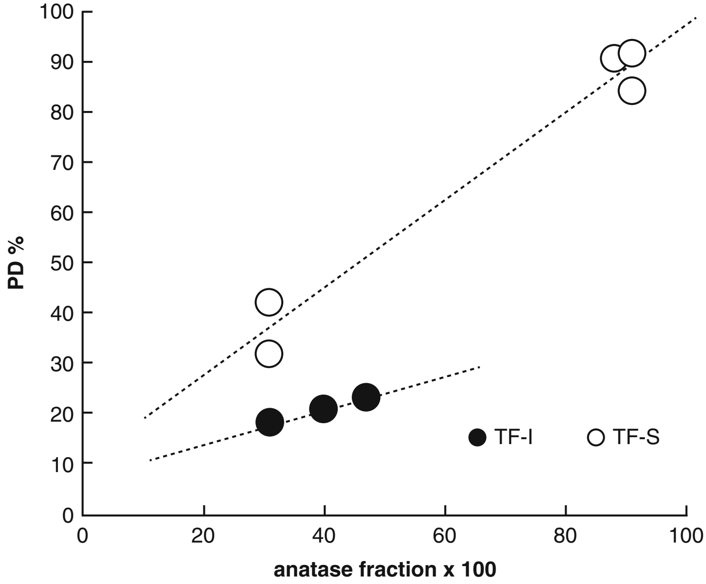

Fig. 10.10 Percentage (PD %) of 2-hydroxybenzoic acid removed against the crystallinity of mesoporous anatase films (expressed as a fraction relative to the content of amorphous TiO_2) deposited on indium tin oxide (*filled circles*) or silicon (*open circles*) (Reprinted with the permission from Ref. [76]. Copyright 2007 American Chemical Society)

photoproduced charges. However, the simultaneous decreases in surface area and surface coverage by hydroxyl groups associated with increased crystallinity can be detrimental to the photocatalytic efficiency.

In practice, because of these opposite effects, tests for the targeted photocatalytic application will hence be needed after increasing the crystallinity via adjustment of the preparation parameters and/or post-preparation sintering, even though amorphous samples are, in general, poorly efficient.

10.5.2 Effect of the Allotropic Form

In a previous review [48], this author drew the attention on the fact that it cannot be claimed that one TiO_2 allotropic form is always more photocatalytically efficient than another one. Obviously, as in thermally activated catalysis, many factors intervene, so that the efficiency of a given allotropic form covers a wide range. Accordingly, the photocatalytic efficiency of powder anatase and rutile samples (and other allotropic forms) overlaps. Valuable comparisons between fully crystallized allotropic forms should involve (1) samples of similar size, porosity, and morphology, (2) the use of a series of probe molecules to test the efficiency, and (3) irradiance conditions under which the number of potentially absorbable photons is equivalent. In the case of single crystals, a comparison of the anatase 001 face with the rutile 110 face has shown close initial rates of CO_2 formation from an adsorbed layer of trimethylacetate [77].

Perhaps principally because P-25 contains anatase and about 20 % of rutile, there has been a lot of research on the interest of utilizing anatase/rutile mixtures to increase the photocatalytic efficiency. Many reasons for the "high" efficiency of P-25 have been suggested as was effectively summarized by Henderson [13]. In particular, the properties of the interfaces between the two allotropic forms were thought to facilitate the separation of the photoproduced charges because of appropriate energy differences in either the conduction band edges or the electron trap sites. However, the use of various anatase/rutile ratios did not really clarify the interpretation of the presumed synergistic effect. The optimal ratio was found to be comprised between <10 % and >70 % of rutile depending on both the preparation method and the photocatalytic reaction. This last dependency stresses again the need of employing a series of adequately selected probe molecules [9]. Indeed, it was shown by use of 5 reactions that the photocatalytic efficiency of 35 commercial powders could be represented by a linear combination of 6 TiO_2 characteristics, viz., the contents in anatase and rutile, the particle shape and the particle size (see the following Sections), the surface area, and the density of lattice defects. The weight of each characteristic depended on the reaction [78].

10.5.3 Effect of the Particle Shape: Case of TiO_2 Nanotubes

The importance of the particle shape is related to the development of facets with differing photocatalytic efficiencies [78–80]. Consequently, polyhedral particles have been reported to exhibit, in general, a higher efficiency than spherical ones (Fig. 10.11) [81]. In addition to the effects of facets per se, the shape can also influence the density of surface structural defects [82]. These defects have been shown to modify the efficiency by both attracting or repelling one of the charge carriers and changing the adsorption properties.

TiO_2 can be shaped as tubes (or also rods and wires). TiO_2 nanotubes (TNT) have mainly been used in dye-sensitized solar cells, essentially because of a higher transport rate of electrons. Regarding the use of TNT for the photocatalytic removal of pollutants, reports are scarce. Nevertheless, an analysis of the only studies allowing meaningful comparisons has shown no major improvement with TNT compared to nanoparticles [83]. This result could partially be due to TNT texture disorders and/or to the question of the exposed planes of TiO_2. It could also come from the fact that the properties influencing the efficiency are more numerous, their interrelations more complex, and their effects more important for pollutant removal than for dye-sensitized solar cells and photoelectrocatalysis where the electron transport rate is the crucial parameter. The issue of the long-term stability of the photocatalytic efficiency of the TNT during the photocatalytic removal of pollutants should also be addressed

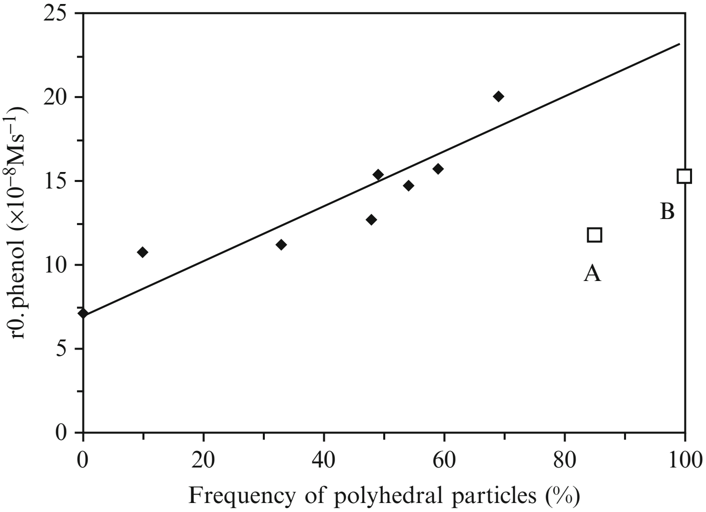

Fig. 10.11 Initial rate of phenol photocatalytic removal in liquid water against the frequency of particles with polyhedral shape (as determined by statistical examination of TEM images) for various flame-reactor-prepared TiO_2. The *open squares* correspond to two P-25 batches of same surface area containing, respectively, 20 % (A) or 10 % (B) of rutile (Reprinted from Ref. [81]. Copyright 2008, with permission from Elsevier)

10.5.4 Effect of the Particle Size

As aforementioned, there is a trade-off between: (1) the adsorbed amounts of the reactants and the surface coverage in hydroxyl groups both of which are considered to be favorable factors for the photocatalytic rates (these factors increase with the surface area and hence with decreasing particle sizes) and (2) the unfavorable recombination rate of the photoproduced charges at the structural irregularities whose density should be higher on smaller particles [84]. Also, the effect of the actual particle size on the absorption and scattering of useful photons is a parameter to be taken into account [8] (see Sect. 10.2.1). *In practice*, appropriate trials are required.

10.5.5 Effect of Porosity

Pores can affect, positively or negatively, the adsorbed amounts of the compounds to be transformed and the absorption and scattering of useful photons. *In practice*, case-by-case trials are necessary to evaluate the photocatalytic influence of the porosity of given specimens of TiO_2.

10.5.6 Effect of Film Thickness

With increasing film thickness, favorable photon absorption and ordering of TiO_2 tetrahedrons increase, whereas unfavorable nanostructural clustering decreases. An optimal film thickness is thus found for each film preparation and each photocatalytic reaction.

From the practical viewpoint regarding the cost of a photocatalytic treatment of water, the possible higher efficiency of suspended TiO_2 relative to that of TiO_2 films can prevail over the separation cost of the TiO_2 powder at the end of the treatment. Filtration on a ceramic membrane – which does not need to be cleaned – and continuous reuse of TiO_2 have also been patented and claimed to be cost-effective (http://www.purifics.com).

10.6 Photocatalytic Effects of TiO_2 Modifications

10.6.1 Effects of Metal Deposits

The deposition on TiO_2 of Pt and other group VIII metals, such as Rh, Pd, and Ir, was essentially motivated by the expectancy of (1) obtaining better charge carrier separation, the electrons being attracted to the metal particles, while the holes mainly remain on TiO_2, and (2) taking advantage of the known catalytic properties of these metals to recombine H atoms to produce H_2 from some organic compounds, in particular alcohols (methanol was most often used in the tests), and possibly from water. The first property was also expected to make the reduction of O_2 easier and hence improve the formation of $^{\bullet}OH$ radicals through this pathway. Other beneficial effects can also occur. For instance, the adsorption on the metal of a reactant or an intermediate product, e.g., CO [85–88] that is poorly adsorbed on TiO_2, can be favorable. In several cases, it has also been observed that the metal particles facilitate the de-agglomeration of the TiO_2 grains and thereby could allow, inter alia, a better contact of TiO_2 with the reactants and improved irradiation (however, see Sect. 10.2.1).

Regarding the photocatalytic efficiency for H_2 formation particularly from alcohols, the existence of an optimal and low amount of metal was pointed out early. Depending on the TiO_2 sample, the metal, the deposition/reducing method, and the photocatalytic reaction, it varied between ~0.5 wt% and ~1 wt% (Fig. 10.12 from Ref. [89]). Several reasons have been suggested to explain this optimum. At a too high amount, the blocking/shielding of the TiO_2 surface by the metal particles [90] and/or, possibly, a decrease in the density of surface OH groups would overcome the advantages of the metal deposits. However, calculations based on the relative sizes of TiO_2 and Pt particles for a series of samples where the Pt particle size did not vary much with the Pt % allowed one to show that the increase in the blocking/shielding of the TiO_2 surface was not a major factor [91]. It was then suggested that the unfavorable recombination of photoproduced charges at the numerous Pt particles beyond the optimum became dominant with respect to charge carrier separation because of the increased probability of encounters between opposite charges at the Pt particles.

An effect of the metal particle size on the photocatalytic efficiency has also been observed, especially with Ag and Au whose particle size varies more with the loading and the deposition method than that of group VIII metals. Increased TiO_2-metal interfacial area in the case of smaller metal particles has been found to be favorable as one would a priori expect.

The presence of metal ions in the metal deposits can be significant in the case of group Ib metals (Cu, Ag, Au). Not surprisingly, the photocatalytic efficiency can be affected; however, in practice, it is difficult to indicate favorable ionic/metallic ratios. For Pt deposits, XPS spectra showed that Pt• was the sole species present, at least for samples prepared using thermal reduction in a hydrogen flow [91].

Even with TiO_2 samples having the optimal content of Pt (as was determined in the case of photocatalytic dehydrogenation reactions), a positive effect on photocatalytic oxidations that do not involve H_2 evolution has not always been observed. This suggests that the influence of Pt deposits on charge separation was not really fundamental and/or that the overall reduction of O_2 was not really improved contrary to the aforementioned expectancies. The role of Pt to combine H atoms is therefore essential [91] as was recently confirmed in a study which also concluded that H^+ reduction occurs first on TiO_2 [92].

Metal deposits can also induce a sensitivity of the metal/TiO_2 photocatalyst to the visible spectral region because of metal plasmonic transitions. That has been

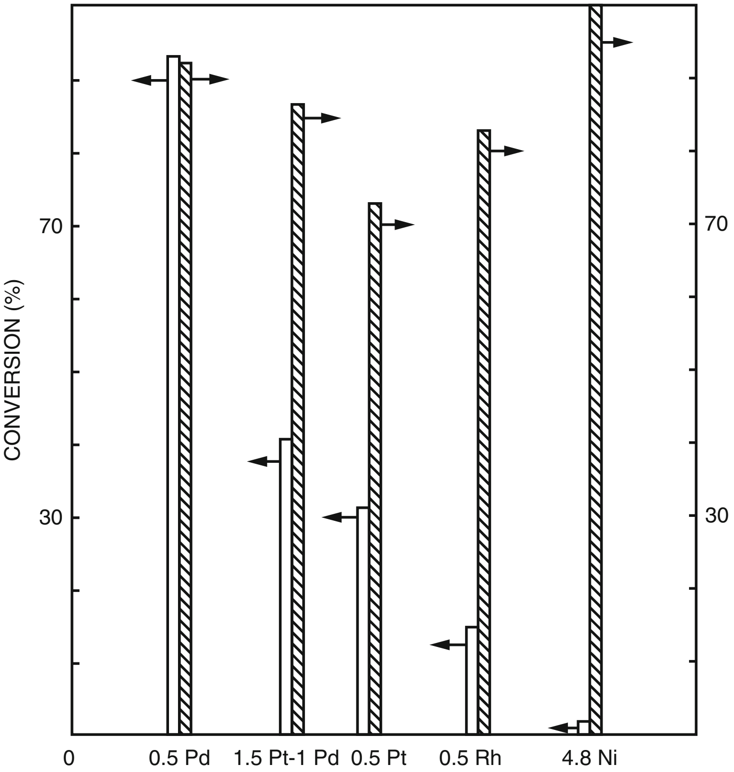

Fig. 10.12 Influence of the nature of the metal deposited on TiO_2 upon the photocatalytic hydrogenation of diphenylethyne using propan-2-ol as hydrogen source. The ordinate axes show the total conversion of diphenylethyne and the selectivity (diphenyl ethane was also formed) toward cis and trans diphenylethenes (or stilbenes) after irradiation of suspensions containing 70 mg of metal/TiO_2 photocatalyst and 0.94 mmol of reactant in 20 mL of propan-2-ol for 3 h (radiant power: ~56 mW cm^{-2} at 365 nm (mercury lamp)). The numbers below the abscissa axis indicate the wt% of deposited metal(s) (Reprinted from Ref. [89]. Copyright 1994, with permission from Elsevier)

reported for Ag in particular [93]. Although this sensitivity undoubtedly presents a fundamental interest, it can be questioned whether it might be exploitable.

In practice, the metals found to be the most efficient (Fig. 10.12) [89] are expensive and could be not cost-effective for producing H_2 from organic compounds [87, 94]. In the case of water splitting, the critical issue remains that of the efficiency, not the cost of the photocatalyst.

10.6.2 Effects of Doping

The main objective of doping TiO_2 is to create additional electronic states, especially within the bandgap, in attempts to use longer wavelengths to effect photocatalytic reactions – particularly for taking advantage of the visible region

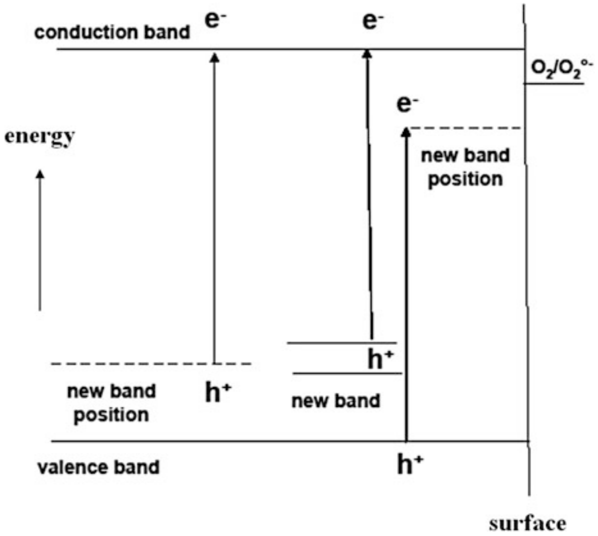

Fig. 10.13 Schematic illustration of the potential possibilities of reducing the photon energy needed to promote electrons in an n-type semiconductor like TiO_2 by shifting the bands or creating a new band within the bandgap. Band bending near the surface is not shown

of solar light. Doping can be achieved by making TiO_2 nonstoichiometric via reduction and, above all, by substitution of foreign atoms for Ti or O atoms or inclusion of foreign atoms at interstitial locations in the TiO_2 lattice. Depending on various factors, these foreign ions can form either a band (Fig. 10.13) or be discrete. In the latter case, the mobility of charges located in these energy states is low, so that these charges are prone to recombine before reaching the surface and thus do not participate in photocatalytic reactions. Furthermore, native point defects, corresponding to charge imbalance, may behave as recombination centers of photoproduced charges and be thereby counterproductive.

10.6.2.1 Effects of Self-Doping

Reduction of TiO_2 can provide samples that can be excited under visible light (in the blue spectral region). This excitation is thought to be due to Ti^{3+} sites, mostly interstitial, arising from O loss and thus corresponding to n-type self-doping. Multiple Ti^{3+} sites can exist as was deduced from EPR signals long ago. At 77 K, these signals can disappear under sub-bandgap irradiation and reappear in the dark, illustrating that a photoinduced, reversible transition of electrons to the CB had occurred.

It has been shown that irreversible oxygen vacancies can result from a plasma treatment of TiO_2 and that the samples obtained are photocatalytically active under visible-light irradiation [95].

10.6.2.2 Effects of Cation Doping

Many cations and methods have been used for doping TiO_2 [13, 71]. Apart from a few other attempts, these cations were based on elements pertaining, like Ti, to the period 4 of the Mendeleev table. Doping with two cations has also been investigated with the expectation that each cation would trap opposite charges. Obviously, substitutional doping can occur merely if the size of the foreign cation is relatively close to that of the Ti^{4+} cation and if the percentage of cations introduced is sufficiently low.

The photocatalytic efficiency of the doped TiO_2 specimens has been tested in both the gas phase and the aqueous phase with only a few probe molecules and, in general, with only one probe molecule for each TiO_2 specimen. Moreover, some of these tests were performed with dyes whose use for determining the photocatalytic efficiency must be ruled out [96–98].

Many doped TiO_2 specimens were photocatalytically inactive under sub-bandgap irradiation in spite of their absorption in the visible spectral region. If they were active, their efficiency under visible irradiation was considerably lower than that of undoped TiO_2 under UV irradiation (note that correct efficiency comparisons must take into account the number of incident photons that are potentially absorbable). The zero or low efficiency under visible irradiation has been attributed to electron–hole recombination at the foreign cations; furthermore, this recombination can also decrease or even suppress the photocatalytic activity under UV irradiation. In contrast, it has been speculated that the recombination rate was markedly lower for TiO_2 with deeply implanted foreign cations whose efficiency under UV irradiation was unchanged and which were active under visible irradiation [99]; that might have arisen from the fact that the charge carriers formed in the deep TiO_2 layers (where the foreign cations were located) encountered almost no foreign cations when they moved to the surface [48].

Concerning the activity under sub-bandgap irradiation of TiO_2, e.g., [100–103], on the basis of an ensemble of experimental and theoretical methods [102, 103], it was determined that, in some cases, this activity was really due to the existence of new energy levels corresponding to the foreign cations. However, in other cases, depending on the preparation of doped TiO_2, other phenomena might be at the origin of the observed activity, viz., a photo-Fenton reaction occurring between hydrogen peroxide formed in situ and the cations located at the surface (potentially, partially dissolved in the case of aqueous-phase reactions); surface complexes, formed with the foreign cations, which are susceptible to be excited by sub-bandgap irradiation.

From the practical viewpoint, the results of cation doping of TiO_2 have been rather disappointing regarding an improved use of the solar spectrum in photocatalysis.

10.6.2.3 Effects of Anion Doping

Several anions have been used in attempts to render TiO_2 active under visible-light irradiation by introducing energy states forming a band above the VB and/or moving the VB top toward higher energy (Fig. 10.13). These anions were based on the following elements: N, S, B, P, halides, and even C; they were used either alone or combined: e.g., [104–118]. The objective was, in principle, to replace O^{2-} anions. Extremely diverse synthesis methods have been used and have resulted in samples having very different photocatalytic activity whether it was under visible or UV irradiation, even when the foreign element introduced was the same.

Regarding N for which more papers have been published, there are uncertainties about the chemical state and location of the N atoms depending on the preparation method, the amount and source of N atoms, and other factors [13, 119]. Furthermore, the interpretation of the results issued from the characterization methods is sometimes debated. In addition to the existence of substitutional and interstitial N (in the form of N^{-2} and N^{-3} anions), the formation of Ti-O-N bonds and the presence of embedded N_2 and NO have been reported. It has also been suggested that inorganic and organic N-containing surface species could also act as sensitizers beyond 400 nm [120]. New energy levels within the bandgap (Fig. 10.13) could also be associated not directly with N atoms but with oxygen vacancies arising from the preparation [13, 119]. Similar uncertainties have been reported for the other aforementioned nonmetals, although the picture may be less complex for halides.

For photocatalytic reactions, the key factor is the charge trapping and detrapping rates at these new energy levels. Cases have been reported where oxidations supposed to proceed with direct transfer of VB holes to the target molecules did not occur with holes located within the bandgap (i.e., upon visible-light excitation; Fig. 10.13) because the trapping and detrapping rates were too slow, e.g., [116, 117]. Consequently, the observed visible-light photocatalytic activity was suggested to mainly be mediated by the initial excitation of electrons from mid-gap energy levels to the CB; for this mechanism, the hole detrapping rate would matter less than for transport to the surface and direct transfer to adsorbed molecules. Subsequently, the CB electrons would form $^{\bullet}OH$ radicals via the reduction of O_2, first to superoxide (Eq. 10.1) and then to hydrogen peroxide (Eqs. 10.4, 10.5, and 10.6), as it is supposed to take place under bandgap irradiation. Anyhow, the low rates regarding the reactions of holes formed at levels within the bandgap are unfavorable for the overall photocatalytic rate under visible irradiation compared with UV irradiation.

From the practical viewpoint, these results have restrained the development of commercially available TiO_2 modified with nonmetals, even though these modifications might be cost-effective because some of the chemicals that could be utilized as “anion” sources have reasonable prices. Although researches aiming at modifying TiO_2 to better take advantage of the solar spectrum continue, TiO_2 KRONOClean (kronosww.com) seems to be one of the rare products presently on the market until now; it has been used as a reference for testing laboratory-prepared samples [121].

10.7 Photocatalytic Interest of Combining TiO_2 with Another Oxide

Very likely on the basis of methods commonly utilized in thermal catalysis, the combination of TiO_2 with another insulating or semiconducting oxide was used (1) to induce appropriate textural/structural modifications, e.g., increased dispersion of the TiO_2 particles and/or more homogeneous TiO_2 particle size; (2) to positively modify the surface characteristics, e.g., the acidity/basicity [122] or the adsorption of water (Fig. 10.14) [3]; and (3) to offer new types of adsorption sites (especially for O_2) and reaction sites. Although some positive results have been obtained in particular cases, the addition of a second oxide to TiO_2 has been shown to be difficult to tailor without detrimental effects to the photocatalytic efficiency, such as (1) blocking the access to the TiO_2 sites [31], (2) decreasing the photoexcitation of TiO_2 [123], and (3) increasing the recombination rate of the charge carriers because of the supplementary solid interfaces [124].

On the other hand, considering the fundamental mechanism of TiO_2 photocatalysis, the main reason for combining TiO_2 with another semiconductor has been to facilitate separation of the photoproduced charges through charge transfer between the two semiconductors. That requires adequately matched energies of the VB and CB of both semiconductors. On this basis, TiO_2 has been combined with several semiconductor oxides among which are: Cu_2O [125], CuO [126], ZrO_2 [127], ZnO [128], SnO_2 [129], RuO_2 [130], WO_3 [131], MoO_3 [131], In_2O_3 [132], Nb_2O_5 [133], Bi_2O_3 [125], $SrTiO_3$ [134], and oxides of rare earths [135, 136]. Sulfides or even other chalcogenides have also been used but, in general, they are not as stable and/or cost-effective as oxides. Coupled semiconductors that do not include TiO_2 have also been proposed. Charge transfer between the two

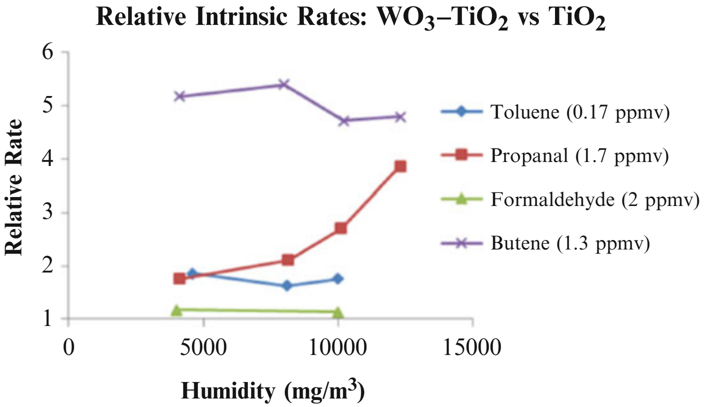

Fig. 10.14 Graphs showing that the photocatalytic efficiency, at various humidity levels, was enhanced for the air pollutants indicated, with the exception of formaldehyde, when the surface of P-25 was partially coated with 3 % WO_3. The relative rate is the rate for WO_3/P-25 minus the rate, r, for P-25 divided by r (Reprinted from Ref. [3])

combined semiconductors has been evidenced by photoelectrochemical and photoconductivity measurements, photoacoustic spectroscopy, Kelvin probe force microscopy, and other techniques. For most TiO_2–semiconductor oxide couples tested in diverse laboratory experiments, the maximum increase in photocatalytic efficiency for the removal of various single compounds in water and air was found to be comprised between approximately 1.5 and 3 relative to TiO_2 alone. These increases have been attributed to both the aforementioned charge transfer between the two semiconductor oxides and the textural/structural modifications indicated in the preceding paragraph.

From the practical viewpoint, the future of these combined materials will depend on their cost balanced against the improved photocatalytic efficiency; some of the added elements are indeed rarer than Ti and therefore more expensive. Possible alterations of the mechanical and optical properties, durability, etc. will also have to be assessed in regard to the envisaged application.

10.8 Photocatalytic Interest of Combining TiO_2 with a High-Surface-Area Adsorbent

Adding activated carbon (AC) to TiO_2 appears as a good means to overcome the problem of the approach of organic pollutants [9, 14, 47] to TiO_2 across the well-organized layers of adsorbed water [45]. With AC being hydrophobic and organophilic, the trace organic pollutants will be attracted to it and then could be transferred to TiO_2 through the interfaces between the two solids. Alternatively, a transfer over several tens of μm of active species from TiO_2 to the pollutants adsorbed on AC has been postulated because of both remote degradation of soot [137, 138] and experiments using well-defined structures consisting of alternate microstripes of TiO_2 on Si [139].

To increase the efficiency, the area of the TiO_2–AC interfaces must obviously be maximized, while both preserving irradiation of TiO_2 and avoiding blockage of AC pores by TiO_2. Because of the variety of the parameters that can be modified, including the morphology of each solid, preparation recipes rather than clear guidance have been reported [140].

In practice, $TiO_2 + AC$ materials are commercialized, though not on a large industrial scale. At least for water purification, added assets of these materials are: (1) the well-known use of AC alone, (2) an affordable price of AC, (3) the increased duration of AC usage without regeneration because of in situ photocatalytic cleaning, (4) the easy recovery of the material by filtering if granular AC is utilized, and (5) the enhanced adsorption of intermediate products of photocatalytic degradation which can be toxic and whose complete mineralization can be too costly. By contrast, the oxidizing capability of photoexcited TiO_2 toward carbon materials (cf. the case of soot) would need further assessment regarding the long-term durability as opposed to the cleaning (point (3) above).

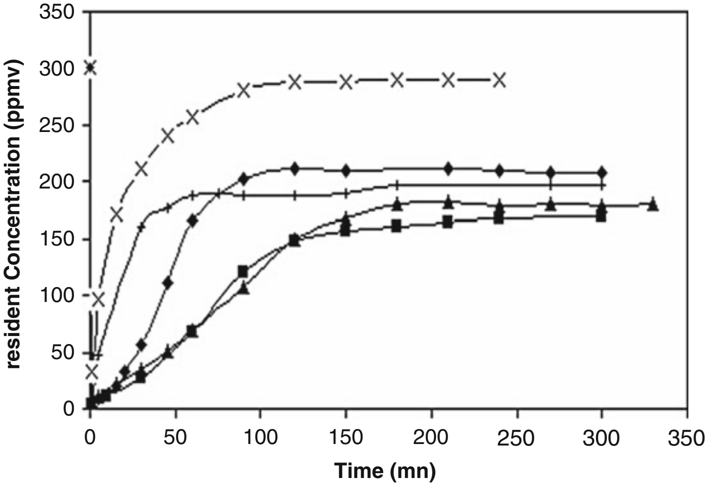

Fig. 10.15 Kinetic variations in methanol concentration in flowing dry air at the photocatalytic reactor exit using the following photocatalysts: +- P-25; x- Na bentonite calcined at 673 K; ♦- TiO_2 (1 mmol/g)-pillared bentonitecalcined at 673 K; ▲- TiO_2 (10 mmol/g)-pillared bentonite calcined at 673 K; and ■- TiO_2 (10 mmol/g)-pillared bentonite calcined by microwave (Reprinted from Ref. [144], with kind permission from Springer Science + Business Media)

AC can be replaced by other high-surface-area adsorbents, such as zeolites [141–143] and clays [144–146], which are hydrophobic or can be made hydrophobic by proper treatment. Because of their particular texture, these adsorbents (either synthesized or natural) may allow easier design of the mixed materials than AC. The combinations of these adsorbents with TiO_2 have been tested for the removal of pollutants in both air and water, unfortunately often with dyes as probes, which is not recommended from the fundamental viewpoint as aforementioned [96–98] but can be justified if the dye used is in fact the targeted compound. Positive results have been reported for several pollutants (e.g., Fig. 10.15). To the author's knowledge, none of these materials are commercially available so far.

Much more recently, the combination of TiO_2 with graphene or its oxide has been proposed not only because of the high surface area of these materials but also because of their high electrical conductivity susceptible to facilitate the transport of TiO_2 photoproduced electrons and finally because of their adjustable shape. Application of TiO_2/graphene materials to pollutant removal is still not developed. Moreover, not surprisingly, the photocatalytic long-term stability has been questioned [147] as in the case of other carbon materials.

10.9 Conclusions

The basic phenomena of photocatalysis using TiO_2-based materials are known in great detail even if some questions remain still open to debate according to specialists in surface science [13] and theoreticians [14]. Progress in this research field has arisen from both the development of various techniques (or expert application of older techniques, e.g., infrared spectroscopy [148], in TiO_2 photocatalysis), especially the availability of time-resolved devices operating at shorter timescales, and the use of advanced theoretical methods.

From the practical viewpoint, one of the messages from the fundamental results about the respective timescales of electron (or hole) transport, trapping, detrapping, and transfers is that the energy spent to promote electrons out of the VB can be extremely rapidly lost before useful chemical reactions can be accomplished, even if these reactions are thermodynamically downhill as in the case of the applications to self-cleaning materials [1] and air [2, 3, 47] or water purification [4]. Another message based on the interpretations of the fundamental events occurring upon photoexcitation of variously modified TiO_2 allows one to understand why these materials have been somewhat disappointing with respect to the initial expectations regarding each of them. Until now, none of them seem to be at the basis of significant commercial development capable of penetrating a market. In the author's view, the combination of TiO_2 with AC (or possibly zeolites and clays because of their photocatalytic stability) appears to offer reasonable perspectives in environmental detoxification. Photocatalytic formation of H_2 from certain alcohols and polyols over metal/TiO_2 could also be of interest [91], perhaps at temperature higher than ambient [94], but cost issues have to be considered.

In spite of intense research, the use of photocatalysts for endergonic water splitting and carbon dioxide reduction seems still far away from implementation, even though solids much more expensive than pristine TiO_2 could be taken into account for these reactions contrary to the cases of depollution applications, in general. These topics are not covered in this chapter devoted mainly to photocatalysis using conventional TiO_2-based materials. They are treated in other chapters of this book.

References

1. Pichat P (2013) Self-cleaning materials based on solar photocatalysis. In: Suib SL (ed) New and future developments in catalysis, vol 7, Solar photocatalysis. Elsevier, Amsterdam, pp 167–190
2. Mo J, Zhang Y, Xu Q, Lamson JJ, Zhao R (2009) Photocatalytic purification of volatile organic compounds in indoor air: a literature review. Atmos Environ 43(14):2229–2246
3. Hay SO, Obee T, Luo Z, Jiang T, Meng Y, He J, Murphy SC, Suib S (2015) The viability of photocatalysis for air purification. Molecules 20(1):1319–1356
4. Pichat P (ed) (2013) Photocatalysis and water purification: from fundamentals to recent applications. Wiley, Weinheim
5. Omote M, Kitaoka H, Kobayashi E, Suzuki O, Aratake K, Sano H, Mizutani G, Wolf W, Podloucky R (2005) Spectral, tensor, and ab initio theoretical analysis of optical second harmonic generation from the rutile TiO_2 (110) and (001) faces. J Phys Condens Matter 17 (8):S175

6. Manzhos S, Jono R, Yamashita K, Fujisawa J-i, Nagata M, Segawa H (2011) Study of interfacial charge transfer bands and electron recombination in the surface complexes of TCNE, TCNQ, and TCNAQ with TiO_2. J Phys Chem C 115(43):21487–21493
7. Agrios AG, Gray KA, Weitz E (2004) Narrow-band irradiation of a homologous series of chlorophenols on TiO_2: charge-transfer complex formation and reactivity. Langmuir 20 (14):5911–5917
8. Egerton TA (2014) UV-absorption – the primary process in photocatalysis and some practical consequences. Molecules 19(11):18192–18214
9. Enríquez R, Agrios AG, Pichat P (2007) Probing multiple effects of TiO_2 sintering temperature on photocatalytic activity in water by use of a series of organic pollutant molecules. Catal Today 120(2):196–202
10. Turner GM, Beard MC, Schmuttenmaer CA (2002) Carrier localization and cooling in dye-sensitized nanocrystalline titanium dioxide. J Phys Chem B 106(45):11716–11719
11. Grela M, Colussi A (1999) Photon energy and photon intermittence effects on the quantum efficiency of photoinduced oxidations in crystalline and metastable TiO_2 colloidal nanoparticles. J Phys Chem B 103(14):2614–2619
12. Xu C, Yang W, Ren Z, Dai D, Guo Q, Minton TK, Yang X (2013) Strong photon energy dependence of the photocatalytic dissociation rate of methanol on TiO_2 (110). J Am Chem Soc 135(50):19039–19045
13. Henderson MA (2011) A surface science perspective on photocatalysis. Surf Sci Rep 66 (6):185–297
14. De Angelis F, Di Valentin C, Fantacci S, Vittadini A, Selloni A (2014) Theoretical studies on anatase and less common TiO_2 phases: bulk, surfaces, and nanomaterials. Chem Rev 114 (19):9708–9753
15. Lantz JM, Corn RM (1994) Time-resolved optical second harmonic generation measurements of picosecond band flattening processes at single crystal TiO_2 electrodes. J Phys Chem 98(38):9387–9390
16. Salafsky J (1999) Exciton dissociation, charge transport, and recombination in ultrathin, conjugated polymer-TiO_2 nanocrystal intermixed composites. Phys Rev B 59(16):10885
17. Salvador P (2007) On the nature of photogenerated radical species active in the oxidative degradation of dissolved pollutants with TiO_2 aqueous suspensions: a revision in the light of the electronic structure of adsorbed water. J Phys Chem C 111(45):17038–17043
18. Nakamura R, Nakato Y (2010) Molecular mechanism of water oxidation reaction at photo-irradiated TiO_2 and related metal oxide surfaces. Solid State Phenom 162:1–27
19. Ikeda S, Sugiyama N, Murakami S-y, Kominami H, Kera Y, Noguchi H, Uosaki K, Torimoto T, Ohtani B (2003) Quantitative analysis of defective sites in titanium (IV) oxide photocatalyst powders. Phys Chem Chem Phys 5(4):778–783
20. Warren DS, McQuillan AJ (2004) Influence of adsorbed water on phonon and UV-induced IR absorptions of TiO_2 photocatalytic particle films. J Phys Chem B 108(50):19373–19379
21. Planelles J, Movilla J (2006) Trapping electrons in semiconductor air bubbles: a theoretical approach. Phys Rev B 73(23):235350
22. Deskins NA, Rousseau R, Dupuis M (2009) Localized electronic states from surface hydroxyls and polarons in TiO_2 (110). J Phys Chem C 113(33):14583–14586
23. Szczepankiewicz SH, Moss JA, Hoffmann MR (2002) Slow surface charge trapping kinetics on irradiated TiO_2. J Phys Chem B 106(11):2922–2927
24. Kuznetsov A, Kameneva O, Alexandrov A, Bityurin N, Chhor K, Kanaev A (2006) Chemical activity of photoinduced Ti3+ centers in titanium oxide gels. J Phys Chem B 110(1):435–441
25. Kormann C, Bahnemann DW, Hoffmann MR (1988) Preparation and characterization of quantum-size titanium dioxide. J Phys Chem 92(18):5196–5201
26. Rabani J, Yamashita K, Ushida K, Stark J, Kira A (1998) Fundamental reactions in illuminated titanium dioxide nanocrystallite layers studied by pulsed laser. J Phys Chem B 102 (10):1689–1695

27. Van de Lagemaat J, Frank A (2001) Nonthermalized electron transport in dye-sensitized nanocrystalline TiO_2 films: transient photocurrent and random-walk modeling studies. J Phys Chem B 105(45):11194–11205
28. Huber R, Spörlein S, Moser JE, Grätzel M, Wachtveitl J (2000) The role of surface states in the ultrafast photoinduced electron transfer from sensitizing dye molecules to semiconductor colloids. J Phys Chem B 104(38):8995–9003
29. Peiró AM, Colombo C, Doyle G, Nelson J, Mills A, Durrant JR (2006) Photochemical reduction of oxygen adsorbed to nanocrystalline TiO_2 films: a transient absorption and oxygen scavenging study of different TiO_2 preparations. J Phys Chem B 110 (46):23255–23263
30. Cai Y, Strømme M, Welch K (2013) Photocatalytic antibacterial effects are maintained on resin-based TiO_2 nanocomposites after cessation of UV irradiation. PLoS One 8(10)
31. Coronado JM, Maira AJ, Martínez-Arias A, Conesa JC, Soria J (2002) EPR study of the radicals formed upon UV irradiation of ceria-based photocatalysts. J Photochem Photobiol A 150(1):213–221
32. Berger T, Diwald O, Knözinger E, Sterrer M, Yates JT Jr (2006) UV induced local heating effects in TiO_2 nanocrystals. Phys Chem Chem Phys 8(15):1822–1826
33. Hurum DC, Gray KA, Rajh T, Thurnauer MC (2005) Recombination pathways in the Degussa P25 formulation of TiO_2: surface versus lattice mechanisms. J Phys Chem B 109 (2):977–980
34. Lawless D, Serpone N, Meisel D (1991) Role of hydroxyl radicals and trapped holes in photocatalysis. A pulse radiolysis study. J Phys Chem 95(13):5166–5170
35. Furube A, Asahi T, Masuhara H, Yamashita H, Anpo M (2001) Direct observation of interfacial hole transfer from a photoexcited TiO_2 particle to an adsorbed molecule SCN-by femtosecond diffuse reflectance spectroscopy. Res Chem Intermed 27(1):177–187
36. Tamaki Y, Furube A, Murai M, Hara K, Katoh R, Tachiya M (2006) Direct observation of reactive trapped holes in TiO_2 undergoing photocatalytic oxidation of adsorbed alcohols: evaluation of the reaction rates and yields. J Am Chem Soc 128(2):416–417
37. Shkrob IA, Sauer MC, Gosztola D (2004) Efficient, rapid photooxidation of chemisorbed polyhydroxyl alcohols and carbohydrates by TiO_2 nanoparticles in an aqueous solution. J Phys Chem B 108(33):12512–12517
38. Tachikawa T, Tojo S, Fujitsuka M, Majima T (2004) Direct observation of the cascade hole transfer giving free radical cations of trans-stilbenes during TiO_2 photocatalytic reactions. Chem Phys Lett 392(1):50–54
39. Ferry JL, Glaze WH (1998) Photocatalytic reduction of nitroorganics over illuminated titanium dioxide: electron transfer between excited-state TiO_2 and nitroaromatics. J Phys Chem B 102(12):2239–2244
40. Minero C, Maurino V, Pelizzetti E (2003) Mechanisms of the photocatalytic transformation of organic compounds. In: Ramamurthy V, Schanze KS (eds) Molecular and supramolecular photochemistry, vol 10, Semiconductor photochemistry and photophysics. Marcel Dekker, New York, pp 211–230
41. Muggli DS, Falconer JL (1999) UV-enhanced exchange of O_2 with H_2O adsorbed on TiO_2. J Catal 181(1):155–159
42. Pang X, Chen C, Ji H, Che Y, Ma W, Zhao J (2014) Unraveling the photocatalytic mechanisms on TiO_2 surfaces using the oxygen-18 isotopic label technique. Molecules 19 (10):16291–16311
43. Du Y, Deskins NA, Zhang Z, Dohnalek Z, Dupuis M, Lyubinetsky I (2009) Two pathways for water interaction with oxygen adatoms on TiO_2 (110). Phys Rev Lett 102(9):096102
44. Obee TN, Brown RT (1995) TiO_2 photocatalysis for indoor air applications: effects of humidity and trace contaminant levels on the oxidation rates of formaldehyde, toluene, and 1, 3-butadiene. Environ Sci Technol 29(5):1223–1231
45. Tilocca A, Selloni A (2004) Vertical and lateral order in adsorbed water layers on anatase TiO_2 (101). Langmuir 20(19):8379–8384

46. Zhao Z, Li Z, Zou Z (2012) Structure and properties of water on the anatase TiO_2 (101) surface: from single-molecule adsorption to interface formation. J Phys Chem C 116 (20):11054–11061
47. Pichat P (2010) Some views about indoor air photocatalytic treatment using TiO_2: conceptualization of humidity effects, active oxygen species, problem of C1–C3 carbonyl pollutants. Appl Catal Environ 99(3):428–434
48. Pichat P (2003) Photocatalytic degradation of pollutants in water and air: basic concepts and applications. In: Tarr MA (ed) Chemical degradation methods for wastes and pollutants: environmental and industrial applications. Marcel Dekker, New York, pp 77–119
49. Coronado JM, Soria J (2007) ESR study of the initial stages of the photocatalytic oxidation of toluene over TiO_2 powders. Catal Today 123(1):37–41
50. Kataoka S, Tejedor-Tejedor MI, Coronado JM, Anderson MA (2004) Thin-film transmission IR spectroscopy as an in situ probe of the gas–solid interface in photocatalytic processes. J Photochem Photobiol A 163(3):323–329
51. Sawyer DT, Valentine JS (1981) How super is superoxide? Acc Chem Res 14(12):393–400
52. Pichat P, Guillard C, Amalric L, Renard A-C, Plaidy O (1995) Assessment of the importance of the role of H_2O_2 and $O_2^{\bullet-}$ in the photocatalytic degradation of 1,2-dimethoxybenzene. Sol Energy Mater Sol Cells 38(1):391–399
53. Cermenati L, Pichat P, Guillard C, Albini A (1997) Probing the TiO_2 photocatalytic mechanisms in water purification by use of quinoline, photo-fenton generated OH radicals and superoxide dismutase. J Phys Chem B 101(14):2650–2658
54. Nosaka Y, Nosaka AY (2013) Identification and roles of the active species generated on various photocatalysts. In: Pichat P (ed) Photocatalysis and water purification: from fundamentals to recent applications. Wiley, Weinheim, pp 1–24
55. Jenks WS (2013) Photocatalytic reaction pathways–effects of molecular structure, catalyst, and wavelength. In: Pichat P (ed) Photocatalysis and water purification: from fundamentals to recent applications. Wiley, Weinheim, pp 25–51
56. Shao M-h, Liu P, Adzic RR (2006) Superoxide anion is the intermediate in the oxygen reduction reaction on platinum electrodes. J Am Chem Soc 128(23):7408–7409
57. Mattioli G, Filippone F, Amore Bonapasta A (2006) Reaction intermediates in the photoreduction of oxygen molecules at the (101) TiO_2 (anatase) surface. J Am Chem Soc 128 (42):13772–13780
58. Pichat P, Courbon H, Enriquez R, Tan TT, Amal R (2007) Light-induced isotopic exchange between O_2 and semiconductor oxides, a characterization method that deserves not to be overlooked. Res Chem Intermed 33(3):239–250
59. Pichat P, Enriquez R, Mietton E (2010) Investigations of photo-excited TiO_2 based on time resolved microwave conductivity and oxygen isotopic exchange. Solid State Phenom 162:41–48
60. Lu G, Linsebigler A, YatesJr JT (1995) Photooxidation of CH_3Cl on TiO_2 (110): a mechanism not involving H_2O. J Phys Chem 99(19):7626–7631
61. von Sonntag C (2006) Free-radical-induced DNA damage and its repair. Springer, Heidelberg
62. Carteau D, Pichat P (2010) Degradation of an ether–alcohol (3-ethoxypropan-1-ol) by photo-Fenton-generated OH radicals: products analysis and formation pathways; relevance to atmospheric water-phase chemistry. Res Chem Intermed 36(2):141–153
63. Irawaty W, Friedmann D, Scott J, Pichat P, Amal R (2011) Photocatalysis in TiO_2 aqueous suspension: effects of mono-or di-hydroxyl substitution of butanedioic acid on the disappearance and mineralisation rates. Catal Today 178(1):51–57
64. Pichat P, Disdier J, Hoang-Van C, Mas D, Goutailler G, Gaysse C (2000) Purification/deodorization of indoor air and gaseous effluents by TiO_2 photocatalysis. Catal Today 63 (2):363–369
65. Taranto J, Frochot D, Pichat P (2007) Combining cold plasma and TiO_2 photocatalysis to purify gaseous effluents: a preliminary study using methanol-contaminated air. Ind Eng Chem Res 46(23):7611–7614

66. Jenny B, Pichat P (1991) Determination of the actual photocatalytic rate of hydrogen peroxide decomposition over suspended titania. Fitting to the Langmuir-Hinshelwood form. Langmuir 7(5):947–954
67. Nandi D, Krishnakumar E, Rosa A, Schmidt W-F, Illenberger E (2003) Dissociative electron attachment to H_2O_2: a very effective source for OH and OH− generation. Chem Phys Lett 373(5):454–459
68. Rengifo-Herrera JA, Rincón AG, Pulgarin C (2013) Waterborne escherichia coli inactivation by TiO_2 photoassisted processes: a brief overview. In: Pichat P (ed) Photocatalysis and water purification: from fundamentals to recent applications. Wiley, Weinheim, pp 295–309
69. Byrne JA, Dunlop PSM, Hamilton JWJ, Fernández-Ibáñez P, Polo-López I, Sharma PK, Vennard ASM (2015) A review of heterogeneous photocatalysis for water and surface disinfection. Molecules 20(4):5574–5615
70. Zubkov T, Stahl D, Thompson TL, Panayotov D, Diwald O, Yates JT (2005) Ultraviolet light-induced hydrophilicity effect on TiO_2 (110) (1 × 1). Dominant role of the photooxidation of adsorbed hydrocarbons causing wetting by water droplets. J Phys Chem B 109 (32):15454–15462
71. Fujishima A, Zhang X, Tryk DA (2008) TiO_2 photocatalysis and related surface phenomena. Surf Sci Rep 63(12):515–582
72. Li Y, Wen B, Ma W, Chen C, Zhao J (2012) Photocatalytic degradation of aromatic pollutants: a pivotal role of conduction band electron in distribution of hydroxylated intermediates. Environ Sci Technol 46(9):5093–5099
73. Li Y, Wen B, Yu C, Chen C, Ji H, Ma W, Zhao J (2012) Pathway of oxygen incorporation from O_2 in TiO_2 photocatalytic hydroxylation of aromatics: oxygen isotope labeling studies. Chem Eur J 18(7):2030–2039
74. Hathway T, Jenks WS (2008) Effects of sintering of TiO_2 particles on the mechanisms of photocatalytic degradation of organic molecules in water. J Photochem Photobiol A 200 (2):216–224
75. Zayani G, Bousselmi L, Pichat P, Mhenni F, Ghrabi A (2006) Photocatalytic degradation of four textile azo dyes in aqueous TiO_2 suspensions: practical outcomes and revisited pathways. J Adv Oxid Technol 9(1):65–78
76. Angelomé PC, Andrini L, Calvo ME, Requejo FG, Bilmes SA, Soler-Illia GJ (2007) Mesoporous anatase TiO_2 films: use of Ti K XANES for the quantification of the nanocrystalline character and substrate effects in the photocatalysis behavior. J Phys Chem C 111 (29):10886–10893
77. Ohsawa T, Lyubinetsky IV, Henderson MA, Chambers SA (2008) Hole-mediated photodecomposition of trimethyl acetate on a TiO_2 (001) anatase epitaxial thin film surface. J Phys Chem C 112(50):20050–20056
78. Ohtani B (2013) Design and development of active titania and related photocatalysts. In: Pichat P (ed) Photocatalysis and water purification: from fundamentals to recent applications. Wiley, Weinheim, pp 73–102
79. Liu G, Jimmy CY, Lu GQM, Cheng H-M (2011) Crystal facet engineering of semiconductor photocatalysts: motivations, advances and unique properties. Chem Commun 47 (24):6763–6783
80. Jiang Z, Tang Y, Tay Q, Zhang Y, Malyi OI, Wang D, Deng J, Lai Y, Zhou H, Chen X (2013) Understanding the role of nanostructures for efficient hydrogen generation on immobilized photocatalysts. Adv Energy Mater 3(10):1368–1380
81. Balázs N, Mogyorósi K, Srankó DF, Pallagi A, Alapi T, Oszkó A, Dombi A, Sipos P (2008) The effect of particle shape on the activity of nanocrystalline TiO_2 photocatalysts in phenol decomposition. Appl Catal Environ 84(3):356–362
82. Dimitrijevic NM, Saponjic ZV, Rabatic BM, Poluektov OG, Rajh T (2007) Effect of size and shape of nanocrystalline TiO_2 on photogenerated charges. An EPR study. J Phys Chem C 111 (40):14597–14601

83. Pichat P (2014) Are TiO_2 nanotubes worth using in photocatalytic purification of air and water? Molecules 19(9):15075–15087
84. Almquist CB, Biswas P (2002) Role of synthesis method and particle size of nanostructured TiO_2 on its photoactivity. J Catal 212(2):145–156
85. Vorontsov A, Savinov E, Barannik G, Troitsky V, Parmon V (1997) Quantitative studies on the heterogeneous gas-phase photooxidation of CO and simple VOCs by air over TiO_2. Catal Today 39(3):207–218
86. Einaga H, Harada M, Futamura S, Ibusuki T (2003) Generation of active sites for CO photooxidation on TiO_2 by platinum deposition. J Phys Chem B 107(35):9290–9297
87. Gong D, Subramaniam VP, Highfield JG, Tang Y, Lai Y, Chen Z (2011) In situ mechanistic investigation at the liquid/solid interface by attenuated total reflectance FTIR: ethanol photooxidation over pristine and platinized TiO_2 (P25). ACS Catal 1(8):864–871
88. Rosseler O, Ulhaq-Bouillet C, Bonnefont A, Pronkin S, Savinova E, Louvet A, Keller V, Keller N (2015) Structural and electronic effects in bimetallic PdPt nanoparticles on TiO_2 for improved photocatalytic oxidation of CO in the presence of humidity. Appl Catal Environ 166:381–392
89. Hoang-Van C, Pichat P, Mozzanega M-N (1994) Room-temperature hydrogen transfer from liquid methanol or 2-propanol to diphenylacetylene over group VIII metal/TiO_2 photocatalysts. J Mol Catal 92(2):187–199
90. Driessen M, Grassian V (1998) Photooxidation of trichloroethylene on Pt/TiO_2. J Phys Chem B 102(8):1418–1423
91. Pichat P (1987) Surface-properties, activity and selectivity of bifunctional powder photocatalysts. New J Chem 11(2):135–140
92. Joo JB, Dillon R, Lee I, Yin Y, Bardeen CJ, Zaera F (2014) Promotion of atomic hydrogen recombination as an alternative to electron trapping for the role of metals in the photocatalytic production of H_2. Proc Natl Acad Sci 111(22):7942–7947
93. Hirakawa T, Kamat PV (2005) Charge separation and catalytic activity of Ag@ TiO2 core-shell composite clusters under UV-irradiation. J Am Chem Soc 127(11):3928–3934
94. Highfield J, Chen M, Nguyen P, Chen Z (2009) Mechanistic investigations of photo-driven processes over TiO_2 by in-situ DRIFTS-MS: part 1. Platinization and methanol reforming. Energy Environ Sci 2(9):991–1002
95. Takeuchi K, Nakamura I, Matsumoto O, Sugihara S, Ando M, Ihara T (2000) Preparation of visible-light-responsive titanium oxide photocatalysts by plasma treatment. Chem Lett 29 (12):1354–1355
96. Yan X, Ohno T, Nishijima K, Abe R, Ohtani B (2006) Is methylene blue an appropriate substrate for a photocatalytic activity test? A study with visible-light responsive titania. Chem Phys Lett 429(4):606–610
97. Mills A (2012) An overview of the methylene blue ISO test for assessing the activities of photocatalytic films. Appl Catal Environ 128:144–149
98. Ollis D, Silva CG, Faria J (2015) Simultaneous photochemical and photocatalyzed liquid phase reactions: dye decolorization kinetics. Catal Today 240:80–85
99. Iino K, Kitano M, Takeuchi M, Matsuoka M, Anpo M (2006) Design and development of second-generation titanium oxide photocatalyst materials operating under visible light irradiation by applying advanced ion-engineering techniques. Curr Appl Phys 6(6):982–986
100. Lee K, Lee N, Shin S, Lee H, Kim S (2006) Hydrothermal synthesis and photocatalytic characterizations of transition metals doped nano TiO_2 sols. Mater Sci Eng B 129(1):109–115
101. Sun B, Reddy EP, Smirniotis PG (2005) Visible light Cr (VI) reduction and organic chemical oxidation by TiO_2 photocatalysis. Environ Sci Technol 39(16):6251–6259
102. Yalçın Y, Kılıç M, Çınar Z (2010) Fe^+ 3-doped TiO_2: a combined experimental and computational approach to the evaluation of visible light activity. Appl Catal Environ 99(3):469–477

103. Gurkan YY, Kasapbasi E, Cinar Z (2013) Enhanced solar photocatalytic activity of TiO_2 by selenium (IV) ion-doping: characterization and DFT modeling of the surface. Chem Eng J 214:34–44
104. Ohno T, Mitsui T, Matsumura M (2003) Photocatalytic activity of S-doped TiO_2 photocatalyst under visible light. Chem Lett 32(4):364–365
105. Sakthivel S, Kisch H (2003) Daylight photocatalysis by carbon-modified titanium dioxide. Angew Chem Int Ed 42(40):4908–4911
106. Kitano M, Funatsu K, Matsuoka M, Ueshima M, Anpo M (2006) Preparation of nitrogen-substituted TiO_2 thin film photocatalysts by the radio frequency magnetron sputtering deposition method and their photocatalytic reactivity under visible light irradiation. J Phys Chem B 110(50):25266–25272
107. Mitoraj D, Kisch H (2008) the nature of nitrogen-modified titanium dioxide photocatalysts active in visible light. Angew Chem Int Ed 47(51):9975–9978
108. Sun H, Wang S, Ang HM, Tadé MO, Li Q (2010) Halogen element modified titanium dioxide for visible light photocatalysis. Chem Eng J 162(2):437–447
109. Dozzi MV, Livraghi S, Giamello E, Selli E (2011) Photocatalytic activity of S-and F-doped TiO_2 in formic acid mineralization. Photochem Photobiol Sci 10(3):343–349
110. Liu G, Zhao Y, Sun C, Li F, Lu GQ, Cheng HM (2008) Synergistic effects of B/N doping on the visible-light photocatalytic activity of mesoporous TiO_2. Angew Chem Int Ed 47 (24):4516–4520
111. Dong F, Guo S, Wang H, Li X, Wu Z (2011) Enhancement of the visible light photocatalytic activity of C-doped TiO_2 nanomaterials prepared by a green synthetic approach. J Phys Chem C 115(27):13285–13292
112. McEvoy JG, Cui W, Zhang Z (2013) Degradative and disinfective properties of carbon-doped anatase–rutile TiO_2 mixtures under visible light irradiation. Catal Today 207:191–199
113. Pelaez M, Nolan NT, Pillai SC, Seery MK, Falaras P, Kontos AG, Dunlop PS, Hamilton JW, Byrne JA, O'Shea K (2012) A review on the visible light active titanium dioxide photocatalysts for environmental applications. Appl Catal Environ 125:331–349
114. Xu QC, Wellia DV, Yan S, Liao DW, Lim TM, Tan TTY (2011) Enhanced photocatalytic activity of C–N-codoped TiO_2 films prepared via an organic-free approach. J Hazard Mater 188(1):172–180
115. Zhang K, Wang X, He T, Guo X, Feng Y (2014) Preparation and photocatalytic activity of B–N co-doped mesoporous TiO_2. Powder Technol 253:608–613
116. Su W, Zhang Y, Li Z, Wu L, Wang X, Li J, Fu X (2008) Multivalency iodine doped TiO_2: preparation, characterization, theoretical studies, and visible-light photocatalysis. Langmuir 24(7):3422–3428
117. Tojo S, Tachikawa T, Fujitsuka M, Majima T (2008) Iodine-doped TiO_2 photocatalysts: correlation between band structure and mechanism. J Phys Chem C 112(38):14948–14954
118. Dolat D, Mozia S, Wróbel R, Moszyński D, Ohtani B, Guskos N, Morawski A (2015) Nitrogen-doped, metal-modified rutile titanium dioxide as photocatalysts for water remediation. Appl Catal Environ 162:310–318
119. Serpone N, Emeline AV, Kuznetsov VN, Ryabchuk VK (2010) Second generation visible-light-active photocatalysts: preparation, optical properties, and consequences of dopants on the band gap energy of TiO_2. In: Anpo M, Kamat PV (eds) Environmentally benign photocatalysts: applications of titanium oxide-based materials. Springer, New York, pp 35–111
120. Cheng YH, Subramaniam VP, Gong D, Tang Y, Highfield J, Pehkonen SO, Pichat P, Schreyer MK, Chen Z (2012) Nitrogen-sensitized dual phase titanate/titania for visible-light driven phenol degradation. J Solid State Chem 196:518–527
121. Pelaez M, Armah A, Stathatos E, Falaras P, Dionysiou DD (2009) Visible light-activated NF-codoped TiO_2 nanoparticles for the photocatalytic degradation of microcystin-LR in water. Catal Today 144(1):19–25

122. Noguchi H, Nakajima A, Watanabe T, Hashimoto K (2002) Removal of bromate ion from water using TiO_2 and alumina-loaded TiO_2 photocatalysts. Water Sci Technol 46 (11–12):27–31
123. Puzenat E, Pichat P (2003) Studying TiO_2 coatings on silica-covered glass by O_2 photosorption measurements and FTIR–ATR spectrometry: correlation with the self-cleaning efficacy. J Photochem Photobiol A 160(1):127–133
124. Beydoun D, Amal R, Low G, McEvoy S (2002) Occurrence and prevention of photodissolution at the phase junction of magnetite and titanium dioxide. J Mol Catal A 180 (1):193–200
125. Bessekhouad Y, Robert D, Weber J-V (2005) Photocatalytic activity of Cu_2O/TiO_2, Bi_2O_3/TiO_2 and $ZnMn_2O_4/TiO_2$ heterojunctions. Catal Today 101(3):315–321
126. Bandara J, Udawatta C, Rajapakse C (2005) Highly stable CuO incorporated TiO_2 catalyst for photocatalytic hydrogen production from H_2O. Photochem Photobiol Sci 4(11):857–861
127. Zorn ME, Tompkins DT, Zeltner WA, Anderson MA (1999) Photocatalytic oxidation of acetone vapor on TiO_2/ZrO_2 thin films. Appl Catal Environ 23(1):1–8
128. Chen D, Zhang H, Hu S, Li J (2008) Preparation and enhanced photoelectrochemical performance of coupled bicomponent ZnO-TiO_2 nanocomposites. J Phys Chem C 112 (1):117–122
129. Vinodgopal K, Kamat PV (1995) Enhanced rates of photocatalytic degradation of an azo dye using SnO_2/TiO_2 coupled semiconductor thin films. Environ Sci Technol 29(3):841–845
130. Amama P, Itoh K, Murabayashi M (2004) Effect of RuO_2 deposition on the activity of TiO_2: photocatalytic oxidation of trichloroethylene in aqueous phase. J Mater Sci 39 (13):4349–4351
131. Papp J, Soled S, Dwight K, Wold A (1994) Surface acidity and photocatalytic activity of TiO_2, WO_3/TiO_2, and MoO_3/TiO_2 photocatalysts. Chem Mater 6(4):496–500
132. Shchukin D, Poznyak S, Kulak A, Pichat P (2004) TiO_2-In_2O_3 photocatalysts: preparation, characterisations and activity for 2-chlorophenol degradation in water. J Photochem Photobiol A 162(2):423–430
133. Cui H, Dwight K, Soled S, Wold A (1995) Surface acidity and photocatalytic activity of Nb_2O_5/TiO_2 photocatalysts. J Solid State Chem 115(1):187–191
134. Tuan AC, Kaspar TC, Droubay T, Rogers J, Chambers SA (2003) Band offsets for the epitaxial $TiO_2/SrTiO_3/Si$ (001) system. Appl Phys Lett 83(18):3734–3736
135. Reszczyńska J, Grzyb T, Sobczak JW, Lisowski W, Gazda M, Ohtani B, Zaleska A (2014) Lanthanide co-doped TiO_2: the effect of metal type and amount on surface properties and photocatalytic activity. Appl Surf Sci 307:333–345
136. Tobaldi D, Pullar R, Škapin AS, Seabra M, Labrincha J (2014) Visible light activated photocatalytic behaviour of rare earth modified commercial TiO_2. Mater Res Bull 50:183–190
137. Lee MC, Choi W (2002) Solid phase photocatalytic reaction on the soot/TiO_2 interface: the role of migrating OH radicals. J Phys Chem B 106(45):11818–11822
138. Lee S-K, McIntyre S, Mills A (2004) Visible illustration of the direct, lateral and remote photocatalytic destruction of soot by titania. J Photochem Photobiol A 162(1):203–206
139. Haick H, Paz Y (2001) Remote photocatalytic activity as probed by measuring the degradation of self-assembled monolayers anchored near microdomains of titanium dioxide. J Phys Chem B 105(15):3045–3051
140. Puma GL, Bono A, Krishnaiah D, Collin JG (2008) Preparation of titanium dioxide photocatalyst loaded onto activated carbon support using chemical vapor deposition: a review paper. J Hazard Mater 157(2):209–219
141. Vaisman E, Cook RL, Langford CH (2000) Characterization of a composite photocatalyst. J Phys Chem B 104(36):8679–8684
142. Kamegawa T, Ishiguro Y, Kido R, Yamashita H (2014) Design of composite photocatalyst of TiO_2 and Y-zeolite for degradation of 2-propanol in the gas phase under UV and visible light irradiation. Molecules 19(10):16477–16488

143. Yasumori A, Yanagida S, Sawada J (2015) Preparation of a titania/X-zeolite/porous glass composite photocatalyst using hydrothermal and drop coating processes. Molecules 20(2):2349–2363
144. Pichat P, Khalaf H, Tabet D, Houari M, Saidi M (2005) Ti-montmorillonite as photocatalyst to remove 4-chlorophenol in water and methanol in air. Environ Chem Lett 2(4):191–194
145. Belessi V, Lambropoulou D, Konstantinou I, Katsoulidis A, Pomonis P, Petridis D, Albanis T (2007) Structure and photocatalytic performance of TiO_2/clay nanocomposites for the degradation of dimethachlor. Appl Catal Environ 73(3):292–299
146. Kibanova D, Cervini-Silva J, Destaillats H (2009) Efficiency of clay – TiO_2 nanocomposites on the photocatalytic elimination of a model hydrophobic air pollutant. Environ Sci Technol 43(5):1500–1506
147. Radich JG, Krenselewski AL, Zhu J, Kamat PV (2014) Is graphene a stable platform for photocatalysis? Mineralization of reduced graphene oxide with UV-irradiated TiO_2 nanoparticles. Chem Mater 26(15):4662–4668
148. Pichat P (2014) Representative examples of infrared spectroscopy uses in semiconductor photocatalysis. Catal Today 224:251–257

Chapter 11
Fundamental Processes in Surface Photocatalysis on TiO_2

Qing Guo, Chuanyao Zhou, Zhibo Ma, Zefeng Ren, Hongjun Fan, and Xueming Yang

Abstract Due to the potential applications of TiO_2 in photocatalytic hydrogen production and pollutant degradation, over the past few decades, we have witnessed the fast-growing interest and effort in developing TiO_2-based photocatalysts, improving the efficiency, and exploring the reaction mechanism at the atomic and molecular level. Since surface science studies on single crystal surfaces under UHV conditions could provide fundamental insights into these important processes, both thermal chemistry and photo-chemistry on TiO_2, especially on rutile TiO_2(110) surface, have been extensively investigated with a variety of experimental and theoretical approaches. In this chapter, we start from the properties of TiO_2 and then focus on charge transport and trapping and electron transfer dynamics. Next, we summarize recent progresses made in the study of elementary photocatalytic chemistry of oxygen and methanol on mainly rutile TiO_2(110) along with some studies on rutile TiO_2(011) and anatase TiO_2(101) and (001). These studies have provided fundamental insights into surface photocatalysis as well as stimulated new investigations in this exciting area. At the end of this chapter, implications of these studies for the development of new photocatalysis models are also discussed.

Keywords Photocatalysis • Titanium dioxide • Charge trapping • Charge transfer dynamics • Oxygen vacancies • Methanol • Ground state reaction

11.1 Introduction

Because the rapid consumption of fossil fuels and the pollution caused severe impact on the earth's environment, developing new and environmentally friendly energy sources is of the greatest importance for human kind on a global scale and is

---

Q. Guo • C. Zhou • Z. Ma • H. Fan • X. Yang (✉)
State Key Laboratory of Molecular Reaction Dynamics, Dalian Institute of Chemical Physics,
457 Zhongshan Road, Dalian 116023, Liaoning, People's Republic of China
e-mail: xmyang@dicp.ac.cn

Z. Ren
International Center for Quantum Materials and School of Physics, Peking University, Beijing
100871, People's Republic of China

J.C. Colmenares, Y.-J. Xu (eds.), *Heterogeneous Photocatalysis*, Green Chemistry
and Sustainable Technology, DOI 10.1007/978-3-662-48719-8_11

one of the biggest challenges facing the scientific community in the world. The most important clean energy source on the earth is clearly the solar energy, which is crucial in supporting the earth's ecological system as well as the energy for the earth's environment suitable for human being's living. Solar energy contains light in a wide spectral range from infrared to ultraviolet, the light energy in these wavelengths can also be used to drive energy and chemical conversion so that clean chemical energy source can be developed. For example, when light can be used to split water into hydrogen and oxygen, it will provide clean hydrogen energy for combustion with little pollution, unlike fossil fuels. Thus, it should be our priority to develop ecologically clean, environmentally harmonious, and sustainable, safe, and energy-efficient chemical technologies using solar energy [1]. Developing clean energy sources requires knowledge of photocatalysis on surfaces of photocatalysts.

Heterogeneous photocatalysis is basically a process of surface chemical reactions driven by photons. Therefore, there are at least two essential steps in photocatalysis. The first step is the photoexcitation of the photocatalyst, normally a semiconductor. Photoexcitation usually generates pairs of electrons and holes or excitons, below or at a photocatalyst surface. The energy carried by these excitons is then used to drive the chemical reactions of molecules adsorbed on the photocatalyst surface. The second step involves chemical reaction processes induced by the excitons. These processes must also avoid causing chemical changes for the photocatalysts [2]. Understanding the fundamental processes in heterogeneous photocatalysis is important for this field of study. Generally, heterogeneous photocatalysis of organic and inorganic compounds by TiO_2 is driven by photogenerated electrons or holes in the semiconductor particles, suggesting that the reactions occur on the excited electron state after photogenerated electrons or holes transfer to organic and inorganic compounds on the surface. Recently, however, detailed studies of photocatalysis on single crystal surfaces suggest that photocatalytic reactions can also possibly occur on the ground state, which is driven by the energy from exciton recombinations. It is therefore useful for us to review these studies to seek a more in-depth understanding of the entire heterogeneous photocatalysis process.

The study of heterogeneous photocatalysis has made tremendous progresses since the discovery of photocatalytic water splitting on TiO_2 by Fujishima and Honda in 1972 [3]. The photocatalytic properties of certain materials, normally semiconductors or doped semiconductor materials, have been used to convert solar energy into chemical energy to reduce or oxidize reagents to obtain useful target products including hydrogen and hydrocarbons and to remove pollutants and bacteria on wall surfaces and in air and water [4]. Among the many different photocatalysts, TiO_2, as a model of semiconductor photocatalyst, has been most widely investigated because of its exceptionally efficient photoactivity, high chemical stability, low cost, as well as its low toxicity for both humans and the environment. TiO_2, as a versatile material, has extensive applications in various fields. As an n-type semiconductor photocatalyst that has been widely used, one meaningful potential application of TiO_2 is the photocatalytic fuel generation reaction such as hydrogen production process [5].

Even though a great amount of studies has been carried out on the development of photocatalytic materials and the characterization of photocatalytic processes, however, studies on fundamental mechanisms about detailed surface photocatalytic processes on model photocatalysts such as TiO_2 are still lacking. A few fundamental issues need to be investigated in detail in typical photocatalytic reaction processes. Firstly, we need to learn how the energy of excitons created by photon excitation on or below the surface of a semiconductor photocatalyst is converted to the energy to drive a surface chemical reaction. Secondly, we need to investigate the elementary photocatalytic chemical reaction steps and thus the whole photocatalytic chemical process. Only when these processes are understood at the very fundamental level, a clear physical picture of surface photocatalysis at the molecular level can be obtained. Understanding of surface photocatalysis at the molecular level is crucial for the future development of the photocatalysis research field. In this chapter, we will provide a comprehensive review on previous studies of the mechanisms and dynamics of photocatalytic reactions on a few TiO_2 surfaces and TiO_2-based photocatalysts. A detailed discussion on possible new picture of photocatalysis from a different perspective is also provided at the end of this chapter.

11.2 TiO_2 Semiconductor Photocatalysts

11.2.1 Crystal Structures of TiO_2

TiO_2 can exist in one of the three major bulk crystalline forms, rutile, anatase, and brookite, all of which can be described in terms of distorted TiO_6 octahedra with different symmetries or arrangements. The anatase structure consists of edge-sharing TiO_6 octahedra, while the rutile and the brookite frameworks exhibit both corner and edge-sharing configurations (Fig. 11.1) [6]. The different characteristics of the Ti–O bonds play a very important role in the structural and electronic features of different phase forms of TiO_2 [7]. The knowledge of bulk properties of TiO_2 with different crystal structures has been comprehensively reviewed by Diebold [8]. Thermodynamically, rutile is the most stable phase in the bulk form, while bulk anatase and bulk brookite are the metastable ones. Upon heating, both anatase and brookite can transform irreversibly to rutile. Li and coworkers have investigated the phase transformation process from anatase to rutile systematically [9–11]. These authors found that the phase transformation of TiO_2 anatase nanoparticles to TiO_2 rutile nanoparticles starts from the interfaces between the agglomerated anatase particles, leading to a bulk phase transformation. Meanwhile, the surface defect sites on anatase particles are suggested to play an important role in the phase transformation process. The phase transformation from brookite to rutile phase undergoes brookite to anatase transition first with an intermediate structure of a quasi-$H_2Ti_3O_7$ and then transforms to rutile [12, 13]. Furthermore, the transformation of anatase and brookite to rutile phase strongly depends on the particle size of the initial TiO_2. For example, at temperatures ranging between

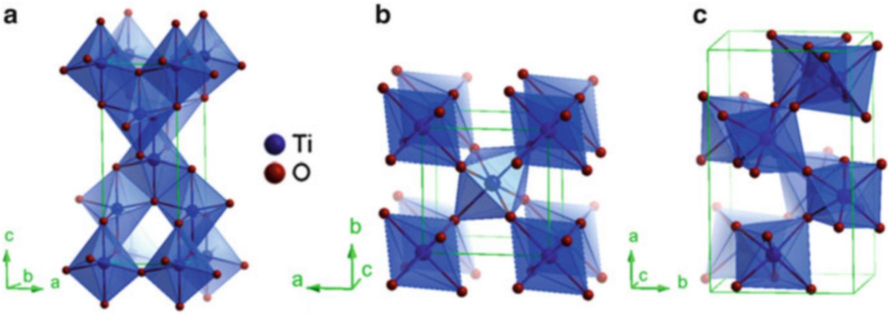

Fig. 11.1 Representations of the TiO_2 anatase (**a**), rutile (**b**), and brookite (**c**) forms. Anatase (tetragonal, a = 3.785 Å, c = 9.513 Å), rutile (tetragonal, a = 4.593 Å, c = 2.959 Å), and brookite (orthorhombic, a = 9.181 Å, b = 5.455 Å, c = 5.142 Å)

325 °C and 750 °C, rutile is the most stable phase with particle sizes above 35 nm, anatase is the most stable phase particle sizes under 11 nm, and brookite is the most stable phase between 11 and 35 nm [14].

The three polymorphs of TiO_2 have been enormously applied in many fields based on their different physical/chemical properties. However, in general, the most dominant research on TiO_2 is still focusing on its applications in solar energy conversion, which is mainly studied on rutile and anatase phase. Up to now, various research works have been performed with TiO_2 as a model semiconductor photocatalyst to yield H_2 from water splitting, biomass reforming, and industrial waste reforming. One limitation of TiO_2 as a photocatalyst is its wide bandgap (i.e., bandgap for bulk materials: anatase 3.20 eV corresponding to 384 nm and rutile 3.02 eV corresponding to 410 nm), which makes TiO_2 only sensitive to the UV light which covers less than 5 % of the solar spectrum. However, TiO_2 serves as a good model semiconductor photocatalyst for understanding and exploring the elemental processes and mechanisms of photocatalysis. These fundamental understandings obtained through investigation of TiO_2-based photocatalysts might be helpful for the development of more efficient photocatalysts for photocatalytic reactions such as water splitting and CO_2 reduction.

The photocatalytic activities of anatase and rutile forms of TiO_2 are quite different. The larger bandgap makes anatase have a slightly higher redox driving force than rutile, although the sensitive range of the light absorption for anatase is slightly less than that of rutile. Due to the lower thermodynamic stability of anatase, few laboratories have accomplished the synthesis of anatase single crystals [15]. Up to date, most of the investigations of anatase TiO_2-based photocatalysts have been carried out in the nanocrystalline regime, and the anatase crystal structure usually has a much higher surface area than rutile, resulting in enhanced adsorption capability and more active sites (i.e., oxygen vacancies). In addition, although rutile has a better charge carrier mobility than anatase because of its higher crystallinity, the latter can generate more efficient charge separation due to the existence of more oxygen vacancies. Due to these advantages of anatase, it usually shows much higher photocatalytic activity than rutile [5]. However, on anatase single crystal surfaces (such as anatase $TiO_2(001)$ [16] and $TiO_2(101)$ [17]), the surface point defects can hardly be formed through UHV annealing at temperatures as high as 600 °C, a condition under which significant reduction is known to take place on rutile single crystal surfaces. Therefore, the physical/chemical properties of a material may be quite different for their various phase structures, as well as the particle sizes.

11.2.2 Electronic Structures of TiO_2

Photocatalysis refers to light-induced acceleration of a reaction in the presence of a light-sensitive catalyst and can be compared to the way plants use chlorophyll to convert water and carbon dioxide into oxygen and glucose fueled by sunlight (thereby commonly also referred to as artificial photosynthesis) [18]. Figure 11.2 presents a simple model that compiles the essential features in the process of light-induced water splitting to yield hydrogen and oxygen with a photocatalyst; it also describes the preferred energy band level alignment between energy band edges of the photocatalyst and the reactant to drive a redox reaction via charge transfer from the catalyst to the reactant [19].

In general, the valence and conduction bands of rutile, anatase, and brookite TiO_2 are mainly comprised of O_2 p and Ti 3d states, respectively, at the band edges. Furthermore, a detailed molecular orbital bonding energy diagram of TiO_2, constructed from the individual atomic energy levels of Ti and O atoms, not only

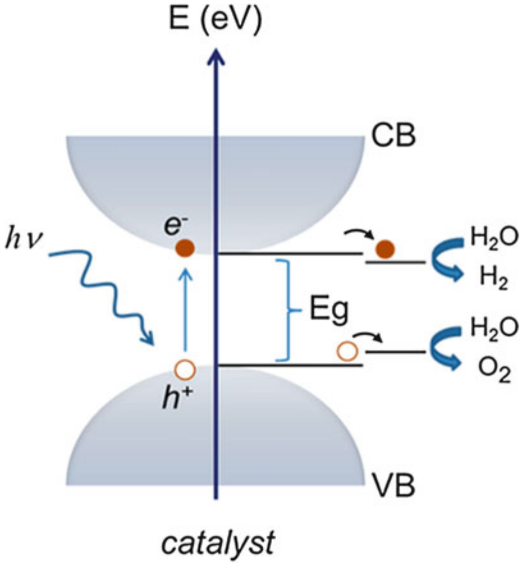

Fig. 11.2 Schematic presentation of the typical light-induced decomposition of water molecules, wherein (i) hydrogen is produced via a reduction process at the conduction band assisted by a photoelectron and (ii) oxygen is produced via an oxidation process assisted by a photoinduced hole in the valence band of the photocatalyst (Reproduced with permission from Ref. [19]. Copyright 2014 American Chemical Society)

provides a clear insight in the chemical bonds formed between the constituent atoms in TiO_2 but also serves as an excellent tool to visualize the hybridization between the different energy levels/orbitals within the cation and anion, as well as the change upon doping. Asahi et al. [20] have investigated the chemical bonding in anatase TiO_2 by decomposing its densities of states (DOSs) spectra into Ti e_g and t_{2g} (d_{yz}, d_{zx}, and d_{xy}), O p_σ (in the TiO_3 cluster plane), and O p_π (out of plane) carefully, and then a molecular orbital bonding energy diagram of anatase TiO_2 could be further constructed from these orbitals (Fig. 11.3); it now more clearly shows that (i) the valence band (VB) of anatase TiO_2 is comprised of O p_π (higher energy region), p_σ and p_π (intermediate energy region), and p_σ (lower energy region) and (ii) the conduction band (CB) is comprised of Ti 3d and 4s, and the lower energy regions of the conduction band are constructed by the degenerate e_g-like and threefold t_{2g}-like states resulting from the crystal field splitting of Ti 3d.

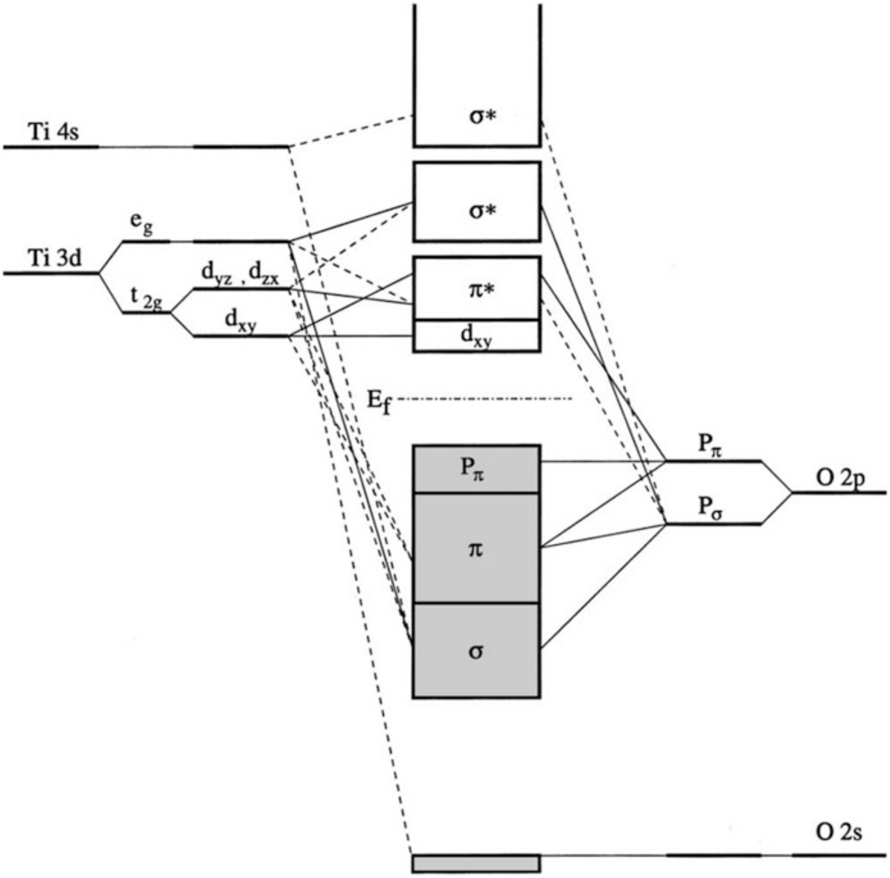

Fig. 11.3 Detailed molecular orbital bonding diagram of anatase TiO_2 (Reprinted with permission from Ref. [20]. Copyright 2000 American Physical Society)

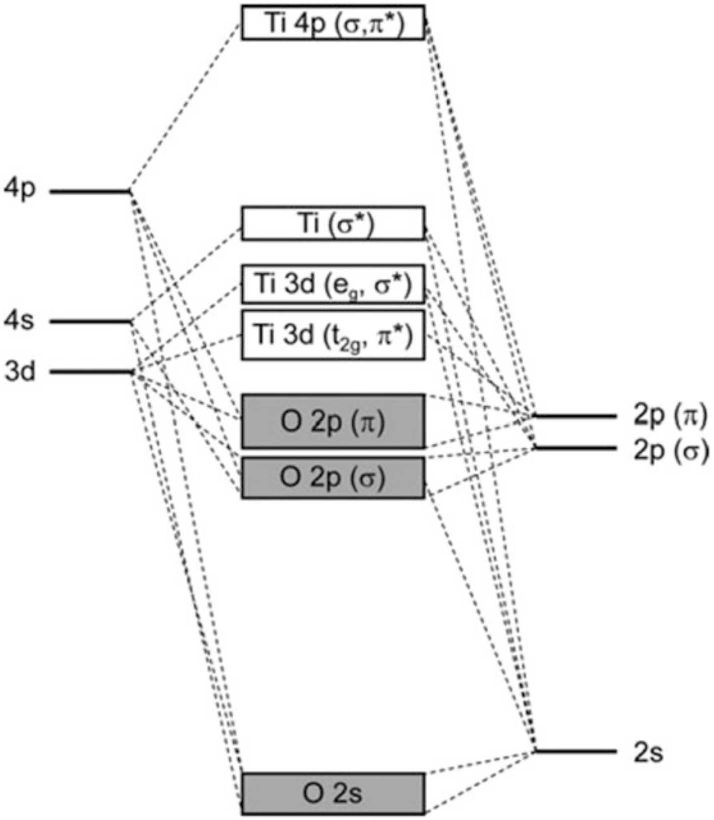

Fig. 11.4 Simplified molecular orbital diagram of rutile TiO_2 summarized by Van de Krol (Reprinted with permission from Ref. [21]. Copyright 2012 Springer)

Similarly, a simplified molecular orbital bonding energy diagram for rutile TiO_2 has been summarized by Krol [21], as shown in Fig. 11.4.

11.2.3 Band Bending

Before focusing on the processes occurring in TiO_2 under UV light irradiation, the situation before UV light exposure needs to be understood. The band bending concept was first proposed by Schottky and Mott to explain the rectifying effect observed from the contact of metal and semiconductor in 1930s [22–25]. As show in Fig. 11.5, the work functions of metal (ϕ_m) and semiconductor (ϕ_s) are usually not the same. With the contact of metal and semiconductor, the free electrons will flow between the metal and the semiconductor because of the work function difference. When the n-type semiconductor (electrons as majority charge carriers)

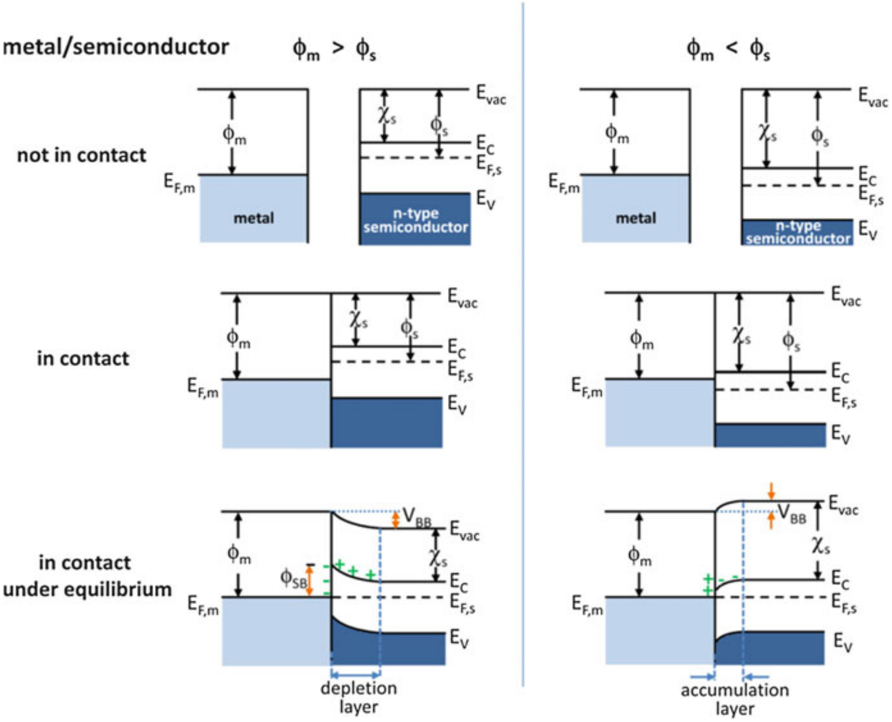

Fig. 11.5 Energy band diagrams of metal and n-type semiconductor contacts. E_{vac} vacuum energy; E_c energy of conduction band minimum; E_v energy of valence band maximum; ϕ_m metal work function; ϕ_s semiconductor work function; χ_s electron affinity of the semiconductor (Reprinted with permission from Ref. [26]. Copyright 2012 American Chemical Society)

contacts with the metal and when ϕ_m is higher than ϕ_s, as shown in the left of Fig. 11.5, the electrons will transfer from the semiconductor to the metal continually until the Fermi levels of metal ($E_{F,m}$) and semiconductor ($E_{F,s}$) are aligned. Under equilibrium, a Helmholtz double charge layer will be formed at the metal/semiconductor interface, where the metal is negatively charged and the semiconductor is positively charged near its surface. As a result, the concentration of the free charge carriers near the semiconductor surface is depleted compared with that of the bulk. This near-surface region of the semiconductor is defined as the space charge region. When ϕ_m is higher than ϕ_s, the electrons are depleted in the space charge region, and thus this region is called the depletion layer with excess positive charge. When ϕ_m is lower than ϕ_s, as shown in the right side of Fig. 11.5, the electrons flow from the metal to the semiconductor, leading to an accumulation of electrons in the space charge region, and this region is called the accumulation layer. Generally, when the $E_{F,m}$ is below the $E_{F,s}$, charge will transfer to the metal resulting in the $E_{F,s}$ to decrease and vice versa.

In the space charge region, due to the electric field formed between the semiconductor and the metal as a result of the charge transfer, the energy band edges in the semiconductor are also shifted continuously, which is called band bending. When ϕ_m is higher than ϕ_s, the energy bands bend upward toward the interface, while the edges of the energy bands bend downward toward the interface when ϕ_m is smaller than ϕ_s. In Fig. 11.5, compared with the bulk, the degree of bending of the energy band of the semiconductor at the interface equals to the work function difference between metal and semiconductor [26]:

$$\mathrm{V}_{\mathrm{BB}} = |\phi_m - \phi_s| \tag{11.1}$$

When ϕ_m is higher than ϕ_s in an n-type semiconductor, there is also a barrier formed at the metal/semiconductor interface, which is called the Schottky barrier (ϕ_{SB}) [26]:

$$\phi_{SB} = (\phi_m - \chi_s) \tag{11.2}$$

where χ_s is the electron affinity of the semiconductor. When ϕ_m is lower than ϕ_s in an n-type semiconductor, there is no Schottky barrier.

As mentioned above, the contact between TiO_2 and another phase (i.e., liquid, gas, or metal) generally involves the distribution of electric charges and the formation of a double charge layer. The transfer of mobile charge carriers between TiO_2 and the contact phase, or the trapping of charge carriers at surface states of the interface, leads to a space charge layer. For TiO_2–gas phase interactions, surface states available for electron trapping exist, resulting in a negative space charge layer at the interface. To preserve electrical neutrality, a positive space charge layer forms just within TiO_2 causing a shift in electrostatic potential and a bending of bands upward toward the surface [27]. Even for a clean surface with surface states, that is, of a single crystal TiO_2 surface in contact with vacuum, surface states will be formed which alter the electronic structure drastically.

For stoichiometric TiO_2 single crystal surfaces (such as rutile (100) and (110)), flat bands have been demonstrated from photoemission experiments [28]. However, TiO_2, as an n-type semiconductor, is largely used in photocatalytic systems; the surface inevitably contains a lot of defects, which are usually surface oxygen vacancies (O_v). During the process of the removal of the corresponding oxygen atom to form an O_v, the initially located electrons in an O 2p orbital are transferred into the conduction band formed by Ti 3d orbitals and then exist in the form of unpaired electrons [29]. After a careful analysis of this electronic situation, Diebold [8] concluded that the excessive electrons in the oxygen vacancies act as donor-like states, developing an accumulation layer in the near-surface region that leads to a downward band bending (Fig. 11.6). However, it is very important to take a careful note that the direction of band bending strongly depends on the surface structure and the adsorbates. For realistic cases, with the adsorption of different kinds of molecules at the electron-rich surface, the direction of band bending may even be reverted via excessive charge transfer between surface and adsorbate [30, 31]. More details about the effect of band bending on photochemical reactions can be obtained in Ref. 26.

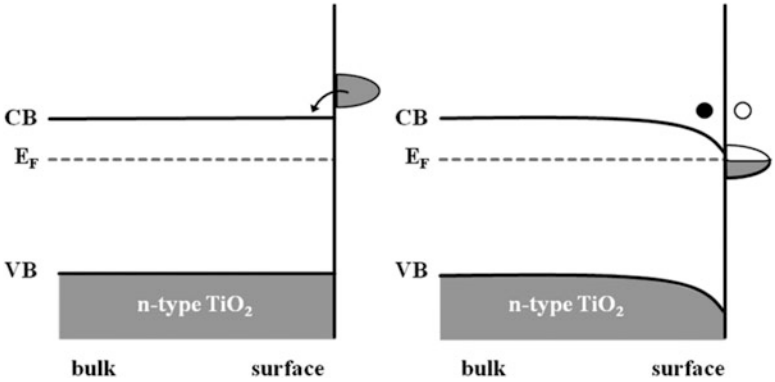

Fig. 11.6 Schematic diagram of the surface band bending of a clean n-type TiO_2 in vacuum due to the presence of donor-like surface defect states (● electron; ○ hole). An alternative energy diagram of a clean n-type TiO_2 has been suggested by Diebold [8] (Reproduced with permission from Ref. [1]. Copyright 2014 American Chemical Society)

11.3 Charge Transport and Trapping

The photon absorption in a photocatalytic reaction is typically viewed as a bulk (i.e., subsurface) process. However, unlike metals which have a continuum of electronic states, TiO_2 possess a wide bandgap which extends from the top of the filled VB to the bottom of the vacant CB, where no electron energy level is available. The VB of TiO_2 is formed by the interaction of the highest occupied molecular orbital (HOMO), while the CB is formed by the interaction of the lowest unoccupied molecular orbital (LUMO). The band structure, including the bandgap (denoted as E_g) and the positions of CB and VB, is one of the important properties for TiO_2 photocatalyst, as well as other semiconductor photocatalysts, because it determines the light absorption property and the redox capability of a semiconductor photocatalyst. Once photoexcitation occurs across the bandgap, the electrons in VB will be excited to CB, leaving the holes in VB. This electron–hole pair generation process in TiO_2 can be expressed as follows:

$$\mathrm{TiO_2} + h\nu \rightarrow \mathrm{e^-(TiO_2)} + \mathrm{h^+(TiO_2)}$$

These photogenerated electron–hole pairs may further be involved in the following three possible processes: (i) the electron–hole pairs are separated and successfully migrate to the surface of TiO_2 and then transfer to adsorbed organic or inorganic species or to the solvent (processes 1 and 3 in Fig. 11.7); (ii) the separated charge carriers are captured by the defect sites in bulk and/or on the surface region of TiO_2; (iii) the separated charge carriers recombine and release the energy in the form of heat or photon in bulk and/or on the surface region of TiO_2 (processes 2 and 4 in Fig. 11.7). Usually, the last two processes are thought as deexcitation processes, because the photogenerated charges do not have the opportunity to drive the photocatalytic reaction. Only the photogenerated charges that transfer to the reactants via the surface

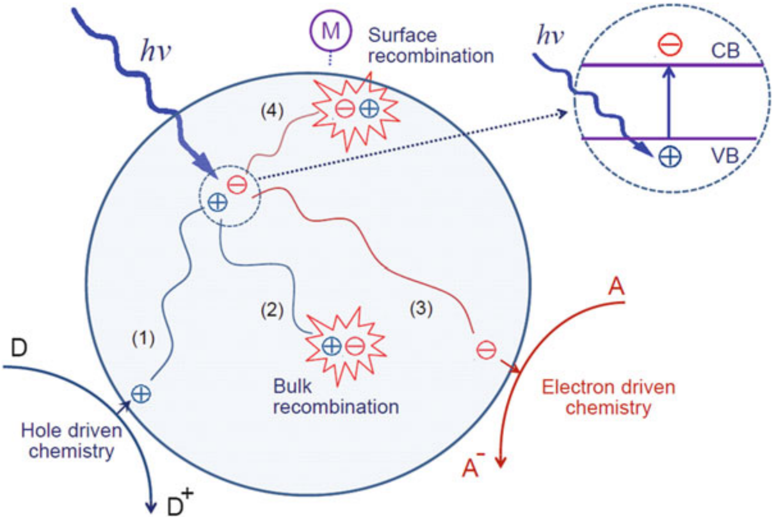

Fig. 11.7 Important processes in the surface photocatalysis processes: photoexcitation of electron–hole pair, charge transfer processes, bulk and surface recombination processes, and electron- and charge-induced chemistry at surfaces (Reproduced with permission from Ref. [27]. Copyright 1995 American Chemical Society)

of TiO_2 could contribute to photocatalytic reactions. The defect sites on the surface and in the bulk of TiO_2 may serve as the recombination centers for the photogenerated electrons and holes, which will decrease the efficiency of the photocatalytic reaction.

In principle, a photocatalytic reaction can be divided into two half reactions, reduction reaction and oxidation reaction. The photoexcited electrons in the CB may initiate a reduction reaction with electron acceptors, and the reduction capability depends on the position of CB minimum (CBM); the holes in the VB drive the oxidation reaction with electron donors, and the oxidation capability is determined by the position of VB maximum (VBM). For the generation of hydrogen from the water splitting reaction, the position of CBM of a semiconductor photocatalyst needs to be located at a more negative potential than the redox potential of H^+/H_2(0 V vs. NHE, pH = 7), while the position of VBM needs to be located at a more positive potential than the redox potential of O_2/H_2O (1.23 V vs. NHE, pH = 7). Although the energy required for the complete redox reaction in this case does not exceed ca. 1.23 eV (Fig. 11.8), the energy required for generating the electron–hole pairs in the catalyst through photoexcitation still needs to be higher than E_g.

As mentioned above, photocatalytic reactions occur at the surface, and photogenerated charge carriers must transfer to the surface and be stabilized at the surface for the electron–hole transfer to the reactants (and not for recombination events). This situation raises questions about how charge carriers transfer through a lattice to a surface. What are the relative timescales for charge separation, thermalization, transport, and trapping? What are the typical charge trapping surface sites? However, characterizations of exciton (electron–hole) thermalization, lifetimes, transport kinetics, trapping, and quenching are all difficult tasks [32].

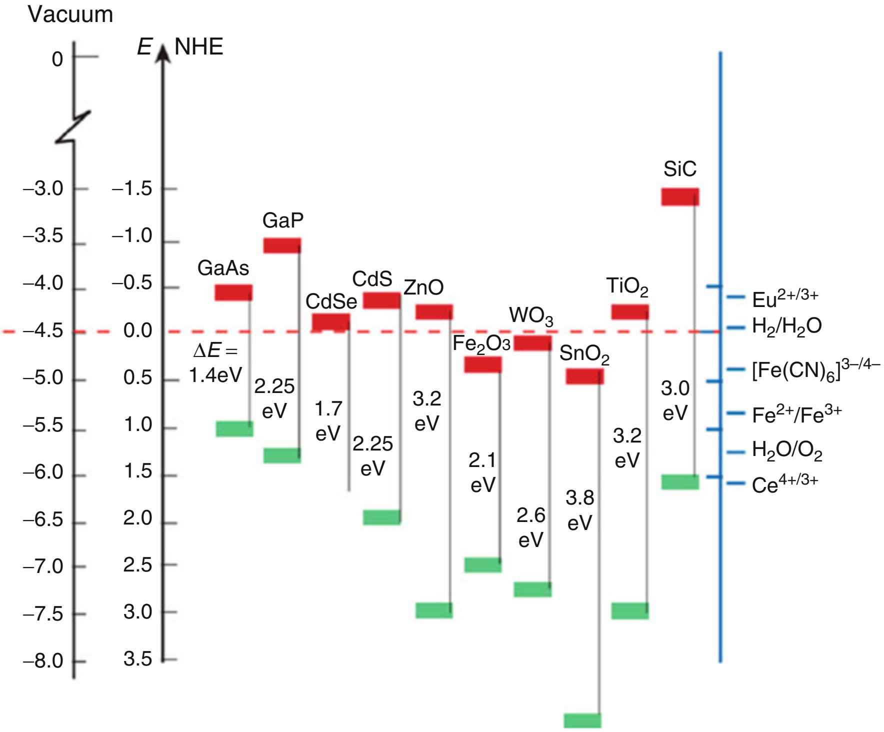

Fig. 11.8 Compilation of energy band positions for some selected semiconductors in contact with an aqueous electrolyte at pH 1 with respect to NHE and the vacuum level as a reference. The scale on the right presents the potentials of several redox couples (Reprinted with permission from Ref. [19]. Copyright 2014 American Chemical Society)

11.3.1 Charge Separation

The efficiency of photocatalytic processes can be evaluated by the measurement of the photonic efficiency ζ, which is defined as the rate of the formation of reaction products divided by the incident photon flow [33]. Unfortunately, the ζ of semiconductor photocatalysts (including TiO_2) usually is found to be rather small. In fact, time-resolved spectroscopic studies demonstrate that most of the photogenerated electron–hole pairs (~90 %) recombine rapidly after excitation. This is proposed to be one main reason for the relatively low ζ (<10 %) for most semiconductor-based photocatalytic reactions.

Therefore, a variety of approaches are investigated to promote the efficiency of charge separation in TiO_2 such as heterojunction, supported charge trap, and bulk dopant for separating one carrier from the other. Of course, the efficiency of charge separation in TiO_2 may be affected by the energy of the charge carriers, as well as temperature. “Hot” electrons and deep holes may be more likely to separate than charge carriers generated with near-bandgap energy light, whereas, according to the work of Berger et al. [34], higher temperatures can decrease the charge separation efficiency of some trapping sites.

11.3.2 Charge Thermalization

In an ideal photocatalyst, all photon energy invested in the generation of charge carriers would be available for redox chemistry. The higher the potential energy of the electron (or hole) is, the more reductive (or oxidative) the capacity is [32]. As a result, a tunable energy of a carrier could be useful for promoting desired electron (or hole) transfer reactions. However, thermalization of charge carrier is rapid. For example, Gundlach and coworkers [35, 36] used 2PPE to track thermalization following electron injection from two dyes adsorbed on rutile $TiO_2(110)$. The authors found that fast initial decay of the 2PPE signal resulting from thermalization of the injected electron occurs on the 10 fs timescale. This result suggests that excess potential energy is lost to the lattice via strong coupling with phonon modes, thus reducing the potential advantage gained by the specificity in the absorption event. Additional evidence for the rapid thermalization of electrons comes from photoemission spectra of Ag clusters on rutile $TiO_2(110)$ [37] as a function of injection electron energy and from photoluminescence spectra of rutile $TiO_2(110)$ [38, 39] with 3.35 eV photon irradiation. In both studies, a constant energy of the emitted photons was observed (at and below the bandgap energy of 3.05 eV), independent of the energy of the exciting electron or photon. Furthermore, experimental investigations indicate that the photodesorption yield and translational energy of O_2 from an O_2-adsorbed rutile $TiO_2(110)$ surface are independent of the excitation photon energy above 3.4 eV, but dependent on the photon flux [40, 41]. Using time-resolved terahertz spectroscopy, Turner et al. [42] investigated the thermalization following electron injection from an adsorbed R535 dye (excited with 100 fs pulses of 400 nm light) on P25 nanoparticles. These authors found that injected electron thermalization to the CB edge occurs on the $\sim$300 fs timescale.

Conversely, hole thermalization in the VB is always accompanied by electron thermalization in the CB, which makes it difficult to distinguish the two processes. Through examining the rate of salicylate photooxidation on suspended TiO_2 nanoparticles ($\leq$5 nm) as a function of excitation energy, Grela and coworkers showed [43] that higher energy photons are always more efficient, resulting in higher quantum yields. Similarly, in another study [44], the quantum yields for 3-nitrophenol photooxidation were also shown to be greater for higher energy photons (Fig. 11.9). These results were consistent with the action spectroscopy study of "hot" hole oxidation of various aromatic molecules on colloidal TiO_2 by this group [45]. Thus, these authors proposed that hole transfer can precede hole thermalization in TiO_2.

Using femtosecond transient reflecting grating (TRG) method to observe the photoinduced ultrafast relaxation dynamics at $TiO_2(001)$/KSCN (aq) interfaces, Morishita and coworkers [46] found that the hole transfer time at TiO_2/SCN^- interfaces is on the 110–690 fs timescale, which is much faster than the estimated

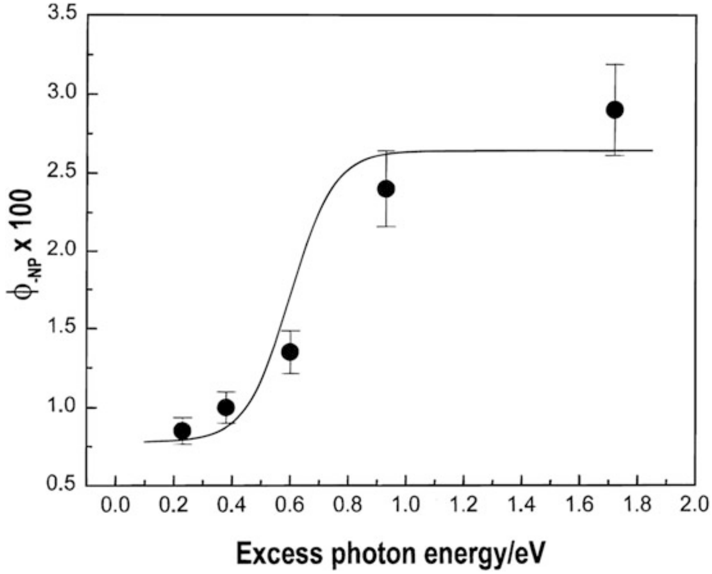

Fig. 11.9 Quantum yields for photooxidation of 3-nitrophenol over suspended TiO_2 as a function of "excess photon energy" (defined as the photon energy in excess of the TiO_2 bandgap energy) (Reprinted with permission from Ref. [44]. Copyright 1999 American Chemical Society)

(1.8 ns by Marcus theory) and reported (5 μs by Bahnemann et al. [47]) values, indicating that the nonequilibrium holes in the VB of TiO_2 may be involved in interface reactions. Similarly, Tamaki et al. [48, 49] have measured the lifetimes of electron and hole trapping in nanocrystalline films of anatase (particles of $\leq$20 Å) with transient absorption method. Based on their assignments of the absorption spectrum of trapped holes, these authors suggested that in some cases hole trapping preceded hole thermalization by up to 100 ps. However, the charge carrier thermalization does not actually correspond to chemical reactions.

11.3.3 Electron Trapping

Electron traps are believed to be localized in the lattice of TiO_2 as Ti^{3+} sites, although the degree of localization remains unclear. The potential energies of surface electron trap states is a little lower than that of the CB (in a range between 0.1 and 1 eV) [32, 50] which is compatible with previous photoemission results for electronic defect state on the surface of TiO_2 single crystal surfaces [8]. It is universally accepted that electron trap sites are located at the surfaces of TiO_2 (irrespective of the polymorph) [32]. However, there are also reports of electron being trapped in the bulk of TiO_2 [51, 52], and theoretical calculations [53, 54] propose that electrons prefer trapping in the bulk (subsurface) rather than trapping at the surface. Other theoretical work [55] suggests that the under-coordinated Ti cation sites on surfaces are the most stable electron trap sites. Similarly, other groups propose that electron traps locate at TiO_2–TiO_2 particle interfaces [56] or at grain boundaries [57]. The electron trap stabilities of TiO_2 can be affected by structure and dielectric properties or by the presence of adsorbates. For example, Planelles and Movilla [58] have investigated the effect of nanopore sizes in TiO_2 on its ability to trap electrons using theoretical method. They found that at low temperature, electron trapping holding by nanopores occurs for the diameter of pores <14 nm, with the trapping stability depending mostly on the nanopore diameter and the chosen permittivity, as well as temperature.

Although the electron trap ability of TiO_2 can be very useful for hole-mediated photochemistry, electron trapping inhibits some processes relying on rapid electron transport (such as photovoltaic application). Thus, rapid electron detrapping is more important in these applications. Electron detrapping usually occurs in two ways: (1) polaronic hopping, which involves in a "trap-to-trap" hopping process [59], and (2) complete detrapping, in which a trapped (localized) electron is converted to a free (delocalized) electron. Detrapping can be induced by thermal activation with low barriers in the range of 0.1–0.3 eV [60–62], or by nonthermal activation through sub-bandgap light excitation [63, 64]. Usually, both polaronic hopping and complete detrapping can be easily accomplished via thermal activation. According to sensitization studies on TiO_2 films by van de Lagemaat and coworkers [65], the average thermal detrapping time is on the order of 10 ns at room temperature, which is rather rapid. Conversely, nonthermal detrapping by sub-bandgap light excitation is mainly governed by the optical properties of the trap state. Based on transient absorbance (TA) studies, Shkrob and Sauer [63] found that as the trapped electron is detrapped by 1064 or 532 nm photoexcitation, the resultant-free, mobile electron rapidly recombines with the hole on a timescale of 3 ns. Beerman et al. [64] and Komaguchi et al. [66] also observed the similar results, while Komaguchi and coworkers monitored Ti^{3+} electron spin resonance (ESR – essentially the same technique as EPR) signals for thermally reduced anatase (○), rutile (Δ), and P-25 (□) during and after visible light irradiation (Fig. 11.10). Upon irradiation of the reduced samples with white light at 77 K, the Ti^{3+}EPR signals for these three samples all decreased in intensity and disappeared entirely after a few minutes of illumination. After the light was turned off, the Ti^{3+}EPR signals begun to reappear and increase in intensity at 77 K. Finally, the signals for the anatase and rutile were restored to 100 % of the initial intensity within 30 min, whereas in the P-25 samples, a certain amount of the electrons detrapped from the anatase phase could transfer through the interfacial boundaries to be retrapped on the rutile phase, leading to the Ti^{3+}EPR signal restoration, which significantly exceeds the initial value.

Although EPR technique is an extremely powerful tool to detect and characterize trapped electrons (and holes) on/in TiO_2, with surface and subsurface trap sites distinguished using chemical adsorbates (hole scavenger and electron scavenger), it is not very convenient for many researchers due to the high requirements of operation, such as low temperature and high intensity of magnetic field. Thus, other easy-to-use techniques have been innovated for detection and characterization

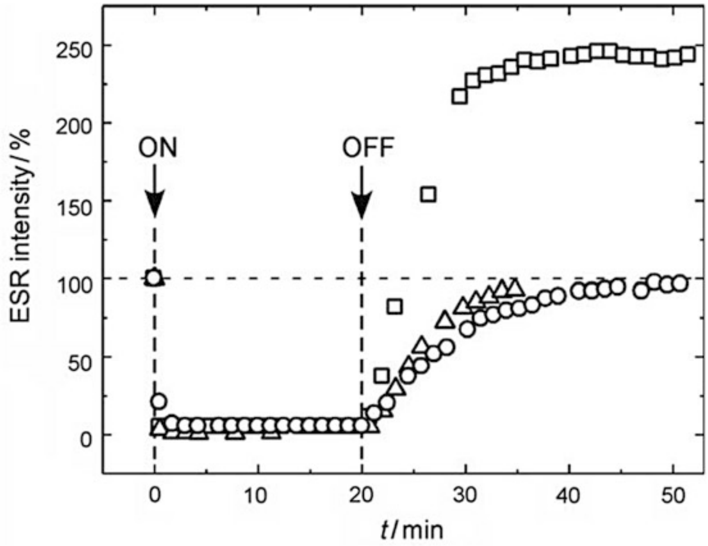

Fig. 11.10 Relative changes in the EPR (ESR) signals associated with trapped electrons in anatase (○), rutile (Δ), and P-25 (□) resulting from visible light irradiation in air (Reprinted with permission from Ref. [66]. Copyright 2006 Elsevier)

of trapped electrons in TiO_2. Nowadays, based on the optical properties of trapped electrons, several optical spectroscopies have been used for detecting trapped electrons. However, a big challenge for optical spectroscopies is correlating absorption events at specific wavelengths, which are typically very broad, with specific trap sites in or on TiO_2, while identification of the excited state level of an optical transition is another challenge. Readers could get more detailed information about optical spectroscopies for detecting trapped electrons in Ref. 32.

11.3.4 Hole Trapping

According to a series of EPR studies [32], a surface $Ti4^+–O^-$ site is proposed to be the most likely hole trap site, where the hole locates at an under-coordinated surface oxygen atom. However, it is unclear whether bridged or oxo type is the preferred coordination of such a site. Additionally, some groups have also found evidence for subsurface hole traps [50, 67, 68]. Recently, Kerisit et al. [69] carried out calculations on the sites of hole (and electron) trapping at the unrelaxed rutile $TiO_2(110)$ surface. Their results indicate that holes prefer to trap in the near-surface region, as opposed to on surface sites or in the bulk (Conversely, electrons prefer to trap at subsurface sites). Their results are consistent with the early findings by Shapovalov et al. [70] using an ab initio embedded cluster approach.

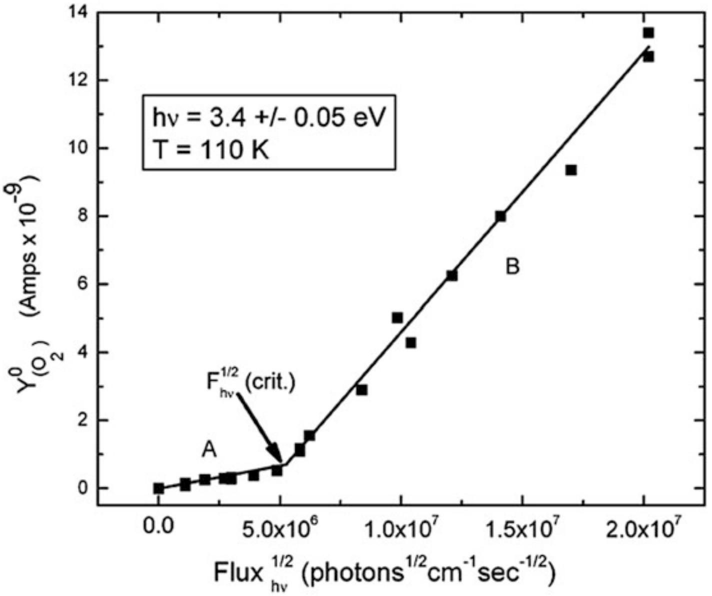

Fig. 11.11 Dependence of the $^{18}O_2$ photodesorption yield on the incident UV photon flux for $^{18}O_2$ adsorbed on the rutile $TiO_2(110)$ surface at 110 K (Reprinted with permission from Ref. [73]. Copyright 2005 American Chemical Society)

Compared to electron trapping studies performed via sensitization, there are no convenient methods to inject holes into the VB of TiO_2. Thus, hole trapping studies always initiate with band-to-band excitation processes. Although optical spectroscopies have been used for detecting trapped holes based on comparisons before and after exposure to hole scavengers, the nature of the adsorption events (the excited state level of an optical transition) is not known. For example, by time-resolved transient absorption studies, Tamai and coworkers [71] observed a broad transient absorption signal at ~520 nm and assigned it to excitation of trapped holes initiating from excitation of colloidal anatase with a 200 fs 360 nm pulsed laser source based on comparisons before and after exposure to hole scavengers, such as SCN^-, and the hole trapping timescale at the surface of colloidal anatase particles is about 50 fs. Similarly, Tamaki and coworkers [50, 72] assigned the spectral region at ~500 nm to excitation of trapped holes from excitation of nanocrystalline films of anatase (diameter of particles ≤20 Å) using the same method. These authors also estimated a hole trapping timescale of ~200 fs for "hot" holes, and then, the trapped holes thermalized over the next 100+ ps.

Thompson and Yates [73] were perhaps the first to quantify bulk concentration of hole traps in the near-surface region of a reduced rutile $TiO_2(110)$ surface, by increasing the photon flux and using photodesorption yield of $^{18}O_2$ to monitor the rate of hole delivery to the surface (Fig. 11.11). These authors observed two linear branches, A and B, in the relationship between the photodesorption yield of $^{18}O_2$

and the photon flux. At low fluxes (branch A), the photodesorption yield of $^{18}O_2$ was significantly lower than at high fluxes, which is proposed to result from preferential trapping of holes away from adsorbed O_2 molecules, presumably in the subsurface. At F_{hv}(crit), the holes transferring to the surface fill all the hole traps, leading to a more efficient branch B photodesorption process. By assuming that the fluence of photons at F_{hv}(crit) is entirely consumed by trap filling by holes, an upper limit for the hole trap density of $\sim 2.5 \times 10^{18}$ cm^{-3} ($\sim$0.003 % of the atomic sites in the bulk lattice) is estimated by these authors. Moreover, Berger and coworkers [74] found that reduced TiO_2, produced by annealing in vacuum, is less efficient in hole trapping than oxidized TiO_2, indicating that these bulk traps are related to reduced centers resulting from vacuum annealing.

11.3.5 Charge Recombination

The photocatalytic efficiency of TiO_2 photocatalysts is usually limited due to the fast recombination of the electron–hole pairs. Although this recombination process is undesirable, its study can provide a deep insight into the charge carrier dynamics in TiO_2. The recombination of the charge carriers can occur via two pathways: irradiative and non-irradiative routes. The irradiative pathway involves light emission. Non-irradiative recombination can occur through energy release via phonon emission. Generally, the non-irradiative recombination in TiO_2 is believed to be the main charge recombination pathway, while the charge recombination processes can be strongly affected by chemical adsorbates (i.e., hole or electron scavengers) or additives (such as supported metal particles, dopants, or interfacial heterojunctions).

Photoluminescence (PL) induced by irradiative recombination is usually at sub-bandgap energies because of charge carrier thermalization and trapping. As a result, PL spectroscopy can give valuable information in the energetic distribution of sub-bandgap states and the dynamics of TiO_2 related to thermalization and trapping. For both anatase and rutile, the PL spectra are detected from the visible to the near-IR wavelength range, whereas the PL for anatase is related to self-trapped excitons and, for rutile, to intrinsic sites (such as defects or impurities) or to surface-bound species [11, 75–78]. For example, Knorr and coworkers [79] found that the PL spectrum of the anatase nanocrystalline film spans a broad range of visible wavelengths centered at 520 nm, while the PL spectrum of the rutile nanocrystalline films is observed in the near-infrared range centered at 840 nm. In the combination of time-resolved PL, transient absorption (TA), and photoconductivity (PC) measurements, Yamada and Kanemits [80] have investigated the electron and hole relaxation dynamics in rutile and anatase TiO_2 single crystals. These authors showed that the lifetimes of electrons and holes in rutile are on a few nanosecond timescales (24 ns for electron, 48 ns for hole), whereas the carrier decay dynamics in anatase are completely different from those in rutile. In anatase crystals, the interaction between electrons and holes is weak because of its indirect-gap band structure, the lifetime of electrons in anatase is longer than 1 μs, while the decay for the holes occurs on the nanosecond timescale, indicating the presence of multiple carrier trapping processes. These authors also suggested that the long electron lifetime is related to the high photoactivity of anatase.

Furthermore, from time-resolved photoluminescence (PL) spectroscopy analysis, Dozzi et al. [81] found that the photoactivity of the anatase TiO_2 materials doped with fluorine increases with the increasing long-lasting component of the PL signal, suggesting that long-living photoproduced charge couples are beneficial in photoactivity, while systems with other TiO_2-related interfaces indicate that surface structure and the presence of adsorbates on both rutile and anatase TiO_2 surfaces play an important role in guiding neutralization events toward emission [32].

As mentioned above, photogenerated electron–hole pairs in TiO_2 predominantly recombine through non-irradiative pathways. The non-irradiative recombination occurs upon the rapid release of heat, making it difficult to be directly detected. Thus, it is usually detected by indirect methods, such as time-resolved photoacoustic spectroscopy (TRPAS). With this method, Leytnar and Hupp [82] found that about 60 % of all trapped electron–hole pairs generated in their colloidal anatase samples recombine on the timescale of about 25 ns, releasing 154 kJ/mol of energy as heat. In contrast, irradiative recombination is not expected to contribute significantly to heat generation.

As in the case of photoluminescence, surfaces, defects, adsorbates, and impurities all likely play roles in promoting or inhibiting charge recombination [32]. However, temperature can strongly affect the proportion of irradiative versus non-irradiative recombination in TiO_2. For example, using anatase TiO_2(001) thin films fabricated on $LaAlO_3$(001) substrates by a laser molecular beam epitaxy (MBE) method, Murakami and coworkers [77] observed a PL band with the peak maximum at 2.2 eV due to recombination of self-trapped excitons at 5 K. As sample temperature was higher than 200 K, the PL was significantly quenched, suggesting that charge recombination at higher temperature became non-irradiative, likely resulting from increased lattice motions. From these previous studies, it is clear that charge (electron and hole) recombination is a main pathway for excited state energy relaxation; it is therefore interesting to ask whether this large amount of energy released will have a significant effect on surface chemical reactions for adsorbed molecules. If it does have an effect, it means that ground state surface reaction of adsorbed molecules is possible. This kind of mechanism is obviously very different from the hole- or electron-induced reaction mechanisms, which are widely believed to be the mechanism for photocatalysis. It is therefore very necessary to investigate this important issue of how charge recombination will affect the surface chemical reactions.

11.4 Electron Transfer Dynamics

Interfacial electron transfer between a surface and a chemisorbed (or physisorbed) species is a fundamental process that is relevant to many applications in heterogeneous photocatalysis. The interaction is essentially interpreted as a donor/acceptor (D/A) model initiated by a photoexcitation event. There are commonly four types of electron transfer processes. The first type involves electron transfer from the TiO_2 CB to an electron acceptor ("1" in Fig. 11.7); the second ("3" in Fig. 11.7) involves hole transfer from the TiO_2 VB to a hole acceptor (i.e., electron transfer from an electron donor into a VB hole state); the third involves electron transfer from a donor into the TiO_2 CB; and the fourth involves hole transfer from a donor into the TiO_2 VB, which is not commonly observed for TiO_2 (i.e., electron transfer from a TiO_2 VB state to an unoccupied state of an acceptor). The first two types of electron transfer correspond to photoexcitation occurring in TiO_2 and the last two correspond to photoexcitation occurring in an adsorbate or attached entity (such as dopants or impurities). It is worth noting that not all electron transfer processes lead to chemistry (i.e., old bond brokenness and new bond formation) or involve ground state configurations.

11.4.1 TiO_2 Conduction Band to Electron Acceptor

In the past, a photocatalytic reaction is normally divided into two half reactions, reduction reaction and oxidation reaction. A reduction reaction may be initiated by coupling of a CB electron to acceptor states of an adsorbed species (i.e., electron in the CB transfer to the LUMO of the adsorbed species). However, the coupling should be strong enough and energetically downhill to inhibit back-electron transfer to the higher DOS in the TiO_2 CB. For example, using time-of-flight quadrupole mass spectrometry, Weitz and coworkers [83, 84] have investigated the substrate-mediated photodesorption of CH_3X ($X = I$ and Br) on rutile $TiO_2(110)$ for low fluence irradiation. These authors found that the CB electrons generated from bandgap excitation of TiO_2 transfer to these adsorbed CH_3X molecules do not drive appreciable photochemical reaction. On the contrary, an Antoniewicz-type desorption process occurs due to the rapid back-electron transfer to the surface [85]. As shown in Fig. 11.12, starting from the neutral ground state (and following the dashed lines), an electron attachment causes a Franck–Condon transition from the ground state of the adsorbate–substrate system to antibonding states, which leads to the excited/ground ion state. The ion created in the excitation process sees an attractive image potential. The new equilibrium position of the ionized adsorbate is considerably closer to the surface than the ground-state adsorbate equilibrium position. Thus, the newly formed ion relaxes toward the surface and is neutralized via back-electron transfer to the surface, which is described by a vertical jump from the upper to the lower curve. During the vertical jump process, the kinetic energies (KE) of the ion and the neutral adsorbate are the same, so the total energy of the neutral adsorbate is the kinetic energy before neutralization plus the potential energy at the position of the neutralization. If the total energy is greater than the adsorption energy, the adsorbate will desorb from the surface after breaking the adsorption bond. The desorption events strongly depend on the potential energy surfaces of ion and molecule and the lifetime of excited states as well.

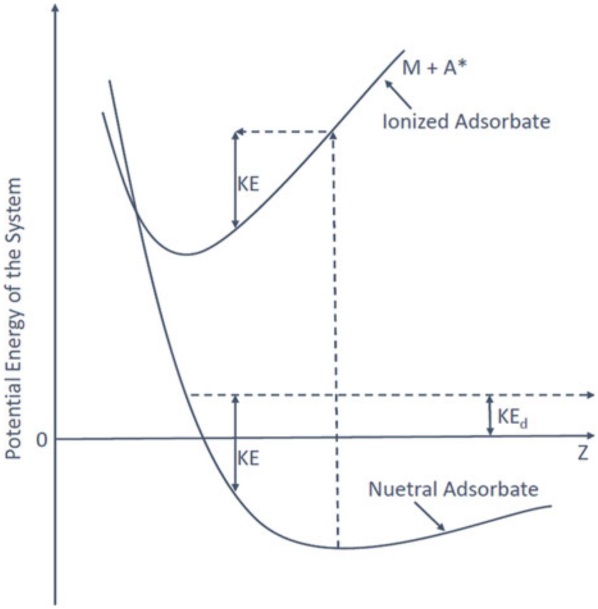

Fig. 11.12 Schematic model of the Antoniewicz model for excitation-induced desorption from surfaces. The *vertical dashed arrow* corresponds to the initial charge transfer event, placing the adsorbate on an "ionized adsorbate" potential energy surface. Prompt re-neutralization back to the "neutral" adsorbed potential energy surface results in the adsorbate retaining sufficient kinetic energy ("KE") for desorption (Reprinted with permission from Ref. [85]. Copyright 1980 American Physical Society)

While there are many studies involving the mechanistic details of photoreduction processes on TiO_2 (such as H_2O and CO_2 photoreduction), there are only few photodynamic studies focusing on a photoreduction process. The main limitation is the unavailability of convenient molecular markers that are sensitive to electron attachment. One of the convenient molecular markers is the methyl viologen divalent cation (MV^{2+}). Using TA method, Asahi and coworkers [86] found that electron transfers from photoexcited colloidal anatase TiO_2 to MV^{2+}adsorbed on the TiO_2 surface in the few picosecond to nanosecond timescale, as monitored by the appearance of the 605 nm absorption feature of MV^{+}. The timescales are comparable to the electron trapping times in TiO_2, indicating that the reduction of MV^{2+}-adsorbed on the surface is likely due to trapped electrons and not free CB electrons, while similar studies performed by Martino et al. [87] also support these conclusions. Although so many dynamic works have been done on electron transfer from TiO_2 to an electron acceptor by molecular sensitization studies, the dynamics of real photoreduction reactions (i.e., H_2O reduction to produce H_2) are not well understood.

11.4.2 Electron Donor to TiO_2 Valence Band Hole

Generally, an oxidation reaction may be initiated by coupling of a VB hole state to donor states of an adsorbed species (i.e., electron transfer from an electronic state of an adsorbate to a more or less localized VB hole state generated in TiO_2 by a band-to-band photoexcitation). Similar to CB electron photoreduction, VB hole photooxidation also initiates from photoinduced band-to-band transitions in TiO_2 leading to charge carriers with a broad range of energies, generated at near or at the TiO_2 surface.

Compared to extensive dynamic studies of CB electron transfer to acceptor states of an adsorbed species, the dynamics of hole transfer on TiO_2 are less investigated. Usually, thiocyanate (SCN^-), as the most effective adsorbate (or hole scavenger), is chosen for probing the dynamics of hole transfer. An early dynamical study of SCN^- photooxidation on TiO_2 carried out by Colombo and coworkers [88] demonstrates that interfacial charge transfer of an electron from the SCN^- to a VB hole generated in TiO_2 effectively competes with electron–hole recombination on an ultrafast timescale. Similarly, by the analysis of rise and decay dynamics of TA spectra of nanosized anatase TiO_2 colloidal system without SCN^-, Yang and Tamai [71] estimate the hole and electron trapping times to be <50 and 260 fs, respectively, while the rate of the hole transfer from nanosized anatase TiO_2 colloid to SCN^- is comparable to that of the hole trapping, implying that the hole transfer process occurs on a similar timescale. The similar conclusion is further verified by Morishita et al. [46] and Furube et al. [89].

However, the timescale of hole transfer varies significantly according to the different kinds of adsorbates (hole scavengers). For example, using I^- as a hole scavenger, Rabani and coworkers [90] found that hole transfer from packed films of 5 nm TiO_2 particles to I^- occurs within less than 10 ns, while the decay of the electron absorption is only slightly different than in I^- free solutions. In contrast, the adsorbed alcohols (methanol or isopropanol) are more reactive for recombination after trapping holes. Other groups have observed reactive trapped holes in TiO_2 with adsorbed alcohols. Shkrob and coworkers [91] have investigated hole transfer to chemisorbed diols and carbohydrates on TiO_2 nanoparticle ($PH = 4$, ~4.6 nm diameter) with time-resolved transient absorption spectroscopy. These authors found that on the timescale of the 355 nm laser pulse width (3.3 ns), 50–60 % of the generated holes react with chemisorbed diols and carbohydrates rather than recombine, while the examination of hole transfer to glycerol bound to TiO_2 nanoparticle by Shkrobet al. [63] obtained the similar results.

According to above studies, the hole transfer rates seem not to be the key factor for the inefficient photooxidations on TiO_2. For example, the single electron transfer from SCN^- to a VB hole is fast and efficient. Actually, an overall reaction generally requires many charge transfer process, and not all the steps are as fast and efficient as SCN^- photooxidation. And every electron transfer step in a photooxidation reaction is governed by the properties of VB hole and the electron donor. Thus, how to identify and improve the slow and inefficient steps is still a key challenge.

11.4.3 Electron Donor to TiO_2 Conduction Band

The dynamics of electron transfer from an electron donor to TiO_2 CB have been intensely studied. Normally, a dye molecule is chosen as an electron donor. With dye sensitization, the molecular dye (sensitizer) acts as the "photocatalyst," efficiently absorbing light to generate charge carriers, and then the excited electrons inject into the TiO_2 CB with high efficiency. Because of the well-known optical properties and energy levels of dye chromophores and the ability to spectroscopically track the injected electron, ultrafast dynamic studies of the electron transfer processes with TiO_2/dye systems are tailor-made. A series of results [32] reveal that the coupling of electronic states between the excited electronic states of dyes and the TiO_2 CB "continuum" is strong, leading to electron transfer processes between the two that are fast with injection yields approaching 100 % for many different dyes. In some cases, due to the strong coupling, back-electron transfer processes are also fast (see the work of Lian et al. [92]), whereas, in almost all cases, the CB "continuum" takes over in thermalizing the transferred electron, so that the process does not occur.

11.4.4 TiO_2 Valence Band to Acceptor Hole

Until now, no examples of studies involving hole photochemically generated in an adsorbed species injection into the TiO_2 VB have been reported. In this case, the HOMO levels of the chosen dyes should be below the energy level of the TiO_2 VB edge, and the electronic excited states of dye should reside mid-gap (far below the energy level of the TiO_2 CB edge) to avoid electron transfer from dye to the TiO_2 CB. In early studies, Hagfeidt and coworkers [93, 94] have constructed such a model solar cell system using NiO and proper dyes, but a similar model system has not been identified for TiO_2. Similar to back-electron transfer for photoreduction, back-hole transfer for photooxidation between an adsorbate and the TiO_2 VB (i.e., a VB hole generated on TiO_2 transfers transiently to an adsorbate and flows back the TiO_2 VB) provides another potential ground for examining hole injection to the TiO_2 VB, which may be very universal in photooxidation with TiO_2 catalysts. However, reliable photochemical "markers" are required for identifying and studying such a hole transfer process.

11.5 Mechanisms of Photocatalytic Chemical Reactions

The mechanism for a whole photocatalysis process is usually quite complicated. In this section, we will describe recent studies of detailed photocatalytic reactions of two important molecules on various TiO_2 surfaces: oxygen (electron scavenger) and methanol (hole scavenger), which are representative photooxidation and photoreduction reactions on TiO_2.

11.5.1 Oxygen

Oxygen (O_2) is usually present in the photooxidation of organic pollutants and photocatalytic splitting of water over TiO_2. In addition, oxygen can act as an electron scavenger, realizing the photoexcited electron–hole separation [26, 33, 95–97]. These crucial roles oxygen plays have stimulated the extensive studies of the interaction between oxygen and TiO_2 which are of both fundamental and applicable significance.

11.5.1.1 Adsorption of Oxygen on TiO_2 Surfaces

Adsorption of O_2 on TiO_2, which is both coverage and temperature dependent, requires the charge which is usually introduced by point defects such as surface oxygen vacancies (O_v) and subsurface Ti^{3+} interstitials (Ti_{int}) transfer from the substrate [30, 59, 98–103]. This is the reason why O_2 adsorbed only physically (desorbing below 75 K) on stoichiometric rutile $TiO_2(110)$ [104]. At elevated adsorption temperatures (above 150 K), spontaneous dissociation of O_2 at O_v's has been well established. An oxygen molecule healed an O_v, leaving another O_a at a neighboring Ti_{5c} site [101, 105–109]. Aside from the dissociation at O_v's, Besenbacher et al. discovered another channel for oxygen dissociation, i.e., splitting of O_2 at Ti_{5c} sites, producing O_a pairs, which was proposed to be facilitated by the excess charge transfer from the subsurface Ti_{int}'s [106, 108].

Despite the spontaneous dissociation of O_2 at both O_v and Ti_{5c} sites at elevated temperatures, molecular adsorption has also been investigated with temperature below 100 K. O_2 is adsorbed preferentially at O_v sites at this temperature range [110–113]. Temperature programmed desorption (TPD) experiments performed by Henderson et al. showed that chemisorbed O_2 desorbed at around 410 K with first-order kinetics [99]. Kimmel and Petrik [110] reported the saturation coverage of chemisorbed O_2 was twice of the O_v concentration, which meant two O_2 per O_v ($2\ O_2/O_v$). Based on the TPD and electron-stimulated desorption (ESD) results, these authors proposed a tetraoxygen species when the initial $2\ O_2/O_v$ structure was annealed between 200 and 400 K. This finding was consistent with earlier calculation by Pillay et al. [114], which showed the O_4^{2-} structure was more stable by 0.6–0.9 eV than $2\ O_2^-$. Site-specific adsorption of O_2 on rutile $TiO_2(110)$ has been investigated using high-resolution scanning tunnel microscope (STM) in Diebold's and Lyubinetsky's groups [111–113]. Briefly, driven by STM tip, molecularly adsorbed O_2 at both O_v and Ti_{5c} sites became dissociated (Fig. 11.13) [112]. Chemisorbed O_2 at O_v was invisible. However, since O_v appeared as bright spots on the dark bridging oxygen row in the empty state STM, one can easily see the difference before (Fig. 11.13Aa) and after (Fig. 11.13Ab) O_2 exposure, while molecular adsorbed oxygen at Ti_{5c} displayed as even brighter spot on the bright Ti troughs. To retain the chemisorbed structure, mild tunneling condition should be chosen. For example, that in Fig. 11.13Ab was taken at $V = 0.8$ V and $I = 3$ pA,

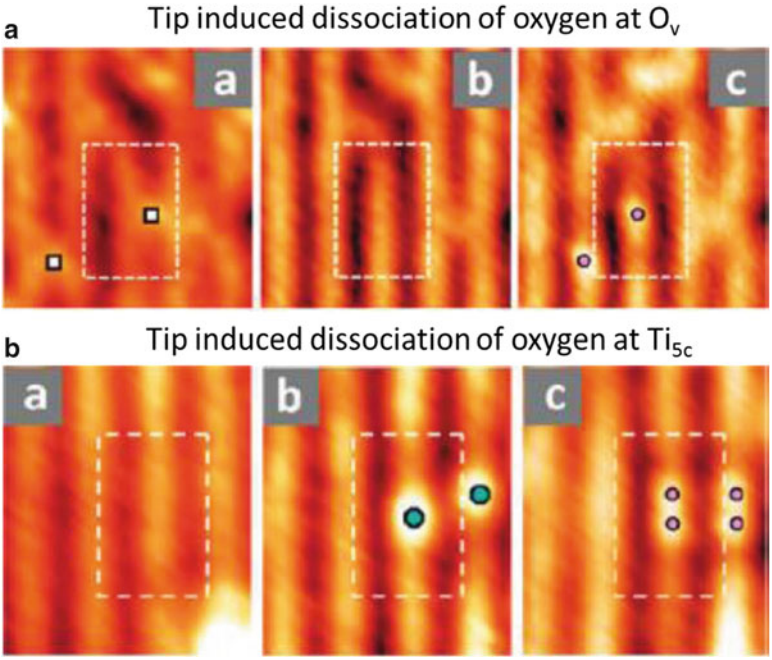

Fig. 11.13 STM images showing the tip-induced dissociation of oxygen molecules at O_v (**a**) and Ti_{5c} (**b**) sites respectively. *a*, *b*, and *c* represent the $TiO_2(110)$ surface before and after O_2 exposure and after UV illumination (Modified with permission from Ref. [112]. Copyright 2010 American Chemical Society)

while that in Fig. 11.13Bb was acquired under V = 0.3 V and I = 1 pA. Under higher voltage and current (1.5 V and 3 pA in Fig. 11.13Ac, 0.6 V and 3 pA in Fig. 11.13Bc), chemisorbed O_2 were dissociated. The dissociation of an O_2 at an O_v resulted in the appearance of an O_a on top of the Ti_{5c} adjacent to the original O_v, while that at Ti_{5c} lead to O_a pair at the Ti trough.

The charge state of the chemisorbed O_2 species is a crucial property which affects the related chemistry. Peroxo (O_2^-) [99, 106, 115–118], superoxo (O_2^{2-}) [30, 115, 118–120], and tetraoxygen (O_4^{2-}) [110, 114] have all been suggested for O_2 adsorption on rutile $TiO_2(110)$. For example, using quantum-chemical, ab initio periodic Hartree–Fock calculations, Lara-Castells and coworkers found O_2^- was the most stable O_2 species adsorbed at the defect sites of rutile $TiO_2(110)$ [116]. Based on the O_v to O_2 charge transfer and the absence of magnetic moment, Tilocca and Selloni proposed the O_2^{2}-like species using first-principle string molecular dynamic approach [103]. Changing the number of chemisorbed O_2 per O_v, Pillay et al. calculated the structure, bonding, and energetics of these O_2 species and proposed a tetraoxygen structure, i.e., O_4^{2-} [114], which was consistent with an experimental finding [110]. Direct spectroscopic investigation of the charge state of chemisorbed O_2 on rutile $TiO_2(110)$ has been performed by Henderson et al. [99, 119]. These authors found that a new loss feature appeared at 2.8 eV at the expense of the Ti 3d derived defect states in electron energy loss spectroscopy (EELS) spectra. Examination of the loss feature at 2.8 eV, however, gave rise to different conclusions in Refs. 99 and 119. The loss feature was assigned to O_2^- in Ref. 99 and superoxo species in Ref. 119. No consensus has been reached and thus far suggests the complexity of O_2 adsorption on TiO_2.

O_2 adsorption on anatase surface has also been investigated [98, 121–128]. Due to the absence of surface O_v on anatase TiO_2(101) [129], subsurface O_v's are responsible for the charge transfer from this TiO_2 substrate to O_2 [98]. DFT calculations by Aschauer et al. [122] suggested that the O_2 coverage increased from below 1 O_2 per defect to above 1.5 O_2 per defect and the most stable species varied from peroxo to superoxo. Combined STM and DFT calculations carried out by Setvin and coworkers [127] showed that reacting with a subsurface O_v, the superoxo was transformed into a peroxo and further placed into an anion surface lattice, generating a bridging dimmer $(O_2)_2$. Chemisorption and tip-induced dissociation of O_2 at Ti^{3+}-related point defects on anatase TiO_2(001)-(1 × 4) surface at 80 K have recently been reported by Hou and Wang's group [130]. At room temperature, O_2 was still adsorbed molecularly at these point defects and dissociated at even higher temperature.

11.5.1.2 Photochemistry of Oxygen on TiO_2 Surfaces

Existing photochemistry of O_2 on rutile TiO_2(110) includes the extensively studied photostimulated desorption (PSD) [119, 40, 73, 131–135] and a new topic of photoinduced dissociation [136–140]. Yates' group has systematically studied the PSD of O_2 from rutile TiO_2(110) and built a hole-mediated desorption model [141–143], which consisted of bandgap excitation, diffusion of holes to the surface, trapping of holes at the surface, and finally the transfer of positively charged holes to the anion O_2 ($O_{2(a)}{}^-$), leading to the desorption (reaction 11.3).

$$O_{2(a)^-} + h^+ \rightarrow O_2(\mathrm{gas}) \tag{11.3}$$

Lu et al. [131, 132] discovered two chemisorption states of O_2 on a reduced rutile TiO_2(110), of which one could assist the photooxidation of CO, while the other could not. The finding of two different O_2 adsorption states was consistent with the velocity distribution measurements using time-of-flight (TOF) method by Sporleder et al. [40]. Coverage-dependent O_2 PSD has been further quantitatively investigated by Petrik and Kimmel (Fig. 11.14) [138]. On a reduced rutile TiO_2(110) with 0.08 ± 0.01 ML (1 ML $= 5.2 \times 10^{14}$ molecules/cm^2) O_v, adsorption of $^{18}O_2$ at 28 K was followed by a subsequent TPD to 100 K (Square in Fig. 11.14). Thereafter, 300 s PSD was performed at 28 K (triangle in Fig. 11.14). No $^{18}O_2$ TPD signal was detected until the saturated chemisorption (2 O_2/O_v [110]) was reached, since ramping to 100 K could only remove the physisorbed species [104, 144]. The increase of $^{18}O_2$ PSD signal with initial $^{18}O_2$ coverage could be fitted by two

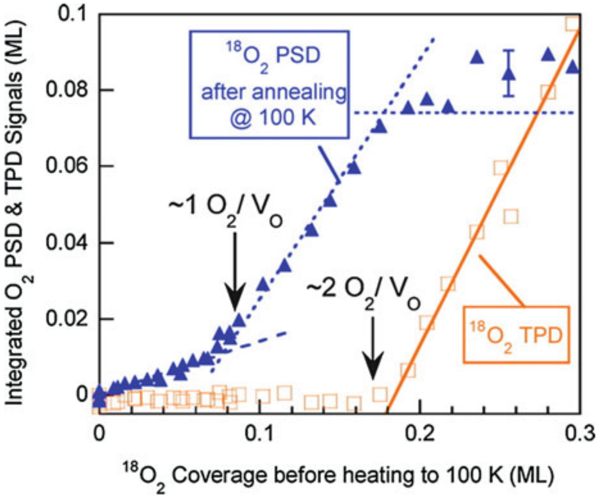

Fig. 11.14 $^{18}O_2$ PSD (*blue*) and TPD (*orange*) signal as a function of initial coverage (Reproduced with permission from Ref. [138]. Copyright 2011 American Chemical Society)

straight lines with slopes of 0.14 and 0.57 below 1 O_2/O_v and between 1 O_2/O_v and 2 O_2/O_v, respectively. The authors argued the increase of the slope resulted from the sharing of the excess electrons of the chemisorbed oxygen, which meant the charge state was more O_2^{2}-like before all the O_v sites were occupied and favored O_2^- which was the reagent of the hole-mediated O_2 desorption thereafter. Photodesorption of O_2 at Ti_{5c} sites (O_2^-/Ti_{5c}) has recently been imaged by Lyubinetsky et al. using high-resolution STM (Fig. 11.15a) [139]. Therefore, reaction 11.3 could be revised as follows (reaction 11.4):

$$O_2^-/Ti_{5c} + h^+ \rightarrow O_2(gas) \tag{11.4}$$

Besides PSD, ultraviolet (UV) light-induced dissociation of O_2 on rutile $TiO_2(110)$ has also been examined [138–142]. Figure 11.16 summarized the quantitative analysis of the chemisorbed, photodesorbed, and photodissociated O_2 species by Petrik and Kimmel using a combined TPD and PSD study [138]. θ_{rem}, θ_X, and θ_{diss} stood for the coverage of oxygen that retained on the surface, remained undissociated, and became dissociated after UV irradiation, respectively, while θ_{occ} and θ_{2nd} represented the amount of occupied and unoccupied sites after exposure to UV light, respectively, where the latter was determined by the TPD measurements after a second O_2 exposure following the UV irradiation. The authors proposed an electron-mediated mechanism of photoinduced dissociation at O_v sites to form a bridging-bonded oxygen (O_b) and a surface O^-/Ti_{5c} (reaction 11.5):

$$O_2^{2-}/O_v + h^+ \rightarrow O_b^{2-} + O^-/Ti_{5c} \tag{11.5}$$

which was complemented by the hole-mediated photodesorption. The increase of photodesorption and decrease of photodissociation fractions (Fig. 11.16) with the initial O_2 coverage agreed well with the proposal. The amount of O_2^- increased at

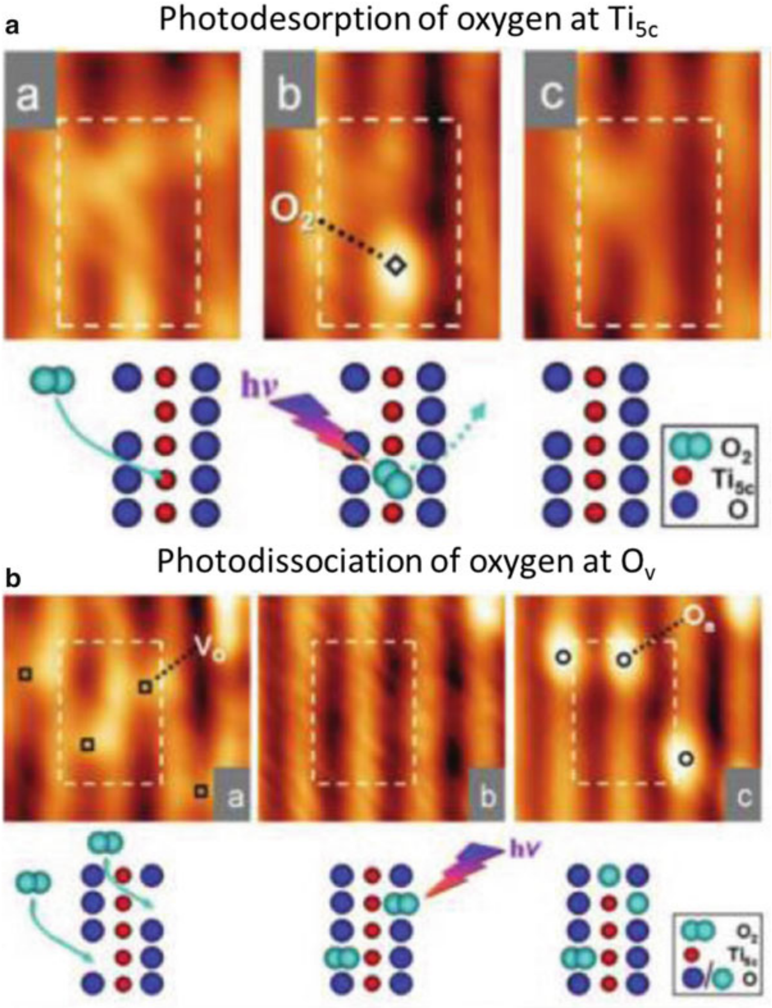

Fig. 11.15 STM images and cartoons showing the photodesorption of O_2 at Ti_{5c} sites (**a**) and photodissociation of O_2 at O_v's (**b**) (Modified with permission from Ref. [139]. Copyright 2012 American Chemical Society)

the expense of O_2^{2-} with the O_2 coverage due to charge sharing. Therefore, enhanced photodesorption and depressed photodissociation could be expected. Petrik and Kimmel's further work using isotope labeling showed that although there were chemisorbed O_2 species which were photoinactive, they could exchange atoms with physisorbed O_2 [139]. The exchange rate reached a maxima if the O_2 covered rutile $TiO_2(110)$ was preheated to 350 K. Though the exact structure of this O_2 species remained unclear, the authors proposed two possible candidates, i.e., O_2 at O_v sites and tetraoxygen. Understanding of the photodissociation of oxygen on

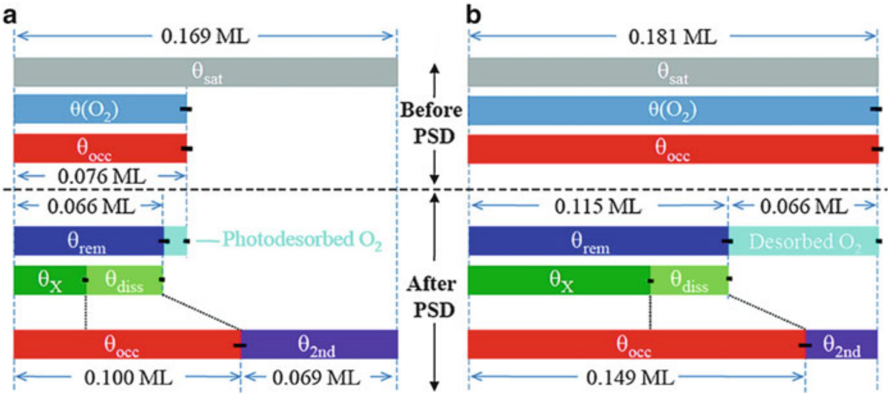

Fig. 11.16 The amount of adsorbed, photodesorbed, photodissociated, and nondissociated O_2 before and after UV irradiation for (**a**) $\theta(O_2) = \theta(O_v)$ and (**b**) $\theta(O_2) = 2\theta(O_v)$ (Reproduced with permission from Ref. [138]. Copyright 2010 American Chemical Society)

rutile $TiO_2(110)$ at the molecular level was provided by Lyubinetsky et al. [139]. Using high-resolution STM, photoinduced desorption at Ti_{5c} sites (Fig. 11.15a) and photoinduced dissociation at O_v sties (Fig. 11.15b) have been directly imaged. While complementary oxidative and reductive reaction in photocatalysis was expected to proceed at substantial and balanced rates, the observed kinetics of hole-mediated photodesorption and electron-mediated photodissociation in this study differed significantly from each other (Fig. 11.17). Despite the generally accepted fact that holes diffuse more slowly than electrons [32, 141], hole-mediated desorption proceeded much faster than the electron-mediated dissociation of O_2. The authors speculated the deviation from expectation originated from the difference of the dynamics of charge transfer to the surface reagents.

11.5.2 *Methanol*

Photocatalytic reactions of alcohols on TiO_2 are important in a number of technological applications. Due to the prominent use of alcohols in reforming reactions to produce H_2, oxidative remediation of organic wastes, and biomass conversion to fuels and useful synthetic chemicals, great interest has been attracted to the reactivity of TiO_2 with alcohols, especially methanol (CH_3OH) and ethanol. Since surface science studies on single crystal surfaces under UHV conditions could provide fundamental insights into these important processes, both thermal chemistry and photo-chemistry on the TiO_2, especially rutile $TiO_2(110)$ surface, have been investigated with a variety of experimental and theoretical approaches. In this part, we described the thermal and photo-chemistry of CH_3OH on TiO_2 surfaces.

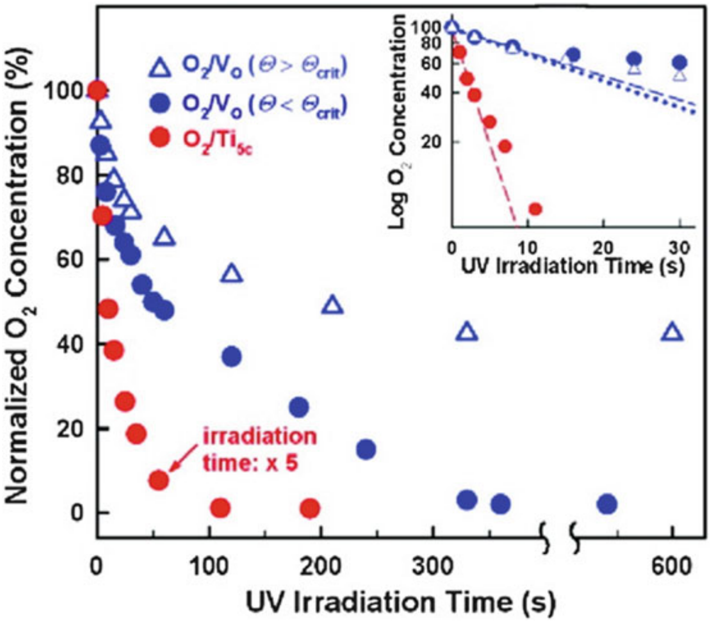

Fig. 11.17 Normalized UV irradiation time-dependent amount of O_2 at O_v and Ti_{5c} sites. Inset graph shows the initial regions of the plot in a semilog scale (Reproduced with permission from Ref. [139]. Copyright 2012 American Chemical Society)

11.5.2.1 Adsorption of Methanol on TiO_2 Surfaces

On reduced rutile $TiO_2(110)$, TPD spectra of CH_3OH yielded five prominent features at 150, 165, 295, 350, and 480 K [145]. The 150 and 165 K peaks were assigned to multilayer desorption, the feature at 295 K was assigned to the desorption of molecularly adsorbed CH_3OH on Ti_{5c} sites, and the broad tail around 480 K was attributed to the recombinative desorption of dissociated CH_3OH at O_v's. The 350 K shoulder was difficult to assign. Because both high-resolution EELS (HREELS) and static secondary ion mass spectroscopy (SSIMS) spectra were inconclusive, Henderson et al. [146] suggested that the 350 K shoulder was due to CH_3OH dissociated at non-defective sites of the surface, probably Ti_{5c}, on the basis of similar behavior of the 350 and 480 K peaks following electron bombardment. However, no obvious 350 K shoulder was shown in recent TPD studies of CH_3OH on reduced rutile $TiO_2(110)$ with gentle surface treatment [147]. The assignment of the 350 K shoulder is still not conclusive.

Peteket al. [148, 149] provided some indirect evidence that part of CH_3OH was adsorbed at Ti_{5c} sites dissociatively. Using two-photon photoemission spectroscopy (2PPE), an empty wet electron state at about 2.3 ± 0.2 eV above Fermi level (E_F) was detected on both reduced and stoichiometric rutile $TiO_2(110)$. However, in the case of H_2O, this excited state could only be observed on reduced rutile $TiO_2(110)$ surfaces with simultaneous presence of monolayer water and bridging hydroxyls

(OH_{br}) (resulting from spontaneous dissociation of water at O_v's [49]), and the electron distribution in this state was reported to encompass several adsorbate H sites [150]. While on the water covered stoichiometric rutile TiO_2 surface, this state was totally absent. By analogy with the properties of the excited state at H_2O/rutile $TiO_2(110)$ interface, those authors argued the partial dissociation of methanol on rutile $TiO_2(110)$ surface.

In a recent STM work, Zhang et al. [151] found that CH_3OH dissociated at the O_v sites spontaneously to form methoxy (CH_3O) and hydroxyl on the primarily neighboring O_b sites. Further investigation showed that molecular methanol can diffuse along the Ti_{5c} rows at room temperature (RT), indicating that CH_3OH is not dissociated at these sites. Theoretical work regarding CH_3OH adsorption on rutile $TiO_2(110)$ was also carried out [152, 153, 154]. Most results indicated that the molecular state of CH_3OH was nearly iso-energetic to the dissociated state with the former slightly more stable, and the energy barrier for the transformation between these two states was very small. This suggested that molecular adsorption of CH_3OH on the rutile $TiO_2(110)$ surface was more stable, which was consistent with STM observation at both liquid nitrogen temperature [155] and RT [151]. Theoretical result showed that dissociative adsorption of CH_3OH on O_v sites is thermodynamically more favorable than molecular adsorption by 0.5 eV [153], also consistent with TPD and STM experimental results.

11.5.2.2 Photocatalytic Chemistry of Methanol on TiO_2 Surfaces

Methanol (CH_3OH)/TiO_2 is an important model system because of remarkable enhancement of photocatalytic hydrogen production from water–methanol mixture over TiO_2 [156], the potential applications of CH_3OH in photocatalytic selective oxidation [157], environmental photocatalysis [158], and photocatalytic reforming reactions [159]. Meanwhile, as one of the simplest organic compounds, CH_3OH is often chosen as a probe for the fundamental studies of photocatalytic chemistry on oxide surfaces.

Recently, the methanol/rutile $TiO_2(110)$ system was studied using 2PPE, STM, and DFT calculations by Zhou et al. [155]. These authors also observed an excited state at about 2.4 eV above E_F by irradiating a saturated layer of CH_3OH (0.77 ML) [161]. In the original paper, a saturated layer was regarded as 1 ML covered rutile $TiO_2(110)$ surface with 400 nm femtosecond laser pulse, which was very similar to the previous 2PPE measurements on this surface, where the unoccupied excited state was assigned to be an intrinsic "wet electron state" on the CH_3OH covered rutile $TiO_2(110)$ surface. By contrast, Zhou et al.'s results showed the excited resonance peak was absent immediately after the laser irradiation (Fig. 11.18a). It increased with the laser irradiation time and saturated after a 15 min irradiation, accompanied by a peak shift toward lower energy. The interesting result unambiguously demonstrated that the excited resonance state, which was located at 2.4 eV above E_F, was a photoinduced surface state rather than a wet electron state that was intrinsically present on the freshly prepared

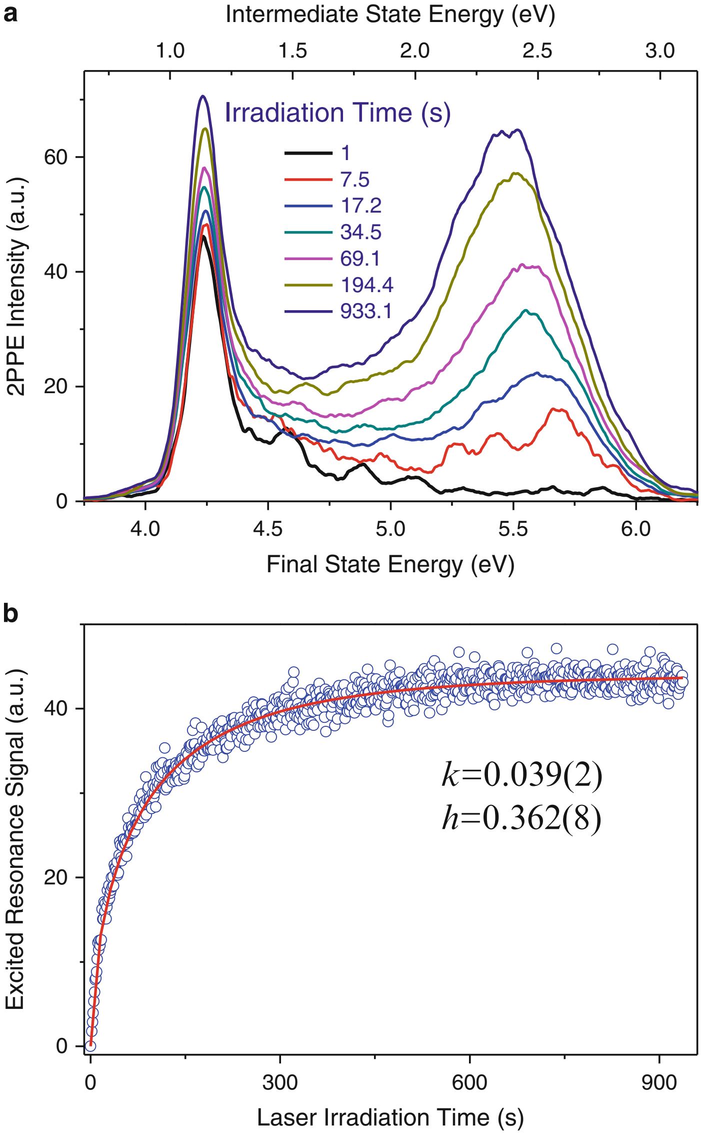

Fig. 11.18 (**a**) 2PPE spectra for CH_3OH adsorbed stoichiometric rutile $TiO_2(110)$ after the interface was exposed to the probe light for different periods. (**b**) Time-dependent excited resonance signal integrated from (**a**) and the fractal-like kinetics model fitting (Modified with permission from Refs. [155, 162]. Copyright 2010, 2012 the Royal Society of Chemistry)

CH_3OH/rutile $TiO_2(110)$ surface. The lifetime of the excited state was measured to be ~20 fs by time-resolved two-pulse correlation [162]. This value was in accord with Petek's results [149].

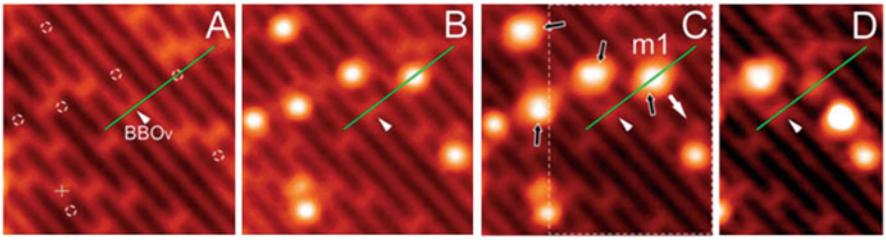

Fig. 11.19 STM images (acquired at bias of 1.0 V and set point current of 10 pA, size of 7.3×7.3 nm^2) showing the photocatalyzed dissociation of methanol. (**a**) Bare $TiO_2(110)$-1×1 surface. (**b**) Surface with adsorbed CH_3OH (0.02 ML). (**c**) After 10 min. irradiation by 400 nm light. *Dashed circles* in (**a**), sites for CH_3OH adsorption on Ti_{5c} row. *Cross*, sites for CH_3OH on O_V (labeled as BBO_V in the figure). *Black arrows* in (**c**) indicate the four dissociated molecules after UV irradiation. (**d**) STM image after manipulation (0.4 V, 700 pA) of the dissociated molecule m1 in the marked area of (**c**) (Modified with permission from Ref. [155]. Copyright 2010 the Royal Society of Chemistry)

In order to understand this photoinduced process, Zhou et al. [155] employed STM (acquired at 80 K) to reveal the nature of the photochemical changes detected by 2PPE (Fig. 11.19). Figure 11.19a shows an STM image of the bare rutile $TiO_2(110)$ surface with about 4 % O_v's (labeled as "BBOv" in the figure). The bright and dark lines corresponded to the Ti_{5c} and O_b rows, respectively, while the bright spots on the dark lines represented the O_v's. After adsorption of 0.02 ML CH_3OH, most of the CH_3OH molecules were adsorbed on the Ti_{5c} sites (CH3OH/Ti_{5c}) and appeared as clear bright round spots (Fig. 11.19b). These bright round spots could move along the Ti_{5c} row as a whole or desorb driven by the STM tip, implying that CH_3OH molecules were adsorbed on the Ti_{5c} sites molecularly, which was consistent with previous STM results [151]. After a 10 min UV (<400 nm) irradiation, the majority of the bright round spots became elongated (marked by black arrows in Fig. 11.19c). By manipulating one of these altered species (labeled "m1" in Fig. 11.19c) with the STM tip, the elongated spots after UV irradiation were separated into two components. One of the components left on the O_b site was confirmed to be an OH_b group [163], while the other was likely a CH_3O on a Ti_{5c} site (CH_3O/Ti_{5c}). This clearly suggested that the CH_3OH molecule after UV irradiation was dissociated. Similar STM experiments using >400 nm light have also been carried out. No evidence for CH_3OH dissociation was found, indicating the dissociation of methanol was a substrate-mediated photocatalytic process.

Given the coverage difference in the 2PPE and STM experiments, the authors performed additional 2PPE measurements at low coverage. The irradiation dependences of the excited resonance state were all similar when the methanol coverage was set to 0.77, 0.39 and 0.12 ML, suggesting the photochemical change was independent on the methanol coverage, although the reaction kinetics were likely dependent. Therefore, the STM and 2PPE results could be directly related. The photocatalyzed dissociation of methanol imaged by STM suggested the photoinduced resonance detected by 2PPE arose from photodecomposition of CH_3OH on this surface. And DFT calculations of the electronic structure were consistent with experimental results. Molecularly adsorbed methanol had little effect on the density of states (DOS) of Ti 3d due to the relative weak interaction between methanol and Ti_{5c}; however, the adsorbate–substrate interaction became much stronger when methanol deprotonated. The strong interaction between CH_3O and the Ti_{5c} ion led to the appearance of a new band which was centered at 2.5 eV above the E_F, in agreement with the 2PPE measurements. Since both initial state (bandgap states in these measurements) and intermediated state of the 2PPE were of Ti 3d character, the transition between them was forbidden in octahedral field. However, due to the presence of the surface, the octahedra became distorted, allowing weak $d \rightarrow d$ transition.

Zhou et al. then suggested a photodissociation of CH_3OH through O–H bond cleavage with the H atom transferring to an O_b site nearby, as illustrated in reaction 11.6:

$$CH_3OH/Ti_{5c} + O_b + h\nu \rightarrow CH_3O/Ti_{5c} + OH_{br} \tag{11.6}$$

Since the excited state was associated with the dissociation of CH_3OH, the irradiation time-dependent excited resonance signal illustrated essentially the kinetics of photocatalyzed dissociation of CH_3OH on rutile $TiO_2(110)$. The integrated time-dependent excited resonance signal (Fig. 11.18b) could not be described by a single exponential model, while a fractal-like kinetic model (Eq. 11.7) [164, 165] stimulated the data well:

$$I = I_0\left(1 - \exp\left(-\frac{k_0}{1-h}t^{1-h}\right)\right) \tag{11.7}$$

where k_0 is the rate at $t = 1$ and h is equal to $1 - d_s/2$, where d_s is the spectral dimension of the heterogeneous reaction media. The fractal-like kinetics of photochemistry on TiO_2 surface were reported to result from the trapping and detrapping of charge carriers [137].

As a model photoreaction, photocatalyzed decomposition of CD_3OD on TiO_2 has been used by Zhou et al. [166] to study the differences in the photocatalytic activities of the stoichiometric and reduced rutile $TiO_2(110)$ surfaces. The excited resonance state at around 5.5 eV was observed by 2PPE on both surfaces precovered with CD_3OD, whereas the rise times of the excited resonance signal on these two surfaces were significantly different (Fig. 11.20). It took 37 s for the excited resonance signal to reach 90 % of its maximum level on the reduced surface, whereas on the stoichiometric one, the rise time was 640 s. The varied photoactivity was attributed to the concentration difference of point defects on these two surfaces. The amount of both surface and subsurface defects on the reduced rutile $TiO_2(110)$ surface was significantly larger than those on the stoichiometric surface. These authors suggested that the surface and/or subsurface defects could accelerate methanol photolysis on rutile $TiO_2(110)$ surface.

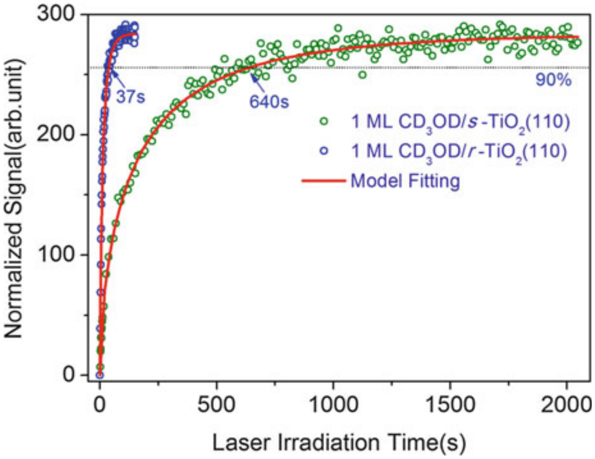

Fig. 11.20 Normalized time-dependent signal of the excited resonance of 0.77 ML CD_3OD covered stoichiometric (*olive circle*) and reduced (*blue circle*) rutile $TiO_2(110)$ surface and the fractal-like kinetics model fitting (*red line*) (Reproduced with permission from Ref. [166]. Copyright 2011 the Royal Society of Chemistry)

Unfortunately, it was difficult to characterize whether the surface defects or subsurface defects play a more important role in the acceleration of methanol photolysis on TiO_2 [167] due to the difficulty in quantitative characterization of the density of the subsurface defects. The observed higher photoactivity on reduced TiO_2 surface was consistent with improved photocatalytic hydrogen production via self Ti^{3+} doping, probably due to the enhanced light absorption [168].

As discussed above, dissociation of the CH_3O–H bond occurred on CH_3OH covered reduced and stoichiometric rutile $TiO_2(110)$ surfaces under UV irradiation. However, both 2PPE and STM methods were not able to identify the photochemical species on the surface. Recently, CH_3OH photolysis on rutile $TiO_2(110)$ has been studied using TPD method by Henderson et al. 147, 169, 170]. These authors proposed that the adsorption state of CH_3OH was crucial to its photochemistry on TiO_2. By coadsorption of CH_3OH and O_2 on rutile $TiO_2(110)$ to control the thermal dissociation of CH_3OH, CH_3O is formed on $TiO_2(110)$ from the reaction of molecularly adsorbed CH_3OH and an O adatom on Ti_{5c} sites:

$$CH_3OH/Ti_{5c} + O/Ti_{5c} \rightarrow CH_3O/Ti_{5c} + OH_t \qquad (11.8)$$

where OH_t is a thermal hydroxyl group on a Ti_{5c} site. Henderson et al. [147] concluded that CH_3O, rather than molecular CH_3OH, was the photoactive species in photochemical reactions of CH_3OH on TiO_2. Their results also suggested that formaldehyde (CH_2O) was produced from photochemistry of thermally dissociated methanol on the Ti_{5c} sites, which was initiated by defects and coadsorbed O/Ti_{5c} or OH_t groups, but not by O_v sites (under UHV conditions) and not from photodissociation of molecular CH_3OH/Ti_{5c}.

Guo et al. [171] have extended the investigation of CH_3OH photolysis systematically using TPD method, in combination with laser surface photocatalysis. These authors investigated the photoinduced dissociation of partially deuterated methanol (CD_3OH) on rutile $TiO_2(110)$ using 400 nm laser irradiation without coadsorbed

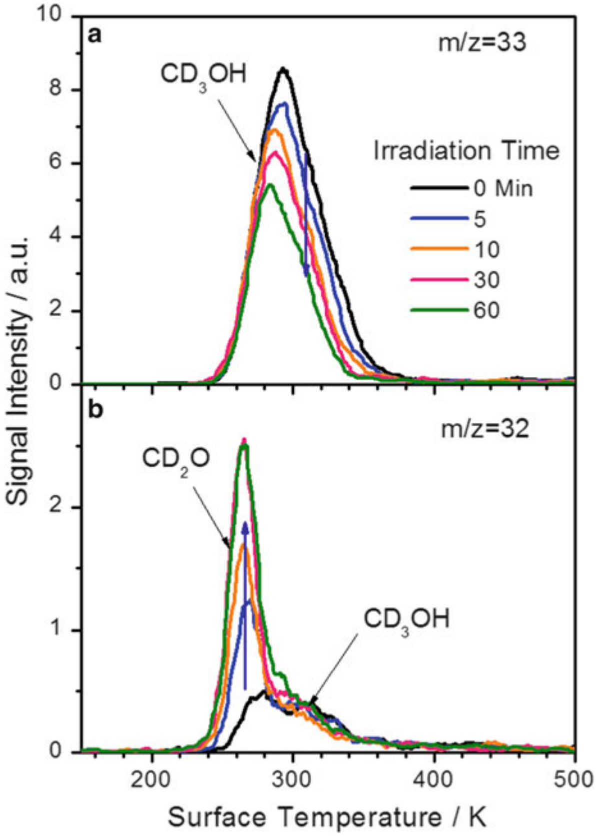

Fig. 11.21 (**a**) Typical TPD spectra collected at $m/z = 33$ (CD_2OH^+) following different laser irradiation times. CD_2OH^+ is formed by dissociative ionization of the desorbed parent CD_3OH molecule in the electron-bombardment ionizer. (**b**) Typical TPD spectra collected at $m/z = 32$ (CD_2O^+) following different laser irradiation times. The $m/z = 32$ (CD_2O^+) signal has three components: the parent ion signal of formaldehyde (CD_2O), the ion-fragment signals of the parent CD_3OH molecule, and the photocatalyzed CD_3OD product (Reproduced with permission from Ref. [171]. Copyright 2012 American Chemical Society)

O_2. Figure 11.21a shows TPD spectra collected at a mass-to-charge ratio (m/z) of 33 (CD_2OH^+) after surfaces of rutile $TiO_2(110)$ were dosed with 0.5 ML CD_3OH and then irradiated by the laser for various durations. The observed CD_3OH signal decreased monotonically with the laser irradiation time, suggesting that the CD_3OH molecules adsorbed on the Ti_{5c} sites of rutile $TiO_2(110)$ were photocatalytically dissociated. Concomitant to the decrease of the CD_3OH TPD peak, a new peak at 270 K appeared in the TPD spectra for $m/z = 32(CD_2O^+)$ and increased with laser irradiation time (Fig. 11.21b), corresponding to desorption of molecularly adsorbed CH_2O from the Ti_{5c} sites. The released H/D atoms transferred to the O_b sites were confirmed by the characteristic recombinative desorption of bridging hydroxyls from this surface around 460 K [172, 173].

DFT calculations on the ground state potential surface showed that the O–H dissociation energy of CH_3OH was slightly endoergic by 0.03 eV, with a barrier of 0.25 eV, while the dissociation energy of the second dissociation step (the C–H dissociation) to produce CH_2O and H was highly endoergic (1.03 eV), and the barrier was also much higher (1.57 eV). The barrier for the reverse reaction was therefore 0.54 eV (Fig. 11.22). Similar energetics for the methanol/rutile $TiO_2(110)$

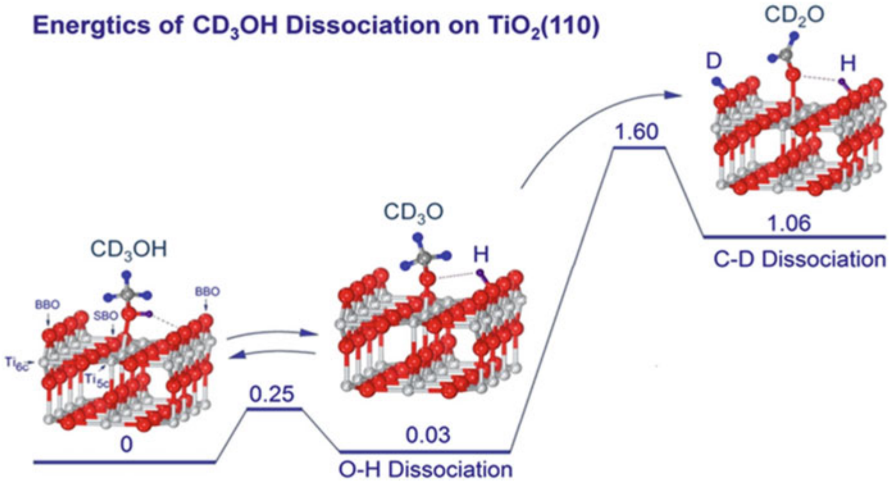

Fig. 11.22 Calculated energetics of the two-step dissociation of CD_3OH on the rutile $TiO_2(110)$ surface. The structures shown are simplified schematics (Modified with permission from Ref. [171]. Copyright 2012 American Chemical Society)

model system have been reported by Lang et al. [174]. A recent study on the recombination of formaldehyde and H_b atoms by Mao et al. [175] using 2PPE and STM suggested the above-calculated energetics were reasonable. CH_3OH at Ti_{5c} sites could only be dissociated under UV irradiation (spontaneous and tip-induced ($V = +1.25$ V, $I = 100$ pA) dissociation of methanol at Ti_{5c} sites was not observed).However, spontaneous and tip-induced recombination of CH_2O and H_b atoms was detected, suggesting the lower stability of the products and a high and low barrier for the forward (dissociation) and reverse (recombination) reaction, respectively. This was consistent with the calculation of the energetics for the methanol/rutile $TiO_2(110)$ system.

Therefore, Guo and coworkers proposed that CD_3OH was photodissociated into CD_2O at Ti_{5c} sites (CD_2O/Ti_{5c}) in a two-step process, leaving H and D atoms on the O_b sites:

$$CD_3OH/Ti_{5c} + O_b \xrightarrow{hv,\,TiO_2(110)} CD_3O/Ti_{5c} + OH_{br} \tag{11.9}$$

$$CD_3O/Ti_{5c} + O_b \xrightarrow{hv,\,TiO_2(110)} CD_2O/Ti_{5c} + OD_{br} \tag{11.10}$$

These experimental results clearly demonstrated that photocatalytic CH_3OH dissociation on rutile $TiO_2(110)$ occurred on Ti_{5c} sites rather than O_v's.

Photocatalyzed splitting of CH_3OH on rutile $TiO_2(110)$ clearly provided a strategy to continuously vary the surface hydroxyls without affecting the subsurface defects. Mao et al. thus revisited the long-standing issue of the origin of bandgap states in rutile $TiO_2(110)$ by exploring the correlation between the DOS of the bandgap states and the concentration of surface hydroxyls prepared via CH_3OH

photodissociation [176]. The intensity of bandgap states measured by ultraviolet photoelectron spectroscopy (UPS) scaled linearly with surface hydroxyls characterized by TPD with a small intercept, suggesting surface defects made a major contribution to the bandgap states, which in turn indicates the importance of surface defects in changing the electronic structure of TiO_2 which dictated the surface chemistry.

In addition to the formation of CH_2O from CH_3OH photocatalysis on rutile $TiO_2(110)$, Guo et al. [177] observed further photocatalytic oxidation to form methyl formate ($HCOOCH_3$) with 0.5 ML CH_3OH covered rutile $TiO_2(110)$ surface. As seen in Fig. 11.23, during the first 10 min of irradiation, the amount of CH_2O formed rose rapidly to a maximum, while little $HCOOCH_3$ was formed. Longer irradiation times lead to a steady decrease of the amount of CH_2O and a concomitant increase of that of $HCOOCH_3$. After 90 min of irradiation, very little CH_2O remained on the surface. Thus, the formation of $HCOOCH_3$ appeared to be directly correlated with the depletion of CH_2O. Similar phenomena were also observed by Phillips et al. [178] and Yuan et al. [179].

According to a series of thermal catalytic investigations on gas phase dehydrogenation of CH_3OH to $HCOOCH_3$ over copper-based catalysts [180–182], Guo et al. [177] suggested that $HCOOCH_3$ was produced through cross-coupling of CH_2O and CH_3O:

$$CH_2O/Ti_{5c} + CH_3O/Ti_{5c} \xrightarrow{hv,\, TiO_2(110)} HCOOCH_3/Ti_{5c} + OH_{br} \tag{11.11}$$

while Phillips et al. [178] proposed that CH_3O on Ti_{5c} sites underwent photooxidation to $HCOOCH_3$ in a two-step process where the CH_3O dissociated to CH_2O and a cross-coupling reaction involving a formyl (HCO) intermediate led to the formation of $HCOOCH_3$:

$$CHO/Ti_{5c} + CH_3O/Ti_{5c} \xrightarrow{hv,\, TiO_2(110)} HCOOCH_3/Ti_{5c} \tag{11.12}$$

Recently, Lang and coworkers [174] have investigated the two pathways mentioned above for CH_3OH oxidation into $HCOOCH_3$ on perfect and defect rutile $TiO_2(110)$ based on first-principle calculations. The huge difference in the energy barriers for HCO and hemiacetal production suggested that CH_3OH oxidation on both surfaces facilely proceeded through the intermediate hemiacetal to produce $HCOOCH_3$.

Photooxidation of CH_3OH has recently been chosen by Mao et al. [183] to assess the photoactivity of rutile $TiO_2(110)$-(1 × 1) and $TiO_2(011)$-(2 × 1), with the latter being reported to be of high activity toward photooxidation reactions [68, 184]. The reaction pathways were similar to these two surfaces. CH_2O and $HCOOCH_3$ have been detected. The most prominent difference of the photooxidation of CH_3OH on these two surfaces came from the reaction kinetics. The reaction rate on rutile $TiO_2(011)$-(2 × 1) was only 42% of that on rutile $TiO_2(110)$-(1 × 1), contradicting

Fig. 11.23 (**a**) TPD spectra acquired at $m/z = 31$ (CH_3O^+) after 0.5 ML CH_3OH was adsorbed on rutile $TiO_2(110)$ at 120 K and irradiated at 400 nm for various times. (**b**) TPD spectra acquired at 30 (CH_2O^+) after 0.5 ML CH_3OH was adsorbed on rutile $TiO_2(110)$ at 120 K and irradiated at 400 nm for various times. (**c**) Yields of CH_3OH, CH_2O, and $HCOOCH_3$ as a function of irradiation time, derived from data in Fig. 11.16a and b (Modified with permission from Ref. [177]. Copyright 2013 American Chemical Society)

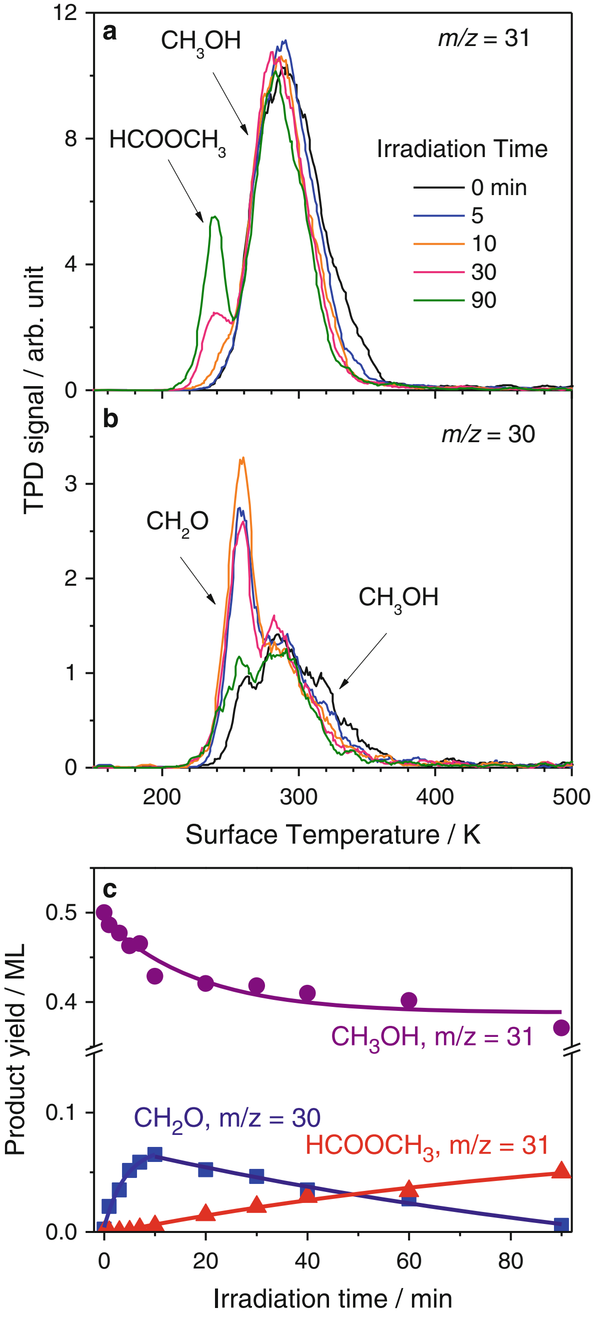

with the previous reports in aqueous environments where characterization of TiO_2 structure was difficult [68, 184].

Conventionally, the effect of surface atomic structure on the activity of a crystal in heterogeneous reactions is greatly related to the percentage of under-coordinated atoms. The higher the percentage of under-coordinated surface atoms is, the more reactive the crystal is. The results obviously did not comply with this rule since the percentage of Ti_{5c} was 100% on rutile $TiO_2(011)$-(2 × 1) and 50% on rutile $TiO_2(110)$-(1 × 1). In addition, this result was not in agreement with a previous electronic structure study which expected that the electron trapping and electron–hole separation on rutile $TiO_2(011)$-(2 × 1) surface were more efficient than on rutile $TiO_2(110)$-(1 × 1) based on the higher binding energy of the bandgap states of the former [185]. Through examining the energetics of the CH_3OH/TiO_2 system [185], the authors discovered the rate determining step of photooxidation of CH_3OH on both surfaces was the cleavage of C–H; however, the barrier of this elementary step was 0.2 eV higher on rutile $TiO_2(011)$-(2 × 1) due to the distinct atomic configuration. Mao et al. then tentatively linked the correlation between the photoactivity and the surface structure of TiO_2.

From above experimental studies of CH_3OH photolysis on rutile $TiO_2(110)$, it is quite clear that photooxidation of CH_3OH on rutile $TiO_2(110)$ proceeded through multiple elementary reaction steps. After CH_3OH dissociation, the dissociated H atoms transferred to nearby O_b sites, prompting the question of how molecular hydrogen might be formed during CH_3OH photocatalysis. Recent experimental investigation on the photocatalysis of CD_3OD on rutile $TiO_2(110)$ by Xu and coworkers [186] suggested that molecular hydrogen (D_2) was not formed from photoinduced recombination of dissociated D atoms, whereas during TPD process, D atoms are desorbed from the surface in the forms of D_2O and D_2 (Fig. 11.24):

$$2OD_{br} \xrightarrow{\text{heat}, TiO_2(110)} D_2O(\text{gas}) + O_v \tag{11.13}$$

$$2OD_{br} \xrightarrow{\text{heat}, TiO_2(110)} D_2(\text{gas}) + 2O_b \tag{11.14}$$

Both the D_2O and D_2 recombination signals increased with laser irradiation time and the peaks gradually shift to lower temperature, while the desorption of D_2 starts from ~375 K, which is about 50 K higher than that of D_2O, indicating that D_2 desorption was more difficult than D_2O desorption. The yields of these two products indicated that less than ~7 % of total D atoms from CD_3OD photolysis are desorbed as D_2, demonstrating that D_2 formation is much less important than D_2O formation.

It is generally believed that the thermalization of charge carriers produced from UV irradiation of TiO_2 surface and relaxation of their respective band edges occurs in the hundred fs scale. As a result, photolysis on TiO_2 is driven by separated electrons or holes that are energetically located at the band edges. The reaction rate will depend on the photon flux rather than on the wavelength of the incident light [32]. As a result, excess potential energy was lost to the lattice via strong coupling with phonon modes, thus reducing the potential advantage gained by the specificity

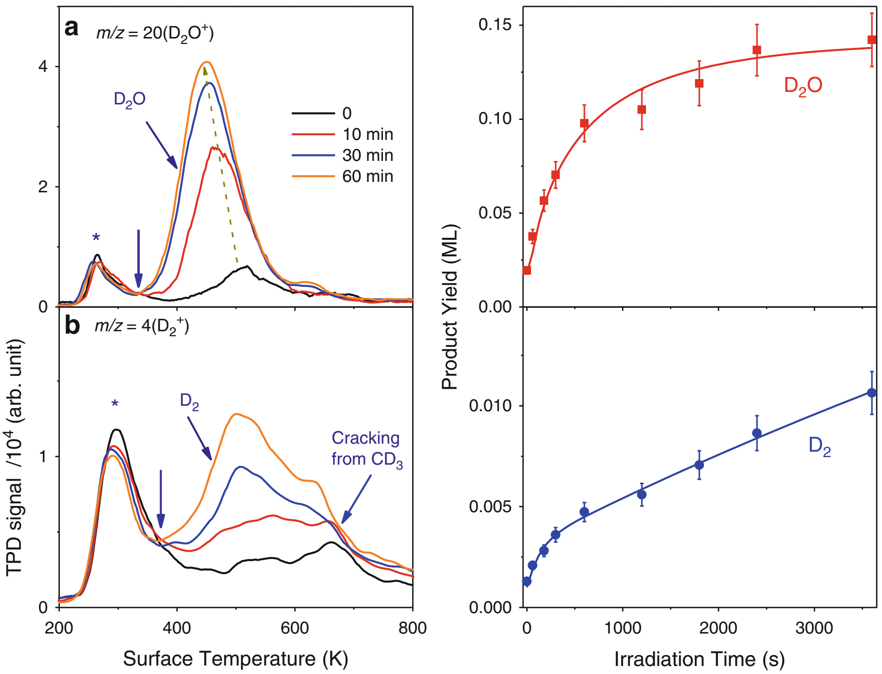

Fig. 11.24 (**a**) Typical TPD spectra collected at $m/z = 20$ (D_2O^+) following different laser irradiation times at 400 nm; the peak (marked with *) slightly below 300 K is attributed to the dissociative ionization signal of molecular adsorbed CD_3OD in the electron-impact ionizer and impurity of D_2O in CD_3OD. (**b**) Typical TPD spectra collected at $m/z = 4(D_2^+)$ following different laser irradiation times at 400 nm; the peak (marked with *) slightly below 300 K is attributed to the dissociative ionization signal of molecular adsorbed CD_3OD in the electron-impact ionizer. The right shows TPD product yield for D_2O and D_2 as a function of irradiation time, derived from data in Fig. 11.17a and b (Modified with permission from Ref. [186]. Copyright 2013 American Chemical Society)

in the absorption event. Xu and coworkers [187] have tested this idea by measuring the initial dissociation rate of CH_3OH on rutile $TiO_2(110)$ with two irradiation wavelengths, 355 and 266 nm. Because CH_3OH and CH_2O may be desorbed by irradiation [187], monitoring the yields of CH_3OH reactant and CH_2O product was not the best approach to measure the product formation rate. Another major product from CH_3OH dissociation on rutile $TiO_2(110)$ was atomic H on the O_b sites, resulting from reactions 11.9 and 11.10. Due to the high adsorption energy, these products did not desorb easily by light. While upon heating, two bridging H atoms abstracted an O_b to form a H_2O molecule, and then the H_2O molecules desorbed around 500 K, leaving behind an O_v on the surface (reaction 11.13).

Thus, monitoring H atom production through the desorption of H_2O was the preferred way to measure the product formation rate as CH_3OH underwent photocatalytic dissociation. As shown in Fig. 11.25, the initial rate of H_2O production was found to be strongly dependent on photon energy, with the initial rate being about two orders of magnitude higher at 266 nm than at 355 nm. This striking

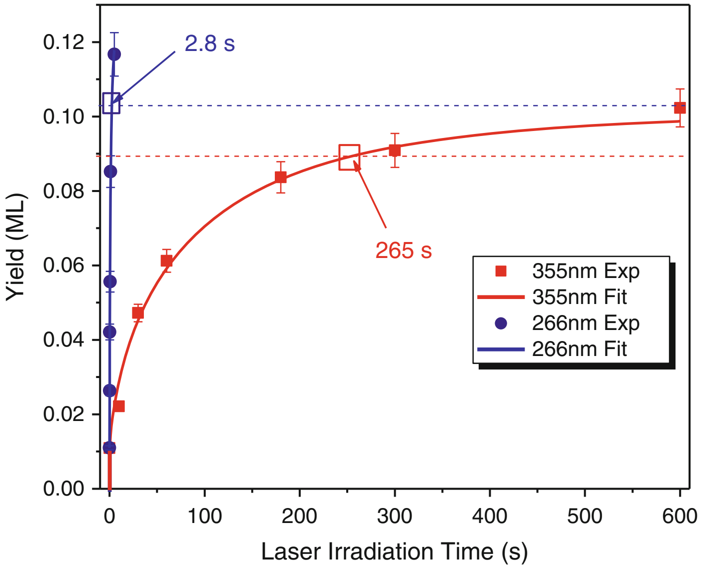

Fig. 11.25 The laser irradiation time dependence of the water (from BBO) TPD yield at both 355 nm (*left panel*) and 266 nm (*right panel*) photolysis from a 0.5 ML methanol covered rutile $TiO_2(110)$ surface. The *solid squares* and *circles* are the experimental data (calibrated), while the *solid lines* are the fits using the fractal models described in the text. The *unfilled squares* indicate the rise times at 90 % of the asymptotic values of the fits for both 355 and 266 nm photocatalysis (Reprinted with permission from Ref. [187]. Copyright 2013 American Chemical Society)

result was clearly in conflict with the traditional electron–hole photocatalysis model in that charge carriers in TiO_2 rapidly thermalize to their respective band edges via strong coupling with phonon modes first, which predicted that photocatalysis should not depend strongly on the photon energy. These authors speculated that reactions may occur on the ground electronic state, where increased converted photon energy should be more efficient in driving chemical reactions. The new phenomenon reported by Xu and coworkers challenges the traditional electron–hole photocatalysis model and calls for the development of a more sophisticated surface photocatalysis model that incorporates the effect of photon energy, which is expected to enhance the understanding of fundamental processes in photocatalysis.

Kavan and colleagues [188] found that anatase is the more photoactive polymorph for the photocatalytic production of hydrogen from H_2O oxidation and is the only polymorph that can produce hydrogen without applying an external bias. However, the availability of large size and high-quality single crystal anatase is very limited. As yet, only a few experimental studies [189, 190] on CH_3OH chemistry on a well-defined anatase $TiO_2(101)$ surface have been done. On the reduced anatase $TiO_2(101)$ surface, five desorption features are observed at 142, 188, 270, 410, and 650 K in TPD spectra of CH_3OH (Fig. 11.26) [189, 190]. By analogy with the behavior of CH_3OH on $TiO_2(110)$, the 142 and 188 K peaks are assigned to multilayer desorption, the feature at 270 K is assigned to the desorption of molecularly adsorbed CH_3OH on the Ti_{5c} sites, and the broad

Fig. 11.26 CH_3OH TPD spectra ($m/z = 31$) spectra from various exposures of CH_3OH on the anatase $TiO_2(101)$ surface at 100 K (Reprinted with permission from Ref. [190]. Copyright 2014 American Chemical Society)

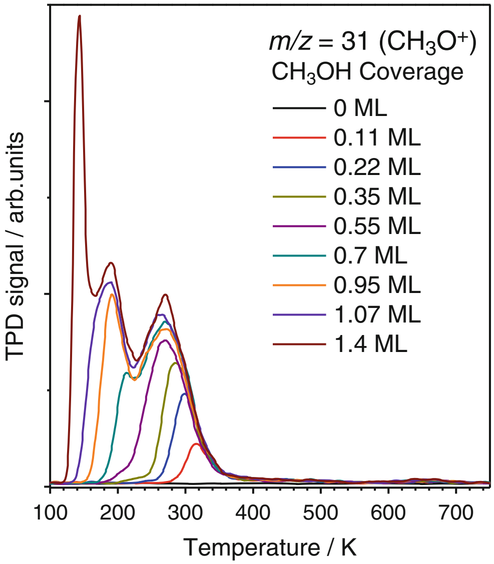

tail around 410 K is attributed to the recombinative desorption of dissociated CH_3OH on defect sites. The 650 K peak is likely due to CH_3O disproportionation at Ti_{5c} sites, as on the rutile $TiO_2(110)$ surface [169]:

$$CH_3OH/Ti_{5c} \xrightarrow{A-TiO_2(101)} CH_3O/Ti_{5c} + H - O_b \tag{11.15}$$

$$2CH_3O/Ti_{5c} \xrightarrow{heat,\, A-TiO_2(101)} CH_3OH(gas) + CH_2O(gas) \tag{11.16}$$

Recently, Xu and coworkers [190] have done some preliminary study of methanol photolysis on anatase $TiO_2(101)$ using TPD method. As shown in Fig. 11.27, the 650 K peak in mass 30 and 31 TPD decreased rapidly after 5 s irradiation, while the 300 K peak changed little, implying that CH_3O has a much higher reactivity than molecular CH_3OH on this surface. Photocatalytic products, CH_2O and $HCOOCH_3$, have been detected after different laser irradiation times (Fig. 11.27b and c), implying that the photocatalytic mechanisms for the formation of these products are similar to that on the rutile $TiO_2(110)$ surface [171]. These authors also detected dissociated H atoms from photocatalysis of CH_3OH on the anatase $TiO_2(101)$ surface by collecting TPD spectra of H_2O and H_2 products (Fig. 11.28a and b), whereas a rather sharp peak at $m/z = 18$ was observed near 260 K with different laser irradiation times, which was assigned to H_2O desorption from Ti_{5c} sites (H_2O/Ti_{5c}), and no obvious water desorption signal was detected at higher temperature. Concomitant to the increase of the H_2O TPD peak, a broad methyl radical feature stretching from 400 to 700 K was also detected at mass

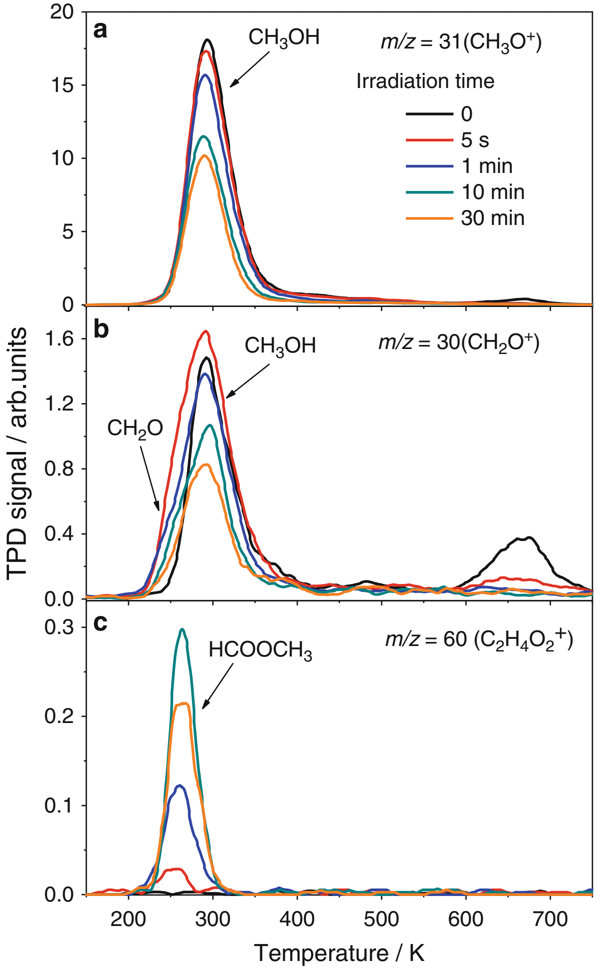

Fig. 11.27 0.38 ML of CH_3OH were dosed to the anatase $TiO_2(101)$ surfaces at 100 K. (**a**) Typical TPD spectra collected at $m/z = 31$ (CH_2OH^+) as a function of irradiation time with a photon flux of 1.9×10^{17} photons cm^{-2} s^{-1}. CH_2OH^+ is formed by dissociative ionization of the desorbed parent CH_3OH molecule in the electron-bombardment ionizer. (**b**) Typical TPD spectra collected at $m/z = 30$ (CH_2O^+) as a function of irradiation time irradiation time. The $m/z = 30$ (CH_2O^+) signal has two components: the parent ion signal of CH_2O and the ion-fragment signals of the parent CH_3OH molecule. (**c**) Typical TPD spectra collected at $m/z = 60$ ($C_2H_4O_2{}^+$) as a function of irradiation time irradiation time. The $m/z = 60$ ($C_2H_4O_2{}^+$) signal is from the parent ion signal of $HCOOCH_3$ molecule (Reprinted with permission from Ref. [190]. Copyright 2014 American Chemical Society)

15, keeping the same increasing rate with that of H_2O. Referring to earlier theoretical work by Tilocca and Selloni [191], theses authors suggest that the H_2O TPD peak at 260 K is due to the following thermally driven exchange reaction:

Fig. 11.28 TPD spectra collected at $m/z = 2$ and 18, from photocatalysis of 0.38 ML of CH_3OH covered anatase$TiO_2(101)$ at 100 K with a photon flux of 1.9×10^{17} photons $cm^{-2}\ s^{-1}$ (Fig. 11.21c). Yields of the molecular hydrogen (H_2), water (H_2O) TPD product as a function of laser irradiation time, derived from data in Fig. 11.11a and b (Modified with permission from Ref. [190]. Copyright 2014 American Chemical Society)

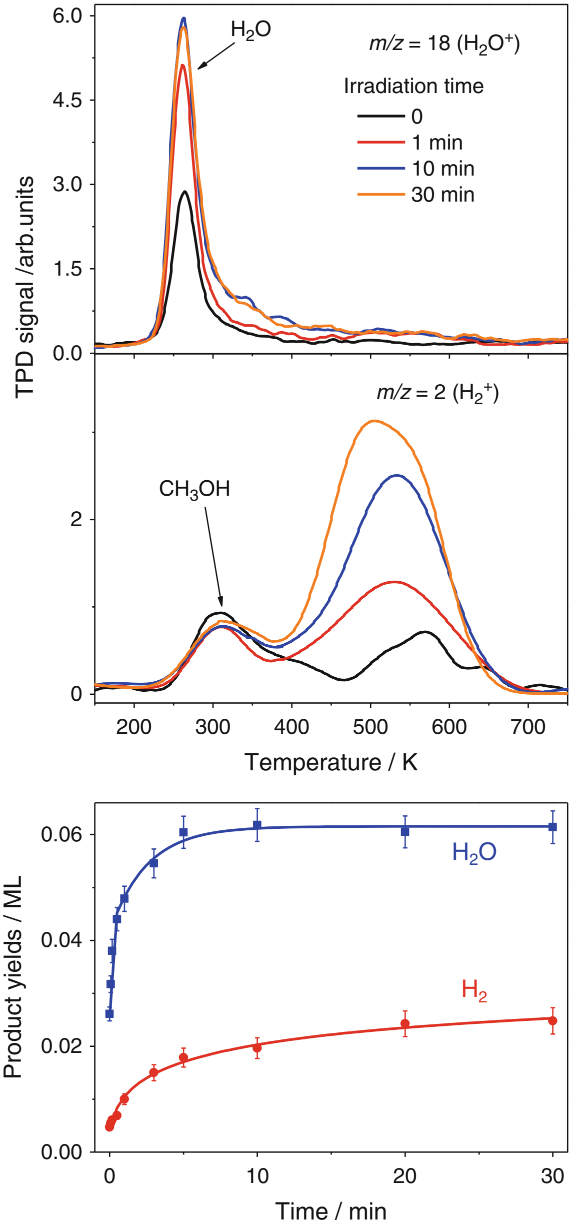

$$CH_3OH/Ti_{5c} + H - O_b \xrightarrow{\text{heat},\ A-TiO_2(101)} CH_3 - O_b + H_2O/Ti_{5c} \qquad (11.17)$$

On the basis of the analogy to the behavior of D_2 formation on rutile $TiO_2(110)$, H_2 formation from CH_3OH photocatalysis on anatase $TiO_2(101)$ likely occurs via photocatalytic dissociation of CH_3OH followed by thermal recombination of H–O_b, while the formation of molecular H_2 and H_2O was comparable on the anatase TiO_2(101) surface, indicating that the H_2 formation process should be more efficient on the anatase TiO_2(101) surface relative to rutile TiO_2(110) surface.

11.6 Conclusions

Based on the molecular level studies of photocatalysis processes on TiO_2 conducted using various surface science techniques, this chapter highlighted some of the most significant advances made in many related areas of research, particularly on charge transfer dynamics and photocatalysis of O_2 and CH_3OH on TiO_2 surfaces. However, numerous opportunities and challenges still remain, for example:

1. Understanding how additives (i.e., dopants, cocatalysts, etc.) influence the photon absorption, electron transfer, and thermal/nonthermal chemistry at TiO_2 surfaces at the molecular level
2. More detailed knowledge about the effect of the charge transfer process on surface photocatalytic reactions
3. Detailed knowledge about the charge transfer dynamics and mechanistic studies of important "up-hill" reactions such as water photooxidation at the molecular level
4. The role of recombination energy on the photocatalytic reaction processes

In addition to these big challenges of experimental photocatalysis studies, the development of theoretical understanding of photocatalysis processes at the most fundamental level from chemical dynamic perspective is also very important and potentially rewarding. According to the recently published works [43–45, 171, 187], one surprising fact is that the experimental results of photooxidation obtained from methanol, water, and other organic chemicals are not quite consistent with the simplistic photocatalysis picture based on the traditional concept that thermalized electrons and holes are the driving force of chemical reactions. For example, the traditional photocatalysis model cannot explain why methanol can be photocatalyzed on rutile TiO_2(110) at 400 nm, while water cannot at the exactly same wavelength [171]. The strong photon energy dependence of methanol and water photocatalysis on rutile TiO_2(110) is also not explainable using the traditional photocatalysis model [187]. It is therefore fair to question whether this traditional photocatalysis model can explain all photocatalytic processes. Based on the results of methanol and water photocatalysis on rutile TiO_2(110), a new photocatalysis model (Fig. 11.29) [192] based on nonadiabatic dynamics and ground state surface reactions was proposed by Yang and coworkers, which can qualitatively explain the new experimental results obtained recently for photocatalysis of water and methanol on rutile TiO_2(110). It is clear that surface dynamics is a crucial factor in photocatalysis, which is well described in this new model. However, it is necessary to point out that this new model proposed is based on studies of photocatalysis of

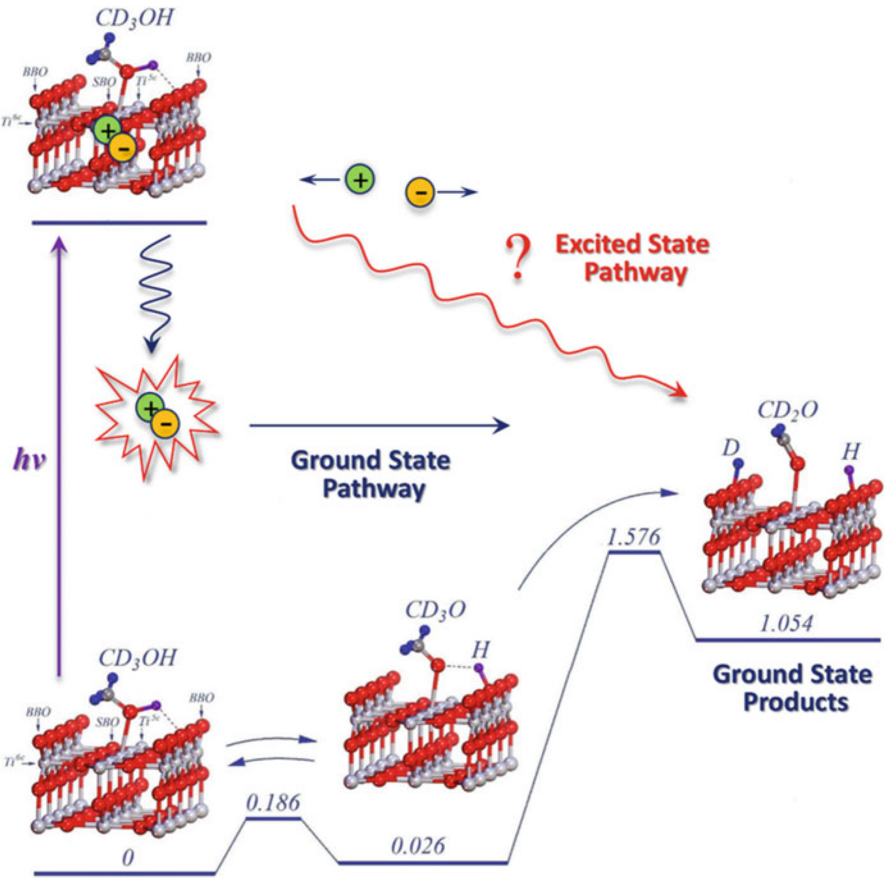

Fig. 11.29 A newly proposed photocatalysis model based on nonadiabatic chemical dynamical processes and ground state reactions. In this model, photoexcited electron–hole pairs are nonadiabatically recombined to convert the excited electronic state energy to the ground state energy, which drives the chemical reactions on the ground state surface (Reprinted with permission from Ref. [192]. Copyright 2015 Dalian Institute of Chemical Physics, the Chinese Academy of Sciences)

methanol and water on TiO_2 under vacuum conditions only, and the applicability of this model to other photocatalysis systems or photocatalysis under realistic conditions needs to be rigorously tested in the future with well-controlled photocatalysis experiments. In addition, theoretical studies of surface nonadiabatic processes and surface reaction dynamics are also urgently needed in order to gain clear and important insights to the fundamental understanding of photocatalysis processes.

References

1. Schneider J, Matsuoka M, Takeuchi M et al (2014) Understanding TiO_2 photocatalysis: mechanisms and materials. Chem Rev 114:9919–9986
2. Fujishima A, Zhang X, Tryk DA (2008) TiO_2 photocatalysis and related surface phenomena. Surf Sci Rep 63:515–582
3. Fujishima A, Honda K (1972) Electrochemical photolysis of water at a semiconductor electrode. Nature 238:37–38
4. Nakata K, Fujishima A (2012) TiO_2 photocatalysis: design and applications. J Photochem Photobiol C Photochem Rev 13:169–189
5. Ma Y, Wang X, Li C et al (2014) Titanium dioxide-based nanomaterials for photocatalytic fuel generations. Chem Rev 114:9987–10043
6. Dambournet D, Belharouak I, Amine K (2010) Tailored preparation methods of TiO_2 anatase, rutile, brookite: mechanism of formation and electrochemical properties. Chem Mater 22:1173–1179
7. Nosheen S, Galasso FS, Suib SL (2009) Role of Ti–O bonds in phase transitions of TiO_2. Langmuir 25:7623–7630
8. Diebold U (2003) The surface science of titanium dioxide. Surf Sci Rep 48:53–229
9. Zhang J, Li MJ, Li C et al (2006) UV Raman spectroscopic study on TiO_2. I. Phase transformation at the surface and in the bulk. J Phys Chem B 110:927–935
10. Su WG, Zhang J, Li C et al (2008) Surface phases of TiO_2 nanoparticles studied by UV Raman spectroscopy and FT-IR spectroscopy. J Phys Chem C 112:7710–7716
11. Shi JY, Chen J, Li C et al (2007) Photoluminescence characteristics of TiO_2 and their relationship to the photoassisted reaction of water/methanol mixture. J Phys Chem C 111:693–699
12. Zhang J, Xu Q, Li C et al (2009) UV Raman spectroscopic study on TiO_2. II. effect of nanoparticle size on the outer/inner phase transformations. J Phys Chem C 113:1698–1704
13. Xu QA, Zhang J, Li C (2010) Surface structural transformation and the phase transition kinetics of brookite TiO_2. Chem Asian J 5:2158–2161
14. Zhang HZ, Banfield JF (2000) Understanding polymorphic phase transformation behavior during growth of nanocrystalline aggregates: insights from TiO_2. J Phys Chem B 104:3481–3487
15. Yang HG, Sun CH, Lu GQ et al (2008) Anatase TiO_2 single crystals with a large percentage of reactive facets. Nature 453:638–641
16. Liang Y, Gan S, Chambers SA, Eltman EI (2001) Surface structure of anatase TiO_2(001): reconstruction, atomic steps, and domains. Phys Rev B 63:303–306
17. He Y, Dulub O, Diebold U (2009) Evidence for the predominance of subsurface defects on reduced anatase TiO_2(101). Phys Rev Lett 102:106105
18. Tachibana Y, Vayssieres L, Durrant JR (2012) Artificial photosynthesis for solar water-splitting. Nat Photonics 6:511–518
19. Kapilashrami M, Zhang Y, Guo J (2014) Probing the optical property and electronic structure of TiO_2 nanomaterials for renewable energy applications. Chem Rev 114:9662–9707
20. Asahi R, Taga Y, Mannstadt W, Freeman A (2000) Electronic and optical properties of anatase TiO_2. J Phys Rev B 61:7459–7465
21. Tuller HL, Series ED (2012) Photoelectrochemical hydrogen production; electronic materials: science & technology, vol 102. Springer, New York/Dordrecht/Heidelberg/London
22. Schottky WZ (1939) Zur halbleitertheorie der sperrschicht- und spitzengleichrichter. Zeitschrift Für Physik 113:367–414
23. Schottky W (1938) Halbleitertheorie der sperrschicht. Naturwissenschaften 26:843–843
24. Mott NF (1939) The theory of crystal rectifiers. Proc R Soc London Ser A 171:27–38
25. Mott NF (1938) Note on the contact between a metal and an insulator or semi-conductor. Proc Camb Philos Soc 34:568–572

26. Zhang Z, Yates JT Jr (2012) Band bending in semiconductors: chemical and physical consequences at surfaces and interfaces. Chem Rev 112:5520–5551
27. Linsebigler AL, Lu G, Yates JT Jr (1995) Photocatalysis on TiO_2 surfaces: principles, mechanisms, and selected results. Chem Rev 95:735–758
28. Hardman PJ, Raikar GN, Bullett DW et al (1994) Valence-band structure of TiO_2 along the Γ-Δ-X and Γ-Σ-M directions. Phys Rev B 49:7170
29. Lindan PJD, Harrison NM, Gillan MJ et al (1997) First-principles spin-polarized calculations on the reduced and reconstructed TiO_2 (110) surface. Phys Rev B 55:15919
30. Deskins NA, Rousseau R, Dupuis M (2010) Defining the role of excess electrons in the surface chemistry of TiO_2. J Phys Chem C 114:5891–5897
31. Martinez U, Hammer B (2011) Adsorption properties versus oxidation states of rutile TiO_2 (110). J Chem Phys 134:194703
32. Henderson MA (2011) A surface science perspective on photocatalysis. Surf Sci Rep 66:185–297
33. Hoffmann MR, Martin ST, Choi W et al (1995) Environmental applications of semiconductor photocatalysis. Chem Rev 95:69–96
34. Berger T, Sterrer M, Diwald O et al (2005) Charge trapping and photoadsorption of O_2 on dehydroxylated TiO_2 nanocrystals–an electron paramagnetic resonance study. Chemphyschem 6:2104–2112
35. Gundlach L, Felber S, Willig F et al (2005) Surface electron transfer dynamics in the presence of organic chromophores. Res Chem Intermed 31:39–46
36. Gundlach L, Ernstorfer R, Willig F (2006) Escape dynamics of photoexcited electrons at catechol: TiO_2 (110). Phys Rev B 74:035324
37. Nilius N, Ernst N, Freund H (2001) On energy transfer processes at cluster–oxide interfaces: silver on titania. J Chem Phys Lett 349:351–357
38. Yamada Y, Kanemitsu Y (2010) Blue photoluminescence of highly photoexcited rutile TiO_2: nearly degenerate conduction-band effects. Phys Rev B 82:113103
39. Yamada Y, Kanemitsu Y (2011) Photoluminescence spectrum and dynamics in highly photoexcited rutile TiO_2. Phys Status Solidi C 8:104–107
40. Sporleder D, Wilson DP, White MG (2009) Final state distributions of O_2 photodesorbed from TiO_2 (110). J Phys Chem C 113:13180–13191
41. Diwald O, Thompson TL, Yates JT Jr (2004) The effect of nitrogen ion implantation on the photoactivity of TiO_2 rutile single crystals. J Phys Chem B 108:52–57
42. Turner GM, Beard MC, Schmuttenmaer CA (2002) Carrier localization and cooling in dye-sensitized nanocrystalline titanium dioxide. J Phys Chem B 106:11716–11719
43. Grela MA, Brusa MA, Colussi AJ (1997) Harnessing excess photon energy in photoinduced surface electron transfer between salicylate and illuminated titanium dioxide nanoparticles. J Phys Chem B 101:10986–10989
44. Grela MA, Colussi AJ (1999) Photon energy and photon intermittence effects on the quantum efficiency of photoinduced oxidations in crystalline and metastable TiO_2 colloidal nanoparticles. J Phys Chem B 103:2614–2619
45. Grela MA, Brusa MA, Colussi AJ (1999) Efficiency of hot carrier trapping by outer-sphere redox probes at quantum dot interfaces. J Phys Chem B 103:6400–6402
46. Morishita T, Hibara A, Sawada T, Tsuyumoto I (1999) Ultrafast charge transfer at TiO_2/SCN-(aq) interfaces investigated by femtosecond transient reflecting grating method. J Phys Chem B 103:5984–5987
47. Bahnemann DW, Hilgendorff M, Memming R (1997) Charge carrier dynamics at TiO_2 particles: 090009 reactivity of free and trapped holes. J Phys Chem B 101:4265–4275
48. Yoshihara T, Katoh R, Tachiya M et al (2004) Identification of reactive species in photoexcited nanocrystalline TiO_2 films by wide-wavelength-range (400–2500 nm) transient absorption spectroscopy. J Phys Chem B 108:3817–3823

49. Tamaki Y, Furube A, Murai M et al (2006) Direct observation of reactive trapped holes in TiO_2 undergoing photocatalytic oxidation of adsorbed alcohols: evaluation of the reaction rates and yields. J Am Chem Soc 128:416–417
50. Tamaki Y, Furube A, Tachiya M et al (2007) Dynamics of efficient electron–hole separation in TiO_2 nanoparticles revealed by femtosecond transient absorption spectroscopy under the weak-excitation condition. Phys Chem Chem Phys 9:1453–1460
51. Nakaoka Y, Nosaka Y (1997) ESR investigation into the effects of heat treatment and crystal structure on radicals produced over irradiated TiO_2 powder. J Photochem Photobiol A 110:299–305
52. Jenkins CA, Murphy DM (1999) Thermal and photoreactivity of TiO_2 at the gas-solid interface with aliphatic and aromatic aldehydes. J Phys Chem B 103:1019–1026
53. Kowalski PM, Camellone MF, Nair NN, Meyer B, Marx D (2010) Charge localization dynamics induced by oxygen vacancies on the TiO_2 (110) surface. Phys Rev Lett 105:146405
54. Ganduglia-Pirovano MV, Hofmann A, Sauer J (2007) Oxygen vacancies in transition metal and rare earth oxides: current state of understanding and remaining challenges. Surf Sci Rep 62:219–270
55. Qu ZW, Kroes G-J (2006) Theoretical study of the electronic structure and stability of titanium dioxide clusters $(TiO_2)_n$ with $n = 1–9$. J Phys Chem B 110:8998–9007
56. Miyagi T, Kamei M, Mitsuhashi T et al (2004) Charge separation at the rutile/anatase interface: a dominant factor of photocatalytic activity. Chem Phys Lett 390:399–402
57. Kamei M, Miyagi T, Ishigaki T (2005) Strain-induced charge separation in the photocatalytic single crystalline anatase TiO_2 film. Chem Phys Lett 407:209–212
58. Planelles J, Movilla JL (2006) Trapping electrons in semiconductor air bubbles: a theoretical approach. Phys Rev B 73:235350
59. Deskins NA, Dupuis M (2007) Electron transport via polaron hopping in bulk TiO_2: a density functional theory characterization. Phys Rev B 75(19):195212
60. Agrell HG, Boschloo G, Hagfeldt A (2004) Conductivity studies of nanostructured TiO_2 films permeated with electrolyte. J Phys Chem B 108:12388–12396
61. Mora-Sero I, Bisquert J (2003) Fermi level of surface states in TiO_2 nanoparticles. Nano Lett 3:945–949
62. Barzykin AV, Tachiya M (2002) Mechanism of charge recombination in dye-sensitized nanocrystalline semiconductors: random flight model. J Phys Chem B 106:4356–4363
63. Shkrob IA, Sauer MC Jr (2004) Hole scavenging and photo-stimulated recombination of electron-hole pairs in aqueous TiO_2 nanoparticles. J Phys Chem B 108:12497–12511
64. Beermann N, Boschloo G, Hagfeldt A (2002) Trapping of electrons in nanostructured TiO_2 studied by photocurrent transients. J Photochem Photobiol A 152:213–218
65. van de Lagemaat J, Frank AJ (2001) Nonthermalized electron transport in dye-sensitized nanocrystalline TiO_2 films: transient photocurrent and random-walk modeling studies. J Phys Chem B 105:11194–11205
66. Komaguchi K, Nakano H, Araki A et al (2006) Photoinduced electron transfer from anatase to rutile in partially reduced TiO_2(P-25) nanoparticles: an ESR study. Chem Phys Lett 428:338–342
67. Peiro AM, Colombo C, Doyle G et al (2006) Photochemical reduction of oxygen adsorbed to nanocrystalline TiO_2 films: a transient absorption and oxygen scavenging study of different TiO_2 preparations. J Phys Chem B 110:23255–23263
68. Takahashi H, Watanabe R, Miyauchi Y et al (2011) Discovery of deep and shallow trap states from step structures of rutile TiO_2 vicinal surfaces by second harmonic and sum frequency generation spectroscopy. J Chem Phys 134:154704
69. Kerisit S, Deskins NA, Rosso KM et al (2008) A shell model for atomistic simulation of charge transfer in titania. J Phys Chem C 112:7678–7688
70. Shapovalov V, Stefanovich EV, Truong TN (2002) Nature of the excited states of the rutile TiO_2(110) surface with adsorbed water. Surf Sci 498:L103–L108

71. Yang XJ, Tamai N (2001) How fast is interfacial hole transfer? In situ monitoring of carrier dynamics in anatase TiO_2 nanoparticles by femtosecond laser spectroscopy. Phys Chem Chem Phys 3:3393–3398
72. Tamaki Y, Furube A, Katoh R et al (2006) Trapping dynamics of electrons and holes in a nanocrystalline TiO_2 film revealed by femtosecond visible/near-infrared transient absorption spectroscopy. C R Chim 9:268–274
73. Thompson TL, Yates JT Jr (2005) Monitoring hole trapping in photoexcited TiO_2(110) using a surface photoreaction. J Phys Chem B 109:18230–18236
74. Berger T, Sterrer M, Diwald O et al (2005) Light-induced charge separation in anatase TiO_2 particles. J Phys Chem B 109:6061–6068
75. Tang H, Levy F, Berger H (1995) Urbach tail of anatase TiO_2. Phys Rev B 52:7771
76. Stevanovic A, Buettner M, Zhang Z et al (2012) Photoluminescence of TiO_2: effect of UV light and adsorbed molecules on surface band structure. J Am Chem Soc 134:324
77. Murakami M, Matsumoto Y, Nakajima K et al (2001) Anatase TiO_2 thin films grown on lattice-matched LaAlO3 substrate by laser molecular-beam epitaxy. Appl Phys Lett 78:2664–2666
78. Shi J, Chen J, Feng Z et al (2007) Photoluminescence characteristics of TiO_2 and their relationship to the photoassisted reaction of water/methanol mixture. J Phys Chem C 111:693–699
79. Knorr FJ, Mercado CC, McHale JL (2008) Trap-state distributions and carrier transport in pure and mixed-phase TiO^2: influence of contacting solvent and interphasial electron transfer. J Phys Chem C 112:12786–12794
80. Yamada Y, Kanemitsu Y (2012) Determination of electron and hole lifetimes of rutile and anatase TiO_2 single crystals. Appl Phys Lett 101:133907
81. Dozzi MV, D’Andrea C, Ohtani B et al (2013) Fluorine-doped TiO_2 materials: photocatalytic activity vs time-resolved photoluminescence. J Phys Chem C 117:25586–25595
82. Leytner S, Hupp JT (2000) Evaluation of the energetics of electron trap states at the nanocrystalline titanium dioxide/aqueous solution interface via time-resolved photoacoustic spectroscopy. Chem Phys Lett 330:231–236
83. Kim SH, Stair PC, Weitz E (1999) UV-induced desorption of $CH_3X(X=I$ and Br)/ TiO_2(110). J Chem Phys 108:5080–5088
84. Kim SH, Stair PC, Weitz E (1999) Substrate-mediated photodesorption from multilayers of CH_3I on TiO_2(110) at 90 K. Chem Phys Lett 302:511–516
85. Antoniewicz PR (1980) Model for electron-stimulated and photo-stimulated desorption. Phys Rev B 21:3811–3815
86. Asahi T, Furube A, Masuhara H (1997) Direct measurement of picosecond interfacial electron transfer from photoexcited TiO_2 powder to an adsorbed molecule in the opaque suspension. Chem Phys Lett 275:234–238
87. Martino DM, van Willigen H, Spitler MT (1997) FT-EPR study of photoinduced electron transfer at the surface of TiO_2 nanoparticles. J Phys Chem B 101:8914–8919
88. Colombo DP, Bowman RM (1996) Does interfacial charge transfer compete with charge carrier recombination? A femtosecond diffuse reflectance investigation of TiO_2 nanoparticles. J Phys Chem 100:18445–18449
89. Furube A, Asahi T, Masuhara H et al (2001) Direct observation of interfacial hole transfer from a photoexcited TiO_2 particle to an adsorbed molecule SCN- by femtosecond diffuse reflectance spectroscopy. Res Chem Intermed 27:177–187
90. Rabani J, Yamashita K, Ushida K et al (1998) Fundamental reactions in illuminated titanium dioxide nanocrystallite layers studied by pulsed laser. J Phys Chem B 102:1689–1695
91. Shkrob IA, Sauer MC (2004) Efficient, rapid photooxidation of chemisorbed polyhydroxyl alcohols and carbohydrates by TiO_2 nanoparticles in an aqueous solution. J Phys Chem B 108:12512–12517

92. Wang YH, Hang K, Anderson NA et al (2003) Comparison of electron transfer dynamics in molecule-to-nanoparticle and intramolecular charge transfer complexes. J Phys Chem B 107:9434–9440
93. He JJ, Lindstrom H, Hagfeldt A et al (1999) Dye-sensitized nanostructured p-type nickel oxide film as a photocathode for a solar cell. J Phys Chem B 103:8940–8943
94. Borgstrom M, Blart E, Boschloo G et al (2005) Sensitized hole injection of phosphorus porphyrin into NiO: toward new photovoltaic devices. J Phys Chem B 109:22928–22934
95. Fujishima A, Rao TN, Tryk DA (2000) Titanium dioxide photocatalysis. J Photochem Photobiol C Photochem Rev 1:1–21
96. Fox MA, Dulay MT (1993) Heterogeneous photocatalysis. Chem Rev 93(1):341–357
97. Ni M, Leung MK, Leung HDYC et al (2007) A review and recent developments in photocatalytic water-splitting using TiO_2 for hydrogen production. Renew Sustain Energy Rev 11:401–425
98. Li YF, Aschauer U, Chen J et al (2014) Adsorption and reactions of O_2 on anatase TiO_2. Acc Chem Res 47:3361–3368
99. Henderson MA, Epling WS, Perkins CL et al (1999) Interaction of molecular oxygen with the vacuum-annealed TiO_2(110) surface: molecular and dissociative channels. J Phys Chem B 103:5328–5337
100. Rasmussen MD, Molina LM, Hammer B (2004) Adsorption, diffusion, and dissociation of molecular oxygen at defected TiO_2(110): a density functional theory study. J Chem Phys 120:988–997
101. Du YG, Deskins NA, Zhang ZR et al (2010) Formation of O adatom pairs and charge transfer upon O_2 dissociation on reduced TiO_2(110). Phys Chem Chem Phys 12:6337–6344
102. Di Valentin C, Pacchioni G, Selloni A (2009) Reduced and n-type doped TiO_2: nature of Ti^{3+} species. J Phys Chem C 113:20543–20552
103. Tilocca A, Selloni A (2005) O_2 and vacancy diffusion on rutile(110): pathways and electronic properties. Chem Phys Chem 6:1911–1916
104. Dohnálek Z, Kim J, Bondarchuk O et al (2006) Physisorption of N_2, O_2, and CO on fully oxidized TiO_2(110). J Phys Chem B 110:6229–6235
105. Bikondoa O, Pang CL, Ithnin R et al (2006) Direct visualization of defect-mediated dissociation of water on TiO_2(110). Nat Mater 5:189–192
106. Wendt S, Sprunger PT, Lira E et al (2008) The role of interstitial sites in the Ti 3d defect state in the band gap of titania. Science 320:1755–1759
107. Petrik NG, Zhang ZR, Du YG et al (2009) Chemical reactivity of reduced TiO_2(110): the dominant role of surface defects in oxygen chemisorption. J Phys Chem C 113:12407–12411
108. Lira E, Hansen JO, Huo P, Bechstein R et al (2010) Dissociative and molecular oxygen chemisorption channels on reduced rutile TiO_2(110): an STM and TPD study. Surf Sci 604:1945–1960
109. Papageorgiou AC, Beglitis NS, Pang CL et al (2010) Electron traps and their effect on the surface chemistry of TiO_2 (110). Proc Natl Acad Sci U S A 107:2391–2396
110. Kimmel GA, Petrik NG (2008) Tetraoxygen on reduced TiO_2(110): oxygen adsorption and reactions with bridging oxygen vacancies. Phys Rev Lett 100:3937–3940
111. Scheiber P, Riss A, Schmid M et al (2010) Observation and destruction of an elusive adsorbate with STM: O_2/TiO_2(110). Phys Rev Lett 105:5332–5337
112. Wang ZT, Du YG, Dohnalek Z et al (2010) Direct observation of site-specific molecular chemisorption of O_2 on TiO_2(110). J Phys Chem Lett 1:3524–3529
113. Tan S, Ji Y, Zhao Y et al (2011) Molecular oxygen adsorption behaviors on the rutile TiO_2(110)-1 x 1 surface: an in situ study with low-temperature scanning tunneling microscopy. J Am Chem Soc 133:2002–2009
114. Pillay D, Wang Y, Hwang GS (2006) Prediction of tetraoxygen formation on rutile TiO_2(110). J Am Chem Soc 128:14000–14001
115. Opel W, Rocker G, Feierabend R (1983) Intrinsic defects of TiO_2(110)-interaction with chemisorbed O_2, H_2, CO, and CO_2. Phys Rev B 28:3427–3438

116. de Lara-Castells MP, Krause JL (2002) Theoretical study of the interaction of molecular oxygen with a reduced TiO_2 surface. Chem Phys Lett 354:483–490
117. Henrich VE, Dresselhaus G, Zeiger HJ (1978) Chemisorbed phase of O_2 on TiO_2 and $SrTiO_3$. J Vac Sci Technol 15:534–537
118. Wang Y, Pillay D, Hwang GS (2004) Dynamics of oxygen species on reduced TiO_2(110) rutile. Phys Rev B 70:3352–3359
119. Henderson MA, Shen M, Wang ZT et al (2013) Characterization of the active surface species responsible for UV-induced desorption of O_2 from the rutile TiO_2(110) surface. J Phys Chem C 117:5774–5784
120. Wu XY, Selloni A, Lazzeri M et al (2003) Oxygen vacancy mediated adsorption and reactions of molecular oxygen on the TiO_2(110) surface. Phys Rev B 68:241402
121. Filippone F, Mattioli G, Bonapasta AA (2007) Reaction intermediates and pathways in the photoreduction of oxygen molecules at the (101) TiO_2 (anatase) surface. Catal Today 129:169–176
122. Aschauer U, Chen J, Selloni A (2010) Peroxide and superoxide states of adsorbed O_2 on anatase TiO_2 (101) with subsurface defects. Phys Chem Chem Phys 12:12956–12960
123. Zeng W, Liu TM, Wang ZC, Tsukimoto S et al (2010) Oxygen adsorption on anatase TiO_2 (101) and (001) surfaces from first principles. Mater Trans 51:171–175
124. Li YF, Selloni A (2013) Theoretical study of interfacial electron transfer from reduced anatase TiO_2(101) to adsorbed O_2. J Am Chem Soc 135:9195–9199
125. Setvín M, Aschauer U, Scheiber P et al (2013) Reaction of O_2 with subsurface oxygen vacancies on TiO_2 anatase (101). Science 341:988–991
126. Liu LL, Liu Q, Zheng YP et al (2014) O_2 adsorption and dissociation on a hydrogenated anatase (101) aurface. J Phys Chem C 118:3471–3482
127. Setvin M, Daniel B, Aschauer U et al (2014) Identification of adsorbed molecules via STM tip manipulation: CO, H_2O, and O_2 on TiO_2 anatase (101). Phys Chem Chem Phys 16:21524–21530
128. Zeng W, Liu T, Li T et al (2015) First principles study of oxygen adsorption on the anatase TiO_2 (101) surface. Physica E 67:59–64
129. He YB, Dulub O, Cheng HZ et al (2009) Evidence for the Predominance of Subsurface Defects on Reduced Anatase TiO_2 (101). Phys Rev Lett 102:106105
130. Wang Y, Sun H, Tan S et al (2013) Role of point defects on the reactivity of reconstructed anatase titanium dioxide (001) surface. Nat Commun 4:375–381
131. Lu G, Linsebigler A, Yates JT (1995) The photochemical identification of 2 chemisorption states for molecular oxygen on TiO_2(110). J Chem Phys 102:3005–3008
132. Lu GQ, Linsebigler A, Yates JT (1995) The adsorption and photodesorption of oxygen on the TiO_2(110) surface. J Chem Phys 102:4657–4662
133. Rusu CN, Yates JT (1997) Defect sites on TiO_2(110). Detection by O_2 photodesorption. Langmuir 13:4311–4316
134. Perkins CL, Henderson MA (2001) Photodesorption and trapping of molecular oxygen at the TiO_2(110)-water ice interface. J Phys Chem B 105:3856–3863
135. Thompson TL, Yates JT (2006) Control of a surface photochemical process by fractal electron transport across the surface: O_2 photodesorption from TiO_2(110). J Phys Chem B 110:7431–7435
136. Petrik NG, Kimmel GA (2010) Photoinduced dissociation of O_2 on rutile TiO_2(110). J Phys Chem Lett 1:1758–1762
137. Petrik NG, Kimmel GA (2011) Oxygen photochemistry on TiO_2(110): recyclable, photoactive oxygen produced by annealing adsorbed O_2. J Phys Chem Lett 2:2790–2796
138. Petrik NG, Kimmel GA (2011) Electron- and hole-mediated reactions in UV-irradiated O_2 adsorbed on reduced rutile TiO_2(110). J Phys Chem C 115:152–164
139. Wang ZT, Aaron Deskins N, Lyubinetsky I (2012) Direct imaging of site-specific photocatalytical reactions of O_2 on TiO_2(110). J Phys Chem Lett 3:102–106

140. Petrik NG, Kimmel GA (2014) Probing the photochemistry of chemisorbed oxygen on TiO_2(110) with Kr and other coadsorbates. Phys Chem Chem Phys 16:2338–2346
141. Thompson TL, Yates JT (2006) Surface science studies of the photoactivation of TiO_2-new photochemical processes. Chem Rev 106:4428–4453
142. Yates JT Jr (2009) Photochemistry on TiO_2: mechanisms behind the surface chemistry. Surf Sci 603:1605–1612
143. Thompson TL, Yates JT (2005) TiO_2-based photocatalysis: surface defects, oxygen and charge transfer. Top Catal 35:197–210
144. Epling WS, Peden CHF, Henderson MA et al (1998) Evidence for oxygen adatoms on TiO_2(110) resulting from O_2 dissociation at vacancy sites. Surf Sci 413:333–343
145. Henderson MA, Otero-Tapia S, Castro ME (1999) The chemistry of methanol on the TiO_2(110) surface: the influence of vacancies and coadsorbed species. Faraday Discuss 114:313–329
146. Henderson MA, Otero-Tapia S, Castro ME (1998) Electron-induced decomposition of methanol on the vacuum-annealed surface of TiO_2(110). Surf Sci 412/413:252–272
147. Shen MM, Henderson MA (2012) Role of water in methanol photochemistry on rutile TiO_2(110). J Phys Chem C 116:18788–18795
148. Onda K, Li B, Zhao J et al (2005a) The electronic structure of methanol covered TiO_2(110) surfaces. Surf Sci 593:32–37
149. Li B, Zhao J, Onda K et al (2006) Ultrafast interfacial proton-coupled electron transfer. Science 311:1436–1440
150. Onda K, Li B, Zhao J et al (2005b) Wet electrons at the H_2O/TiO_2(110) surface. Science 308:1154–1158
151. Zhang ZR, Bondarchuk O, White JM (2006) Imaging adsorbate O−H bond cleavage: methanol on TiO_2(110). J Am Chem Soc 128:4198–4199
152. Bates SP, Gillan MJ, Kresse G (1998) Adsorption of methanol on TiO_2(110): a first-principles investigation. J Phys Chem B 102:2017–2026
153. de Armas RS, Oviedo J, San Miguel MA et al (2007) Methanol adsorption and dissociation on TiO_2(110) from first principles calculations. J Phys Chem C 111:10023–10028
154. Zhao J, Yang JL, Petek H (2009) Theoretical study of the molecular and electronic structure of methanol on a TiO_2(110) surface. Phys Rev B 80:235416
155. Zhou C, Ren ZF, Tan SJ et al (2010) Site-specific photocatalytic splitting of methanol on TiO_2(110). Chem Sci 1:575–580
156. Kawai T, Sakata T (1980) Photocatalytic hydrogen production from liquid methanol and water. J Chem Soc Chem Comm 15:694–695
157. Palmisano G, Augugliaro V, Pagliaro M et al (2007) Photocatalysis: a promising route for 21st century organic chemistry. Chem Commun 33:3425–3437
158. Muggli DS, Odland MJ, Schmidt LR (2001) Effect of trichloroethylene on the photocatalytic oxidation of methanol on TiO_2. J Catal 203:51–63
159. Chen X, Chen S, Guo L et al (2010) Semiconductor-based photocatalytic hydrogen generation. Chem Rev 110:6503–6570
160. Li Z, Smith RS, Kay BD et al (2011) Determination of absolute coverages for small aliphatic alcohols on TiO_2(110). J Phys Chem C 115:22534–22539
161. Shen MM, Acharya DP, Dohnálek Z et al (2012) Importance of diffusion in methanol photochemistry on TiO_2(110). J Phys Chem C 116:25465–25469
162. Zhou C, Ma Z, Ren Z (2012) Surface photochemistry probed by two-photon photoemission spectroscopy. Energy Environ Sci 5:6833–6844
163. Cui XF, Wang Z, Tan SJ (2009) Identifying hydroxyls on the $TiO_2(110)-1 \times 1$ surface with scanning tunneling microscopy. J Phys Chem C 113:13204–13208
164. Klymko PW, Kopelman R (1983) Fractal reaction kinetics: exciton fusion on clusters. J Phys Chem 87:4565–4567
165. Kopelman R (1988) Fractal reaction kinetics. Science 241:1620–1626

166. Zhou C, Ma Z, Ren Z et al (2011) Effect of defects on photocatalytic dissociation of methanol on TiO_2(110). Chem Sci 2:1980–1983
167. Haubrich J, Kaxiras E, Friend CM (2011) The role of surface and subsurface point defects for chemical model studies on TiO_2: a firstprinciples theoretical study of formaldehyde bonding on rutile TiO_2(110). Chem Eur J 17:4496–4506
168. Zuo F, Wang L, Wu T (2010) Self-doped Ti^{3+} enhanced photocatalyst for hydrogen production under visible light. J Am Chem Soc 132:11856–11857
169. Shen MM, Henderson MA (2011a) Identification of the active species in photochemical hole scavenging reactions of methanol on TiO_2. J Phys Chem Lett 2:2707–2710
170. Shen MM, Henderson MA (2011b) Impact of solvent on photocatalytic mechanisms: reactions of photodesorption products with ice overlayers on the TiO_2(110) surface. J Phys Chem C 115:5886–5893
171. Guo Q, Xu C, Ren Z et al (2012) Stepwise photocatalytic dissociation of methanol and water on TiO_2(110). J Am Chem Soc 134:13366–13373
172. Lane CD, Petrik NG, Orlando TM et al (2007) Electron-stimulated oxidation of thin water films adsorbed on TiO_2(110). J Phys Chem C 111:16319–16329
173. Lang X, Wen B, Zhou C et al (2014) First-principles study of methanol oxidation into methyl formate on rutile TiO_2(110). J Phys Chem C 118:19859–19868
174. Petrik NG, Kimmel GA (2009) Nonthermal water splitting on rutile TiO_2: electron-stimulated production of H_2 and O_2 in amorphous solid water films on TiO_2(110). J Phys Chem C 113:4451–4460
175. Mao X, Wei D, Wang Z et al (2015a) Recombination of formaldehyde and hydrogen atoms on TiO_2(110). J Phys Chem C 119:1170–1174
176. Mao X, Lang X, Wang Z et al (2013) Band-gap states of TiO_2(110): major contribution from surface defects. J Phys Chem Lett 4:3839–3844
177. Guo Q, Xu C, Yang W et al (2013) Methyl formate production on TiO_2(110), initiated by methanol photocatalysis at 400 nm. J Phys Chem C 117:5293–5300
178. Phillips KR, Jensen SC, Baron M et al (2013) Sequential photo-oxidation of methanol to methyl formate on TiO_2(110). J Am Chem Soc 135:574–577
179. Yuan Q, Wu Z, Jin Y et al (2013) Photocatalytic cross-coupling of methanol and formaldehyde on a rutile TiO_2(110) surface. J Am Chem Soc 135:5212–5219
180. Domokos L, Katona T, Molnar A (1996) Dehydrogenation of methanol to methyl formate: deuterium labeling studies. Catal Lett 40:215–221
181. Liu JL, Zhan ES, Cai WJ et al (2008) Methanol selective oxidation to methyl formate over ReO_x/CeO_2 catalysts. Catal Lett 120:274–280
182. Minyukova TP, Simentsova II, Khasin AV et al (2002) Dehydrogenation of methanol over copper-containing catalysts. Appl Catal A Gen 237:171–180
183. Mao X, Wang Z, Lang X et al (2015b) Effect of surface structure on the photoreactivity of TiO_2. J Phys Chem C 119:6121–6127
184. Ohno T, Sarukawa K, Matsumura M (2002) Crystal faces of rutile and anatase TiO_2 particles and their roles in photocatalytic reactions. New J Chem 26:1167–1170
185. Tao JG, Batzill M (2010) Role of surface structure on the charge trapping in TiO_2 photocatalysts. J Phys Chem Lett 1:3200–3206
186. Xu C, Yang W, Guo Q et al (2013a) Molecular hydrogen formation from photocatalysis of methanol on TiO_2(110). J Am Chem Soc 135:10206–10209
187. Xu C, Yang W, Ren Z et al (2013b) Strong photon energy dependence of the photocatalytic dissociation rate of methanol on TiO_2(110). J Am Chem Soc 135:19039–19045
188. Kavan L, Gratzel M, Gilbert SE et al (1996) Electrochemical and photoelectrochemical investigation of single-crystal anatase. J Am Chem Soc 118:6716–6723
189. Herman GS, Dohnalek Z, Ruzycki N et al (2003) Experimental investigation of the interaction of water and methanol with anatase$-TiO_2$(101). J Phys Chem B 107:2788–2795
190. Xu C, Yang W, Guo Q et al (2014) Molecular hydrogen formation from photocatalysis of methanol on anatase-TiO_2(101). J Am Chem Soc 136:602–605

191. Tilocca A, Selloni A (2004) Methanol adsorption and reactivity on clean and hydroxylated snatase(101) surfaces. J Phys Chem B 108:19314–19319
192. Guo Q, Minton TK, Yang X (2015) Elementary processes in photocatalysis of methanol and water on rutile TiO_2(110): a new picture of photocatalysis. Chin J Catal. doi:10.1016/S1872-2067(15)60935-4